Comptes Rendus
de l'Académie des sciences

Chimie

Volume 27, Special Issue S2, 2024

Special issue / *Numéro spécial*

Women Chemists in France in 2024 / *Femmes chimistes en France en 2024*

Guest editor / *Rédactrice en chef invitée*

Janine Cossy

ACADÉMIE DES SCIENCES
INSTITUT DE FRANCE

Académie des sciences — Paris

ISSN: 1878-1543 (electronic)

CENTRE MERSENNE

Comptes Rendus

Chimie

Objective of the journal

Comptes Rendus Chimie is a peer-reviewed electronic journal of international standing, covering all areas of the discipline. It publishes mainly special issues, but also original research articles, preliminary announcements, review articles, historical perspectives, pedagogical texts or conference proceedings, without length limit, in English or in French. Comptes Rendus Chimie is published according to a virtuous policy of diamond open access, free for authors (no publication fees) as well as for readers (immediate and permanent open access).

About the journal

All journal's information, including the text of published articles, which is fully open access, is available from the journal website at https://comptes-rendus.academie-sciences.fr/chimie/.

Author enquiries

For enquiries relating to the submission of articles, please visit this journal's homepage at https://comptes-rendus.academie-sciences.fr/chimie/.

Contact

Académie des sciences
23, quai de Conti, 75006 Paris, France
CR-Chimie@academie-sciences.fr

Comptes Rendus
Chimie
2024, 27, nº S2

Contents / *Sommaire*

Guest Editor 1-1

Janine Cossy
A Collection of Articles Highlighting Women Chemists in France in 2024 3-3

Odile Eisenstein
Nucleophilic addition to carbonyl groups from qualitative to quantitative computational studies. A historical perspective 5-19

Sabine Choppin, Joanna Wencel-Delord, Françoise Colobert
Control of atropoisomerism: an access to valuable compounds 21-32

Lucas Bacheley, Gérard Guillamot, Phannarath Phansavath, Virginie Ratovelomanana-Vidal
Direct ring fluorination of 3-substituted 5-(1,3-dioxane) acetal isoxazoles: application to the formal synthesis of a bioactive fluorinated isoxazole 33-38

Anne-Marie Caminade, Valérie Maraval
Selected properties of phosphorus dendrimers: green approaches to catalysis 39-55

Léa Ibos, Emmanuelle Schulz
Non-covalent interactions in supported asymmetric catalysis: a brief account 57-83

Arthur Lasbleiz, Franck Pelissier, Jean-Hugues Renault, Claire M. Grison, Yves-Marie Legrand, Claude Grison
A new generation of ecocatalysts®—from Invasive Alien Species to sustainable and biosourced glyceryl fatty esters 85-97

Juliette Martin
The need for Open Labs for fostering interdisciplinarities in Modern Chemistry. Biocatalysis: a necessary tool for synthetic chemists 99-115

Clotilde Policar, Nicolas Delsuc, Hélène Charlotte Bertrand
Metal complexes in cells: from design of catalytic antioxidants to imaging metal ions and designing metal-based probes in X-ray fluorescence and IR-imaging, a multidisciplinary collaborative journey in bioinorganic chemistry and inorganic chemical biology 117-141

Alexandra Fillion, Sophie Vichier-Guerre, Paola Barbara Arimondo
Adenine, a key player in biology and medicinal chemistry 143-160

Daouda Ndiaye, Éva Tóth
Stable and inert manganese complexes for magnetic resonance imaging 161-177

Jonathan Daniel, Ophélie Dal Pra, Eleonore Kurek, Chloé Grazon, Mireille Blanchard-Desce
Dye-based fluorescent organic nanoparticles made from polar and polarizable chromophores for bioimaging purposes: a bottom-up approach 179-195

Stéphanie Swiha, Valérie Pichon, Thierry Fournier, Sophie Gil, Nathalie Delaunay
Development of an analytical method for the simultaneous determination of 22 Polycyclic Aromatic Hydrocarbons (PAHs) in maternal and umbilical cord blood 197-212

ACADÉMIE DES SCIENCES
INSTITUT DE FRANCE

Comptes Rendus. Chimie
2024, Vol. 27, Special issue S2, p. 1
https://doi.org/10.5802/crchim.312

Women Chemists in France in 2024

Guest Editor

Janine Cossy

Janine Cossy studied at the Université Champagne-Ardenne in Reims, where she completed her PhD in photochemistry under the supervision of Professor Jean-Pierre Pète. After a two-year post-doctoral stay with Professor Barry M. Trost, at the University of Wisconsin (USA), she returned to Reims where, in 1990, she became Director of Research at the CNRS. The same year, she was appointed Professor of Organic Chemistry at the ESPCI Paris. Janine Cossy's research focuses on the synthesis of natural products and biologically active molecules (mainly with anti-tumor and anti-inflammatory properties) and on the development of selective synthetic methods in a variety of fields (photochemistry, radical chemistry, rearrangements, organometallic couplings, enzymatic reactions, etc.). Currently, her work is focused on green chemistry, where she is developing catalytic synthetic methods using low-pollution reagents.

Her research work has resulted in over 560 publications and 18 patents. She was elected to the Académie des Sciences in 2017 and to the Académie nationale de pharmacie in 2022. She was President of the Organic Chemistry Division of the SFC (now SCF), a member of the Organic and Biomolecular Chemistry Division at IUPAC. She was associate editor of *Organic Letters* (ACS) and she is currently associate editor of *Tetrahedron* and associate editor of the *Chimie* edition of the *Comptes rendus de l'Académie des sciences* (a.k.a. *Comptes Rendus. Chimie*). She is the co-founder of two companies, CDP-Innovation and Acanthe Biotech.

ACADÉMIE DES SCIENCES
INSTITUT DE FRANCE

Comptes Rendus. Chimie
2024, Vol. 27, Special issue S2, p. 3
https://doi.org/10.5802/crchim.302

Foreword

Women Chemists in France in 2024

A Collection of Articles Highlighting Women Chemists in France in 2024

Janine Cossy

Women in science are achieving groundbreaking research across the world. But despite their involvement, their dedication to research, and their discoveries, women still represent only around 33% of researchers, and less than 4% of Nobel Prizes for science have been awarded to women. In addition, only 11% of senior research roles are held by women in Europe. Their work rarely gains the recognition it deserves.

However, different institutions and organizations are fighting to encourage women to take a scientific career, to recognize their merits in sciences (IUPAC, L'Oreal, UNESCO, UN etc.) and to advocate the cause of women in science. We can cite Audrey Azoulay, General Director of the United Nations Educational Scientific and Cultural Organization, who said "by advancing the cause of women, we can drive progress in science".

If, in 2024, we still have special prizes to help empower more women scientists and to recognize women's scientific excellence, this means that we still have a lot of work to do to reach gender equality and to encourage young girls to pursue a scientific career. Women scientists still need to fight to be judged purely on the merit of their discoveries and the potential of their work to change the world.

In this context, the editorial board of the *Compte Rendus Chimie* of the Academy of Sciences has decided to have a special issue to highlight the scientific achievements of women chemists in France in different areas of chemistry and to encourage younger generations to pursue careers in chemistry. This issue brings together 12 outstanding contributions in different fields of chemistry.

In 2025, a second issue is planned and we do hope that the Compte Rendus of the Academy of Sciences will act as spokespersons for women scientists in France in various fields.

For this 2024 special issue, I would like to thank P. Braunstein for enthusiastically accepting my proposals, Justine Fabre and Julien Desmarets for all their help and advice in producing this special issue. Thanks also to all the authors and co-authors for their willingness to take part in the adventure. I hope that this special issue will be a source of inspiration for readers and that it will lead to new collaborations.

Janine Cossy
ESPCI Paris
PSL University
France
janine.cossy@espci.fr

ACADÉMIE DES SCIENCES
INSTITUT DE FRANCE

Comptes Rendus. Chimie
2024, Vol. 27, Special issue S2, p. 5-19
https://doi.org/10.5802/crchim.298

Research article

Women Chemists in France in 2024

Nucleophilic addition to carbonyl groups from qualitative to quantitative computational studies. A historical perspective

Odile Eisenstein [a, b]

[a] ICGM Université de Montpellier, CNRS, ENSCM, Montpellier, France

[b] Department of Chemistry and Hylleraas Center for Quantum Molecular Science 0315 University of Oslo, Norway

E-mail: odile.eisenstein@umontpellier.fr

Abstract. Nucleophilic addition to carbonyl groups is one of the most important reactions in organic synthesis. In the case of a prochiral carbonyl group, the preference for the addition of a nucleophile to one face of the π system leads to unequal amounts of the two possible diastereoisomers. The mechanism of this reaction for various nucleophiles (especially the early main group hydride and the Grignard reagents) and the various noncyclic and cyclic aldehydes or ketones has fascinated computational chemists for nearly 40 years. This article describes the research that has been done on this topic, the incentive for the present author being that she started her research with this topic and is returning to it in recent years.

Keywords. Reaction mechanism, Stereochemistry, Nucleophile, Carbonyl, Computational chemistry, Analysis of intramolecular interactions.

Funding. French National Center for scientific Research (CNRS), Center of Excellence Hylleraas Center for Quantum Molecular Science (Grant 262695), Pioneer Research Grant MetalSynergy (Grant 314009), Norwegian Supercomputing Program (NOTUR) (Grant NN 4654K).

Manuscript received 27 January 2024, revised 1 February 2024 and 7 February 2024, accepted 7 February 2024.

1. Introduction

Nucleophilic addition to unsaturated organic molecules is an essential reaction for the formation of new bonds and, in particular new carbon–carbon bonds. It has been a key reaction in organic synthesis since Victor Grignard discovered the so-called Grignard reagent in 1900. This groundbreaking achievement, published in a concise two-page single-author communication in the 'Comptes-Rendus de l'Académie des sciences' [1] earned Grignard the Nobel Prize in 1912. The citation reads "for his discovery that has greatly advanced the progress of organic chemistry". The prize was shared with Paul Sabatier for the discovery of the hydrogenation reaction in presence of metal [2]. The discovery of the Grignard reaction is described in detail together with the author's life in a review article by Bram et al. published in 1997 [3].

Subsequently, numerous methods of forming new bonds have been discovered and studied using both experimental and various theoretical methods. This short review aims to outline a subset of this extensive body of research. Specifically, it focuses on describing the theoretical studies related to the reaction mechanism of nucleophilic addition

to carbonyl groups and to the understanding of its stereoselectivity, a very important aspect of this reaction. Given the importance of the topic, considerable work was done. Therefore, this review gives the opportunity to illustrate the evolution of computational methods applied to reaction mechanism in organic chemistry. It is remarkable that the earlier studies using very simple computational methods and models were able to capture the essence of this reaction. Recently, computations with elaborated methods have provided information that could not be obtained from experiments. Moreover, this reaction is of particular interest to the author as it was the subject of her early research and she has returned to it in the most recent years. A fuller description of this author's scientific work, with a different focus than this article, can be found in a Perspective article [4].

2. Directionality of the nucleophilic addition from crystal structures and early calculations

2.1. *Bürgi–Dunitz reaction path and Felkin–Anh rule*

In the mid-1970s, Hans-Beat Bürgi and Jack Dunitz proposed to use a structure correlation method, extracted from the Cambridge data base, to obtain information about the molecular potential energy hypersurface which is itself informative about chemical reaction dynamics [5]. The basic assumption is that the observed structures tend to concentrate on the low-lying regions of the potential energy surface. This also implies that the crystalline environment has little influence on the molecular structure. By collecting a series of related species and by looking for correlations between the relevant structural parameters, Bürgi and Dunitz established the pathways for several reactions, namely the nucleophilic substitution, the nucleophilic addition to an aldehyde or a ketone, and the Berry rotation on phosphorus. The same method was later used by Crabtree et al. to propose the pathway for C–H bond activation by an unsaturated metal complex [6]. This input, derived from crystal structures, is very useful although it was only applied to few reactions.

The nucleophilic addition of an amine to a carbonyl group was studied by looking at the relative arrangement of the amino and carbonyl groups in the crystal structures of 14 molecules and by showing the correlation between the N(amino)···C(carbonyl) distance and the N···C=O angle (Figure 1) [7].

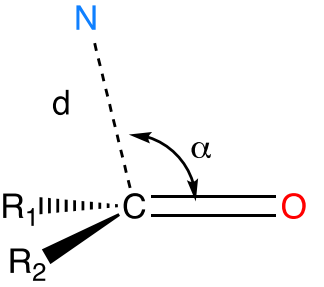

Figure 1. Structural variables used by Bürgi and Dunitz to define the reaction path of the nucleophilic addition to a carbonyl group [5,7].

This study suggested that the amino group approaches the carbonyl group from the back of the molecule ($\alpha > 90°$). This trajectory was later confirmed by ab initio calculations performed by Lehn and Wipff et al. [8,9]. The theoretical model was incredibly simple. The nucleophile was an isolated hydride and the substrate was formaldehyde, with all species in the gas phase. Optimization of the whole system using the Hartree–Fock method and a small basis set (the state of the art at the time) for different distances between the hydride and the carbon mirrored the path established by the crystal structures.

This first computational study identified the most important feature of the nucleophilic addition to a carbonyl group, namely that the nucleophile does not add perpendicularly to the C=O bond. This feature was important because it provided information about the short contacts that could occur during the addition. Indeed, this pathway contributed to a more robust interpretation of 1,2-asymmetric induction. The preferred face for the addition of a nucleophile to an aldehyde or a ketone, bearing an α chiral carbon (with small S, medium M and large L or polar X substituents), has been a topic of great interest for organic synthesis. Several empirical rules, proposed by Cram, Cornforth, Karabatsos and Felkin, have been used to rationalize the formation of the major diastereoisomer. In these models, the nucleophile preferentially attacked the less hindered face of the carbonyl with a given conformation of the chiral carbon. The problem was that each author had chosen

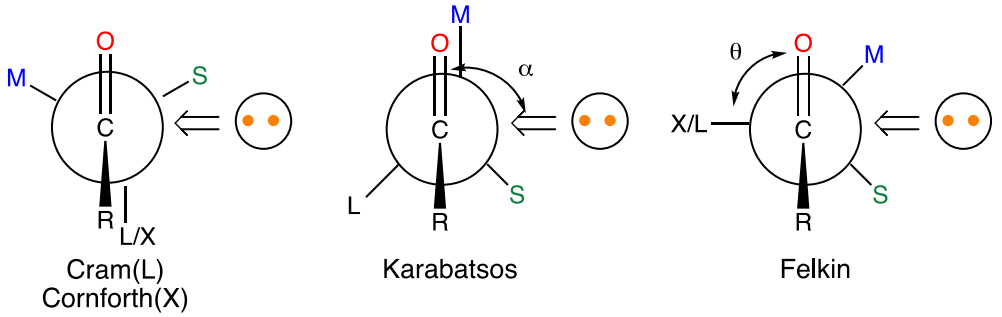

Figure 2. Cram–Cornforth, Karabatsos and Felkin models for the nucleophilic addition to an α substituted carbonyl compound. Only the approach leading to the major diastereoisomer is shown. The nucleophile is represented by a circle with 2 orange dots. The α angle is shown to be equal to 90° as assumed in the original models. In the calculations R = H, X = Cl, L = CH_2CH_3, M = CH_3, S = H, the nucleophile is H^-, θ was rotated by 30° steps and α was optimized for each θ value (average value around 105°).

a different conformation resulting in different rules (Figure 2). The purpose of the computational study was to establish which conformation determines the diastereoisomeric preference.

The substrates chosen were $Cl(CH_3)HC–CH=O$ and $(CH_3CH_2)(CH_3)HC–CH=O$ to mimic systems with polar (Cl) or large (CH_2CH_3), small (H), medium (CH_3) and small (H) groups [10]. A naked hydride was positioned at 1.5 Å from the carbon with an optimized H···C=O α angle (average value around 105°). The Hartree–Fock/STO-3G energies were calculated as a function of the conformation of the chiral carbon described by the θ dihedral angle, X–C–C–O, (X = Cl or CH_3CH_2) (Figure 2) without further geometry optimization. There was a clear preference for the Felkin model, especially when the α angle was greater than 90°. Thus, the nucleophile prefers to add antiperiplanar to the substituent that is either polar (Cl) or the largest (CH_3CH_2) on the face containing the smallest substituent (H).

This conformational preference is rationalized by being associated with the largest interactions between the highest occupied orbital (HOMO) of the nucleophile (the doubly occupied 1s orbital of the hydride) and the lowest unoccupied molecular orbital LUMO π^*_{CO} of the carbonyl group (Figure 3). The stabilizing interaction between these two frontier orbitals increases as the energy gap between them decreases and the overlap increases. Thus, lowering the energy of π^*_{CO} and increasing the overlap between H^- and π^*_{CO} is favorable. Interestingly, the energy of the π^*_{CO} orbital depends on the conformation of the chiral carbon especially in the case of a polar X group or an atom such as Cl. In fact, the polar C–Cl bond is associated with a low-lying unoccupied $\sigma^*_{C–Cl}$ orbital. When this orbital is parallel to the π^*_{CO} orbital (θ = 90° or 270°), the two orbitals overlap and form a low-lying in-phase combination of π^*_{CO} and $\sigma^*_{C–X}$ (Figure 3). This interaction between the π and σ orbitals is known as hyperconjugation. The best overlap between the hydride and π^*_{CO} is obtained for an obtuse α angle to reduce the overlap of the hydride with the oxygen. Some direct overlap of the hydride with $\sigma^*_{C–X}$ could also contribute. This obtuse α angle brings the hydride in close proximity to either the S or M group, with a natural preference for the former. This explains why the nucleophile enters antiperiplanar to the X group and on the side containing the smallest group, as suggested by Felkin.

It should be emphasized that the Felkin rule was associated with the best conformation for the nucleophile addition and not with the most stable conformation of the isolated substrate. However, the transition state was not really determined but assumed by following the Bürgi–Dunitz studies. This approach was acceptable until methodological advances made it possible to locate a transition state on a potential energy surface. Naturally, the first studies that included a transition state determination used highly simplified models of the reacting partners. Remarkably, these simplified models were useful and encouraged further studies with better representation of the chemical systems and higher levels of computation.

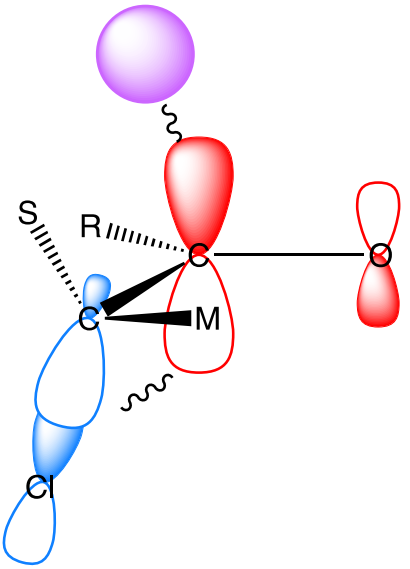

Figure 3. The H^- occupied orbital (purple) stabilized by the substrate LUMO in the Felkin conformation. The substrate LUMO is the in-phase combination of π^*_{CO} (red) and σ^*_{C-Cl} (blue). The main in-phase interactions are indicated by wiggly lines. See ref [10] for further details.

2.2. *The Felkin–Anh and the Cieplak model, the two visions of the antiperiplanarity rule*

Interpreting the results in a language that chemists could understand was considered as important by many computational chemists. Explaining the stereoselectivity of the nucleophilic addition to cyclic ketones was particularly challenging. One of the first reviews that attempted to discuss the stereoselectivity of the nucleophilic addition to acyclic and cyclic carbonyls was published by Nguyen Trong Anh, the author's PhD supervisor [11]. The Felkin–Anh model was not easy to apply. Therefore, an alternative interpretation of the stereoselectivity was presented by Cieplak [12–14]. This author presented an interpretation in which the bond antiperiplanar to the incoming nucleophile acts as a donor towards the incipient σ^*_{C-Nu} empty orbital that is formed when the nucleophile interacts with the carbon of the carbonyl group. The preferred stereoselectivity would be associated with the stronger donor *trans* to the incoming nucleophile. This was a rather heterodox proposal as it was pointed out by Frenking et al. [15] and by Tomoda [16]. It does not follow the rules of orbital interactions, as established by the frontier orbital theory derived from quantum chemistry [17]. It is also unclear how the C–Nu bond would be formed by the delocalization of electrons into its σ^*_{C-Nu} orbital. Although the Cieplak rule has been shown to account for the observed stereoselectivity in some cases [18–21], it will not appear any longer in the most recent studies because it contradicts basic principles of quantum chemistry. In contrast, the Felkin–Anh rule, which obeys the frontier orbitals theory, gives a qualitative interpretation of how the electron density of the nucleophile is best transferred to the carbonyl substrate and thus contributes to the formation of the incipient bond. It has been used extensively and is still a subject of debate, as illustrated by selected recent literature [22–26]. A publication, in the 2023 issue of Helvetica Chimica Acta, dedicated to the memory of J. D. Dunitz, used the crystallographic method of Bürgi and Dunitz to rationalize the diastereoselectivity in a *peri*-naphthalene derivative [27]. However, these antiperiplanarity rules were not sufficient to explain the stereoselectivity of the nucleophilic addition to carbonyl groups and the numerous studies described in the following sections, show the other effects that need to be considered.

2.3. *The case of the 1,3-asymmetric induction*

The stereoselectivity of 1,3-asymmetric induction was considered in the case of β-ketoester with $NaBH_4$. The hypothesis in this work was that the transition state is reactant like in non-chelating conditions. Consequently, the preferred conformations of the substrates were considered to determine the selectivity. This proposal gave results in good agreement with experimental data. This is a rare case where the nucleophile was not included in the study [28].

2.4. *Energetic aspects of the nucleophilic addition to carbonyl*

Ion cyclotron resonance studies and Hartree–Fock calculations for the reaction of alkoxy anions with B_2H_6 provided information on the thermochemical factors that are determining in these reaction pathways [29]. Later, the affinity of the carbonyl groups

for anions was calculated with the MP2 method (currently used in the 1990s for organic species) for hydride to XYC=O (X, Y = H, CH_3, NH_2, OH, and F) and selected additional electrophilic compounds (α,β-unsaturated carbonyl, cycloalkanone, heterocarbonyl molecular compounds) with data in good agreement with available experimental data [30]. This study was extended with the calculation of the affinity of various anions Z^- (Z = H, CH_3, NH_2, OH, F, $CH{=}CH_2$, CH=O, C≡CH, C≡N) for a large variety of carbonyl systems [31].

The interpretation of the obtuse α angle for the nucleophilic addition to a carbonyl, currently called the Bürgi–Dunitz angle, has recently been reconsidered and quantified using energy decomposition analysis (EDA) [32] and the activation strain model [33] in the case of the addition of CN^- to $(CH_3)_2C{=}O$. With the EDA analysis, Bickelhaupt et al. showed that the obtuse bond angle results from the combination of three effects: the Pauli repulsion between the HOMO of the nucleophile and the occupied π orbitals of the substrate, the stabilizing interaction between the HOMO of the nucleophile and the LUMO, π^*_{CO}, of the substrate and the electrostatic interaction between the nucleophile and the substrate. Combining the strain and the EDA analyses, it was found that the preference for an obtuse α angle results from a delicate balance between the strain and the stabilizing energies. The strain energy, associated with the deformation of the different chemical species prevents the α angle from becoming too large. In contrast, the stabilizing energy, dominated by the Pauli repulsion, prevents the same angle from getting smaller (i.e. < 90°). These recent studies demonstrate the importance of quantitative analysis tools to determine the relative importance of the attractive and repulsive interactions. This enriches and quantifies the earlier qualitative analyses.

3. Early studies of the reaction pathway

3.1. *Early studies with non-cyclic carbonyls*

A quantitative computational study of the reaction mechanism requires a reasonable representation of all the reagents and the environment, in particular the solvent, as well as an extensive exploration of the chemical spaces and a proper calculation of the thermodynamics of the chemical systems in solution. These features have been slowly achieved over the years and this section describes, through selected examples, the information that has been gained about the nucleophilic addition to carbonyls and illustrates the improvements in modeling and computation.

Soon after the very first studies, the naked hydride was replaced by more realistic model of the nucleophile. Borohydride was one of them but the cation and the solvent were not yet included. The Hartree–Fock study of the reaction of BH_4^- with formaldehyde showed that the formation of the anionic $CH_3OBH_3^-$ was thermodynamically favored and led to the localization of a transition state. The reaction was found to be concerted although significantly nonsynchronous with the C–H bond being essentially formed while the O···B bond was not. The two-step pathway was also identified and found to be at higher energy than the concerted pathway. Both mechanisms were associated with high energy barriers probably due to an overly simplistic modeling of the chemical species which neither included the cation nor the solvent [34]. A related study using B_2H_6 as nucleophile showed that a BH_3 coordinates the oxygen [35]. Calculations showed that the addition of AlH_3 to formaldehyde proceeds via a 4-centered transition state and forms an energetically favorable aluminum methoxide product [36].

A computational model still using a naked hydride was proposed in the 1990s to analyze the face selectivity in the case of sterically unbiased ketones. Using also semi-empirical method (MNDO), the authors were able to consider large molecules like substituted norbornanones and other bicyclic ketones. The experimental selectivity was well reproduced. The authors point out that the geometrical details of the transition state seemed unimportant but the presence of a hydride was necessary in the calculations [37].

3.2. *Early studies with cyclic ketones*

Considerable efforts have been devoted to the study of the face selectivity for the addition of various nucleophiles to substituted cyclohexanones. These 6-membered ring ketones posed a great computational challenge due to their ring flexibility. The studies were all based on the determination of the reaction pathway by identifying the transition states with different nucleophiles that were modeling as well

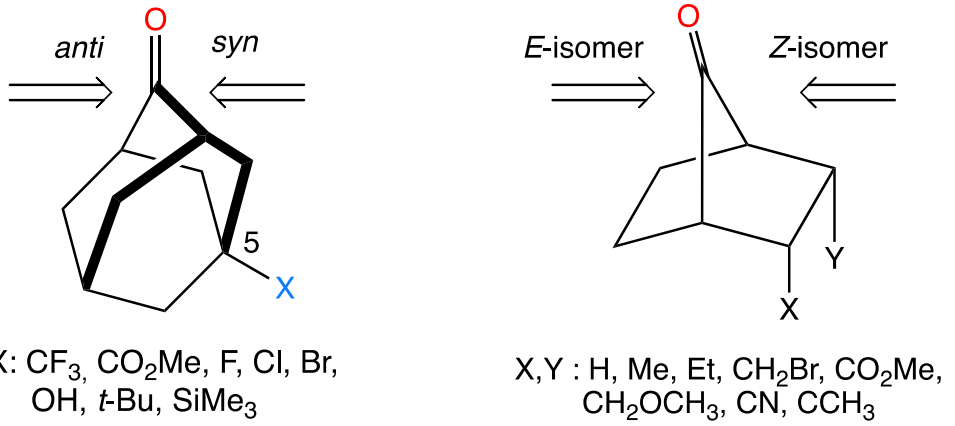

Figure 4. 5-Substituted adamantanones (left) and substituted 7-norbornanones (right) and labels of the isomers resulting from the addition of a nucleophile to the two faces of the carbonyl group.

as possible those used in the experiments. The solvent also began to be included in the computational studies, usually by means of a continuum method, although not yet systematically. This improved the representation of the electrostatic contribution. The studies were aimed at finding the facial preferences and also at understanding, at least in a qualitative way, the various factors that determine these preferences.

The study of the addition of AlH_3 to 5-substituted adamantanones (Figure 4) confirmed the involvement by hyperconjugation of the bond that is antiperiplanar to the incoming nucleophile (the essence of the Felkin–Anh model) and pointed out the importance of torsional effects in the face selectivity [38]. A study of the reduction of substituted 7-norbornanones (Figure 4) using the AM1 method emphasized the importance of determining the transition state and not just looking at the electrostatic properties of the substrate. Using AlH_3 to model the reactivity of $NaAlH_4$ reproduced the stereoselectivity for a whole series of substituted norbornanones [39].

LiH was shown to be associated with a 4-centered transition state and a preference for addition of the hydride to the axial face of the cyclohexanone (Figure 5). This preference, established for a small nucleophile, was related to a distortion of the π^*_{CO} orbital, which was more developed toward the axial face. This distortion was shown to be due to the hyperconjugation with the neighboring C–H and C–C orbitals. Large nucleophiles had a preference for the

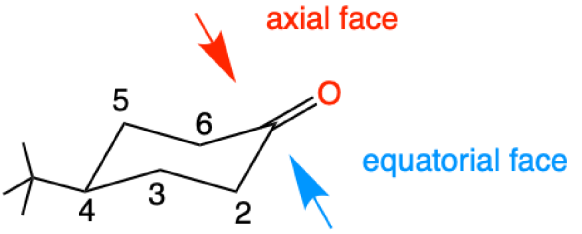

Figure 5. The two non-equivalent faces of 4-*tert*-butylcyclohexanone and the numbering of the carbon atoms.

equatorial approach due to steric hindrance on the axial face [15]. Around the same time, the relative importance of torsional strain and electrostatic interactions was studied, with LiH and NaH as nucleophiles and cyclohexanone and related substituted cyclic carbonyl molecules. Some general trends have emerged. Torsional strain at the transition state disfavors the equatorial attack, steric effects often disfavor the axial attack and the electrostatic interactions can dominate when polar substituents are present on the ring. Substituents have stronger effects at the axial site than at the equatorial site [40,41], and for substituted 7-norbornanones [42]. In 1992, Li and le Noble considered all the rules that have been proposed and favored a rational that mixes the torsional effects, the Felkin–Anh and Cieplak rules in different amounts for each system [43].

Ion mass spectrometry studies showed that pentacoordinated silicon hydride is also a nucleophile

that can add to cyclohexanone and related molecules [44]. This was of interest for the computational studies because gas phase and solution chemistry could be compared. Using SiH_5^- as a simplified model of the experimental pentacoordinated alkoxide silicon hydride, the selectivity of the reduction of several cyclohexanone derivatives was studied using Hartree–Fock and MP2 methods in the gas-phase and the solution [45]. The transition state is dominated by the hydride transfer and very little Si–O bond formation. Axial reduction is preferred for the cyclohexanone but the equatorial reduction is preferred for dithianone, the preferences being similar in the gas phase and in solution. However, for dioxanone, the gas phase favors the equatorial addition and the solution (methanol) favors the axial addition. These computational results were consistent with the observed selectivity of the reactions with $NaBH_4$, $LiAlH_4$ and Grignard reagents in solution. They were qualitatively rationalized as coming from a balance between electrostatic interactions which disfavors the axial approach and torsional strain which disfavors the equatorial attack. Further studies with hindered cyclohexanones and various nucleophiles (hydride, methyl, acetylenic Grignard and lithium reagents) were performed. The reaction of CH_3Li or HC≡CLi with non-substituted cyclohexanone was carried out with an ab-initio Hartree–Fock study but the same method could not be applied for hindered cyclohexanones. In this latter case an adapted MM2 force field method was used. This approach led to a good reproduction of the observed selectivity. In this case also, the selectivity resulted from a balance between steric and torsional effects [46]. The intrinsic diastereoselectivity of the reduction of a large series of cyclic ketones by pentacoordinated silicon hydride ions was investigated in the gas phase using the flowing afterglow-triple quadrupole technique [47]. The percent axial reduction was determined by collision-induced dissociation experiments. The trend observed in the condensed phase is consistent with the results observed in the gas phase suggesting that environmental effects are either unimportant or cancel each other out. Consequently, the diastereoselectivity was proposed to be related to the intrinsic nature of the substrate and rationalized as resulting from a competition between steric, torsional and electrostatic effects.

3.3. *The relative importance of the effects influencing selectivity*

Calculations were clearly able to reproduce the observed stereoselectivity but they were not easy to interpret. The energy difference between the approach to the two faces of the carbonyl group is small (usually less than 1 kcal/mol) and it is a real challenge to identify the driving effect (if there is one) among the several competing interactions. The following factors have been mentioned: (i) the charge transfer of the nucleophile to the substrate also called delocalization or hyperconjugation (i.e. the Felkin–Anh or Cieplak rules), (ii) the electrostatic interaction, (iii) the steric [48] and strain energies, and (iv) the chelation. Another indicator of stereogenicity has been proposed. It is intrinsic to the prochiral substrate and can be derived from its molecular orbitals. The determination of the transition state of the nucleophilic addition can thus be avoided. In a prochiral carbonyl group, the two faces of the π bond are not equivalent. It means that the occupied π orbital as well as the LUMO π^*_{CO} have greater extension toward one of the two faces of the carbonyl. Authors have analyzed these distortions focusing on the carbon contribution. These different extensions result from the mixing of the 2p and 2s carbon orbitals (Figure 6). An earlier version of this indicator was used to justify the Cram rule [49]. This dissymmetry in the occupied or empty orbitals has been considered by Klein in particular for 5- and 6-membered ring ketones [50,51]. An elaborate quantitative evaluation of the expansion of the LUMO π^*_{CO} orbital was developed by Tomoda [16].

The relative importance and validity of these various criteria were the subject of an entire issue of *Chem. Rev.* in 1999, indicating how important these criteria were to the community of chemists. For example, in this issue, Dannenberg nicely discussed the pros and cons of electronic criteria that were used in those years [52]. He pointed out that it was unlikely that a single rule could rationalize all cases. Ohwada described how to use orbitals to rationalize the face selection in sterically unbiased cyclic systems [53]. Cieplak presented his interpretation of the effect of substituents on π-face selection [14]. Wipf and Jung discussed the role of dipole effects [54], Mehta and Chandrasekhar discussed various electronic effects for sterically unbiased ketones and olefins [55].

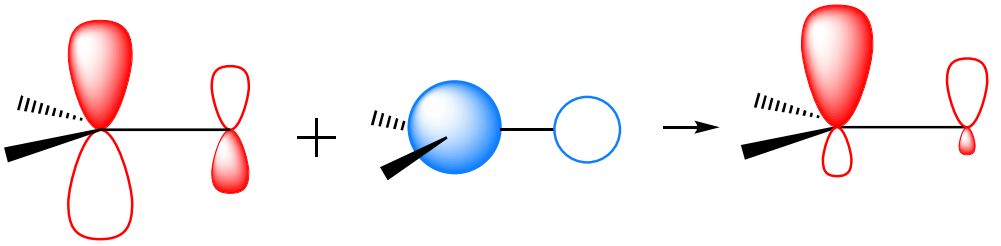

Figure 6. Qualitative illustration of the mixing of 2p and 2s orbitals for C and O when the carbonyl group is prochiral. The mixing at carbon was the focus of attention.

Adcock and Trout discussed the case of rigid saturated model substrates and in particular the influence of the substituents [56].

A study by Rosenberg et al. is notable by the number of systems studied experimentally and computationally and by the careful consideration of a large number of factors [57]. These authors considered a series of 2-X-4-*tert*-butylcyclohexanones (X = H, CH_3, OCH_3, F, Cl, Br; with X equatorial or axial), studied their reactivity with $LiAlH_4$ and, performed computational studies of the face selectivity. They used the simplified model of the hydride that was currently selected in the early 2000s (LiH, NaH, BH_3, AlH_3). They determined the transition states for all the systems and obtained a calculated selectivity which correctly identified the main isomer. The experimental trends were better reproduced by the calculations when the X substituent was equatorial than axial. The controlling factors appeared to be the electrostatic interactions between the nucleophile and the substituent X. When X was axial, the electrostatic effect or the Felkin–Anh rule rationalized the results but the Cieplak model failed.

Thus, in the early 2000s, it was clear that a large number of factors were controlling the face selectivity and that none was dominant. It was also encouraging that calculations were successful to determine the major isomer, although the observed trends were sometimes difficult to reproduce. Given the very small energy difference between the transition states of the addition of the nucleophile on the two faces of the carbonyl, this was very encouraging. Thus, in the following years, improved calculations were performed. This includes a more realistic modeling of the nucleophile, the presence of the counter cation, the almost systematic inclusion of the solvent which was represented either implicitly (by a continuum) or explicitly by the presence of one or two solvent molecules. This also includes the use of more elaborate computational methods, in particular DFT methods that were successful at representing together the strong covalent bonding and the weak non covalent interactions. The determination of the reaction pathway (transition states and intermediates) was systematic. This "static approach" was the state of the art for many years. It was powerful, relatively inexpensive and usually successful in calculating selectivity in good agreement with the experimental data. However, with this static approach, the ability to accurately represent the thermodynamics of a very complex system of solute and solvent could be limited.

3.4. *Studies with improved representation of the nucleophilic reagent*

Calculations were performed with $LiBH_4$, $NaBH_4$ or $LiAlH_4$ as reagents. This allowed to understand how the cation and the element (B or Al) carrying the hydride cooperate to transfer the hydride to the carbonyl carbon. The solvent was often but not always included although its presence seemed necessary in presence of charged species. Besides the determination of the reaction pathway, the stereoselectivity for acyclic and cyclic carbonyl remained the main goal of these studies.

The computational study of the reaction of $LiAlH_4$ with formaldehyde and cyclohexanone was carried out in the gas phase [58]. The authors stated that neglecting the solvent was justified because similar stereoselectivity had been observed in the gas phase and in solution [47]. Under these conditions, the calculations were performed with the DFT method with the widely popular B3LYP functional and a 6–31G**

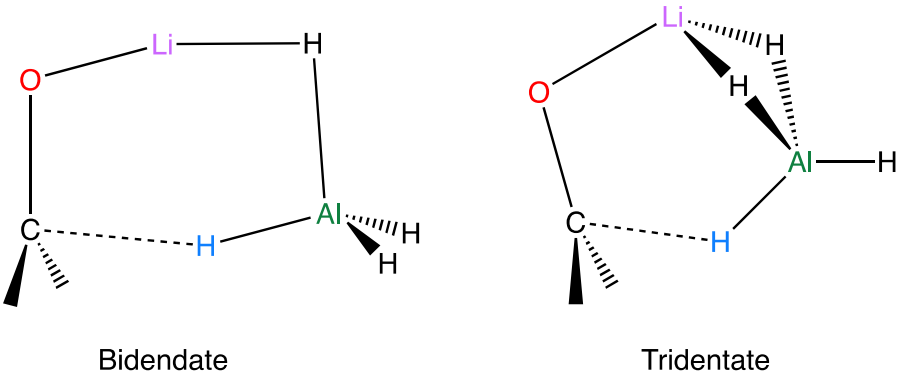

Figure 7. Transition states for the addition of $LiAlH_4$ to formaldehyde. Similar transition states were located with cyclohexanone [58].

basis set (a good level of calculation in the early 2000s). Two types of transition states with either bidentate (preferred) or tridentate Li/AlH_3 bonding were identified (Figure 7). All transition states yielded the same intermediate where Li is still bound to the oxygen. It rearranges to the more stable Al–O bound final product.

The calculations carried out for the cyclohexanone show a preference for an axial approach, which has already been found with nucleophiles such as LiH, SiH_5^-, BH_3 etc. The strain energy is again mentioned as disfavoring the equatorial attack. The hyperconjugation effect is suggested to be small since the C–H and C–C σ bonds, next to the reactive carbonyl group, do not lengthen or contract significantly. Thus, the greater extension of the π^*_{CO} LUMO towards the axial face was suggested to be a favorable factor for the attack on this face. A similar study was carried out on the reduction of 2-X-substituted cyclohexanones (X = OMe, SMe, SeMe) with $LiAlH_4$ in the gas phase [59]. To interpret the results, the extension of the π^*_{CO} LUMO towards one of the faces of the carbonyl and the electrostatic potential were considered. However, this was not sufficient because the conformations of the 6-membered ring and the complexation of X by lithium (Li) had a determining role in the stereoselectivity. To study cases where the X···Li interactions did not exist, calculations were also performed for X = CH_3 and $CH(CH_3)_2$ [60]. The conformational preferences of the 2-X-substituted cyclohexanones in the transition state gave a preference for the *trans*-isomer (Figure 8).

The reaction mechanisms for the addition of $LiBH_4$ and $LiAlH_4$ to formaldehyde were compared with the CAM-B3LYP/Aug-cc-pVTZ level for geometry optimization and with single point calculations at the CCSD(T)/Aug-cc-pVTZ level [61]. The solvent (THF) was represented by an SCRF/PCM continuum and selected calculations included an explicit molecule of THF. The energy barrier was significantly higher for $LiBH_4$ than for $LiAlH_4$. Thus, in agreement with the Hammond postulate, the transition state is product like for $LiBH_4$ and reactant like for $LiAlH_4$. In the product, O–B or O–Al bonds are formed and Li interacts either with the oxygen only (case of $LiAlH_4$) or with the oxygen and the hydride (case of $LiBH_4$). From, the evolution of the charge density along the reaction pathway, the authors suggested that the reaction started with an electron transfer from the hydride to the carbon of the carbonyl and is followed by the hydrogen transfer. This mechanism has not been suggested in other studies.

The experimental conditions were well represented in the relatively recent computational study of the face selectivity for reactions of small and large hydride species to 4-*tert*-butylcyclohexanone, *cis*-2,6-dimethyl *N*-acylpiperidone and *N*-acyltropinone (Figure 9) [62]. The substrates were considered in full and, small and large hydrides were represented by $LiAlH_4$ and by $LiBH(CH_3)_3$, respectively. $LiBH(CH_3)_3$ was used as a model for the experimental lithium tri-*sec*-butylborohydride, L-Selectride, whose conformational complexity was beyond the reach of calculations. The geometry optimization was carried out at the B3LYP/6-31(d,p) and the energies were refined by single point calculations with a larger basis set and implicit solvent effect represented with a recently developed powerful continuum method

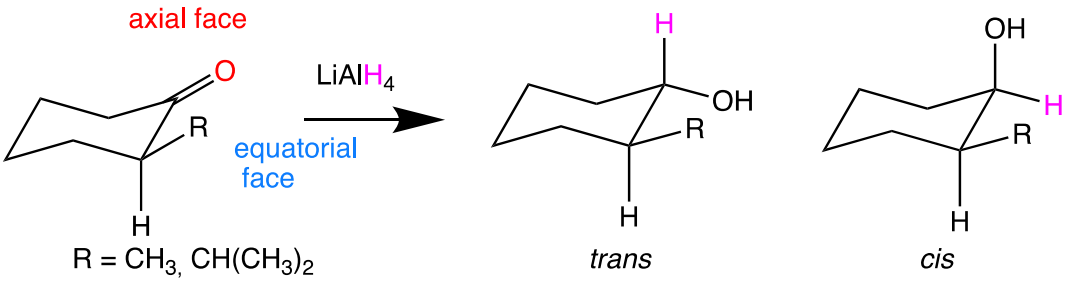

Figure 8. Products resulting from the reaction of $LiAlH_4$ with 2-alkylcyclohexanones.

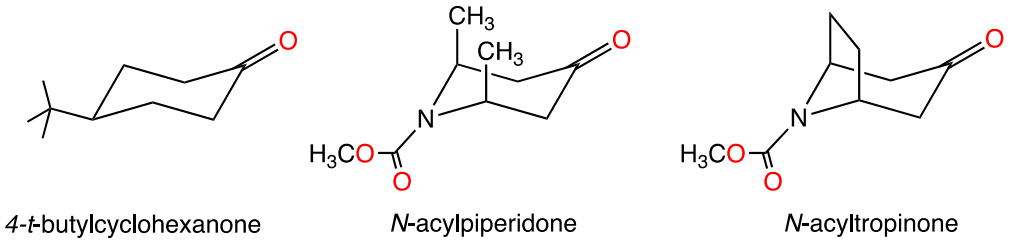

Figure 9. 6-Membered ring ketones whose reactivity with small and large hydride species were studied by calculations.

(SMD). These were high level calculations for such systems 10 years ago. The calculated free energies of activation ($\Delta G^{\neq}$) for the addition of the nucleophile to the two faces of the carbonyls differ by less than 1 kcal/mol and systematically, the transition state that yields the observed major isomer is calculated to have the lower energy. Thus, small diastereoisomeric excesses were correctly calculated. Small hydride species preferentially added to the axial face of the substituted cyclohexanones and tropinone. However, an equatorial attack to a twist boat conformation was preferred for the piperidone. In the case of the bulky hydride, the equatorial face was preferred in all systems. Torsional strain and steric effects control the selectivity and steric effects dominate in the case of large hydride.

Recent years have seen an improved representation of solvation. Solvation has been implemented in calculations for many years using a continuum model which in particular allowed a correct representation of the electrostatic effects in solution. However, microsolvation was not present in implicit solvation and its omission was becoming increasingly questionable because microsolvation is recognized to be important when polar reagents are used. Thus, the selectivity of the reduction of 4-*tert*-butylcyclohexanone by $LiAl(OR)_3H$ (R = *tert*-butyl for the experiments and methyl for the calculations) with THF mono- and bi-solvation was studied computationally with three functionals, B3LYP, B3LYP-D3 and M06-2X [63]. Implicit solvation was also included with the SMD method. Bi-solvation was found to be preferred. A two-step reaction was identified, with the first step describing the hydride transfer to the carbonyl carbon and the second step describing the formation of the Al–O bond. However, the intermediate between the two transition states is energetically high and close to the two transition states, questioning the existence of a two-step reaction and a strongly non-synchronous reaction cannot be ruled out. In fact, a recent high-level calculation of the reduction of 2-X-substituted cyclohexanones (X = H, Cl, Br) by $NaBH_4$ in which the solvent is explicitly represented by microsolvation and implicitly represented by a continuum showed a single transition state pathway [64]. This recent study highlights the need for this dual representation of the solvent. The calculations gave a late transition state with an almost formed C–H bond as actually found in most previous studies. This late transition state was said to be consistent with the mild reducing power of $NaBH_4$. The observation that 2-halo cyclohexanones are more reactive than cyclohexanone was only well represented when both solvation and microsolvation

were considered. Thus, even if the solvent (ethanol) does not change the face selectivity, its explicit inclusion is necessary to better model a reaction pathway involving polar transition states. Today, the need for an explicit representation of the solvent molecules especially when highly polar or ionic species are present is fully recognized. The question remains on how to represent this explicit solvation. For years, calculations were performed with a reasonably small number of solvent molecules following some computational tests and chemical intuition. Today, this is an important issue in the study of reaction pathways and other methods are starting to be used [65] (see also below).

Computational chemists have also been concerned with the quality of the calculations and in particular with the method and level of calculation that must be used to represent the strong bonds and the weak interactions in a balanced way in order to correctly determine the face selectivity. Such a study has been carried out for substituted 2-X-substituted cyclohexanones (X = Me, OMe, SMe, Cl) and $LiAlH_4$ with eight different functionals, MP2 and CCSD(T) methods [66]. The energy barrier is found to be more sensitive to the calculation method than the conformational properties of the substrate. MP2 appears one of the poorest methods in this particular study. The coordination mode of AlH_4 to Li at the transition state was found to depend on the calculation method but not the face selectivity which is the same for all methods. An interesting analysis of the strain energy and steric effects, reinforces the accepted understanding that face selectivity results from a balance between them. The fact that the selectivity of the reaction does not vary with these already high-level computational methods is encouraging for further studies with more complex substrates and nucleophiles.

4. What is in solution? Searching for the structure of the alkali and alkalino earth complexes

4.1. *The metal hydride cases*

The nature of the solvated species present in ethereal solutions of $LiAlH_4$ has been studied by combining experiments and computations based on IR spectroscopy. The result of this study is that $LiAlH_4$ in ethereal solutions forms contact ion pairs. The dissociated species are higher in energy than the associated species by about 2.3 kcal/mol and 4 kcal/mol for THF and dimethyl ether, respectively [67].

Car–Parrinello molecular dynamics simulation of $NaBH_4$ in methanol also suggested a preference for a solvated contact ion pair and found that the dissociation pair to be more than 4 kcal/mol higher in energy [68]. This led the authors to propose a transition state for the reduction of ketone that incorporates this finding in a set of static calculations. Using this solvated contact ion pair as reagent for the reaction with cyclohexanone derivatives dramatically lowers the activation energy. It also leads to calculated selectivities in very good agreement with observed values (4-methylcyclohexanone axial/equatorial: exp = 86:14, calc = 80.9:19.1; 2-*tert*-butcyclohexanone axial/equatorial: exp = 50:50, calc = 41:59). These results were used to calculate the complete mechanism for the reduction of resorufin by $NaBH_4$ in water [69]. As mentioned above, the effect of the solvent (ethanol) on the stereoselectivity and reactivity was also investigated in the case of the reduction of 2-X-substituted cyclohexanones (X = H, Cl, Br) by $NaBH_4$ [64].

4.2. *The Grignard reaction*

The Grignard reaction is a prominent process in organic synthesis for the formation of carbon–carbon bonds. Despite extensive experimental studies, the mechanism of the reaction at the molecular level remains unknown. This is because the nature of the Grignard reagent in solution is still unknown. As summarized by Dietmar Seyferth, “Generally written as RMgX, the Grignard reagents in ethereal solution are more complicated than this simple formula indicates” [70]. It is currently recognized that the nominal reagent, RMgX is a condensed representation of numerous mono- and poly-metallic species in rapid equilibrium and that the exact nature of the species is determined by the solvent. Thus, unfortunately, most of the studies attempting to characterize these species by the most advanced and diverse spectroscopic methods [71], and crystallization have identified them under conditions different from those of the reaction itself. Traditional static computational methods would also fail because they cannot properly calculate the free energy changes of the solvent

organization and dynamics at close and intermediate distances from the organomagnesium species. A method of calculations capable of representing the thermodynamics of the solute and the solvent, as accurately as possible, is the ab initio molecular dynamics (AIMD). This method has been used to describe solvated $NaBH_4$ as mentioned above [68] and has thus been used to uncover the diversity of species representing the global Grignard reagent in ethereal solution and to propose a mechanism for the Schlenk equilibrium (Equation (1)), for CH_3MgCl in THF [72].

$$2RMgX \rightleftharpoons MgR_2 + MgCl_2. \quad (1)$$

It appears that the solvation of the magnesium species is highly variable and also very dynamic. It takes very little energy to add or remove a solvent molecule from the coordination sphere of magnesium. As expected, solvation is higher when Mg is bound to the electron withdrawing-chloride atom than to the electron-donating methyl group. Thus, dimethyl magnesium is best solvated by two THF molecules, while magnesium dichloride prefers three THF molecules in its coordination sphere. Thus, a higher positive charge on Mg increases the solvation. Several chloride and methyl-bridged dinuclear magnesium species, which differ in their solvation, are present in equilibrium, (Figure 10). The calculations suggest that the Cl/Me exchange between the two magnesium centers is initiated by a solvation imbalance between the two metal centers. The least solvated attracts a bridging chloride more strongly. The chloride unequally bound to the two magnesium centers becomes terminal to the closer magnesium promoting the transfer of a methyl group from the terminal to the bridging position. This chloride-methyl-bridged dimer achieves the Cl/Me exchange. The dynamics of the solvent is thus essential in the Schlenk equilibrium.

The Grignard reaction itself was studied with the AIMD method by considering the reaction of acetaldehyde with all identified forms of CH_3MgCl in THF [73]. It was found that all forms are competent in the Grignard reaction as the free energies of activation are within a narrow energy range. Since the different Grignard species are in rapid equilibria, they can all contribute to the reaction in parallel. Therefore, the reaction can occur via competing parallel pathways resulting in unclear kinetic order. Additional solvation may also be required to achieve the reaction. This is the case for the monomeric species, of which $Mg(CH_3)_2$ is found to be the most reactive. A highly solvated μ^2-Cl dimagnesium species is the most reactive dinuclear species. Importantly, the substrate and the nucleophile are initially bound to different magnesium centers and, in the transition state the acetaldehyde is strongly electrophilically activated by being O-coordinated to both magnesium centers (Figure 11). Previous studies of the reaction using traditional (static) DFT calculations also identified dinuclear magnesium complexes as the most reactive [74–76]. The direct role of the solvent in modulating the reaction pathway is the main reason for the structural and energetic differences between the earlier and later studies. Indeed, the AIMD calculations indicate that the solvent is an essential active partner in the reaction.

This study also clarified the issue of nucleophile vs single electron transfer (SET) mechanism. The SET mechanism has been proposed for substrates with low reduction potential. Recent studies have shown that the SET is rare and occurs only with aromatic carbonyl compounds [77,78]. The computational study was limited to the formation of the organic radical and thus to the calculation of the bond dissociation energy (BDE) of the homolytic cleavage of the CH_3–Mg bond (DFT static calculations). The carbon–magnesium BDE in CH_3MgCl was calculated to be high (about 60 kcal/mol) with very little influence of the solvent. This high BDE would indicate that the radical cannot be formed. However, when the substrate is bonded to the magnesium, the carbon–magnesium BDE drops dramatically and the drop is increased as the energy of the π^*_{CO} orbital of the substrate is decreasing. The reason is that the single electron of the magnesium species remains located on Mg in solvated MgCl species. However, the MgCl(substrate) species has a low-lying LUMO that is localized on the π^*_{CO} empty orbital of the coordinated substrate. Thus, the single electron goes to the coordinated substrate π^*_{CO} orbital, where it is stabilized compared to be located on Mg. In other words, the substrate itself assists the formation of the organic radical and the lowering of its reduction potential reinforces the assistance. The calculations show that the SET mechanism becomes competitive with the nucleophilic addition in the case of fluorenone in excellent agreement with Woerpel's experimental results [77,78].

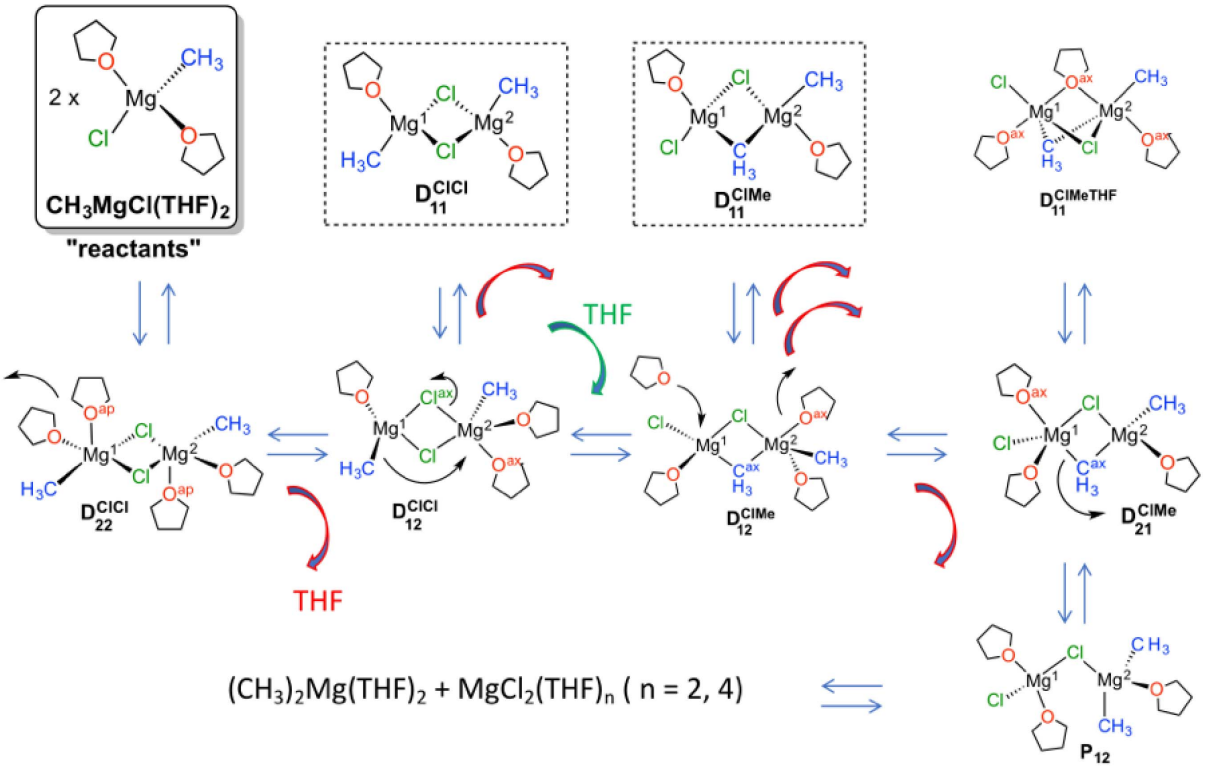

Figure 10. Methyl magnesium chloride in THF. Species present in solution and involved in the Schlenk equilibrium proposed by AIMD calculations. The red (green) arrow represents the loss (addition) of a molecule of THF from (to) the coordination of the magnesium atoms. D_{ij}^{XY} labels the dinuclear species with i/j coordinated THF molecules on the left/right magnesium center with XY (Cl or Me) are the bridging atom or group. Adapted from ref [72].

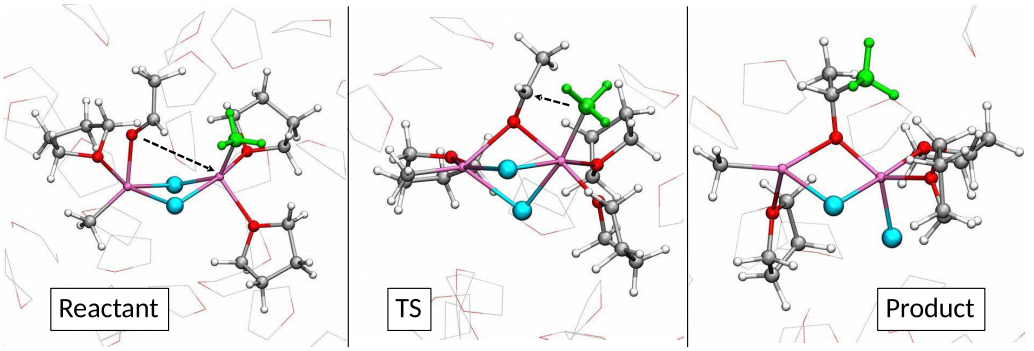

Figure 11. The most reactive species in the Grignard reaction. The substrate (acetaldehyde) is coordinated to the left-hand side magnesium, and the nucleophilic methyl group (green color) is on the right-hand side magnesium. Copyright from [73].

5. Conclusion and perspective

This topic was of interest to the author as she was an active member in the construction of the Felkin–Anh rule. Recently, she returned to the addition of nucleophiles to carbonyl groups with the Grignard reaction. The description of important work done in the field of nucleophilic addition to carbonyl groups by many authors described in this perspective is well representative of the way in which computational chemistry has developed and accompanied experimental studies. It is noteworthy that the direction of approach of a nucleophile to a carbonyl group has long been correctly captured with very simple calculations. The attempts to quantitatively reproduce the face selectivity illustrate the courage of computational chemists to try to capture small energy differences that are computationally challenging but chemically significant. Trying to interpret the factors that control the selectivity has also been a struggle. Now everyone seems to accept that many factors contribute and none of them dominate. There have been great improvements in the representation of chemical systems and in computational methods over the past 40 years. This has allowed small diastereomeric excesses can be calculated quite accurately. Getting it right was not and is still not easy. One of the greatest difficulties is to decide which species to include in a model. Unfortunately, there are no entities present in the experimental systems that should be ignored a priori in the modeling. In particular, it would be a serious mistake to ignore the solvent. None of the species present in the reactive media are total spectators but representing the entire media is simply not possible. Computational chemists will proceed step by step using either (or both) static and ab initio molecular dynamics calculations. Static calculations, including explicit and implicit solvation, will be useful for well-identified reactive systems as illustrated by the cases reported in this article. Ab initio molecular dynamics will be needed to study cases where the dynamics of the solvent plays a role. It will also be needed to analyze highly complex chemical media with unknown solvent-dependent reactive systems as illustrated by the Grignard reaction. This topic is indeed pursued with the study of the synergistic role of lithium salts [79] in the so-called Turbo Grignard [80]. This author is involved in the exploration of this subject [81] in a collaboration with Professor Michele Cascella of the Hylleraas Center at the University of Oslo.

Declaration of interests

The author does not work for, advise, own shares in or receive funds from any organization that could benefit from this article, and has declared no affiliations other than her research organizations.

Funding

Early work by this author was supported by the French National Center for scientific Research (CNRS). More recent work by this author was supported by the Research Council of Norway through the Center of Excellence Hylleraas Center for Quantum Molecular Science (Grant 262695) and the Pioneer Research Grant MetalSynergy (Grant 314009) and by the Norwegian Supercomputing Program (NOTUR) (Grant NN 4654K).

References

[1] V. C. Grignard, *Compt. Rend. Hebd. Séances Acad. Sci.*, 1900, **130**, 1322-1324.
[2] Nobel Prize organisation web site, https://www.nobelprize.org/prizes/chemistry/1912/summary/.
[3] G. Bram, E. Peralez, J.-C. Négel, M. Chanon, *Compt. Rend. Hebd. Séances Acad. Sci. Sér. II*, 1997, **325**, 235-240.
[4] O. Eisenstein, *Isr. J. Chem.*, 2022, **62**, article no. e202100138.
[5] H. B. Bürgi, J. D. Dunitz, *Acc. Chem. Res.*, 1983, **16**, 153-161.
[6] R. H. Crabtree, E. M. Holt, M. Lavin, S. Morehouse, *Inorg. Chem.*, 1985, **24**, 1986-1992.
[7] H. B. Bürgi, J. D. Dunitz, E. Shefter, *J. Am. Chem. Soc.*, 1973, **95**, 5065-5067.
[8] H. B. Bürgi, J.-M. Lehn, G. Wipff, *J. Am. Chem. Soc.*, 1974, **96**, 1956-1957.
[9] H. B. Bürgi, J. D. Dunitz, J.-M. Lehn, G. Wipff, *Tetrahedron*, 1974, **30**, 1563-1572.
[10] N. T. Anh, O. Eisenstein, *Nouv. J. Chem.*, 1977, **1**, 61-70.
[11] N. T. Anh, *Top. Curr. Chem.*, 1980, **88**, 145-162.
[12] A. S. Cieplak, *J. Am. Chem. Soc.*, 1981, **103**, 4540-4552.
[13] A. S. Cieplak, B. D. Tait, C. R. Johnson, *J. Am. Chem. Soc.*, 1989, **111**, 8447-8462.
[14] A. S. Cieplak, *Chem. Rev.*, 1999, **99**, 1265-1336.
[15] G. Frenking, K. F. Köhler, M. T. Reetz, *Angew. Chem. Int. Ed.*, 1991, **30**, 1146-1149.
[16] S. Tomoda, *Chem. Rev.*, 1999, **99**, 1243-1263.
[17] K. Fukui, *Acc. Chem. Res.*, 1971, **4**, 57-64.
[18] S. Srivastava, W. J. Le Noble, *J. Am. Chem. Soc.*, 1987, **109**, 5874-5875.

[19] K. Okada, S. Tomita, M. Oda, *Bull. Chem. Soc. Jpn.*, 1989, **62**, 459-468.

[20] Y. Senda, S. Nakano, H. Itoh, *J. Chem. Soc. Perkin Trans.*, 1993, **2**, 1009-1010.

[21] Y. Senda, H. Sakurai, S. Nakano, H. Itoh, *Bull. Chem. Soc. Jpn.*, 1996, **69**, 3297-3303.

[22] R. E. Rosenberg, W. J. Kelly, *J. Phys. Org. Chem.*, 2015, **28**, 47-56.

[23] N. D. Bartolo, J. A. Read, E. M. Valentin, K. A. Woerpel, *Chem. Rev.*, 2020, **120**, 1513-1619.

[24] N. D. Bartolo, K. M. Demkiw, E. M. Valentin, C. T. Hu, A. A. Arabi, K. A. Woerpel, *J. Org. Chem.*, 2021, **86**, 7203-7217.

[25] N. D. Bartolo, K. M. Demkiw, J. A. Read, E. M. Valentin, Y.-G. Yang, A. M. Dillon, C. T. Hu, M. D. Ward, K. A. Woerpel, *J. Org. Chem.*, 2022, **87**, 3042-3065.

[26] T. Bettens, M. Alonso, P. Geerlings, F. de Proft, *J. Org. Chem.*, 2023, **88**, 2046-2056.

[27] J. C. Bristow, R. Leslie, J. D. Wallis, *Helv. Chim. Acta*, 2023, **106**, article no. e202300021.

[28] C. Bonini, V. Esposito, M. D'Auria, G. Righi, *Tetrahedron*, 1997, **53**, 13419-13426.

[29] O. Eisenstein, M. Kayser, M. Roy, T. B. McMahon, *Can. J. Chem.*, 1985, **63**, 281-287.

[30] R. E. Rosenberg, *J. Am. Chem. Soc.*, 1995, **117**, 10358-10364.

[31] R. E. Rosenberg, *J. Org. Chem.*, 2008, **73**, 6636-6641.

[32] H. A. Rodriguez, F. M. Bickelhaupt, I. Fernández, *ChemPhysChem*, 2023, **24**, article no. e202300379.

[33] I. Fernández, F. M. Bickelhaupt, D. Svatunek, *J. Chem. Theory Comput.*, 2023, **19**, 7300-7306.

[34] O. Eisenstein, H. B. Schlegel, M. M. Kayser, *J. Org. Chem.*, 1982, **47**, 2886-2891.

[35] S. Masamune, R. M. Kennedy, J. S. Petersen, K. N. Houk, Y. D. Wu, *J. Am. Chem. Soc.*, 1986, **108**, 7404-7405.

[36] J. M. Coxon, R. T. Luibrand, *Tet. Lett.*, 1993, **34**, 7093-7096.

[37] B. Ganguly, J. Chandrasekhar, F. A. Khan, G. Mehta, *J. Org. Chem.*, 1993, **58**, 1734-1739.

[38] J. M. Coxon, K. N. Houk, R. T. Luibrand, *J. Org. Chem.*, 1995, **60**, 418-427.

[39] G. M. Keserü, Z. Kovári, G. Náray-Szabó, *J. Chem. Soc. Perkin Trans.*, 1996, **2**, 2231-2234.

[40] Y. D. Wu, J. A. Tucker, K. N. Houk, *J. Am. Chem. Soc.*, 1991, **113**, 5018-5027.

[41] Y.-D. Wu, K. N. Houk, M. N. Paddon-Row, *Angew. Chem. Int. Ed.*, 1992, **31**, 1019-1021.

[42] M. N. Paddon-Row, Y. D. Wu, K. N. Houk, *J. Am. Chem. Soc.*, 1992, **114**, 10638-10639.

[43] H. F. Li, W. J. Le Noble, *Rec. Trav. Chim. Pays-Bas*, 1992, **111**, 199-210.

[44] Y.-G. Ho, R. R. Squires, *J. Am. Chem. Soc.*, 1992, **114**, 10961-10963.

[45] Y. D. Wu, K. Houk, *J. Am. Chem. Soc.*, 1993, **115**, 10992-10993.

[46] K. Ando, K. N. Houk, J. Busch, A. Ménassé, U. Séquin, *J. Org. Chem.*, 1998, **63**, 1761-1766.

[47] A. Artau, Y.-G. Ho, H. Kenttämaa, R. R. Squires, *J. Am. Chem. Soc.*, 1999, **121**, 7130-7137.

[48] I. C. Lagerstedt, T. Olsson, *J. Chem. Inf. Comput. Sci.*, 1993, **33**, 896-904.

[49] N. T. Anh, O. Eisenstein, J. M. Lefour, M. E. Trân Huu Dâu, *J. Am. Chem. Soc.*, 1973, **95**, 6146-6147.

[50] J. Klein, *Tet. Lett.*, 1973, 4307-4310.

[51] J. Klein, *Tetrahedron*, 1974, **30**, 3349-3353.

[52] J. J. Dannenberg, *Chem. Rev.*, 1999, **99**, 1225-1242.

[53] T. Ohwada, *Chem. Rev.*, 1999, **99**, 1337-1376.

[54] P. Wipf, J.-L. Jung, *Chem. Rev.*, 1999, **99**, 1469-1480.

[55] G. Mehta, J. Chadrasekhar, *Chem. Rev.*, 1999, **99**, 1437-1468.

[56] W. Adcock, N. A. Trout, *Chem. Rev.*, 1999, **99**, 1415-1436.

[57] R. R. Rosenberg, R. L. Abel, M. D. Drake, D. J. Fox, A. K. Ignatz, D. M. Kwiat, K. M. Schaal, P. R. Virkler, *J. Org. Chem.*, 2001, **66**, 1694-1700.

[58] R. T. Luibrand, I. R. Taigounov, A. A. Taigounov, *J. Org. Chem.*, 2001, **66**, 7254-7262.

[59] C. C. Bocca, G. F. Gauze, E. A. Basso, *Chem. Phys. Let.*, 2005, **413**, 434-439.

[60] C. C. Bocca, R. Rittner, A. P. da Silva, E. Basso, *J. Phys. Org. Chem.*, 2011, **24**, 241-248.

[61] Y. Hori, T. Ida, M. Mizuno, *Comput. Theor. Chem.*, 2016, **1076**, 86-93.

[62] S. R. Neufeldt, G. Jiménez-Osés, D. L. Comins, K. N. Houk, *J. Org. Chem.*, 2014, **79**, 11609-11618.

[63] G. J. Tanoury, S. Roeper, *Tetrahedron*, 2018, **74**, 7103-7110.

[64] D. Rodrigues Silva, L. A. Zeoly, P. Vermeeren, R. A. Cormanich, T. A. Hamlin, C. Fonseca Guerra, M. P. Freitas, *J. Phys. Org. Chem.*, 2023, **36**, article no. e4556.

[65] G. Norjmaa, G. Ujaque, A. Lledós, *Top. Catal.*, 2022, **65**, 118-140.

[66] X. Deraet, T. Woller, R. Van Lommel, F. De Proft, G. Verniest, M. Alonso, *ChemistryOpen*, 2019, **8**, 788-806.

[67] D. E. Bikiel, F. Di Salvo, M. C. González Lebrero, F. Doctorovich, D. A. Estrin, *Inorg. Chem.*, 2005, **44**, 5286-5292.

[68] Y. Suzuki, D. Kaneno, S. Tomoda, *J. Phys. Chem. A.*, 2009, **113**, 2578-2583.

[69] P. Son, M. B. Ruan, X. J. Sun, Y. W. Zhang, W. L. Xu, *J. Phys. Chem. B*, 2014, **118**, 10224-10231.

[70] D. Seyferth, *Organometallics*, 2009, **28**, 1598-1605.

[71] C. Schnegelsberg, S. Bachmann, M. Kolter, T. Auth, M. John, D. Stalke, K. Koszinowski, *Chem. Eur. J.*, 2016, **22**, 7752-7762.

[72] R. M. Peltzer, O. Eisenstein, A. Nova, M. Cascella, *J. Phys. Chem. B*, 2017, **121**, 4226-4237.

[73] R. M. Peltzer, J. Gauss, O. Eisenstein, M. Cascella, *J. Am. Chem. Soc.*, 2020, **142**, 2984-2994.

[74] S. Yamazaki, S. Yamabe, *J. Org. Chem.*, 2002, **67**, 9346-9353.

[75] T. Mori, S. Kato, *J. Phys. Chem. A*, 2009, **113**, 6158-6165.

[76] S. Yamabe, S. Yamazaki, in *The Chemistry of Organomagnesium Compounds* (Z. Rappoport, I. Marek, eds.), Wiley-VCH, Weinheim, 2008, 369-402.

[77] D. A. L. Otte, K. A. Woerpel, *Org. Lett.*, 2015, **117**, 3906-3909.

[78] N. Bartolo, K. A. Woerpel, *J. Org. Chem.*, 2020, **85**, 7848-7862.

[79] S. D. Robertson, M. Uzelac, R. E. Mulvey, *Chem. Rev.*, 2019, **119**, 8332-8405.

[80] A. Krasovskiy, P. Knochel, *Angew. Chem. Int. Ed.*, 2004, **43**, 3333-3336.

[81] M. de Giovanetti, S. H. Hopen Eliasson, A. C. Castro, O. Eisenstein, M. Cascella, *J. Am. Chem. Soc.*, 2023, **145**, 16305-16309.

ACADÉMIE DES SCIENCES
INSTITUT DE FRANCE

Comptes Rendus. Chimie
2024, Vol. 27, Special issue S2, p. 21-32
https://doi.org/10.5802/crchim.274

Review article

Women Chemists in France in 2024

Control of atropoisomerism: an access to valuable compounds

Sabine Choppin[a], **Joanna Wencel-Delord**[a] **and Françoise Colobert**[*,a]

[a] Laboratoire d'Innovation Moléculaire et Applications, ECPM, UMR 7042, Université de Strasbourg/Université de Haute-Alsace, 25 rue Becquerel, Cedex 67087, Strasbourg, France

E-mail: francoise.colobert@unistra.fr (F. Colobert)

Abstract. Many natural, biologically active compounds are stereogenic with a unique tridimensional structure that is on the origin of the specific interactions with the active binding site.

This concept of chirality goes beyond chiral stereocenters, englobing also atropoisomerism related to a hindered rotation around an axis with the isolation of atropostable conformers at room temperature. Atropoisomerism is well-known in biaryls, however this phenomenon is encountered in many pharmaceutically relevant compounds such as heterobiaryl, diarylamines, benzamides and anilides.

Currently four FDA-approved drugs are atropostable and many others are in clinical trials. It is also important to note that almost 30% of recent FDA-approved small molecules are "proatropisomeric" and interact with a target in a specific chiral conformation.

Given this vivid interest in C–C but also C–N atropisomerically stable compounds, this account will detail the new atropoisomeric strategies we developed and their applications in the synthesis of relevant molecules and ligands.

Keywords. Atropoisomerism, C–H activation, Chiral sulfoxide, Natural products, Terphenyl ligands, C–N coupling.

Manuscript received 8 November 2023, revised and accepted 13 November 2023.

1. Introduction

The importance of axially chiral biaryl compounds is rapidly expanding. The main reason is their presence in numerous biologically active natural products and therapeutic agents. They are also the privileged backbone of ligands and catalysts in asymmetric catalysis. Regarding the importance of these scaffolds, numerous strategies have been reported and among them atropo-enantioselective metallo- or organo-catalyzed cross-coupling reactions have been successfully employed to efficiently synthesize a large panel of these scaffolds (for recent reviews on the synthesis of axially chiral biaryls see [1–5]). Recently asymmetric C–H activation has proved to be efficient to control the chirality and more particularly to synthesize axially chiral biaryls [6,7].

Over the past decade our laboratory has embarked on a research program dedicated to the control of atropoisomerism and we targeted at first differently substituted biaryl and triaryl skeletons bearing one or two atropisomeric axis. Our idea was to use a Pd-catalyzed atropo-diastereoselective C–H functionalization process using as chiral auxiliary an enantiopure sulfoxide, fixed on a configurationally unstable biaryl. Secondly, we turned our attention to the control of a C–N atropisomeric axis in N–Ar units via a Cu-catalyzed atroposelective aryl amination using hypervalent iodines as coupling partners (Figure 1).

* Corresponding author

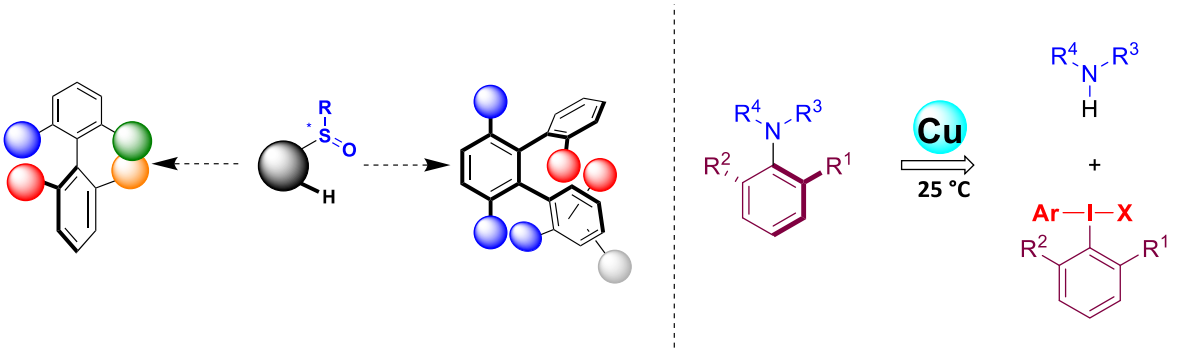

Figure 1. Csp^2-H activation: Axially chiral biaryl and triaryl compounds/Control of C–N atropisomeric axis via Ullmann-type C–N coupling reaction.

Capitalizing on our experience in total synthesis of biologically active compounds, we applied our atroposelective methods towards the synthesis of natural products as well as a new family of terphenyl ligands.

2. Results and discussion

Our first successful contribution to control atropoisomerism through a C–H activation-type protocol concerns a diastereoselective approach by using a chiral Directing Group (DG*). The chiral DG is utilized in stoechiometric amount and several criteria need to be fulfilled: the chiral DG must be (1) easy to install and not expensive (2) traceless or highly recyclable. The advantage compared to the enantioselective approach is the obtention of separable atropo-diastereomers. In addition the stereogenic center is in close proximity to both metal and substrate insuring an efficient chiral induction. We chose a sulfinyl moiety as chiral DG because we had already an extensive experience in the use of sulfoxides as chiral auxiliary (for the use of sulfoxides in Suzuki coupling reactions [8–10]). Moreover chiral sulfoxides are easily accessible on a large scale and the most important is its traceless character [11]. Sulfoxyde motif can be easily transformed via sulfoxide lithium exchange followed by electrophilic trapping with a myriad of electrophiles. Our initial hypothesis envisioned to start from a preformed biaryl, bearing the sulfinyl group in *ortho* position, and to introduce a substituent at the *ortho* position to the Ar–Ar′ linkage through a C–H functionalization process. One atropo-diastereomeric metallacycle was expected to be favored and the subsequent functionalization should thus occur in a stereoretentive manner, keeping the already fixed chirality. The removal or modification of the chiral sulfinyl group would allow the modular synthesis of axially chiral biaryls (Figure 2).

Thus, the hypothesis was validated by designing a Fujiwara–Moritani reaction with methyl acrylates or styrenes. We were delighted to obtain the corresponding coupling products in high yields and high atropo-diastereoselectivities [12–14]. Remarkably, the reaction is very tolerant towards many functional groups. Progressively, similar C–H acetoxylation in the presence of AcOH as well as the C–H iodination in the presence of *N*-iodosuccinimide (NIS) were developed, delivering the atropostable biaryls in excellent yields and stereoselectivities (Scheme 1) [15].

To rationalize these experimental results, a phenomenon of dynamic kinetic asymmetric transformation has been proposed and corroborated by DFT calculations. It was thus shown that the rotational barrier between the two substrates **S1** and **S2** is much higher than between the two palladacycles **C1** and **C2** (a difference of 10 kcal/mol) (Figure 3). Accordingly, the dynamic character of the overall transformation arises from a possible rotation around the chiral axis once the metallacyclic intermediates are formed whereas the substrate remains atropostable under the reaction conditions.

To demonstrate the broad synthetic utility of this atroposelective method, sulfinyl/Li exchange was performed at −78 °C to avoid the epimerisation of the atropisomeric axis and quenching with different electrophiles allows the introduction of different

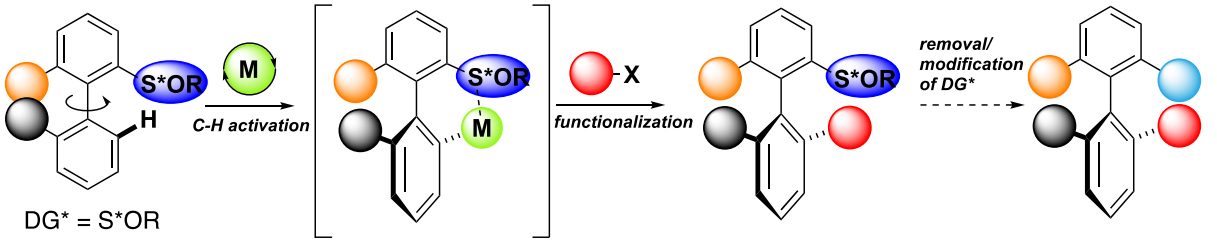

Figure 2. Axially chiral C–H functionalization of a biaryl moiety.

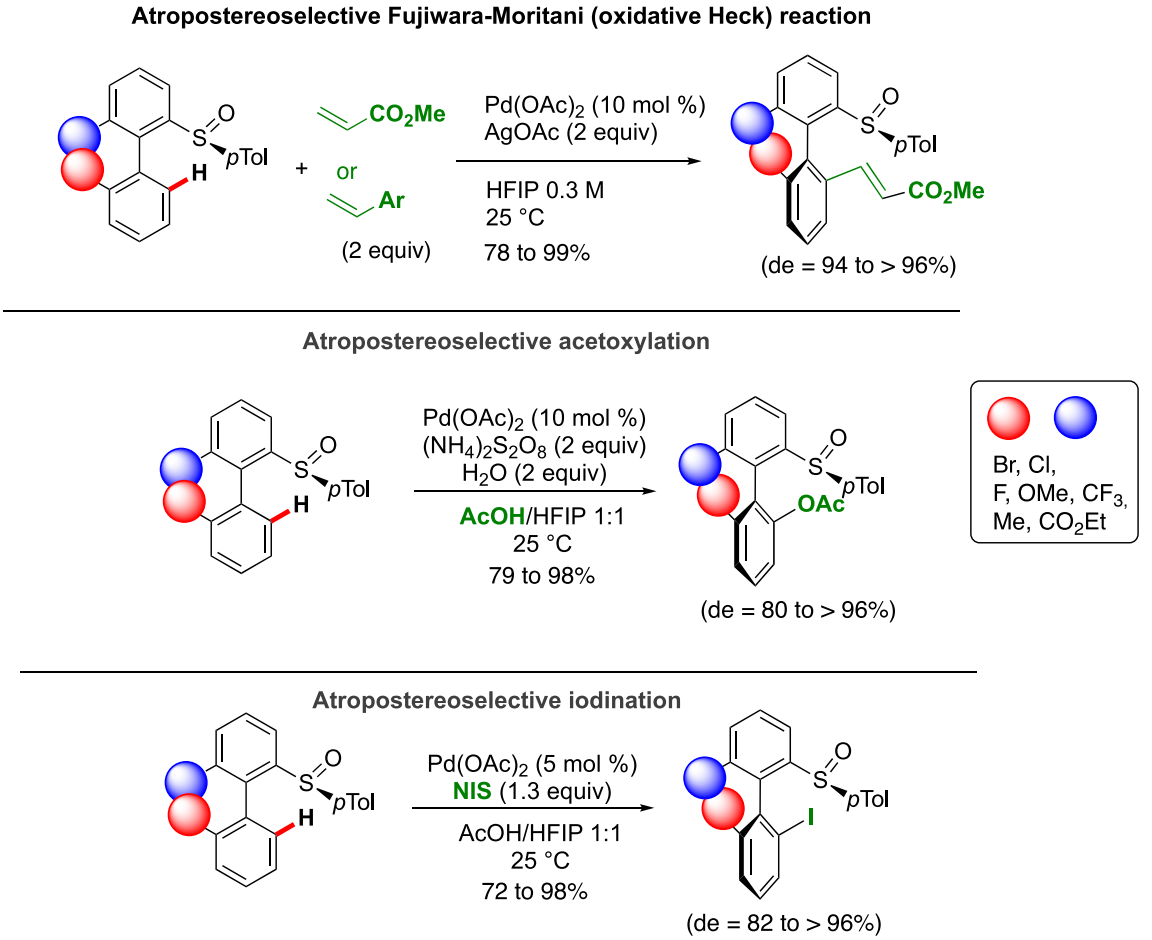

Scheme 1. Atropodiastereoselective oxidative Heck, acetoxylation and iodination.

functional groups with a total retention of the axial chirality (Scheme 2).

We applied this strategy to the formal synthesis of the biaryl subunit of (-)steganone that has been often used to illustrate the efficiency of a new atroposelective method. Starting from bromobenzodioxole we performed the most expedient synthesis in 10 steps with a 42.3% overall yield and with a total atropostereoselectivity (Scheme 3) [16].

Moreover, in collaboration with Speicher et al., we applied our method towards the first total synthesis of atropopure isoriccardin C. An atropostereose-

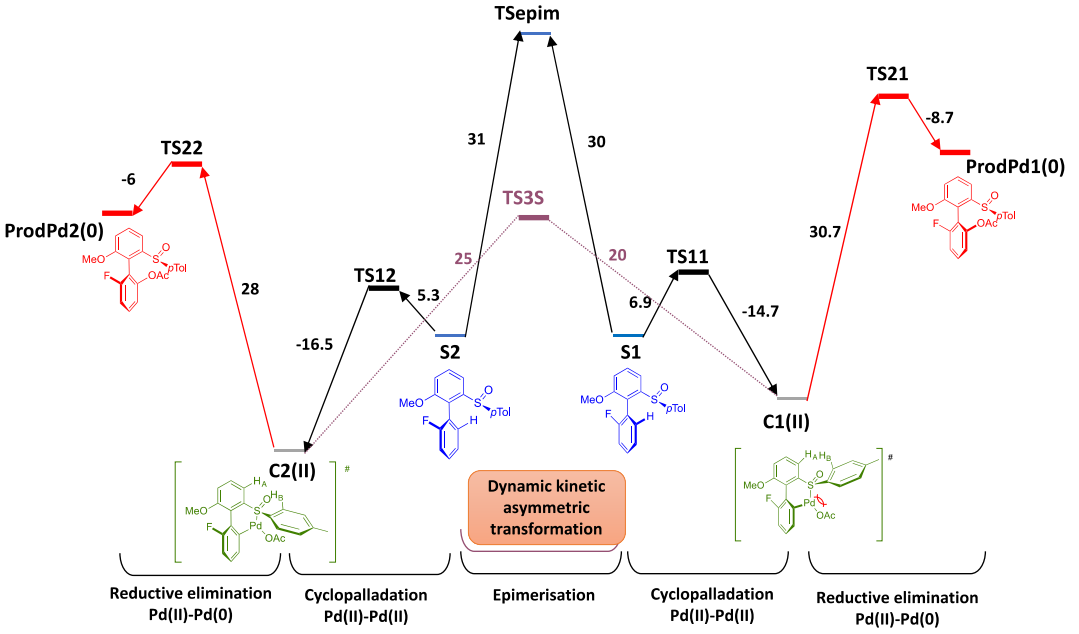

Figure 3. Conventional DFT studies in gazeous phase without solvatation.

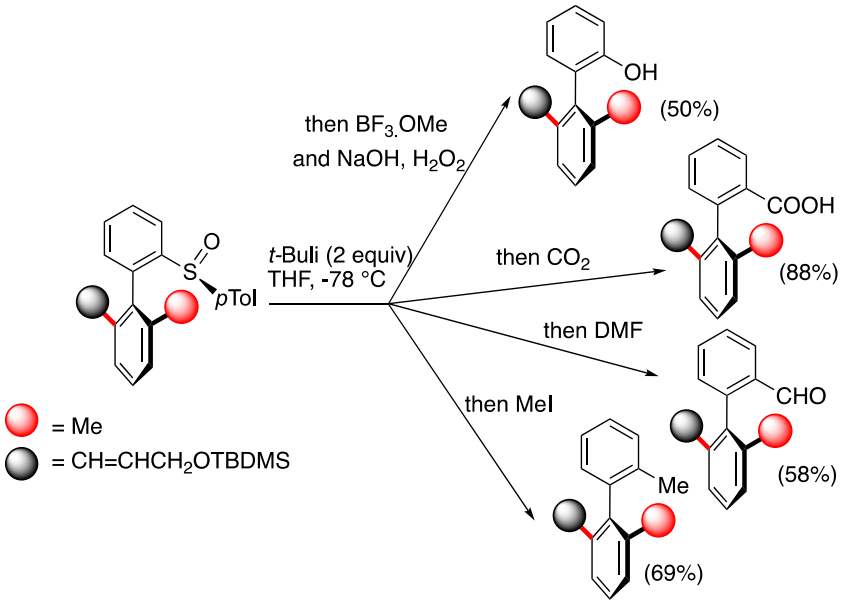

Scheme 2. Traceless character of the sulfinyl group.

lective macrocyclization through an oxidative Heck type C–H activation process allowed complete control of the atroposelectivity (de > 98%) and the traceless character of the sulfinyl moiety in *ortho* position of the biaryl enabled the introduction of an OH group (Scheme 4) [17].

Following this work, we were interested in the synthesis of doubly atropoisomeric, *ortho*-orientated

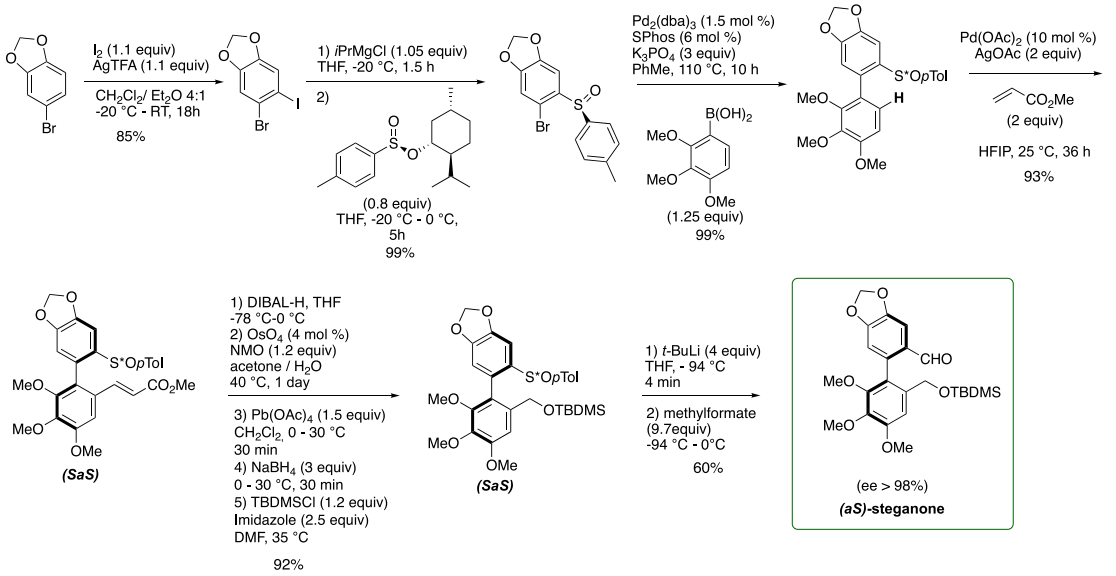

Scheme 3. Formal synthesis of the biaryl subunit of (-)steganone.

dissymmetrical terphenyls that are truly appealing for the design of chiral ligands. Following this idea we explored the C–H arylation of a biaryl bearing in the *ortho* position the chiral sulfinyl DG with *ortho*-substituted aryl iodides. After an extensive optimization of the reaction conditions, we succeeded in obtaining the terphenyl in moderate to good yields but with excellent atropo-diastereoselectivity. What is remarkable in this reaction is the control of the two contiguous chiral axes in one step. An X-ray crystal structure highlighted a unique architecture of these scaffolds, featuring a cavity comparable to the one of a seashell well designed for the coordination with metal in organometallic catalysis (Scheme 5) [18].

Of particular interest is the atropoenantiopure terphenyl scaffold **A**, bearing the sulfinyl group and the bromine which can be obtained in good yield (49%), with total atroposelectivity (>98:2) and on a gram scale in one day, this compound can be transformed by simple chemoselective lithium exchange and then quenched by various electrophiles to give access to a large variety of ligands. On the one hand, we performed the double exchange with Li base giving access to diphosphines BiaxPhos (Scheme 6) and, on the other hand, we developed an elegant two-step sequential chemoselective functionalization to install different coordinating groups like two different phosphines BiaxPhos* (Scheme 7) [19].

With the new ligands in hand, their potential in asymmetric catalysis, focusing mainly on the Ir-catalyzed hydrogenation of imines, was explored [20]. After optimization of the reaction conditions and catalyst screening, the desired chiral amines were isolated in high yields and excellent enantioselectivities under a remarkably low hydrogen pressure (Scheme 8) [19].

Intrigued by the growing interest of compounds with C–N atropoisomeric axes in medicinal chemistry with unique kinase inhibitor activities [21–31], we turned our attention to their atroposelective synthesis. However, the stereoselective control of the C–N axially chiral compounds remains a big challenge due to their low configurational stability compared to the well-developed C–C atropisomers and also due to the harsh reaction conditions generally required for the C–N coupling reaction. The extremely challenging character of these transformations is unambiguously illustrated by the lack of literature precedents on asymmetric Ullmann and Buchwald–Hartwig couplings.

Following such an ambitious goal, our idea was to use highly electrophilic coupling partners such as hypervalent iodines to perform the Cu-catalyzed C–N Ullmann-type coupling at low temperature to ensure the configurational stability of the C–N atropoisomer formed. Besides, the sterecontrol could

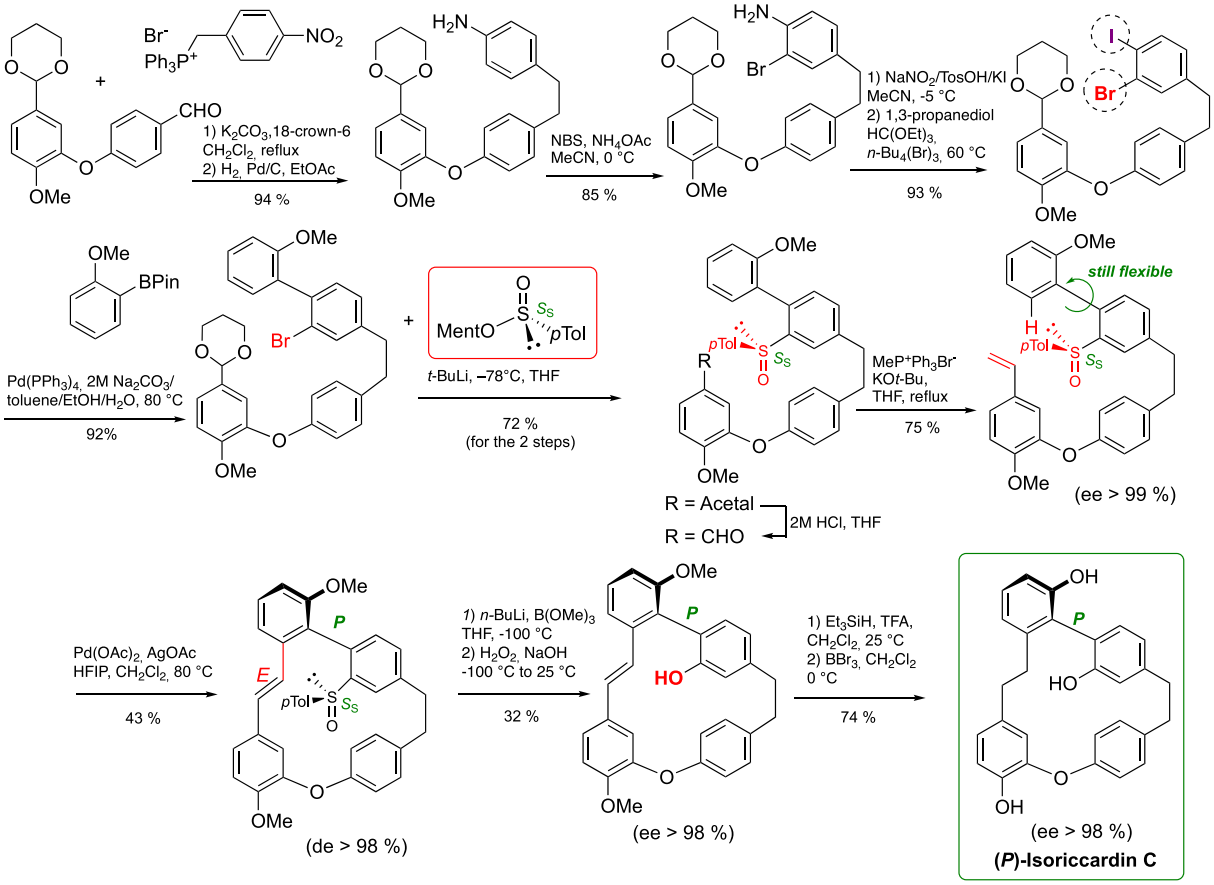

Scheme 4. Total synthesis of atropopure isoriccardin C.

be reached either with enantiomerically pure, stereogenic iodanes bearing a sulfinyl moiety allowing an atropo-diastereoselective C–N coupling with different N-coupling partners or using chiral ligands compatible with an atropo-enantioselective C–N coupling (Figure 4).

If we consider the atropo-diastereoselective C–N coupling occurring via the chiral transfer from the iodanes (sulfoxide-substituted iodanes were prepared by C–H functionalization of the arylsulfoxide with Koser's reagent), we studied the C–N coupling with indolines first as standard substrates, and we obtained the desired coupling products at room temperature in excellent yield and high atropopurity. However, in the first two examples, we noticed a slow racemization of the product at room temperature. Therefore, to increase the atropostability of the coupling products, substituted indolines at the C7 position or iodanes *ortho*-substituted by a methyl, instead of a methoxy, were used as coupling partners to obtain atropostable products [32].

Remarkably, the reaction tolerates many functional groups including chlorine, bromine, methoxy, benzyloxy but also boronic ester compatible for further functionalization (Scheme 9).

Subsequently, an atropo-enantioselective version of this C–N coupling was explored. Drawing inspiration from Gaunt et al. and Mc Millan et al. who investigated asymmetric copper-catalyzed coupling reaction with hypervalent iodines, the BOX-type ligand was preselected as the chirality source. We rapidly established that a free amide as DG on the iodine substrate was important to reach high enantioselectivity whereas the optimization of the BOX ligand revealed that the presence of benzyl

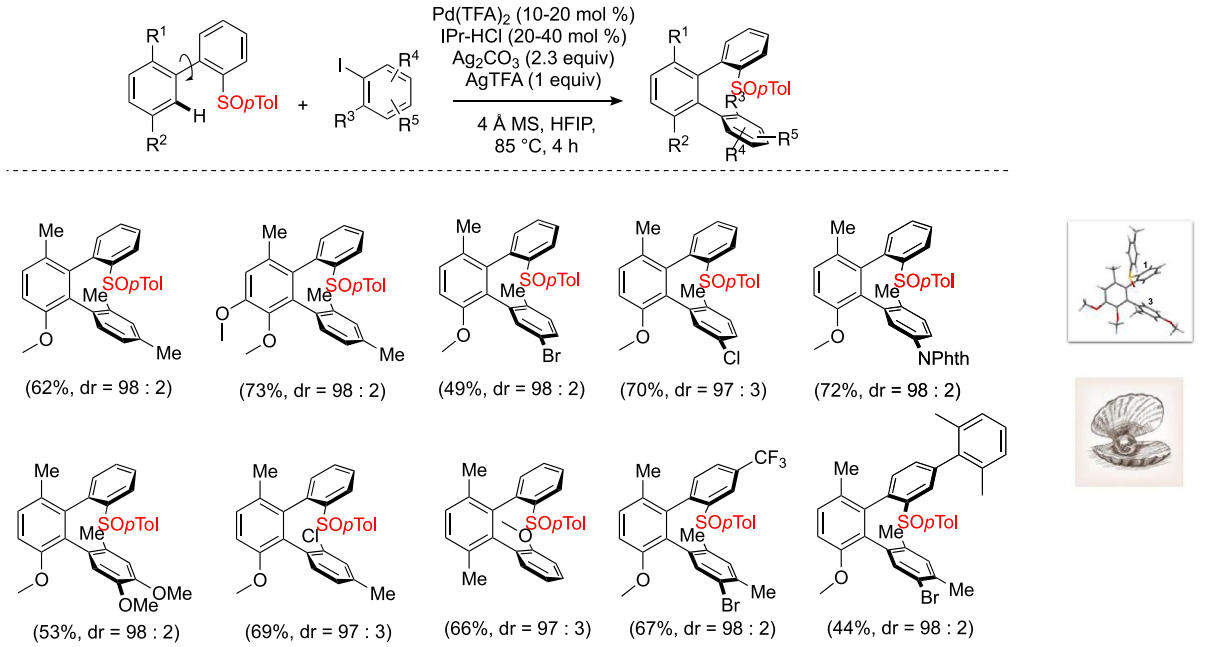

Scheme 5. Synthesis of terphenyls with two chiral axes.

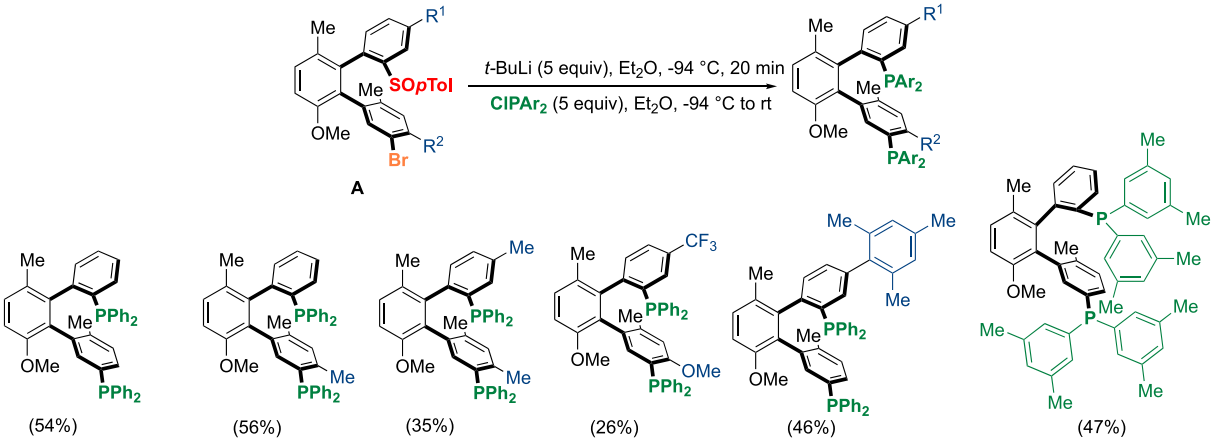

Scheme 6. Synthesis of diphosphines BiaxPhos bearing the same phosphorus moiety.

groups as well as gem-dimethyl group was essential. Optimization of the reactions conditions indicated that the addition of a Lewis acid such as $BF_3{\cdot}OEt_2$ warrants significantly increased yields [33].

The results, in most of the examples, show excellent enantioselectivities with moderate to good yields. As previously, a substituent in the C7 position of the indoline is necessary to guarantee atropostability of the newly formed axis. The presence of Cl-, Br-, F-substituents is well tolerated either on the indoline or the iodane.

The X-ray crystal structure which shows the absolute *aR*-configuration and a hydrogen bonding between the N atom of indoline and the free NH_2 is in

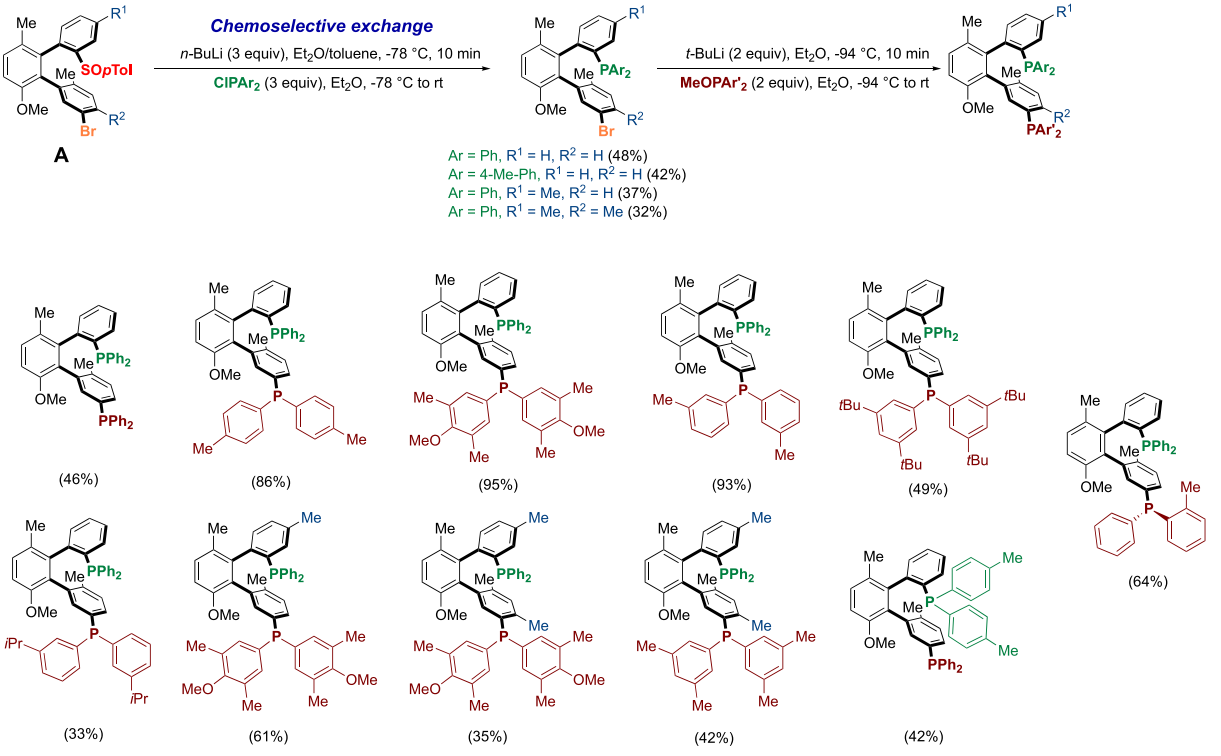

Scheme 7. Synthesis of diphosphines BiaxPhos* bearing different phosphorus moieties.

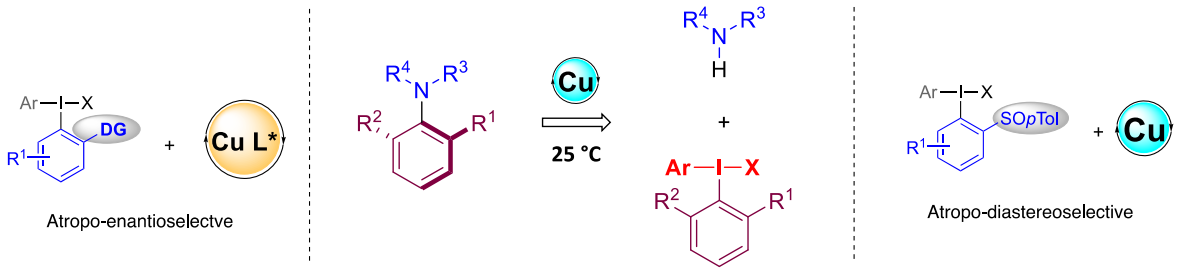

Figure 4. Cu-catalyzed atropo-stereoselective C–N coupling reaction.

agreement with the importance of the free amide as DG (Scheme 10).

In order to highlight the synthetic potential of this method, the post-modifications of the coupling products were studied. Thanks to the traceless character of the sulfoxide, various functional groups could be introduced such as, for example, an aldehyde. The halogenated substrates allow mild Stille- and Suzuki-coupling under micellar conditions, thus overcoming the racemization issues. Oxydation of indoline to indole works very well with sulfinyl or amide DG. Moreover, indoline-2,3-dione, a privileged synthetic intermediate of oxindole scaffolds could also be obtained by oxydation with *t*-butylhydroperoxide in presence of copper. The amide DG can be transformed in two steps into a carboxylic acid with a complete atropostability (Figure 5).

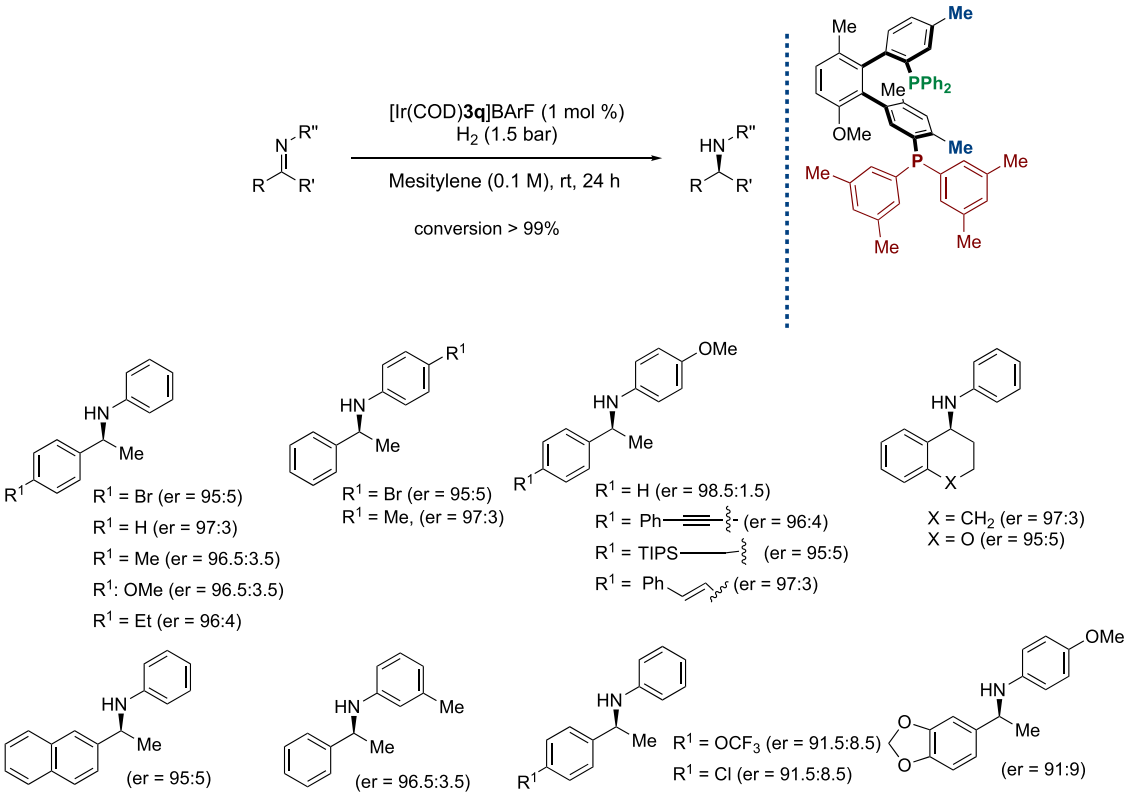

Scheme 8. Ir-catalyzed asymmetric hydrogenation of imines with BiaxPhos* ligands.

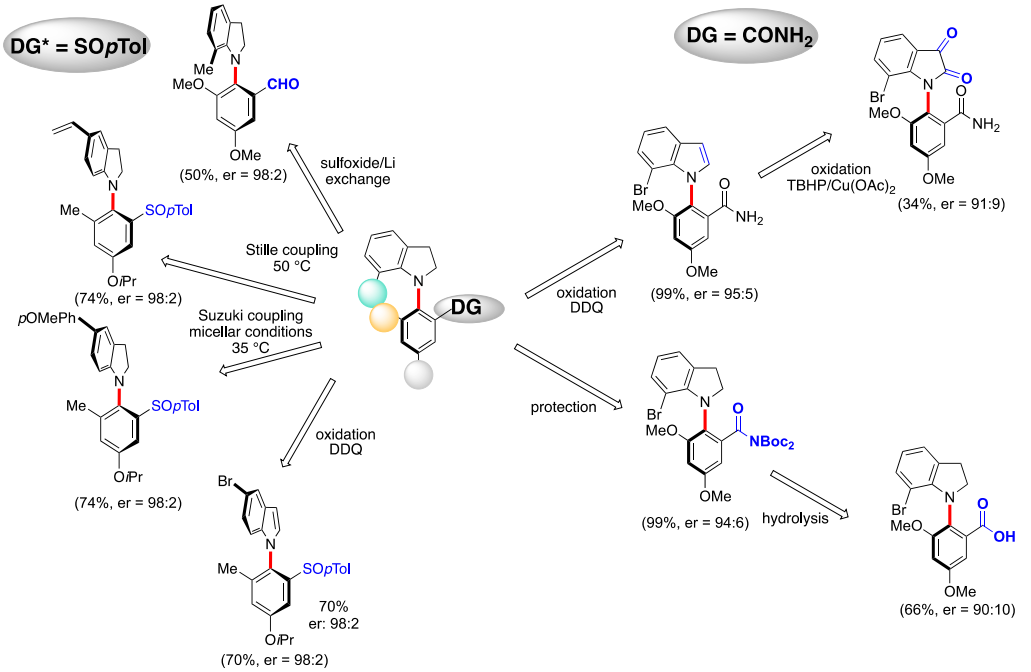

Figure 5. Postfunctionalization of the C–N atropoenriched coupling products.

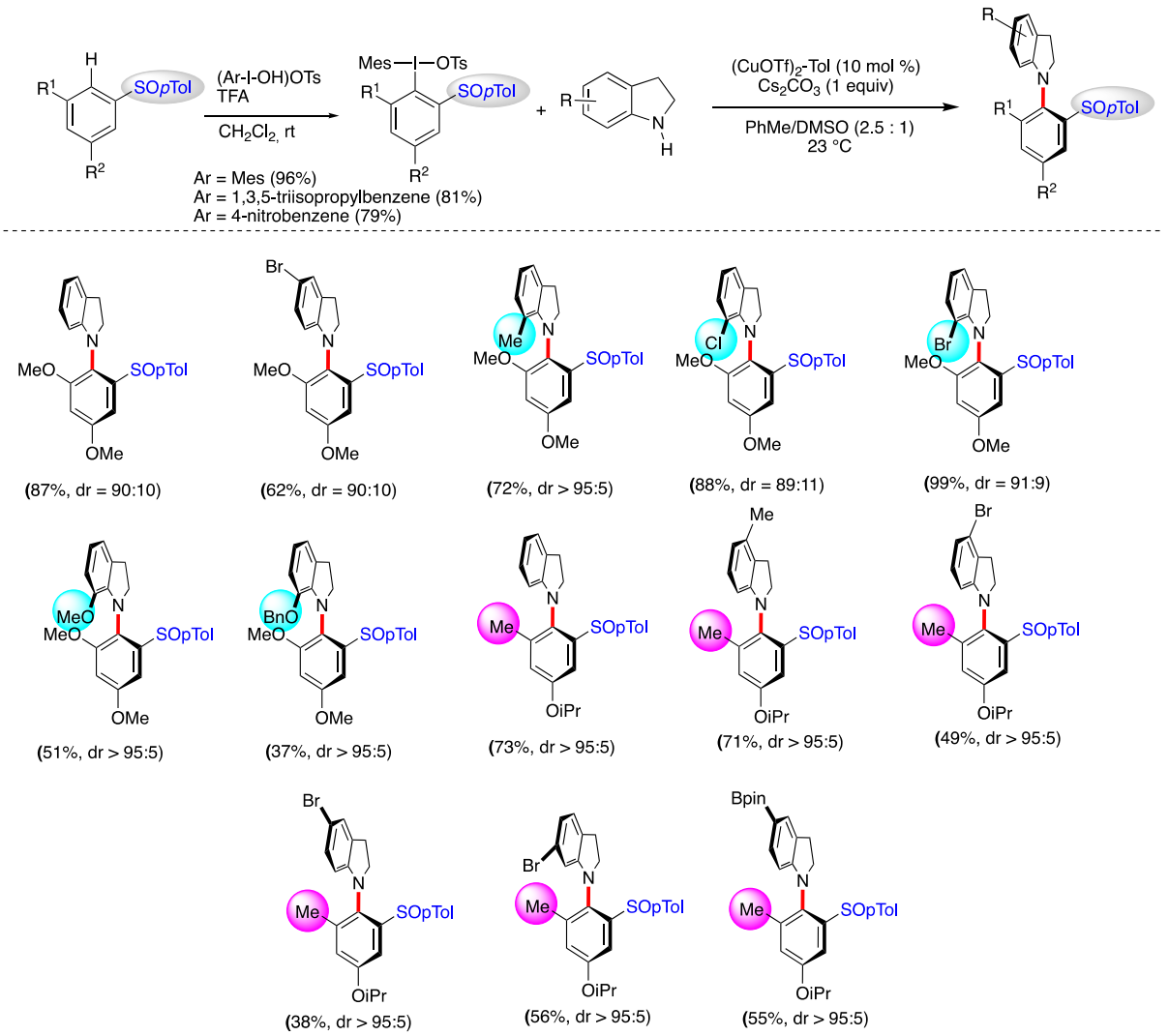

Scheme 9. Cu-catalyzed Ullmann-type C–N coupling using a chiral sulfinyl directing group.

In conclusion, this account summarizes our recent efforts to control atropoisomerism in both biaryl and aryl-N-(het)aryl molecules. The general methods described such as the C–H functionalization of the biarylsulfoxide afforded complex molecules such as biologically active natural products: steganone and isoriccardin C. In parallel, the challenging C–H arylation gives access to unprecendented terphenyl ligands with two atropisomeric axes that have been demonstrated to be highly efficient in Ir-catalyzed asymmetric hydrogenation. Their original scaffold as well as their modularity are appealing candidates for asymmetric catalysis in the future.

In addition, the use of hypervalent iodines in Ullmann type C–N coupling at room temperature solved the problem of the weak atropostability of the C–N axis leading to C–N axially chiral compounds in high stereoselectivities. This first example of atroposelective N-arylation, using hypervalent iodines, is opening the way to synthesize different C–N axially chiral products with different N-coupling partners.

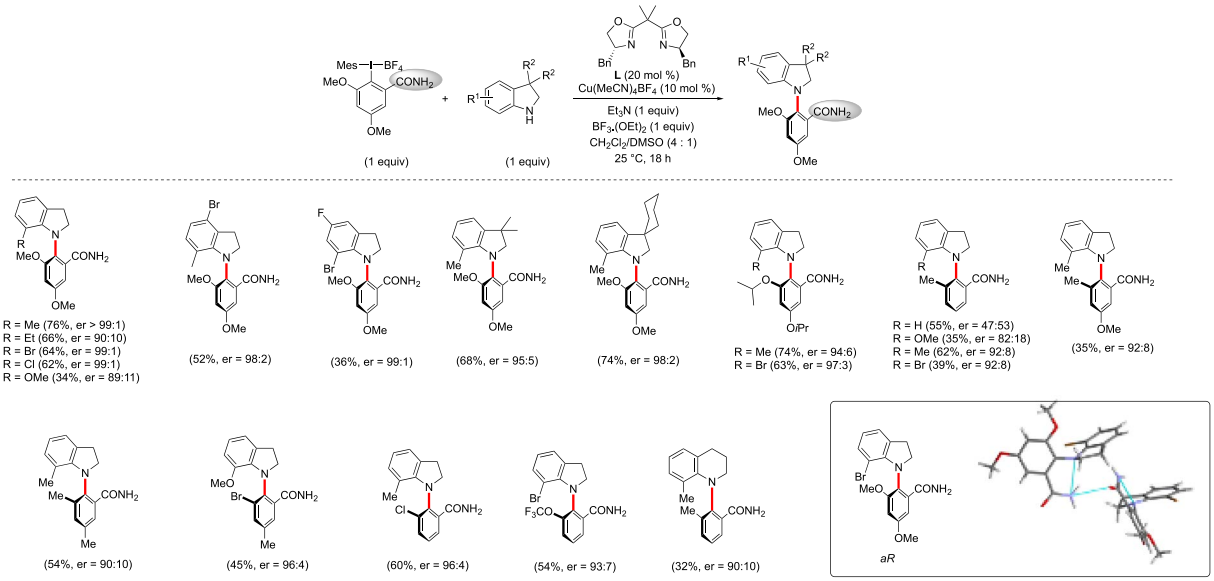

Scheme 10. Cu-catalyzed Ullmann-type C–N coupling using a BOX ligand.

Declaration of interests

The authors do not work for, advise, own shares in, or receive funds from any organization that could benefit from this article, and have declared no affiliations other than their research organizations.

References

[1] J. Wencel-Delord, A. Panossian, F. R. Leroux, F. Colobert, *Chem. Soc. Rev.*, 2015, **44**, 3418-3430.

[2] G. Bringmann, T. Gulder, T. A. M. Gulder, M. Breuning, *Chem. Rev.*, 2011, **111**, 563-639.

[3] M. C. Kozlowski, B. J. Morgan, E. C. Linton, *Chem. Soc. Rev.*, 2009, **38**, 3193-3207.

[4] G. Bringmann, A. J. Price Mortimer, P. A. Keller, M. J. Gresser, J. Garner, M. Breuning, *Angew. Chem. Int. Ed.*, 2005, **44**, 5384-5427.

[5] O. Baudoin, *Eur. J. Org. Chem.*, 2005, **2005**, 4223-4229.

[6] G. Liao, T. Zhou, Q. Yao, B.-F. Shi, *Chem. Commun.*, 2019, **55**, 8514-8523.

[7] J. Wencel-Delord, F. Colobert, *Synlett*, 2015, **26**, 2644-2658.

[8] F. Colobert, V. Valdivia, S. Choppin, F. R. Leroux, I. Fernández, E. Álvarez, N. Khiar, *Org. Lett.*, 2009, **11**, 5130-5133.

[9] P.-E. Broutin, F. Colobert, *Org. Lett.*, 2005, **7**, 3737-3740.

[10] T. Leermann, P.-E. Broutin, F. R. Leroux, F. Colobert, *Org. Biomol. Chem.*, 2012, **10**, 4095-4102.

[11] F. R. Leroux, A. Berthelot, L. Bonnafoux, A. Panossian, F. Colobert, *Chem. Eur. J.*, 2012, **18**, 14232-14236.

[12] T. Wesch, F. R. Leroux, F. Colobert, *Adv. Synth. Cat.*, 2013, **355**, 2139-2144.

[13] J. Wencel-Delord, F. Colobert, *Chem. Eur. J.*, 2013, **19**, 14010-14017.

[14] Q. Dherbassy, G. Schwertz, M. Chessé, C. Kumar Hazra, J. Wencel-Delord, F. Colobert, *Chem. Eur. J.*, 2016, **22**, 1735-1743.

[15] C. K. Hazra, Q. Dherbassy, J. Wencel-Delord, F. Colobert, *Angew. Chem. Int. Ed.*, 2014, **53**, 13871-13875.

[16] Q. Dherbassy, J. Wencel-Delord, F. Colobert, *Tetrahedron*, 2016, **72**, 5238-5245.

[17] L. Marx, D. Lamberty, S. Choppin, F. Colobert, A. Speicher, *Eur. J. Org. Chem.*, 2021, **9**, 1351-1354.

[18] Q. Dherbassy, J.-P. Djukic, J. Wencel-Delord, F. Colobert, *Angew. Chem. Int. Ed.*, 2018, **57**, 4668-4672, *Nature*, research highlight, April 10 2018. Patent 14/12/2017 N° EP17306779.4.

[19] G. Hedouin, R. A. A. Abdine, Q. Dherbassy, I. Funes-Ardoiz, F. Colobert, J. Wencel-Delord, *Adv. Synth. Catal.*, 2023, **365**, 1995-2005.

[20] R. A. A. Abdine, G. Hedouin, F. Colobert, J. Wencel-Delord, *ACS Catal.*, 2021, **11**, 215-247.

[21] P. W. Glunz, *Bioorg. Med. Chem. Lett.*, 2018, **28**, 53-60.

[22] S. T. Toenjes, J. L. Gustafson, *Future Med. Chem.*, 2018, **10**, 409-422.

[23] S. R. LaPlante, L. D. Fader, K. R. Fandrick, D. R. Fandrick, O. Hucke, R. Kemper, S. P. F. Miller, P. J. Edwards, *J. Med. Chem.*, 2011, **54**, 7005-7022.

[24] G. Beutner, R. Carrasquillo, P. Geng, Y. Hsiao, E. C. Huang, J. Janey, K. Katipally, S. Kolotuchin, T. La Porte, A. Lee *et al.*, *Org. Lett.*, 2018, **20**, 3736-3740.

[25] J. Chandrasekhar, R. Dick, J. Van Veldhuizen, D. Koditek, E.-

I. Lepist, M. E. McGrath, L. Patel, G. Phillips, K. Sedillo, J. R. Somoza *et al.*, *J. Med. Chem.*, 2018, **61**, 6858-6868.

[26] T. Sugane, T. Tobe, W. Hamaguchi, I. Shimada, K. Maeno, J. Miyata, T. Suzuki, T. Kimizuka, S. Sakamoto, S. Tsukamoto, *J. Med. Chem.*, 2013, **56**, 5744-5756.

[27] J. Wang, W. Zeng, S. Li, L. Shen, Z. Gu, Y. Zhang, J. Li, S. Chen, X. Jia, *ACS Med. Chem. Lett.*, 2017, **8**, 299-303.

[28] S. H. Watterson, G. V. De Lucca, Q. Shi, C. M. Langevine, Q. Liu, D. G. Batt, M. Beaudoin Bertrand, H. Gong, J. Dai, S. Yip *et al.*, *J. Med. Chem.*, 2016, **59**, 9173-9200.

[29] S. R. Selness, R. V. Devraj, B. Devadas, J. K. Walker, T. L. Boehm, R. C. Durley, H. Shieh, L. Xing, P. V. Rucker, K. D. Jerome *et al.*, *Bioorg. Med. Chem. Lett.*, 2011, **21**, 4066-4071.

[30] A. L. Leivers, M. Tallant, J. B. Shotwell, S. Dickerson, M. R. Leivers, O. B. McDonald, J. Gobel, K. L. Creech, S. L. Strum, A. Mathis *et al.*, *J. Med. Chem.*, 2014, **57**, 2091-2106.

[31] F. Hasegawa, K. Kawamura, H. Tsuchikawa, M. Murata, *Bioorg. Med. Chem.*, 2017, **25**, 4506-4511.

[32] J. Rae, J. Frey, S. Jerhaoui, S. Choppin, J. Wencel-Delord, F. Colobert, *ACS Catal.*, 2018, **8**, 2805-2809.

[33] J. Frey, A. Malekafzali, I. Delso, S. Choppin, F. Colobert, J. Wencel-Delord, *Angew. Chem. Int. Ed.*, 2020, **59**, 8844-8848.

ACADÉMIE DES SCIENCES
INSTITUT DE FRANCE

Comptes Rendus. Chimie
2024, Vol. 27, Special issue S2, p. 33-38
https://doi.org/10.5802/crchim.278

Research article

Women Chemists in France in 2024

Direct ring fluorination of 3-substituted 5-(1,3-dioxane) acetal isoxazoles: application to the formal synthesis of a bioactive fluorinated isoxazole

Lucas Bacheley [a,b], Gérard Guillamot [b], Phannarath Phansavath [*,a] and Virginie Ratovelomanana-Vidal [*,a]

[a] PSL University, Chimie ParisTech, CNRS UMR 8060, Institute of Chemistry for Life and Health Sciences, CSB2D Team, 75005 Paris, France

[b] SEQENS, 2-8 rue de Rouen, ZI de Limay-Porcheville, 78440 Porcheville, France

E-mails: phannarath.phansavath@chimieparistech.psl.eu (P. Phansavath), virginie.vidal@chimieparistech.psl.eu (V. Ratovelomanana-Vidal)

Abstract. The access to a novel variety of 4-fluorinated isoxazoles bearing an aryl or alkyl group at the C-3 position and an acetal fragment at the C-5 position has been achieved through a direct fluorination using N-fluorobenzenesulfonimide (NFSI) with yields up to 75%. This method was transposed to gram-scale and has been applied to the formal synthesis of a bioactive compound that increases CFTR (Cystic Fibrosis Transmembrane Conductance Regulator) activity.

Keywords. Fluorination, Isoxazoles, Heterocycles.

Funding. This work was supported by the Ministère de l'Enseignement Supérieur et de la Recherche (MESR) and the Centre National de la Recherche Scientifique (CNRS). LB is grateful to SEQENS for a grant (2021–2024).

Manuscript received 24 November 2023, revised and accepted 6 December 2023.

1. Introduction

Heterocyclic scaffolds represent the largest family of organic compounds and have a role in many fields of sciences such as medicinal chemistry [1,2], biochemistry [3] or agrochemistry [4,5]. More specifically, the isoxazole skeleton is a very important motif found in natural products or synthetic products such as antibiotics [6], analgesics [7], antirheumatic [8], anti-inflammatory [9] or antidepressant compounds [10].

Furthermore, the interest of fluorine and its methods of introduction are still gaining increasing interest as fluorination of an organic molecule significantly impacts its biological characteristics. In spite of the significant fascination for fluorine, the challenge of integrating this element into essential building blocks has postponed the examination and comprehension of its impacts as well as its utilization. Nonetheless, notable advancement has been achieved in the field over the previous decade. Considering the size of the fluorine atom and its electronegativity, the incorporation of a fluorine or a trifluoromethyl group profoundly modifies both the pharmacodynamics and pharmacokinetics of the compounds such as lipid solubility, metabolic stabil-

* Corresponding authors

ity or acidity [11]. Moreover, it can increase the potency of a substance's engagement with a specific target protein.

Roughly 30% of all agrochemicals and 20% of all pharmaceuticals encompass fluorine [12] within their structures.

With the aim of continuing our investigations into the synthesis of fluorinated carbocycles and heterocycles [13–17], we envisaged to focus on a synthetic pathway for the fluorination of an isoxazole functionalized at C-5 by an acetal fragment, an area that has been relatively overlooked in the literature despite numerous molecules of interest featuring this motif (Figure 1) [18–23]. The synthesis of 4-fluorinated 3,5-disubstituted isoxazole was reported by either condensation of 2-fluoro-1,3-diketone [24,25] or gold-catalyzed cascade cyclization-fluorination of 2-alkynone *O*-methyl oximes [26] but only one method for the direct fluorination in this position was reported relying on the use of Selectfluor as the fluorinating agent and delivering the desired products in moderate chemical yields ranging from 16% to 44% (Figure 2) [27,28]. Furthermore, the products generated during the reaction cannot undergo additional post-functionalization. In this context, the direct fluorination at the C-4 position of the 3,5-disubstituted isoxazole core, as a late-stage functionalization, was explored. With the substitution of an acetal group at the C-5 position, the resulting fluoroisoxazoles can undergo deprotection, opening-up numerous possibilities for additional functionalization.

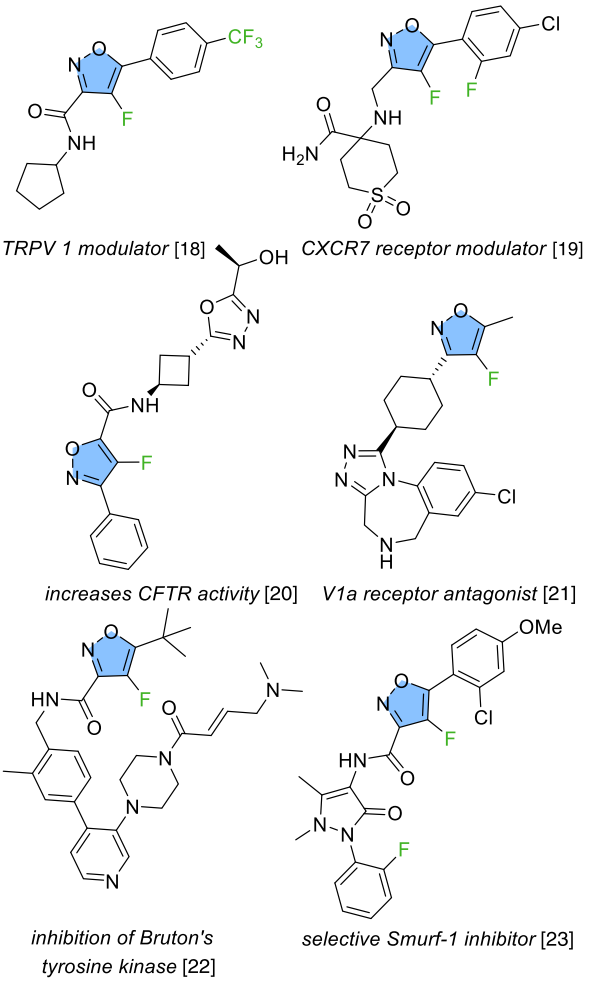

Figure 1. Examples of bioactive molecules containing a 4-fluorinated isoxazole core.

2. Results and discussion

A range of 3,5-disubstituted isoxazoles **1a-1k** were prepared from diversely substituted chloroximes and bromovinyl acetals, according to a three-step procedure developed previously [29]. Having those substrates in hand, our study started with a series of optimization experiments on 5-(1,3-dioxan-2-yl)-3-phenylisoxazole **1a** (Table 1). The first experiment required 3.5 equiv of base and N-fluorobenzenesulfonimide (NFSI) to afford the fluorinated isoxazole **2a** in 47% yield for a conversion of 63% at −78 °C (Table 1, entry 1). Other commercially available electrophilic fluorinated agent such as Selectfluor or *N*-fluoropyridinium triflate were tested but no conversion was observed under these conditions. Reducing the quantity of base and fluorinating agent to 1.2 and 2.0 equiv respectively led to better conversions (72–74%) and higher yields in **2a** (60–62%) (Table 1, entries 2–3). Subsequently, the impact of the starting material concentration in THF on the reaction outcome was examined. The concentration was gradually increased step by step from 0.1 mol/L to 1.0 mol/L (Table 1, entries 4–9), leading to an optimized yield of 75% at 0.4 mol/L (Table 1, entry 6). In fact, for a concentration higher than 0.6 mol/L, the reaction medium reaches such a viscosity that stirring stops after addition of the electophile.

Carrying out the reaction at −40 °C to achieve a full conversion led to complete degradation of the

Table 1. Optimisation of the reaction conditions[a]

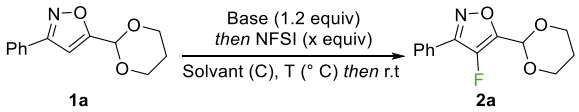

Entry	Base	Solvent	x (equiv)	c (mol/L)	T	t (h)	Conversion[b] (%)	Yield[c] (%)
1	*n*-BuLi	THF	3.5[d]	0.05	−78 °C	20	63	47
2	*n*-BuLi	THF	2.5[e]	0.05	−78 °C	20	72	62
3	*n*-BuLi	THF	2.0	0.05	−78 °C	2	74	60
4	*n*-BuLi	THF	2.0	0.1	−78 °C	2	78	61
5	*n*-BuLi	THF	2.0	0.2	−78 °C	2	82	73
6	*n*-BuLi	THF	2.0	0.4	−78 °C	1	85	75
7	*n*-BuLi	THF	2.0	0.6	−78 °C	0.5	89	71
8	*n*-BuLi	THF	2.0	0.8	−78 °C	0.5	91	70
9	*n*-BuLi	THF	2.0	1.0	−78 °C	0.5	90	70
10	*n*-BuLi	THF	2.0	0.2	−40 °C	1	100	0[f]
11	*n*-BuLi	Et_2O	2.0	0.2	−78 °C	3	20	nd
12	*n*-BuLi	MeTHF	2.0	0.2	−78 °C	1	58	nd
13	LiHMDS	THF	2.0	0.4	−78 °C	0.5	0	nd
14	LiHMDS	THF	2.0	0.4	0 °C	0.5	0	nd
15	LiTMP	THF	2.0	0.3	−78 °C	0.5	100	0[f]
16	LDA	THF	2.0	0.1	−78 °C	1.5	81	67
17	NaH	THF	2.0	0.1	0 °C	2	0	nd

[a]Reaction conditions: (**1a**, 0.43 mmol, 1.0 equiv), *n*BuLi (0.52 mmol, 1.2 equiv), NFSI (0.86 mmol, 2.0 equiv), THF (0.4 M, 1.1 mL), −78 °C to rt, under argon.

[b]After NMR ^{1}H analysis of the crude reaction mixture.

[c]After isolation by column chromatography.

[d]3.5 equiv of base were used.

[e]1.5 equiv of base were used.

[f]Only degradation was observed.

starting material (Table 1, entry 10). Other solvents were tested such as Et_2O or 2-MeTHF, but lower conversions were observed (20% and 58% respectively, Table 1, entries 11 and 12). The influence of the base was also studied. The starting material was fully recovered when treated with LiHMDS at −78 °C and 0 °C or with NaH at 0 °C (Table 1, entries 13, 14 and 17). Unfortunately, LiTMP led to a complete degradation of the isoxazole (Table 1, entry 15). Using LDA gave an encouraging result of 81% conversion and 67% yield in **2a** but was still inferior when *n*-BuLi was used (Table 1, entries 16 vs 6).

Having these optimized conditions in hand, we further explored the scope and limitations of the reaction with 3,5-disubstituted isoxazoles previously synthesized. This process allowed us to obtain the corresponding fluorinated isoxazoles bearing various electron-donating or -withdrawing substituents in the *para*-position of the aryl ring such as *t*-butyl-**2b**, chlorine **2c**, fluorine **2d** or trifluoromethyl **2e** groups in yields between 59–70%. Compounds **2g** and **2h** having a 3-chloro-4-fluorophenyl or a 2,6-dichlorophenyl substituent were obtained in 44% and 21% yield, respectively (Figure 3). Having a

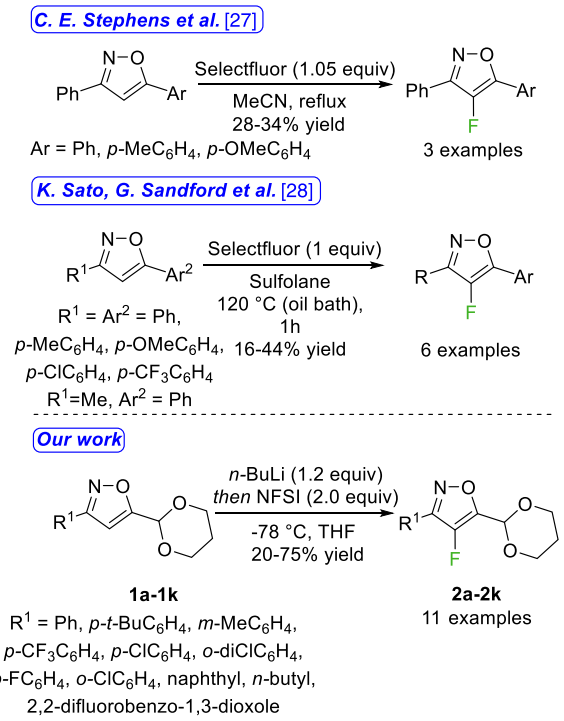

Figure 2. Synthesis of a 4-fluorinated 3,5-disubstituted isoxazoles by direct fluorination.

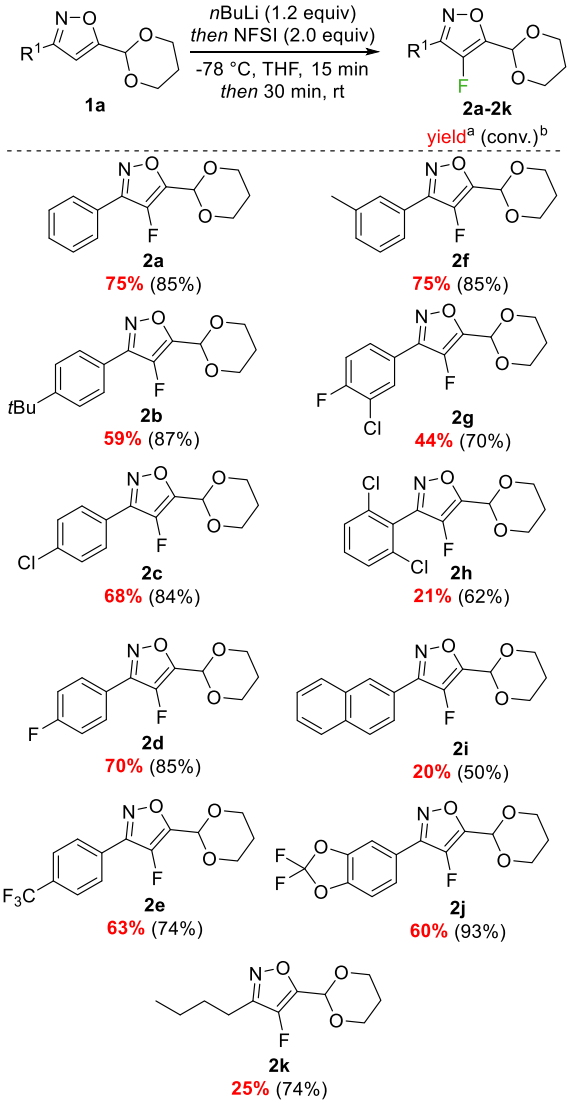

[a] isolated yield after column chromatography [b] after ^{1}H NMR analysis of the crude reaction mixture.

Figure 3. Scope of the fluorination.

methyl in *meta*-position (**1f**) led to 75% isolated yield of the corresponding fluorinated product **2f**. To extend the feasibility of our process, a bulky group such as a naphthyl or a 2,2-difluorobenzodioxole was also investigated and afforded the products **2i** and **2j** in 20% and 60% yields, respectively. The reaction was also suitable for isoxazoles bearing a non-aromatic substituent at the C-3 position and compound **2k**, bearing a *n*-butyl chain, was synthesized in 25% yield.

Furthermore, our goal was to obtain a range of fluorinated isoxazoles that could be subsequently modified after deprotection of the acetal fragment at the C-5 position. In this context, the acetal was deprotected in acidic media (HCl 1N, 5 equiv), in a mixture of water/acetone (1/1) for 4 days at 90 °C affording the corresponding aldehyde **3a** in 65% yield (Figure 4).

Isoxazole **3a** is an intermediate in the preparation of a bioactive compound that increases Cystic Fibrosis Transmembrane Conductance Regulator (CFTR) activity [15]. Cystic fibrosis is a result of genetic mutations in the CFTR gene, responsible for encoding a chloride channel that spans multiple cell membranes in epithelial tissues. The loss of a functional CFTR channel leads to a reduced lung function and increases mucus viscosity resulting in chronic infection and inflammation [30]. Besides respiratory impairment, CFTR also affects the regular operation of additional organs such as the pancreas, intestine, or gall bladder.

The effectiveness of this fluorination process was supported by a scale-up experiment conducted

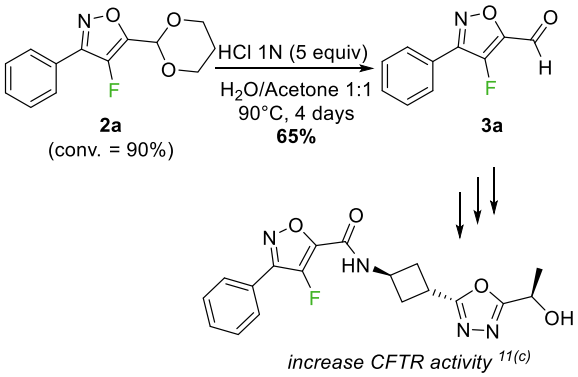

Figure 4. Formal synthesis of a bioactive compound that increases CFTR activity.

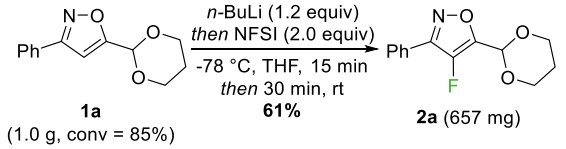

Figure 5. Scale-up experiment of the fluorination of **1a**.

under the defined standard conditions using 5-(1,3-dioxan-2-yl)-3-phenylisoxazole **1a** (Figure 5) to obtain the desired fluorinated product **2a** in 61% yield.

3. Conclusion

In conclusion, we succeeded in synthesizing a range of new 4-fluorinated 3,5-disubstituted isoxazoles bearing various substituents on the aromatic ring at the C-3 position in 20–75% yields. This process was also tolerant to bulkier substituents such as a naphthyl or a difluorodioxobenzene and even a non-aromatic substituent such as a *n*-butyl fragment. The objective of this project was also to obtain a substrate that could be subsequently functionalized. This was achieved through the deprotection of the acetal, resulting in a much more advantageous aldehyde for subsequent post-functionalization. The usefulness of this method was demonstrated through the formal synthesis of a bioactive compound that increases CFTR activity.

Declaration of interests

The authors do not work for, advise, own shares in, or receive funds from any organization that could benefit from this article, and have declared no affiliations other than their research organizations.

Acknowledgement

We thank Dr. C. Fosse (Chimie ParisTech - PSL) for HRMS analysis.

Supplementary data

Supporting information for this article is available on the journal's website under https://doi.org/10.5802/crchim.278 or from the author.

References

[1] J. Jampilek, *Molecules*, 2019, **24**, article no. 3839.
[2] A. Amin, T. Qadir, P. K. Sharma, I. Jeelani, H. Abe, *Open J. Med. Chem.*, 2022, **16**, article no. e187410452209010.
[3] E. Kabir, M. Uzzaman, *Results Chem.*, 2022, **4**, article no. 100606.
[4] C. Lamberth, *Pest Manag. Sci.*, 2013, **69**, 1106-1114.
[5] E. A. Al-Harbi, W. A. Gad, *Agri. Res. Tech.: Open Access J.*, 2018, **16**, 60-61.
[6] R. Sutherland, E. A. P. Croydon, G. N. Robinson, *Br. Med. J.*, 1970, **4**, 455-460.
[7] R. Pollak, G. A. Raymond, R. M. Jay, H. J. Hillstrom, K. T. Mahan, D. Riff, E. L. Jacobs, M. T. Brown, K. M. Verburg, *J. Am. Podiatr. Med. Assoc.*, 2006, **96**, 393-407.
[8] M. M. Goldenberg, *Clin. Ther.*, 1999, **21**, 1837-1852.
[9] G. Cingolani, A. Panella, M. G. Perrone, P. Vitale, G. Di Mauro, C. G. Fortuna, R. S. Armen, S. Ferorelli, W. L. Smith, A. Scilimati, *Eur. J. Med. Chem.*, 2017, **138**, 661-668.
[10] I. Fagervall, S. B. Ross, *Biochem. Pharmacol.*, 1986, **35**, 1381-1387.
[11] H.-J. Böhm, D. Banner, S. Bendels, M. Kansy, B. Kuhn, K. Müller, U. Obst-Sander, M. Stahl, *ChemBioChem*, 2004, **5**, 637-643.
[12] K. Müller, C. Faeh, F. Diederich, *Science*, 2007, **317**, 1881-1886.
[13] A. Westermeyer, G. Guillamot, P. Phansavath, V. Ratovelomanana-Vidal, *New J. Chem.*, 2020, **44**, 20535-20543.
[14] R. Molina Betancourt, P. Phansavath, V. Ratovelomanana-Vidal, *J. Org. Chem.*, 2021, **86**, 12054-12063.
[15] R. Molina Betancourt, P. Phansavath, V. Ratovelomanana-Vidal, *Molecules*, 2022, **27**, 1-15.
[16] R. Molina Betancourt, L. Bacheley, A. Karapetyan, G. Guillamot, P. Phansavath, V. Ratovelomanana-Vidal, *ChemCatChem*, 2022, **14**, article no. e202200595.

[17] L. Bacheley, R. Molina Betancourt, R. Ravindra, G. Guillamot, P. Phansavath, V. Ratovelomanana-Vidal, *Eur. J. Org. Chem.*, 2023, **26**, article no. e202300383.
[18] A. L. Roughton, K.-K. Ho, M. Ohlmeyer, I. Neagu, S. G. Kultgen, N. Ansari, Y. Rong, P. D. Ratcliffe, R. Palin, 2009, WO 2009/016241.
[19] H. Aissaoui, P. Guerry, F. Lehembre, J. Pothier, L. Pouzol, S. Richard-Bildstein, S. Yuan, 2018, WO 2018/019929.
[20] C. Bastos, B. Munoz, B. Tait, 2016, WO 2016/105485.
[21] C. Dolente, P. Schnider, 2011, US 2011/0275801.
[22] B. T. Hopkins, I. Marx, J. Schulz, G. Vandeveer, R. Prince, M. Nevalainen, T. Y. Chen, Z. Yousaf, M. Himmel-Bauer, V. Pattaropong, J. H. Jones, R. Gilfillan, E. Y. S. Lin, F. Gonzales Lopez De Turiso, 2022, WO 2022/032019.
[23] L. Arista, S. Cotesta, P. D'Alessandro, A.-M. D'Souza, R. Lattmann, D. Lizos, A. P. Pulz, A. L. Rooney, N. Smith, L. J. Taylor, T. J. Troxler, 2015, WO 2015/173656.
[24] C. L. Baumgartner, J. C. Sloop, *J. Fluorine Chem.*, 1992, **56**, 141-146.
[25] J. C. Sloop, C. L. Bumgardner, W. D. Loehle, *J. Fluorine Chem.*, 2002, **118**, 135-147.
[26] Y. Jeong, B. Kim, J. K. Lee, J.-S. Ryu, *J. Org. Chem.*, 2014, **79**, 6444-6455.
[27] C. E. Stephens, J. A. Blake, *J. Fluorine Chem.*, 2004, **125**, 1939-1945.
[28] K. Sato, G. Sandford, K. Shimizu, S. Akiyama, M. J. Lancashire, D. S. Yufit, A. Tarui, M. Omote, I. Kumadaki, S. Harusa wa, A. Ando, *Tetrahedron*, 2016, **72**, 1690-1698.
[29] Q. Llopis, G. Guillamot, P. Phansavath, V. Ratovelomanana-Vidal, *Org. Lett.*, 2017, **19**, 6428-6431.
[30] R. C. Boucher, *J. Intern. Med.*, 2007, **261**, 5-16.

ACADÉMIE DES SCIENCES
INSTITUT DE FRANCE

Comptes Rendus. Chimie
2024, Vol. 27, Special issue S2, p. 39-55
https://doi.org/10.5802/crchim.277

Research article

Women Chemists in France in 2024

Selected properties of phosphorus dendrimers: green approaches to catalysis

Anne-Marie Caminade [a, *, b] **and Valérie Maraval** [a, b]

[a] Laboratoire de Chimie de Coordination (LCC) du CNRS, 205 route de Narbonne, 31077 Toulouse Cedex 4, France

[b] LCC-CNRS, Université de Toulouse, CNRS, Toulouse, France

E-mails: anne-marie.caminade@lcc-toulouse.fr (A.-M. Caminade), valerie.maraval@lcc-toulouse.fr (V. Maraval)

Abstract. This review describes the synthesis of polyphosphorhydrazone (PPH) dendrimers, which are highly branched macromolecules, having a phosphorus atom at each branching point. The properties of these PPH dendrimers in the field of catalysis are then described. The review is organized to illustrate in the first part how the specificities of dendrimers could contribute to green chemistry. This concerns in particular the dendritic effect that is an increased efficiency (yield, enantioselectivity, etc.) when the size of the dendrimer increases, the recovery and reuse of the dendritic catalyst, the decreased leaching, and the entrapping of nanoparticles. In a second part, some even greener approaches of catalysis with dendrimers will be displayed, such as catalysis in water, switchable catalysis, and organocatalysis (no metal used). Different types of catalytic reactions have been studied, such as Stille, Suzuki and Sonogashira couplings, Knoevenagel condensations, Michael additions, asymmetric allylic alkylations, *O*- and *N*-arylation and vinylation reactions, [2+2+2]-cycloaddition reactions, isomerization of 1-octan-3-ol, Friedel–Crafts acylations, Heck reactions, hydrogenations, hydrations, transfer hydrogenations, amination of β-dicarbonyl compounds, etc.

Keywords. Dendrimer, Dendron, Phosphorus chemistry, Catalysis, Organocatalysis, Nanoparticles, Green chemistry.

Manuscript received 16 November 2023, revised 28 November 2023 and 30 November 2023, accepted 30 November 2023.

1. Introduction

The word "dendrimer" was created by Tomalia *et al.* [1] to name a new class of hyperbranched polymers, constituted of branched monomers associated stepwise and not by polymerization reactions. Most dendrimers are synthesized by a divergent process, starting from a multifunctional core, which is modified to become suitable for reaction with a branched monomer. Such process affords the first generation of the dendrimer. If both steps are quantitative, they can be repeated, by modifying the terminal functions of the dendrimer, to render it suitable for the reaction with the branched monomer, affording the second generation of the dendrimer (Scheme 1). Quantitative reactions are the key-point for the synthesis of dendrimers [2]. Each time the number of terminal functions is multiplied, generally by two [3] or three [4], a new generation is created. When the number of generations increases, it becomes more and more difficult to draw the full structures, thus dendrimers can also be represented by a linear structure, with parentheses after each level of branching points, associated to a number which

* Corresponding author

corresponds to the number of divergent ramifications for the branching point considered. Both the full structure and the linear structure of the second-generation dendrimer are represented in Scheme 1. Dendrimers have a bowl-shaped structure, in particular for high generations. There is a limit to the number of generations attainable with dendrimers, which depends on the length of the branches [5]. Indeed, the surface available to accommodate the terminal functions increases more slowly than the number of terminal functions. Polyamidoamine (PAMAM) dendrimers [6] and poly-L-lysine dendrimers [7] were the first dendrimers synthesized up to the tenth generation. Polyphosphorhydrazone (PPH) dendrimers [8], which will be the main topic of this review, were synthesized up to generation 12 [9], and were, for a long time, the largest type of dendrimers ever synthesized. Relatively recently, generation 13 was obtained with polytriazine dendrimers [10].

The presence of a large number of functional groups, easily accessible on the surface, and potentially modifiable at will, make dendrimers unique objects in the field of nanotechnologies. Indeed, dendrimers have a nanometric size, but contrarily to classical metal nanoparticles of the same size [11], which pertain to hard matter, dendrimers pertain to soft matter, as micelles and liposomes [12]. Modification of the terminal functions of diverse families of dendrimers has already opened the way towards many potential applications in the fields of catalysis, nanomaterials, biology [13], and also sensors, or electronic, to name a few [14].

Most dendrimers comprise a nitrogen atom at each branching point. This is the case of the PAMAM dendrimers [15], and poly-L-lysine dendrimers [16], but also of polypropyleneimine (PPI) dendrimers [17]. Besides, dendrimers constituted of more inorganic elements such as phosphorus [18] and silicon [19] particularly carbosilane [20] are also known and have been reviewed [21,22]. The case of phosphorus is particularly attractive for several reasons, due to the richness of its chemistry [23], the sensitivity and the wide window of ^{31}P NMR [24], as well as the potential biocompatibility, as phosphates are for instance the cement of DNA.

In this review, we will present the synthesis of polyphosphorhydrazone dendrimers, and then selected examples of their properties in the field of catalysis, to illustrate the dendritic effect, the recycling, the decreased leaching, and the entrapping of nanoparticles. In a second part, other green approaches of catalysis with dendrimers will be displayed, such as catalysis in water, switchable catalysis, and organocatalysis. An overview of the different types of catalysis carried out with phosphorhydrazone dendrimers has been published [25], but no emphasis on their specific properties has been reported.

2. Synthesis of polyphosphorhydrazone (PPH) dendrimers

Two steps are used for the synthesis of polyphosphorhydrazone (PPH) dendrimers, as for most dendrimers. The core bears P–Cl functions in most cases, based either on the thiophosphoryl trichloride $P(S)Cl_3$ (**1a**-$\mathbf{G_0}$) [8] or the hexachlorocyclotriphosphazene $N_3P_3Cl_6$ (**2a**-$\mathbf{G_0}$) [26]. Starting from the core, the first step is the reaction with 4-hydroxybenzaldehyde (**AB**) in basic conditions, either using NaH or cesium carbonate. The second step is the condensation of the aldehydes of **1b**-$\mathbf{G_0}$ or **2b**-$\mathbf{G_0}$ with the thiophosphorhydrazide $H_2NNMeP(S)Cl_2$ ($\mathbf{CD_2}$) used as branched monomer, and obtained by reaction of methylhydrazine with $P(S)Cl_3$ at low temperature (−60 °C). This second reaction permits to double the number of chlorides compared to the core **1a**-$\mathbf{G_0}$ or **2a**-$\mathbf{G_0}$, and thus affords the first generation of the dendrimer **1a**-$\mathbf{G_1}$ (Scheme 2A) or **2a**-$\mathbf{G_1}$ (Scheme 2B). Both steps are quantitative, thus they can be used again to get the second generation **1a**-$\mathbf{G_2}$ or **2a**-$\mathbf{G_2}$, then the third **1a**-$\mathbf{G_3}$ or **2a**-$\mathbf{G_3}$, and so on. By starting from $N_3P_3Cl_6$ as the core, by using the same principle, the 8th generation **2b**-$\mathbf{G_8}$ can be obtained (Scheme 2B) [27], whereas the 12th generation **1a**-$\mathbf{G_{12}}$ can be obtained when $P(S)Cl_3$ is used as the core (Scheme 2A) [9].

Several other methods to prepare phosphorus dendrimers have been elaborated, often based on the Staudinger reaction [28] between phosphines and azides, in particular using thiophosphoryl azides [29], for the synthesis of highly sophisticated dendritic structures [30]. However, this family of phosphorus dendrimers has not found any practical use up to now, and the selected properties of PPH dendrimers in the field of catalysis will only be described.

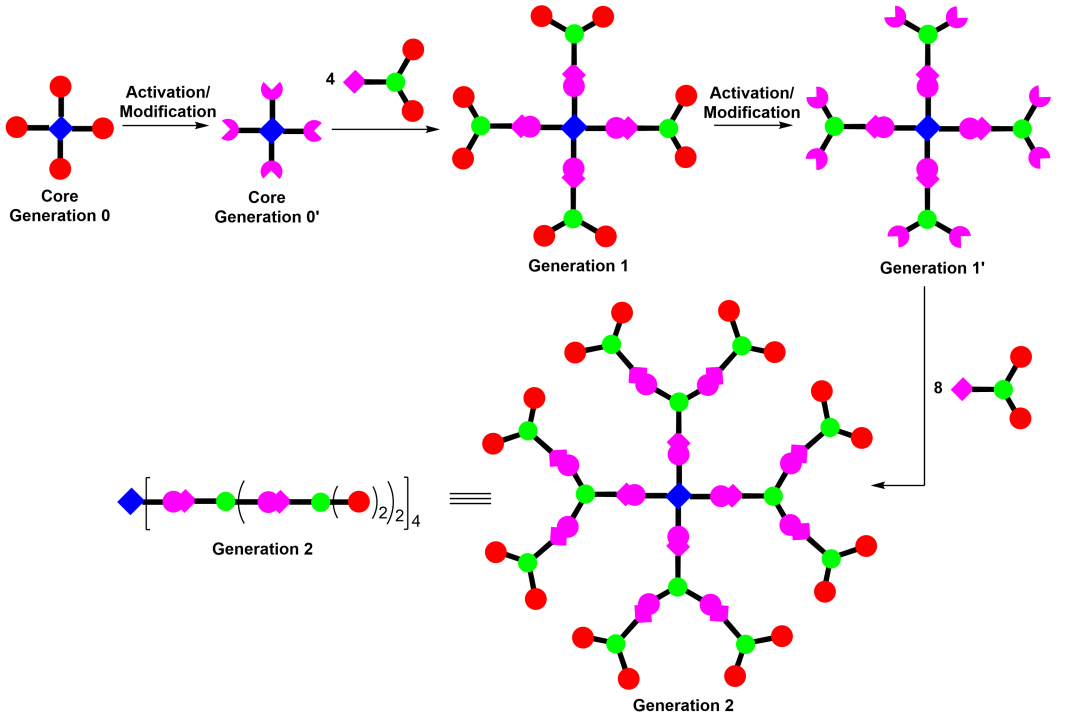

Scheme 1. Divergent synthesis of dendrimers. Generation 2 is represented twice: both the full structure, and the corresponding linear representation with parentheses after each branching point.

3. Specificities of dendrimers as catalysts

The very first examples of dendritic catalysts, were a silane dendrimer functionalized with aryl nickel complexes, which was used in the Kharasch addition of polyhalogenoalkanes to carbon–carbon double bonds [31], and a small polyphosphine dendrimer complexing palladium used in the electrochemical reduction of CO_2 to CO [32].

Different types of ligands have been grafted very early on the surface of PPH dendrimers, in particular phosphines [33] for the complexation of metals such as gold, enabling the characterization by High Resolution Transmission Electron Microscopy (HRTEM) [26], but also the complexation of iron and tungsten [34], palladium, platinum and rhodium [35], ruthenium [36], and zirconium [37] but none of them were used as catalysts. The first examples of PPH dendrimers used as catalysts concerned palladium and ruthenium complexes which were utilized in Stille couplings, Knoevenagel condensations, and Michael additions [38]. Other examples of PPH dendritic catalysts concerned Pd complexes for asymmetric allylic alkylations [39], and C–C cross-coupling reactions [40].

3.1. *Dendritic effect in catalysis*

One of the most intriguing properties of dendrimers is the so-called "dendritic effect" [41]. This effect is observed when a functional group behaves differently when it is alone or linked to a dendrimer, and the effect is also depending on the generation of the dendrimer. This effect is essentially unexplained, even if it is believed that it is related to the multivalency effect, which is well-known in biology [42]. In the case of catalysis, a spectacular example of dendritic effect concerned the ester hydrolysis catalyzed by peptide dendrimers composed of histidine–serine. The generation 4 peptide dendrimer was 140,000-fold more efficient than the reference catalyst for ester hydrolysis, with a 4500-fold acceleration per histidine side-chain [43]. In the case of PPH dendrimers, another intriguing example of the dendritic effect concerned pyridineimine ligands used for the complexation of copper.

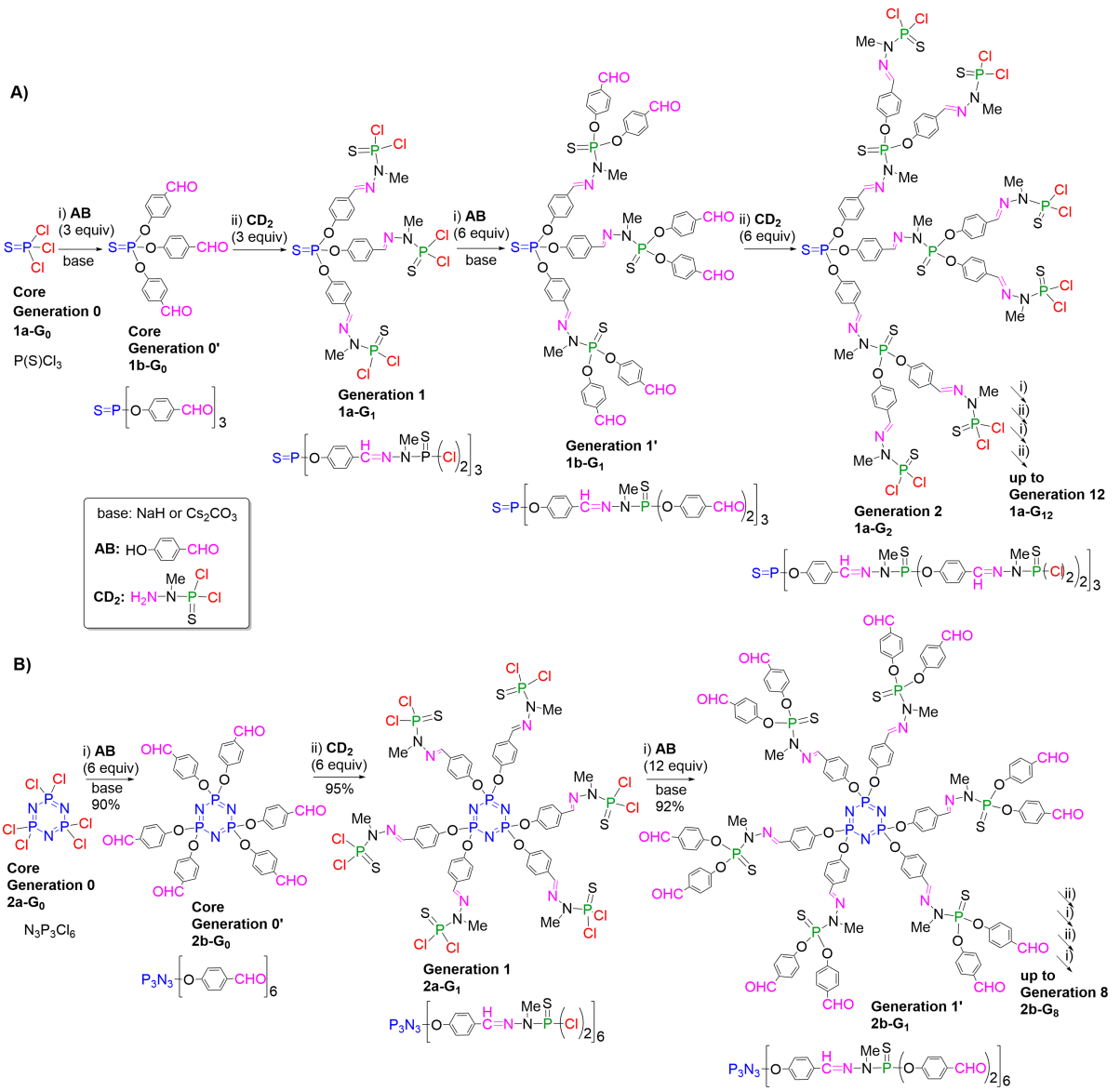

Scheme 2. Synthesis of polyphosphorhydrazone dendrimers, starting from either $P(S)Cl_3$ (A) or $N_3P_3Cl_6$ (B) as core.

The monomer and generations 1 to 3 of the PPH dendrimers were synthesized, and used as catalysts for *O*- and *N*-arylation as well as for vinylations. The most spectacular example concerned the arylation of pyrazole, using the same quantity of copper (10 mol%) for all the generations used. The efficiency of 1 equiv of generation 3 (**2c**-$\mathbf{G_3}$) was compared to that of 2 equiv of generation 2 (**2c**-$\mathbf{G_2}$), or 4 equiv of generation 1 (**2c**-$\mathbf{G_1}$), or 48 equiv of monomer (**2c**-**M**), as in all the examples displayed in this review (Scheme 3). The monomeric catalyst **2c**-**M** was found almost inactive as only 2% yield in 1-phenylpyrazole **3** was obtained when pyrrole was treated with phenylbromide. The yield in **3** was increased with generation 1 (40% yield), generation 2 (44% yield), and the best yield in **3** was obtained with generation 3 (80% yield) [44].

A strong positive dendritic effect has been also

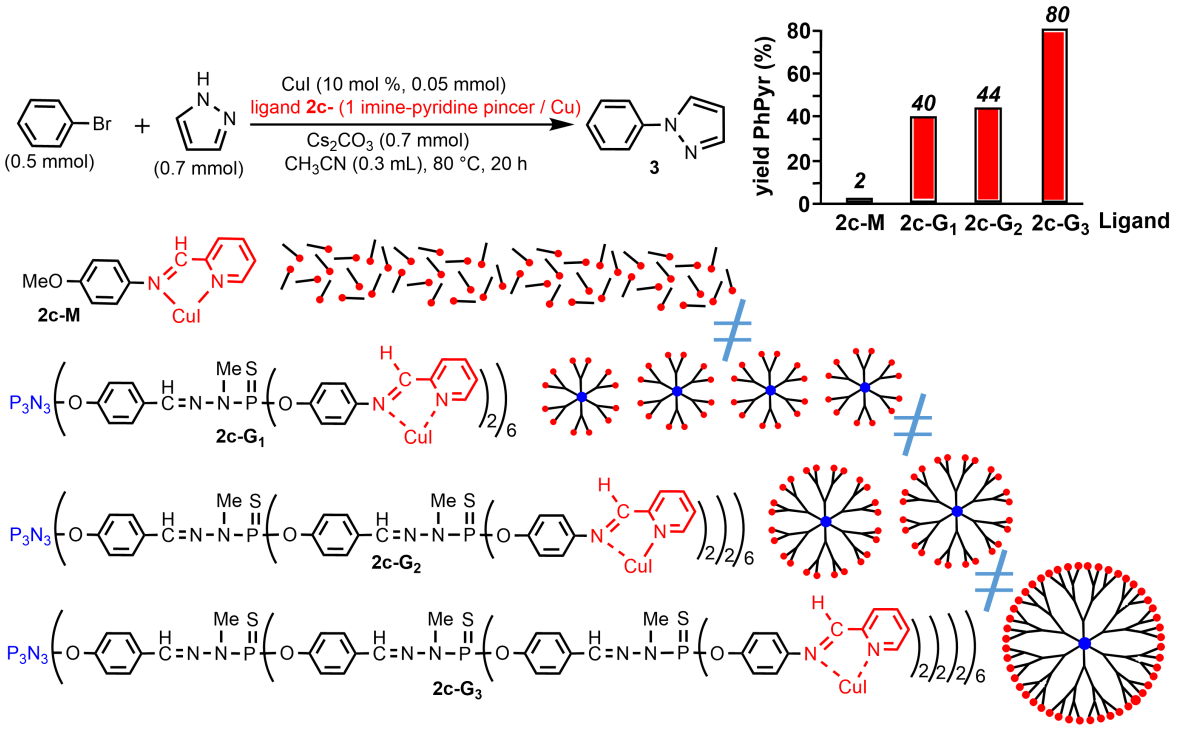

Scheme 3. Illustration of the "dendritic effect" with copper complexes of pyridine-imine ligands used for the arylation of pyrazole, using the same quantity of copper.

observed in both the yield and the enantioselectivity of Rh-catalyzed [2+2+2]-cycloadditions with dendritic phosphoramidite chiral ligands, leading to axially chiral biaryl compounds. As previously, the same quantity of catalytic sites is used in all cases [45] (Scheme 4). The monomer complex **2d-M-Rh** and the branch complex **2d-B-Rh** have practically no activity and no selectivity in the synthesis of the biarylic compound **4**. On the contrary, all the dendrimers are active, and display an increasing efficiency on going from the first generation **2d-G$_1$-Rh** to the third generation **2d-G$_3$-Rh**, in both yield and enantioselectivity.

Other examples of positive dendritic effects have been observed in the isomerization of 1-octan-3-ol catalyzed by dendritic Ru-complexes [46]. However, it should be emphasized that a positive dendritic effect is not always observed with dendrimers. In some cases, there is no change when using a dendrimer compared to a monomer [47], or there is only a slight difference, which depends on the reagents used [48]. In some cases, the absence of dendritic effect is due to the cleavage of the catalytic entity from the dendrimer when using hard conditions [49]. Some negative dendritic effects have been also reported [50], but there is probably a bias in the reported number of positive dendritic effects, as most negative results have never been published.

3.2. *Recovery and reuse of dendritic catalysts*

Another important benefit of using dendritic catalysts is the possibility to recover and reuse them in several catalytic runs. The main reason is that dendrimers are quite large compared to the reagents and products, and thus they can be less soluble in some solvents than small molecules. This is in particular the case of phosphorhydrazone dendrimers, which are soluble in several organic solvents, but not in diethylether. Thus, the dendritic catalyst can be recovered by precipitation in ether. This concept has been applied several times generally for three runs (see for example: [38,39,45,48]), but such property was applied in particular to the 4th generation dendrimer

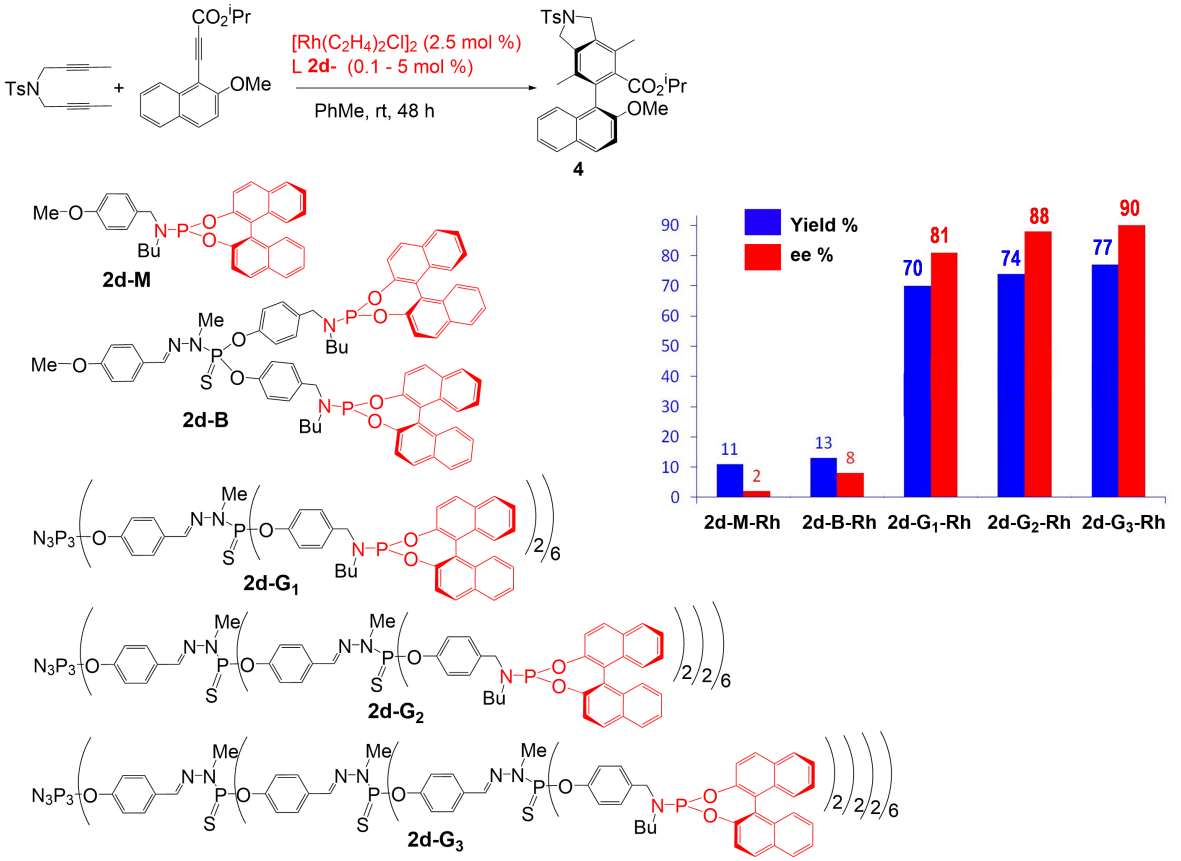

Scheme 4. Catalyzed [2+2+2]-cycloadditions using monomeric (**2d**-**M**), branch (**2d**-**B**), and dendritic (**2d**-$\mathbf{G_1}$ to **2d**-$\mathbf{G_3}$) Rh complexes. Influence of the generation on the yield and the enantioselectivity.

2e-$\mathbf{G_4}$ bearing terpyridine terminal functions, suitable for the complexation of scandium. This dendrimer was used in Friedel–Crafts acylations, under microwave irradiation. It is worth mentioning that 12 runs can be achieved, with different substrates at each run, and the efficiency of this dendrimer was still very high even after 12 runs [51] (Scheme 5).

Another example of the dendritic catalyst recovery concerned a biphasic experiment (water/heptane 1:1), utilizing dendritic ruthenium complexes of PTA (1,3,5-triaza-7-phosphaadamantane) [52] in the isomerization of 1-octan-3-ol **5**. The dendrimers are soluble in water, whereas the reagents and products are soluble in heptane. Catalysis occurred at the interface, upon strong stirring. After stopping the magnetic stirring, two phases are rapidly formed and easily separated, the organic phase containing the products, and the water phase containing the dendritic catalysts. A positive dendritic effect on the yield was observed from the monomer **2f**-**M** (38% conversion of **5**) to the third generation **2f**-$\mathbf{G_3}$ (98% conversion of **5**). The water phase was recovered and reused in another run, including for the first generation **2f**-$\mathbf{G_1}$, which was efficiently reused for 3 runs [46] (Scheme 6).

The third recycling method used to recover the dendritic phosphorhydrazone catalysts is very original, as it uses magnetic nanoparticles as supports of the dendritic catalysts, which are easily recovered with a magnet [53]. The very first example concerning the use of dendritic catalysts in such process was obtained with generations 0 (**6**-$\mathbf{G_0}$) and 1 (**6**-$\mathbf{G_1}$) of PPH dendrimers having phosphine palladium complexes on the surface and a single pyrene linked to the core. At room temperature, the pyrene interacts by π-stacking with a few graphene layers encapsulating the magnetic cobalt nanoparticles. The efficiency of the π-stacking decreased when heating,

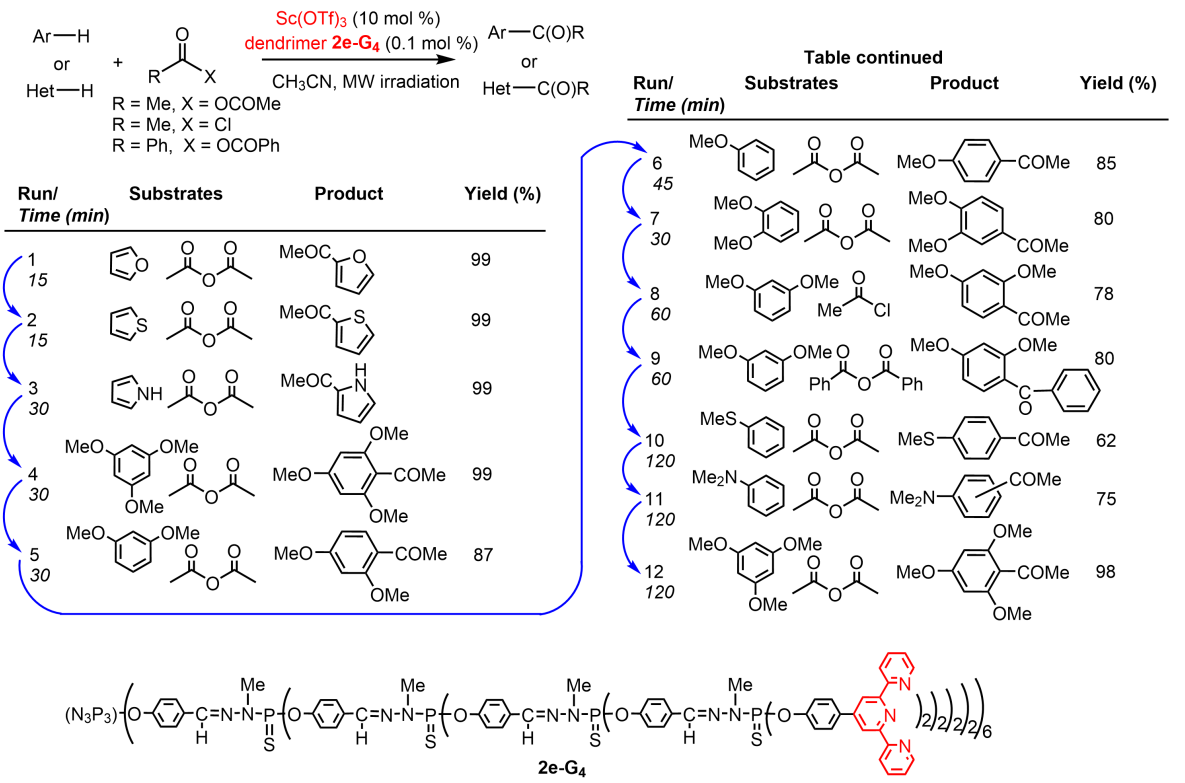

Scheme 5. Generation 4 dendrimer complexing scandium used as catalyst in Friedel–Crafts acylation, under microwave irradiation. Recovery and reuse of the dendritic catalyst in 12 runs, using different substrates at each step. Blue arrows indicate the recycling.

thus catalysis with these dendritic catalysts is performed in solution. After completion of the catalysis, the reaction medium is cooled down to room temperature, the dendrimers go back to the graphene entrapping magnetic nanoparticles, which are easily recovered using a magnet, as illustrated in Scheme 7. Such process has been applied to Suzuki couplings of boronic acids with various aryl bromides, and in particular for the synthesis of an anti-inflammatory drug, Felbinac, which was isolated in 100% yield even after 12 runs [54].

3.3. *Decreased metal leaching*

Leaching of metals during catalytic processes is an important problem for both the loss of precious/expensive metals, and the difficult purification of products, especially for the pharmaceutical industry [55]. As shown in the previous paragraphs, it is possible to recover and reuse dendritic catalysts with a good efficiency even after several runs, thus it is presumed that leaching should be reduced when using dendrimers compared to monomers, but it might also depend on the type of ligands. Two families of dendrimers (monomer, generations 1 and 3) were synthesized, decorated with either triphenylphosphine (**2g**-**MPPh$_3$**, **2g**-**G$_1$PPh$_3$**, **2g**-**G$_3$PPh$_3$**) or thiazolyldiphenyl phosphine (**2h**-**MthiazolP**, **2h**-**G$_1$thiazolP**, **2h**-**G$_3$thiazolP**). They were involved in Suzuki coupling reactions, after complexation of palladium. Both families demonstrated a better efficiency of the first generations, compared to the corresponding monomers (Scheme 8). Thus, their recycling was studied. It was shown that the 1st generation dendrimer decorated with Pd complexes of thiazolyl phosphine (**2h**-**G$_1$thiazolP**-**Pd**) was efficiently recovered and reused, without loss of activity for at least 5 runs. On the contrary, the efficiency of the 1st generation dendrimer decorated with Pd

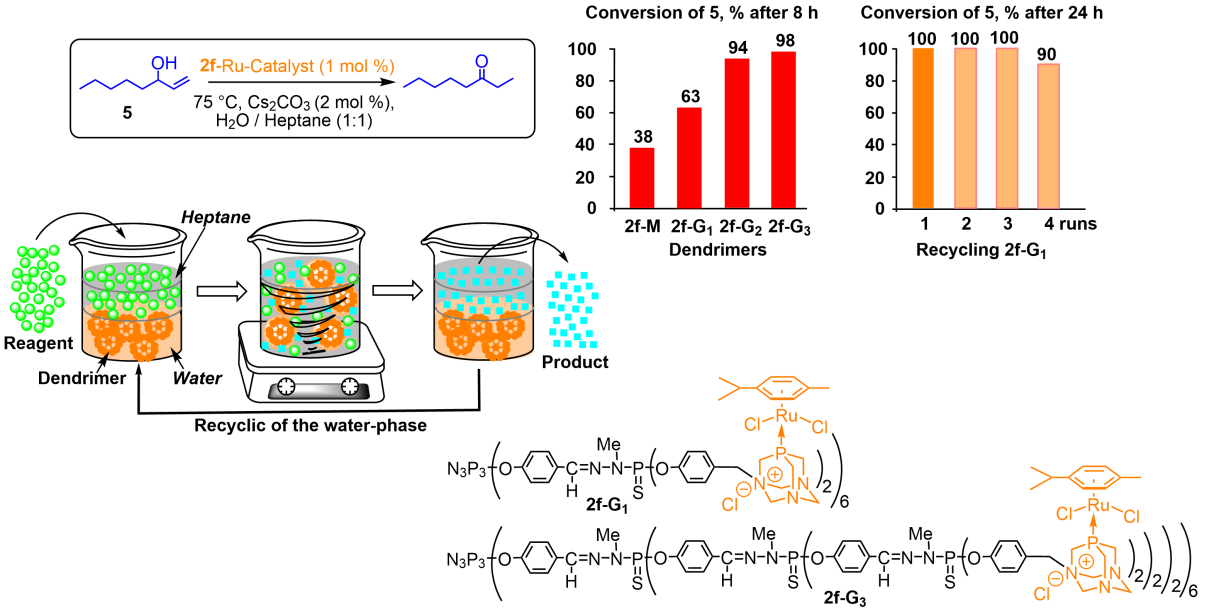

Scheme 6. Water-soluble dendrimers used in catalyzed biphasic isomerization of allylic alcohols to ketones. Positive dendritic effect, and recycling of **2f-G$_1$** by phase separation.

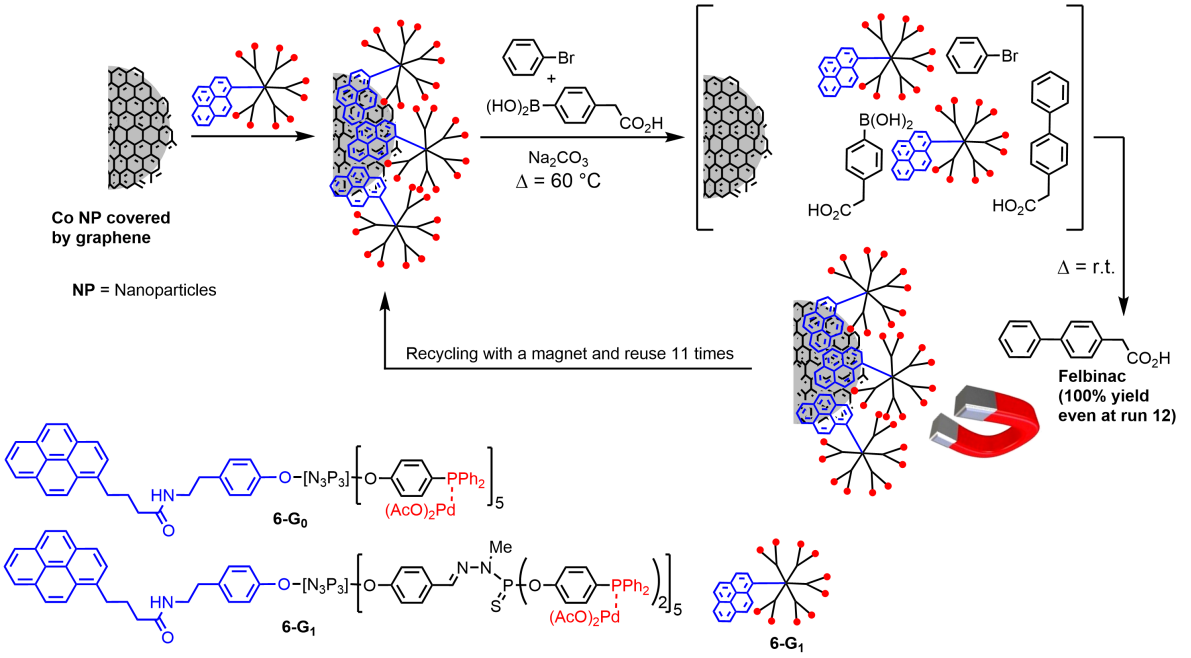

Scheme 7. Magnetic cobalt nanoparticles covered by graphene interacting with a pyrene catalytic dendron at room temperature, and used for the synthesis of Felbinac. Recovery using a magnet was carried out 11 times.

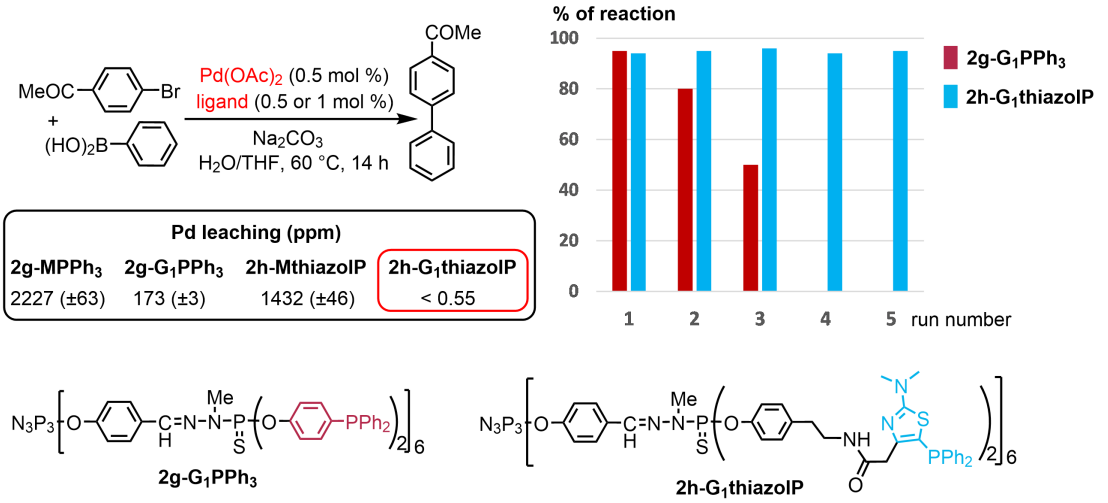

Scheme 8. Two types of dendrimers suitable for the complexation of palladium, and used in Suzuki couplings. Recycling was only efficient with the dendrimer bearing the thiazolyl phosphine complexes, thanks to undetectable palladium leaching.

complexes of triphenylphosphine (**2g-G$_1$PPh$_3$-Pd**) decreased rapidly, and disappeared after 3 runs. To elucidate this difference, palladium leaching with the monomers and the 1st generation dendrimers was measured by Inductively Coupled Plasma Mass Spectrometry (ICP-MS). Leaching was found very high with both monomers, reduced for the triphenylphosphine linked to the dendrimer, and undetectable for the thiazolyl phosphine linked to the dendrimer (Scheme 8). Such a low level of palladium leaching is very rare for Suzuki reactions in homogeneous conditions, and explains the efficiency of the recovery and reuse of the dendritic catalyst [56].

3.4. *Entrapping catalytic nanoparticles*

Beside the grafting of discrete complexes on the surface of dendrimers, examples of dendrimers incorporating metal nanoparticles used for catalysis have been largely explored [57]. Most generally, the starting complex has to be reduced to generate the nanoparticles and to stabilize them, by entrapping them inside the dendrimers or in between dendrimers. A series of phosphorhydrazone dendrimers was functionalized with 15-membered triolefinic triazamacrocycles, generation 0 built from P(S)Cl$_3$ as core (**1i-G$_0$**) and generations 0, 1 and 4, built from $N_3P_3Cl_6$ as core (**2i-G$_0$**, **2i-G$_1$**, and **2i-G$_4$**). These macrocycles are suitable for complexing Pd(0), issued from $Pd_2(dba)_4$ (dba = dibenzylidene acetone). The use of a stoichiometric amount of palladium (1 Pd per macrocycle) induces the formation of discrete complexes, whereas the use of an excess of Pd induces the formation of Pd(0) nanoparticles, stabilized by the dendrimers. The average diameters of the nanoparticles are between 3 and 5 nm, irrespective of the size (generation) of the dendrimers. Both the discrete complexes and the nanoparticles stabilized by the dendrimers were tested as catalysts in Heck reactions, using the same quantity of palladium in all cases. Generation 0 built from the P(S) trifunctional core (compound **1i-G$_0$**) was found the most efficient after 4 h, with both the discrete complex and the nanoparticles. However, no large differences were observed after 24 h. In both cases, recycling was attempted 5 times (Scheme 9). The most important differences were observed after 4 h. The discrete complex is easily recovered and reused with the same efficiency. Surprisingly, the nanoparticles complexed by the generation 0 dendrimers (**1i-G$_0$**) displayed an increasing activity with the number of recycling runs, with a yield in butyl cinnamate after 4 h increasing from 36% after run 1 to 98% after run 6. This contra-intuitive result is due to the decrease of the nanoparticles size, with an average size from 4.1 nm at the first run to 2.3 nm at the sixth run [58].

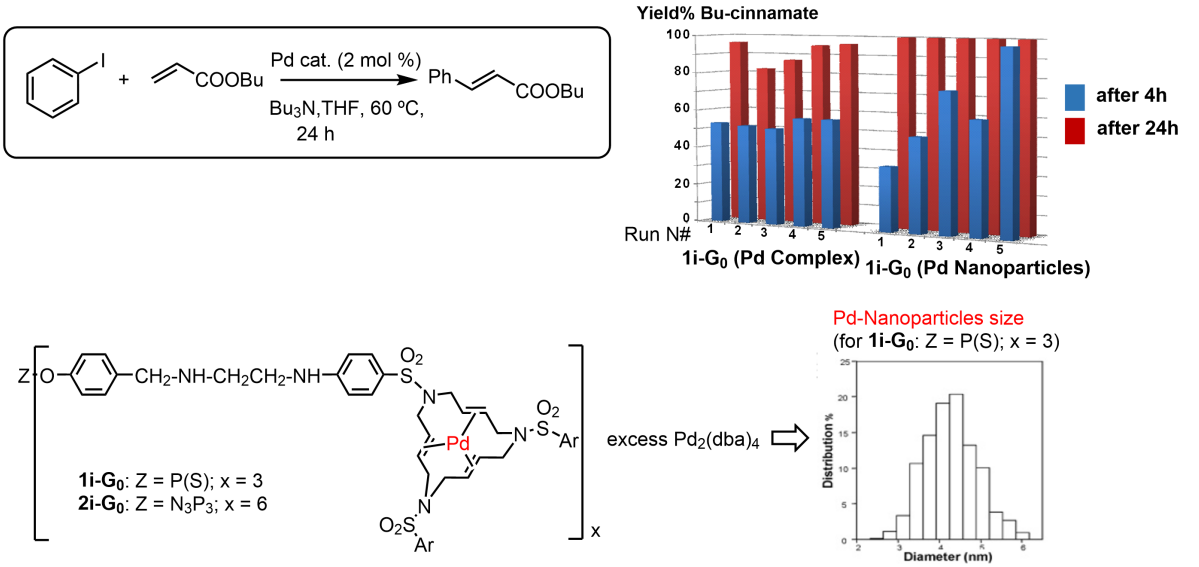

Scheme 9. Macrocycles on the surface of dendrimers, used for complexing palladium as discrete complexes or as palladium nanoparticles. Heck coupling reactions, and recycling.

Another way to generate catalytic nanoparticles consisted in milling, under air, ruthenium chloride ($RuCl_3$), sodium borohydride ($NaBH_4$) and polyphosphorhydrazone (PPH) dendrons of generations 0 to 2, having an alkyl chain (C12 or C16) at the focal point and triarylphosphines on the surface (compounds **7-G$_0$**, **7-G$_1$**, and **7-G$_2$**). Ru nanoparticles obtained in these conditions, were then used as efficient catalysts in the hydrogenation of styrene, to afford ethylbenzene **8** (Scheme 10). No effect of the alkyl chain length on the efficiency was observed. However, a positive dendrimer effect was observed, as the Ru particles stabilized with the second generation dendron (**Ru@7-G$_2$**) were the most efficient (85% yield with generation 0; 96% yield with generation 2). This is probably due to the fact that the surface of the nanocomposite systems is less hindered when higher generation dendrons are involved, as illustrated in Scheme 10 [59].

4. Additional green approaches of catalysis

The different specificities of dendrimers in catalysis shown in Section 3 are all relevant for green chemistry processes by decreasing the leaching of metal, and by decreasing either the time or the temperature of the reaction, reusing the catalyst to decrease the quantity of metal needed, and simplifying the purification of the products. Other types of green approaches are more classical and are known also with monomeric catalysts.

4.1. *Catalysis in water*

Water can be considered as a green solvent, compared to classical organic solvents. As the internal structure of the phosphorhydrazone dendrimers contains numerous aromatic cycles, they are rather hydrophobic, and can be soluble in water only if the terminal functions are hydrophilic, bearing either positive charges such as ammoniums [60–62] or negative charges such as carboxylates [63–65], phosphonates [66,67] or sulfonates [68], or neutral polyethyleneglycol (PEG) [69,70].

As shown in Scheme 6, the positive charge on the PTA (PhosphaTriazaAdamantane) ligand induces a solubilization of the dendrimers in water and at the interface between water and heptane [46]. Generations 0 (**2f-G$_0$**) to 3 (**2f-G$_3$**) of the same family of PTA dendrimers have been also investigated, both as catalysts for the hydration of phenylacetylene in H_2O/*i*PrOH, and for their interaction in phosphate buffer (excepted **2f-G$_3$**) with supercoiled DNA, to afford relaxed DNA [71].

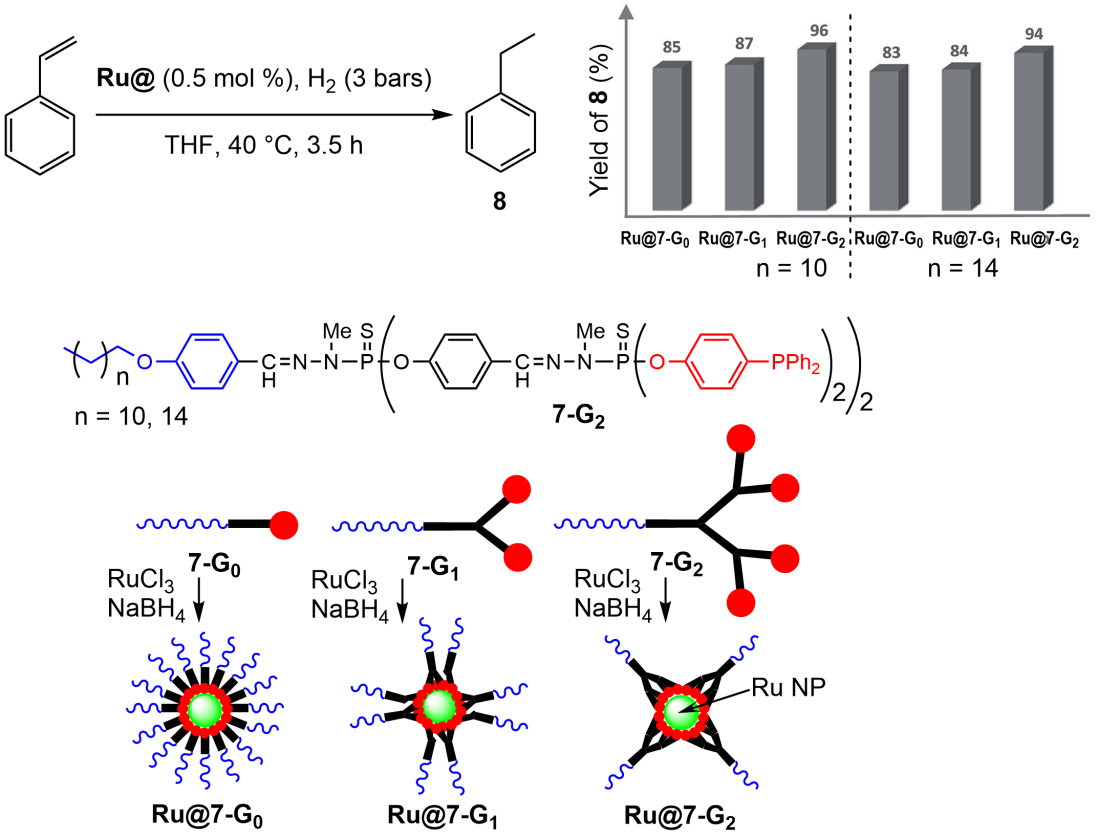

Scheme 10. Dendrons for the synthesis of Ru nanoparticles. Catalysts for the hydrogenation of styrene.

Scorpionates such as tris(pyrazolyl) ligands, have been grafted to the surface of a 1st generation dendrimer **2j-G$_1$**, and used for the complexation of palladium. Complexes of the dendrimer (**2j-G$_1$-Pd**) and of the corresponding monomer (**2j-M-Pd**) have been used as catalysts in both Sonogashira and Heck C–C cross-coupling reactions in a H_2O/CH_3CN (1:6) mixture (Scheme 11) [72]. Monomer **2j-M-Pd** and dendrimer **2j-G$_1$-Pd** complexes afford analogous efficiency in the Sonogashira coupling, whereas the dendrimer **2j-G$_1$-Pd** is more efficient than the monomer **2j-M-Pd** in Heck coupling.

4.2. *Switchable catalysts*

Redox-switchable catalysis concerns an emerging field of research, in which a redox-active functionality is incorporated within a ligand framework. As the redox process influences the electron-donating ability of the ligands, the coordinated metal centers can be influenced *in situ*, thus modifying the catalytic activity [73]. It has never been applied to dendritic catalysts before our work. Ferrocene is a widely used redox-active group, which displays a high degree of reversibility. Furthermore, it can be easily functionalized and has been frequently grafted to dendrimers, including to phosphorus dendrimers [74]. The presence of an additional functionalization such as phosphine complexes of palladium, enabled their use in asymmetric allylic substitution reactions [47]. Later on, a monomer and a 1st generation dendrimer (**2k-G$_1$**) were functionalized with unsymmetrically disubstituted 1,1′-ferrocenylphosphine, in which one cyclopentadienyl (Cp) ring is substituted with a phenol for the grafting to the dendrimer, and the other Cp is substituted with an aryl phosphine. The phosphines were then used for complexing

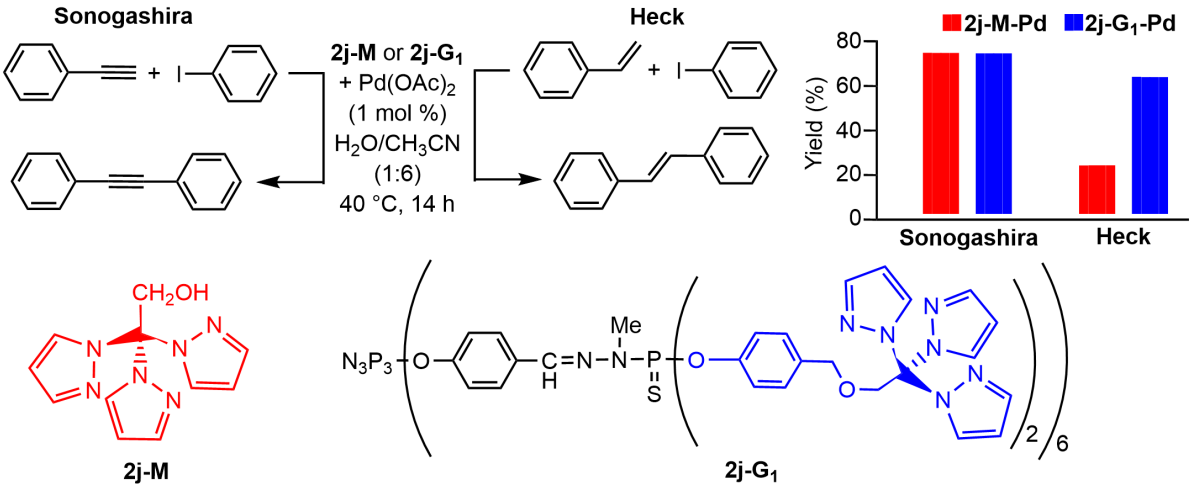

Scheme 11. Monomer and dendrimer bearing scorpionates for the complexation of palladium. Sonogashira and Heck coupling reactions.

ruthenium, and the complexes efficiently catalyzed the isomerization of 1-octen-3-ol to 3-octanone. Upon oxidation of the ferrocene (**2k-G$_1$-Red**) to ferrocenium (**2k-G$_1$-Ox**), the experimental rate constant dramatically decreased, due to the precipitation of the oxidized dendritic catalysts **2k-G$_1$-Ox** in the medium. Upon reduction to **2k-G$_1$-Red**, the dendritic catalysts became again soluble, and the rate constant dramatically increased, displaying an ON/OFF/ON switching process (Scheme 12) [75]. This family of redox-switchable dendrimers was expanded up to generation 3, and with the use of either no linker or a biphenyl linker between the ferrocene and the phosphine [76].

More recently, the same switching process was successfully applied to dendrimers bearing chiral ferrocenyl phosphines as terminal functions for ruthenium-catalyzed transfer hydrogenation [77] of acetophenone [78].

4.3. *Organocatalysis*

Organocatalysis, i.e. catalysis in the absence of any metal, is particularly attractive in relation to the principles of "green chemistry", being both cheaper and safer. The use of dendrimers as organocatalysts has been recognized early and reviewed [79]. Phosphorhydrazone dendrimers have been used as supports of known organocatalysts in several cases. In a first example, small polymers linked to the surface of cobalt nanoparticles **2l-NP** (identical to those used in Scheme 7) as well as dendrimers of generations 1 to 3 (**2l-G$_1$**, **2l-G$_2$** and **2l-G$_3$**) were functionalized with the Jørgensen–Hayashi catalyst [(*S*)-α,α-diphenylprolinol trimethylsilyl ether]. Both families of compounds were used as catalysts in the Michael additions of a wide range of aldehydes to different nitroolefins. The addition of propanal to β-nitrostyrene was particularly studied to demonstrate the recycling ability (Scheme 13). Among the dendrimers, generation 3 (**2l-G$_3$**) was the most efficient at the first run, and remained highly efficient over 4 runs. The cobalt nanoparticles covered with the catalysts **2l-NP** were found as efficient as the dendrimer **2l-G$_3$**, but the recycling was surprisingly poorly efficient. Indeed, at run 4, the catalytic efficiency of the dendrimer **2l-G$_3$** was still 98%, whereas that of the nanoparticles **2l-NP** was only 34% [80].

Cinchona alkaloids are natural products, which derivatives have been used in many catalytic asymmetric reactions [81]. One of these derivatives, (+)-cinchonine, has been grafted on the surface of phosphorhydrazone (PPH) dendrimers in two different ways for two different purposes. In the first attempt, (+)-cinchonine was modified with a phenol, to be reacted with the P(S)Cl$_2$ terminal functions of the dendrimers of generations 1 (**2m-G$_1$**) and 4 (**2m-G$_4$**). A branch derivative (**2m-B**) was also synthesized as a model compound bearing two (+)-

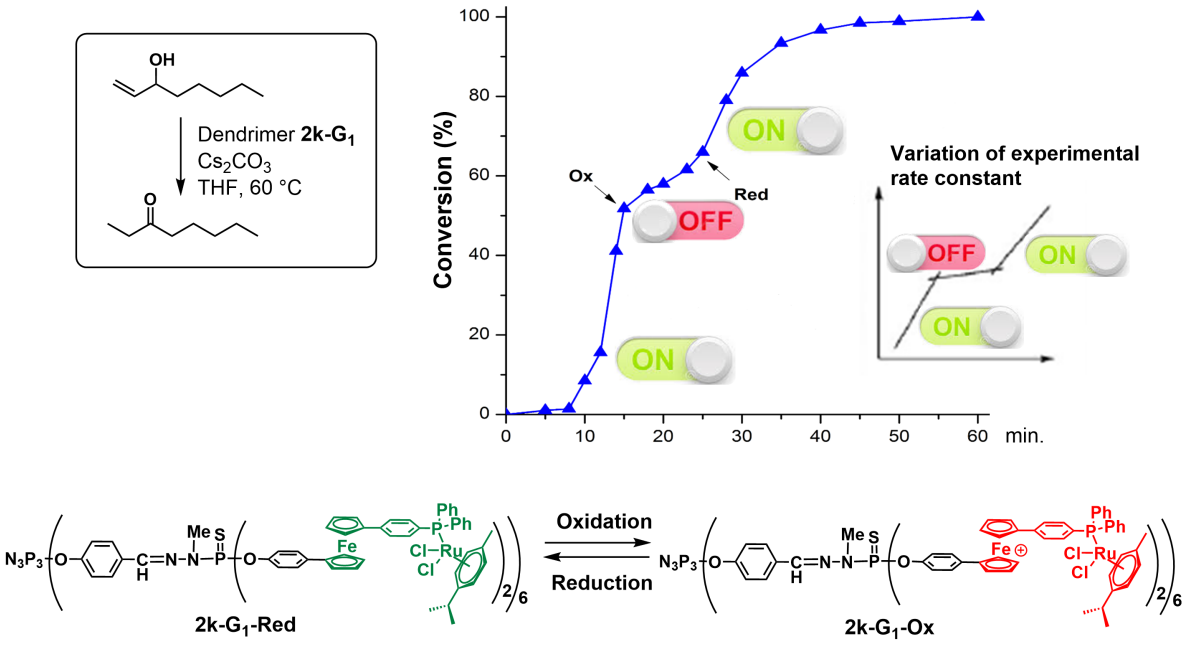

Scheme 12. Dendrimer bearing redox switchable phosphines complexing ruthenium, and its use as catalyst in the isomerization of 1-octen-3-ol to 3-octanone. Influence of the oxidation and reduction of the ferrocenes on the catalytic rate.

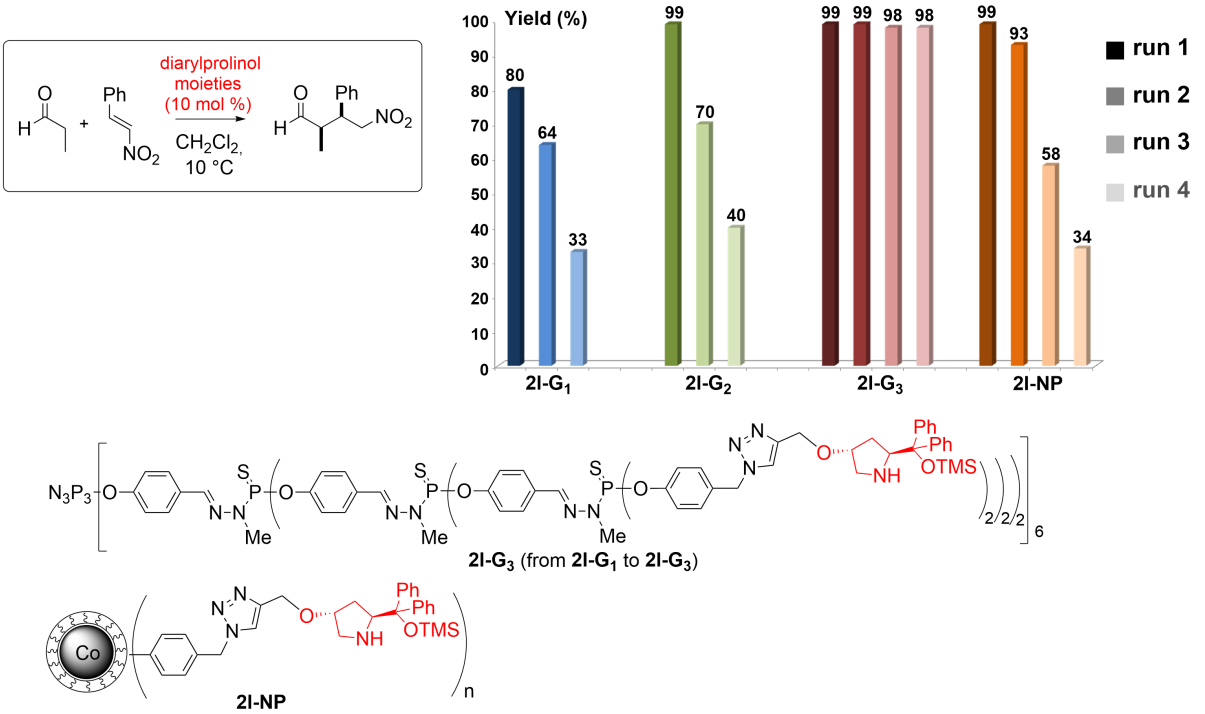

Scheme 13. Dendrimers and cobalt nanoparticles as support of the Jørgensen–Hayashi organocatalyst. Coupling of propanal to β-nitrostyrene. Comparison of the efficacy in recycling experiments.

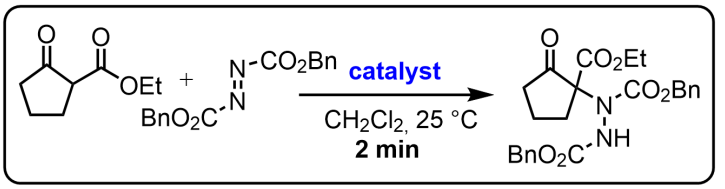

Cat. (mol %)	Yield (%)	ee (%)
2m-M (20)	87	62
2m-B (4)	96	81
2m-G$_1$ (4)	95	75

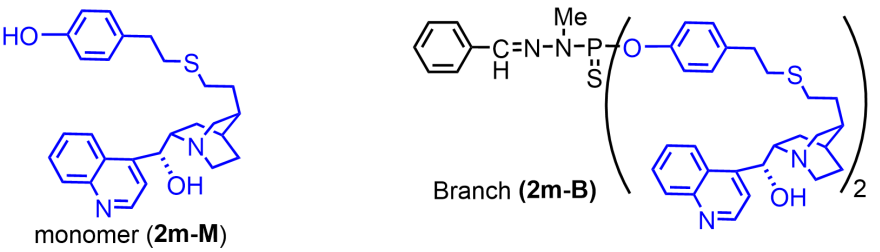

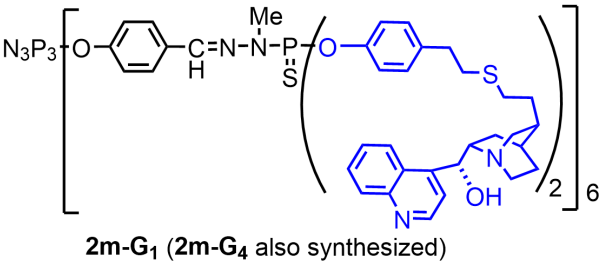

Scheme 14. (+)-Cinchonine derivative linked to a monomer (**2m**-**M**), a branch (**2m**-**B**) and to generation 1 of dendrimer (**2m**-**G$_1$**), and their use as organocatalysts for the α-amination of β-dicarbonyl compounds.

cinchonine derivatives (Scheme 14). These compounds were tested in the α-amination of several β-dicarbonyl compounds. The reactions were very fast, even with only 4 mol% of catalyst (to be compared with 20 mol% in the case of the monomer **2m**-**M**), and went to completion in 2 min at 25 °C, and in 10 min at −25 °C with the smallest compounds (branch **2m**-**B**, and 1st generation dendrimer **2m**-**G$_1$**). The best enantiomeric excesses were obtained with the branch and the 1st generation dendrimer. Recycling experiments were successfully carried out with the 1st generation **2m**-**G$_1$**, and ten runs were carried out without loss of activity and enantioselectivity. The scope of the catalytic enantioselective amination of various active methylene compounds was then evaluated, using cyclic and noncyclic esters, cyclic β-diketones and opened chain esters [82].

The second way to graft (+)-cinchonine required the modification of the surface of the dendrimers in three steps from the aldehydes, e.g. reduction with $BH_3{\cdot}SMe_2$, transformation to benzylic chloride with $SOCl_2$ [83], and reaction with NaI to give benzyl iodide terminal functions. The next step was the quaternization of the nitrogen of the quinuclidine of (+)-cinchonine, containing different R groups in the O-9 hydroxy group of the cinchonine unit. A small quantity (0.1 mol%) of these functionalized dendrimers **2n**-**G$_1$a**-**d** was then used as a phase transfer catalyst in the asymmetric alkylation of a glycinate Schiff base with benzyl bromide, at 25 °C, 0 °C, and even −20 °C (Scheme 15). To simplify the analysis, the resulting imines **9** were derivatized to the corresponding trifluoroacetamides **10** by their hydrolysis with citric acid, followed by the protection of the generated primary amines by reaction with trifluoroacetic anhydride. The best results concerning the yield and the enantiomeric excess were obtained for **2n**-**G$_1$b** (R = allyl). This dendrimer was also used in recycling experiments, at 0 °C. Five runs were carried out, and yields were similar for

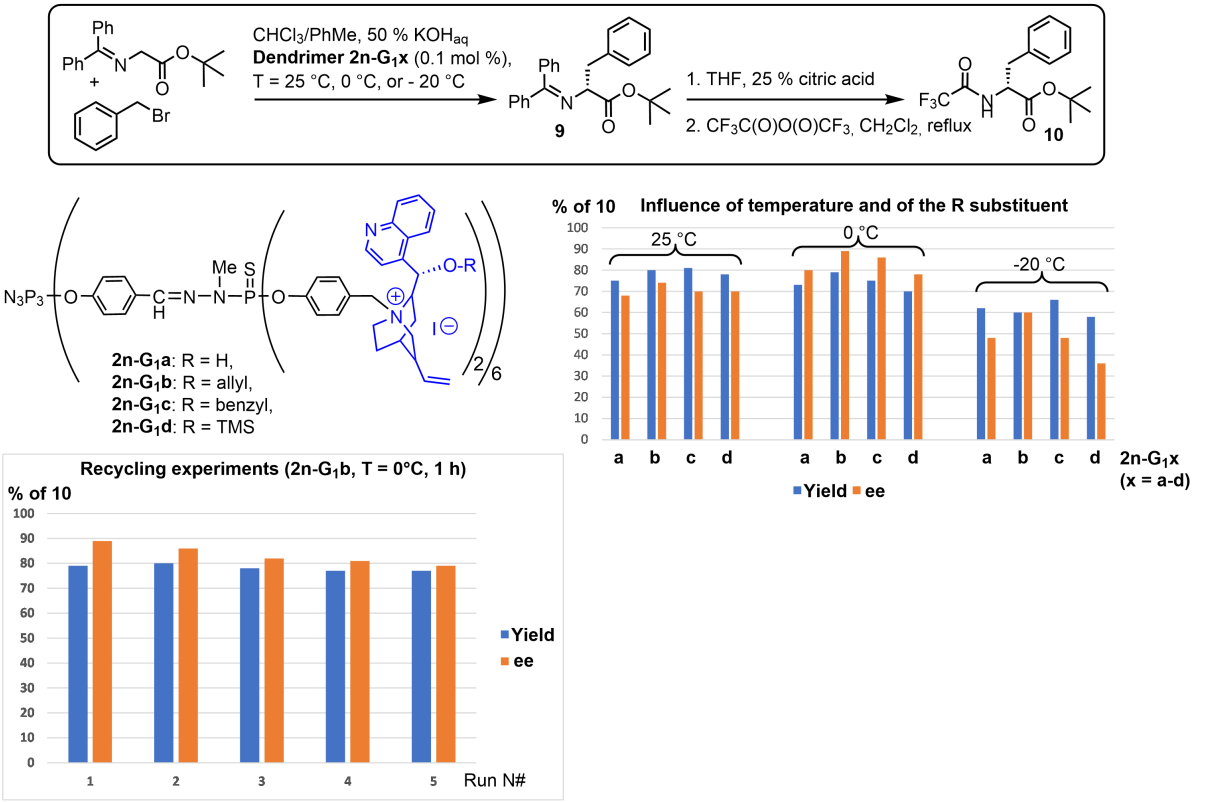

Scheme 15. Alkylation of the nitrogen of the quinuclidine of (+)-cinchonine for the grafting to the 1st generation dendrimer. Phase transfer catalyst in the asymmetric alkylation of a glycinate Schiff base with benzyl bromide. Influence of the temperature and the R substituent. Recycling experiments with **2n-G$_1$b**.

each run, but a slight decrease of ee was observed. The scope of the catalytic enantioselective alkylation of the *N*-(diphenylmethylene)glycine *tert*-butyl ester with various alkylating agents was then also evaluated. Good yields (76–87%) and enantioselectivities (76–89%) were obtained in most cases [84].

5. Conclusions

We have shown in this review different aspects of the use of dendrimers in catalysis. Very positive influences on the yield, the enantioselectivity, the easy recovery and reuse, make dendrimers especially attractive in the field of catalysis. However, it should be emphasized that catalysis is only a part of the fields that benefit from the use of dendrimers. The PPH (polyphosphorhydrazone) dendrimers in particular gave birth to two start-ups, one in the field of materials, in particular biosensors for diagnosis [85,86], and one in the field of biology, in particular an anti-inflammatory drug [87,88]. Thus, there is still plenty of room to expand the use of dendrimers in general, and more specifically of PPH dendrimers.

Declaration of interests

The authors do not work for, advise, own shares in, or receive funds from any organization that could benefit from this article, and have declared no affiliations other than their research organizations.

References

[1] D. A. Tomalia, H. Baker, J. Dewald, M. Hall, G. Kallos, S. Martin, J. Roeck, J. Ryder, P. Smith, *Polymer J.*, 1985, **17**, 117-132.

[2] E. Buhleier, F. Wehner, F. Vögtle, *Synthesis*, 1978, **78**, 155-158.
[3] G. R. Newkome, C. D. Shreiner, *Polymer*, 2008, **49**, 1-173.
[4] G. R. Newkome, C. Shreiner, *Chem. Rev.*, 2010, **110**, 6338-6442.
[5] P. G. De Gennes, H. Hervet, *J. Phys. Lett.*, 1983, **44**, L351-L360.
[6] B. L. Schwartz, A. L. Rockwood, R. D. Smith, D. A. Tomalia, R. Spindler, *Rapid Commun. Mass Spectrom.*, 1995, **9**, 1552-1555.
[7] R. G. Denkewalter, J. F. Kolc, W. J. Lukasavage, "Macromolecular highly branched homogeneous compound", U.S. Patent (1981), 4,410,688.
[8] N. Launay, A. M. Caminade, R. Lahana, J. P. Majoral, *Angew. Chem.-Int. Edit. Engl.*, 1994, **33**, 1589-1592.
[9] M. L. Lartigue, B. Donnadieu, C. Galliot, A. M. Caminade, J. P. Majoral, J. P. Fayet, *Macromolecules*, 1997, **30**, 7335-7337.
[10] J. Lim, M. Kostiainen, J. Maly, V. C. P. da Costa, O. Annunziata, G. M. Pavan, E. E. Simanek, *J. Am. Chem. Soc.*, 2013, **135**, 4660-4663.
[11] C. Amiens, B. Chaudret, D. Ciuculescu-Pradines, V. Colliere, K. Fajerwerg, P. Fau, M. Kahn, A. Maisonnat, K. Soulantica, K. Philippot, *New J. Chem.*, 2013, **37**, 3374-3401.
[12] A. Sangtani, O. K. Nag, L. D. Field, J. C. Breger, J. B. Delehanty, *Wiley Interdiscip. Rev.-Nanomed. Nanobiotechnol.*, 2017, **9**, article no. e1466.
[13] A. M. Caminade, C. O. Turrin, R. Laurent, A. Ouali, B. Delavaux-Nicot (eds.), *Dendrimers: Towards Catalytic, Material and Biomedical Uses*, Wiley, Chichester, UK, 2011.
[14] D. Astruc, E. Boisselier, C. Ornelas, *Chem. Rev.*, 2010, **110**, 1857-1959.
[15] D. A. Tomalia, A. M. Naylor, W. A. Goddard, *Angew. Chem.-Int. Edit. Engl.*, 1990, **29**, 138-175.
[16] S. M. Aharoni, C. R. Crosby, E. K. Walsh, *Macromolecules*, 1982, **15**, 1093-1098.
[17] E. M. M. de Brabander van den Berg, E. W. Meijer, *Angew. Chem.-Int. Edit. Engl.*, 1993, **32**, 1308-1311.
[18] K. Rengan, R. Engel, *J. Chem. Soc.-Chem. Commun.*, 1990, 1084-1085.
[19] E. A. Rebrov, A. M. Muzafarov, V. S. Papkov, A. A. Zhdanov, *Dokl. Akad. Nauk SSSR*, 1989, **309**, 376-380.
[20] A. W. Van der Made, P. W. N. M. Van Leeuwen, *J. Chem. Soc.-Chem. Commun.*, 1992, 1400-1401.
[21] J. P. Majoral, A. M. Caminade, *Chem. Rev.*, 1999, **99**, 845-880.
[22] A. M. Caminade, *Chem. Soc. Rev.*, 2016, **45**, 5174-5186.
[23] K. B. Dillon, F. Mathey, J. F. Nixon (eds.), *Phosphorus: The Carbon Copy, from Organophosphorus to Phosphaorganic Chemistry*, John Wiley & Sons, Chichester, UK, 1998.
[24] L. B. Krivdin, *Magn. Reson. Chem.*, 2020, **58**, 478-499.
[25] A.-M. Caminade, R. Laurent, *Coord. Chem. Rev.*, 2019, **389**, 59-72.
[26] M. Slany, M. Bardaji, M. J. Casanove, A. M. Caminade, J. P. Majoral, B. Chaudret, *J. Am. Chem. Soc.*, 1995, **117**, 9764-9765.
[27] N. Launay, A. M. Caminade, J. P. Majoral, *J. Organomet. Chem.*, 1997, **529**, 51-58.
[28] H. Staudinger, J. Meyer, *Helv. Chim. Acta*, 1919, **2**, 635-646.
[29] V. Maraval, A. M. Caminade, J. P. Majoral, J. C. Blais, *Angew. Chem. Int. Ed.*, 2003, **42**, 1822-1826.
[30] C. Galliot, C. Larre, A. M. Caminade, J. P. Majoral, *Science*, 1997, **277**, 1981-1984.
[31] J. W. J. Knapen, A. W. Van der Made, J. C. De Wilde, P. W. N. M. Van Leeuwen, P. Wijkens, D. M. Grove, G. Van Koten, *Nature*, 1994, **372**, 659-663.
[32] A. Miedaner, C. J. Curtis, R. M. Barkley, D. L. Dubois, *Inorg. Chem.*, 1994, **33**, 5482-5490.
[33] A. M. Caminade, R. Laurent, B. Chaudret, J. P. Majoral, *Coord. Chem. Rev.*, 1998, **178**, 793-821.
[34] M. Slany, M. Bardaji, A. M. Caminade, B. Chaudret, J. P. Majoral, *Inorg. Chem.*, 1997, **36**, 1939-1945.
[35] M. Bardaji, M. Kustos, A. M. Caminade, J. P. Majoral, B. Chaudret, *Organometallics*, 1997, **16**, 403-410.
[36] M. Bardaji, A. M. Caminade, J. P. Majoral, B. Chaudret, *Organometallics*, 1997, **16**, 3489-3497.
[37] V. Cadierno, A. Igau, B. Donnadieu, A. M. Caminade, J. P. Majoral, *Organometallics*, 1999, **18**, 1580-1582.
[38] V. Maraval, R. Laurent, A. M. Caminade, J. P. Majoral, *Organometallics*, 2000, **19**, 4025-4029.
[39] R. Laurent, A. M. Caminade, J. P. Majoral, *Tetrahedron Lett.*, 2005, **46**, 6503-6506.
[40] P. Servin, R. Laurent, A. Romerosa, M. Peruzzini, J. P. Majoral, A. M. Caminade, *Organometallics*, 2008, **27**, 2066-2073.
[41] A. M. Caminade, A. Ouali, R. Laurent, C. O. Turrin, J. P. Majoral, *Chem. Soc. Rev.*, 2015, **44**, 3890-3899.
[42] O. Rolland, C. O. Turrin, A. M. Caminade, J. P. Majoral, *New J. Chem.*, 2009, **33**, 1809-1824.
[43] E. Delort, T. Darbre, J. L. Reymond, *J. Am. Chem. Soc.*, 2004, **126**, 15642-15643.
[44] A. Ouali, R. Laurent, A. M. Caminade, J. P. Majoral, M. Taillefer, *J. Am. Chem. Soc.*, 2006, **128**, 15990-15991.
[45] L. Garcia, A. Roglans, R. Laurent, J. P. Majoral, A. Pla-Quintana, A. M. Caminade, *Chem. Commun.*, 2012, **48**, 9248-9250.
[46] P. Servin, R. Laurent, L. Gonsalvi, M. Tristany, M. Peruzzini, J. P. Majoral, A. M. Caminade, *Dalton Trans.*, 2009, 4432-4434.
[47] L. Routaboul, S. Vincendeau, C. O. Turrin, A. M. Caminade, J. P. Majoral, J. C. Daran, E. Manoury, *J. Organomet. Chem.*, 2007, **692**, 1064-1073.
[48] M. Koprowski, R. M. Sebastian, V. Maraval, M. Zablocka, V. Cadierno, B. Donnadieu, A. Igau, A. M. Caminade, J. P. Majoral, *Organometallics*, 2002, **21**, 4680-4687.
[49] M. Keller, M. Ianchuk, S. Ladeira, M. Taillefer, A. M. Caminade, J. P. Majoral, A. Ouali, *Eur. J. Org. Chem.*, 2012, **2012**, 1056-1062.
[50] S. Gatard, S. Kahlal, D. Mery, S. Nlate, E. Cloutet, J. Y. Saillard, D. Astruc, *Organometallics*, 2004, **23**, 1313-1324.
[51] A. Perrier, M. Keller, A. M. Caminade, J. P. Majoral, A. Ouali, *Green Chem.*, 2013, **15**, 2075-2080.
[52] A. D. Phillips, L. Gonsalvi, A. Rornerosa, F. Vizza, M. Peruzzini, *Coord. Chem. Rev.*, 2004, **248**, 955-993.
[53] V. Polshettiwar, R. Luque, A. Fihri, H. B. Zhu, M. Bouhrara, J. M. Bassett, *Chem. Rev.*, 2011, **111**, 3036-3075.
[54] M. Keller, V. Colliere, O. Reiser, A. M. Caminade, J. P. Majoral, A. Ouali, *Angew. Chem. Int. Ed.*, 2013, **52**, 3626-3629.
[55] M. Pagliaro, V. Pandarus, R. Ciriminna, F. Beland, P. D. Cara, *ChemCatChem*, 2012, **4**, 432-445.
[56] M. Keller, A. Hameau, G. Spataro, S. Ladeira, A. M. Caminade, J. P. Majoral, A. Ouali, *Green Chem.*, 2012, **14**, 2807-2815.
[57] V. S. Myers, M. G. Weir, E. V. Carino, D. F. Yancey, S. Pande, R. M. Crooks, *Chem. Sci.*, 2011, **2**, 1632-1646.
[58] E. Badetti, A. M. Caminade, J. P. Majoral, M. Moreno-Manas, R. M. Sebastian, *Langmuir*, 2008, **24**, 2090-2101.

[59] N. G. Garcia-Pena, A. M. Caminade, A. Ouali, R. Redon, C. O. Turrin, *RSC Adv.*, 2016, **6**, 64557-64567.
[60] C. Larre, B. Donnadieu, A. M. Caminade, J. P. Majoral, *Eur. J. Inorg. Chem.*, 1999, **1999**, 601-611.
[61] L. Chen, J. Li, Y. Fan, J. Qiu, L. Cao, R. Laurent, S. Mignani, A.-M. Caminade, J.-P. Majoral, X. Shi, *Biomacromolecules*, 2020, **21**, 2502-2511.
[62] L. Chen, L. Cao, M. Zhan, J. Li, D. Wang, R. Laurent, S. Mignani, A.-M. Caminade, J.-P. Majoral, X. Shi, *Biomacromolecules*, 2022, **23**, 2827-2837.
[63] G. Soler-Illia, L. Rozes, M. K. Boggiano, C. Sanchez, C. O. Turrin, A. M. Caminade, J. P. Majoral, *Angew. Chem. Int. Ed.*, 2000, **39**, 4250-4254.
[64] D. H. Kim, P. Karan, P. Goring, J. Leclaire, A. M. Caminade, J. P. Majoral, U. Gosele, M. Steinhart, W. Knoll, *Small*, 2005, **1**, 99-102.
[65] J. Ledall, S. Fruchon, M. Garzoni, G. M. Pavan, A. M. Caminade, C. O. Turrin, M. Blanzat, R. Poupot, *Nanoscale*, 2015, **7**, 17672-17684.
[66] L. Griffe, M. Poupot, P. Marchand, A. Maraval, C. O. Turrin, O. Rolland, P. Metivier, G. Bacquet, J. J. Fournie, A. M. Caminade, R. Poupot, J. P. Majoral, *Angew. Chem. Int. Ed.*, 2007, **46**, 2523-2526.
[67] A. M. Caminade, S. Fruchon, C. O. Turrin, M. Poupot, A. Ouali, A. Maraval, M. Garzoni, M. Maly, V. Furer, V. Kovalenko, J. P. Majoral, G. M. Pavan, R. Poupot, *Nat. Commun.*, 2015, **6**, article no. 7722.
[68] O. Rolland, C. O. Turrin, G. Bacquet, R. Poupot, M. Poupot, A. M. Caminade, J. P. Majoral, *Tetrahedron Lett.*, 2009, **50**, 2078-2082.
[69] A. Hameau, S. Fruchon, C. Bijani, A. Barducci, M. Blanzat, R. Poupot, G. M. Pavan, A. M. Caminade, C. O. Turrin, *J. Polym. Sci. Part A-Polym. Chem.*, 2015, **53**, 761-774.
[70] A. Sourdon, M. Gary-Bobo, M. Maynadier, M. Garcia, J. P. Majoral, A. M. Caminade, O. Mongin, M. Blanchard-Desce, *Chem.-Eur. J.*, 2019, **25**, 3637-3649.
[71] P. Servin, R. Laurent, M. Tristany, A. Romerosa, M. Peruzzini, F. Garcia-Maroto, J.-P. Majoral, A.-M. Caminade, *Inorg. Chim. Acta*, 2018, **470**, 106-112.
[72] L. Martins, R. Wanke, T. F. S. Silva, A. J. L. Pombeiro, P. Servin, R. Laurent, A. M. Caminade, *Molecules*, 2018, **23**, article no. 3066.
[73] A. M. Allgeier, C. A. Mirkin, *Angew. Chem. Int. Ed.*, 1998, **37**, 894-908.
[74] C.-O. Turrin, E. Manoury, A.-M. Caminade, *Molecules*, 2020, **25**, article no. 447.
[75] P. Neumann, H. Dib, A. M. Caminade, E. Hey-Hawkins, *Angew. Chem. Int. Ed.*, 2015, **54**, 311-314.
[76] P. Neumann, H. Dib, A. Sournia-Saquet, T. Grell, M. Handke, A. M. Caminade, E. Hey-Hawkins, *Chem.-Eur. J.*, 2015, **21**, 6590-6604.
[77] J. Cossy, F. Eustache, P. I. Dalko, *Tetrahedron Lett.*, 2001, **42**, 5005-5007.
[78] J. Popp, A.-M. Caminade, E. Hey-Hawkins, *Eur. J. Inorg. Chem.*, 2020, **2020**, 1654-1669.
[79] A. M. Caminade, A. Ouali, M. Keller, J. P. Majoral, *Chem. Soc. Rev.*, 2012, **41**, 4113-4125.
[80] M. Keller, A. Perrier, R. Linhardt, L. Travers, S. Wittmann, A. M. Caminade, J. P. Majoral, O. Reiser, A. Ouali, *Adv. Synth. Catal.*, 2013, **355**, 1748-1754.
[81] C. E. Song (ed.), *Cinchona Alkaloids in Synthesis and Catalysis: Ligands, Immobilization and Organocatalysis*, Wiley-VCH, Weinheim, 2009.
[82] J. Rull, M. Casals, R. M. Sebastian, A. Vallribera, J. P. Majoral, A. M. Caminade, *ChemCatChem*, 2015, **7**, 2698-2704.
[83] E. Cavero, M. Zablocka, A. M. Caminade, J. P. Majoral, *Eur. J. Org. Chem.*, 2010, **2010**, 2759-2767.
[84] J. Rull, J. J. Jara, R. M. Sebastian, A. Vallribera, C. Najera, J. P. Majoral, A. M. Caminade, *ChemCatChem*, 2016, **8**, 2049-2056.
[85] https://dendris.fr/ (accessed on November 13, 2023).
[86] J. P. Majoral, J. M. Francois, R. Fabre, A. Senescau, S. Mignani, A. M. Caminade, *Sci. China-Mater.*, 2018, **61**, 1454-1461.
[87] https://www.imd-pharma.com/ (accessed on November 13, 2023).
[88] A.-M. Caminade, C.-O. Turrin, R. Poupot, *Wiley Interdiscip. Rev.-Nanomed. Nanobiotechnol.*, 2022, **14**, article no. e1783.

ACADÉMIE DES SCIENCES
INSTITUT DE FRANCE

Comptes Rendus. Chimie
2024, Vol. 27, Special issue S2, p. 57-83
https://doi.org/10.5802/crchim.287

Research article

Women Chemists in France in 2024

Non-covalent interactions in supported asymmetric catalysis: a brief account

Léa Ibos [a] and Emmanuelle Schulz [b, *, a]

[a] Université Paris-Saclay, CNRS, Institut de Chimie Moléculaire et des Matériaux d'Orsay, Site Henri Moissan, 17, avenue des Sciences, 91400 Orsay, France

E-mail: emmanuelle.schulz@universite-paris-saclay.fr (E. Schulz)

Abstract. Recent developments in asymmetric catalysis involve the heterogeneization of chiral complexes so that they can be easily immobilized on different supports. This account focuses on procedures that lead to the formation of non-covalent interactions between the chiral active sites and the chosen support, as they generally involve less tedious synthetic modifications and can allow either the chiral catalyst or the support to be easily recovered, at will. As a result, electrostatic interactions between inorganic supports and chiral organometallic complexes have been described to lead to efficient and recoverable catalysts. More recently, other weak interactions, such as π-interactions, but also donor–acceptor complexes, have been implicated for implementation of robust immobilizing procedures. There are also many examples of the use of coordination links, such as those present in metal organic frameworks for supported asymmetric catalysis, which pave the way for efficient cooperative or tandem asymmetric catalysis.

Keywords. Asymmetric catalysis, Recycling, Heterogeneous catalysis, Electrostatic interactions, π-interactions, Donor–acceptor complexes, Metal organic frameworks.

Funding. We are grateful to the CNRS, the Université Paris-Saclay for their support and to the Agence Nationale de la Recherche (ANR-22-CE07-0A40-01, PhD financial support to LI).

Manuscript received 20 December 2023, revised 5 January 2024, accepted 19 January 2024.

1. Introduction

Since its discovery over 50 years ago, asymmetric catalysis has enabled the preparation of a wide variety of enantioenriched synthons with different functionalities, with an efficiency in line with green chemistry concepts. A step forward has been taken with the development of heterogeneous asymmetric catalysis, aimed at separating the catalyst from the substrates and reaction products in two different phases (usually a solid and a liquid phase) for easy recovery and reuse of the precious chiral active species. This process has made it possible both to increase the turnover number of the catalysts by recycling them, and to implement flow procedures to best meet industry needs. Kagan and his group pioneered this field by describing the covalent attachment of a chiral rhodium complex analogous to the DIOP ligand to oxidized Merrifield resin and demonstrating its activity in asymmetric hydrogenation and hydrosilylation reactions [1]. They already highlighted the effect of the nature of the support on the activity and enantioselectivity of these reactions, which were subsequently studied and optimized by Stille group [2,3].

In Kagan's seminal paper, the rhodium active sites were covalently anchored to the support to prevent leaching of the metal and hence loss of activity, or even contamination of the products. This type of

* Corresponding author

supported catalyst preparation may, however, require several synthesis steps to modify at least the ligand, but sometimes also the support, for strong grafting *via* the formation of covalent chemical bonds. Interest has therefore been focused on the immobilization of chiral catalysts *via* non covalent interactions on different supports, with the aim of offering robust systems with simpler preparation but also enabling both the catalyst and/or the released support to be recovered at will, for another use.

Original and long-standing approaches to supported asymmetric catalysis involving the modification of natural chiral supports by metal catalysts should be mentioned here, as did Schwab and Rudolph who studied metal-supported cleaved quartz surfaces [4] or Izumi et al., who used Pd dispersed on silk fibers [5]. This has led to disappointing results in terms of activity and enantioselectivity values, but nevertheless remains a fundamental proof of concept. On the other hand, other procedures were examined in which a conventional metal catalyst was modified by adsorption of natural chiral molecules. This is the case, for example, with highly efficient hydrogenation catalysts such as tartaric acid-modified Ni catalysts or cinchona-modified Pt catalysts. In the presence of such metallic surfaces modified by these chiral inducers, the asymmetric transformation is due to the selective adsorption of the substrate onto the chiral surface, leading to very convincing results, for the hydrogenation of β-ketoesters or β-diketones for the first catalyst, and for the hydrogenation of α-ketoesters for the second one. This field of research has been the subject of numerous reports, including a comprehensive review by Blaser [6], and these methods have also been successfully applied on a large scale, for example in the preparation of Benazepril, an angiotensin-converting enzyme inhibitor intermediate [7].

However, major difficulties have arisen in achieving reproducible reaction rates and optical yields, as the selectivity of the transformations is highly dependent on the catalyst preparation procedure and/or its modification with the chiral inducer. Enantioselectivity indeed results from specific interactions between the substrate, the chiral modifier and the metal, the nature of which remains largely unknown and uncontrolled. Work in this field has now mostly shifted to the use of well-defined chiral active catalysts whose activity is more predictable and reproducible thanks to their immobilization on different supports [8–14].

Non-covalent immobilization of enantioselective catalysts was described in exhaustive reviews nearly 15 years ago, concerning organometallic [15] or organic catalysts [16], organized according to the immobilization method used. At that time, most of them involved electrostatic, acid-base, hydrophobic or coordination interactions, adsorption or some entrapment methods. Since then, new strategies have emerged involving π-stacking or charge-transfer interactions, coming from our group and others. Accordingly, this account will highlight some of the most recent results describing non-covalent interactions for the easy recovery and reuse of enantioselective catalysts, starting with a selection of articles dealing with the use of ionic interactions with inorganic supports to immobilize catalysts. Then asymmetric catalysis with active chiral species immobilized by π-stacking interactions will be summarized, as well as examples implying the formation of charge transfer complexes. Finally, we have chosen to present some of the most recent examples of coordination interactions, such as those leading to metal organic frameworks (MOFs), as they also enable recent, contextual and valuable asymmetric multicatalysis. The vast majority of the examples we have chosen to highlight here involve the use of the well-known salen complexes, due to their ease of access and their high efficiency in a very large number of asymmetric catalysis reactions.

2. Electrostatic interactions with inorganic supports

As previously mentioned, the non-covalent immobilization of chiral catalysts has already been widely developed and mainly involved anchoring complexes on silica supports, modified accordingly to allow predominantly ionic interactions *via* sulfonic acid bonds. As an example, Kim and coworkers have described the hydrothermal synthesis of sulfonic acid-functionalized SBA-16 mesoporous silica [17]. The incorporation of active Co-salen moieties was achieved by the addition of Co(II) complexes in solution and subsequent oxidation in air leading to a stable linkage in the form of ionic pairs with sulfonate anions on the surface. The robustness of the solid

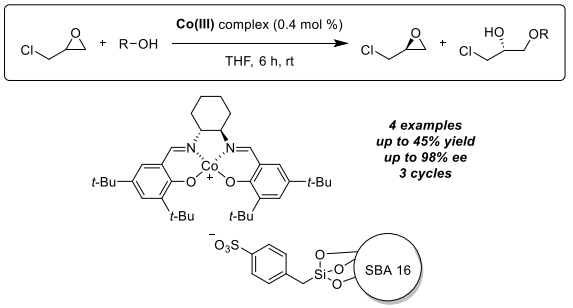

Scheme 1. Immobilization by ion pair interactions for the ARO of epoxides.

catalyst was tested for the Asymmetric Ring Opening (ARO) of *rac*-epichlorohydrin by water or phenol derivatives. The reactions even gave better results than those carried out with analogous homogeneous catalysts, i.e. with lower catalyst loading and shorter reaction time. The targeted products were recovered, after simple solid filtration, with enantioselectivity values exceeding 98% in some cases and yields reaching 45% (Scheme 1). A slight drop in activity was observed when recycling was attempted in the hydrolytic kinetic resolution of *rac*-epichlorohydrin, leading to a polar diol, which may compromise ionic pairing on silica. In the case of the formation of less polar compounds, using phenols as nucleophiles for example, no loss of activity was observed and the catalyst could be reused. The authors proved that the support could be recovered and reused after a new Co-salen re-attachment; they also demonstrated that no reaction occurred in the supernatant after catalyst removal before complete conversion, as a proof of the effectiveness of the heterogeneous procedure.

New developments include the use of a different support, namely chiral silica, in the hope of synergy for possible matching effects between the two chiral elements, the support and the complex. In this context, Sun and his group prepared a series of helical silica materials in a sol–gel procedure doped with sodium lactate to affect chirality, and carried out subsequent phenylsulfonylation before immobilizing Mn-salen complexes in ionic pairs [18]. Comprehensive analytical studies were performed to prove the immobilization of the chiral catalysts and the integrity of the helical structure. These new structures were tested as catalysts to promote the hetero-Diels–Alder reaction between Danishefsky's diene and various aldehydes. Active and enantioselective catalysts were obtained after immobilization of achiral Mn-complexes, demonstrating the chiral induction induced by the support alone. Immobilization of a chiral catalyst improved enantioselectivity values, the molecular catalyst being responsible for product configuration and the chiral environment for enantioselectivity enhancement. The authors describe a series of four different aldehydes and the reaction with acetophenone with varying success, which they attribute to restricted conformational changes by hydrogen bond or other adsorptions on the support, depending on the substrate structure. The transformation of heptaldehyde, however, has been described with total conversion and selectivity (Scheme 2). A major influence of solvents was observed, with ionic liquids influencing the product configuration and promoting catalyst recyclability. Six cycles of the solid catalyst in $BMImBF_4$ gave stable results in terms of product yield (74%) and enantioselectivity (>99%). These chiral helical silica supports have also been studied for their ability to promote asymmetric epoxidations of non-functionalized alkenes, in the presence of PhIO or *m*-CPBA [19]. In this case the silica support has been modified with pendant ammonium groups and the Mn-salen derivative was modified on the aryl moieties by a sulfonyl group, remote from the catalytic center, to enable ion pair formation. Again, an enantioselective transformation occurred in the presence of the exclusive helical chirality, and synergistic effects were highlighted between the mesoscopic and the molecular chirality, with match or *mis*-match properties.

Other types of supports, namely layered zinc or Lanthanum Hydroxide Nitrates (LHS, Layered Hydroxide Salts) have also been used as ion-exchangeable supports to immobilize Mn-salen complexes modified with sodium sulfonate groups [20]. The lower inter-layer forces allowed indeed the intercalation of larger anions, even though FT-IR analyses revealed only partial exchange of nitrates by the anionic catalyst. The benchmark reaction involved the enantioselective epoxidation of styrene derivatives and the Zn-LHS-supported Mn-salen sandwich structure gave the best results in terms of activity and selectivity, achieving 79% conversion and 99% ee for the epoxidation of α-methylstyrene with iodosylbenzene (Scheme 3). Re-

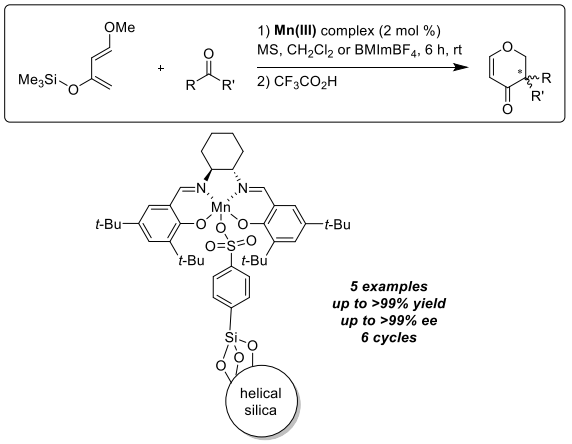

Scheme 2. Immobilization by ion pair interactions on chiral silica for the hetero Diels–Alder reaction.

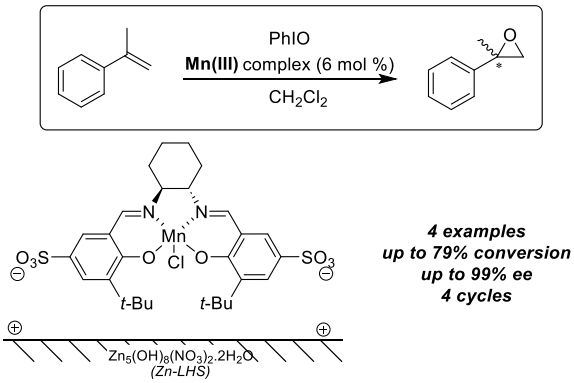

Scheme 3. Layered Hydroxide Salts as ion-exchangeable supports for alkenes epoxidation.

cycling can be achieved after simple filtration and the epoxidation was successful for the following four cycles.

Ionic links of different nature have further been exploited towards immobilization of metal-salen derivatives on silica supports. Bhaumik, Islam et al. prepared a chemically transformed carboxylic acid functionalized mesoporous silica (AFS-1) by modification of the SBA-15 outer sphere [21]. A methylammonium-modified Co-salen complex was then immobilized by ionic exchange interactions between the anionic support and the cationic complex. Asymmetric aminolysis of racemic and *meso* epoxides (10 examples) has been achieved with excellent results under solvent-free conditions, leading for example to the formation of 2-(phenylamino)phenol in 97% isolated yield and >99% ee. The high recyclability of the catalyst has been described, as it can be engaged in successive transformations up to 5 times with almost no loss of efficiency (Scheme 4A). An analogous catalytic material was also prepared with the corresponding Cu-complex and found to promote the asymmetric nitroaldol reaction between various aryl- or alkylaldehydes and nitromethane (11 examples) with high enantioselectivity (up to 94%) and TONs [22]. The recyclability of the procedure was demonstrated by performing the multiple reaction of *p*-nitrobenzaldehyde with nitromethane with the same batch of catalyst in dichloromethane, which proceeded successfully with only a slight loss in activity (95% to 84% conversion) and an identical enantioselectivity value (91%) for eight consecutive cycles (Scheme 4B). Interestingly, this supported catalyst has been used to prepare (*R*)-isoproterenol, a non-selective β-adrenoreceptor agonist.

The last example we have chosen to present concerns the preparation of heterogeneous Mn-salen complexes anchored on mesoporous materials functionalized with imidazole groups [23]. Modified silica supports were obtained by co-condensation of tetraethyl orthosilicate and *N*-(3-triethoxysilylpropyl) imidazole, resulting in functionalized MCM-41, favoring homogeneous distribution of organic species. Immobilization of the Mn-salen complex was achieved in refluxing toluene to form electrostatic bonds with the imidazole group, resulting in a solid catalyst offering high activity and enantioselectivity similar to that obtained with soluble catalysts, in the epoxidation of olefins (3 examples, up to 99% conversion and 85% ee for the oxidation of indene) (Scheme 5). It should be noted that very small quantities of catalyst could be used, due both to the high electron-donating capacity of the imidazole ligand and the good accessibility of the catalytic sites. Virtually no metal leaching was detected by ICP-AES analysis (Inductively Coupled Plasma Atomic Emission Spectrometry); nevertheless, the supported catalyst progressively lost its efficiency when subjected to recycling experiments (3 runs).

Other types of electrostatic interaction than those reported previously are existing, namely hydrogen bonding which has been used, however not specif-

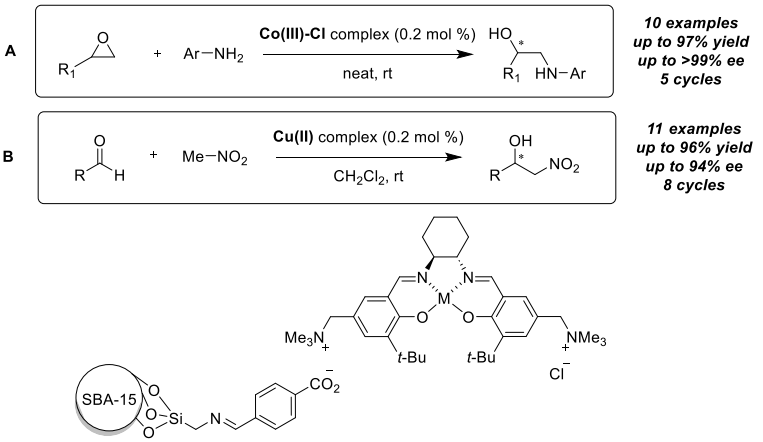

Scheme 4. Immobilization by ion pair interactions on mesoporous silica for aminolysis of epoxides and nitroaldol reactions.

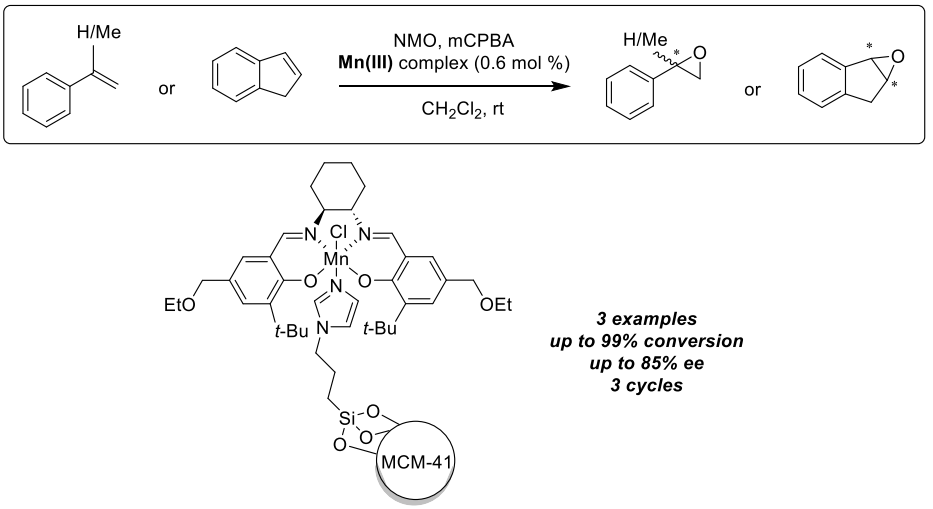

Scheme 5. Immobilization by ion pair interactions on MCM-41 for alkenes epoxidation.

ically for the immobilization of catalysts on a solid support, but to bring two salen complexes together, with the aim of promoting their cooperativity [24]. Hong and his group have prepared unsymmetrical Co-salen complexes bearing complementary 2-pyridone/aminopyridine moieties on each phenolic group, capable of creating self-assembled dimers in solution *via* hydrogen bonding. The reaction tested was the Henry reaction, in which both the aldehyde and the nitronate ion are activated by the cobalt center so that the asymmetric catalysis can take place in the presence of a tertiary amine, as a base. Control experiments revealed significant rate acceleration using this assembled catalyst, as well as kinetic studies indicated a second order relative to the cobalt concentration, with excellent enantioselectivity values for a range of aldehydes (8 examples, up to 96% ee, Scheme 6A). These authors demonstrated that other functionalities, notably the urea unit, could be used to create directional hydrogen-bonding interactions for self-assembly [25]. Therefore, they prepared various symmetrical Co-salen complexes functional-

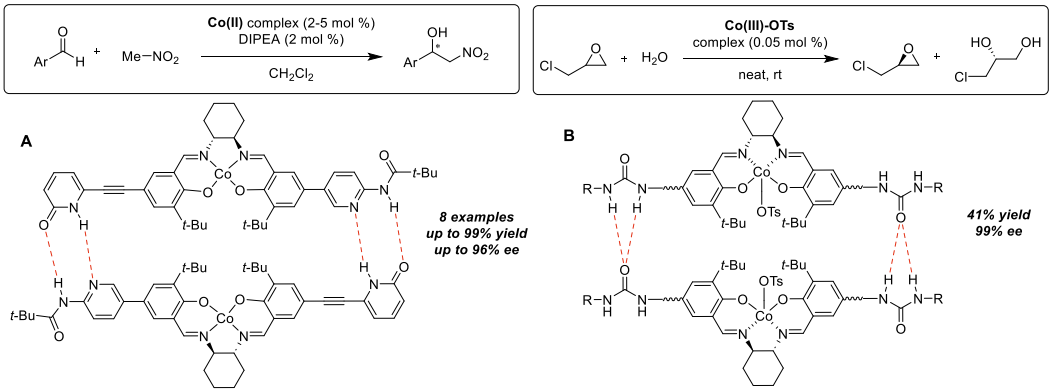

Scheme 6. Immobilization by hydrogen bonding for nitroaldol reactions and hydrolysis of epoxides.

ized with bis-urea units and studied their efficiency in catalyzing the HKR (Hydrolytic Kinetic Resolution) of *rac*-epichlorohydrin; these dimeric species (11 examples) were found to exhibit a significant rate acceleration compared with the monomeric catalyst, both in solution (in THF, up to 92% ee) and under solvent-free conditions (up to 93% ee), and this proved true for the transformation of four different terminal epoxides (Scheme 6B). In this case, kinetic studies also showed that the rate laws were second-order in the cobalt concentration and further mechanistic studies were carried out, consistent with the fact that the observed rate enhancement was due to the self-assembly by urea-urea hydrogen bonding.

3. π-stacking interactions with carbon supports

In 2008, Zhou et al. reported an example of enantioselective hydrogenation of α-dehydroamino esters catalysed by a Rh(I) complex immobilized *via* a pyrene-modified PyrPhos ligand on Carbon Nanotubes (CNTs) [26]. This ligand is readily accessible by simple amide coupling, and both the activity and enantioselectivity of the corresponding catalyst are unaffected by the presence of the pyrene-tag. Various examples of substrates containing electron-donating or electron-withdrawing *para*-substituted aromatic groups have led to the targeted products in excellent yields (>99%) and very good enantiomeric excess values (92–96% ee). The main advantage of these modified catalysts remains their solvent-dependent adsorption capacity. As such, reactions can be carried out under homogeneous conditions, and the catalyst recovered by filtration after a simple change of solvent for precipitation. The authors showed that the lowest adsorption rate on CNTs was obtained when using dichloromethane (50%), which was considered the best solvent because the catalyst was fairly mobile and the active sites easily accessible. On the contrary, the use of a solvent with a high adsorption rate on CNT, as ethyl acetate, led to the precipitation of the complex, making it suitable for catalyst recovery and recycling by filtration. By playing on this difference of adsorption, easy catalysts recycling was performed by a simple solvent change and 9 cycles were realized without affecting either the conversion or the enantioselectivity (Scheme 7A). A similar transformation was reported by Fernández, Khiar and their group in 2017, for which they proposed a pyrene-tagged carbohydrate-based phosphorus/sulfur ligand for Rh(I) catalysis immobilized on Single-Walled Carbon Nanotubes (SWCNTs) [27]. Here, the effect of carbon linker length on catalytic activity was investigated for the hydrogenation of methyl α-acetoamido-cinnamate. Notably, they demonstrated low activity using a one-carbon linker, whereas a three-carbon linker achieved the same conversion and enantioselectivity as with a traditional Rh complex in dichloromethane (>99% conversion, 90% ee). In addition, they also showed that the presence of this pyrene-tag made the reaction efficiency more solvent-dependent, probably due to possible competitive complexation of Rh(I) with the aromatic rings to form Rh(I)-η^6-arene complexes.

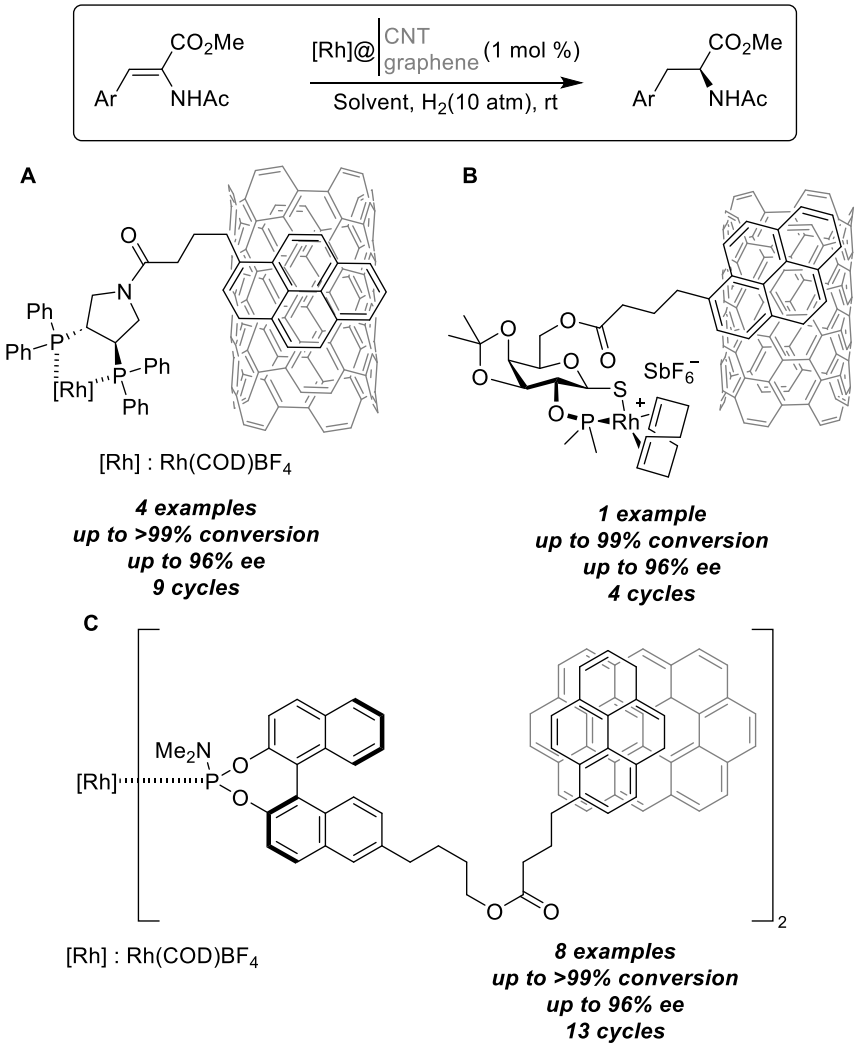

Scheme 7. π-stacking interactions on CNTs for Rh-catalyzed asymmetric hydrogenation.

As mentioned previously [26], the solvent also influenced the catalyst adsorption on CNTs, allowing reactions to be carried out under homogeneous conditions and the catalyst to be recovered by changing the solvent. Here also, dichloromethane was the solvent of choice to carry out the reaction. On the other hand, while the reaction went poorly in ethyl acetate, the use of this solvent enabled almost complete adsorption onto the CNTs after one hour of sonication, which allowed to switch to heterogeneous conditions for easy catalyst recovery. Based on these results, four successive runs were carried out with the same batch of catalyst, starting with excellent conversion (>99%) and enantiomeric excess (96%) to dramatically decreased values at the end (<10% conversion, 40% ee), probably due to the intrinsic instability of the catalyst (Scheme 7B). Later, in 2020, Shi et al. described a method for the asymmetric hydrogenation of dehydroamino acid esters under heterogeneous conditions [28]. They employed pyrene-modified MonoPhos-Rh(I) complexes immobilized on graphene, demonstrating both high catalytic activity and enantioselectivity. The use of ethyl acetate enabled the achievement of comparable catalytic performance to classical homogeneous conditions, coupled with high adsorption on graphene. The

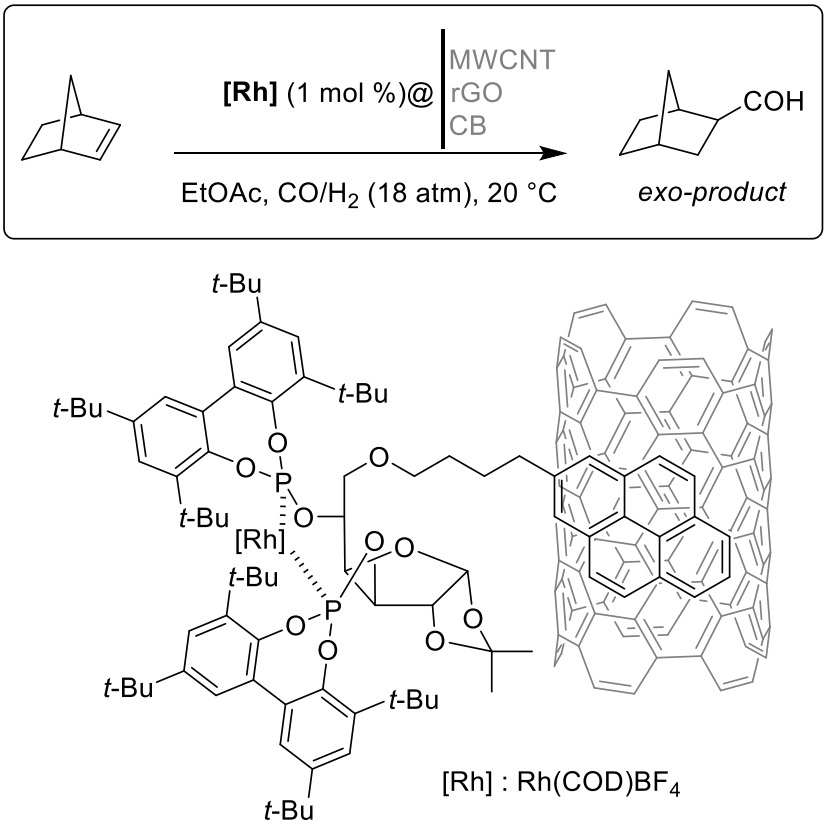

Scheme 8. π-stacking interactions on CNTs for Rh-catalyzed asymmetric hydrogenation of norbornene.

study encompassed eight examples of substrates featuring variously substituted aromatic groups. This resulted quantitative yields and enantiomeric excess values ranging from 91 to 96% for the targeted products (Scheme 7C). Notably, diverse analytical methods were employed to confirm well-defined immobilisation. ^{31}P Cross-polarization magic-angle spinning (CP-MAS) NMR spectra demonstrated that the Rh complexation pattern remained unchanged after adsorption on graphene surfaces with a 3×10^{-4} mmol·mg^{-1} loading on graphene. Additionally, EDS TEM analyses (Energy Dispersive Spectroscopy for elemental mapping in Transmission Electron Microscopy) illustrated a homogeneous distribution of the Rh complex on the surface. BET (Brunauer–Emmett–Teller) measurements indicated a surface area for the immobilized catalyst reduced by half compared to the raw graphene. The catalyst exhibited reusability for up to 13 cycles without compromising the conversion of the starting material or enantiomeric excess values. However, it is worth mentioning that the reaction time had to be extended from 2 h to 10 h after seven cycles, likely due to the instability of the filtrated intermediate in the absence of a hydrogen atmosphere.

Another example of immobilised Rh(I)-catalysed reaction on carbon surfaces has been developed by Godard and his group in 2019 [29]. The authors focused on the asymmetric hydroformylation of norbornene to preferentially obtain the *exo*-product, utilizing new pyrene-tagged diphosphite ligands supported on various carbon materials and adapted for continuous flow conditions (Scheme 8). Initially, the authors designed new sugar-based ligands to achieve good *exo*-product yields (>99%) and enantiomeric excess values (62%) under homogeneous conditions. Optimization efforts revealed that glucofuranose-diphosphite ligands exhibited better enantioselectivity than xylofuranose-derivatives, especially when introducing substituents on the

biphenyl moiety. Moreover, the *O*-alkylation at the glucofuranose-C5-position played a crucial role in catalyst activity. Subsequently, the heterogenization of the reaction was undertaken by adding a pyrene-tag to the effective ligand, ensuring no modification of the catalyst activity. The immobilization of the tagged Rh(I)-complexes was studied on different carbon materials (Multi-Walled Carbon NanoTubes (MWCNTs), Reduced Graphene Oxide (rGO) and Carbon Black (CB)). The results were consistent when using MWCNTs or rGO but significantly increased on CBs, likely due to the entrapment of the complexes in the material structure. The effect of carbon-linker length was highlighted, with the four-carbon linker on MWCNT showing the best results being selected for the rest of the study. However, heterogeneous catalysis resulted in significantly lower enantioselectivity values, and in terms of the recycling ability of the immobilized catalyst in batch conditions, no conversion of the starting material was observed after three runs. ICP-MS (Inductively Coupled Plasma Mass Spectrometry) analysis demonstrated high Rh leaching during the reaction. Nevertheless, with the most optimized conditions in hand, the authors have tested continuous flow conditions. Injecting the syngas mixture *via* a mass flow controller, they optimized the reaction at 10 bar pressure to achieve higher enantioselectivity in the flow mode (72%) than in batch (62%). This improvement was attributed to more efficient gas-mass transfer which increased gas solubility, and better exposure of substrates to the catalyst, resulting in a higher local catalyst concentration. Subsequently, the support was changed for rGO or CBs, and similar enantioselectivity was obtained with approximately the same substrate conversion and lower decay. This was explained by a larger surface area of rGO (450 $m^2 \cdot g^{-1}$) and CBs (211 $m^2 \cdot g^{-1}$) compared to MWCNTs (80 $m^2 \cdot g^{-1}$) and improved ligand interactions with those supports, facilitated by the presence of functional groups on rGO or entrapment in mesoporous CBs. Although increasing the catalyst loading in CBs support allowed to increase the conversion up to 35% with the same enantiomeric excess value, Rh leaching remained a significant drawback for this reaction.

In 2013, Schulz et al. described the use of immobilized bis(oxazoline)-ligands for both copper-catalyzed Henry and ene reactions (Scheme 9) [30]. The use of anthracene-tagged ligands was favored to optimize the reaction conditions and study the recyclability of the supported catalysts. First, the Henry reaction between benzaldehyde and nitromethane was carried out using an anthracene-bis(oxazoline)-tagged $Cu(OAc)_2$ complex in ethanol under homogeneous conditions, which furnished excellent yield (89%) and enantiomeric excess (90%). However, after immobilization on activated carbon, the yield and enantioselective excess value slightly decreased (68% isolated yield, 69% ee), indicating that the support interferes with the reaction, leading to less accessible active sites. Moreover, formation of traces of elimination by-products was observed, probably due to the non-negligible acidity of the support, explaining the loss of yield. Then, recycling of the catalyst was achieved after centrifugation of the reaction medium to recover the catalyst. After 6 runs, the reaction time increased from 24 to 120 h for moderate yields and enantiomeric excesses. A test reaction performed with the supernatant after a recycling cycle gave comparable results, showing that a non-negligible amount of catalyst had been solubilized during the washing. Then, the reaction scope was extended to the ene reaction between ethyl glyoxylate and α-methyl-styrene with the anthracene-bis(oxazoline)-tagged $Cu(OTf)_2$ catalyst in dichloromethane. In this case, the same activity and enantioselectivity were obtained compared with homogeneous conditions (89% yield, 67% ee). However, throughout the runs, a slight decrease in activity and enantiomeric excesses was observed, as in the previous case. The catalyst immobilization on charcoal was then experimented and gave similar good results (85% yield, 70% ee). Attempts to recover and reuse the free ligand, exempt of the anthracene-tag, gave poor results during the recycling, indicating that those tags are really necessary for the catalyst recovery, without affecting its activity. Finally, to diversify supports, studies using a pyrene-tag instead of an anthracene one has been conducted to compare the effect of various carbon surfaces: charcoal, fullerene and SWCNT. After one run, some differences were already observable: all supported $Cu(OTf)_2$-supported catalysts allowed to obtain the desired product of the ene reaction with excellent yields (89%) but with variable enantioselectivity. The best enantiomeric excess was obtained with the catalyst supported on charcoal (69% ee), followed by SWNCT-supported reaction (64% ee) and then fullerene (56% ee). Pyrene- or anthracene-tags

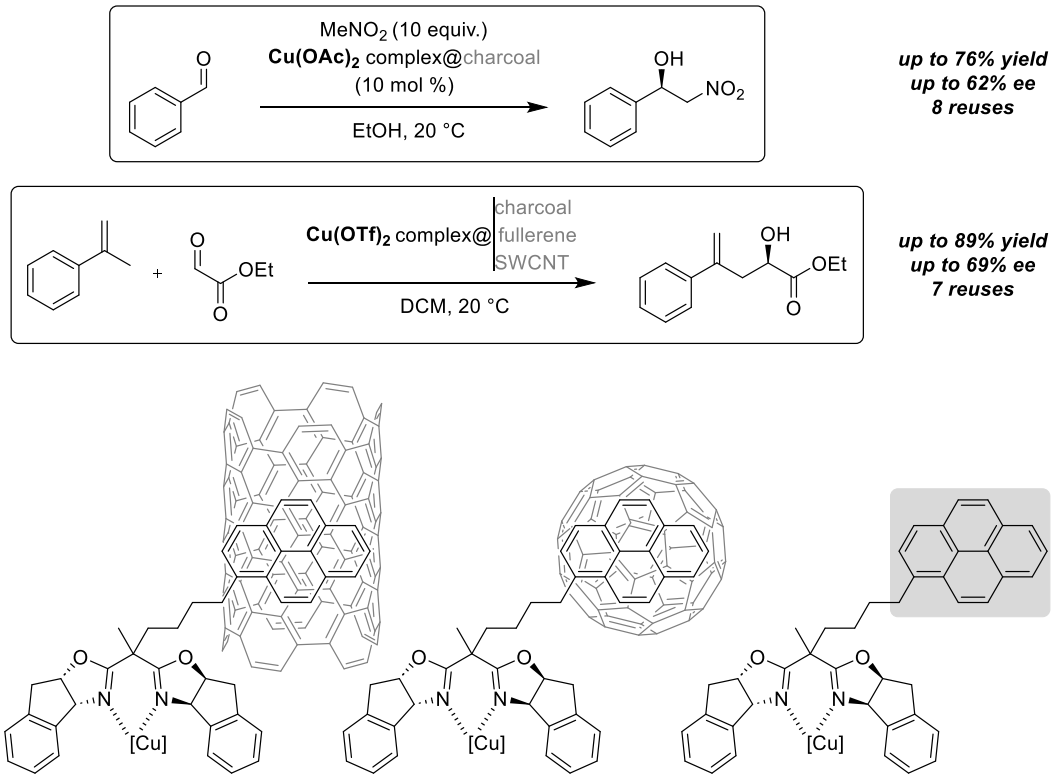

Scheme 9. π-stacking interactions on carbon supports for Cu-catalyzed nitroaldol and ene reactions.

showed no change in recyclability, despite a stronger π–π interaction in the former case. After seven runs, the charcoal-supported catalyst showed a slight decrease in yield and enantiomeric excesses. For the fullerene-based catalyst, the values remained more stable due to strong stacking with the pyrene-tag, which allowed easy recyclability throughout the cycles, but with lower enantioselectivity. On the other hand, the SWCNT-supported $Cu(OTf)_2$ complex gave better results in terms of activity, and values remained constant. This support seemed to be the best immobilization method, avoiding leaching, and promoting strong interactions with the pyrene-tag to ensure a good anchoring of the catalyst for recycling.

Later, in 2021, Schulz et al. described the immobilization of another type of organometallic complex *via* a pyrene-tagged salen ligand for both the Asymmetric Ring-Opening (ARO) of a *meso*-epoxide and the hetero-Diels–Alder reaction (HDA) (Scheme 10) [31]. Herein, different types of chromium salen complexes have been designed and their activity studied for the cyclohexene oxide ARO. Indeed, *one*- and *four*-carbon linkers have been synthesized and then, both respective symmetric and unsymmetric ligands have been accessed to finally compare the four ligand-tagged activity. First, in homogeneous conditions, those new-designed catalysts have shown a better activity with improved conversion rates of starting materials compared to the classical Jacobsen ligand, probably explained by possible π-stacking interactions between two catalysts to form bi-metallic more active complexes. However, symmetric catalysts seemed to be considerably less enantioselective than unsymmetric ones. Then, the immobilization of unsymmetric complexes on rGO as a suspension with a 4:1 mass ratio, characterised by UV–Vis and XPS (X-Ray Photoelectron Spectroscopy) analyses, has been performed to switch to heterogeneous conditions. Interestingly, in this case, the catalyst activity was not affected by the heterogenization although the enantioselectivity slightly decreased after the first run. Nevertheless,

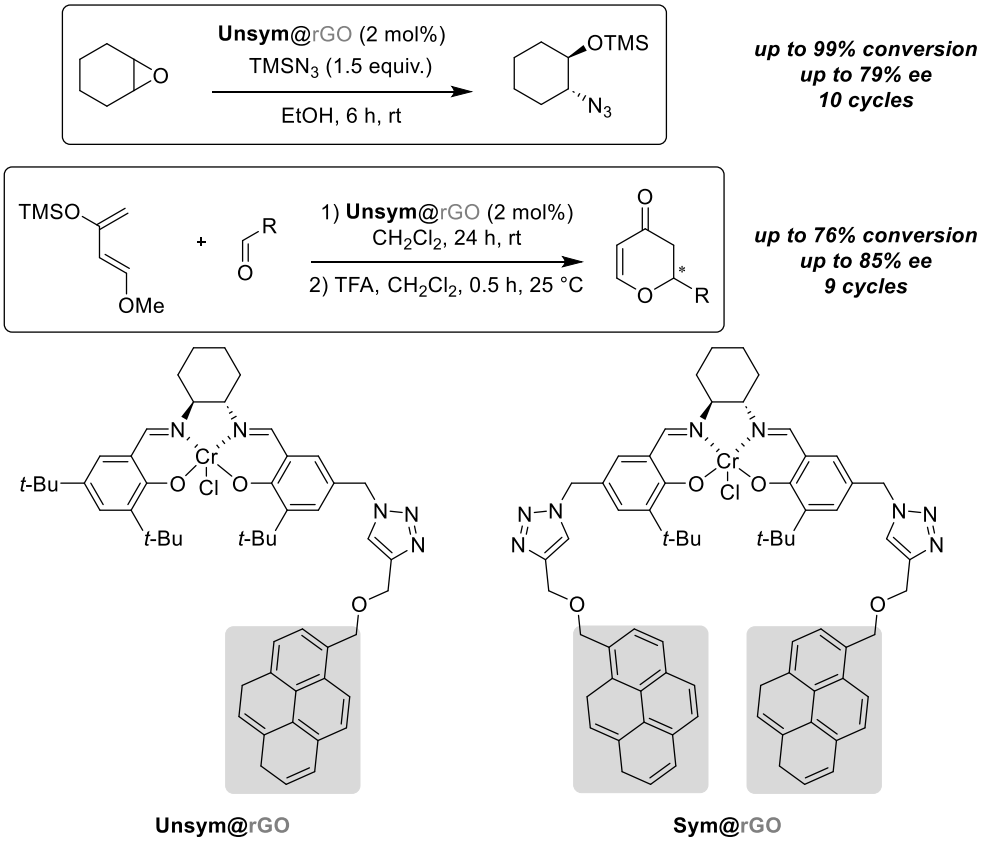

Scheme 10. π-stacking interactions on rGO for epoxides aminolysis and hetero Diels–Alder reaction.

as the recycling progressed, the enantiomeric excesses increased to reach the same values as the ones obtained under homogeneous conditions. Next, HDA of different aldehydes with Danishefsky's diene has been then performed to extend the application scope of this new-designed unsymmetrical salen chromium complex immobilized on rGO. Again, the catalyst efficiency was not affected in terms of yields and enantioselectivity with benzaldehyde compared to the use of the classic salen complex. Concerning the immobilization procedure, the nature of the washing solvent which allowed the supported catalyst recovery after one run proved to be very important. Indeed, both cold dichloromethane and acetone afforded a non-negligible leaching of the catalyst which affected the conversion of the starting materials. Diethyl ether finally allowed to perform seven cycles without any impact on either the conversion or the enantioselectivity. Moreover, the authors studied the ability of using the same immobilized-catalyst batch for the transformation of three different aldehydes, successively. Interestingly, the reactivity, with the three different substrates, remained stable even after two runs, showing the robustness of the recovery procedure.

In the same year, Schulz and her group developed heterogeneous conditions to perform the enantioselective formal [3 + 2]-cycloaddition of oxaziridine with ammonium enolates described by Smith group [32]. This reaction was promoted by an IsoThioUrea (ITU) catalyst on phenyl acetic anhydrides allowing to study the heterogenization of the organocatalytic transformation by π-stacking interactions (Scheme 11). Indeed, the organic catalyst has been tagged with a pyrene group on the benzotetramisole phenyl ring and the activity of this newly designed species has been first evaluated under homogeneous conditions. Fortunately, the

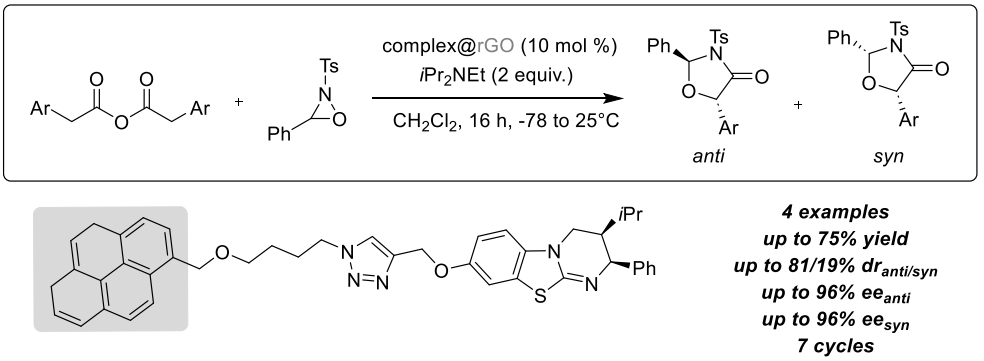

Scheme 11. π-stacking interactions on rGO for the enantioselective synthesis of oxaziridine derivatives.

same high activity as described with the unmodified ITU was recorded and it was shown that using the soluble Hünig base instead of inorganic Cs_2CO_3 resulted in improving the yields (92%) despite a slight decrease in selectivity (55/45% $dr_{(anti/syn)}$, 89/89% $ee_{(anti/syn)}$) and the formation of a small amount of *N*-tosylbenzylimine by-product. With those results in hands, the immobilised catalyst on rGO has been engaged and both organic and inorganic bases have been tested allowing to maintain quite the same activity, a stable good activity along three runs (60% yield, $dr_{(anti/syn)}$ about 50:50, and ee values for both products varying between 85 and 93%). Using dichloromethane was preferred as both reaction and washing solvent. Finally, an extended scope was developed, using four different substituted homoanhydrides, and the same batch of reused catalyst enabled the four different product mixtures to be obtained successively in good yields, with moderate diastereoselectivity and high enantioselectivity values.

4. Formation of charge-transfer complexes

Schulz and collaborators, using Atomic Force Microscopy (AFM), were able to visualize the formation of weak bonds between two acceptor–donor aromatic molecules, forming Charge-Transfer Complexes (CTC). They indeed successfully functionalized a tip and a probe with electron-deficient TriNitroFluorenone (TNF, (acceptor)) and electron-rich 1-methanolanthracene siloxane (donor), respectively, to quantify the reversible pull-off force between the two species [33]. Furthermore, they showed that CTC interactions could be influenced by the presence of competitive species. For instance, employing an apolar dodecane solvent revealed stronger interactions (6.6 ± 3.5 nN) than using aromatic apolar 1-methylnaphthalene (1.7 ± 0.5 nN), which engaged in competitive π-stacking interactions and saturated the tip-accessible sites, leading to decreased measurements. Various factors, such as time of contact between the species, medium concentration, viscosity, sweep time, and tip geometry, played crucial roles in measuring bonding forces [34]. Building on these results, Schulz et al. exploited CTC interactions for asymmetric catalysis. They developed an innovative recycling method by creating solid CTC between a donor-tagged catalyst and a good acceptor additive, facilitating simple recovery through filtration at the end of the reaction. The first described example involved the design of new anthracene-tagged bis(oxazoline) ligands complexed with Cu(II) to proceed enantioselective Diels–Alder reaction [35]. First, the activity of the new designed complex was evaluated under homogeneous conditions in dichloromethane and showed no impact on both conversion (>99%) and selectivity (93% de, 84% ee) after the first run, for the reaction between cyclopentadiene and 3-acryloyl-oxazolidin-2-one. CTC formation was then achieved by adding TNF, and the resulting complex precipitated thanks to pentane addition, enabling easy catalyst recovery for subsequent runs without compromising activity. Switching to another dienophile with the same recovered catalyst allowed for five more cycles at 20 °C. Eleven runs were successfully processed with the same batch, recovered by precipitation, and washing

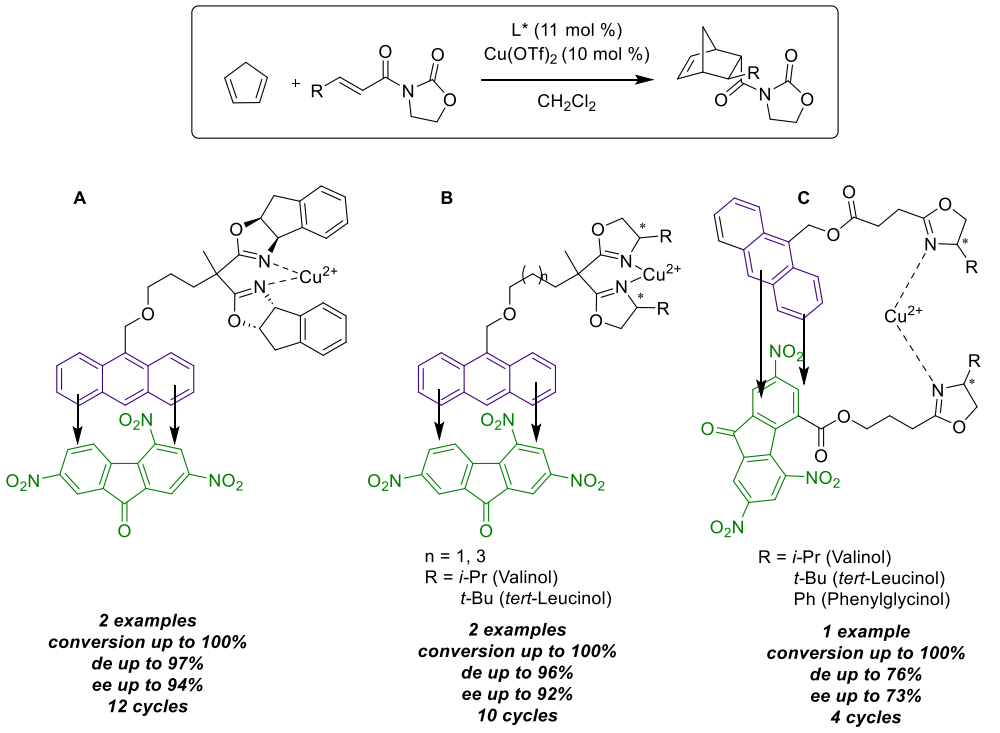

Scheme 12. Immobilization by CTC interactions for the Diels–Alder reaction.

with pentane, without impacting yields and enantioselectivity (Scheme 12A). The following year, in 2007, the method was extended to three newly designed bis(oxazoline) ligands in the Cu(II) promoted Diels–Alder reaction [36], involving one (*R*)-valinol and two *tert*-leucinol bis(oxazoline) derivatives, each tagged with anthracene. At first, the reaction was conducted under homogeneous conditions to assess the impact of ligand modification on catalyst activity. Concerning the (R)-valinol derivative, there was a significant decrease on selectivity (22% ee), mainly explained by the partial loss of the C_2 symmetry of the ligand after functionalization on the *gem*-dimethyl group compared to classical bis(oxazoline). Then, regarding the catalyst recovery, CTC were prior prepared *ex-situ* before being introduced to the reaction solvent with substrates. Fortunately, over six runs, the recovered catalyst was re-engaged with new substrates without compromising the enantioselectivity. In parallel, similar study was conducted with the two *tert*-leucinol derivatives as ligand (three- and five-carbon linker) which appeared to have a lesser impact on enantioselectivity than the first one (97% ee after one run under homogeneous conditions). However, initial tests in the presence of the corresponding CTC-based catalysts were much less effective (15 and 33% ee). The reuse for a second attempt with the same CTCs and new substrates surprisingly resulted in significantly improved enantiomeric excesses in both cases. Notably, the addition of molecular sieves was mandatory to prevent the detrimental effect of water on copper complex. PM3 calculations also revealed that in these latter complexes, the distortion degree between *tert*-leucinol-derivative ligands and the catalytic site was larger than with (R)-valinol one, involving more steric hindrance around the copper center. To overcome this activity loss, it was demonstrated that the first run needed to proceed without the electron-deficient precursor to achieve better results (89% yield, 87% ee), and the formation of the CTC must be executed only at the end of the first transformation. By adopting this approach, improved yields (89%) and enantiomeric excesses (87% ee) were achieved

after the second run with the same catalyst batch and remained stable along two additional cycles. Finally, three more cycles were conducted by switching from previously used 3-(but-2-enoyl)-oxazolidin-2-one to 3-acryloyloxazolidin-2-one, sustaining satisfactory activity (Scheme 12B). In 2008, our group proposed to use CTC interactions to prepare mimic bidentate complexes from anthracene- and TNF-tagged monodentate bis(oxazoline) [37]. We focused on the design of reversible copper(II) catalysts from copper triflate for use in asymmetric Diels–Alder cycloaddition. Initially, unsymmetrical modified bis(oxazoline) was prepared by deriving from *(S)*-valinol, (R)-phenylglycinol and *(S)*-*tert*-leucinol. These three ligands were respectively tagged with both anthracene as a donor and TNF as an acceptor. With these six ligands in hand, catalytic tests were attempted under homogeneous conditions to evaluate the tag impact on reactivity. Fortunately, good conversion and enantioselectivities were achieved using monodentates species independently, resulting in major formation of the *endo*-product with the anthracene-tagged electron-rich ligand and *exo*-product with the TNF-tagged electron-deficient one. This phenomenon was particularly evident with *tert*-leucinol derivatives and was explained by likely π-stacking interactions between the tags, favoring the formation of homodimeric copper complexes well known to efficiently catalyze asymmetric transformations. Subsequently, mixtures of one electron-rich and one electron-deficient ligand equivalent (1:1) afforded heterodimeric CTC. Unfortunately, as previously demonstrated [33,34], competitive π-stacking could occur between aromatic moieties, leading to the formation of homo-and hetero-dimeric bidentate complexes, resulting in poor yields and enantiomeric excesses for the *endo* and *exo* products. Nevertheless, a method has been developed for easily recovering the catalyst by precipitating the CTCs, facilitated by a simple pentane addition. The reuse of those CTC complexes did not affect conversion and enantioselectivity in two runs, demonstrating the efficiency of the procedure for recycling (Scheme 12C).

In the same year, Gennari et al. also reported the formation of bidentate complexes *via* CTC interactions between modified ligands, applied to Rh-catalysed hydrogenation [38]. They first prepared a library of tagged-ligands, consisting in eight electron-rich (six BINOL-and two octahydro-BINOL-based) and two electron-deficient pentafluorobenzyl phosphites (*R* and *S*). After isolating these compounds, they engaged them separately into a solution with the $Rh(cod)BF_4$ pre-catalyst (L/Rh = 2:1) to form homodimeric complexes, characterized by ^{31}P NMR. In parallel, they applied the same method to obtain heterodimeric CTC by mixing an equimolar ratio of electron-rich, electron-poor, and Rh pre-catalyst. In these cases, they observed the formation of the desired hetero-CTC (50%), but unfortunately, also the formation of homo-complexes (50%) due to competitive interactions. Consequently, they decided to conduct attempts with homodimeric and heterodimeric complexes in the enantioselective hydrogenation of dimethyl itaconate (Scheme 13). The best outcome was achieved with the mixture of (R)-electron-poor phosphite and (R)-*meta*-dimethoxybenzylalcohol-modified electron-rich ligand (99% ee). Other heterodimeric derivatives yielded moderate to excellent enantioselectivities, generally exhibiting higher activity with (R)/(R) mixtures compared to (R)/(S) ones. Additionally, concerning homodimeric species, methoxyphenol derivatives led to improved enantioselectivities (92–99% ee) compared to methoxybenzylalcohol ones, which delivered poor enantiomeric excesses (70–84% ee) and octahydro-BINOL ones, which provided moderate values (50–54% ee). Finally, they applied their library of bidentate complexes to the same reaction on methyl acetamido acrylate and, again, heterodimeric (R)-dimethoxybenzylalcohol derivative/(R)-pentafluorobenzyl one was the most successful trial (93% ee). Despite the heterodimeric catalyst not being pure, the corresponding heterodimeric/homodimeric mixture turned out to be the most active catalytic species.

In 2010, the Schulz group described a new immobilization method based on the same CTC interactions but involving the use of a modified-resin solid support [39]. In this case, they thought to functionalize a Merrifield resin with a TNF moiety as an acceptor for immobilizing anthracene-tagged ligands. The advantage of this method is that it facilitates catalyst recovery and allows one catalyst to be replaced by another to carry out different reactions in sequence, while using the same support. The reaction chosen to highlight this strategy was the Cu(II) enantioselective Diels–Alder reaction between 3-but-2-enoyl-oxazolidin-2-one and cy-

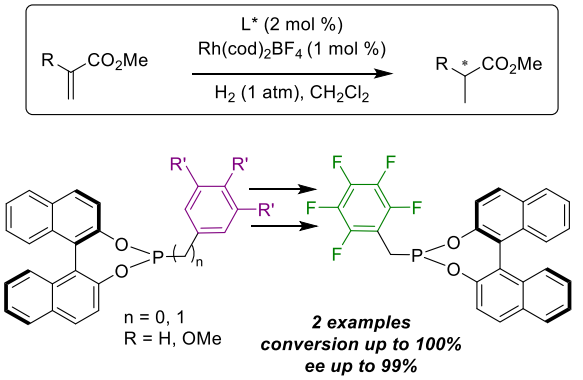

Scheme 13. CTC interactions for hydrogenation reactions.

clopentadiene. Initially, the efficiency of the newly designed tagged ligand was evaluated under homogeneous conditions without any detrimental effect on activity (83% ee, 78% de). Subsequently, the newly formed Cu(II)-catalyst was engaged under the same reaction conditions after its immobilization was conducted *ex situ* by CTC formation with the modified resin (0.5 mmol/g TNF loading, <50 mesh particle size). Once again, the same activity was achieved, leading to the desired *endo* product as the major compound (91% yield, 76% ee). Five additional runs were achieved using the same immobilized catalyst batch, recovered by simple filtration, and washing with pentane. During the first two reuses, the activity seemed stable, but from the fourth recycling, the yield and selectivity began to decrease, reaching very low values after the sixth reuse (28% yield, 39% ee). Test reactions indicated a partial leaching of the catalyst and weak CTC interactions (Scheme 14A). Finally, the same support was tested for different reactions; to this end, the first attempts were run with a single anthracene-tagged catalyst over four successive runs, revealing a loss of activity during the last two runs. To change the catalyst, toluene was introduced as a competitive solvent for CTC interactions, facilitating the removal of the catalyst from the solid support. The *ent*-catalyst was then easily added in dichloromethane to bind it to the recovered TNF-tagged solid support, and the same antagonistic reaction was conducted. Four additional runs were carried out using the same conditions, furnishing the opposite enantiomer of the target product with the same enantiomeric excesses as before. This method has proved to be an effective approach for the recycle of the catalysts and conducting multiple reactions using the same support, which could prove particularly useful in flow chemistry, for example. The same group also described another multi-reaction approach facilitated by CTC assistance for Cu(II)-catalyst recycling [40]. In this context, the aim was to use the same catalyst batch for the asymmetric Henry nitroaldolization, applied to multiple substrates. The study focused on an anthracene-tagged bis(oxazoline) ligand, as previously described, complexed with $Cu(OAc)_2 \cdot H_2O$. The presence of the anthracene moiety was proven to be not detrimental to the reaction activity (89% yield, 90% ee). Conveniently, catalyst recovery was achieved by adding TNF for CTC formation and subsequent precipitation in pentane at the end of the first run. After one recycling, the enantioselectivity remained stable, indicating that the CTC formation had no negative impact on the catalyst activity. Notably, the reaction time increased over the other runs, probably due to a leaching of the catalyst, but six reuses were successfully conducted while maintaining good results. This method was then applied to various substrates, including five aldehydes and two nitroalkane derivatives, resulting in seven different products with good yields and enantiomeric excesses. Especially, reactions involving nitroethane yielded a diastereoisomer mixture, with the *anti*-isomer as the major product. With these results in hands, they accomplished the recycling of one catalyst batch for nine different transformations, demonstrating that no impact on selectivity was observed over the runs. Despite a slight increase in reaction time during the subsequent runs, it is important to note that no traces of the previous product were observed during the next run, indicating that the recycling and washing procedures had been well optimized. Finally, they switched to heterogeneous conditions by grafting TNF moieties onto activated silica and immobilizing an anthracene-tagged Cu(II) catalyst *via* CTC interactions. The Henry reaction could be performed five successive times with the same catalyst batch, without additional precipitation in pentane, affording the desired product with the same yields and enantioselectivity values as under homogeneous conditions (Scheme 14B). This method represents another original example of immobilization and recovery of

catalysts on a solid support by non-covalent CTC interactions.

In 2011, our group proposed a new asymmetric multi-reaction method facilitating the promotion of additional Cu-catalyzed transformations, namely ene and cyclopropanation reactions [41]. These transformations were already known to process by bis(oxazoline) ligands with $Cu(OTf)_2$. This study reported the use of anthracene-modified bis(oxazoline) for the easy recovery and recycling of the catalyst. The ene reaction was firstly carried out under homogeneous conditions between α-methylstyrene and ethyl glyoxylate, resulting in a similar yield (89%) and enantiomeric excess (67% ee) as with the parent symmetrical ligands. Secondly, after the first run and TNF addition, a further nine cycles of catalyst recycling were carried out with no effect on catalyst activity. CTC Precipitation in pentane was employed to ensure effective recovery and similar results were achieved on the analogous 3,3,3-trifluoro-2-oxo-propionic acid methylester over seven reuses using the same method. Likewise, the cyclopropanation of styrene with ethyl diazoacetate was investigated with the same Cu-complex. The initial trial also showed a good yield (69%) with a mixture of diastereoisomers (2:3 ratio) and good enantiomeric excesses (72% and 69% ee for each diastereoisomers), in agreement with the results obtained using conventional homogeneous catalysts. These results were replicated over five cycles, with a slight loss in activity observed from the sixth run (41% yield, 67 and 69% ee). The main objective of this work was therefore to execute these different reactions using a single catalyst batch, thanks to the precipitation of CTC for catalyst recycling (Scheme 15). As previously reported [35,36], Diels–Alder cycloaddition was also achieved *via* this procedure and was consequently considered. The reaction was first carried out twice between 3-acryloyloxazolidin-2-one and cyclopentadiene, then twice more times between 3-(but-2-enoyl)-oxazolidin-2-one and the same diene to yield another derivative. Subsequently, the ene reaction was conducted three times with α-methylstyrene and ethyl glyoxylate, yielding good results. Finally, the same batch of catalyst was again used for cyclopropanation, giving results in line with those described above. This unprecedented multi-reaction approach enabled the same catalyst batch to be reused nine times without any loss of activity in successive reactions with different substrates.

On another hand, in 2012, Schulz and Didier described the immobilization of the same bis(oxazoline) structures but tagged with an electron-deficient TNF moiety [42]. Immobilization *via* CTC interactions was therefore considered by adding anthracene after the first reaction and introducing apolar pentane to precipitate the formed CTC, facilitating a good catalyst recovery. The first attempt involved the TNF-modified ligand and $Cu(OTf)_2$ in the well-known Diels–Alder cycloaddition between cyclopentadiene and 3-but-2-enoyloxazolidin-2-one. At the end of the reaction, a precipitation procedure and filtration were conducted to recover the solid. Surprisingly, all the anthracene was recovered in solution, indicating that the interactions with the CTC were not sufficiently strong. In fact, regarding the solubility of the TNF-tagged Cu-complex in different solvents, it precipitated on its own when the solvent was changed, and the addition of anthracene for the CTC formation was not necessary for the catalyst recovery. Subsequently, the solid TNF-complex was reused with new substrates and proved effective in fourteen runs with the same reactant, followed by a further six runs with analogous 3-acryloyloxazolidin-2-one. A lower temperature was required with this latter substrate to inhibit competitive racemic transformation. More recently, in 2019, Liang and collaborators described the use of CTC in the Hydrolytic Kinetic Resolution (HKR) of epichlorohydrin, catalyzed by Co(III)-salen complexes [43]. Since this transformation involves a bimetallic system, where one metal acts as a Lewis acid to activate the epoxide and the other to activate the hydroxide, the formation of donor–acceptor complexes to bring two salen molecules together was found to be highly beneficial. Modification of the symmetrical salen-ligands with two electron-poor diimide tags facilitated interactions with additional polyaromatic species, allowing the formation of acceptor–donor–acceptor CTC sandwiches at an ideal distance of around 7–8 Å, optimal for enhancing HKR reactions. The group synthesized three generations of modified salen ligands to explore various parameters. Their results revealed that flexible alkyl ester linkers between the acceptor and the salen core were more efficient than rigid conjugated phenyl linkers, enabling favorable orientation and geometrical arrangement of the bimetallic system. In addition, the choice of polyaromatic

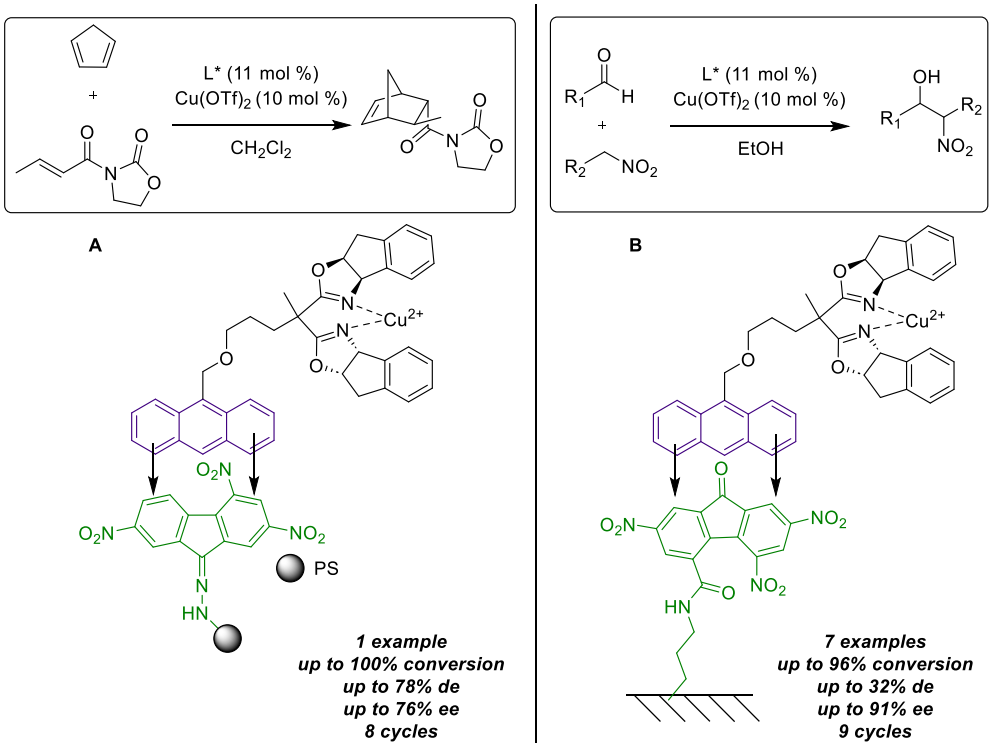

Scheme 14. Immobilization by formation of CTC with organic and inorganic supports.

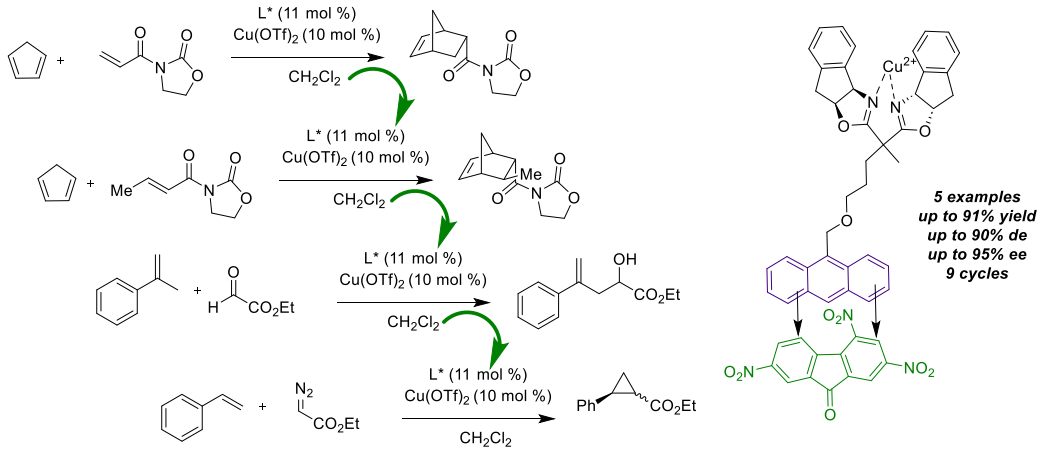

Scheme 15. CTC interactions for an asymmetric multi-reaction procedure.

donor species played a crucial role, improving the catalyst activity when used in the proper quantity. In this case, the best results were obtained with the symmetrical di-Pyromellitic DiImide (PDI) acceptor in the presence of pyrene or perylene (conversion rates of 52% and 54%, >99% ee, respectively), outperforming the classical Jacobsen salen (10 h vs. 42 h). The face-to-face stacking of the bimetallic CTC probably optimally aligned the Co(III)-salen cores, optimizing the interactions between both substrates. This was

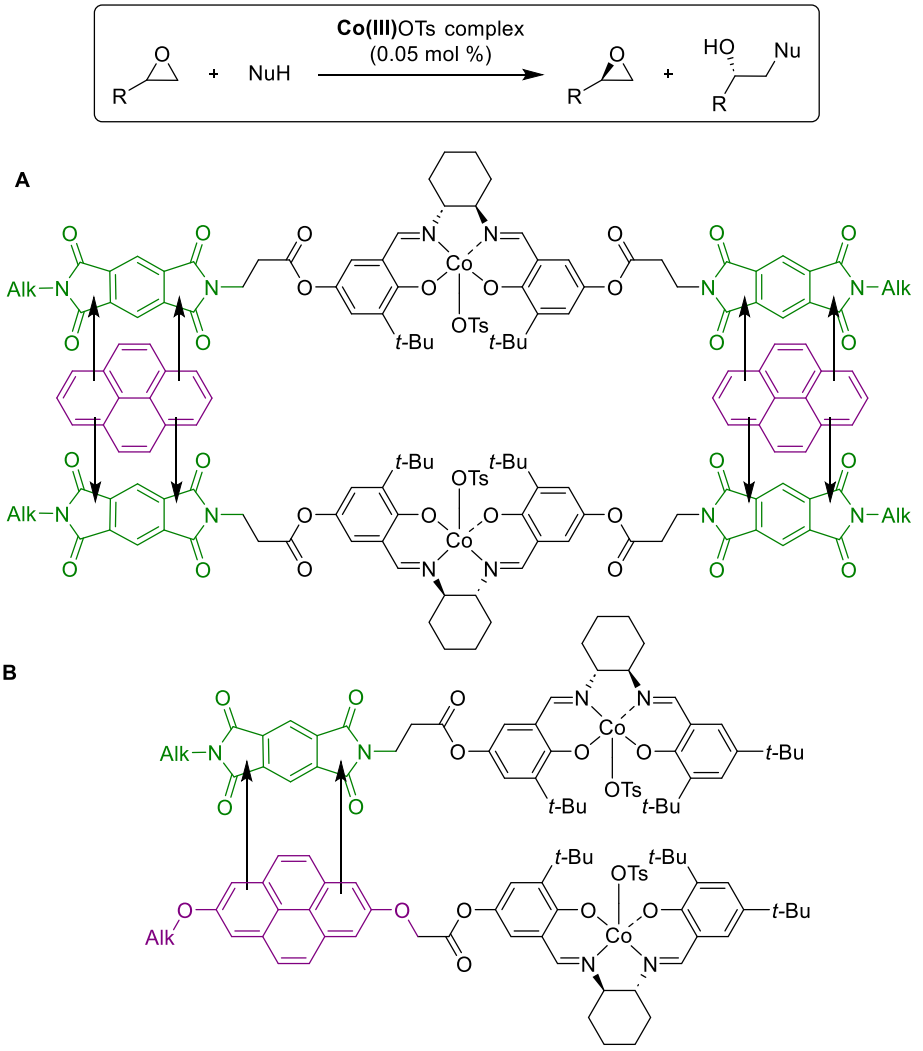

Scheme 16. CTC formation for ARO of epoxides.

supported by ^{1}H NMR and UV–Vis studies, highlighting donor–acceptor interactions between PDI and pyrene moieties (Scheme 16A). In addition to this, the same group reported another CTC-immobilized bimetallic system for the same reaction, expanding the scope to other epoxides and nucleophiles [44]. They designed new modified salen ligands, including unsymmetrical Naphtalene DiImide (NDI)/pyrene-bi-tagged, mono-NDI or mono-pyrene, and symmetrical bi-NDI or bi-pyrene-tagged ligands, comparing their activity with the non-substituted Jacobsen complex. In the epichlorohydrin HKR, all catalysts led to improved yields (50%–59%) and enantioselectivity (>99%) compared to the classical salen, with particularly decreased reaction rates obtained in the presence of the unsymmetrical acceptor–donor tagged ligand (3.5 h). Another noteworthy attempt, involving a mixture of both mono-substituted acceptor and donor (1:1 ratio), yielded similar results (59% yield, >99% ee). Further experiments involved committing both CTCs to other terminal epoxides HKR, which gave satisfactory results, with slightly better activity observed with the mixture of two differently tagged complexes, particularly on aliphatic and hindered substrates. It also allowed to reduce reaction time for the transformation of 1,2-epoxybutane and 1,2-

epoxyhexane epoxide without affecting the selectivity. The higher activity was attributed to a more flexible bi-complex between two mono-tagged than two bi-tagged ones, allowing an optimized arrangement in the space between the two salen catalytic moieties (Scheme 16B). Overall, these results were also observed on more complex substrates, demonstrating good solvent adaptability, high catalytic activity, and enantioselectivity in the asymmetric ring opening of epoxides.

5. Coordination links—Metal Organic Frameworks (MOF)

Another strategy has been developed for the immobilization of chiral organometallic catalysts involving the heterocombination or homocombination of different mutitopic ligands with metal ions, leading to self-supported catalysts, active as heterogeneous species, or to self-supported dynamic catalysts, mainly effective as homogeneous species [45]. To illustrate the first case, Ding and coworkers prepared two different ligands both possessing ditopic sites in the form of a bridged BINAP and a bridged diphenyldiamine (Scheme 17) [46]. After coordination of ruthenium in the presence of the two ligands, a one-dimensional structure is formed as a self-supported Noyori-type catalyst, in the form of an *iso*-propanol-insoluble light-brown solid. The selectivity of this catalyst proved superior to that of its homogeneous counterpart, promoting the hydrogenation of acetophenone and seven other arylketones with enantioselectivities in excess of 94.5% ee, thus demonstrating the synergistic impact of the supramolecular self-supported assembly on the catalytic behavior. The insoluble catalyst was recovered by filtration and reused seven consecutive times without losing its efficiency.

Another related approach involves the homoassembly of multitopic ligands by metal coordination leading to a polymeric structure. What is looked for in this case, is a catalyst that remains heterogeneous in its resting state at the end of catalysis, yet capable of undergoing a reversible partial decoordination process in the reaction mixture to become the active species. This concept was demonstrated by García et al., who prepared a new chiral ditopic ligand bearing two azabis(oxazoline) groups (Scheme 18) [47]. Using copper salts of weakly coordinating anions with an equimolar amount of the ditopic ligand in a non-coordinating solvent, formation of the desired coordination polymer occurred. The reaction tested involved the cyclopropanation of styrene with ethyldiazoacetate, as a strongly coordinating species, leading to a de-coordination process upon its addition and a reaction taking place in the homogeneous phase with even higher enantioselectivity values for both cyclopropane isomers (ee up to 97% for the *trans* product). After completion of the reaction, the coordination polymer is formed again, and can be easily recovered by filtration for its efficient recycling (14 cycles).

This procedure was subsequently studied by the Bellemin-Laponnaz group for the enantioselective α-hydrazination of β-ketoesters with polytopic (bis-, tris- and tetratopic) bisoxazoline as ligands [48]. The use of the ditopic ligand in combination with $Cu(OTf)_2$ led to a highly efficient self-supporting catalyst for reacting with acyclic and cyclic β-ketoesters (5 examples) delivering the desired products with almost complete conversion and enantioselectivity values of 99%. Depending on the substrate structure, six to ten runs could be performed without loss of efficiency. Interestingly, increasing the topicity of the ligand led to a worse recycling and more catalyst leaching. The authors also studied NonLinear Effects (NLE) to better understand the aggregation state of the active species, conducting experiments in which the optical purity of the ligand varied. Negative NLE was observed, consistent with the preferential formation of a homochiral metallopolymer, in equilibrium with the active monomeric species. These authors applied further this concept for the preparation of air- and moisture-stable nickel metallopolymers efficient as enantioselective catalysts for the Michael addition of diester malonates to nitroalkenes [49]. A chiral ditopic cyclohexyldiamine-based ligand was prepared generating a self-supported catalyst in the presence of nickel salts (Scheme 19). The substrate displaces a diamine ligand and generates an active catalyst that contains only a single diamine ligand, giving an efficient catalyst with greater activity than the corresponding monomer and similar enantioselectivity. Five examples were described (complete conversion and up to 93% ee), along with a procedure for efficient recovery of the catalytic species. It involves the addition of diethylether for

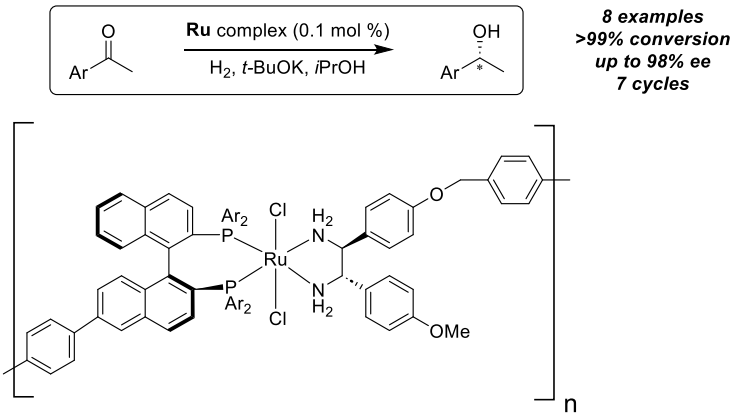

Scheme 17. Immobilization by heterocombination of mutitopic ligands for asymmetric hydrogenation.

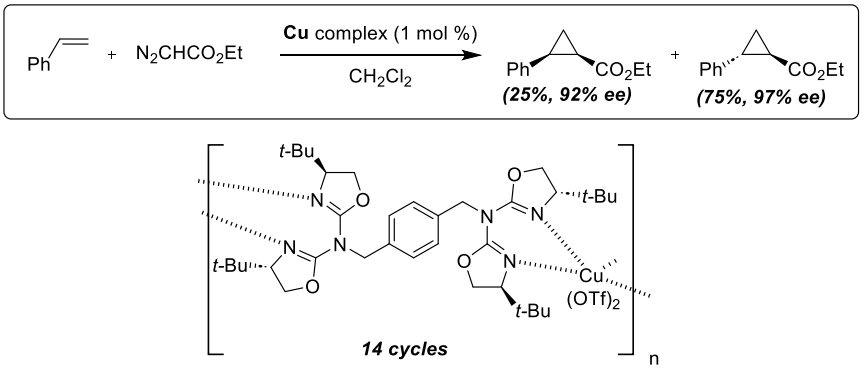

Scheme 18. Self-supported dynamic copper catalysts for cyclopropanation reactions.

catalyst precipitation, filtration, washing and subsequent reuse in up to 13 cycles with stable enantioselectivity and a slight decrease in substrate conversion.

For over fifteen years now, metal organic frameworks (MOFs) have also been studied as a response to certain challenges in supported asymmetric catalysis [50,51]. The activity of these heterogeneous catalysts comes either from unsaturated metal coordination sites, or from active linkers between metals, or both, particularly if these linkers are chiral organometallic complexes. In addition, the wide choice of porous structures available allows selective limitations in terms of size and shape through well-defined channels and pores. Thus, MOFs have been reported fairly recently as effective heterogeneous catalysts for a number of transformations, including enantioselective reactions. A relatively early example was described by the Lin's group for the preparation of homochiral porous MOFs from BINOL derivatives as chiral bridging ligands containing bipyridyl units as orthogonal functional groups (Scheme 20) [52]. They were able to produce colorless crystals in the presence of $CdCl_2$ while the chiral dihydroxy groups were accessible for reaction with Ti(O*i*-Pr)$_4$, enabling the formation of an active heterogeneous catalyst for the addition of Et_2Zn to aromatic aldehydes. The authors showed activity and enantioselectivity equivalent to those obtained when homogeneous BINOL was used as a ligand (8 examples compared), except for some substrates bearing Frechet-type dendrons, which were probably unable to access the catalytic sites because they were too large. This result proved that catalysis occurred inside the MOF pores, and

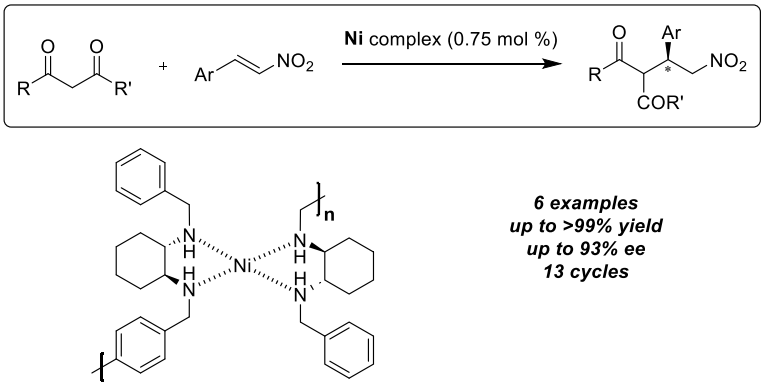

Scheme 19. Ditopic cyclohexyldiamine-based ligand as self-supported nickel catalyst.

control experiments were also carried out to confirm the heterogeneous nature of the reaction.

One year later, Nguyen and Hupp prepared another microporous MOF with Mn-salen struts for asymmetric epoxidation [53]. The Mn-salen was modified with two pyridine units, and a robust structure, in the form of a pair of interpenetrating networks, was obtained from zinc salts associated with biphenyldicarboxylate as the second ligand. For the asymmetric epoxidation of chromene derivatives and 2-(*tert*-butylsulfonyl)iodosylbenzene as oxidant, the heterogeneous catalyst proved to be almost four times more active than the corresponding homogeneous catalyst, with only a slight decrease in enantioselectivity (from 88 to 82% ee). Simple recovery of the MOF catalyst by filtration enabled it to be reused for three cycles without any decrease in enantioselectivity and with a slight loss of activity, probably due to partial fragmentation of the particles.

Since these early examples, a great deal of work has been devoted to the precise optimization of the MOF structure in order to enhance its reactivity and selectivity according to the target. For instance, a family of isoreticular chiral MOFs has been prepared under solvothermal conditions from Mn-salen derivatives bearing dicarboxylic acids functions attached by spacer bonds of different sizes [54]. The corresponding materials therefore had different structures depending on the solvent used to synthesize them and adjustable open channel sizes, which in some cases led to heterogeneous catalysts that were as effective as homogeneous ones for the asymmetric epoxidation of alkenes, while at the same time being recoverable and reusable after simple filtration.

The versatility of these crystalline structures for asymmetric heterogeneous catalysis was demonstrated by Liu and Cui, who prepared a porous Cr-salen MOF (Scheme 21) and subjected it to a series of four catalytic transformations involving different mechanisms [55]. The crystalline catalyst was obtained by heating the corresponding salen complex with CdI_2 and NaOAc and was tested in the Nazarov reaction of alkoxydienones, affording functionalized cyclopentenones with high selectivity. Although the enantioselectivity remained slightly lower than the value obtained with the homogeneous analog, a higher diastereoselectivity was observed, which was attributed to the steric constraints of the confined network. Used in other reactions such as the asymmetric aminolysis of *trans*-stilbene oxide, the Diels–Alder and hetero-Diels–Alder reactions, it has led to increased enantioselectivity values compared with homogeneous cases, with confinement effects allowing ideal location of the active sites. Size selectivity was also demonstrated as a bulky benzaldehyde derivative could not undergo an hetero-Diels–Alder reaction, indicating a unique catalytic activity within the MOF pores. The catalyst was reused in four aminolysis cycles, showing good stability.

Other advances involving the manipulation of such heterogeneous catalysts concern their post-synthesis modification. Ren and Jiang, for instance, synthesized and fully characterized a 3D Cu-salen MOF possessing a 1D open channel [56]. They then carried out a reduction step in the presence of

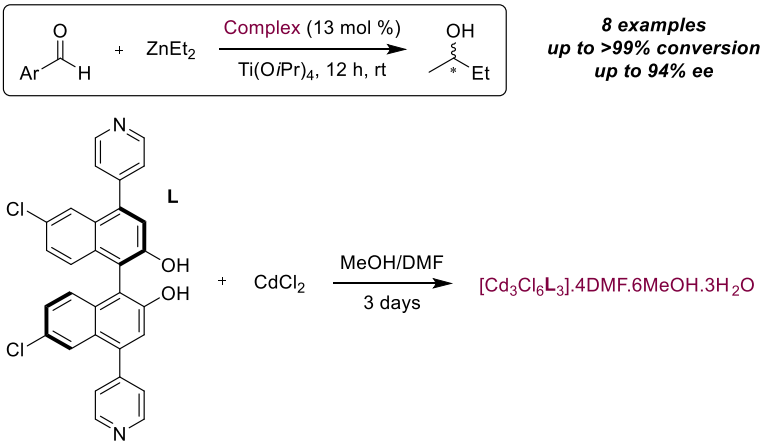

Scheme 20. BINOL-based homochiral porous MOF for the $ZnEt_2$ addition on aldehydes.

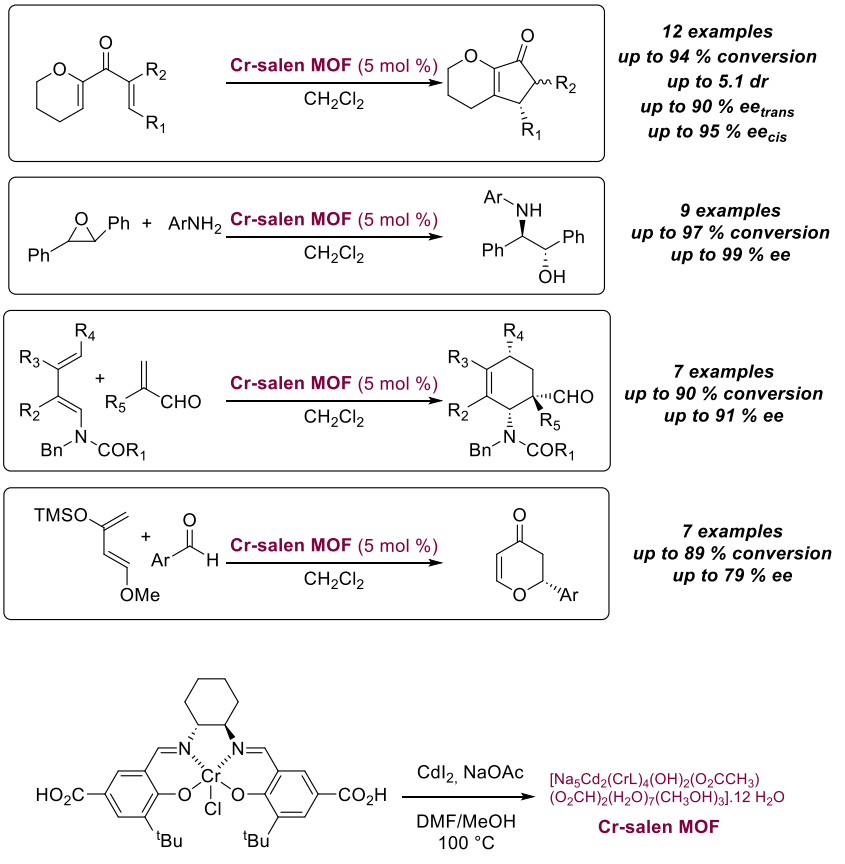

Scheme 21. Porous Cr-salen MOF efficient for four catalytic transformations.

$NaBH_4$, leading to the reduction of the salen imine groups to a more basic and flexible skeleton, while retaining its structural integrity. Although the Cu-salen MOF proved to be a poor catalyst in the Henry reaction, the corresponding salan derivative afforded the expected products with higher activity and enantioselectivity (15 examples and ee up to 98%) and was successfully recovered and reused for five successive runs. Another post-modification of an existing MOF was described by Liu and Cui, when they heated a VO-salen MOF in the presence of a Cr-salen complex with exactly the same structure; this solvent-assisted linker exchange resulted in the partial replacement of certain VO-salen units by Cr-ones as shown by Inductively Coupled Plasma – Optical Emission Spectrometry (ICP-OES analyses) [57]. While the first catalyst was active in the cyanosilylation of aldehydes (with up to 95% ee, 11 examples), the MOF exchanged by Cr-salen was engaged in asymmetric kinetic resolution with aniline, a reaction that is not catalyzed by VO-salen complexes. *Cis*-stilbene oxide was efficiently converted (87%) to aminoalcohol (76% ee), demonstrating the introduction, by exchange, of chiral Cr-salen species leading to mixed MOF, promising for cooperative or tandem catalysis. To illustrate cooperative catalysis, the authors demonstrated the presence of a synergistic pathway resulting from the close location of two V-salen units in the open channels of a MOF [58]. They prepared two different heterogeneous MOFs catalysts resulting from $Cd(NO_3)_2$ and a VO-salen complex or a mixture of a Cu- and a VO-salen complex. Once the two networks had been fully characterized, they were used in the test reaction involving the asymmetric cyanation of aldehydes. The homometallic heterogeneous catalyst was very active and selective, particularly at low loadings, highlighting the positive effect of confinement. As a result, the bimetallic Cu- and V-containing MOF was far less active, as the synergistic VO–VO pathway was blocked by the presence of the copper sites, resulting in less efficient unimolecular activation of the substrates. In the context of tandem catalysis, they proposed a similar strategy for the post-synthetic exchange of achiral ligands from Zr-based UiO-68 MOF with chiral salen complexes, bearing the same or different metal centers [59]. Consequently, a Mn-salen derived UiO-68 was obtained, which cannot be achieved by direct solvothermal synthesis. Then, from Mn-salen derived UiO-68, mixed salen-containing MOFs were obtained (Mn/Cr and Mn/V) by another solvent-assisted linker exchange procedure. These highly stable platforms were precisely characterized using NMR spectroscopy, ICP-OES, and Powder X-Ray Diffraction (PXRD). Excellent heterogeneous asymmetric activity of the newly formed UiO-68-(monometallic salen) MOFs was achieved depending on the nature of the trapped metal, such as epoxidation for the Mn-containing material and epoxide ring opening for Cr-one, for example. Finally, in the presence of the MOF UiO-68-(bimetallic Mn/Cr salen), a sequential tandem transformation (i.e. epoxidation followed by ring opening with anilines) was carried out to give the targeted amino alcohol in very high yield and almost complete enantioselectivity, with a low catalyst loading (0.5 mol%). This bimetallic catalyst was recycled after extraction of the products for at least 10 cycles without any loss of efficiency.

A variation in the structure of MOFs was also proposed by Ren, Jiang and their group when they heated a mixture of tetracarboxyphenylporphyrin and a Ni-salen complex in the presence of $Cd(NO_3)_2$ [60]. They obtained a porphyrin-salen based chiral MOF, with two different interpenetrated networks, one in which the porphyrin core contains Cd^{2+}, the other being metal-free. Efficient cooperativity could be demonstrated using this MOF in catalytic asymmetric cyanosilylation (8 examples), due to the presence of the high Lewis acidic sites of the Cd^{2+} ion in the porphyrin ring. The close location to the enantiopure Ni-salen complex led to high values in terms of activity (up to 96% conversion) and enantioselectivity (up to 98% ee). Finally, we chose to highlight the immobilization of bulky Spinol-based chiral phosphoric acids in stable Zr-MOFs, and their use as asymmetric Brønsted acid catalysts to promote enantioselective multicomponent tandem reactions [61]. The structure of the chiral organocatalysts was designed to protect them from coordinating with metal ions and to allow the formation of MOFs with different channel sizes. The corresponding heterogeneous catalysts were found to be more active than analogous homogeneous catalysts, with increased acidity in the two-component acetalization/Friedel–Crafts tandem reaction for the synthesis of enantioenriched 2,3-dihydroquinazolinones (11 examples, up to full conversion and enantioselectivity) or

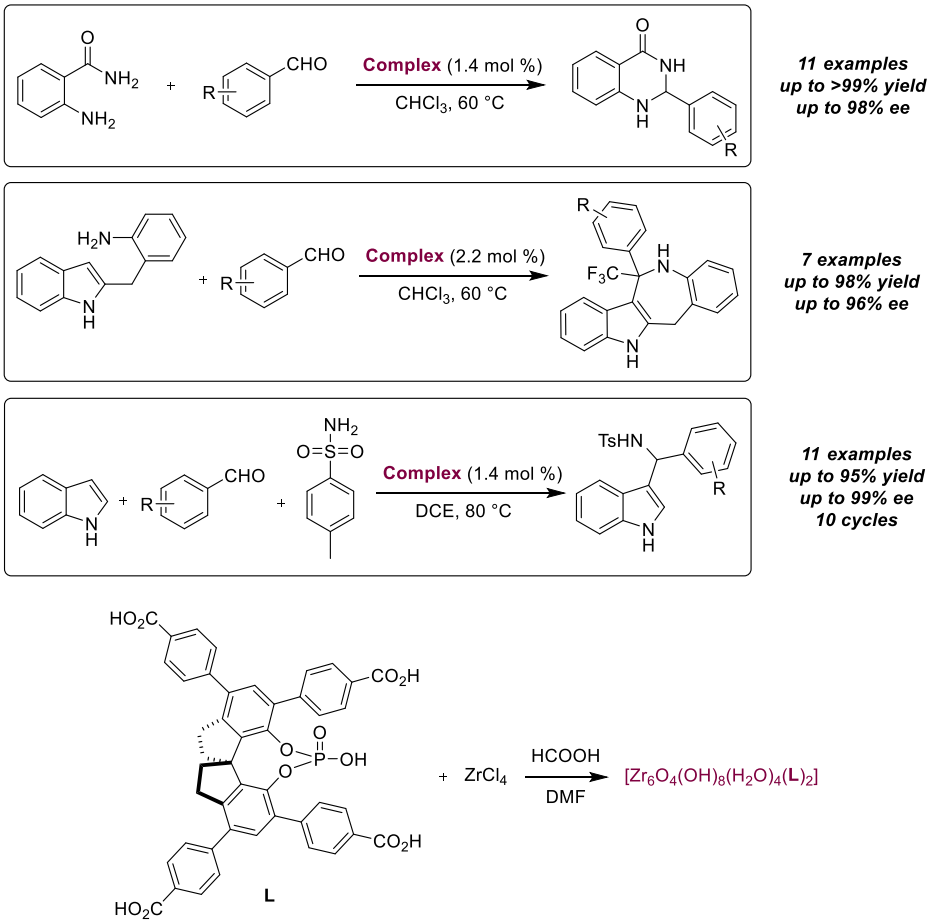

Scheme 22. Immobilization of a Spinol-based chiral phosphoric acid in Zr-MOFs for multi-component tandem reactions.

iso-Pictet–Spengler reaction of *o*-aminobenzylindole with trifluoromethylated ketones (7 examples, up to 98% yield and 96% ee). The catalyst was reused 10 times for the first transformation without losing its activity or enantioselectivity. A successful three-component tandem reaction using indole, aldehydes and *p*-toluenesulfonalide as substrates (Scheme 22) demonstrated interesting synergistic effects with the Lewis acid Zr(IV) sites.

Similarly, the recent description of supramolecular coordination cages has also produced excellent results for asymmetric catalysis [62]. For example, various tetrahedral cages were prepared by mixing four clusters of Cp_3Zr_3 with six dicarboxylate ligands derived from metal-salen complexes. These new nanoreactors were described in detail and the authors succeeded in obtaining cages containing identical or different active catalytic sites [63]. Cages containing Mn-salen were used for the epoxidation of chromene derivatives with iodosylbenzene derivatives with enantioselectivity values higher than those obtained with the monomer. On the other hand, Cr-salen cages have been used successfully for the ring-opening of epoxides with aniline or trimethylsilylazide. Consequently, the mixed Cr/Mn-salen cage was tested in the sequential asymmetric epoxidation/ring-opening reaction of alkenes with $TMSN_3$ (3 examples) or anilines (9 examples) and gave excellent results in terms of activity and enantioselectivity, outperforming those obtained using a 1/1 mixture of each cage containing either Cr-salen or Mn-salen as the active species, demonstrating the

positive confining effect of a mixed cage. These few examples are only representative of a growing number of articles in this field, which show the value of these crystalline objects, which are perfectly defined and whose structure has been precisely targeted to carry out extremely varied asymmetric catalysis and asymmetric multicatalysis reactions, in highly efficient recycling procedures.

6. Ship in a bottle procedure

Finally, a last strategy based on non-covalent interactions to immobilize chiral catalysts is worth mentioning, namely the "ship in a bottle" strategy, which consists of trapping a homogeneous catalyst in a solid porous matrix, leaving the space for the entry of substrates and the exit of products. This procedure proved effective in immobilizing a chiral Co-salen complex inside the mesoporous cage of SBA-16, by controlling the size of the pore entrance, adapting the autoclaving time and the silylation process [64]. The corresponding heterogeneous chiral catalyst was successfully used for the asymmetric hydrolytic ring-opening of epichlorohydrin and propylene oxide with, in each case, values corresponding those obtained with the homogeneous counterpart. Furthermore, this catalyst was reused after simple filtration in ten recycles with propylene oxide as substrate, showing almost no loss in activity or selectivity, as a proof of the stability of the material and its ability to effectively trap active salen species. Another more recent example concerns the encapsulation of Mn-salen complexes in a one-step procedure for the synthesis of a highly porous MOF, namely NH_2-MIL-101(Al), implying the linker, the Mn-salen complex and $AlCl_3$ [65]. The corresponding crystalline material was characterized indicating the presence of a salen complex in one cage out of six. Although a lower conversion was obtained compared to the homogeneous catalyst, the enantioselectivity for the epoxidation of dihydronaphthalene remained unchanged at 70% ee, probably due to the soft encapsulation strategy where the catalyst structure remained unchanged, without influence of the MOFs walls. The MOF-cage thus assembled around the Mn-salen complex was tested for four recycles with a slight decrease in activity and no loss of selectivity. Further analytical studies of the solid catalyst and filtrate were carried out, showing an unchanged structure and no leaching, demonstrating the stability and truly heterogeneous nature of the catalyst. A final example involves the entrapment of a chiral Co-salen catalyst in IRMOF-3 nanocages by adsorption. As this support is derived from tetranuclear Zn_4O clusters linked to 1,4-dicarboxylic benzene linkers with a functional amino group, subsequent acylation of the free amino groups *via* the post-synthetic modification technique enabled the catalytic sites to be trapped by reducing pores size and, therefore, access [66]. The synthesis of enantioenriched cyclic carbonates from epoxides and CO_2 was used as a test reaction resulting in a product with slightly reduced activity compared with the homogeneous case, probably due to reduced diffusion. The control experiments nevertheless proved the existence of heterogeneous activity inside the pores, with the catalyst easily recovered and effectively reused over four repeated runs.

7. Conclusion and outlook

The immobilization of enantiopure catalysts, whether organic species or organometallic complexes, *via* non-covalent interactions on various support is constantly evolving. The use of weak and reversible interactions could lead to leaching of the catalyst and hinder, for example, efficient recycling or promote metal contamination of the target product. While this may still be true for certain methods of immobilization by electrostatic interactions on silica-type supports, partly because of their polar nature, many other solutions have been found, for example by adapting the solvent so that the effective recycling number reaches very high values. More recently, π-interactions with carbon supports have also been exploited in the field of asymmetric catalysis, enabling simple procedures to be implemented since no modification of the support is required. The conservation of the activity and enantioselectivity of the immobilized catalyst was described, as well as numerous effective recycles, right up to implementation in flow procedures as proof of the robustness of this heterogenization process. Future developments of this method should involve the co-immobilization

of different (chiral) active species on the same support in order to promote ambitious asymmetric multicatalytic reactions. The formation of charge transfer complexes for the recycling of chiral catalysts is rarer, but has also proved its worth, either by acting in the homogeneous phase and being easily recovered by the addition of an apolar solvent before filtration, or by direct filtration when the CTC is formed directly with a species anchored on a support. Examples of numerous recycling processes are also described here as an interesting method for recovering and reusing, not only the catalyst but also the support, through easy exchanges of active species thanks to non-covalent interactions. These immobilization procedures have also been used in multi-substrates reactions, as well as in multi-reaction procedures proving both their applicability and their robustness. The use of MOFs for supported asymmetric catalysis is growing rapidly; in fact, today's perfect mastery of the synthesis of these crystalline materials, whose structure and porosity are controlled, means that we can decide on the exact location of the catalytic sites, spacing them out or bringing them closer together as required, depending on the desired reactivity, whether individual or cooperative. These perfectly designed nanoreactors offer size selectivity, multiple recycling without metal contamination and asymmetric multicatalysis. The field of supported asymmetric catalysis, involving the use of non-covalent bonds, is still wide open to creativity, to easily carry out numerous transformations using the support, not only for the purposes of economy and recycling, but also to control the placement of numerous active catalytic sites for the discovery of increasingly complex reactivities.

Declaration of interests

The authors do not work for, advise, own shares in, or receive funds from any organization that could benefit from this article, and have declared no affiliations other than their research organizations.

Acknowledgments

We are grateful to the CNRS, the Université Paris-Saclay for their support and to the Agence Nationale de la Recherche (ANR-22-CE07-0A40-01, PhD financial support to LI). For the purpose of Open Access, a

References

[1] W. Dumont, J.-C. Poulin, T.-P. Dang, H. B. Kagan, *J. Am. Chem. Soc.*, 1973, **95**, 8295-8299.
[2] N. Takaishi, H. Imai, C. A. Bertelo, J. K. Stille, *J. Am. Chem. Soc.*, 1976, **98**, 5400-5402.
[3] N. Takaishi, H. Imai, C. A. Bertelo, J. K. Stille, *J. Am. Chem. Soc.*, 1978, **100**, 264-268.
[4] G. M. Schwab, I. Rudolph, *Naturwissen*, 1932, **20**, 362.
[5] S. Akabori, S. Sakurai, Y. Izumi, Y. Fujii, *Nature*, 1956, **178**, 323-324.
[6] H. U. Blaser, *Asymm*, 1991, **2**, 843-866.
[7] M. Studer, S. Burkhardt, A. F. Indolese, H. U. Blaser, *Chem. Commun.*, 2000, 1327-1328.
[8] M. Berthod, G. Mignani, G. Woodward, M. Lemaire, *Chem. Rev.*, 2005, **105**, 1801-1836.
[9] C. Baleizao, H. Garcia, *Chem. Rev.*, 2006, **106**, 3987-4043.
[10] J. M. Fraile, J. I. García, J. A. Mayoral, *Coord. Chem. Rev.*, 2008, **252**, 624-646.
[11] A. F. Trindade, P. M. P. Gois, C. A. M. Afonso, *Chem. Rev.*, 2009, **109**, 418-514.
[12] A. Zulauf, M. Mellah, X. Hong, E. Schulz, *Dalton Trans.*, 2010, **39**, 6911-6935.
[13] S. Matsunaga, M. Shibasaki, *Synthesis*, 2013, **45**, 421-437.
[14] M. Abd El Sater, N. Jaber, E. Schulz, *ChemCatChem*, 2019, **11**, 3662-3687.
[15] J. M. Fraile, J. I. García, J. A. Mayoral, *Chem. Rev.*, 2009, **109**, 360-417.
[16] L. Zhang, S. Luo, J. P. Cheng, *Catal. Sci. Technol.*, 2011, **1**, 507-516.
[17] Y.-S. Kim, X.-F. Guo, G.-J. Kim, *Chem. Commun.*, 2009, 4296-4298.
[18] L. Li, Y. Li, D. Pang, F. Liu, A. Zheng, G. Zhang, Y. Sun, *Tetrahedron*, 2015, **71**, 8096-8103.
[19] J. Zhang, L. Li, Y. Li, G. Zhang, A. Zheng, J. Zhang, Y. Sun, *Catal. Lett.*, 2015, **145**, 1148-1161.
[20] X. Li, Q. Shen, G. Zhang, D. Zhang, A. Zheng, F. Guan, Y. Sun, *Catal. Commun.*, 2013, **41**, 126-131.
[21] M. M. Islam, P. Bhanja, M. Halder, S. K. Kundu, A. Bhaumik, S. M. Islam, *RSC Adv.*, 2016, **6**, 109315-109321.
[22] M. Halder, P. Bhanja, M. M. Islam, A. Bhaumik, S. M. Islam, *New J. Chem.*, 2018, **42**, 11896-11904.
[23] L.-L. Lou, H. Du, K. Tu, S. Jiang, W. Yu, S. Liu, *J. Mol. Cat. A: Chem.*, 2013, **377**, 85-91.
[24] J. Park, K. Lang, K. A. Abboud, S. J. Hong, *J. Am. Chem. Soc.*, 2008, **130**, 16484-16485.
[25] J. Park, K. Lang, K. A. Abboud, S. J. Hong, *Chem. Eur. J.*, 2011, **17**, 2236-2245.
[26] L. Xing, J.-H. Xie, Y.-S. Chen, L.-X. Wang, Q.-L. Zhou, *Adv. Synth. Catal.*, 2008, **350**, 1013-1016.
[27] J. F. Moya, C. Rosales, I. Fernández, N. Khiar, *Org. Biomol. Chem.*, 2017, **15**, 5772-5780.

[28] E.-J. Hao, G.-X. Li, Z.-Z. Lv, F.-S. Li, Y.-Q. Chen, S.-J. Lin, C.-Z. Shib, L. Shi, *Org. Chem. Front.*, 2020, **7**, 345-349.
[29] A. Cunillera, C. Blanco, A. Gual, J. M. Marinkovic, E. J. Garcia-Suarez, A. Riisager, C. Claver, A. Ruiz, C. Godard, *ChemCatChem*, 2019, **11**, 2195-2205.
[30] D. Didier, E. Schulz, *Tetrahedron Asymmetry*, 2013, **24**, 769-775.
[31] M. Abd El Sater, M. Mellah, D. Dragoe, E. Kolodziej, N. Jaber, E. Schulz, *Chem. Eur. J.*, 2021, **27**, 9454-9460.
[32] Y.-C. Yuan, M. Abd El Sater, M. Mellah, N. Jaber, O. R. P. David, E. Schulz, *Org. Chem. Front.*, 2021, **8**, 4693-4699.
[33] R. Gil, J.-C. Fiaud, J.-C. Poulin, E. Schulz, *Chem. Comm.*, 2003, 2234-2235.
[34] R. Gil, M.-G. Guillerez, J.-C. Poulin, E. Schulz, *Langmuir*, 2007, **23**, 542-548.
[35] G. Chollet, F. Rodriguez, E. Schulz, *Org. Lett.*, 2006, **8**, 539-542.
[36] G. Chollet, M.-G. Guillerez, E. Schulz, *Chem. Eur. J.*, 2007, **13**, 992-1000.
[37] O. Chuzel, C. Magnier-Bouvier, E. Schulz, *Tetrahedron Asymmetry*, 2008, **19**, 1010-1019.
[38] B. Lynikaite, J. Cvengros, U. Piarulli, C. Gennari, *Tetrahedron Lett.*, 2008, **49**, 755-759.
[39] G. Chollet, D. Didier, E. Schulz, *Catal. Commun.*, 2010, **11**, 351-355.
[40] D. Didier, C. Magnier-Bouvier, E. Schulz, *Adv. Synth. Catal.*, 2011, **353**, 1087-1095.
[41] D. Didier, E. Schulz, *ChemCatChem*, 2011, **3**, 1880-1884.
[42] D. Didier, E. Schulz, *Synlett*, 2012, **23**, 1309-1314.
[43] D. R. Blechschmidt, M. D. Woodhouse, S. Inagaki, M. Whitfield, A. Ogunsanya, A. Yoder, D. Lilly, E. W. Heim, L. N. Soucie, J. Liang, Y. Liu, *Org. Biomol. Chem.*, 2019, **17**, 172-180.
[44] J. Liang, L. N. Soucie, D. Bleschmidt, A. Yoder, A. Gustafson, Y. Liu, *Org. Lett.*, 2019, **21**, 513-518.
[45] S. Bellemin-Laponnaz, T. Achard, D. Bissessar, Y. Gieger, A. Maisse-François, *Coord. Chem. Rev.*, 2017, **332**, 38-47.
[46] Y. Liang, Q. Jin, X. Li, L. Shi, K. Ding, *J. Am. Chem. Soc.*, 2005, **127**, 7694-7695.
[47] J. I. García, B. López-Sánchez, J. A. Mayoral, *Org. Lett.*, 2008, **10**, 4995-4998.
[48] M. Torres, A. Marie-Fraçois, S. Bellemin-Laponnaz, *ChemCatChem*, 2013, **5**, 3078-3085.
[49] D. Bissessar, T. Achard, S. Bellemin-Laponnaz, *Adv. Synth. Catal.*, 2016, **358**, 1982-1988.
[50] T. Drake, P. Ji, W. Lin, *Acc. Chem. Res.*, 2018, **51**, 2129-2138.
[51] G. Yuan, H. Jiang, L. Zhang, Y. Liu, Y. Cui, *Coord. Chem. Rev.*, 2019, **378**, 483-499.
[52] C.-D. Wu, A. Hu, L. Zhang, W. Lin, *J. Am. Chem. Soc.*, 2005, **127**, 8940-8941.
[53] S.-H. Cho, B. Ma, S. T. Nguyen, J. T. Hupp, T. E. Albrecht-Schmitt, *Chem. Commun.*, 2006, 2563-2565.
[54] F. Song, C. Wang, J. M. Falkowski, L. Ma, W. Lin, *J. Am. Chem. Soc.*, 2010, **132**, 15390-15398.
[55] Q. Xia, Y. Liu, Z. Li, W. Gong, Y. Cui, *Chem. Commun.*, 2016, **52**, 13167-13170.
[56] Y. Fan, Y. Ren, J. Li, C. Yue, H. Jiang, *Inorg. Chem.*, 2018, **57**, 11986-11994.
[57] W. Xi, Y. Liu, Q. Xia, Z. Li, Y. Cui, *Chem. Eur. J.*, 2015, **21**, 12581-12585.
[58] C. Zhu, Q. Xia, X. Chen, Y. Liu, X. Du, Y. Cui, *ACS Catal.*, 2016, **6**, 7590-7596.
[59] C. Tan, X. Han, Z. Li, Y. Liu, Y. Cui, *J. Am. Chem. Soc.*, 2018, **140**, 16229-16236.
[60] J. Li, Y. Ren, C. Qi, H. Jiang, *Chem. Commun.*, 2017, **53**, 8223-8226.
[61] W. Gong, X. Chen, H. Jiang, D. Chu, Y. Cui, Y. Liu, *J. Am. Chem. Soc.*, 2019, **141**, 7498-7508.
[62] C. Tan, D. Chu, X. Tang, Y. Liu, W. Xuan, Y. Cui, *Chem. Eur. J.*, 2019, **25**, 662-672.
[63] J. Jao, C. Tan, Z. Li, Y. Liu, X. Han, Y. Cui, *J. Am. Chem. Soc.*, 2018, **140**, 2251-2259.
[64] H. Yang, L. Zhang, W. Su, Q. Yang, C. Li, *J. Catal.*, 2007, **248**, 204-212.
[65] T. Bogaerts, A. Van Yperen-De Deyne, Y.-Y. Liu, F. Lynen, V. Van Speybroeck, P. Van der Voort, *Chem. Commun.*, 2013, **49**, 8021-8023.
[66] D. Chen, R. Luo, M. Li, M. Wen, Y. Li, C. Chen, N. Zhang, *Chem. Commun.*, 2017, **53**, 10930-10933.

ACADÉMIE DES SCIENCES
INSTITUT DE FRANCE

Comptes Rendus. Chimie
2024, Vol. 27, Special issue S2, p. 85-97
https://doi.org/10.5802/crchim.273

Research article

Women Chemists in France in 2024

A new generation of ecocatalysts®—from Invasive Alien Species to sustainable and biosourced glyceryl fatty esters

Arthur Lasbleiz [a], Franck Pelissier [a], Jean-Hugues Renault [b], Claire M. Grison [a], Yves-Marie Legrand [a] and Claude Grison [*, a]

[a] Laboratory of Bio-inspired Chemistry and Ecological Innovations, UMR 5021, University of Montpellier - CNRS, 34790 Grabels, France

[b] Université de Reims Champagne-Ardenne, CNRS, ICMR 7312, 51097, Reims, France

E-mail: claude.grison@cnrs.fr (C. Grison)

This article is dedicated to Professor Philippe Coutrot in recognition of his significant contributions in the organic chemistry of biomolecules

Abstract. A new generation of ecocatalysts® derived from Invasive Alien Species (IAS) (*Fallopia japonica* and *Arundo donax*) was used as starting material for the preparation of novel biosourced catalysts. The preparation of these ecocatalysts® is a new way to support the management of IAS. These catalysts were characterized by microwave plasma atomic emission spectrometry (MP-AES) and X-ray powder diffraction (XRPD), which revealed basic properties. After calculating Pearson's correlations to evaluate the relative importance of reaction parameters, a design of experiments (DoE) was implemented to synthesize glyceryl caprylate and oleate with a high selectivity. These molecules constitute emollients and non-ionic emulsifiers of high industrial interest. The ecocatalysts® were efficient and recyclable for the transesterification of methyl and ethyl fatty esters, leading to high yields (66–83%). These ecocatalysts® are an alternative to usual base catalysts previously reported for the transesterification of methyl caprylate, methyl oleate and ethyl caprylate with glycerol, which are often non-recyclable, not systematically selective and require questionable preparation conditions.

Keywords. Invasive Alien Species, Ecocatalysts®, Transesterification, Glyceryl esters, Sustainable chemistry.

Funding. French National Centre for Scientific Research (CNRS).

Manuscript received 30 October 2023, revised and accepted 10 November 2023.

1. Introduction

According to recent data from IPBES (Intergovernmental Science-Policy Platform on Biodiversity and Ecosystem Services), 60% of species extinctions are due to Invasive Alien Species (IAS) [1]. These latter constitute one of the five main causes of biodiversity loss on a global scale and cost 400 billion dollars each year. IAS profoundly and negatively affect biodiversity, economy, food security, water security, and human health. Among them, the Japanese knotweed, or *Fallopia japonica*, is one of the most fearsome plant species. It is widely established in wetlands in Europe, Oceania, North and South America [2]. The uncontrolled development of *F. japonica* strongly impacts the biological diversity of wetlands, on uses, the weakening of banks and hinders flood management. *Arundo donax*, also called the giant reed and

* Corresponding author

present in temperate and tropical areas [3], is another demonstrative example. Its long, fibrous, interconnected root mats constitute a frightening obstacle to ecosystems and affect the functioning of wetlands. The growth of *A. donax* is 2–5 times faster than native competitors, and its vegetative reproduction allows it to quickly invade new areas and completely supplant native vegetation. Finally, *A. donax* is extremely flammable, increasing the likelihood and intensity of wildfires.

While they constitute the largest reservoirs of carbonaceous organic matter, wetlands contribute to mitigating extreme climatic phenomena (floods and droughts), water purification, and preserving biodiversity. Thus, the rapid disappearance of wetlands, which no longer ensure their regulatory action, is worryingly reducing the resilience of neighbouring ecosystems. Over the past ten years, wetland managers have made considerable efforts to try to eradicate IAS. The technique is frequently based on the extraction of rhizomes. This method is destructive, expensive and has a major limitation: the slightest residue of rhizomes or roots can grow uncontrollably. The various eradication operations seem so far illusory. Today, it is more realistic to study the implementation of solutions to refrain the proliferation of IAS rather than aiming for their eradication. Thus, for example, a less destructive management of the proliferation of invasive species, *F. japonica* and *A. donax*, is being studied: rather than extracting the rhizomes at the cost of significant and inconclusive efforts, repeated mowing of the aerial parts could deplete the plant. This technique affects the vegetative dynamics of the species and allows native species to recreate habitats. These experiments must be designed over several years to assess the process efficiency of management control for each species. It is therefore essential to find an economically viable valorization of the harvested parts to support the ecological study. To do so and particularly to limit IAS in wetlands over the long term, the Grison group is studying the transformation of harvested aerial parts into essential raw materials for sustainable chemistry (Figure 1). Their particular physiology and vegetative dynamics bear witness to an unusual mineral composition [4]. They complete the family of biosourced metal catalysts, called ecocatalysts® [5–8].

Recently, we showed that ecocatalysts® derived from *F. japonica* were composed of fairchildite, a double carbonate of potassium and calcium, $K_2Ca(CO_3)_2$. This original structure led to very good results in the Michael addition of di-activated methylene to cyclic enones [9]. The study was here extended to a reaction of industrial interest, the transesterification of alkyl esters with glycerol. This new application led to the green and biosourced synthesis of emollients and non-ionic emulsifiers, glyceryl caprylates and oleates. The structure and reactivity of ecocatalysts® derived from *F. japonica* and *A. donax* were compared. After a detailed study of the different parameters influencing the conversion and selectivity of transesterification reactions, the design of an experimental plan was carried out to optimize the reaction conditions. The method was then studied on larger quantities through a scale-up study.

2. Results and discussion

2.1. *Characterisation of ecocatalysts®*

Ecocatalysts®, Eco1-E-FA-JA and Eco1-E-AR-DO, were prepared from aerial parts of *F. japonica* and *A. donax*, including stems, leaves and petioles. The harvested parts were ground and thermally treated under airflow, directly characterised by MP-AES and XRPD and used as catalysts for the transesterification of methyl and ethyl fatty esters.

2.1.1. *Elemental composition of ecocatalysts®*

Metallic compositions of ecocatalysts®, resulting from the thermal treatment of aerial parts of *F. japonica* (Eco1-E-FA-JA) and *A. donax* (Eco1-E-AR-DO), were studied by MP-AES analyses. Assays were performed in triplicate for each sample to determine the standard deviation of the measurement (Table 1). The results showed that potassium was the major mineral element in each ecocatalysts®. These values were significantly higher than the average values of native plants present in the wetlands where the harvests were carried out (potassium content usually around 3–5%). It should be noted that Eco1-E-FA-JA exhibited a high magnesium level, which is consistent with the high level of chlorophyll in the leaf biomass of *F. japonica* [11].

2.1.2. *XRPD analysis of ecocatalysts®*

The structures of Eco1-E-FA-JA and Eco1-E-AR-DO were investigated by XRPD (Table 2, Figures S1

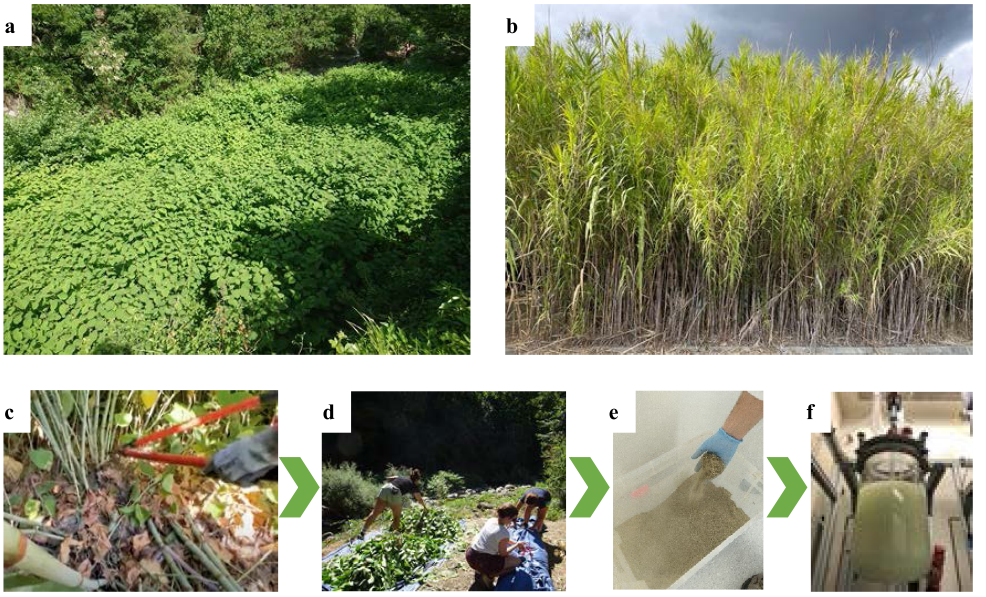

Figure 1. From the management of IAS in wetlands to green synthesis of glyceryl esters. (a) *F. japonica* and (b) *A. donax* [10]; (c, d) massive harvests of aerial parts; (e) transformation of aerial parts into ecocatalysts®; (f) synthesis of glyceryl esters using ecocatalysts®. Pictures taken by the authors.

Table 1. Elemental composition of Eco1-E-FA-JA and Eco1-E-AR-DO determined by MP-AES.

Ecocatalysts®	Composition (wt% (%RSD))					
	Ca	Fe	Mg	Na	K	Al
Eco1-E-FA-JA	9.09 (0.57)	0.28 (4.33)	3.90 (0.5)	0.10 (0.66)	**30.16** (0.7)	0.13 (3.52)
Eco1-E-AR-DO	2.71 (2.29)	0.05 (2.93)	1.49 (4.07)	0.12 (0.63)	**37.16** (0.48)	0.03 (1.10)

and S2 in ESI). The two ecocatalysts® presented mostly crystalline potassium salts; neutral crystalline potassium salts were similar but the basic ones differed. Indeed, Eco1-E-AR-DO exhibited K_2CO_3, while Eco1-E-FA-JA revealed the presence of $KMgPO_4{\cdot}6H_2O$, crystallized as struvite-K. Surprisingly no crystalline phase of fairchildite, $K_2Ca(CO_3)_2$, could be detected within Eco1-E-FA-JA, as it had been previously observed [9]. The difference of structure between the two ecocatalysts®, which both derived from the same plant species *F. japonica*, might be due to different locations and dates of collection. Nevertheless, the presence of struvite-K was of high interest since phosphates possess stronger basic properties than carbonates.

The basicity of the two ecocatalysts® was hence assessed and gave high pH values of 12 for Eco1-E-AR-DO and 11.5 for Eco1-E-FA-JA (Table 2).

These two catalysts being therefore slightly different, it was particularly interesting to compare their reactivity in the basic-catalyzed transesterification of triglycerides.

2.2. *Application of the ecocatalysts® in the transesterification of triglycerides*

The preparation of glyceryl esters is based on three possible strategies (Scheme 1):

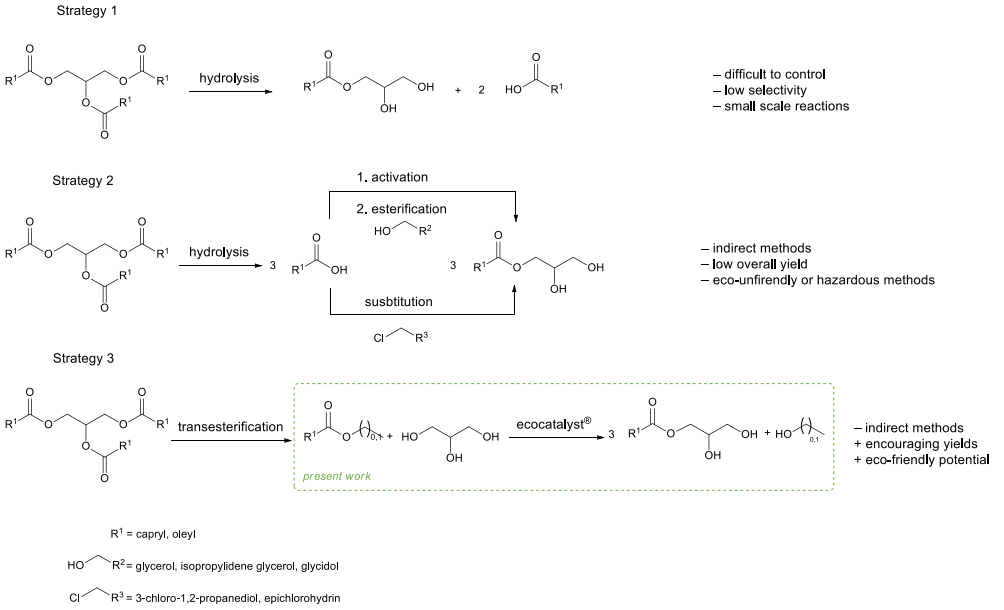

Scheme 1. General routes for the synthesis of glyceryl esters from literature and envisaged strategies for the transesterification of alkyl esters with glycerol using ecocatalysis.

Table 2. Crystalline species of potassium salts Eco1-E-AR-DO and Eco1-E-FA-JA determined by XRPD and pH of a suspension of ecocatalysts® in water

Ecocatalysts®	Crystalline species						pH*
	KCl	K_2SO_4	K_2CO_3	$K_2Ca(CO_3)_2$	$KMgPO_4{\cdot}6H_2O$	$CaCO_3$	
Eco1-E-AR-DO	✓	✓	✓	-	-	-	12
Eco1-E-FA-JA	✓	✓	-	-	✓	✓	11.5

*pH was measured after stirring 100 mg of ecocatalyst® in 1 mL of distilled water for 15 min and decanting.

• Hydrolysis of a triglyceride.
(Strategy 1): This strategy may seem attractive because it is direct. However, the hydrolysis of a triglyceride into a monoglyceride is very difficult to control as hydrolysis is increasingly rapid as the fatty chains of the triglyceride are hydrolyzed [12,13]. The literature is therefore mainly based on enzymatic hydrolysis using specific lipases, which are more suited to this situation [14,15]. However, the selectivities remain moderate (>50%) and the reactions are described on small quantities of substrates.

• Esterification of an activated fatty acid.
(Strategy 2): This sequenced method requires the prior hydrolysis of the triglyceride into fatty acid, followed by the activation of the acid to carry out the esterification. Various activation methods are described: activation of the fatty acid partner by Brønsted acids such as APTS [16], Zn or Ti salts supported on zeolite [17,18], tungsten nanoparticles in ionic liquid [19], cobalt salts supported on hydroxyapatite [20], activation by enzymes [21–23], formation of fatty acid chlorides [24–28], or acid anhydrides [29,30]. Using glycerol as a nucleophile

leads to unsatisfactory results despite the variety of activation agents (drastic conditions in terms of temperature and/or reaction time), and masked forms of glycerol have been described to improve conversion and selectivity. Thus, isopropylidene glycerol [30,31], glycidol [32–36], epichlorohydrin [37] or 3-chloro-1,2-propanediol [38] have been reported. This strategy is hardly compatible with the principles of green chemistry (protection/deprotection sequences of the masked form of glycerol, toxic reagent, moderate or even low overall yields).

• Transesterification of a methyl or ethyl fatty ester. **(Strategy 3)**: This strategy is probably the best compromise between efficiency and number of reaction steps. The key intermediate here is the fatty methyl ester (eventually an ethyl ester), widely described since the emergence of biodiesel. However, only a few examples of monoglyceride formation from fatty esters are described in the literature. Among them, the preparation of glyceryl oleate and caprylate has been reported using sodium carbonate for 5 h at 180 °C [39]. The yield is not specified, but the reaction conditions show that using alkaline carbonates makes it possible to facilitate the transesterification under reasonable reaction conditions in terms of duration and temperature. Our recent work showed that the ecocatalyst® derived from *F. japonica* presented a reactivity that could be higher than the alkaline carbonates reactivity [4]. These encouraging results led us to revisit this third strategy through the transesterification of methyl and ethyl esters with glycerol in caprylic and oleic series (Scheme 1).

2.2.1. *Optimization of the transesterification conditions of methyl caprylate **1** with glycerol*

The preparation of glyceryl caprylate **2** by transesterification of methyl caprylate **1** with glycerol was chosen as the first model reaction. The solvent-free reaction was promoted under microwave activation. Glycerol plays the role of nucleophile as well as a heating source absorbing microwaves (Figure 2). A fine study of the reaction conditions was carried out with Eco1-E-AR-DO. The influence of four parameters were investigated on the conversion and the selectivity of the reaction: temperature, reaction time, catalyst loading and the quantity of glycerol. The detailed results are summarised in the Table S1 of the ESI. Given the number and range of experiments, Pearson's correlations were calculated to statistically analyze these data (Figure 2a). Correlation values greater than 0.50 and p-values less than 0.05 were considered (in bold in Figure 2a). The correlation matrix showing only the correlation of the four parameters and the two responses of the system highlights two statistically significant correlations: conversion rate and selectivity with the catalytic loading and the quantity of glycerol. Both conversion rate and selectivity were positively correlated to the catalytic loading. The influence of glycerol was more complicated: conversion rate was negatively correlated to the quantity of glycerol while selectivity was positively correlated. The correlation coefficient of -0.44 between the conversion rate and the quantity of glycerol was considered, although it does not meet the selectivity criteria. The use of ten equivalents of glycerol was thus chosen, which was a compromise to achieve a sufficient conversion rate without affecting the selectivity. Experimental conditions that take into account these initial results have been tested. Indeed, the transesterification of methyl caprylate **1** with glycerol (10 equiv) at 150 °C for 1 h using Eco1-E-AR-DO (0.5 equiv in potassium) led to an excellent yield (Figure 2b). The use of Eco1-E-FA-JA led to excellent results as well (92% of conversion and 96% of selectivity).

The recyclability of Eco1-E-AR-DO was then studied on a larger scale (8.5 mmol), called the intermediate scale, to allow distillation of the crude mixture. Distillation of a mixture of glycerol and glyceryl caprylate **2** under reduced pressure (145 °C, 0.04 mbar) was used to recover the ecocatalyst® as the distillation residue. Eco1-E-AR-DO was reactivated by thermal treatment and reused, giving comparable yields during at least 4 reaction cycles (Figure 2c).

The MW-transesterification was scaled up on a larger scale (85 mmol), called the large scale, using a specific set-up. The reaction was performed with Eco1-E-AR-DO on a pilot MW 1 L reactor equipped with a distillation apparatus. MeOH was distilled to shift the equilibrium while the temperature of the reaction mixture was maintained at 160 °C, with a high absorbance of MW power. Good conversion (81%) and selectivity (81%) could be preserved at such a scale.

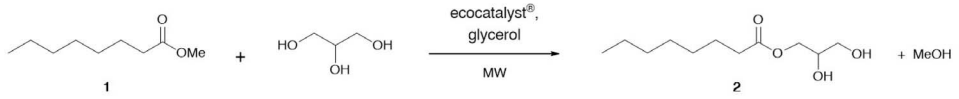

(a)

variables	conversion of **1**	selectivity in **2**
cat. loading	**0.53**	0.18
glycerol	−0.44	**0.51**
time	0.30	0.19
temperature	0.16	0.48
conversion of **1**	**1**	−0.14
selectivity in **2**	−0.14	**1**

(b)

ecocatalyst®	best conditions*	conv.¥ **1**	select.¥ **2**	scale (mmol of methyl caprylate)
Eco1-E-AR-DO	1 h, 150 °C	90%	92%	small (0.85 mmol)
Eco1-E-FA-JA		92%	96%	
Eco1-E-AR-DO	2 h, 150 °C	100%		intermediate (8.5 mmol)
Eco1-E-AR-DO	1 h, 160 °C	81%	81%	large (85 mmol)

(c)

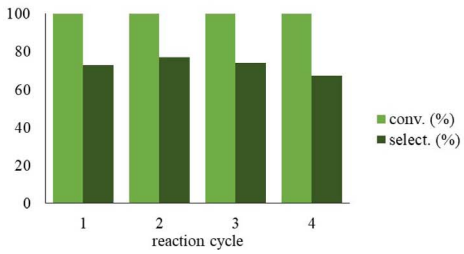

Figure 2. (a) Pearson's correlation matrix of the experimental variables from 16 experiments for determining the key parameters of the transesterification of methyl caprylate **1** with glycerol using Eco1-E-AR-DO, at a small scale (values in bold correspond to a p-value < 0.05); (b) best conditions found at different scales. *methyl caprylate **1** (1 equiv), glycerol (10 equiv) and ecocatalyst® (0.5 equiv in potassium), ¥conversion and selectivity were established using an HPLC-QDa calibration curve; (c) recycling studies of Eco1-E-AR-DO at the intermediate scale.

Depending on the scale of the reaction, the method used here led to yields ranging from 66% to 89%. In the literature, the transesterification of methyl caprylate **1** with glycerol was described using a Ba–Al oxides catalyst at 140 °C for 16 h, leading to a 96% yield [40]. This reaction required a long reaction time and the use of a Ba–Al oxide catalyst, which is questionable from an environmental point of view [41], while our method relied on a biosourced catalyst and a shorter reaction time which could be decreased to 1 h or 2 h according to the reaction scale.

Two work-up conditions were studied to separate glycerol and glyceryl caprylate **2** (Figure S3 in ESI). The first one relies on a conventional treatment by adding water to remove glycerol, followed by a liquid-liquid extraction of glyceryl caprylate **2** with Me-THF. Glyceryl caprylate **2** (100 g) could be obtained with high purity (less than 1 wt% of glycerol) (Table 3).

Based on a cloud point experiment, an alternative work-up was investigated to avoid the use of solvent and prevent waste formation. Glyceryl caprylate **2** was added to a brine solution, and the mixture was stirred at 60 °C. Cloud points were determined visually by noting the formation of two phases: brine water/glycerol and glyceryl caprylate **2**, which were easily separated by hot decantation. This method led to an excellent separation with only 4 wt% of glycerol.

2.2.2. *Extension of the method to the transesterification of methyl oleate **3** with glycerol*

The best conditions obtained during the synthesis of methyl caprylate **1** (150 °C, 10 equiv glycerol, 0.5 equiv in potassium, 1 h, microwave activation) were transposed to the transesterification of methyl oleate **3**. However, the conversion rate collapsed to 5%, probably due to the lengthening of the carbon chain. Eco1-E-FA-JA appeared far more efficient to achieve this reaction with significant conversion (Figure 3b).

A new set of experiments was then conducted to improve the conversion rate and the selectivity by studying the reaction time, the temperature and the catalytic loading (Figure 3a). Results were again statistically analyzed by calculating Pearson's correlations, which showed time and temperature were pos-

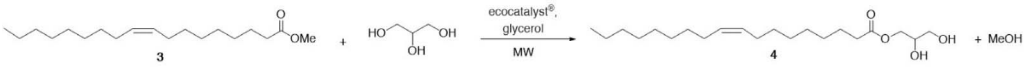

3 **4**

(a)

variables	conversion of **3**	selectivity in **4**
cat. loading	0.43	−0.34
time	**0.51**	−0.15
temperature	**0.54**	−0.23
conversion of **3**	**1**	**−0.55**
selectivity in **4**	**−0.55**	**1**

(b)

ecocatalyst®	conditions*	conv.¥ **3**	select.¥ **4**
Eco1-E-AR-DO	1 h, 150 °C	5%	60%
Eco1-E-AR-DO	1 h, 180 °C	27%	37%
Eco1-E-FA-JA		88%	45%

Figure 3. (a) Pearson's correlation matrix of the experimental variables from 16 experiments for determining the key parameters of the transesterification of methyl oleate **3** with glycerol using Eco1-E-FA-JA (values in bold correspond to a p-value < 0.05). (b) Transposed conditions from transesterification of methyl caprylate **1** and examples of conditions used for the Pearson's correlation matrix, *methyl oleate **3** (17 mmol, 1 equiv), glycerol (10 equiv) and ecocatalyst® (0.5 equiv in potassium), MW activation, ¥conversions and selectivity were established using an HPLC-ELSD calibration curve.

Table 3. Industrial specifications [42] and properties of glyceryl caprylate **2** obtained by extraction with H_2O/Me-THF

	Industrial specifications	Sample properties
Acid value (mg KOH/g)	<2.5	<2.5
Peroxide value (m equiv/kg)	<1	0.6
Free glycerol (%)	<2.5	<1
Monoglycerides (%)	>80	>90
Diglycerides (%)	<20	<10
Triglycerides (%)	<5	<0.1
Methanol (ppm)	-	<0.4

itively correlated to the conversion rate (correlation coefficient > 0.5 and p-value < 0.05). Moreover, the conversion was negatively correlated to the selectivity. For instance, an increase of the temperature led to a conversion rate of 88% but with a selectivity of only 45% selectivity, which can be explained by the beginning of glycerol polymerization.

A design of experiment (DoE) approach was carried out to determine the optimal settings of the transesterification reaction parameters for the production of glyceryl monooleate **4** [43].

The experimental space, shown in Table 5, was defined by the upper and lower limits of three parameters: the temperature of the reaction (160–170 °C), which was limited to 170 °C to avoid the glycerol polymerization side reaction, the reaction time (40–80 min) and the quantity of Eco1-E-FA-JA (0.25–0.5 equiv in K) (Table 5). The studied response was the yield in glyceryl monooleate **4**. A design matrix was generated using Modde 13.0 software according to full fractional design, resulting in 11 experimental points that included 2^3 factor points and three replications at the middle point to evaluate the reproducibility. A polynomial model (see Figure 4b for the corresponding equation) for the glyceryl monooleate **4** yield was obtained with a satisfying R^2 (0.954) and an acceptable fit between prediction and experimental data (Q^2 = 0.800). Figure 4a highlights that increasing the reaction time and quantity of Ecocatalyst® significantly positively impacts glyceryl monooleate **4** synthesis. The other studied parameters have no significant impact. As shown by the contour plots of Figure 4b, the hotspot is located in the top right-hand area (i.e. Eco1-E-FA-JA at 0.5 equiv in potassium and 170 °C), these optimum conditions allowing the prediction of a theoretical yield of 77%. These optimized experimental parameters were then tested in triplicate, leading to a repeatable yield of 82%, slightly higher than the yield predicted by the DoE model.

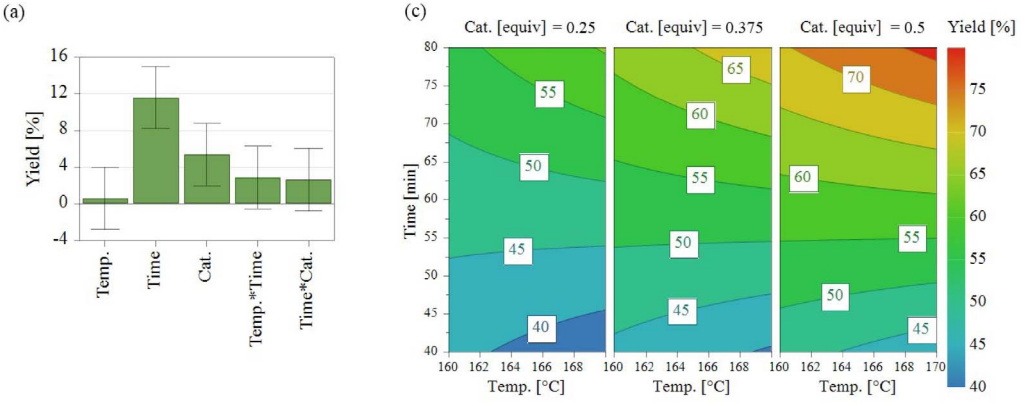

ecocatalyst®	time	temperature	yield.¥	application
Eco1-E-FA-JA (0.5 equiv in K)	1.3 h	170 °C	77%	DoE model
			82%	experiments

Figure 4. (a) Regression coefficients of the model and (b) the associated model equation with normalized coefficients; (c) response contour of yield for the transesterification of methyl oleate **3** with glycerol; (d) theoretical and experimental yields obtained using optimum conditions determined by DoE. ¥Yields in glyceryl oleate **4** were established using an HPLC-ELSD calibration curve.

This result can be advantageously compared to the literature data regarding performances and soft reaction conditions (Table 4). The same reaction was described either with glycerol or using isopropylidene glycerol. The use of glycerol relied on chemical activation by P1 phosphazene [44] or Mg oxides [45] at high temperature or during long reaction time. Isopropylidene glycerol was used in enzymatic catalysis in a hazardous solvent (hexane) and required a strong acid-catalyzed deprotection step [46]. The solvent-free way of synthesis presented here, which needs low reaction times and the use of an eco-friendly catalyst, is particularly attractive from a sustainable point of view.

2.2.3. *Transesterification of ethyl caprylate **5** by glycerol*

The transesterification of ethyl caprylate **5** by glycerol presents a specific interest in producing 100% biosourced monoglyceryl esters. Indeed, ethyl caprylate **5** is derived from the transesterification of triglyceride by ethanol rather than by methanol, which is petroleum-based and neurotoxic. However, ethyl caprylate **5** is less reactive than methyl caprylate **1**. The transesterification of ethyl caprylate **5** by glycerol therefore required a specific study. The strategy previously used for methyl caprylate **1** and oleate **3** was transposed identically. First, the influence of the reaction time, temperature and catalyst loading on the conversion rate and the selectivity was investigated using Pearson's correlations (Figure 5a). The correlation matrix highlights that selectivity shows negative correlations with the reaction time and the catalytic loading, suggesting that decreasing the quantity of ecocatalyst® increases the selectivity (Figure 5b). The reaction time and catalytic loading are positively correlated with the conversion rate and temperature is positively correlated with the selectivity, but their values of correlation coefficient are not statistically significant (p-value > 0.05).

The optimal reaction conditions of ethyl caprylate **5** transesterification were then determined by DoE with regards to three key parameters: the temperature of the reaction (150–160 °C), the reaction time (15–30 min) and the loading of ecocatalyst® Eco1-E-FA-JA (0.025–0.05 equiv). The response was the yield in glyceryl monocaprylate **2**. The same simple systematic design (full factorial design with 11 experimental points) was used to estimate the main effects and potential interactions. The coefficient values of

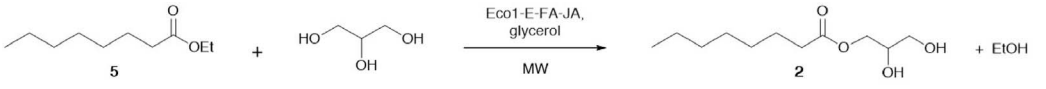

(a)

variables	conversion of **5**	selectivity in **2**
cat. loading	0.46	**−0.94**
time	0.50	**−0.58**
temperature	−0.22	0.57
conversion of **5**	1	**−0.65**
selectivity in **2**	**−0.65**	1

(b)

ecocatalyst®	cat. loading in K	conditions*	conv.¥ **5**	select.¥ **2**
Eco1-E-FA-JA	0.5	30 min, 160 °C	100%	60%
	0.1		100%	67%
	0.05		45%	76%

Figure 5. (a) Pearson's correlation matrix of the experimental variables from 12 experiments for determining the key parameters of the transesterification of ethyl caprylate **5** with glycerol (values in bold correspond to a p-value < 0.05); (b) examples of conditions used for Pearson's correlations. *Ethyl caprylate **5** (17 mmol, 1 equiv), glycerol (10 equiv) and ecocatalyst®, under MW activation, ¥conversions and selectivity were established using HPLC-ELSD and HPLC-PDA (λ = 211.3 nm) calibration curves.

Table 4. Comparison of processes from literature and using ecocatalysis

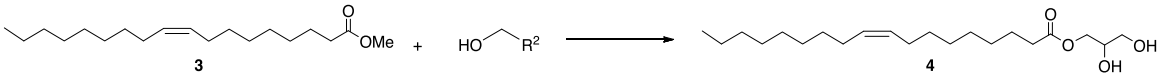

HO R2	Reactant	Conditions	Yield in 4	Ref.
Glycerol	Ecocatalyst®	170 °C (MW), 1.3 h without solvent	82%	Present work
Glycerol	Phosphazene P1	rt, 16 h in DMSO	87%	[44]
Glycerol	Mg salts	220 °C, 5 h	>60%	[45]
Isopropylidene glycerol	Lipase EC 3.1.1.3	(1) 65 °C, 48 h in hexane (2) HCl (50% v/v)	88%	[46]

the polynomial response model (R^2 = 0.905 and Q^2 = 0.677) are all significantly positive, except for the interaction between temperature and reaction time, meaning that an increase in the temperature, time and catalyst tends to increase the yield in glyceryl monocaprylate **2** (Figure 6a and b). Figure 6c shows that the hotspot—again located at the top right-hand zone (i.e. Eco1-E-FA-JA at 0.05 equiv in potassium and 160 °C)—indicates that these optimum conditions predict a theoretical yield of 70%.

Table 5. Factors and their values used for the experimental design.

Factors	Levels	
	−1	+1
Temperature	160 °C	170 °C
Time	40 min	80 min
Eco1-E-FA-JA (equiv K)	0.25	0.5

This prediction was confirmed experimentally, with an isolated yield of 67% of glyceryl monocaprylate **2**, slightly lower than the yield predicted by the 2^3 full factorial design model.

In an attempt to obtain better results, the increase of each parameter independently was tested. It led to similar results, with no increase of the yield (Table S9). To our knowledge, no similar synthesis were reported in the literature except in a patent, which claims the possibility of carrying out the same reaction by enzymatic catalysis, but without quantitative performance indicators [47].

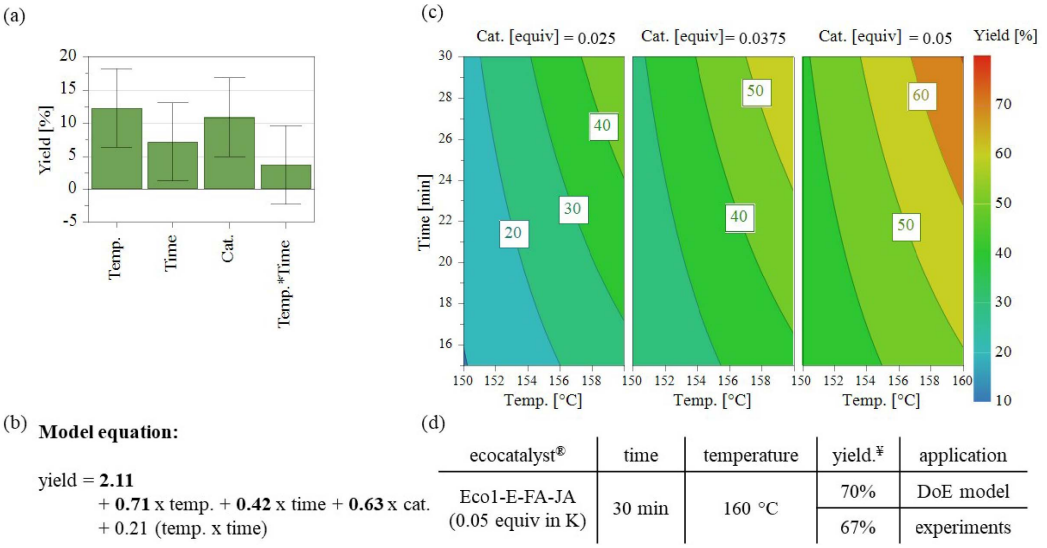

(b) **Model equation:**

yield = **2.11**
+ **0.71** x temp. + **0.42** x time + **0.63** x cat.
+ 0.21 (temp. x time)

(d)

ecocatalyst®	time	temperature	yield.¥	application
Eco1-E-FA-JA (0.05 equiv in K)	30 min	160 °C	70%	DoE model
			67%	experiments

Figure 6. (a) Regression coefficients of the model and the associated model equation with normalized coefficients; (b) response contour of yield for the transesterification of ethyl caprylate **5** with glycerol ¥isolated yield.

3. Conclusion

In conclusion, we exploited two wetland Invasive Alien Species (IAS), *Arundo donax* and *Fallopia japonica*, by transforming these unwanted plant species into valuable resources, ecocatalysts®. Their characterization showed an interesting mineral composition favoring transesterifications in a basic medium. These ecocatalysts® are eco-friendly and harmless catalysts, which have proven to be very effective for the preparation of glyceryl caprylate and oleate. Using statistical tools such as Pearson's correlations and DoE, good to excellent selectivities and yields were obtained under microwave activation, without solvent and with a high degree of naturalness. Finally, this study encourages the valorization of IAS, which aims to explore disruptive solutions to support the management of IAS through their transformation into new useful eco-materials for sustainable chemistry processes.

4. Experimental part

4.1. *Preparation of ecocatalysts®*

Aerial parts of *F. japonica* were harvested in April 2023, in the wetlands of Clapices, Aulas (South of France) by BIOINSPIR company. Aerial parts of *A. donax* were harvested in November 2021, in Montferrier-sur-Lez (South of France). Ecocatalysts® were prepared from aerial parts of the harvested plants, which were first dried in an oven at 30 °C, ground and then thermally treated in an oven under airflow. The following temperature program was used: 20 °C–350 °C in 1 h, 350 °C–550 °C in 1 h, then 4 h at 550 °C.

4.2. *Characterization of ecocatalysts®*

Mineral composition of the ecocatalysts® was determined using an Agilent 4200 Microwave Plasma-Atomic Emission Spectrometer (MP-AES) coupled with an SPS4 autosampler. The samples were digested in 6 mL of reversed aqua regia [hydrochloric acid (37%)/nitric acid (65%) = 1:2] under an Anton Paar Multiwave Go microwave-assisted digestion, with the following program: 20 °C–164 °C in 20 min then 10 min isothermal at 164 °C. Samples were filtered and then diluted to 0.2 $g{\cdot}L^{-1}$ in nitric acid (1%). Three blanks were recorded for each step of the dilute procedure. Three analyses were carried out for each sample to determine the standard deviation of the measurement. X-ray diffraction (XRD) analyses were performed on samples dried

at 110 °C for 2 h by using a BRUKER diffractometer (D8 advance, with a Cu Kα radiation λ = 1.54086 Å) equipped with a LynxEye detector.

4.3. *Procedure for the preparation of glyceryl monocaprylate **2** from methyl caprylate **1***

4.3.1. *Small scale procedure*

Methyl caprylate **1** (0.85 mmol), glycerol (8.5 mmol) and Eco1-E-AR-DO (0.425 mmol of potassium) were stirred in a 10 mL microwave reactor. A microwave oven (CEM Discover 2.0) was programmed as follows: temperature gradient from rt to 150 °C in 2 min, then constant temperature for 1 h. The reaction mixture was filtered using a sintered glass filter (porosity 4) and washed 3 times with isopropanol. The reaction was placed in a 100 mL volumetric flask and analyzed by HPLC-QDa by ion extraction in Single Ion Recording (SIR) mode.

4.3.2. *Intermediate scale procedure*

This procedure allowed the study of the ecocatalyst® recyclability. Methyl caprylate **1** (8.5 mmol), glycerol (85 mmol) and Eco1-E-AR-DO (4.25 mmol of potassium) were stirred in a 20 mL microwave reactor. A microwave oven (CEM Discover 2.0) was programmed as follows: temperature gradient from rt to 150 °C in 2 min, then constant temperature for 2 h. The reaction mixture was filtered using a sintered glass filter (porosity 4), washed with isopropanol and analyzed by HPLC-QDa by ion extraction in Single Ion Recording (SIR) mode.

4.3.3. *Large scale procedure*

Methyl caprylate **1** (595 mmol), glycerol (5.95 mol) and Eco1-E-AR-DO (59.5 mmol of potassium) were stirred in a 1 L flask. A microwave oven (CEM MARS 6) was programmed as follows: temperature gradient from rt to 160 °C in 10 min, then constant temperature for 1 h. During the reaction, the produced methanol was distilled at atmospheric pressure. The reaction mixture was filtered using a sintered glass filter (porosity 4), washed with isopropanol and analyzed by HPLC-QDa by ion extraction in Single Ion Recording (SIR) mode.

4.4. *Procedure for the preparation of glyceryl monooleate **4** from methyl oleate **3***

In a typical procedure, methyl oleate **3** (17 mmol), glycerol (170 mmol) and Eco1-E-FA-JA (8.5 mmol of potassium) were stirred in a 50 mL flask. A microwave oven (CEM Discover 2.0) was programmed as follows: temperature gradient from rt to 150 °C in 5 min, then constant temperature for 1 h 20. During the reaction, the produced methanol was distilled under a vacuum (20 mbar). The reaction mixture was filtered using a sintered glass filter (porosity 4) and washed 3 times with isopropanol. The reaction was placed in a 250 mL volumetric flask, diluted 8 times and analyzed by HPLC-PDA and HPLC-ELSD.

4.5. *Statistical studies for the preparation of glyceryl monooleate **4** from methyl oleate **3***

4.5.1. *Design of experiments*

Using the Modde 13.0 software, a DoE was performed using the following factors to optimize the experimental conditions for the preparation of glyceryl monooleate **4** from methyl oleate **3** using Eco1-E-FA-JA.

A first-order polynomial equation including correlation terms was used to find the relationship between the factors and the response surface (Equation (1)):

$$Y = \alpha_0 + \sum_i \alpha_i X_i + \sum_{i,j} \alpha_{ij} X_i X_j, \qquad (1)$$

where Y is the response (yield), X_i are the factors, α_0 is the constant term of the equation, α_i are the linear coefficients and α_{ij} are the interaction coefficients. The factors and their values are reported in Table 6.

The coefficients were determined using Multiple Linear Regressions (MLR). The validity of the model was assessed by analysis of the variance (ANOVA), R^2, Q^2 and the lack of fit. A full 2^3 factorial design, with 3 replicated centered points to evaluate the reproducibility, was used to fit the model. This design required 11 experiments. The results are presented in Table S5 of the ESI. The order of the experiments was randomized to avoid bias. The yields were obtained by using a calibration curve in HPLC. To obtain a good fit between the dataset and the polynomial equation, the correlation term Temperature

Table 6. Factors and their values used for the experimental design

Factors	Levels	
	−1	+1
Temperature	150 °C	160 °C
Time	15 min	30 min
Eco1-E-FA-JA (equiv K)	0.025	0.05

× Catalyst was removed from the initial polynomial equation. The analysis of variance shows a good correlation between the obtained yield and the factors. The p-value of the regression model ($p = 0.002 < 0.05$) shows that the regression is statistically significant. The lack of fit ($p = 0.571 > 0.05$) shows that the model has low replicate errors. The model gives a very good coefficient of determination ($R^2 = 0.954$) and a good cross-validation coefficient ($Q_2 = 0.800$).

4.6. *Procedure for the preparation of glyceryl monocaprylate **2** from ethyl caprylate **5***

In a typical procedure, ethyl caprylate **5** (17 mmol), glycerol (170 mmol) and Eco1-E-FA-JA (0.85 mmol of K) were stirred in a 50 mL flask. A microwave oven (CEM Discover 2.0) was programmed as follows: temperature gradient from room temperature to 160 °C in 5 min, then constant temperature for 30 min. During the reaction, the methanol produced was distilled under vacuum (220 mbar). The reaction mixture was filtered using a sintered glass filter (porosity 4) and washed 3 times with isopropanol. The reaction was placed in a 250 mL volumetric flask, diluted 8 times with isopropanol and analyzed by HPLC-PDA and HPLC-ELSD.

4.7. *Statistical studies for the preparation of glyceryl monocaprylate **2** from ethyl caprylate **5***

4.7.1. *Design of experiments*

A DoE was performed using the following factors to optimize the experimental conditions for the preparation of glyceryl monocaprylate **2** from ethyl caprylate **5** using Eco1-E-FA-JA.

As in the previous DoE, a first-order polynomial equation including correlation terms was used to find the relationship between the factors and the response surface (Equation (2)):

$$Y = \alpha_0 + \sum_i \alpha_i X_i + \sum_{i,j} \alpha_{ij} X_i X_j, \qquad (2)$$

where Y is the response (yield), X_i are the factors, α_0 is the constant term of the equation, α_i are the linear coefficients and α_{ij} are the interaction coefficients.

The coefficients were determined using Multiple Linear Regressions (MLR). The validity of the model was assessed by analysis of the variance (ANOVA), R^2, Q^2 and the lack of fit. A full 2^3 factorial design, with 3 replicated centered points to evaluate the reproducibility, was used to fit the model. Such a design required 11 experiments. The results are reported in Table S5 of the ESI. The correlation terms Temperature × Catalyst and Time × Catalyst were removed from the initial polynomial equation to obtain a good fit between the dataset and the polynomial equation. The analysis of variance shows a good correlation between the obtained yield and the factors. The p-value of the regression model ($p = 0.003 < 0.05$) and the lack of fit ($p = 0.124 > 0.05$) confirm the statistical significance. Moreover, the model gives a good coefficient of determination ($R_2 = 0.905$) and an acceptable cross-validation coefficient ($Q_2 = 0.677$).

Declaration of interests

The authors do not work for, advise, own shares in, or receive funds from any organization that could benefit from this article, and have declared no affiliations other than their research organizations.

Acknowledgements

The authors thank the French National Centre for Scientific Research (CNRS) for financial support (International program between CNRS and University of Arizona). The authors also thank Professor Laurent Debelle for the fruitful discussions concerning the statistical tests carried out in this work.

Supplementary data

Supporting information for this article is available on the journal's website under https://doi.org/10.5802/crchim.273 or from the author.

References

[1] H. E. Roy, A. Pauchard, P. Stoett, T. Renard Truong, S. Bacher, B. S. Galil *et al.*, *IPBES Invasive Alien Species Assessment: Summary for Policymakers*, Zenodo, Bonn, 2023.

[2] T. Pullalaiah, M. R. Ielmini, *Invasive Alien Species*, vol. 3, John Wiley & Sons, Ltd, Hoboken, NJ, 2021, ISBN 978-1-119-60704-5, i-xv pages.

[3] J. Rojas-Sandoval, P. Acevedo-Rodríguez, *Arundo Donax (Giant Reed)*, CABI Compendium, 2014.

[4] C. Grison, Y. Lock Toy Ki, "Novel compositions for the sustainable catalysis of organic synthesis reactions", WO2023144167A1, January 2022.

[5] C. Grison, Y. Lock Toy Ki, *Curr. Opin. Green Sustain. Chem.*, 2021, **29**, article no. 100461.

[6] V. Escande, L. Garoux, C. Grison, Y. Thillier, F. Debart, J.-J. Vasseur *et al.*, *Appl. Catal. B: Environ.*, 2014, **146**, 279-288.

[7] C. Bihanic, S. Diliberto, F. Pelissier, E. Petit, C. Boulanger, C. Grison, *ACS Sustain. Chem. Eng.*, 2020, **8**, 4044-4057.

[8] G. Clavé, F. Pelissier, S. Campidelli, C. Grison, *Green Chem.*, 2017, **19**, 4093-4103.

[9] Y. Lock Toy Ki, A. Garcia, F. Pelissier, T. K. Olszewski, A. Babst-Kostecka, Y.-M. Legrand *et al.*, *Molecules*, 2022, **27**, article no. 3306.

[10] S. Boudjelas, M. Browne, M. De Poorter, S. Lowe, *100 of the World's Worst Invasive Alien Species: A Selection from the Global Invasive Species Database*, IUCN, Auckland, 2000.

[11] S. Lachowicz, J. Oszmiański, A. Wojdyło, T. Cebulak, L. Hirnle, M. Siewiński, *Eur. Food Res. Technol.*, 2019, **245**, 691-706.

[12] L. Hui, F. Weiyu, L. Yang, Z. Pinhui, N. Guozhi, "Method for preparing fatty acid monoglyceride by taking basic ionic liquid as catalyst", CN103540413A, January 29, 2014.

[13] M. Sutter, W. Dayoub, E. Métay, Y. Raoul, M. Lemaire, *ChemCatChem*, 2013, **5**, 2893-2904.

[14] A. P. D. de Lima, E. M. Aschenbrenner, S. d. N. Oliveira, J.-B. Doucet, C. K. Weiss, U. Ziener *et al.*, *J. Mol. Catal. B: Enzymatic*, 2013, **98**, 127-137.

[15] I. C. Omar, N. Nishio, S. Nagai, *Agric. Biol. Chem.*, 1987, **51**, 2153-2159.

[16] H. D. Kwon, H. M. Lee, "Method for Preparing Monoglycerides", KR102109134B1, May 11, 2020.

[17] D. Singh, P. Patidar, A. Ganesh, S. Mahajani, *Ind. Eng. Chem. Res.*, 2013, **52**, 14776-14786.

[18] M. Kotwal, A. Kumar, S. Darbha, *J. Mol. Catal. A: Chem.*, 2013, **377**, 65-73.

[19] W. N. R. W. Isahak, Z. A. C. Ramli, M. Ismail, M. A. Yarmo, *Ind. Eng. Chem. Res.*, 2014, **53**, 10285-10293.

[20] P. Mukhopadhyay, R. Chakraborty, *Catal. Commun.*, 2017, **94**, 73-76.

[21] A. Ducret, A. Giroux, M. Trani, R. Lortie, *Biotechnol. Bioeng.*, 1995, **48**, 214-221.

[22] T. Yoshio, O. Susumu, I. Mieko, *Biochim. Biophys. Acta (BBA) - Lipids and Lipid Metabolism*, 1977, **489**, 415-422.

[23] M. M. Hoq, H. Tagami, T. Yamane, S. Shimizu, *Agric. Biol. Chem.*, 1985, **49**, 335-342.

[24] X. Shi, K. Guo, Z. Fang, L. Tao, G. Lai, "High-quality vegetable oil polyol as well as preparation method and application thereof", CN109608333A, April 12, 2019.

[25] L. M. Strawn, R. E. Martell, R. U. Simpson, K. L. Leach, *J. Med. Chem.*, 1989, **32**, 2104-2110.

[26] L. Yue, C. Zhang, G. Zhang, *Lipids*, 2006, **41**, 301-303.

[27] S. Narine, S. Li, L. Bouzidi, "Oligomères de triacylglycérol", WO2015168789A1, November 12, 2015.

[28] S. Li, L. Bouzidi, S. S. Narine, *Ind. Eng. Chem. Res.*, 2013, **52**, 2209-2219.

[29] D. I. Batovska, S. Tsubota, Y. Kato, Y. Asano, M. Ubukata, *Tetrahedron: Asymmetry*, 2004, **15**, 3551-3559.

[30] D. Lochmann, S. Reyer, M. Stehr, "Process for producing high-grade tricaprylin", WO 2022/242883, November 24, 2022.

[31] S. C. Sik, C. J. Youl, L. Y. Mi, K. T. Woong, K. H. Jeung, "New 3-acetyl-1-oleoyl-glycerol tetrahydrocuminic acid ester compounds and the method thereof", KR101465899B1, November 26, 2014.

[32] P. Maheswari, "Green synthesis of 1 mono acyl glycerol with medium-chain fatty acid catalysed by fatty acid cuprate complex", IN202143016811, October 14, 2022.

[33] R. Janiš, A. Klásek, J. Bobálová, *J. Food Lipids*, 2006, **13**, 199-209.

[34] J.-P. Jamet, J. Parmentier, G. Vermeersch, Z. Mouloungui, V. Rakotondrazafy, M. Asdih *et al.*, "Process for the manufacture of a glycidic ester from glycidol or derivative", FR2684669B1, March 24, 1995.

[35] Z. Mouloungui, V. Rakotondrazafy, R. Valentin, B. Zebib, *Ind. Eng. Chem. Res.*, 2009, **48**, 6949-6956.

[36] P. Rytczak, M. Koziołkiewicz, A. Okruszek, *New J. Chem.*, 2010, **34**, 1008-1017.

[37] G. T. Topping, "Method of synthesizing glyceryl mono-esters", WO2001079190A1, October 25, 2001.

[38] W. Zhongkai, "Fatty acid monomer, preparation method and thermoplastic macromolecule synthesized through application", CN107032991A, August 11, 2017.

[39] D. G. Nunes, A. d. P. M. da Silva, J. Cajaiba, A. Pérez-Gramatges, E. R. Lachter, R. S. V. Nascimento, *J. Appl. Polym. Sci.*, 2014, **131**, article no. 41085.

[40] M. Sutter, W. Dayoub, E. Métay, Y. Raoul, M. Lemaire, *Green Chem.*, 2013, **15**, 786-797.

[41] H. Jiahu, "Method of preparing barium nitrate and/or barium carbonate from raw materials containing barium carbonate and calcium carbonate", CN103303958A, September 18, 2013.

[42] Unpublished data.

[43] D. C. Montgomery, *Design and Analysis of Experiments*, John Wiley & Sons, Hoboken, NJ, 2017, ISBN 978-1-119-11347-8.

[44] Y. Fu, Y. Weng, W.-X. Hong, Q. Zhang, *Synlett*, 2010, **2011**, 809-812.

[45] P. G. Belelli, C. A. Ferretti, C. R. Apesteguía, R. M. Ferullo, J. I. Di Cosimo, *J. Catal.*, 2015, **323**, 132-144.

[46] C. C. Akoh, *Biotechnol. Lett.*, 1993, **15**, 949-954.

[47] P. N. Golyshin, O. V. Golyshina, K. N. Timmis, T. Chernikova, A. Waliczek, M. Ferrer *et al.*, "Probe compound for detecting and isolating enzymes and means and methods using the same", WO2010105851A1, September 23, 2010.

ACADÉMIE DES SCIENCES
INSTITUT DE FRANCE

Comptes Rendus. Chimie
2024, Vol. 27, Special issue S2, p. 99-115
https://doi.org/10.5802/crchim.281

Research article

Women Chemists in France in 2024

The need for Open Labs for fostering interdisciplinarities in Modern Chemistry. Biocatalysis: a necessary tool for synthetic chemists

Juliette Martin [a]

[a] 70 Allée Graham Bell, 30035 Nîmes – SEQENS, France
E-mail: juliette.martin@seqens.com

Abstract. Among the different fields of chemical approaches available to the synthetic chemists, biocatalysis is only being slowly adopted, especially due to a lack of know-how and practical experience. However, enzymatic catalysis is a mature technology, and this should encourage more chemists to take further ownership and expand applications in modern chemistry.

In the industrial sector, some pharmaceutical companies have been pioneers in the use and acceptance of biocatalysis for the unique properties that enzymes can deliver. In this article, the key concepts for biocatalysis applications will be addressed including some recommendations to new practitioners. Some industrial examples will be presented, such as polycyclization, regioselective acylation, alkene asymmetric bioreduction, *meso* desymmetrization, kinetic resolution and aldolization. Biocatalysis provides economic and environmental benefits, its awareness should be enhanced, especially in a *momentum* of conducting hybrid approaches and multicatalysis. Open your Labs!

Keywords. Biocatalysis, Enzymes, Catalysis, Asymmetric synthesis, Sustainability, Green chemistry.

Manuscript received 15 October 2023, revised 10 November 2023 and 27 November 2023, accepted 11 December 2023.

1. Introduction

For the past decade, the need to produce compounds with more complexity in terms of group functionality and chemical structure has expanded tremendously, including drug discovery in the pharmaceutical field and materials science. Moreover, the increasing pressure to reduce energy consumption, protect the environment and conserve natural resources challenge synthetic methods.

In response to this demand, the execution of complex chemical syntheses requires expert knowledge, usually acquired over many years of study and hands-on laboratory practice. However, when cross-fertilization of multi-competencies is achieved, the outcome may lead to incredible avenue of innovation and enlarge the vision on synthetic methods and strategies. Among the different tools available to synthetic chemists, enzymatic catalysis remains underused. Indeed, there is a lack of knowledge and training in this area which contribute mainly to the slow progress.

Considering the significant advances in biotechnologies over the past two decades, the emergence of plethora new enzymes has occurred. Contemporary tools are facilitating the access to new ways of conducting chemical transformations and should complement chemical intuition.

By examining the current key concepts, this article aims to demystify biocatalysis for bench chemists so that they may embrace it as a tool rather than fear it as a too complex technology. Spur the curiosity of

synthetic chemists who are willing to fulfill the gaps in knowledge and increase the number of successful stories in biocatalysis, especially within the trends of building multicatalysis approaches.

To familiarize yourself with biocatalysis, books by Grogan [1] and Faber [2], and comprehensive contemporary review which have been compiled by Faber *et al.* [3] and Whittall *et al.* [4], are worth reading. The recent review by Lin *et al.* [5] provides a convenient correlation of enzyme catalyzed reactions with named organic chemical reactions that organic chemists are familiar with.

2. Biocatalysis is in its Golden Age

The emergence of catalysis in the 18th century has had a transformative impact over the decades in many fields, including the production of chemicals, healthcare, materials, agriculture and in the environmental sector. A majority of all commercial chemicals are produced by methods involving at least one catalytic step. Still, research in catalysis remains one of the most dynamic areas of chemical synthesis research, and in addition, the quest for more sustainable methods encourages synthetic chemists to consider catalysis as a central science and as a key contributor.

Traditionally, catalysis has been subdivided into three fields: heterogeneous catalysis, homogeneous catalysis and biocatalysis. It can also be classified in terms of thermo-, electro-, and photocatalytic processes within the three fields. These disciplines have been developed mostly independently to address specific scientific and distinct catalytic challenges. Since the late 1990s, a series of fundamental studies on metal-free chiral catalysts, such as ketones, thioureas, amines and amino-acids for asymmetric catalysis have sparked a new craze for organocatalysis [6]. It is a promising alternative, generally exhibiting better moisture and air tolerance, as well as excellent compatibility with various functional groups. However, their main limitation is their low efficiency. In many cases, it is necessary to load a high quantity of catalyst and the selectivity is difficult to control. Besides, in some cases the molecular weight of the catalyst is superior to the weight of the desired product. The need to develop highly chemoselective and efficient catalysts remains a challenge in synthetic chemistry both in organocatalysis and in organometallic catalysis.

In recent years, cross-fertilization between these distinct fields and complementary hybrid approaches to catalysts design have begun to address some of the inherent limitations of the traditional fields. These efforts have enabled combining some of the most attractive features of the disciplines, such as chemocatalysis.

In this article, enzymatic chemistry will be the main focus, highlighting the considerable progress that has been made over the past two decades leading to a mature technology in organic synthesis. Major advances in enzyme discovery and engineering have brought with them a surge in the development and implementation of biocatalytic reactions in organic syntheses executed in both academic and industrial settings. Moreover, they offer retrosynthetic disconnections that can be quite distinct from typical chemical small-molecule-mediated transformations.

2.1. *State-of-the-art*

The amazing efficiency with which living organisms build complex molecules from abundant starting materials has inspired chemists for centuries. To produce natural compounds, there are necessarily individual enzymes that have specific tasks for specific compounds. Enzymes excel at catalyzing chemical transformations in complex cellular media and, despite their selectivity, some of them are even evolving *in vivo* to specifically handle non-natural chemicals [7].

Innovation inspired by nature has led to recent significant achievements in the field of biocatalysis, enabling scientists to mimic this approach by using evolutionary strategies to create and tune enzymes for a broad and diversified applications [8–11]. One of the major advances has been the development of directed evolution of enzymes which has enabled the adaptation of enzymes and their optimization to the needs of catalysis. The work on directed evolution has been rewarded with the Nobel Prize in Chemistry in 2018 to Professor Frances Arnold[1].

[1]Nobel Price received with Gregory Winter and Georges P. Smith, for their work on directed evolution of peptides and antibodies via phages.

Enzymes have a promiscuous behavior which is useful for exploring other types of reactions that have not yet been discovered. Indeed, catalytic promiscuity [12] is defined as the ability of an enzyme to catalyze secondary reactions. Interestingly, promiscuous enzymes provide the opportunity for new reaction applications through molecular evolution in the laboratory, through protein engineering techniques and reaction engineering.

Another major breakthrough for the discovery of new enzymes has been the extraordinary advances in high-throughput DNA sequencing and also the development of computer-assisted tools for protein modeling combined with protein engineering techniques. All these technical advances have made it possible to enlarge the application of biocatalysis in multiple synthetic routes [13,14]. Today, the number of reactions accessible by a biocatalytic approach has considerably expanded [15]. However, for neophytes, its use seems restricted to certain experts, whereas it should be more widespread among synthetic chemists.

For the synthetic chemists, biocatalysis offers a number of advantages:

(1) enzymes as catalysts can typically deliver superior regio-, stereo-, and enantioselectivity,
(2) biocatalysis can significantly shorten multistep synthesis routes by allowing reactions and reaction sequences, which cannot be carried out with classical chemical means,
(3) biocatalysis is generally associated with mild reaction conditions, e.g., avoiding the use of toxic reagents and high temperature or pressure.

However, chemists have preconceived ideas on biocatalysis such as:

(1) enzymatic process is necessarily carried out in very dilute conditions and can only work in water,
(2) the enzymes are not stable,
(3) high-cost contribution of enzymes in the process,
(4) the reaction does not work for compounds that are not soluble in water,
(5) or native enzymes will not be active on substrates that are chemically different from the natural substrate.

These considerations are not anymore valid. Biocatalysis in organic synthesis has faced many challenges related to stability, substrate scope, and restricted reaction conditions. Enzymes can be easy to handle, and it should be acknowledged that enzymatic reactions can be carried out in combination of water with organic solvents (even fully excluding the presence of water) and, in addition the stability and productivity of biocatalysts for commercial applications are now widely demonstrated [16]. Cost contribution of the biocatalyst into the process is an important milestone. General rules for cost analysis have been established for biocatalyst production based on biocatalyst format (whole cells, soluble or immobilized enzyme), product cost, market size and value, and the requirements for the implementation of biocatalytic processes [17] have been carefully analyzed. Enzymes still are the exception rather than the rule in the synthesis of fine chemicals and pharmaceuticals; biocatalysis is often regarded as a second generation process. Although it holds great promise as a powerful tool for application in process chemistry, the number of applications at commercial scale is still low. By means of enzyme and/or reaction engineering, cost-effective process is achievable. For illustration, in one of the following case study referring to enantioselective aldolization to produce D-serine at manufacturing scale, the biocatalyst cost contribution is less than 5%.

2.2. *The experimental method for implementing biocatalysis*

When designing the retrosynthesis pathway to produce the targeted molecule, the integration of the enzymatic approach should be considered as it may enlarge the route alternatives and/or potential shortcuts. To select the enzymatic step, the disconnection approach through functional group consideration, will help to determine the appropriate enzyme family. To plan the required tests to be carried out, the following features have to be considered.

2.2.1. *Access to enzymes*

Enzyme providers, such as Protéus by Seqens, offer enzyme collections in single vials and/or microtiterplate format for rapid screening (Seqenzym® kits) and will ensure availability at larger scale.

Customized Seqenzym® kit.

Cofactor-independent enzymes are usually preferred for organic synthesis because they don't require cofactor recycling. Nevertheless, there are known methods to recycle cofactor-dependent enzymes:

- NADH can be recycled by adding *iso*propanol or using Formate DeHydrogenase (FDH) with formic acid.
- NADPH can be recycled using Glucose DeHydrogenase (GDH) and glucose or NADPH-dependent FDH variants.
- Pyridoxal-5′-phosphate (PLP)-dependent enzymes usually do not need cofactor recycling, but adding a small amount of PLP maybe recommended for stability.
- Thiamine diphosphate in lyases is sufficiently accessible and does not require recycling.
- Efficient ADP recycling systems for ATP-dependent enzymes are currently lacking, so whole cells with glucose supplementation are used.

2.2.2. *Screening conditions*

The enzyme screening approach needs to be combined with adequate reaction conditions to evaluate the technical feasibility and to determine the best enzyme candidates. Once the size of the enzyme library is addressed, the implementation of the most appropriate analytical method is required for activity measurement. Regarding the reaction conditions, the next features should be taken into account:

Most enzymes can tolerate the presence of organic solvents. Typically, the concentration of water-miscible organic solvents (like DMSO, DMF, lower molecular weight alcohols) should not exceed 10–20% (v/v). Enzymes may tolerate water-non-miscible solvents (toluene, ethers), leading to biphasic systems that can ease product isolation and potentially favor product formation. Certain enzymes, especially lipases, can be highly active in pure organic solvents. Noteworthy, maintaining appropriate pH and temperature is crucial for enzyme activity.

When working with enzymes, it is important to evaluate the risk of substrate and product inhibition.

According to the activity results, further confirmation and statement on enzymes performance will need to be carried out independently, in order to select the best enzyme candidate in respect of the targeted criteria, such as stability and robustness under the chosen reaction conditions. At this point, acceptable specifications can be reached within the selected enzyme. For industrial applications, the choice of criteria acceptance and relevance at the screening stage is very important prior to further development studies.

Stability, selectivity and activity, are the prominent criteria for all types of catalysis, homogeneous, heterogeneous and biocatalysis, but they may be evaluated in a very different way. Enzymes are proteins and they may be typically stable in the range of moderate temperatures and moderate pH values, unless using extremozymes [18]. Under these conditions they can be remarkably active. Several enzymes may be limited only by diffusion of the starting material to the active site, allowing however extremely high turnover frequencies once the medium composition is fulfilled. Air is often not a problem for enzymes, while many homogenous and heterogeneous catalysts will be oxidized and deactivated by air, even at room temperature.

Choosing the best route depends on factors like enzyme availability, starting material cost, solubility, product isolation, and productivity. Careful evaluation of the entire process is necessary before making a decision.

2.2.3. *Enzyme properties improvement*

To achieve both an excellent selectivity and a broad substrate scope, modern biocatalysis relies on libraries of enzymes, similar to the catalyst libraries used in chemoselective metal-based catalysis. Noteworthy, compared to other catalyst-based chemical transformations, when observing initial poor performance with an enzyme, such as very low conversion, it remains yet a good starting point for further remarkable improvement, as recognition (or affinity) between the enzyme and the substrate remains the key feature. In the case where the diversity of available libraries does not provide the desired

specifications, nor within studied reaction conditions, it may be required to engineer an existing biocatalyst for a specific substrate shape or even identify/evolve a new biocatalyst for a substrate for which no catalyst is available at all.

Moreover, enzymes have a chiral 3D structure that interacts at multiple contact points with the substrate, thus explaining activity and selectivity. As a result, through protein engineering, modifications of protein sequences and therefore of their 3D structures, will alter the properties of a biocatalyst indefinitely until reaching the targeted specifications. Conversely, the selectivity and reactivity of typical chemical catalysts are more limited to the available structures of the catalysts themselves or of their ligands.

2.3. *In the field of pharmaceuticals manufacturing*

The pharmaceutical industry has already adopted biocatalysis as an essential tool [19] for providing efficient and sustainable catalytic routes toward APIs. The synthesis of active pharmaceutical ingredients (APIs) can be particularly challenging as they become more complex molecules. Chemists recognize the value of enzymes related to exceptional selectivity, in terms of stereo-, regio-, and chemoselectivity in many biotransformations. This field has gained impressive developments offering robust, scalable processes along with a very diversified panel of enzymes that are required.

Today, the pharmaceutical industry is facing significant challenges associated with environmental regulations, including productivity and costs [20], which provides the opportunity to expand synthetic methods within green chemistry technologies. Consequently, the identification of innovative, cost-effective and environmentally responsible synthetic methods becomes a "Must-Have".

2.4. *How sustainable is biocatalysis?*

Enzyme catalysis is a clean, green, and sustainable alternative to traditional synthetic catalysts, as enzymes exhibit an exquisite selectivity and efficiency, and work under mild reaction conditions (significantly less energy consumption), while eliminating the use of hazardous solvents and reagents (less waste), making it a green alternative to classical strategies [21]. The conciseness, environmental friendliness, and atom economy of synthetic methods have become important aspects of synthetic chemistry (Figure 1).

In terms of process-based chemistry, biocatalysis is aligned with all the principles of green chemistry. Alignment with five of the principles is a consequence of enzymes generally exhibiting high chemo-, regio-, and stereoselectivities that are in general difficult to achieve with traditional catalytic methods. In particular, the (near) perfect enantioselectivities observed with highly engineered enzymes are practically inimitable.

The use of enzymes in organic synthesis has clear economic and environmental benefits. Enzymes are produced from readily available and inexpensive renewable resources and the cost of production is, therefore, essentially stable and predictable. This contrasts with the serious environmental costs of precious metals and the disruptive price fluctuations caused by competing demand from other industries [22]. Moreover, the significant costs associated with removing traces of noble metals from end products to the very low levels that are demanded by pharmaceutical regulatory authorities, are prohibitive.

Regarding the production of enzymes, you need to know how they are produced, but a synthetic chemist should focus on their use within the awareness of mechanistic insights in the chemical transformation.

2.5. *How are enzymes produced?*

An enzyme is a polypeptide chain that includes on average 200–600 amino-acids, hence it is necessarily produced by fermentation. At industrial scale, depending on the production host—for example: bacteria or yeast, the cultivation times are around 24 h–72 h.

In most enzyme-based catalysis, the term biocatalyst refers typically to a crude cell extract from the production strain (e.g., *E. coli*), which may contain many other enzymes that, in general, do not interfere with the intended reaction. The whole cells containing the non-natural expressed enzyme may also be used as catalyst preparation, thanks to the recombinant DNA technology. Enzyme purification by chromatography is prohibitively expensive on a large scale, explaining the prevalence of crude

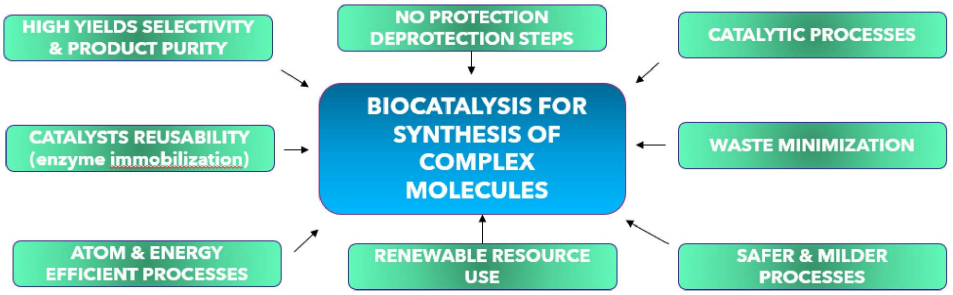

Figure 1. Biocatalysis is aligned with the green chemistry principles.

preparations for biocatalysis applications. Certain production strains (e.g., *Yarrowia lipolytica*, *Pichia pastoris*) allow the secretion of enzymes into the aqueous medium in which the production strain grows, making separation straightforward and leading directly to a rather pure enzyme preparation.

In the following case studies, the use of either a single enzyme (provided as crude preparation) or in combination of different enzymes in one-pot have been implemented. For illustration, below are cited some of our work, where biocatalysis was applied successfully with key considerations for limiting the number of chemical steps, such as protection and deprotection steps. But also, for replacing metal-based catalytic process by an enzyme in an asymmetric reduction of alkenes, desymmetrization of prochiral compounds, and in kinetic resolution steps to avoid separative chromatography.

3. Applications

3.1. *Biocatalytic synthesis of (−)-Ambrox*

The terpenoid molecule: (−)-8,12-epoxy-13,14,15, 16-tetranorlabdane, so-called (−)-Ambrox, is a valuable ingredient related to Ambergris, exhibiting amber and woody scent. It is widely used in the fragrance industry. For a longtime, it has been produced starting from the diterpenic alcohol, sclareol [23,24]. The latter is readily extracted in sufficient quantities from clary sage (*Salvia sclarea* L.). The historical and chemical synthesis consists of seven steps involving long reaction times and hazardous reagents such as peracetic acid, lithium aluminum hydride, and butyllithium, a stoichiometric oxidation with sodium periodate, and the generation of enormous amounts of waste in addition to the 76% global yield of the desired product (Scheme 1).

Later, a green two-step process has been reported [25], which involves the conversion of sclareol to ambradiol, catalyzed by whole cells of *Hyphozyma roseoniger*, followed by cyclization to (−)-Ambrox over a Ca–Y zeolite at ambient temperature, both steps proceeding in 98% yield (Scheme 2).

More recently, Eichhorn and Schroeder described a new industrial method for producing (−)-Ambrox starting from (*E*,*E*)-homofarnesol, which includes a biocatalytic step using a Squalene Hopene Cyclase (SHC) enzyme (Scheme 3) [26].

Squalene-Hopene Cyclase (SHC) enzymes are remarkable because they transform the C30 terpene squalene into the pentacyclic product hopene through a unique cationic polycyclization process involving multiple C–C bond formations. This transformation is initiated by the protonation of the C=C double bond of the terminal isoprene unit. The properties of the SHC enzyme were improved by evolving the wild type enzyme to produce a biocatalyst suited for application at industrial scale (Scheme 4) [27].

The engineering strategy generated a significant range of new variants that were then tested experimentally in the reaction [27]. As a result, the best variants resulted in the following:

- Improved (*E*,*E*)-homofarnesol conversion properties. With one round of random mutagenesis, 1.5- to 10-fold compared to the wild type enzyme.
- Conversion of 125 g/L (*E*,*E*)-homofarnesol. The maximal productivity observed was about 10 g/L/h, with approximately a 10-fold improvement with the best variant compared to the wild type enzyme.

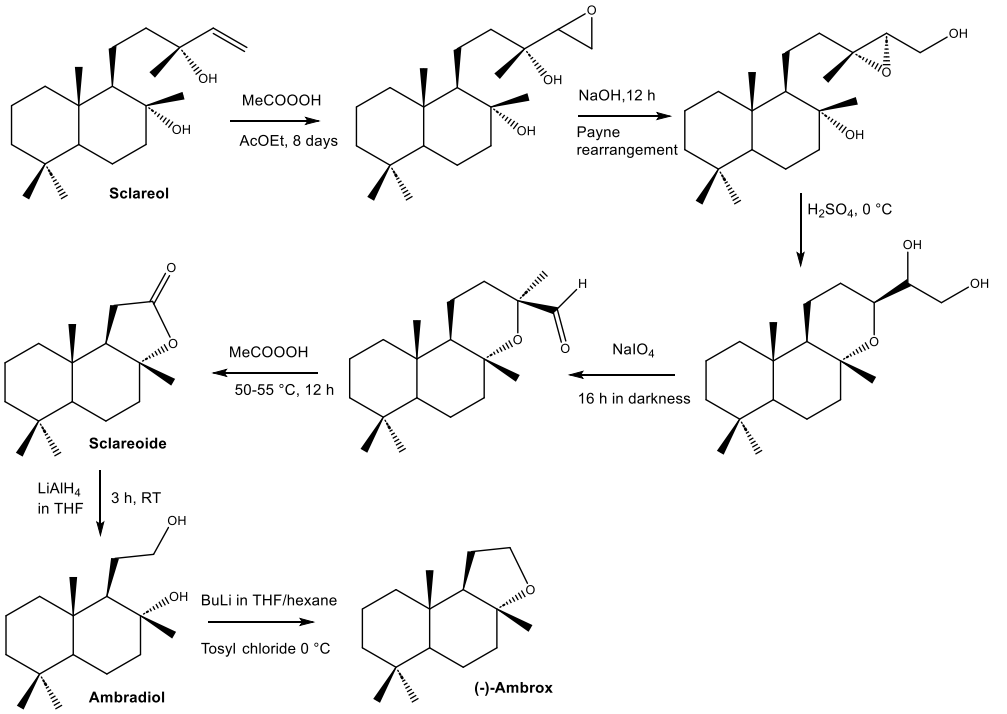

Scheme 1. Chemical route to (−)-Ambrox starting from sclareol [1].

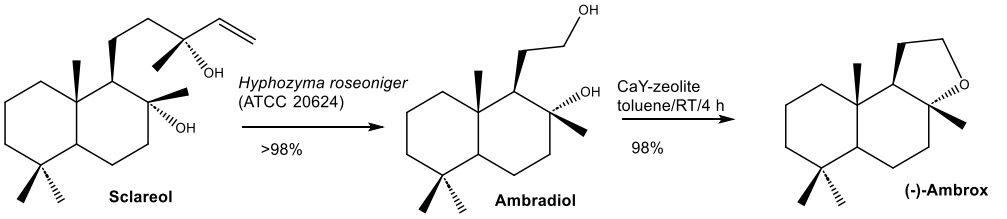

Scheme 2. Chemo-enzymatic route to (−)-Ambrox starting from sclareol.

- Further optimization of the reaction conditions was carried out by DoE (Design of Experiments) with the best performing variant.

3.2. *Regioselective acylation*

Simvastatin is a lipolipidemic compound that lowers the cholesterol and triglycerides circulating in the blood, this drug is marketed by Merck as Zocor. Historically, the manufacturing chemical route synthesis, involved six chemical steps starting from lovastatin, including protection and deprotection steps (Scheme 5).

Following the hydrolysis of the natural product lovastatin to give monacolin J, this latter was then converted to simvastatin by lactonization. Subsequent protection of the hydroxyl group followed by acylation to introduce the dimethylbutyryl side chain yields the protected form of simvastatin, which is then deprotected to yield simvastatin. The overall process needs six steps which are technically and economically demanding.

By integrating an enzymatic approach, the overall chemical steps could be reduced to only two steps (Scheme 6), thanks to a regioselective acylation using an acyl transferase with a cheap acyl donor, e.g.

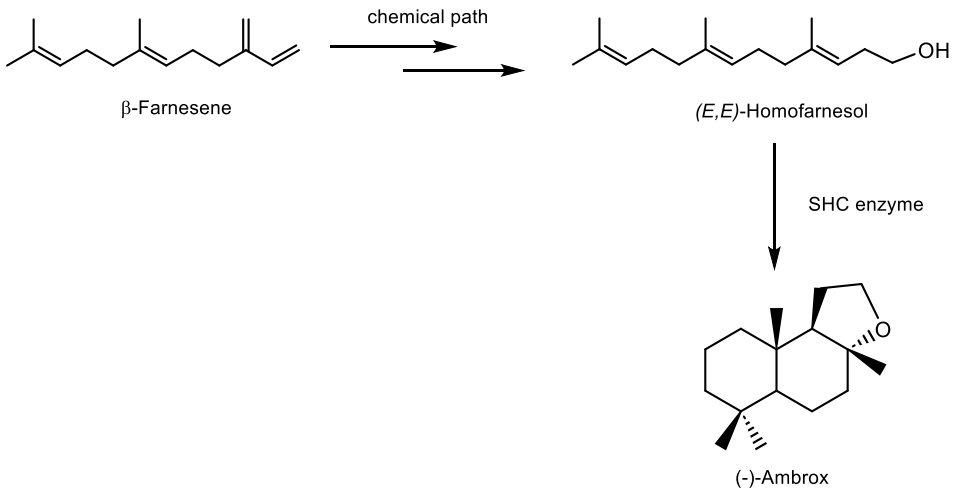

Scheme 3. SHC-mediated (−)-Ambrox synthesis from β-farnesene via (*E*,*E*)-homofarnesol.

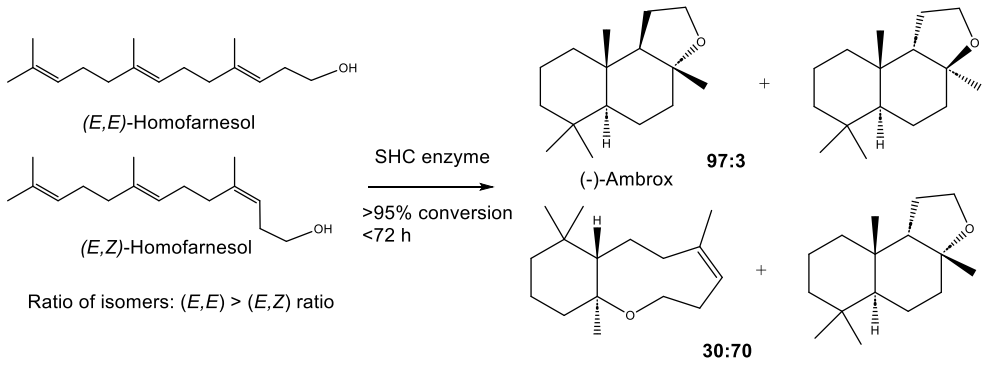

Scheme 4. Biocatalytic reaction with evolved SHC enzyme: work with Protéus by Seqens [4].

dimethylbutyryl phosphonate [28], and starting from the lactone-hydrolyzed form of lovastatin. The benefits of using acyl-phoshonates are:

- low cost acyl donors easy to produce,
- acyl transferases accommodate acyl-phosphonates donors,
- non reactive leaving groups.

3.3. *Alkene asymmetric bioreduction*

Danoprevir is a protease inhibitor used for the treatment of hepatitis C virus (HCV). During the Covid-19 pandemic crisis, some antiviral drugs were evaluated to repositioning on Covid-19 treatment. This product was discovered by Array BioPharma (now Pfizer) and first licensed to Roche for development and commercialization. The modified-peptidic type macrocyclic structure of Danoprevir is built according to a 20 steps convergent synthesis [29]. To build Danoprevir, the retrosynthetic pathway considers three main disconnections, that lead to three fragments: an hydroxy proline **1**, a protected amino ester **2**, and a substituted cyclopropane **3**. The key steps will be two peptide couplings and a ring closing metathesis (Scheme 7).

Regarding the synthesis of **2**, the unnatural α-amino acid derivative possessing a terminal alkene, was produced by a rhodium-catalyzed asymmetric hydrogenation of the dehydroamino ester **4** [30] (Scheme 8).

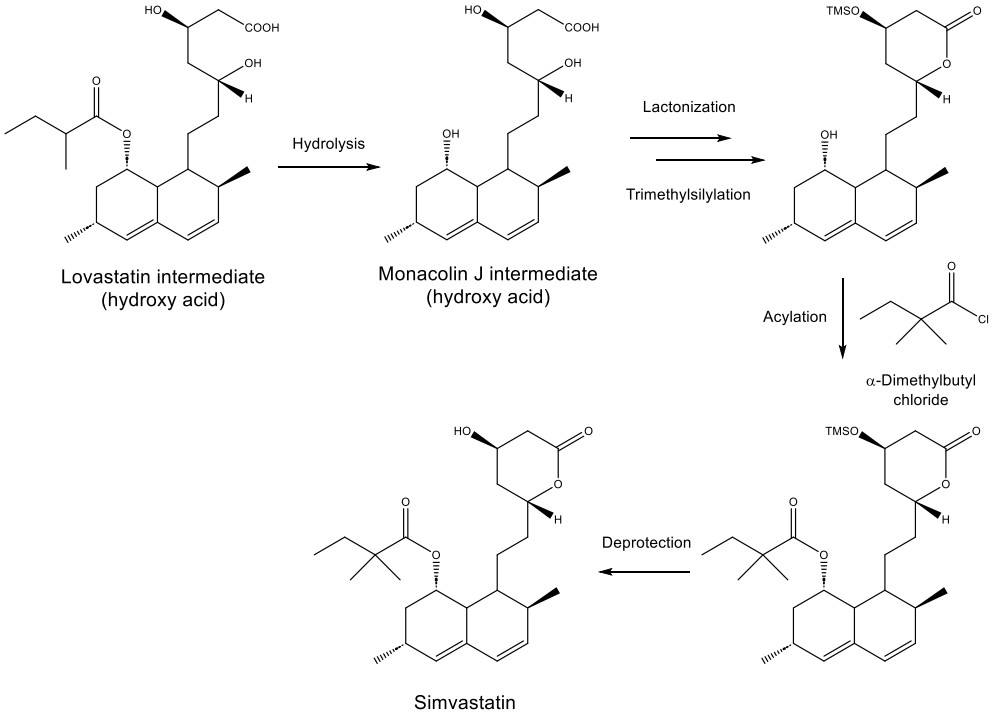

Scheme 5. Chemical route to simvastatin starting from lovastatin.

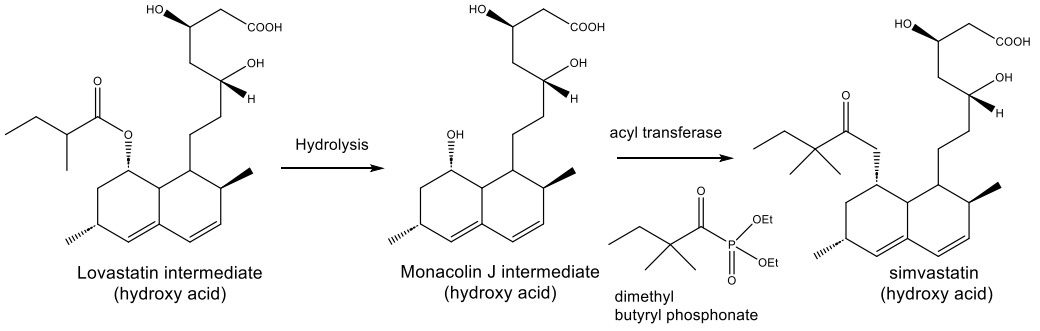

Scheme 6. Biocatalytic route to simvastatin starting from lovastatin.

Despite a perfect enantio- and chemo-selectivity for the conjugated alkene, the use of this transition metal catalyst suffers from a tedious preparation of the chiral diphosphine ligand and from the actual price of rhodium, which has a commercial price that has increased by a factor of 8–13 between 2015–2020.

A cheaper alternative was envisaged by using a metal-free catalytic step, such as the reduction of the enoate analog **4** by an ene reductase (ERED) (Scheme 9) [31].

This NAD(P)-dependent ERED family of enzymes can reduce selectively substituted alkenes conjugated to an electron-withdrawing group meaning that chemo-selectivity between the two alkenes in **4** could be achieved. Generally, the ERED-catalyzed reactions proceed with high enantio-selectivity in mild conditions without hydrogen gas. An efficient system for the regeneration of the NAD(P)H cofactor could be easily implemented to afford a greener process.

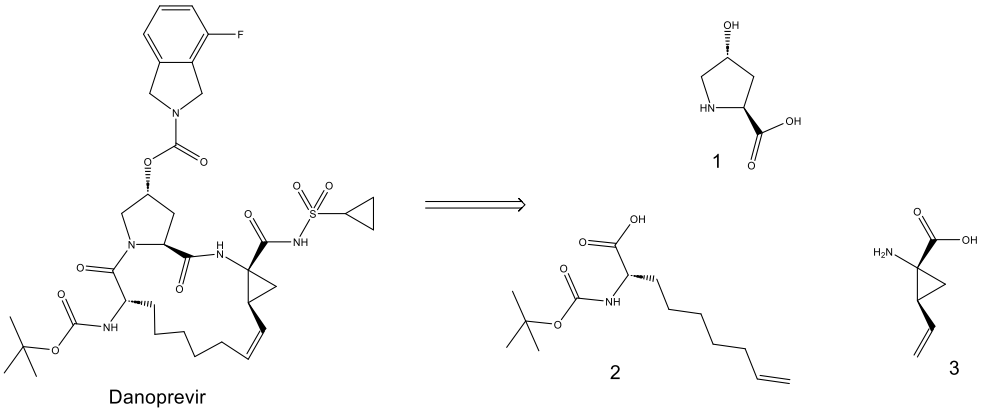

Scheme 7. Retrosynthetic pathway of danoprevir compound.

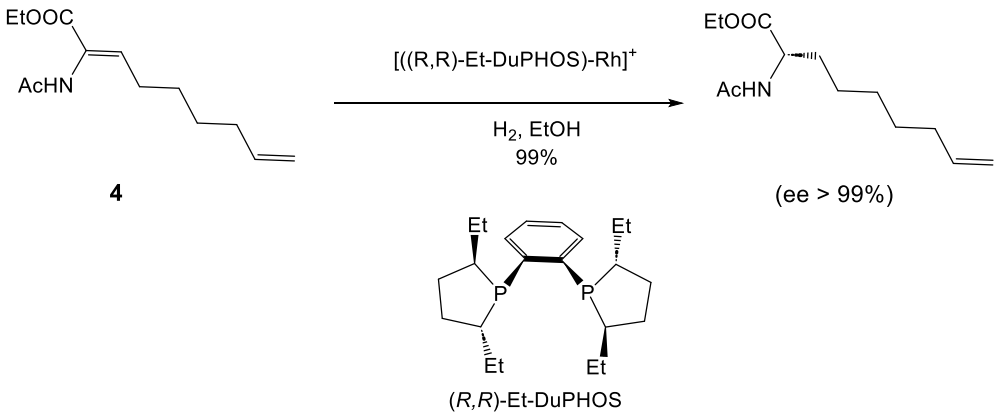

Scheme 8. Asymmetric hydrogenation with a rhodium-based chiral catalyst.

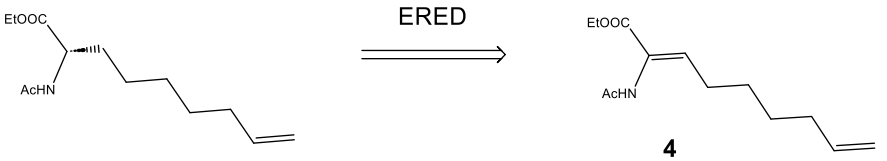

Scheme 9. Enzymatic reduction of a dehydro-amino intermediate.

At Protéus by Seqens, the asymmetric bioreduction of a dehydro-amino ester analog has been carried out (Scheme 10). The EREDs tested have allowed to selectively reduce only one of the alkene functions.

A panel of twenty ene reductases (EREDs) Seqenzym® have been tested. Within the exclusion of two enzyme candidates, all exhibited activity and the conversion rate during this first series of screening was moderate (around 30%) but still high degree of enantioselectivity were detected. Optimization of the reaction conditions is also on its way.

Depending on the scale of production, replacing a reaction catalyzed by a transition metal by an enzymatic reaction can result in a competitive process.

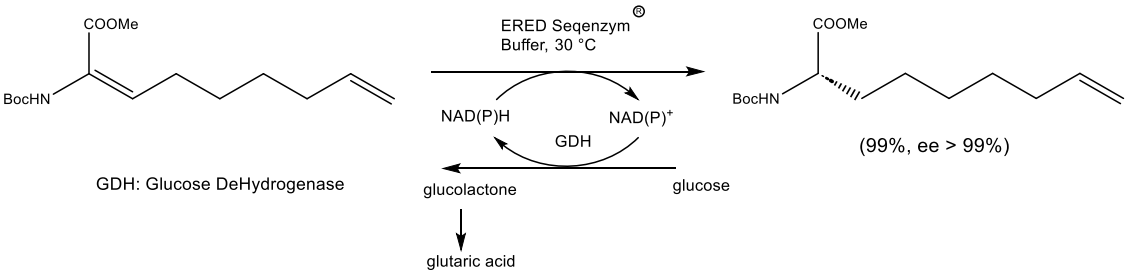

Scheme 10. Bioreduction of dehydro-amino acid derivative with ERED Seqenzym®.

This is explained by the volatility of the price of transition metals compared to the stable prices of raw materials used in the enzyme production (glucose, mineral salts, etc.). In addition, there is a strong scale effect with a cost reduction during the production of a biocatalyst making the latter competitive for the intermediate production on a large scale. Furthermore, when evaluating the manufacturing cost, the overall process must be considered, including potential purification steps to remove some impurities.

3.4. *Desymmetrization strategy*

Understanding that desymmetrization is the transformation of a substrate that results in the loss of a symmetry element, that precludes chirality (plane of symmetry, center of symmetry), this concept is one the most efficient strategy for obtaining enantioenriched molecules, within 100% attainable yield. The exquisite advantage of enzymes being highly specific, makes enzymatic desymmetrization of prochiral molecules an obvious and efficient method for obtaining enantiomerically pure compounds.

To desymmetrize 2-Me-propanedi-acetate and a cyclopentan-diester analog, a screening test of 80 enzymes, such as lipases, were realized and implemented at large scale. In both examples, we reached high enantioselectivity (ee > 98%) (Scheme 11).

Lipases are astonishing catalysts with a vast range of applications including the synthesis of esters/acids, and polymers. The broad specificity of the substrates, as well as their regio-, stereo-, and enantioselectivity, are the differentiating factors of these enzymes. They are also attractive biocatalysts in the kinetic resolution of racemic mixtures and they are highly robust in organic solvents.

3.5. *Kinetic resolution*

For the substituted aminoester **5**, a lipase was identified in the collection of Seqenzym® for the kinetic resolution of racemic 4-amino-butanoate derivative, with high enantioselectivity (Scheme 12).

However, the lipase candidate suffered from thermal stability issue during the course of the reaction. Thus, it was decided to run an experimental statistical strategy with DoE approach (Design of Experiments), to immobilize the enzyme by absorption on the most efficient resin support. Ten different resin carriers were tested. This work resulted in implementing a new biocatalyst. As shown in Figure 2, the new immobilized enzyme, allowed running the resolution process without the presence of the undesired enantiomer, even at prolonged time. The resulting biocatalyst had exclusive stereopreference in favor of the (*R*)-configuration. Figure 2 exhibits the results obtained with the corresponding immobilized enzyme.

We were able to measure the enantiomeric ratio $E = (k^R_{cat}/K^R_m)/(k^S_{cat}/K^S_m)$, which is a measure of the intrinsic selectivity of the catalyst and therefore gives a concise representation of the enantioselective properties of an enzyme in reactions involving chiral compounds [32]. As such, we obtained a value of $E > 150$ with the new immobilized enzyme, to be compared with the initial value of $E = 60$. Consequently, we were able to improve the productivity by a factor of 44. By reaching such high enantiomeric ratio, this leads to the optimum process for ensuring full chirality control, without the presence of the undesired enantiomer at manufacturing scale and in multi-batch campaigns.

In the second example represented in Scheme 13, the kinetic resolution was carried out on a racemic

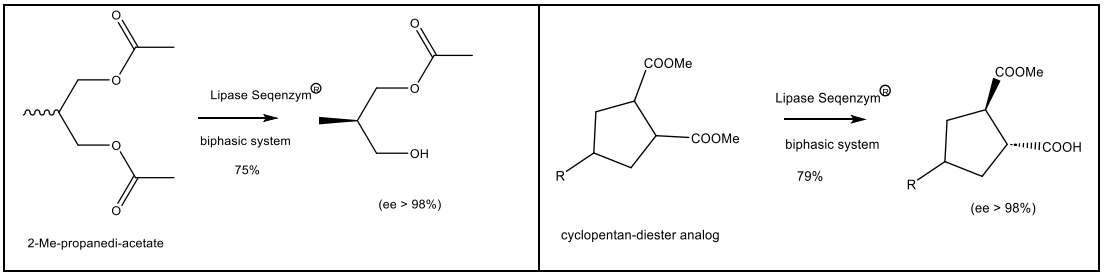

Scheme 11. Enzymatic desymmetrization with lipases starting from 2-Me-propanedi-acetate and cyclopentan-diester analog.

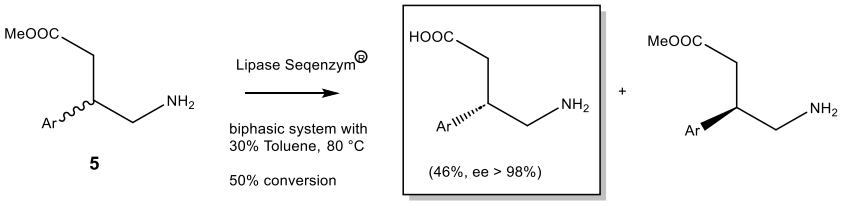

Scheme 12. Resolution of β-aminoester derivative.

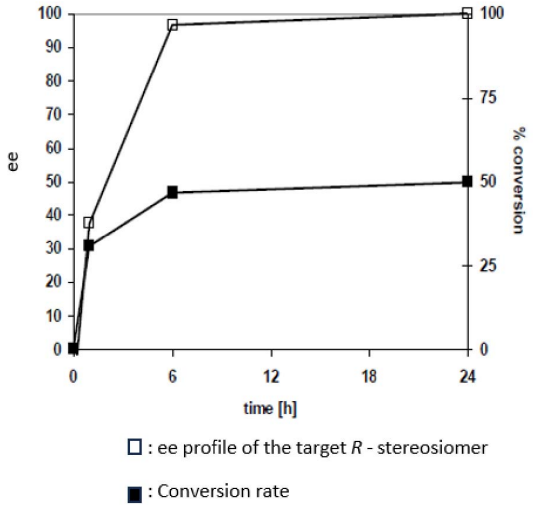

Figure 2. Conversion and enantioselectivity profiles during kinetic resolution with the corresponding immobilized enzyme.

compound: α-methyl α-alkyl aldehyde derivative using a ketoreductase (KRED) from Seqenzym®, leading to the desired enantioenriched β-alcohol product (ee > 98%). By working on the process conditions, we were able to manufacture at large scale starting with 400 g/L of substrate, the cofactor system NAD^+/NADH was regenerated by using *iso*propanol (IPA) as co-substrate. Conversion was completed within 8 h, and the desired product was isolated within 47% yield, after trapping the remaining enantioenriched aldehyde intermediate with bisulfite salt reagent to make the isolation process easier.

The scope with other aldehyde substrates was investigated with KRED Seqenzym® family leading to preferential (*R*)- or (*S*)-enantiomers as presented below (Scheme 14).

3.6. *Enantioselective aldolization*

In this work, an enzymatic process, for producing non-natural amino-acid e.g. D-serine, has been developed and implemented, which is a key building block for the synthesis of several APIs. The enzymatic aldolization step is carried out on glycine as starting material (Scheme 15). This approach is an alternative strategy to access D-serine and to avoid conventional chromatographic separation process.

It is important to mention that this process leading to very high enantioselectivity is also carried out at high substrate concentration (>300 g/L), and that the cost impact of the biocatalyst added in the process contributes to less than 5% of the overall

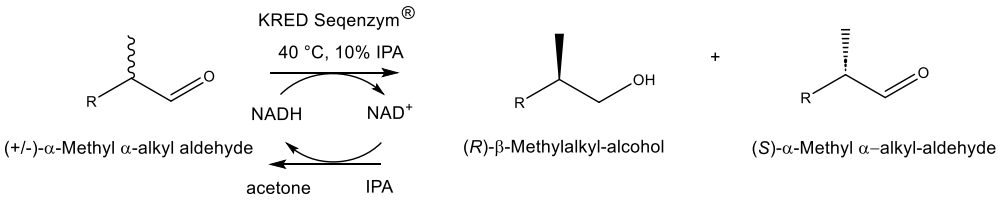

Scheme 13. Kinetic resolution of (±)-α-methyl α-alkyl-aldehyde with KRED Seqenzym®.

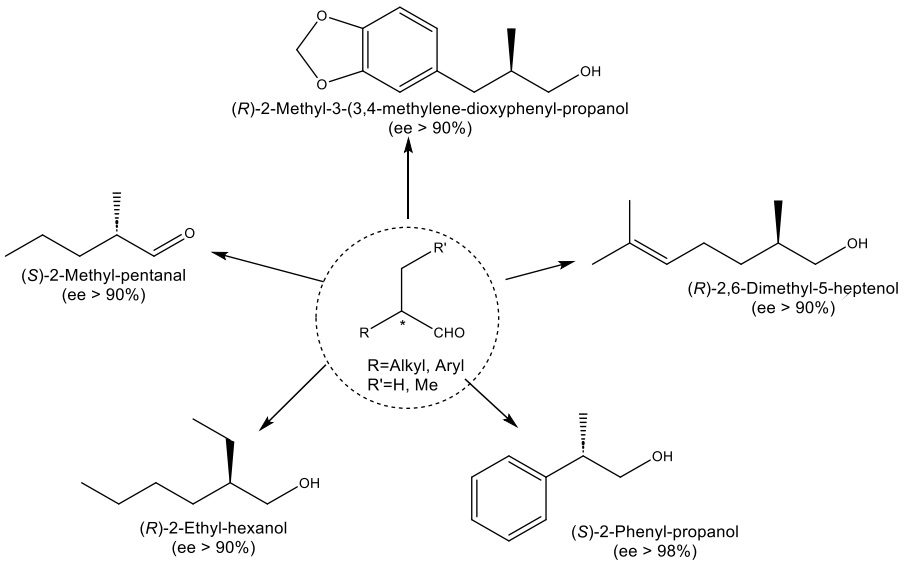

Scheme 14. Scope of products formed with KRED Seqenzym® by kinetic resolution of racemic aldehydes.

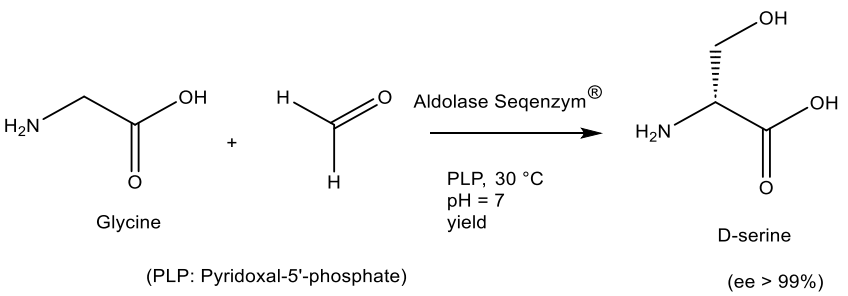

Scheme 15. Enzymatic aldolization of glycine substrate.

chemical production cost. Noteworthy, enzyme residues in the final product isolation are below detection limit. Besides, the enzymatic aldolization conditions were implemented into a cascade reaction for producing (*S*)-ketose [33] (Scheme 16).

4. The emergence of multi-catalysis systems

Driven by the demand for more efficient and sustainable chemical processes, and bringing solutions for more complex molecules, the field of catalysis

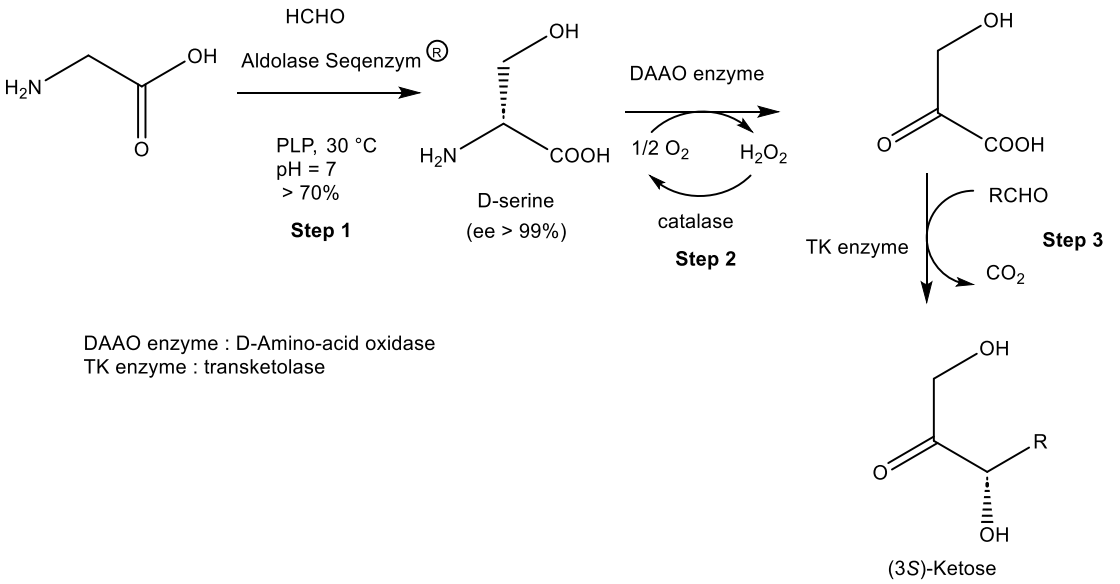

Scheme 16. Enzymatic cascade reaction from glycine to (3S)-ketose derivative. Step 2 and step 3 are simultaneous.

continues to evolve rapidly. With the aim of minimizing isolation and purification steps during multistep syntheses, concurrent catalytic cascades have attracted increasing attention and, recently, there has been a growing interest in developing multi-catalytic systems.

The biocatalytic route developed by Merck & Co. for the manufacture of the anti-HIV drug islatravir illustrates how efficient cascades reactions are, along with protein engineering for fine tuning enzyme performances (Scheme 17) [34].

Multi-catalysis emerges not only to enlarge the avenue of new methods but also to offer potential new valuable short-cuts to the synthetic practitioner. Within multi-catalytic processes, either multiple catalysts execute single reactions, or precise sequences of multiple catalytic reactions occur in a one-pot fashion. Cascade reactions can achieve more than the separated individual steps. This is particularly the case when an equilibrium reaction is coupled with an irreversible catalytic step.

The combination of several catalysts from different fields, such as chemocatalysis and biocatalysis, has been developed. For example, Bornscheuer and coworkers developed a method for producing chiral biaryl amines by combining a biocatalytic method, with an amino transfer using an optimized transaminase enzyme, with a chemocatalysis Suzuki-Miyaura Coupling (SMC) reaction [35] (Scheme 18).

The ability of such species to work under "enzyme-compatible" conditions continues to trigger the development of linear cascades.

5. Perspectives

Remarkably, multi-catalytic sequences can undergo through otherwise unfeasible pathways thanks to, for instance, prospectively unstable intermediates being converted as soon as formed. Complex molecules need to be produced, especially in the pharmaceutical industry and the design of methods to access these compounds in a minimum of steps is highly desirable. For illustration, the synthesis of Eribulin (Figure 3), targeting anticancer treatment, is a highly complex molecule possessing 19 stereogenic centers. It was designed [36] thanks to synthetic chemist's skills. Still, among the first process generation, a 62-step sequence was required for the preparation of this drug which obviously leaves room for further improved productivity and route design, potentially by using some biocatalytic steps.

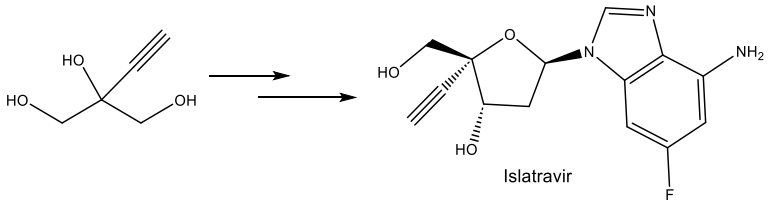

Scheme 17. Chemical structure of islatravir.

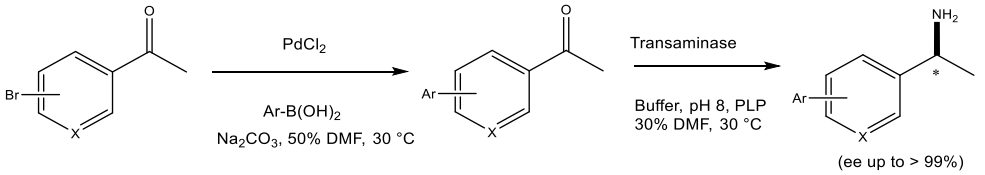

Scheme 18. Combination of the Suzuki–Miyaura cross-coupling reaction with engineered transaminases.

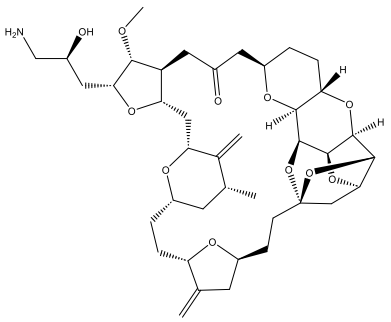

Figure 3. Eribulin structure.

6. The awareness of biocatalysis for synthetic chemists must be strengthen

Some synthetic chemists might be hesitant to adopt biocatalysis due to features like unfamiliarity with the techniques, limited access to biocatalysts, concerns about scalability, and perception that biocatalysis could be more complex than traditional chemical methods. However, as biocatalysis continues to progress, its benefits such as high selectivity (chemo- and enantioselectivity) and environmentally friendly conditions, begin to be recognized and more chemists are going to be motivated to explore its potential. However, most of synthetic chemists are not familiar with the principles, techniques, and applications of biocatalysis. Chemists who are more accustomed to traditional chemical methods might not have the necessary knowledge or experience to effectively use biocatalysis in their work. This lack of "familiarity" could lead to a reluctance to adopt biocatalysis as a viable option for their synthetic processes.

To address the unawareness of synthetic chemists with biocatalysis, several features should be considered:

- *Education and collaborations.* Some academic[2] and industrial organizations[3] can offer workshops, seminars, and training sessions focused on biocatalysis. This would help synthetic chemists understand the principles, advantages, and techniques involved, making them more comfortable with incorporating biocatalysis into their work.
- *Access to biocatalysts.* An increasing number of commercially available enzymes (see footnote 3)—ready to be used are available. Nevertheless, the need to establish repositories or networks that provide synthetic chemists with easy access to enzymes and biocatalyst-related tools.

[2] ESAB: European Society of Applied Biocatalysis.

[3] Such as SEQENS.

- *Practical experience*. Training opportunities where synthetic chemists can work directly with biocatalysts under the guidance of experts. Practical experience will demystify the process and boost confidence in using biocatalysis.

By addressing the unfamiliarity through education, cooperation, and practical experience, the barriers preventing synthetic chemists from using biocatalysis can be gradually overcome. Communicating on success stories with synthetic chemists can inspire others and demonstrate the feasibility and benefits of adopting biocatalytic approaches.

7. Concluding remarks

Current biotechnology offers a comprehensive arsenal of powerful approaches to discover, improve and apply enzymes to produce value-added compounds. Enzyme-catalyzed reactions have already expanded the landscape of attractive retrosynthetic disconnections to selectively build new bonds and design fundamentally new syntheses of complex molecular structures.

Despite the growing impact of biocatalysis in industrial chemistry, the full potential of this technology is yet to be unlocked, especially for reactions that are highly underexplored in enzyme catalysis or not yet known to the enzyme universe. We hope to bring this knowledge to the attention of chemists to bridge the educational gap between organic chemistry and biocatalysis [37–39].

Within industrial organizations, manufacturing active ingredients is paving the way by taking the best from different fields of expertise, including synthetic chemists, process engineers and technobiologists.

This leads to unique opportunity to collaborate across each competency by sharing their knowledge, know-how and perspectives for allowing the discovery of new strategic paths which will enable considerable synthetic economies. Interdisciplinarity is also highly associated with innovation.

Innovative organizations with integrated competencies and capacities, such as high throughput screening platform, can offer these services, such as Seqens.

Declaration of interests

The authors do not work for, advise, own shares in, or receive funds from any organization that could benefit from this article, and have declared no affiliations other than their research organizations.

References

[1] G. Grogan, *Practical Biotransformations: A Beginner's Guide*, Wiley-Blackwell, Hoboken, NJ, 2009, ISBN: 978-1-405-17125-0.
[2] K. Faber, *Biotransformations in Organic Chemistry*, Springer, Cham, 2011, ISBN 978-3-319-61590-5.
[3] K. Faber, W.-D. Fessner, N. J. Turner (eds.), *Biocatalysis in Organic Synthesis. Science of Synthesis*, vol. 1–3, Georg Thieme, Stuttgart, 2015, ISBN 978-3132028715.
[4] J. Whittall, P. W. Sutton, W. Kroutil (eds.), *Practical Methods for Biocatalysis and Biotransformations*, vol. 1–3, Wiley, 2009, 2012, 2016, ISBN: 9780470519271, 9781119991397, 9781118605257.
[5] C.-I. Lin, R. M. McCarty, H.-W. Liu, *Angew. Chem. Int. Ed.*, 2017, **56**, 3446-3489.
[6] B. M. Bhanage *et al.*, *Catal. Sci. Technol.*, 2018, **8**, 955-969.
[7] L. Esquirol, T. S. Peat, M. Wilding, J.-W. Liu, N. G. French, C. J. Hartley, H. Onagi, T. Nebl, C. J. Easton, J. Newman, C. Scott, *J. Biol. Chem.*, 2018, **293**, 7880-7891.
[8] H. Renata, Z. J. Wang, F. H. Arnold, *Angew. Chem. Int. Ed.*, 2015, **54**, 3351-3367.
[9] F. H. Arnold, *Angew. Chem. Int. Ed.*, 2018, **57**, 4143-4148.
[10] C. K. Prier, F. H. Arnold, *J. Am. Chem. Soc.*, 2015, **137**, 13992-14006.
[11] B. A. Sandoval, T. K. Hyster, *Curr. Opin. Chem. Biol.*, 2020, **55**, 45-51.
[12] G. de Gonzalo, I. Lavandera (eds.), *Biocatalysis for Practitioners, Techniques, Reactions and Applications*, Wiley-VCH, Weinheim, 2021, ISBN: 978-3-527-34683-7.
[13] U. Bornscheuer *et al.*, *Angew. Chem. Int. Ed.*, 2021, **60**, 88-119.
[14] M. A. Huffman *et al.*, *Science*, 2019, **366**, 1255-1259, Erratum: *Science*, 2020, PMID: 31806816.
[15] N. Turner *et al.*, *Tetrahedron*, 2021, **82**, article no. 131926.
[16] F. Tonin *et al.*, *React. Chem. Eng.*, 2019, **4**, 1878-1894.
[17] P. Tüfvesson, J. Lima-Ramos, M. Nordblad, J. M. Woodley, *Org. Process Res. Dev.*, 2011, **15**, 266-274.
[18] G. Giannina Espina *et al.*, *Front. Bioeng. Biotechnol.*, 2022, **9**, article no. 752281.
[19] R. Lewis, S. France, C. Martinez, *ACS Catal.*, 2023, **13**, 5571-5577.
[20] S. Sharma, J. Das, W. M. Braje, A. K. Dash, S. Handa, *ChemSusChem*, 2020, **13**, 2859-2875, Epub 2020 May 20. PMID: 32212245.
[21] S. Schmidt, T. Pedroso De Almeida, D. Rother, F. Hollmann, *Green Chem.*, 2017, **19**, 1226-1229.
[22] P. Gilles, J. Martin, *L'Actual. Chim.*, 2022, 26-32.
[23] J. Moulines, J.-P. Bats, A.-M. Lamidey, N. Da Silva, *Helv. Chim. Acta*, 2004, **87**, 2695-2705.
[24] J. Moulines, A.-M. Lamidey, V. Desvergnes-Breuil, *Synth. Commun.*, 2001, **31**, 749-758.

[25] L. H. Steenkamp, M. Taka, "Process for the Production of Ambrafuran", 2010, US Patent Appl. US 2010/0248316 A1.
[26] E. Eichhorn, F. Schroeder, *J. Agric. Food Chem.*, 2023, **71**, 5042-5052.
[27] E. Eichhorn, E. Locher, S. Guillemer, D. Wahler, L. Fourage, B. Schilling, *Adv. Synth. Catal.*, 2018, **360**, 2339-2351.
[28] J. Martin, G. Guillamot, L. Fourage, D. Wahler, "Enzymatic acylation method using an acylphosphonate donor", WO2012013765.
[29] L. Blatt, S. Andrews, K. Condroski *et al.*, "Macrocyclic compounds as inhibitors of viral replication", US20050267018.
[30] M. J. Burk, J. G. Allen, W. F. Kiesman, *J. Am. Chem. Soc.*, 1998, **120**, 657-663.
[31] R. Stürmer, B. Hauer, T. Friedrich, K. Faber, M. Hall, C. Stückler, "Method for the enzymatic reduction of alpha- and beta-dehydroamino acids using enoate reductases", Patent 2009, WO2009074524.
[32] A. J. J. Straathof, J. A. Jongejan, *Enzyme Microb. Technol.*, 1997, **21**, 559-571.
[33] N. Ocal, M. L'Enfant, F. Charmantray, L. Pollegioni, J. Martin, P. Auffray, J. Collin, L. Hecquet, *Org. Process Res. Dev.*, 2020, **24**, 769-775.
[34] J. B. Hedges, K. S. Ryan, *Chem. Rev.*, 2020, **120**, 3161-3209.
[35] A. W. H. Dawood, J. Bassut, R. O. M. A. de Souza, U. T. Bornscheuer, *Chem. Eur. J.*, 2018, **24**, 16009-16013.
[36] H. Ledford, *Nature*, 2010, **468**, 608-609.
[37] C. M. Clouthier, J. N. Pelletier, *Chem. Soc. Rev.*, 2012, **41**, 1585-1605.
[38] R. A. Sheldon, D. Brady, M. L. Bode, *Chem. Sci.*, 2020, **11**, 2587-2605.
[39] R. A. Sheldon, D. Brady, *ChemSusChem*, 2019, **12**, 2859-2881.

ACADÉMIE DES SCIENCES
INSTITUT DE FRANCE

Comptes Rendus. Chimie
2024, Vol. 27, Special issue S2, p. 117-141
https://doi.org/10.5802/crchim.295

Review article

Women Chemists in France in 2024

Metal complexes in cells: from design of catalytic antioxidants to imaging metal ions and designing metal-based probes in X-ray fluorescence and IR-imaging, a multidisciplinary collaborative journey in bioinorganic chemistry and inorganic chemical biology

Clotilde Policar[a,*,a,b], **Nicolas Delsuc**[a,b] **and Hélène Charlotte Bertrand**[a,b]

[a] Laboratoire des Biomolécules (LBM), Département de Chimie, Ecole Normale Supérieure, PSL University, Sorbonne Université, CNRS, 75005 Paris, France

[b] Département chimie de l'ENS-PSL, 24 rue Lhomond, 75005 Paris, France

E-mails: Clotilde.policar@ens.psl.eu (C. Policar), nicolas.delsuc@ens.psl.eu (N. Delsuc), helene.bertrand@ens.psl.eu (H. C. Bertrand)

Abstract. Bioinorganic chemistry and inorganic chemical biology are multidisciplinary fields dealing with metal ions in biological systems. In this article we will describe a research journey in these fields. This journey will take us from chemical design of inorganic metal complexes with a biological activity (catalytic antioxidants) or a biological interest (metal-based probes) and their characterization out of cellular context, typical of bioinorganic chemistry, to their studies in cells, typical of chemical biology.

First, we will focus on the description of a bio-inspired strategy to design metal-based catalytic antioxidants. Starting from the description of the main features of an antioxidant cell-protecting metalloenzyme, the superoxide dismutase (SOD), we will delineate the main parameters to be controlled to design low-molecular weight (LMW) metal complexes meant to mimic its activity: choice of the metal cation, tuning of the redox potential, and modulation of the charge. The effect of the hydration level and inertness with regard to metal ion release have also been explored. Methods to quantify the SOD-like activity, out of cellular context and in cells, and analysis of the integrity of the metal-based antioxidant in cells (through ion mobility coupled with mass spectrometry) will be described. Strategies to develop peptide-based metal complexes through conjugation of a LMW complex with peptides aimed at targeting specific organelle will be presented. Peptides can also be used to coordinate the metal ion: a combinatorial approach, with an activity-based screening, or and a rationale design using three-stranded coil-coiled, will also be presented.

The cellular activity of a molecule is strongly dependent on its sub-cellular location. A second focus of this article will be X-ray fluorescence imaging and infra-red microscopy, as techniques to image metal cations and metal-carbonyls in cells using the metallic core (M and $M(CO)_x$). After a brief overview, we will describe how metal-based probes can be developed, as trackers of organelles

* Corresponding author

or tags, with application to mitochondria tracking and to the imaging of the Mn-based SOD mimics previously described.

Overall, we hope this this story will provide an insight of what are bioinorganic chemistry and inorganic chemical biology, showing how artificial metal-based systems can be chemically designed, associated with their direct study in cells.

Keywords. Bioinorganic chemistry, Inorganic chemical biology, Superoxide dismutase mimics, Superoxide dismutase mimetics, Catalase mimics, X-ray fluorescence microscopy μ-XFM, Infra-red microscopy μ-IR.

Funding. ENS-PSL, PSL University, CNRS, MITI-CNRS, Sorbonne University (SU), ANR-15-CE07-0027 MAGIC, DEI20151234413 (*Fondation pour la recherche médicale* 2016), and BACTMAN and ANACOMDA (*Mission pour les initiatives transverses et interdisciplinaires*-CNRS), the Association François Aupetit (AFA, research fellowship), ANR 21-CE18-0053-02 MOBIDIC, ANR 20-CE07-0039-01-CATMAN, ANR 23-CE23 METALINFY; Idex PSL Qlife project Main ANR Q-life ANR-17-CONV-0005; CEFIPRA project no 6505-1; ANR-16-CE18-0017-01 SATIN; EMERGENCE SU EMRG-24 TOTEM; ANR-22-PEBI-0003 (PEPR).

Manuscript received 3 December 2023, revised 20 December 2023, accepted 31 January 2024.

Introduction

Bioinorganic chemistry is a multidisciplinary field dealing with metal ions in biological systems. This field aims to understand and control inorganic molecules, mainly metal-based, within living organisms and cells, whether endogenous (e.g. metalloproteins) or exogenous (e.g. metallodrugs or probes). The goal is to explain how these inorganic molecules work in a biological context, and to design synthetic inorganic compounds with biological activity. These compounds may be systems with no endogenous equivalent, but which are likely to play a role in a biological environment (such as cis-Pt acting as anticancer drugs or contrast agents). In contrast, they may be inspired by biological molecules (in which case we call them bio-inspired), and reproduce the activity of a biomolecule (typically a metalloenzyme) of industrial or therapeutic value. In this last case, the metal-based compounds, meant to be metallodrugs, should be studied directly in the biological environment. Indeed, biological media display some specific physico-chemical characteristics, such as high viscosity, molecular overcrowding, compartmented environment, high content in Lewis bases and metal ions, that can impact kinetics and thermodynamics [1], and may interplay with the bioactivity of these metal complexes by modifying their nature (speciation), and their reactivity.

In addition, to be active a molecule must reach its target, that can be buried in a specific compartment of the cells: hence the knowledge of the sub-cellular distribution of a molecule of interest is also important to understand its bioactivity. To that extent, metal-based tags and probes are interesting tools to investigate the distribution of a molecule of interest or to develop organelles trackers for non-conventional bio imaging techniques appropriate for metal-based compounds. A very attractive feature of this kind of metal-based probes is the opportunity to perform multimodal imaging using a very compact structure that may not impact in a too large extent the physico-chemical properties of the labeled molecule. Towards this goal, metal carbonyl complexes $[M(CO)_x(L)(L')]$ and, in particular Re complexes, are well-suited and will be discussed.

Below, we describe approaches in inorganic cellular chemistry developed in our group to design and apply bioinspired metal-based antioxidants and metal-based probes, with an interest for pathologies linked to oxidative stress (https://ens-bic.fr/). Subcellular metal imaging can be used to get access to the bio-distribution of the complexes, which is, as said above, a key parameter to their activity. Our approaches are highly integrated, from molecular design to study on cells, and require skills in organic (ligands) and inorganic (complexes) synthesis, physical chemistry, cell biology and imaging techniques.

1. Antioxidant protective metalloenzymes: a source of inspiration for catalytic antioxidants

Aerobic living organisms face a flow of species derived from dioxygen and that are much more kinetically reactive that dioxygen. These Reactive Oxygen Species (ROS), such as superoxide ($O_2^{\bullet -}$),

hydrogen peroxide (H_2O_2) or hydroxyl radical ($HO^\bullet$) are involved in a range of physio-pathological situations [2]. In the eustress mode [3], these species play important physiological roles necessary to the well-functioning of the cell. The natural continuous flow of these ROS is controlled by an arsenal of protective antioxidant enzymes (SuperOxide Dismutase (SOD), CATalase (CAT)...). A distress mode [3] is activated when the natural defenses are overwhelmed and no longer able to maintain a flow weak enough to avoid irreversible oxidative damages to biomolecules. That occurs in pathological or therapeutic situations (for instance leading to side effect of some medicines).

SuperOxide Dismutases (SODs), metalloenzymes that catalyze the dismutation of superoxide $O_2^{\bullet-}$, or CATalases (CATs), metalloenzymes that catalyze the dismutation of H_2O_2, are key players of the cellular antioxidant protective arsenal. Exogenous compounds can limit oxidative distress by acting on the flow of these ROS, either by converting them directly (direct action, as stoichiometric or catalytic antioxidants) or by activating endogenous defenses (indirect action, that will not be described further here but was commented in Ref. [4]).

To date, the conventional drug design consists of the quest for small molecules that stoichiometrically react with biomolecules, including proteins or DNA. One innovative alternative refers to catalytic drugs displaying therapeutic properties based on catalysis [5], which offers the opportunity to decrease the effective dose with promising therapeutic perspectives. Among catalytic drugs, Low Molecular Weight (LMW) complexes catalytically activated anticancer agents [6], complexes mimicking the rhodanese to detoxify cyanide [7], and also complexes mimicking the activity of SOD [4,8,9] or CAT [10] are prominent examples [5,11].

2. SuperOxide Dismutases (SODs) physicochemical characteristics: a guideline for chemists [8]

2.1. *Main features of SODs, relevant to SOD mimics design*

SODs are metalloenzymes with either Cu(II)/Cu(I) (Zn), Mn(III)/Mn(II), Fe(III)/Fe(II) or Ni(III)/(II) ions at the active site for Cu-only SOD, Cu–Zn SOD, Mn and Fe SODs and Ni SODs. They are very efficient enzymes, reacting with superoxide with a kinetics close to the diffusion limit [12], and the parameters responsible for this efficient activity have been carefully analyzed [13]. All SODs show [8]:

(1) A redox potential in a very narrow range [13] (Figure 1). Interestingly, this redox potential is tuned to the optimal value for superoxide dismutation, *id est* the midpoint between the two redox potentials for the redox couples involving superoxide $O_2^{\bullet-}/H_2O_2$ and $O_2/O_2^{\bullet-}$, as indicated in Figure 1.

(2) An electrostatic guidance of the anionic superoxide, with an overall negatively charged protein (surface) but a positively charged funnel of access for superoxide [13] (except for Cu-only SOD in which the active site is close to the protein surface and directly accessible to solvent [14]).

(3) Compartmentalization into specific organelles. Note that in this context of unresolved oxidative stress or distress, mitochondria appear as the fragile organelles to be protected. This is the main cellular location where superoxide is produced through uncoupling of the respiratory complexes involved in the reduction of dioxygen to water. The imbalance in the production of superoxide and the capacity of the protective pathways, associated with other ROS and Reactive Nitrogen species (RNS), induces oxidative damage leading to mitochondria and cell dysfunction.

2.2. *SOD mimics design*

What metal ion to choose for the design of metal-complexes as SOD mimic? Mn ion is described as the "stress reliever" [19,20], as less prone to Fenton chemistry than Fe and Cu, associated with the catalysis of the Haber–Weiss reaction (Figure 2), with potential oxidative stress exaltation by the production of $HO^\bullet$ [4,8,9,21]. This is why, although some neurotoxicity has been described [22], Mn ion is now the leading metal ion in the field of SOD mimics design for therapeutic use. In the literature, peptides-based Cu SOD-mimics are nevertheless developed (Sections 4.2 and 4.3), probably because

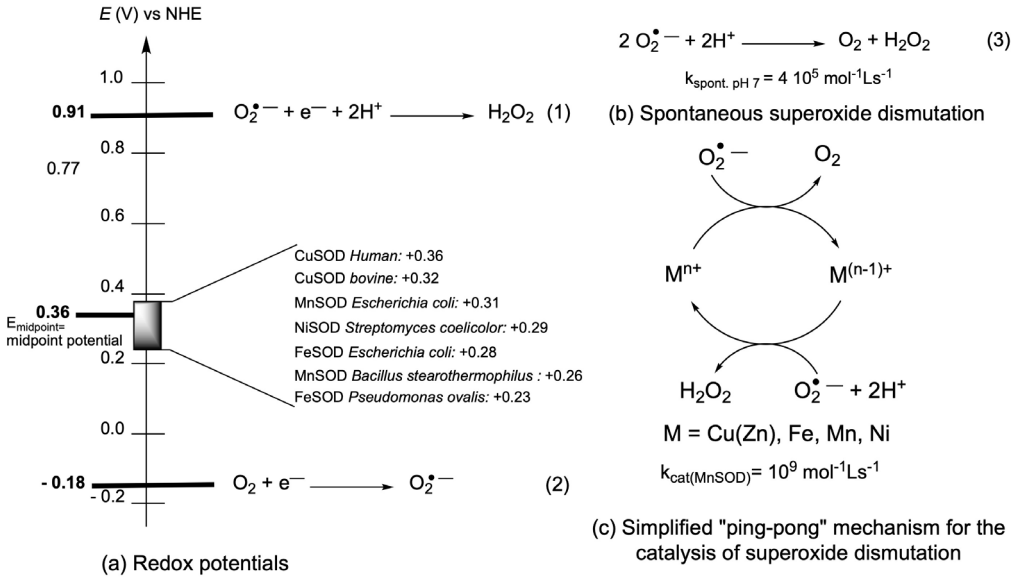

Figure 1. (a) Half-reactions of the redox couples involving superoxide (1) and (2), and standard redox potentials $E^{\circ\prime}$ pH 7 (V versus NHE). These are apparent potentials at pH 7 and with a concentration of dioxygen of 1.23 mM, which is the one found in water under standard conditions, 25 °C and 100 kPa [15] and E_{midpoint} = 0.36 V versus NHE [16,17]. Midpoint potential optimal for catalysis of the dismutation (E_{midpoint}) [17], redox potentials reported for several SOD. (b) Spontaneous superoxide dismutation (3), and (c) simplified ping-pong mechanism for the catalysis of superoxide dismutation. The kinetics are from [12] and [18].

Cu(II)-peptides complexes are easier to characterize than Mn-peptides, as they are more stable.

Mn(II), as a d^5 ion with no ligand-field stabilization energy, has a low association constant for most ligands, one of the lowest within the Irvin and Williams series [23,24]. However, in biological systems, the endogenous ligands competing for Mn(II) binding also have low association constants, rendering the criteria on the association constant within a complex paradoxically less drastic for Mn(II) than for other metal cations [8,25]. This is also why Mn(II) is one of the most bio-available metal ion [26]. In this context, one has to keep in mind that, even if biological media abound with metal ions, the pool of loosely-bound metal ions, able to exchange, although important for biological function such as signaling, is way less abundant.

Nevertheless, exchange with other metal cations, or reaction with an ancillary ligand leading to a ternary complex can occur (for example see [27,28]). Then, characterizing the nature of the Mn-complexes in cells, or manganese speciation, is key.

Most of bioactive molecules are developed for their toxicity, possibly selective towards cancer cells, bacteria or fungi (for example see [29,30]). Therefore, most bioanalyses, even for organometallics bioactive compounds, are meant to evaluate their toxicity. In contrast, SOD mimics must be non-toxic redox catalysts meant to restore the basal activity in cells under oxidative stress. Their characterization requires thus the development of specific non-routine strategies to evaluate their bioactivity.

The main challenge for chemists in the field of antioxidants mimicking SOD [4,8–10,31] is thus to design non-toxic stable and inert complexes, with a tuned redox potential and positive charge for superoxide attraction, which react quickly with superoxide, showing a good cellular availability and possibly an accumulation at the mitochondria, the most fragile organelle in the context of oxidative stress. Even more valuable, a SOD mimic should be a catalyst for superoxide dismutation and, the faster, the better. Indeed, there is a positive correlation between the catalytic kinetic constant for the superox-

$$H_2O_2 + M^{n+} \longrightarrow HO^- + HO^\bullet + M^{(n+1)+} \quad (4)\ \text{Fenton reaction}$$

$$O_2^{\bullet -} + M^{(n+1)+} \longrightarrow O_2 + M^{n+} \quad (5)$$

$$H_2O_2 + O_2^{\bullet -} \xrightarrow{M^{(n+1)+}/M^{n+}} HO^- + HO^\bullet + O_2 \quad (6)\ \text{Haber-Weiss reaction}$$

with M^{n+}: Cu(II) or Fe(II)

Figure 2. Fenton and Haber–Weiss reactions: oxidation of low-oxidation state metal ion (Fe(II) and Cu(I)) by hydrogen peroxide and cycling back to low-oxidation state with superoxide. Haber–Weiss equation, catalysis by $M^{(n+1)+}/M^{n+}$ with (M = Fe or Cu). For (1)–(3), see Figure 1.

ide dismutation, or k_{cat} measured outside of any cellular context (referred below as *intrinsic activity* [8, 32]), and the biological and potential therapeutic effects [8,22]. Characterization in cells, with information about speciation and location, will also be important to the understanding of the bio-activity (Section 5.5).

3. Bio-inspired design of SOD mimics

3.1. *Tuning the ligand to improve SOD activity*

To obtain Mn-complexes with an appropriate redox potential for SOD activity, we have chosen to use an approach bio-inspired from Mn-SOD. In the active site of this protein, the Mn ion is in a Trigonal BiPyramidal (TBP) geometry in an N_3O/water coordination environment, with one monodentate carboxylate from an aspartate and two imidazole moieties from histidine residues in the median triangle/equatorial plane (in green in Figure 3), and a farther histidine with a water molecule (H_2O or HO^-) in the two apical positions.

The particular axially distorted TBP geometry at the active site of SOD probably geometrically favors Mn(III), a d^4 ion $S = 2$ subjected to a Jahn-Teller effect, over Mn(II), a d^5 $S = 5/2$ ion with no electronic geometric preferences. This contributes to the tuning of the redox potential (see above and Figure 1) [34,35], which must be lowered from 1.51 V versus NHE (for hexa-aqua Mn(III)/Mn(II)) down to ca. 0.36 V versus NHE.

Starting from a tripodal amine, functionalized with two imidazole and one carboxylato moieties, we have modified the ligand to tune the redox potential of the Mn(III)/Mn(II) (Figure 4, variations on the nature of the coordinated Lewis bases). Figure 5 shows

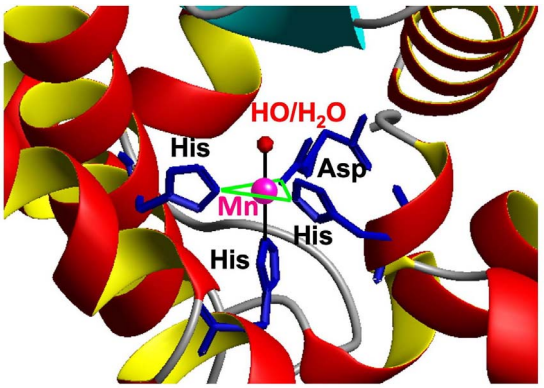

Active site of the mitochondrial human MnSOD

Figure 3. Active site of SOD, structure from Ref. [33].

the k_{cat} for superoxide dismutation plotted against the redox potential of the Mn(III)/Mn(II) redox couples of different SOD mimics. Porphyrins offer a large range of possibilities for redox and charge variations [36,37] and we here compare them with the bio-inspired series centered on a central amine or 1,2-diaminoethane [25,28,32,35,38–40]. These two series of structurally unrelated complexes show a positive slope for $E < 0.4$ V/NHE and a negative slope for $E > 0.4$ V. The two "lines" cross at about 0.4 V, which is close to the optimal value for SODs (Figure 1), in line with this value being the optimal one for SOD-like activity.

We also explored the effect of an increased bulkiness around the metal ion in the complex (picolyl moieties in the Bis-Methyl-Pyridine-Glycinate (BMPG) ligand, hexacoordination in $[Mn(TMIMA)_2]^{2+}$ Figure 4) to disfavor dimerization

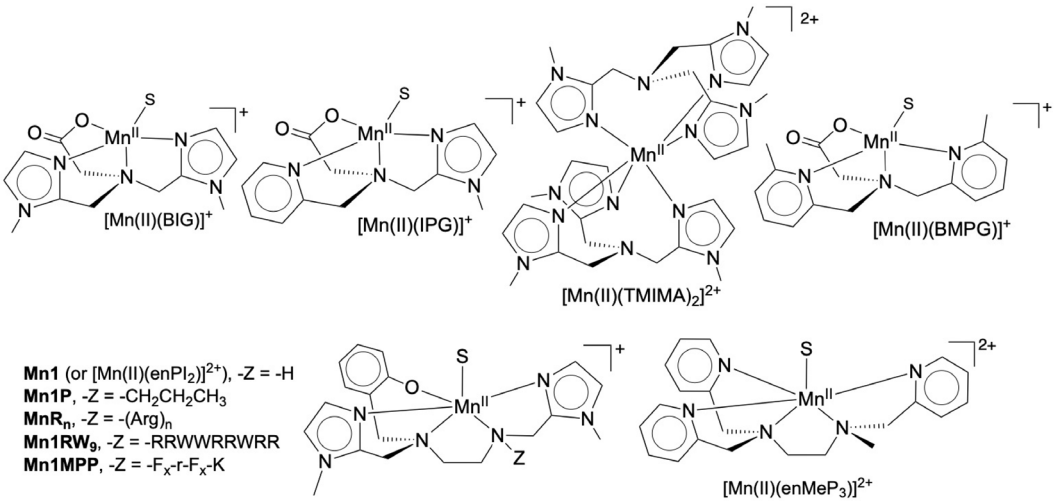

Figure 4. Structure of the complexes discussed in the Section 3.1. S: possible solvent molecule. For the ligands, BIG stands for the bis-imidazole-glycinate, IPG for imidazole, pyridine, glycinate, TMIMA for tris-methyl-imidazole amine, BMPG for bis-methyl-pyridine glycinate. For the peptides: F_x = (L)-cyclohexyl alanine and r = (D)-Arg.

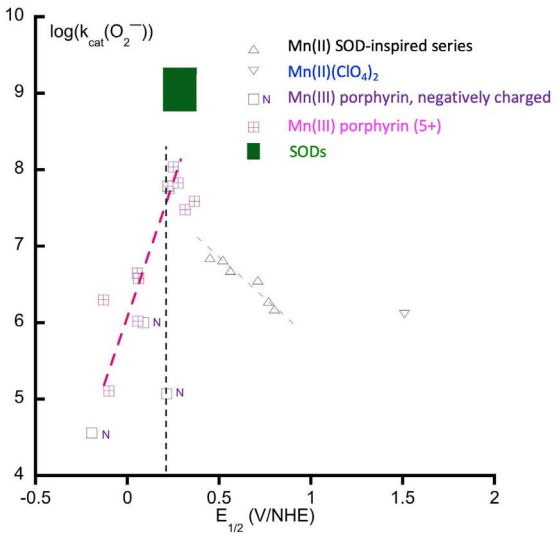

Figure 5. Plot of the log $k_{cat}(O_2^-)$ ($k_{cat}(O_2^-)$ $mol^{-1}{\cdot}L{\cdot}s^{-1}$) as a function of Mn(III)/Mn(II) redox potential ($E_{1/2}$ in V reported against NHE). Triangles, up-ward: Mn(II) complexes directly inspired from SOD active site (see Section 3.1); blue triangle, down-ward: $Mn(II)(ClO_4)_2$ (Mn(II)-hexa-aqua); open-squares, purple (N): negatively charged porphyrins; square with a cross, pink: Mn(III)-porphyrins, 5+ charge. Inspired from [8,22,35].

into Mn(III)–Mn(IV)-di-μ-oxo that is a dead-end for superoxide dismutation [35].

The optimal ligand in the series is enPI2, which displays pentadenticity with the highest association constant for the Mn(II) complex [25,41] and a Mn(III)/Mn(II) redox potential very close to that of SODs (0.36 V/NHE, Section 2 and Figure 1) [42].

3.2. *Modulation of the charge*

The electrostatic attraction of the superoxide anion down a positively charged funnel to the positively charged active site is also key to the fast kinetics of SODs. Can such an effect be seen for SOD mimics? This is obvious along the vertical dash line in Figure 5, with the couple showing a same potential but a negative charge (N), for which the kinetics is much slower than the positive 5+ porphyrin. But the charge is not all, and the topology of its distribution is important. In the SODs, there is an overall negative charge for the protein with a positive channel and a positive area covering less than 1% of the total enzyme surface [43–45]: the negative charge of the surface drives the superoxide away to this positive area where the funnel exerts a directional attraction to the active site. Spasojevic et al. have studied a series of porphyrins bearing pyridinium moieties on the meso-position, with

atropoisomers either with all positive charge as a crown on one side of the porphyrin plane or alternating charges. They have shown that the optimal distribution is that with the positive charges on the same side of the porphyrin plane, hence with a positive crown, as a smaller 3D version of the positive charged funnel in SODs, over the center metal ion [46]. In the *N*-centered series, we have functionalized **Mn1** with an oligoarginine (positive charged amino acid) to modulate the overall charge (Figure 4). Interestingly, an incremental favorable effect on the kinetics was recorded for Arg1 (R) and Arg3 (R3), but no additional effect was observed for Arg6 (R6) and Arg9 (R9). This makes sense as the oligoarginine are not structured and, if too far away and not organized in space as a funnel, they should not display any effect [47].

3.3. *Effect of the hydration level*

The complexes in the *N*-centered series showed different hydration levels when they were isolated in the solid state, with complexes bearing zero, one, or two water molecules coordinated to the Mn(II) ion, as evidenced by crystallography [35,48,49]. The consumption of superoxide as a function of this hydration level in anhydrous dimethylsulfoxide (DMSO) showed that the number of superoxide consumed was correlated with the amount of water on the Mn ion (Figure 6) [35]. This indicates the capacity of the complexes to cycle between the Mn(II) and Mn(III) redox states in the course of the reaction with superoxide (for a detailed description, see also Ref. [8]). Interestingly, H_2O introduced in anhydrous dimethylsulfoxide (DMSO) at the same concentration did not react efficiently with superoxide in the absence of complex.

3.4. *Quantification of the intrinsic SOD activity and in cells*

3.4.1. *Quantification of the intrinsic activity in water*

The reactivity with superoxide can be studied in water using the indirect assay developed by McCord and Fridovich [8,50–52]. The xanthine/xanthine oxidase system produces a slow and continuous flow of superoxide reminiscent of what is found in biological environments. All the complexes were found to be active [28,35,38,47,48,53,54], with kinetic constants k_{McCF} [8,35] in the order of 10^6–10^7 $mol^{-1}{\cdot}L{\cdot}s^{-1}$. The kinetics was also studied using pulsed radiolysis to produce a high concentration of superoxide [39] and stopped-flow, with fast kinetic measurements with a highly concentrated solution of KO_2 in DMSO or acetonitrile (MeCN) and rapid mixing in water [47,53–55], leading to kinetic constants consistent with that from the McCord and Fridovich assay.

3.4.2. *Studies in cells*

To characterize the bio-activity of these SOD mimics, we have developed three cellular models of oxidative stress [56].

The SOD mimics from Figure 4 displayed an intrinsic SOD-activity (ca. k_{cat} from a few 10^7 to a few 10^6 $mol^{-1}{\cdot}s^{-1}$) that is ca. 1% of the enzyme Mn-SOD, which remains quite good since the kinetics of these enzymes is only limited by diffusion [8,12, 13]. Among those SOD mimics, **Mn1** was studied more thoroughly in cells. **Mn1** was shown to limit ROS flow in macrophages [32] and to have an anti-inflammatory activity, both in intestinal epithelial cells, namely HT29-MD2 cells, and in mice [25]. In the rest of this article, we will mainly focus on the HT29-MD2 cells assay [25,27,28,53,54,56]. This cell-model was constructed to increase the inflammatory response involving both ROS production, inflammatory cytokine secretion (interleukin 8 IL8) and expression of inflammatory markers (cyclooxygenase 2 COX2) upon bacterial LipoPolySaccharide (LPS) stimulation [57]. The strong inflammatory effect, reminiscent of what is observed in Inflammatory Bowel Diseases (IBD) [57], provides a large window to observe a return toward the basal state after a 6-hour LPS stimulation upon treatment with a SOD mimic. In this model, we have evidenced that **Mn1** and its derivatives (Figure 4) (**Mn1P**, **Mn1R$_n$**) [25, 27,54] are not toxic up to 200 μM, with an effective anti-inflammatory effect with a dose response in the range 10–100 μM (ca. 35% IL8 secreted in comparison to LPS at 100 μM; see Figures 7c and 20, down-left). The redox inactive Zn(II) analogues, when studied [25,27,28,53,54], were found ineffective, stressing the bioactivity is associated with the redox properties of Mn(II). Interestingly, upon LPS stimulation, cells overexpress mitochondrial MnSOD in an active form, as evaluated by Western Blot (WB), and such an effect has not been seen for the cytosolic CuSOD or CAT. This shows that LPS induces deleterious superoxide flux at the mitochondrial level. HydroEthidine

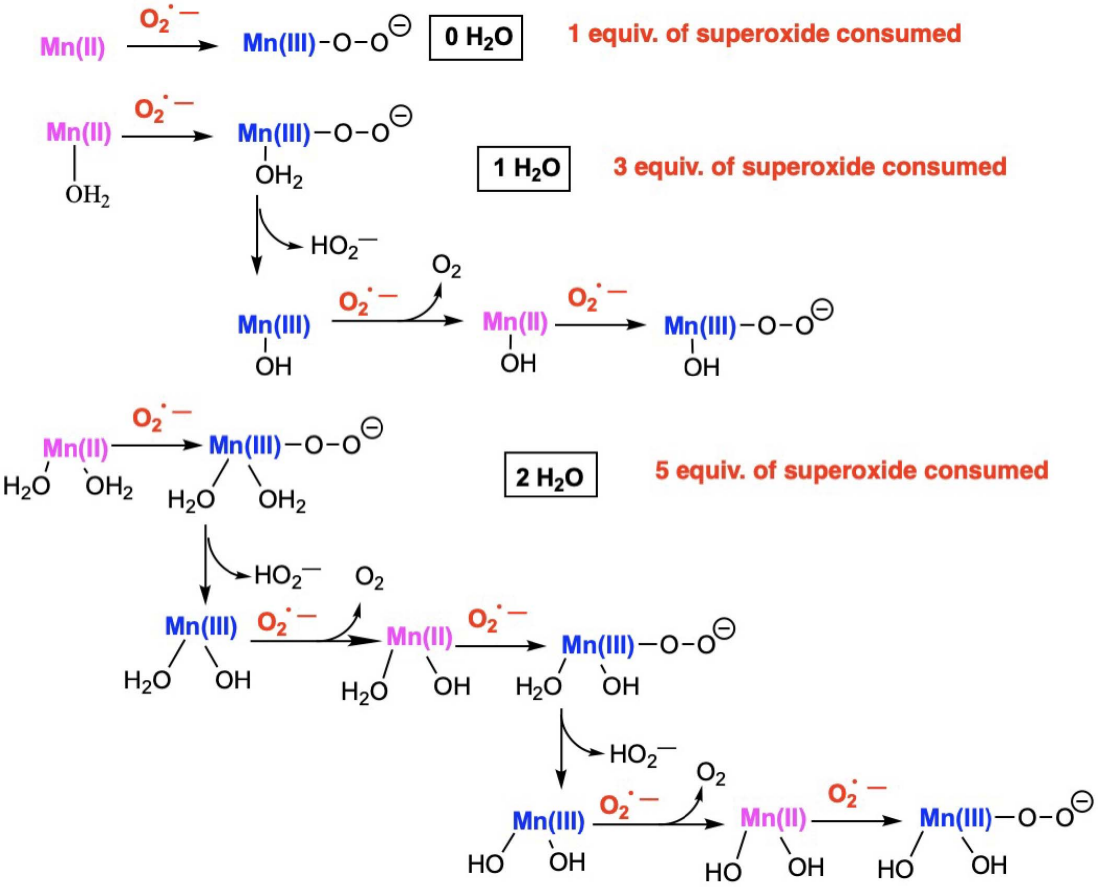

Figure 6. Schematic rationale for the number of superoxide equivalents (with regard to the Mn-complex) consumed in anhydrous DMSO upon the number of bound water molecules. Adapted from Ref. [8]. For details, see Refs [48] and [8].

assay (HE), a fluorescent marker oxidized by superoxide [58], showed that **Mn1** reduces the basal superoxide content [25] but the link with the effect of LPS could not be made and no increase of HE oxidation upon LPS activation could be recorded, in contrast to what was reported before [58]. We believe that this is probably because of the cell antioxidant feedback upon oxidative stress [3]: LPS stimulation induces expression of an active MnSOD that reacts faster with superoxide than HE itself [25].

3.5. *Towards higher inertia*

Inertness and thermodynamic stability are two important features for metal-based drugs, since biological media are very rich in metal ions and Lewis bases that could compete with the native complexes. This is particularly true for complexes involving open-chain ligands such as **Mn1** (Figure 4). Consequently, inspired by the literature [59,60], in order to improve inertness of the SOD mimic we develop, we have replaced the 1,2-diamino group of the ligand by a (±)-trans-1,2-cyclohexyl diamine to rigidify the structure (Figure 7a) [28]. Stability, inertness, and more generally bioactivity of the corresponding complexes have been investigated. Note that the secondary amine was propylated (in **Mn1P** and **Mn1CP**) in view of a detection in cell lysates by mass spectrometry to avoid deprotonation that could occur and would lead to a more complicated mass spectrometry (MS) spectrum.

Thanks to their rigidified skeleton, **Mn1CP**, and to a lesser extent **Mn1C**, were found to be more resistant in the series to metal cation exchanges that

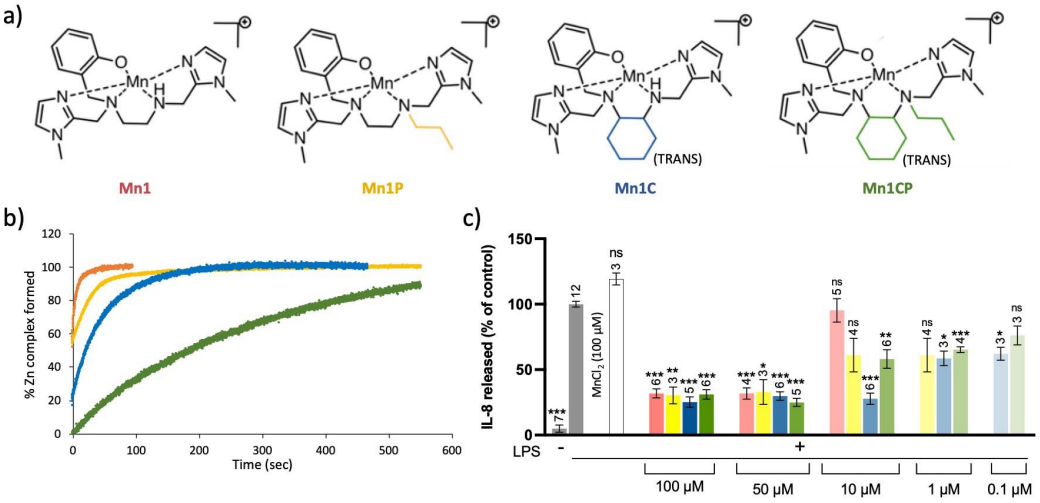

Figure 7. (a) Structures of the manganese(II) complexes; (b) kinetics study of the metal exchanges occurring between the manganese center of the SOD mimics and with Zn^{2+}. The percentage of complexes that underwent metal exchanges was monitored by UV–vis; (c) Quantification of the inflammatory marker IL-8 in intestinal epithelial cells activated with LPS (0.1 µg/mL). IL-8 secretion was measured by ELISA in supernatant of LPS-activated HT29–MD2 cells incubated for 6 h with the SOD mimics at different concentrations. The IL-8 amount measured for LPS-activated cells is set at 100% for each independent experiment. Data represent mean ± SEM for at least three independent experiments: the number of independent experiments is indicated above each column. The p-values were calculated using the student test (bilateral test with equal variances not assumed). The mean ranks of each column were compared to that of the LPS control, each comparison stands alone. (***) $p < 0.001$, (**) $p < 0.01$ and (*) $p < 0.05$ versus LPS control, ns non-significant.

may lead to the formation of redox-inactive analogues in a biological medium (Figure 7b). The modifications of the SOD mimics led to an improvement of their anti-inflammatory and antioxidant activities in epithelial intestinal cells HT29-MD2 under LPS-mediated inflammation. Indeed, **Mn1C** displays the best bioactivity, with significant effects when incubated at 10 µM (Figure 7c). These improved efficacies at low incubation concentrations could be correlated to the higher bioavailability of the new SOD mimics in the cellular environment associated with a higher inertness. Note that, at this stage, we cannot exclude the possibility of a different subcellular location that could also be responsible for the better activity of **Mn1C**. This is now under exploration.

Interestingly, thanks to higher inertness, the intact complex **Mn1CP** could be identified and quantified in cell lysates using Mass Spectrometry (MS), which was not possible with its **Mn1P** analogue, more prone to metal exchange (Section 5.5). After controlling that no exchange occurred during analysis, a known quantity of internal standard (here the cobalt complex having a phenol where the six carbons are ^{13}C in order to distinguish them by mass) was added. Using a previously established calibration curve, we were able to determine the amount of **Mn1CP** in lysates from LPS-activated HT29-MD2 cells incubated for 6 h at 100 µM. The peaks corresponding to **Mn1CP** (m/z = 504.2406), the internal standard **Co1CP** (514.2557 m/z), and the dissociated ligand are clearly identifiable in the mass spectra (Figure 8). We also found that **Mn1CP** partially exchanged with Zn within the cells to give **Zn1CP**, but to a much weaker extent than **Mn1P** (Section 3.6).

3.6. *Ion mobility spectrometry (IMS) coupled to detection in mass spectrometry (MS): an efficient technique to detect and quantify LMW labile complexes in cell lysates*

For the more labile compounds, **Mn1** (m/z = 408.1465) and **Mn1P** (m/z = 450.1935), MS had to be

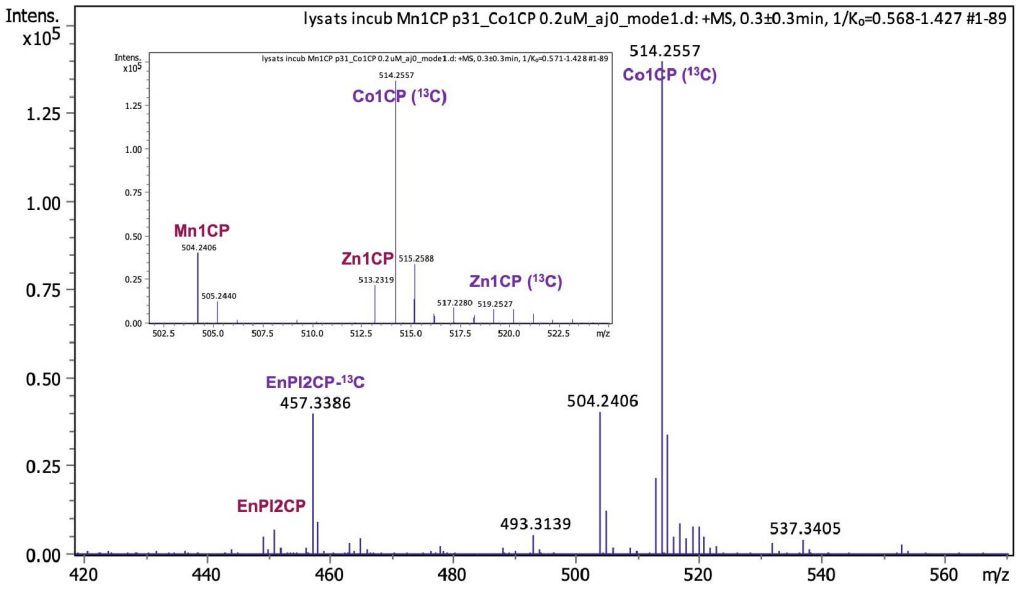

Figure 8. Mass spectrometry analysis of a cell lysate of HT29-MD2 activated cells incubated with **Mn1CP** for 6 h and ultra-centrifugated at 10,000 rpm for 20 min. The lysate was diluted in a solution of 20% NH_4CO_3/80% MeCN and the internal standard **Co1CP** (^{13}C) (0.4 μM) has been spiked before analysis.

coupled with a separation technique. Liquid chromatography (LC)-MS was not effective as metal ions exchanges occurred in the system. We then turned to Ion Mobility Spectrometry (IMS). This technique consists of the separation of the ions according to their size, or Collision Cross-Section (CCS), using an electric field to accelerate ions and a gas flow to push them further or slow them down (depending on the set-up).

Interestingly, we have shown that IMS is capable of separating low molecular weight (LMW) metal complexes built on the same ligand with different divalent metal cations (Mn, Fe, Co, Ni, Cu, Zn) although they exhibit only small differences in ionic radii. The collision cross-section (CCS) correlated with ionic radii [61], as shown in Figure 9. In other words, when a LMW ligand folds around a divalent transition metal cation, the weak difference associated to that of the ionic radii of the metal cation changes the CCS enough for the complexes to be discriminated in IMS (differences down to 1% of the mass can be discriminated). We applied that with a detection in MS, to demonstrate the intracellular presence of two SOD mimics **Mn1** and **Mn1P** in the lysates of cells incubated with the complexes. We were able to estimate the intracellular concentration of **Mn1P** using a similar standard analogue with a heavy ligand (^{13}C) and a Co(II) cation.

4. Peptides-based catalytic antioxidants for SOD and CAT activity

4.1. *Conjugation of **Mn1** with peptides*

A path explored to improve the biological activity of the SOD mimics was their functionalization with peptides [54] and in particular cell penetrating peptides (CPP) [62] -R9 (or -Arg9), and -RW9 (or -RRWWWRRWRR), and a mitochondria targeting peptide MPP designed by Kelley et al. (-Fx-r-Fx-K, with (L)-cyclohexylalanine (Fx), (D)-arginine (r), and (L)-lysine (K) residues) [42] (Figure 4). As indicated previously, mitochondria have been considered as the organelle to be protected against oxidative stress, which is the rationale for choosing these Arg-based CPP and MPP.

These complexes **Mn1-R9**, **Mn1-RW9** and **Mn1-MPP** (Figure 4) have intrinsic SOD activities, and dissociation constants similar to **Mn1**. However, the cell-penetration of **Mn1**, already good probably

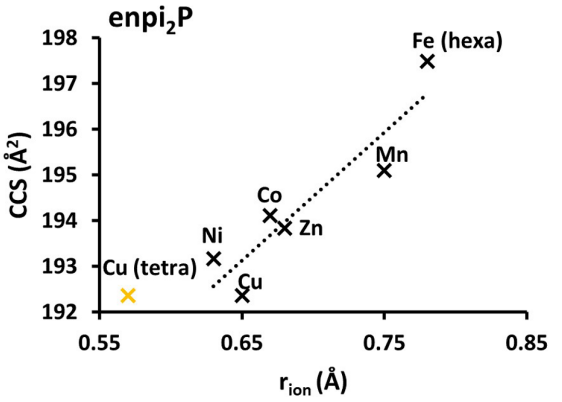

Figure 9. Collision cross-section of complex **Mn1P** in Å^2 plotted against the ionic radius of metal cations in Å. The r_{ion} of any M(II) corresponds to a high spin pentacoordination, except for Fe(II) (high-spin hexa-coordination). The r_{ion} for Cu(II) is also shown (in yellow) for a high-spin tetra-coordination. The r_{ion} values were taken from http://abulafia.mt.ic.ac.uk/shannon/ptable.php [27].

because this is a lipophilic charged compound [25], was deceptively decreased by the functionalization with the CPPs or MPP. The complexes **Mn1-R9**, **Mn1-RW9** and **Mn1-MPP** also showed a cellular distribution different from the homogeneously distributed **Mn1** [25], although this was difficult to follow due to the low intracellular concentration. Their bioactivity in epithelial intestinal cells (HT29-MD2) was similar to that of **Mn1** when assayed at a concentration of incubation of 100 μM. Interestingly, **Mn1-R9**, **Mn1-RW9** and **Mn1-MPP** showed a better anti-inflammatory activity than **Mn1** when incubated at 10 μM. Importantly, the redox-inactive analogue **Zn1-R9** was inactive. The situation was less clear for **Mn1-RW9** and **Mn1-MPP** for which a contribution of the peptidyl moiety to the anti-inflammatory effect independent of redox metal-based regulation was observed as **Zn1-RW9** and **Zn1-MPP** showed a weak activity [54].

Overall, the functionalization with peptides improved the anti-inflammatory activity: indeed, it was possible to reduce the incubation concentration by an order of magnitude, while retaining a significant anti-inflammatory effect and enabling a better activity/concentration ratio, which is interesting for future bio-applications.

4.2. *Metallo-oligopeptides*

Peptides are very attractive as ligand for metal complexes because: (1) peptides are easily synthesized on solid support and their synthesis is very versatile, (2) proteolytic instability and rapid clearance of peptides which were considered as main drawbacks, are nowadays seen as key advantages since peptides do not accumulate in tissues, are not metabolized in the liver avoiding drug-drug interactions [63,64]; (3) peptidyl ligands can be easily conjugated with peptides or molecules in order to address them to specific organs, cells or organelles and (4) peptidyl ligands can be genetically encoded and thus produced by bacteria. However, the design of a sequence that binds selectively a metal cation and leads to a stable complex with the appropriate redox potential—redox potential enabling the targeted antioxidant activity—is very tedious. That is why a combinatorial approach has been combined with activity-based assays to develop efficient catalytic drugs that will be directly usable for oxidative stress resolution (Figure 10). Two antioxidant activities have been targeted leading to the development of SOD mimics and catalase mimics involving copper as the redox center. Catalase is an enzyme able to catalyze the dismutation of H_2O_2 into O_2 and H_2O. For both mimic types, a combinatorial peptide library has been prepared by a split and mix approach on solid support (bead) using a classical Fmoc strategy. This leads to the production a variety of peptides within the beads collection, with one given sequence per bead, each bead bearing several copies of the same peptide. After peptide elongation, the amino acids side chains have been deprotected, and the beads were incubated in a solution containing the metal salts (typically, Cu(II), Fe(II/III), Mn(II), Ni(II), etc.) to generate the complexes. At this stage, washing the beads with 2,2′,2″,2‴-(ethane-1,2-diyldinitrilo)tetraacetic acid (EDTA) enables further increasing the selective pressure and select only stable complexes. The beads bearing peptidyl complexes have been then immobilized in an agarose gel and screened by two different colorimetric assays, one specific to SOD activity [65] and the other to catalase activity [66,67]. This original approach yielded peptide-Cu(II) mimics of SOD [65] or catalase [66,67] that are efficient in test tubes but also in biological contexts. A Mn(II) hit was also obtained but so far the Mn-peptide complex could not

be properly characterized and remains unpublished. This is probably due to the weaker affinity constants of peptides for Mn(II) than for Cu(II) that stem from the intrinsic electronic properties of the metal as previously mentioned and the flexibility of the peptidyl ligands.

Interestingly, even by starting with the same combinatorial library, the two different CAT or SOD assays lead to the selection of different peptide sequences. In addition, in the case of the SOD mimic, the active species for catalysis is the complex involving one ligand for one copper whereas for the CAT mimic, the active species is the one ligand—two copper complex. This is consistent with the fact that superoxide dismutation involves the transfer of a single electron (Figure 1, SOD cycle) whereas H_2O_2 dismutation requires two electrons (Figure 11).

We can thus hypothesize that for the CAT mimic, each copper center brings one electron and cycles between the +II and +I redox states.

Importantly, the CAT mimic was found to have a poor SOD activity and the SOD mimic no CAT activity. This means the screening approach was specific of the activity selected.

4.3. *De novo SOD mimics: rationale design of artificial proteins mimicking SODs*

Expanding the possibilities beyond low-molecular-weight complexes and oligopeptides, rationally designed self-assembling peptide scaffolds with well-defined secondary and tertiary structures are valuable tools for mimicking enzyme structure and activity, leading to artificial *de novo* enzymes [68].

Because of the low association constant of Mn(II) for any ligand (Section 2), we decided to go for a mimic of Cu-based SOD. Designing heteroditopic *de novo* scaffold with specific Cu and Zn sites was not straightforward, as in the native CuZnSOD, and we decided to go for a mimic of Cu-only SOD [14] and not of the Cu–Zn SOD. For that, we used the α3D family of proteins, originally designed by DeGrado et al. and that consists of seven amino acid repeats in which the first and fourth residue of each heptad is hydrophobic [69]. This sequence favors the folding into an antiparallel three helices bundle [69]. A metal-cations binding site can be introduced inside the bundle, at the expense of thermodynamic stability [70] and an elongated version with an additional heptad, called Grα3D, was proposed by Pecoraro et al. to compensate for this loss in thermodynamic stability [70–73].

A series of four structures featuring chelation sites for Cu(II) was generated, with histidine and aspartate residues [73], as in the active site of the Cu-only SOD [14]. More precisely, the chelation sites were H3 (His3), H4 (His4), H2DH (His3Asp with 2 His and 1 Asp in the same plane and one His above) and H3D (His3Asp with 3 His in the same plane and one Asp above). The corresponding complexes were characterized by various techniques (UV-Xis, EPR and XAS), showing they are good structural and spectroscopic mimics of Cu-only SOD. All the complexes show SOD activity with k_{cat} in the range 1–3 $\times$ 10^6 $M^{-1}{\cdot}s^{-1}$ and, although still three orders of magnitude lower than Cu-only SOD, this makes them the first *de novo* Cu-SOD mimics [73]. Note that a Mn-based *de novo* SOD mimic had been previously published, but with a very weak activity (ca. four order of magnitude slower than SOD, ca. 10^5 $M^{-1}{\cdot}s^{-1}$) [74].

5. Imaging metal-based compounds

5.1. *Direct detection of metal-based compounds using micro-X-ray fluorescence or IR-imaging*

Because biological media, and especially cells, are compartmentalized (cytosol, organelles, nucleus, etc.), the bioactivity of a compound depends strongly on its localization and ability to reach a specific target. This target can be a macromolecule (e.g. DNA to silence or modify, or specific protein to activate or inhibit). It can also be a small molecule (e.g. ROS). Note that superoxide because it is negatively charged is not able to cross membrane, whereas hydrogen peroxide can [75].

The development of an innovative cellular inorganic chemistry or inorganic chemical biology can be bolstered by the exploration of analytical techniques adapted to the mapping of metal complexes at the sub-cellular level. Fluorescence in the UV–vis is a widespread technique. A large variety of probes are available, and they can be excited in a range of energies (UV–vis); they can be used as conjugable tags or organelles trackers, conjugated to antibodies and then used to detect specific proteins and map their sub-cellular distribution. Many of

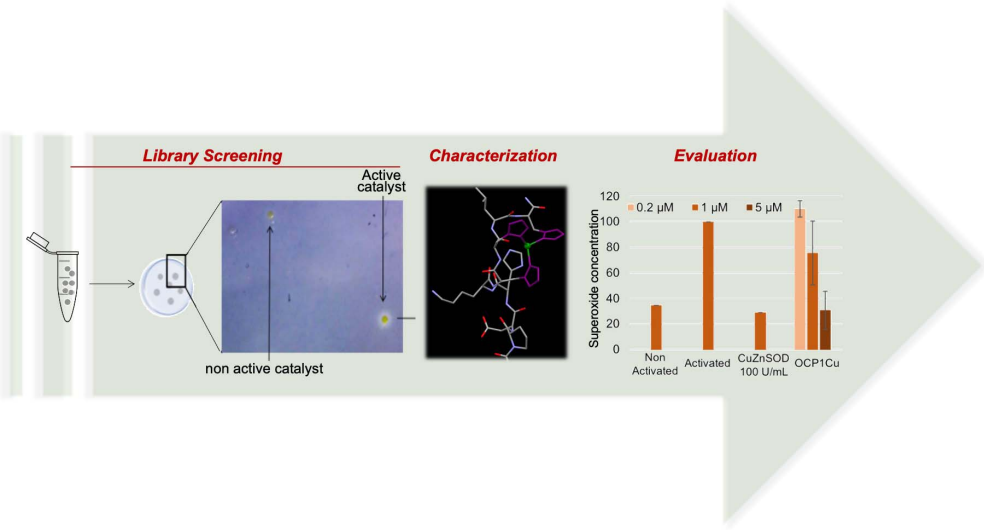

Figure 10. Illustration of the workflow for the development of efficient SOD and CAT mimics involving a peptidyl ligand and active on cellular models.

$$H_2O_2 + 2e^- + 2H^+ \longrightarrow 2\,H_2O \quad (7)$$

$$H_2O_2 \longrightarrow O_2 + 2e^- + 2H^+ \quad (8)$$

$$2\,H_2O_2 \longrightarrow O_2 + 2\,H_2O \quad (9)$$

Figure 11. Half-reactions of the redox couples involving hydrogen peroxide H_2O_2.

the corresponding trackers/tags/antibodies are commercially available [76].

However, these fluorescent probes are mostly large hydrophobic moieties. If used to tag a macromolecule (protein, DNA, antibody ...), the physico-chemical effect of the probe can be minimal and the location of the tagged "chemical object" not modified. But when it comes to tagging a low-molecular weight compound, such as those presented in Sections 3 and 4, a probe will most certainly modify the physico-chemical properties of the compound of interest (as exemplified in Section 5.5). This is why we envisioned to try to detect the metal complexes directly through the metallic core. This can be done using X-ray fluorescence imaging. Another interesting modality is IR absorption. In the mid-IR (4000–400 cm^{-1}), molecules show specific signature (fingerprints) and chemical mappings can be generated.

We detail below some basic principles for X-ray Fluorescence Microscopy (XFM) and IR-microscopy (µ-IR), before explaining the design of multimodal probes for these two modalities and classical fluorescence, along with a few applications.

5.1.1. *X-ray Fluorescence Microscopy (XFM)*

XFM has emerged as a highly efficient technique to image heavy elements, including metal cations. Excellent reviews have detailed the underlying physics, technical characteristics, biological applications [76–81] and possibilities offered by multimodal imaging (coupling of XFM with fluorescence [80] for instance).

In a nutshell, providing its energy is high enough, *id est* above the absorption edge of the core electrons, an X-ray beam can excite a core electron of a heavy element, possibly a metal cation, to a photoelectron. This leads to a more positive ion (+1) in an electronic excited state. Deexcitation pathways, to a cation in a less excited or in the ground state, can occur with an upper electron filling this core hole, with the emission of an X-ray fluorescence light, detected to perform micro-XFM [80]. Note that this emission is isotropic and, to limit incident beam light recording, the detectors are set at ca. 90° from the incident beam. The energy of the emitted light informs on the

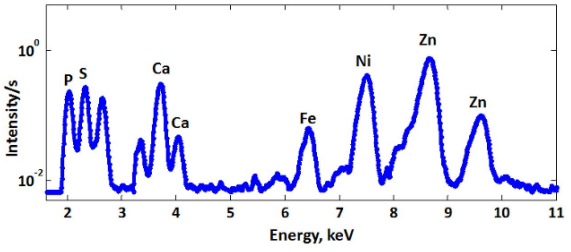

Figure 12. X-ray Fluorescence (XRF) sum spectrum of A549 cells. Conditions: excitation energy: 13.5 keV, pixel size: 300 × 300 nm^2, accumulation time: 4.8 s/pixel [82].

nature of the metal ion and on the two levels involved in the transition. Hence, each element emits a set of X-ray bands that are specific. For elements heavier than Si, these bands are clearly separated (Figure 12), and if there is an overlap, one can expect that at least one band in the emitted set is isolated.

This makes X-ray fluorescence an excellent technique for detection of heavy elements in a sample. Synchrotron-based radiations in the hard X-ray (>2 keV, hence for elements heavier than Si) allow a brightness many orders of magnitude greater than other sources [77]. The incident beam can be focused to a size smaller than that of a cell (typical diameter of 20 µm for eukaryotic cells), while keeping enough power to detect diluted metal ions in the small voxel of observation. Raster scanning the sample through the beam makes subcellular bioimaging of metal ions possible. Recently, resolutions better than 100 nm, down to 30 nm, have been achieved [80,83].

It is possible to grow cells in a monolayer on a window transparent in the X-ray (typically, silicon nitride Si_3N_4 windows, sheets of Kapton® or Ultralene® sheets [78,80,81,84,85]) and map them to determine the metal ions content distribution at the subcellular level. The X-ray incident beam (excitation) and the emitted X-ray signal are penetrating enough to pass through the entire sample (thickness of one cell in case of a monolayer) to provide elemental distribution for the entire cellular depth [80]. Hence, at each pixel, the map describes an integration of the total content in the heavy element over the thickness of the cell. For example, the potassium (K) is homogeneously distributed in cells, and its map in Figure 13 shows its distribution within a cell in false colors indicating the content (red > black). The area with a higher content in potassium (red) corresponds to the location where the cell is the thickest. Interestingly, by rotating the slide in the beam, tomography of cells can be obtained [86], with a very long time of acquisition, but opening new 3D opportunities for the characterization of metal ions distribution in cells.

Sample preparation is a key aspect, for any kind of spectroscopy and imaging. For classical optical fluorescence, several methods of chemical fixation of cells have been developed, such as paraformaldehyde, that are suitable for XFM a priori. However, these techniques show issues associated with possible re-distribution of a molecule of interest. Let us take the example of fixation using paraformaldehyde (H_2C=O, PFA) that reacts with amines present on proteins, peptides, or any other type of molecule. In a way, fixation with PFA casts some sort of a molecular net on the cell, but leaves large holes in which unfixed molecules can move and diffuse away. This can lead to redistribution, either a more even distribution within the cell or an accumulation in some organelles. For X-ray fluorescence, it is necessary to work with dry cells, and the drying process after chemical fixations has been shown to lead to leakage of metal ions, with a significant lowering in the apparent metal content [84]. This has been shown to mostly affect highly diffusible metal ions (Ca, K, Cl), but also the loosely bound transition metal ions pool that is not sequestered at the active site of metalloproteins, whereas metal cations such as Zn or Cu, highly controlled by proteins coordination, are not much redistributed by the fixation-drying procedure [81,87].

Cryofixation, with shock-freezing through plunging in liquid hydrocarbons (ethane, typically), possibly associated with lyophilization (freeze-drying), has been shown to better preserve both the subcellular structure and the distribution of metal ions [84,87]. After cryofixation, the frozen sample can be mapped at low temperatures. An alternative is to lyophilize the sample at low temperature, leading to a sample that can be handled at ambient temperature. But the lyophilization process must be performed steadily to ensure non-transition of ice from amorphous to crystals that would disrupt cell membranes (as crystalline water shows a lower density than liquid water or amorphous ice, such a

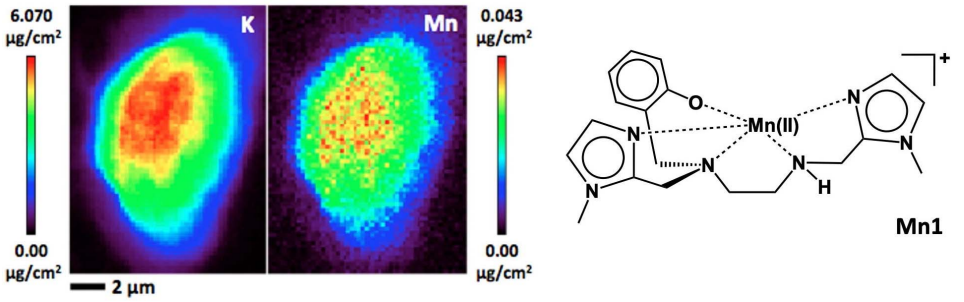

Figure 13. X-ray fluorescence mapping on cryofixed cells (human epithelial intestinal cells, HT29-MD2). Potassium (K) and manganese (Mn) maps by X-ray fluorescence on cryofixed and freeze-dried cells HT29–MD2 incubated with **Mn1** (100 µM). Images recorded on the 2-ID-D beamline of APS synchrotron (excitation at 6.8 keV; integration time, 2 s pixel^{-1}; pixel size, 200 nm) (from Ref. [25]).

transition would lead to a dilatation responsible for the damaging of the sub-cellular structure).

Nowadays, the consensual idea is that the less the sample is manipulated before being mapped the better, so as to avoid the effect of re-distribution but also contamination with metal ions, that in our modern world, can be found everywhere.

We have applied XFM to the imaging of Mn-based SOD mimics. We have used cryofixed/lyophilized cells incubated with the complexes at 100 µM, the typical concentration at which we evaluate their anti-inflammatory activity. As shown in Figure 13 for **Mn1**, the Mn element is distributed over the whole cell, as potassium, whereas a perinuclear distribution is seen for **Mn1Re** (further discussed in Section 5.3).

5.1.2. *Infrared microscopy (µ-IR)*

µ-IR is extensively used for its ability to perform detection using molecular chemical fingerprints in the mid-IR (4000–400 cm^{-1}, energy range where all of the molecular vibrations are excited). IR-maps, or chemical imaging, can be recorded to provide local chemical endogenous information by determining distribution of specific chemical vibrational signatures, for instance, IR-absorption of proteins at ca. 1600–1700 cm^{-1} (amide I), or lipids at ca. 2900–3000 cm^{-1} (CH_2^{asym} and CH_3^{asym}) (Figure 14). IR bio-imaging has been used, for instance, to follow cellular events, such as proteins acetylation [88].

In the course of our work, we have used specific bands (amide, phosphate, lipids), or association of bands (e.g. high amide + phosphate for the nucleus for instance) [89,90], or ratio of bands to identify specific organelles (membrane-rich organelle with very intense CH_2 stretching versus nucleus with more intense CH_3 stretching) [91]. One asset is that this chemical mapping of biological endogenous compounds is label-free, avoiding issues associated with the requirements of tagging [92], and can be implemented easily for bio-medical applications [93], with an easy process using bench IR-microscopes [94]. Synchrotron sources for IR-light are two to three-order of magnitude brighter than thermal source, making SR-FTIR mapping sensitive, with a lateral spatial resolution in the range of the µm (whereas bench-IR-microscope with a thermal source the spatial resolution is no better than 5–10 µm) [95]. The resolution with an optical detection is indeed physically limited by the light diffraction and the Abbe criteria (about $\lambda/2$, which is 2.5 µm at 2000 cm^{-1}).

Sub-micrometric resolutions suitable for intracellular mapping in the IR can be achieved using a near-field technique, which involves exploring mechanically a sample with a probe of sub-cellular dimensions. This was made possible by photothermal induced resonance, coupling an Atomic Force Microscope (AFM) with an IR pulsed-laser. A pulsed irradiation in the IR at a wavelength tuned to the sample IR absorption induces an excitation in the vibrational levels. The only dissipation is heat-release in the near environment. This induces a local dilation [96,97] and the AFM-tip receives a "punch" at every IR laser-pulse. The amplitude of its oscillation has been shown to be proportional to the deformation, and *in fine* to the amount of IR-absorbing compound below the tip. The resolution of the technique is that of the AFM (ca. 10–50 nm).

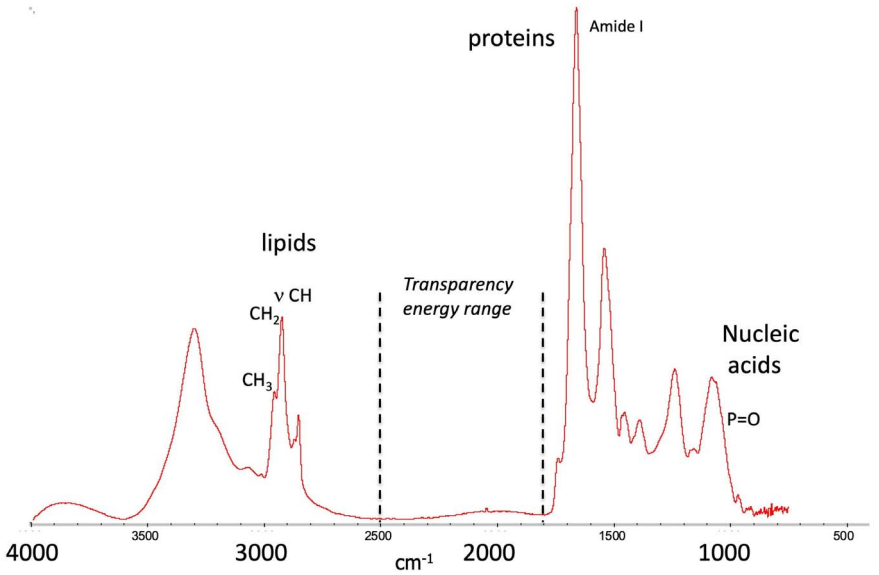

Figure 14. Typical IR-spectrum of a cell showing the main features mentioned in the text. Inspired by C. Sandt, SMIS beamline, synchrotron SOLEIL.

Interestingly, we were able to map the distribution of the [Re(LCp)$(CO)_3$] compound indicated in Figure 15 in MDA-MB231 cells. Its distribution was colocalized with high spots of amide and phosphate, pointed at a nuclear accumulation which is an organelle dense in proteins and DNA [89]. The colocalization with the nucleus was checked in correlative imaging (SR-FTIR imaging and classical fluorescence of DAPI, a nucleus tracker) [98].

For sub-cellular imaging in the IR, the sample has to be on a slide transparent in the IR (thin section of a bio-sample or monolayer of cells grown on the slide):

- CaF_2 slides with chemical fixation (too fragile for plunging and cryofixation). Note that for multimodal imaging in optical fluorescence, optical IR-imaging and AFM-IR [99], thin CaF_2 slides (100–200 μm) can be used. In the case of AFMIR the thin slides can be laid on the sample holder with paraffin oil to ensure a good optical contact and avoid air gap [99]. For instance, we have performed IR-imaging on tissue sections [100,101] or cells grown on the slide [53,90,98,99,102,103], with multimodal imaging (FTIR, AFMIR, and classical X-ray fluorescence) in several cases.
- Si_3N_4 windows than can also be used for multimodal imaging in classical and X-ray fluorescence [104] with chemical or cryofixation.
- ultralene thin film that can be used for multimodal imaging in IR and X-ray fluorescence [101].

Note that mid-IR is absorbed by bio-samples and thin samples (10 μm max) should be used in the case of optical detection (the IR-light passes through the sample). Interestingly, for AFM-IR a set-up (with irradiation from above the sample) [105] allows thick samples. But then they are probed only at the surface (absorption of the IR-light or depth of the penetration of the evanescent wave and the thickness probed depends on the recording parameters [105]).

5.2. *Design of IR or X-ray fluorescence probes*

A wider availability of probes, as tags or organelles trackers, would contribute substantially to the development of these two unconventional bio-imaging techniques to answer key biological questions [106]. Probes that can be detected by several complimentary techniques offer the possibility of cross correlative comparisons. The conventional way to develop a multimodal probe is to covalently conjugate several molecular moieties, one for each modality, leading to large molecular entities, with risk of discrepancy if a

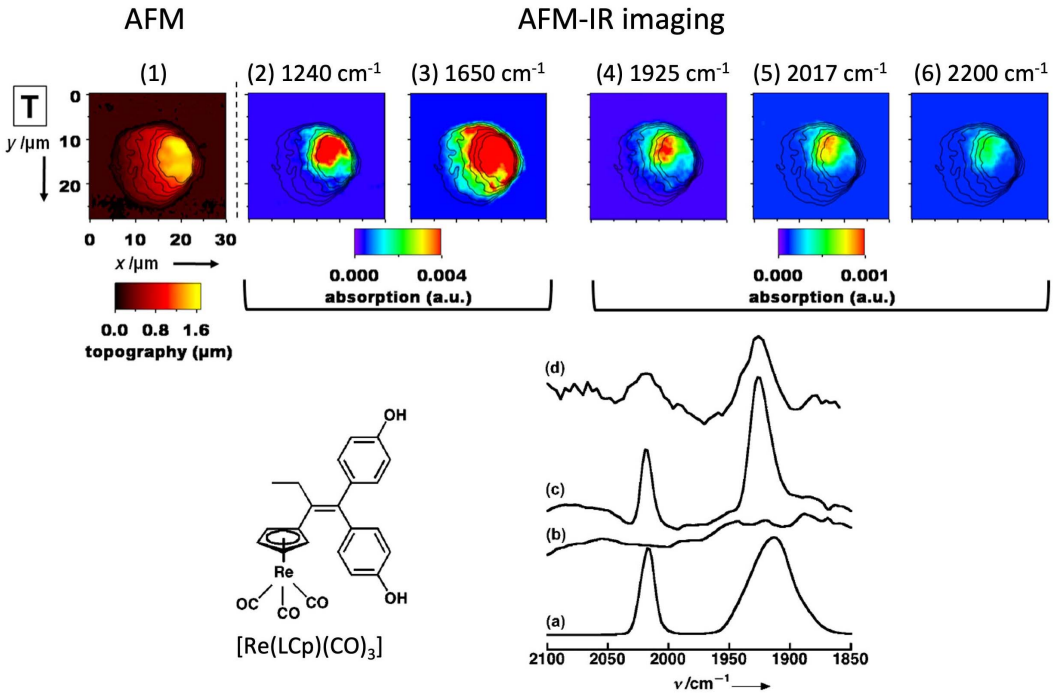

Figure 15. AFM-IR Top: images of MDA-MB-231 cells. MDA-MB321 treated with a 10 µm solution of [Re(LCp)(CO)$_3$] for 1 h at 37 °C. (1) AFM topography; (2–6) AFM-IR mappings at different wavelengths, with the AFM contours superimposed as black lines; the wavelengths correspond to the following bands: phosphate (2), amide (3), tricarbonyl (4 and 5), and out of band (6). Bottom: structure of [Re(LCp)(CO)$_3$]; IR-spectra of (a) pure [Re(LCp)(CO)$_3$], (b) control cells, (c) cells treated with [Re(LCp)(CO)$_3$] (50 µM, ca. 50,000 cells), and (d) AFMIR spectrum recorded at the nucleus for a single cell treated with [Re(LCp)(CO)$_3$] (1 h, incubation concentration: 10 µm). See Ref [89] for details.

moiety is cleaved. In contrast, we wanted to develop a "swiss-knife" probe, more compact, as a single molecular core for multimodal imaging (SCoMPI). To that extent, rhenium(I) tricarbonyl complexes are interesting. Indeed:

- Metal carbonyls (L)M(CO)$_n$ feature intense elongation vibration bands at ca. 2000–2200 cm^{-1} in the transparency window of biological sample in the mid IR (1800–2500 cm^{-1}, see Figure 14). They have been used as markers for immunoassay, for example as pH or cation probes [107]. One can also note that for the IR modality, only vibrational modes are excited and it does not involve transition into an electronic excited state, whose reactivity, different from the ground state, may lead to non-fluorescence species. In other words, unlike what happens for fluorescence probes, no photobleaching of the probes is at stake in IR-imaging [108]. The sole deexcitation pathway after IR excitation is heat release, which opens up possibilities to use them for all imaging techniques relying on the photothermal effect such as IR nanospectroscopy (AFM-IR).
- Rhenium tricarbonyl complexes bearing heteroaromatic ligands with low lying π^* orbitals [Re(N^N)(CO)$_3$]$^{n+}$ display interesting electronic properties at the origin of their development as luminescent probes. They show additional interesting features for use in a biological context such as low toxicity and good chemical inertness. The emission of such complexes mostly arises from triplet metal-to-ligand charge transfer (^{3}MLCT) excited states and they display large Stokes

shift. However, their quantum yield is low (usually around 1%) and their excitation usually occur in the UV-A range.
- Re gives access to detection in X-ray fluorescence, with bands that can be identified in a biological environment at its L-edge (one band, the L-α is superimposed with K-α of Zn, but the L-β is well-separated, as seen in Figure 16).
- Rhenium tricarbonyl complexes with the ligand pyta are easily synthesized and functionalized. The pyta (4-(2-pyridyl)-1,2,3-triazole) ligand seen in Figure 17 is formed through Cu-catalyzed Alkyne-Azide Cycloaddition (CuAAC) chemistry and there is a large variety of possible functionalizations of a R-N_3.

5.3. *Variation of the ligands to control the physico-chemical properties of the probes*

The photophysical properties of these [Re(N^N)$(CO)_3$X] compounds have been well characterized, particularly with the N^N ligand being a bipyridine or a phenanthroline ligand. Their electronic properties can be tuned by modifications of the di-imine or the axial X ligand. We have explored the impact of diverse structural modifications around rhenium tricarbonyl complexes based on a pyridine–triazole N^N ligand (see Figure 17).

To explore questions of cell penetration and toxicity of [Re(pyta)$(CO)_3$Cl] complexes, we have prepared and studied complexes with pyta ligands functionalized with aliphatic chains of increasing length (C4, C8, and C12) [109].

We showed that increasing the lipophilicity of the complex by the increase in the carbon chain length correlated with an enhanced cellular uptake, as quantified by a correlative luminescence and infrared (IR) study, and thus an increased cytotoxicity. This quantitative cellular study stressed out that cytotoxicity values (IC_{50}) reflect intrinsic toxicity but also the ability of the compound to penetrate inside cells. Correlating the toxicity of a compound to its internal concentration and not to an incubation concentration as commonly performed requires the use of such analytical techniques. We also showed that the appendage of a long aliphatic chain (C12) on the pyta ligand strongly impacted the photophysical behavior of the complexes in aqueous medium compared to organic medium (such as acetonitrile) as opposed to shorter chains. The folding of the carbon chain around the metal core in aqueous buffer was proposed to shield the metal center from the emission quenching due to water.

In an attempt to optimize quantum yield and excitation wavelengths—aiming for a bathochromic shift of the Metal-to-Ligand Charge Transfer (MLCT) bands in the visible range that is better adapted for bioimaging—in these complexes, we studied structural variations of the pyta ligand (with X axial ligand as an halogen Cl or Br) [110]. Extending the aromatic surface (from a pyridine to a quinoline) in the quinta series, led to the expected bathochromic shift but it was associated with a decrease in the quantum yield. A satisfying compromise is challenging to reach. We identified the tapy (1-(2-pyridyl)-1,2,3-triazole) ligand as a very interesting scaffold for the design of rhenium tricarbonyl complexes. The common pyta ligand displays a normal or regular coordination through the N3. Inverting the bridge between the pyridine and triazole rings, we generated the tapy ligand showing an inverse coordination through the less donor nitrogen N2. DFT calculations confirmed the poorer electron-donor ability of the tapy ligand in comparison with pyta, with a stabilized LUMO level, leading to a smaller gap and a bathochromic shift of the MLCT absorption band. The enhanced luminescence was proposed later to arise from slower rates of non-radiative decay. The corresponding complexes displayed a strongly enhanced luminescence—particularly with long aliphatic chains—compared to the pyta counterparts, with quantum yields up to 3.5% in aqueous medium. Despite their reduced stability in coordinating solvents, the inverse coordination has interesting potential in organometallic chemistry.

We further modified $Re(CO)_3$ complexes bearing pyta-C12 or tapy-C12 ligands (with long alkyl chains) replacing the axial X ligand [111]. The introduction of benzenethiolate π-donating ligands results in high lying filled orbital on sulfur and benzenethiolate leading to a strong absorption band of mixed MLCT/LLCT (LLCT: Ligand-to-Ligand Charge Transfer) character around 330 nm. The emission of such complexes depends both on the diimine and on the axial benzenethiolate, offering an opportunity to

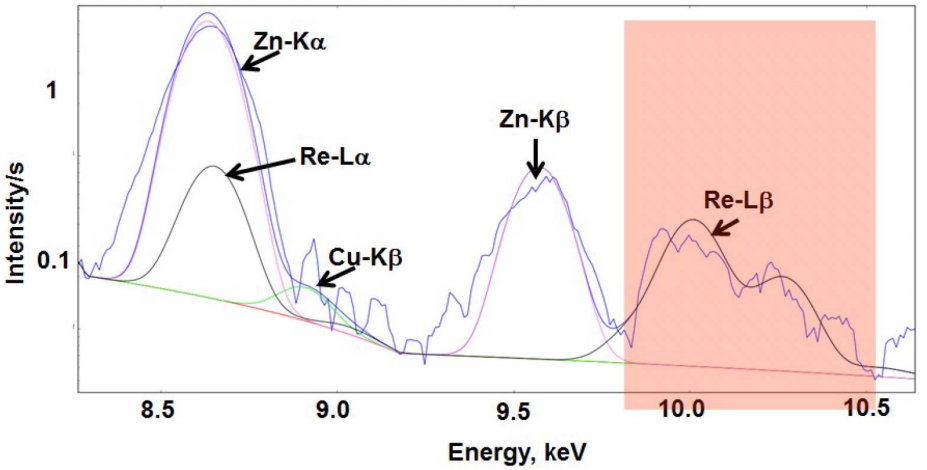

Figure 16. Cu, Zn and Re XRF lines in the mean spectrum of a single Chinese Hamster Ovarian (CHO) cell incubated with an homeodomain trafficking protein tagged with a Re-probe. Recorded data in blue, fits for Cu (green), Zn (violet) and Re (black). For details, see Ref. [82].

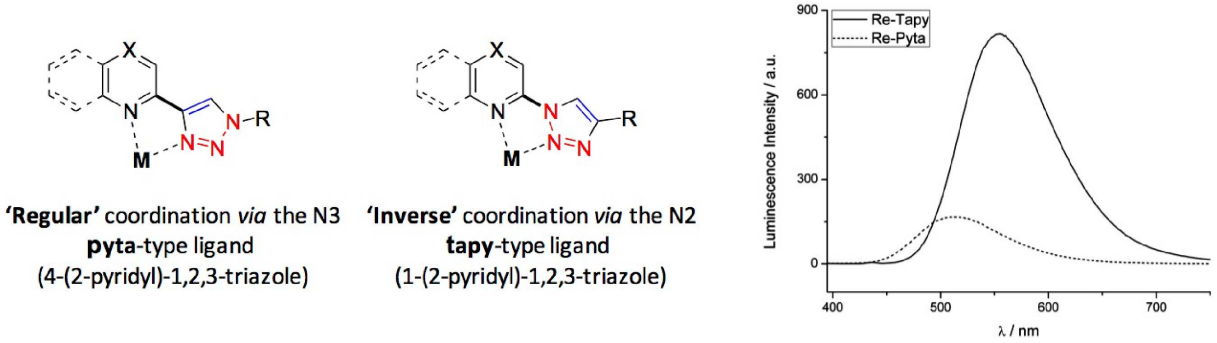

Figure 17. Schematic structures of the [Re(pyta)$(CO)_3$Cl] and [Re(tapy)$(CO)_3$Cl] complexes and their typical luminescence in aqueous medium.

tune the emission wavelength across a wide range extending to the near IR region (Figure 18).

5.4. *LMW organelle trackers working with PFA standard fixation*

For co-localization studies by X-ray Fluorescence (XRF), some endogenous elements can be indicative of a subcellular compartment—e.g. phosphorus, sulfur, copper and zinc reveal nucleus location [112]. Manganese has been shown to accumulate in the Golgi apparatus in neural cells [113]. But this relative metal-specificity cannot be made general for all the organelles. Hence the design of probes for organelle tracking responsive in X-ray fluorescence is of great interest [106]. Sealed carbon nanotubes filled with heavy metals and decorated with organelle-specific peptides have been designed for nucleus targeting. But the attempt to track endoplasmic reticulum failed [114], showing this strategy of peptide-targeting for specific organelle tracking is not easy to extend. Metal-tagged antibodies have been developed, for instance with lanthanides [115, 116] and some used for mitochondria tracking—involving an antibody targeting a protein specific of this organelle [117,118]. But the procedures involve permeabilization with leakage of the loosely-bound metal pool, that can be undesirable. Low-molecular weight complexes targeting organelles can also be used for their tracking [119–121] with compatibility

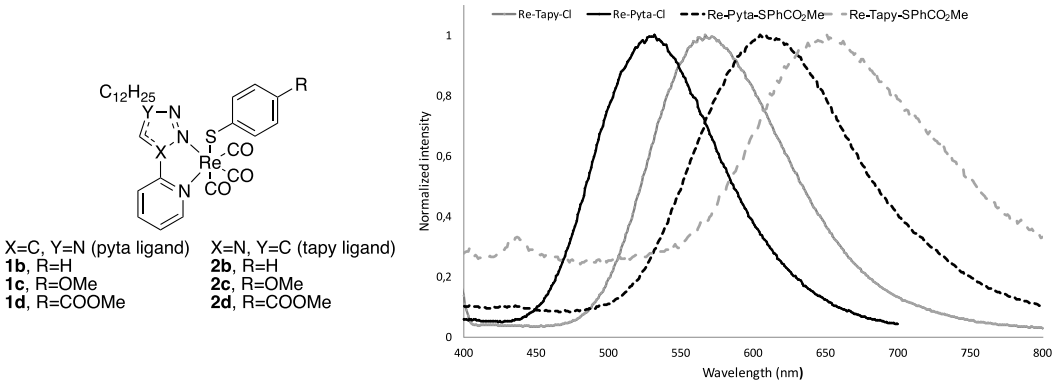

Figure 18. Structural variations on the pyta and tapy ligands, and variation of the fluorescence response.

with cryofixation. Recently, we have conjugated the typical [Re(pyta)(CO)$_3$X] core, with trisphenylphosphonium cations of various lipophilicities (see Figure 19). Trisphenylphosphonium cations are known to accumulate at the mitochondria, due to their delocalized positive charge over a lipophilic trisphenyl core [62]. We chose here a procedure with PFA fixation, more accessible to users than cryofixation, that was hopefully successful. Indeed, using their fluorescent properties, the [Re(L)(CO)$_3$X] probes were first co-localized with a fluorescent mitotracker. Then XFM with the same PFA fixation showed that the Re of the probe was easily detectable for the two more lipophilic probes C2 and C3, and an accumulation of Re (probe) around Zn (nucleus) was clearly seen [121]. This example also shows here the interest of the multimodality of the probes such as the metal-carbonyl probe: the multimodality of a probe means that it can be validated using a tried-and-tested technique, with a view to implementation using a less conventional technique.

In another example, we have tagged a TrisPhenylamine-based (**TP**) mitotracker with a Br (**TP-Br**) or with a [Re(pyta)(CO)$_3$]$^+$ (**TP-Re**) [122]. **TP-Br** can be present in cells in a non-emissive off-state and, as such, fluorescence imaging could not reflect accurately the distribution of the probe. The **TP-Br** was found to be co-localized with a fluorescent mitotracker, whereas the **TP-Re** was co-localized with a lysotracker. In contrast with what happened with the trisphenylphosphonium functionalization, the [Re(pyta)(CO)$_3$X] changed the localization of the **TP** probe. Interestingly, this makes **TP-Br** and **TP-Re** potential new organelle trackers for XFM.

Remembering that some of the [Re(L)(CO)$_3$X] compounds we have studied have been shown to be accumulated at the Golgi [102] or at the nucleus (see Figure 15) [89], these Re(CO)-based compounds constitute a series of multimodal organelle trackers that can be followed by classical fluorescence, in IR-imaging, and X-ray fluorescence.

5.5. *X-ray fluorescence imaging: an original direction to explore metal-complex integrity in cells through distribution*

As mentioned earlier, one challenge faced when studying metal complexes in a biological environment is to ensure that the complex L-M remains intact, despite the abundance of Lewis bases, and the presence of other metal ions, even if they are mostly found coordinated by proteins. One way to interrogate this is to use a ligand tagged with a heavy atom (L*) and check if the two moieties (heavy atom as a covalent tag of the ligand L* and metal ion) are present in cells at the same location [79]. This can be done by recording maps of cells incubated with a L*-M complex in μ-X-ray fluorescence. This has been performed in the literature with a ligand tagged with Br [123] or I [124,125].

As an example, the conjugate of **Mn1** with a multimodal Re-tricarbonyl probe (**Mn1-Re**, Figure 20) was studied in the cellular model HT29-MD2 (Section 3.4b). Its integrity was probed by analyzing the Re and Mn colocalization by X-ray fluorescence imaging, Re tagging the Mn-ligand. The Re-maps and Mn-maps where not fully co-localized, with spots

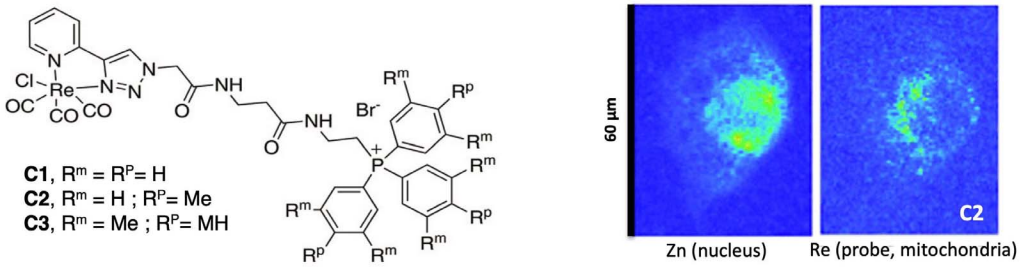

Figure 19. Structures of the $[Re(pyta)(CO)_3]^+$ conjugated with a trisphenylphosphonium moiety and elemental distribution of Zn and Re (XFM) in A549 cells incubated with C2 (4 h, 20 µM) before PFA fixation and air drying (excitation at 14 keV; integration time, 300 ms per pixel; pixel size, 500 nm). XFM recorded at synchrotron SOLEIL, on nanoscopium beamline [121].

where Re (ligand) was present and not Mn, revealing some degree of decoordination in cells, as analyzed by IMS/MS (Section 3.6). Interestingly, Mn and Re showed a perinuclear accumulation (see Figure 20). In contrast, **Mn1** has been seen homogeneously distributed (Figure 13, distribution of Mn similar to that of K). Interestingly, the two compounds, **Mn1** and **Mn1-Re**, showed a similar bioactivity and similar concentration in mitochondria, despite a higher overall cellular concentration of **Mn1-Re** (Figure 20). This is probably because the cellular activity of these compounds is governed by the concentration reached at the mitochondria [53].

6. Conclusion

> "*[Naturam] si sequemur ducem, numquam aberrabimus*", Cicero, *De officiis*, I, 100.
>
> *Let Nature provide us guidance: we shall never get lost.*

We would like to end this article on a less scientific note and comment on the research journey we have just described in the fields of bioinorganic chemistry and inorganic chemical biology, going from chemical design of metal complexes to their studies in cells.

Biomimicry has emerged as a highly heuristic approach: why not learn from the strategies selected by Nature during an evolutionary process spanning millions of years, and put them to use [126]? On a macroscopic scale, this might mean reproducing the movement of an insect to create a highly mobile robot or drawing inspiration from animal skeletons to create highly resistant vaults, as Antoni Gaudi, the precursor of biomimicry in architecture, did. This can be translated to the molecular scale: as chemists, we can seek to reproduce the way a biological system works, and move towards the design of bio-inspired catalysts of industrial or therapeutic value. The use of the term "bio-inspiration" instead of "biomimicry" aims to extend the approach beyond simple copying of structures to the creative development of new systems based on fundamental molecular principles deciphered in biology.

We have tried to illustrate this process in the case of highly efficient SODs, with physico-chemical features that could be implemented in low molecular weight complexes, namely the tuning of the redox potential to an optimal value for this redox catalysis, and a positively charged funnel in an overall negatively charged protein, for the electrostatic attraction of the negative substrate, superoxide. Transposing to a scale other than what nature has set up is not always straightforward, as we saw in the case of electrostatic attraction for the transition from the protein scale to those of low-molecular-weight systems, where simply increasing the overall charge was not enough without 3D organization. However, such approaches enable us to better understand Nature's challenge piece by piece and to learn—or at least make progress in—mastering them at the molecular level.

Came then the need to design dedicated cellular assays to test these catalysts in biological environments. In a way, where biochemistry purifies metalloproteins from biological environments for study in test tubes, cellular and biological inorganic chemistry reverses the process, with the chemical design of metal complexes in the round flask which are then

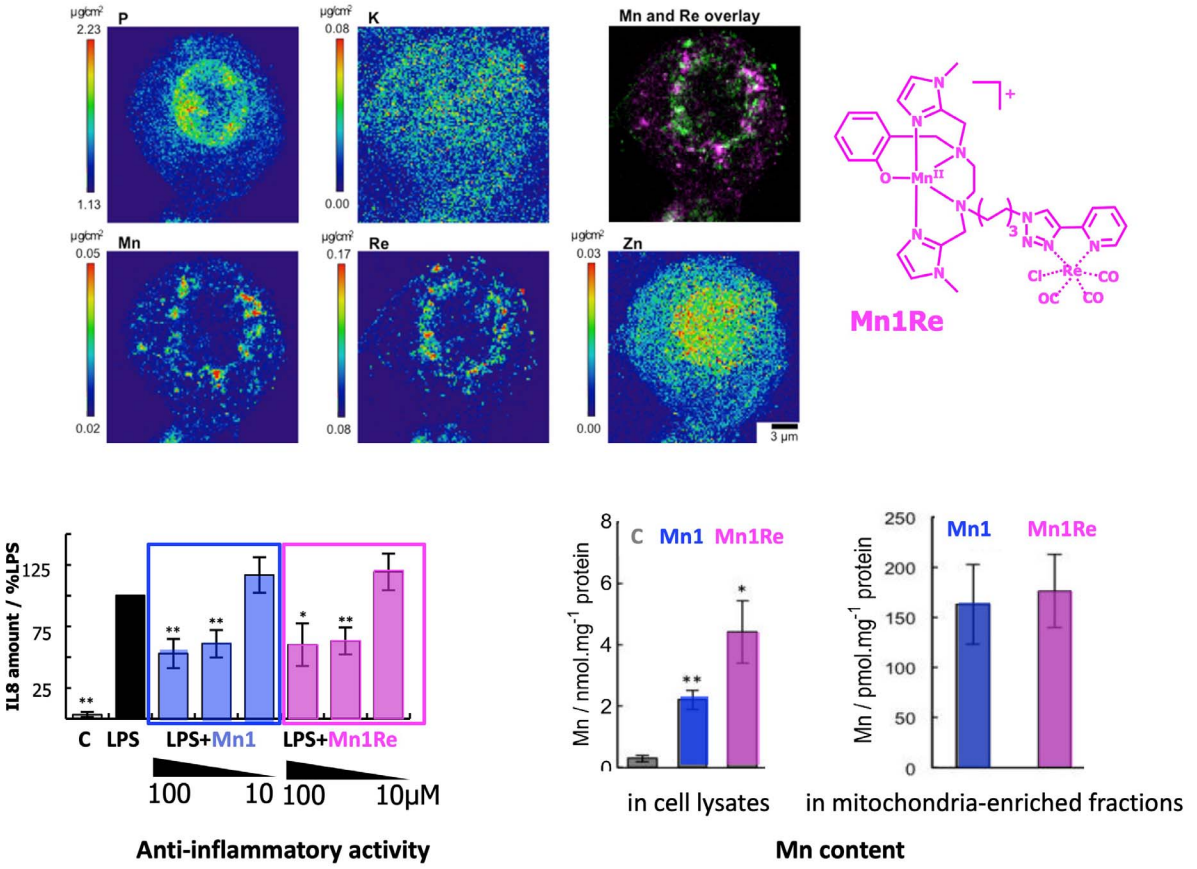

Figure 20. Up: elemental distribution of P, K, Mn, Re, and Zn in an HT29-MD2 cell incubated with **Mn1Re**. The phosphorus (P), and zinc (Zn, Kα-lines) maps are used to identify the nucleus area. The overlay (top right) corresponds to the Mn (Kα-line) (magenta) and Re (Lβ-line) (green) maps. The regions corresponding to an overlap of both elements are displayed in white. Intestinal epithelial cells HT29-MD2 were incubated for 2 h with **Mn1Re** (100 mM, 0.02% DMSO) before cryofixation and freeze-drying. Images were recorded on the 2-ID-D beamline of the APS synchrotron (excitation at 12.0 keV; integration time, 2 s per pixel; pixel size, 200 nm). Down left: C: control HT29-MD2 cells, **Mn1/Mn1Re**: HT29-MD2 cells incubated with **Mn1/Mn1Re** (10 and 100 µM, 6 h). IL8 secretion in HT29-MD2 cells. Intestinal epithelial cells HT29-MD2 were incubated for 7 h under different conditions indicated in the figure. LPS (0.1 µg·mL^{-1}) was added at the end of the first hour. Data represent means ± SEM for 7–10 independent experiments. (*) $p < 0.05$, (**) $p < 0.01$ versus LPS condition. Down right: C-control cells, **Mn1/Mn1Re**-HT29-MD2 cells incubated with **Mn1/Mn1Re** (100 µM, 6 h). The total Mn content in cell lysates was determined in acid-digested cell lysates by titration using EPR. Data represent mean ± SEM for 4 independent experiments. (*) $p < 0.05$, (**) $p < 0.01$ versus C. The total Mn content in mitochondria-enriched fractions was determined by ICP-MS. Mitochondria were isolated using a mitochondria isolation kit (Thermo Fisher Scientific). Data represent mean ± SEM for 7 independent experiments; for details see Ref. [53].

introduced in cellular or biological environments, where they are studied and evaluated.

Immediately, the question of sub-cellular location arose and we embarked on the path of bio-imaging.

XFM, suitable for metal imaging, was an obvious technique to explore as we wanted not to modify the low-molecular weight complex and its physicochemical properties too much.

The idea of developing metal-based IR-probes came about in a different way: this was the story of an encounter, as often in science, with a physicist, Professor A. Dazzi (université Paris-Saclay), who was developing a nano-IR imaging strategy (AFM-IR technique mentioned above). This technique which he had previously used to map biopolymers (DNA, sugars, proteins) was so amazing that we wanted to use it to detect and map non-endogenous molecules. Because of its IR-signature, the $M(CO)_3$ moiety appeared as the ideal molecular core to test that, and their metal-core made them interesting probes to use in XFM.

It also illustrates how science progresses, tackling one question after another, one answer leading to a new more important question or idea to follow. Clearly, Nature is not only a formidable source of inspiration, but also an endless reservoir of interlocking questions and challenges for chemists.

This whole journey was made possible in the context of collaborative work. First, within the research group (https://ens-bic.fr/) where we share a common interest in bioinorganic chemistry and redox aspects, but with complementary expertise (peptide chemistry, organometallic chemistry, ligand synthesis, spectroscopies and now nanoparticles, redox biology and optogenetics). When you do not travel alone, the path is easier and enriched by discussions. But it also means collaborating with other disciplines: physicists, biologists, medical doctors, etc. Working in a multi-disciplinary environment leads to take that step aside that changes everything: it implies being an expert (in one's own field) and at the same time an ignoramus (in another), with a renewed sense of wonder when you begin to grasp something new. It is also sharing with students, especially PhD students, with whom we live in the laboratory for at least a few years, and who bring a new vision and new questions, making research a place where we are always being challenged.

Declaration of interests

The authors do not work for, advise, own shares in, or receive funds from any organization that could benefit from this article, and have declared no affiliations other than their research organizations.

Funding

The authors want to acknowledge ENS-PSL, PSL University, CNRS, MITI-CNRS, Sorbonne University (SU) and the other bodies that funded this work. ANR-15-CE07-0027 MAGIC, DEI20151234413 (*Fondation pour la recherche médicale* 2016), and BACTMAN and ANACOMDA (*Mission pour les initiatives transverses et interdisciplinaires*-CNRS), the Association François Aupetit (AFA, research fellowship), ANR 21-CE18-0053-02 MOBIDIC, ANR 20-CE07-0039-01-CATMAN, ANR 23-CE23 METALINFY; Idex PSL Qlife project Main ANR Q-life ANR-17-CONV-0005; CEFIPRA project no. 6505-1; ANR-16-CE18-0017-01 SATIN; EMERGENCE SU EMRG-24 TOTEM; ANR-22-PEBI-0003 (PEPR).

References

[1] D. Tsiapalis, D. I. Zeugolis, *Biomaterials*, 2021, **275**, article no. 120943.
[2] H. Sies, *Redox Biol.*, 2017, **11**, 613-619.
[3] H. Sies *et al.*, *Nat. Rev. Mol. Cell Biol.*, 2022, **23**, 499-515.
[4] C. Policar, J. Bouvet, H. C. Bertrand, N. Delsuc, *Curr. Opin. Chem. Biol.*, 2022, **67**, article no. 102109.
[5] J. J. Soldevila-Barreda, P. J. Sadler, *Curr. Opin. Chem. Biol.*, 2015, **25**, 172-183.
[6] H. Huang *et al.*, *Nat. Chem.*, 2019, **11**, 1041-1048.
[7] S. G. Suman, in *Targeted Metallo-Drugs: Design, Development, and Modes of Action* (C. J. Marmion, E. Farkas, eds.), CRC Press, Boca Raton, 1st ed., 2023.
[8] C. Policar, in *Redox Active Therapeutics* (I. Batinić-Haberle *et al.*, eds.), Humana Press, published by Springer Nature, Switzerland, 2016, 125-164.
[9] O. Iranzo, *Bioorg. Chem.*, 2011, **39**, 73-87.
[10] S. Signorella, C. Palopoli, G. Ledesma, *Coord. Chem. Rev.*, 2018, **365**, 75-102.
[11] J. J. Soldevila-Barreda, N. Metzler-Nolte, *Chem. Rev.*, 2019, **119**, 829-869.
[12] I. A. Abreu, D. E. Cabelli, *Biochim. Biophys. Acta (BBA) - Proteins Proteom.*, 2010, **1804**, 263-274.
[13] Y. Sheng, I. A. Abreu, D. E. Cabelli, M. J. Maroney, A.-F. Miller, M. Teixeira, J. S. Valentine, *Chem. Rev.*, 2014, **114**, 3854-3918.
[14] J. E. Gleason *et al.*, *Proc. Natl. Acad. Sci. USA*, 2014, **111**, 5866-5871.
[15] W. H. Koppenol, D. M. Stanbury, P. L. Bounds, *Free Radic. Biol. Med.*, 2010, **49**, 317-322.
[16] F. Basolo, R. G. Pearson, *Mechanism of Inorganic Reactions. A Study of Metal Complexes in Solution*, 2nd ed., John Wiley and Sons, New York, 1967.
[17] W. C. Barrette, D. T. Sawyer, J. A. Fee, K. Asada, *Biochemistry*, 1983, **22**, 624-627.

[18] B. H. Bielski, D. E. Cabelli, R. L. Arudi, *J. Chem. Phys. Ref. Data*, 1985, **14**, 1041-1100.
[19] J.-M. Latour, *Metallomics*, 2015, **7**, 25-28.
[20] J. D. Aguirre, V. C. Culotta, *J. Biol. Chem.*, 2012, **287**, 13541-13548.
[21] J. G. Charrier, C. Anastasio, *Atmos. Environ.*, 2011, **45**, 7555-7562.
[22] I. Batinic-Haberle, A. Tovmasyan, E. R. H. Roberts, Z. Vujaskovic, K. W. Leong, I. Spasojevic, *Antioxid. Redox Signal.*, 2014, **20**, 2372-2415.
[23] H. Irving, P. Williams, *Nature*, 1948, **162**, 746-747.
[24] H. Irving, R. J. P. Williams, *J. Chem. Soc. (Resumed)*, 1953, 3192-3210.
[25] E. Mathieu *et al.*, *Inorg. Chem.*, 2017, **56**, 2545-2555.
[26] J. P. Lisher, D. P. Giedroc, *Front. Cell. Infect. Microbiol.*, 2013, **3**, article no. 91.
[27] M. Zoumpoulaki *et al.*, *Angew. Chem. Int. Ed.*, 2022, **61**, article no. e202203066.
[28] G. Schanne *et al.*, *Oxid. Med. Cell. Longevity*, 2022, **2022**, article no. 3858122.
[29] K. J. Franz, N. Metzler-Nolte, *Chem. Rev.*, 2019, **119**, 727-729.
[30] E. Boros, P. J. Dyson, G. Gasser, *Chem*, 2020, **6**, 41-60.
[31] R. Bonetta, *Chem. - A Eur. J.*, 2018, **24**, 5032-5041.
[32] A.-S. Bernard *et al.*, *Dalton Trans.*, 2012, **41**, 6399-6403.
[33] G. E. O. Borgstahl, H. E. Parge, M. J. Hickey, W. F. Beyer Jr, R. A. Hallewell, J. A. Tainer, *Cell*, 1992, **71**, 107-118.
[34] M. G. B. Drew, C. J. Harding, V. McKee, G. G. Morgan, J. Nelson, *J. Chem. Soc., Chem. Commun.*, 1995, 1035-1038.
[35] S. Durot *et al.*, *Eur. J. Inorg. Chem.*, 2005, **2005**, 3513-3523.
[36] I. Batinic-Haberle, I. Spasojevic, *J. Porphyr. Phthalocyan.*, 2019, **23**, 1326-1335.
[37] I. Batinic-Haberle, A. Tovmasyan, I. Spasojevic, *Redox Biol.*, 2015, **5**, 43-65.
[38] F. Cisnetti, A. Lefèvre, R. Guillot, F. Lambert, G. Blain, E. Anxolabéhère-Mallart, C. Policar, *Eur. J. Inorg. Chem.*, 2007, **2007**, 4472-4480.
[39] S. Durot, F. Lambert, J.-P. Renault, C. Policar, *Eur. J. Inorg. Chem.*, 2005, **2005**, 2789-2793.
[40] S. Groni, G. Blain, R. Guillot, C. Policar, E. Anxolabéhère-Mallart, *Inorg. Chem.*, 2007, **46**, 1951-1953.
[41] A. Conte-Daban, V. Ambike, R. Guillot, N. Delsuc, C. Policar, C. Hureau, *Chem. - A Eur. J.*, 2018, **24**, 5095-5099.
[42] K. M. Stewart, K. L. Horton, S. O. Kelley, *Org. Biomol. Chem.*, 2008, **6**, 2242-2255.
[43] W. H. Koppenol, *Oxygen and Oxy-radicals in Chemistry and Biology*, Academics, New York, 1981, 671-674 pages.
[44] J. Benovic, T. Tillman, A. Cudd, I. Fridovich, *Arch. Biochem. Biophys.*, 1983, **221**, 329-332.
[45] E. D. Getzoff, J. A. Tainer, P. K. Weiner, P. A. Kollman, J. S. Richardson, D. C. Richardson, *Nature*, 1983, **306**, 287-290.
[46] I. Spasojević, R. Menzeleev, P. S. White, I. Fridovich, *Inorg. Chem.*, 2002, **41**, 5874-5881.
[47] H. Y. V. Ching, I. Kenkel, N. Delsuc, E. Mathieu, I. Ivanović-Burmazović, C. Policar, *J. Inorg. Biochem.*, 2016, **160**, 172-179.
[48] C. Policar, S. Durot, F. Lambert, M. Cesario, F. Ramiandrasoa, I. Morgenstern-Badarau, *Eur. J. Inorg. Chem.*, 2001, 1807-1818.
[49] S. Durot, C. Policar, G. Pelosi, F. Bisceglie, T. Mallah, J.-P. Mahy, *Inorg. Chem.*, 2003, **42**, 8072-8080.
[50] C. Beauchamp, I. Fridovich, *Anal. Biochem.*, 1971, **44**, 276-287.
[51] K. M. Faulkner, S. I. Liochev, I. Fridovich, *J. Biol. Chem.*, 1994, **269**, 23471-23476.
[52] R. H. Weiss, A. G. Flickinger, W. J. Rivers, M. M. Hardy, K. W. Aston, U. S. Ryan, D. P. Riley, *J. Biol. Chem.*, 1993, **268**, 23049-23054.
[53] E. Mathieu *et al.*, *Chem. Commun.*, 2020, **56**, 7885-7888.
[54] E. Mathieu *et al.*, *Dalton Trans.*, 2020, **49**, 2323-2330.
[55] F. C. Friedel, D. Lieb, I. Ivanović-Burmazović, *J. Inorg. Biochem.*, 2012, **109**, 26-32.
[56] A. Vincent *et al.*, *J. Inorg. Biochem.*, 2021, **219**, article no. 111431.
[57] C. Lenoir *et al.*, *Life Sci.*, 2008, **82**, 519-528.
[58] S.-J. Lee, K.-T. Lim, *Mol. Cell. Biochem.*, 2007, **304**, 13-23.
[59] F. K. Kálmán, G. Tircsó, *Inorg. Chem.*, 2012, **51**, 10065-10067.
[60] D. Ndiaye *et al.*, *Angew. Chem. Int. Ed.*, 2020, **59**, 11958-11963.
[61] R. D. Shannon, *Acta Crystallogr.*, 1976, **A32**, 751-767.
[62] R. A. J. Smith, C. M. Porteous, A. M. Gane, M. P. Murphy, *Proc. Natl. Acad. Sci. USA*, 2003, **100**, 5407-5412.
[63] A. Henninot, J. C. Collins, J. M. Nuss, *J. Med. Chem.*, 2018, **61**, 1382-1414.
[64] J. L. Lau, M. K. Dunn, *Bioorg. Med. Chem.*, 2018, **26**, 2700-2707.
[65] A. Vincent *et al.*, *Chem. Commun.*, 2020, **56**, 399-402.
[66] K. Coulibaly *et al.*, *Inorg. Chem.*, 2021, **60**, 9309-9319.
[67] Y. Ben Hadj Hammouda, K. Coulibaly, A. Bathily, M. Teoh Sook Han, C. Policar, N. Delsuc, *Molecules*, 2022, **27**, article no. 5476.
[68] J. W. Bryson, S. F. Betz, H. S. Lu, D. J. Suich, H. X. Zhou, K. T. O'Neil, W. F. DeGrado, *Science*, 1995, **270**, 935-941.
[69] J. W. Bryson, J. R. Desjarlais, T. M. Handel, W. F. Degrado, *Protein Sci.*, 1998, **7**, 1404-1414.
[70] V. M. Cangelosi, A. Deb, J. E. Penner-Hahn, V. L. Pecoraro, *Angew. Chem. Int. Ed.*, 2014, **53**, 7900-7903.
[71] K. J. Koebke, F. Yu, E. Salerno, C. Van Stappen, A. G. Tebo, J. E. Penner-Hahn, V. L. Pecoraro, *Angew. Chem. Int. Ed.*, 2018, **57**, 3954-3957.
[72] K. J. Koebke *et al.*, *Inorg. Chem.*, 2018, **57**, 12291-12302.
[73] E. Mathieu *et al.*, *Chem. - A Eur. J.*, 2020, **26**, 249-258.
[74] U. P. Singh, R. K. Singh, Y. Isogai, Y. Shiro, *Int. J. Pept. Res. Ther.*, 2006, **12**, 379-385.
[75] H. S. Marinho, L. Cyrne, E. Cadenas, F. Antunes, *Methods in Enzymology*, Elsevier, Amsterdam, 2013, 3-19 pages.
[76] C. M. Ackerman, S. Lee, C. J. Chang, *Anal. Chem.*, 2017, **89**, 22-41.
[77] M. J. Pushie, I. J. Pickering, M. Korbas, M. J. Hackett, G. N. George, *Chem. Rev.*, 2014, **114**, 8499-8541.
[78] F. Porcaro, S. Roudeau, A. Carmona, R. Ortega, *TrAC Trends Anal. Chem.*, 2018, **104**, 22-41.
[79] J. Karges, N. Metzler-Nolte, in *Targeted Metallo-Drugs: Design, Development, and Modes of Action* (C. J. Marmion, E. Farkas, eds.), CRC Press, Boca Raton, 1st ed., 2023, Online at https://www.taylorfrancis.com/books/9781003272250.
[80] M. E. Graziotto, C. J. Kidman, L. D. Adair, S. A. James, H. H. Harris, E. J. New, *Chem. Soc. Rev.*, 2023, **52**, 8295-8318.

[81] S. Matsuyama, K. Maeshima, M. Shimura, *J. Anal. Atom. Spectrom.*, 2020, **35**, 1279-1294.
[82] S. Hostachy *et al.*, *Chem. Sci.*, 2018, **9**, 4483-4487.
[83] T. W. Victor *et al.*, *Sci. Rep.*, 2018, **8**, article no. 13415.
[84] Q. Jin *et al.*, *J. Microsc.*, 2017, **265**, 81-93.
[85] L. Perrin, A. Carmona, S. Roudeau, R. Ortega, *J. Anal. Atom. Spectrom.*, 2015, **30**, 2525-2532.
[86] F. Fus *et al.*, *Angew. Chem. Int. Ed.*, 2019, **58**, 3461-3465.
[87] S. Roudeau, A. Carmona, L. Perrin, R. Ortega, *Anal. Bioanal. Chem.*, 2014, **406**, 6979-6991.
[88] T. Chen *et al.*, *Anal. Chem.*, 2008, **80**, 6390-6396.
[89] C. Policar *et al.*, *Angew. Chem. Int. Ed.*, 2011, **50**, 860-864.
[90] S. Clède, N. Delsuc, C. Laugel, F. Lambert, C. Sandt, A. Baillet-Guffroy, C. Policar, *Chem. Commun.*, 2015, **51**, 2687-2689.
[91] S. Clède, C. Policar, C. Sandt, *Appl. Spectrosc.*, 2014, **68**, 113-117.
[92] M. Hermes *et al.*, *J. Opt.*, 2018, **20**, article no. 023002.
[93] D. Bazin, M. Daudon, C. Combes, C. Rey, *Chem. Rev.*, 2012, **112**, 5092-5120.
[94] L. Henry, D. Bazin, C. Policar, J.-P. Haymann, M. Daudon, V. Frochot, M. Mathonnet, *C. R. Chim.*, 2022, **25**, 503-515.
[95] N. Jamin, P. Dumas, J. Moncuit, W.-H. Fridman, J.-L. Teillaud, G. L. Carr, G. P. Williams, *Proc. Natl. Acad. Sci. USA*, 1998, **95**, 4837-4840.
[96] A. Dazzi, C. Policar, *Biointerface Characterization by Advanced IR Spectroscopy*, Elsevier, Amsterdam, 2011, 245-278 pages.
[97] A. Dazzi, C. B. Prater, *Chem. Rev.*, 2017, **117**, 5146-5173.
[98] S. Clède *et al.*, *Biotechnol. Adv.*, 2013, **31**, 393-395.
[99] Y. Wang *et al.*, *Dalton Trans.*, 2018, **47**, 9824-9833.
[100] L. Henry *et al.*, *Bioconjugate Chem.*, 2018, **29**, 987-991.
[101] S. Clède *et al.*, *ChemBioChem*, 2016, **17**, 1004-1007.
[102] S. Clède *et al.*, *Chem. Commun.*, 2012, **48**, 7729-7731.
[103] S. Clède *et al.*, *Analyst*, 2013, **138**, 5627-5638.
[104] E. A. Carter *et al.*, *Mol. BioSyst.*, 2010, **6**, 1316-1322.
[105] G. Latour, L. Robinet, A. Dazzi, F. Portier, A. Deniset-Besseau, M.-C. Schanne-Klein, *Sci. Rep.*, 2016, **6**, article no. 26344.
[106] S. Roudeau, A. Carmona, R. Ortega, *Curr. Opin. Chem. Biol.*, 2023, **76**, article no. 102372.
[107] G. R. Stephenson, *Bioorganometallic Chemistry. Biomolecules, lebeling, Medecine*, Wiley-VCH Verlag GmbH & Co. KGaA, Hoboken, NJ, 2006, 215-262 pages.
[108] S. Clède, C. Policar, *Chem. - A Eur. J.*, 2015, **21**, 942-958.
[109] S. Clède, F. Lambert, R. Saint-Fort, M.-A. Plamont, H. Bertrand, A. Vessières, C. Policar, *Chem. - A Eur. J.*, 2014, **20**, 8714-8722.
[110] H. C. Bertrand, S. Clède, R. Guillot, F. Lambert, C. Policar, *Inorg. Chem.*, 2014, **53**, 6204-6223.
[111] M. He, H. Y. V. Ching, C. Policar, H. C. Bertrand, *New J. Chem.*, 2018, **42**, 11312-11323.
[112] R. McRae, B. Lai, C. J. Fahrni, *Metallomics*, 2013, **5**, 52-61.
[113] S. Das, A. Carmona, K. Khatua, F. Porcaro, A. Somogyi, R. Ortega, A. Datta, *Inorg. Chem.*, 2019, **58**, 13724-13732.
[114] C. J. Serpell *et al.*, *Nat. Commun.*, 2016, **7**, article no. 13118.
[115] X. Rovira-Clavé *et al.*, *Nat. Commun.*, 2021, **12**, article no. 4628.
[116] Y. Bai *et al.*, *Nat. Commun.*, 2023, **14**, article no. 4013.
[117] R. McRae, B. Lai, S. Vogt, C. J. Fahrni, *J. Struct. Biol.*, 2006, **155**, 22-29.
[118] S. Matsuyama *et al.*, *X-Ray Spectrom.*, 2009, **38**, 89-94.
[119] Y. Chen, T. W. Rees, L. Ji, H. Chao, *Curr. Opin. Chem. Biol.*, 2018, **43**, 51-57.
[120] K. K.-W. Lo, K. K.-S. Tso, *Inorg. Chem. Front.*, 2015, **2**, 510-524.
[121] G. Schanne *et al.*, *Inorg. Chem. Front.*, 2021, **8**, 3905-3915.
[122] S. Nagarajan *et al.*, *Chem. – A Eur. J.*, 2022, **28**, article no. e202104424.
[123] M. D. Hall *et al.*, *J. Struct. Biol.*, 2006, **155**, 38-44.
[124] J. L. Wedding *et al.*, *Metallomics*, 2017, **9**, 382-390.
[125] C. C. Konkankit, J. Lovett, H. H. Harris, J. J. Wilson, *Chem. Commun.*, 2020, **56**, 6515-6518.
[126] J. M. Benyus, *Biomimicry: Innovation Inspired by Nature*, William Morrow, New York, NY, 1997.

ACADÉMIE DES SCIENCES
INSTITUT DE FRANCE

Comptes Rendus. Chimie
2024, Vol. 27, Special issue S2, p. 143-160
https://doi.org/10.5802/crchim.279

Research article

Women Chemists in France in 2024

Adenine, a key player in biology and medicinal chemistry

Alexandra Fillion [a, b], **Sophie Vichier-Guerre** [a] **and Paola Barbara Arimondo** [a, *]

[a] Institut Pasteur, Université Paris Cité, CNRS UMR3523 Chem4Life, Epigenetic Chemical Biology, Department of Structural Biology and Chemistry, 75015 Paris, France

[b] Université Paris Cité, Ecole Doctorale MTCI, Paris, France

Current address: EpiCBio, Institut Pasteur-CNRS UMR3523, Institut Pasteur 28 rue du Dr Roux 75015 Paris, France (P. B. Arimondo)

E-mails: alexandra.fillion@pasteur.fr (A. Fillion), sophie.vichier-guerre@pasteur.fr (S. Vichier-Guerre), paola.arimondo@cnrs.fr (P. B. Arimondo)

Abstract. Adenine is one of the most ubiquitous heterocycles in life. In addition of being one of the four nucleobases constituting DNA and RNA, adenine is also contained in many biological molecules (ATP, SAM, NAD, cAMP, coA…) that have fundamental roles in the functioning of living systems, e.g. energy source, cofactors of enzymes and proteins. As such, the adenine has naturally become a privileged scaffold explored in medicinal chemistry for biomedical applications. Many chemical modifications and Structure-Activity Relationships studies have been carried out on the adenine scaffold to result in potent analogues with various biological activities. Today, numerous adenine-based inhibitors are used to treat a wide range of diseases including cancer, viral and bacterial diseases. This review aims to introduce the adenine and discuss adenine-based inhibitors, their design and use for different therapeutic targets through examples of drugs and compounds that reached clinical and preclinical trials.

Keywords. Adenine, Medicinal chemistry, Inhibitors, Anticancer, Antiviral and antibactirial agents.

Funding. French National Research Priority Plan PPR Antibioresistance (Grant agreement no. AMI-AMR-2020_ANR-20-PAMR-0011) and The French Minister of Higher Education, Research and Innovation.

Manuscript received 1 December 2023, revised and accepted 8 December 2023.

1. Introduction

The purine ring system, and especially *adenine*, is one of the most ubiquitous natural heterocyclic compounds and plays major roles in various biological processes. In addition of being a nucleobase and building block of the genetic material and its transcription and translation in proteins, adenine stores energy in the form of Adenosine TriPhosphate (ATP) and is found in the structure of cofactors of many enzymes such as ATP, *S*-Adenosyl-*L*-Methionine (SAM or AdoMet), Nicotinamide Adenine Dinucleotide (NAD), Flavin Adenine Dinucleotide (FAD) and in substrates of metabolic pathways, as acetyl-Coenzyme A (acetyl-CoA) (Figure 1). ATP is both the source of energy at the cellular level, a precursor to DNA and RNA synthesis and a cofactor of protein kinases to phosphorylate their substrates [1]. SAM is used as methyl donor by MethylTransferases

* Corresponding author

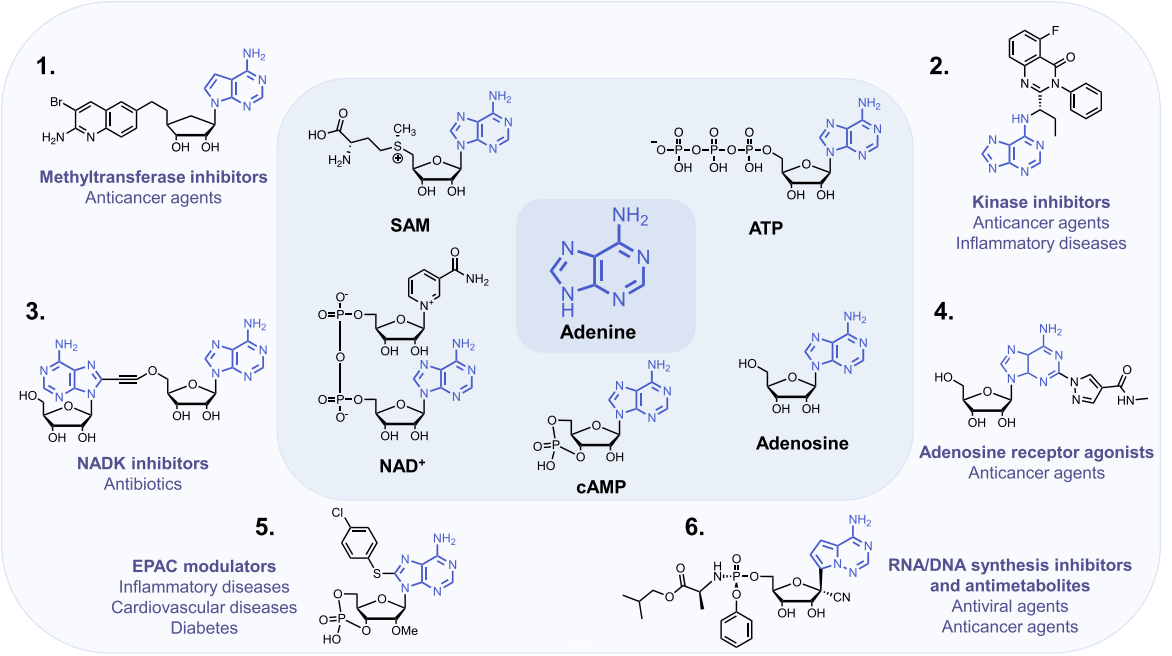

Figure 1. The adenine scaffold (in blue) in biological molecules and therapeutic agents.

(MTases) to methylate histones, DNA, lipids and small biological molecules [2]. NAD^+ is a cofactor for redox reactions and has a central role in energy metabolism. It is also a coenzyme for non-redox NAD^+-dependent enzymes (CD38, sirtuins and poly(ADP-ribose)) and is a substrate for Nicotinamide Adenine Dinucleotide Kinases (NADK) [3]. Some signaling molecules such as cyclic Adenosine MonoPhosphate (cAMP) contain also an adenine scaffold. cAMP is an ubiquitous second messenger that regulates various biological processes, interacting with protein effectors such as Protein Kinase A (PKA), Exchange Proteins Activated by cAMP (EPACs) and Cyclic Nucleotide-Gated (CNG) channels [4].

Importantly, these biological pathways are deregulated in diseases and the aforementioned protein families represent major therapeutic targets. Thus, the adenine scaffold has been exploited to design and develop therapeutic agents [5–7]. Chemical modifications of the adenine scaffold—giving *adenine analogues*—have been carried out to identify inhibitors of these pathways deregulated in diseases. Kinases and MTases inhibitors, based on the adenine scaffold are used for cancer treatment [8,9]. Adenosine analogues inhibiting DNA/RNA synthesis are widely utilized as anticancer and antiviral agents [10,11]. NAD Analogues are investigated to target NADK in the context of bacterial infection [12]. Finally, cAMP analogues are emerging as modulators of EPACs, playing a role in inflammation, diabetes and cardiovascular diseases [13]. Another example is the use of adenosine receptor agonists as anticancer agents [14].

Herein, we review the highlights of the use of the adenine scaffold for the design of versatile therapeutic agents and its role in biological processes. This review is not meant to be exhaustive and presents its chemical modulation in Medicinal Chemistry through chosen examples of approved drugs and inhibitors in clinical trials and preclinical studies for selected therapeutic targets.

2. *S*-Adenosyl-*L*-Methionine/*S*-Adenosyl-*L*-Homocystein (SAM/SAH) analogues to target SAM-dependent methyltransferases

S-Adenosyl-*L*-Methionine is one of the most ubiquitous cofactors. It is mainly used by the SAM-dependent MethylTransferases (MTases) as

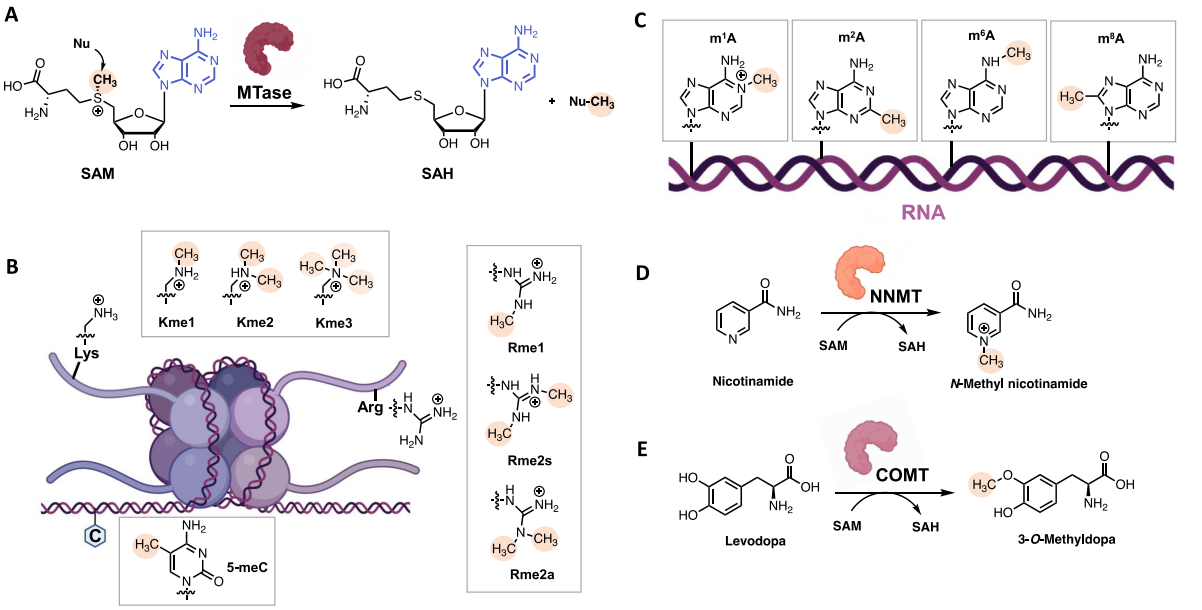

Figure 2. (A) SAM-dependent MTase-catalyzed methylation reaction; (B) examples of methylation products: mammalian histone and DNA methylation by HMTs and DNMTs; (C) examples of adenine methylation on RNA; (D) NNMT-catalyzed methylation of nicotinamide; (E) COMT-catalyzed methylation of Levodopa. (Biorender.com was used to prepare part of the figure.)

methyl donor to methylate their substrates (DNA, RNA, proteins, carbohydrates and metabolites). These methylated substrates contribute for example to the epigenetic regulation, protein function modulation, metabolites synthesis and degradation etc… [15–19].

SAM is a hybrid compound of adenosine bonded to the sulfur atom of methionine. The sulfonium group that bears the methyl group confers the SAM's reactivity. Under the catalytic reaction, the nucleophilic substrate (N-, C-, O- or S-nucleophiles) attacks the electrophilic methyl group through an S_N2-type mechanism generating *S*-Adenosyl-*L*-Homocystein (SAH) as byproduct (Figure 2A) [20,21]. The methyl group transfer happens in the catalytic site of MTase that is composed of two pockets: a SAM binding site and a substrate binding site [15].

SAM-Dependent MTases are a wide and diversified class of enzymes. They can be classified according to their type of substrate. First, Histone MethylTransferases (HMTs) catalyze the transfer of methyl group on lysine and arginine residues of histones and are partitioned into Protein Arginine MethylTransferases (PRMTs) and Lysine MethylTransferases (KMTs) (Figure 2B) [22,23]. Other protein methyltransferases methylate side chains of non-histone proteins [24], especially *N*-Terminal MethylTransferases (NTMTs) have recently raised interest recently [25,26]. Among the DNA MTases, C5 DNA MethylTransferases (DNMTs) catalyze the methylation of C5-position of cytosines (5mC) in DNA (Figure 2B), which plays a major role in human diseases, and for which we and other have developed several inhibitors [27]. Most recently, the biological role of RNA methylation states (as on adenine, Figure 3C) is emergining. Additional MTases are responsible for the methylation of small molecules such as Nicotinamide *N*-MethylTransferases (NNMTs) that methylates nicotinamide and Catechol *O*-MethylTransferases (COMTs) that methylate catecholamines for neurotransmitter degradation [28] (Figure 3D, E).

Due to the plethora of biological functions of MTases but also to their involvement in various diseases, SAM and SAH analogues have been developed and exploited either as MTases inhibitors or as tools to study the functions of MTases [29].

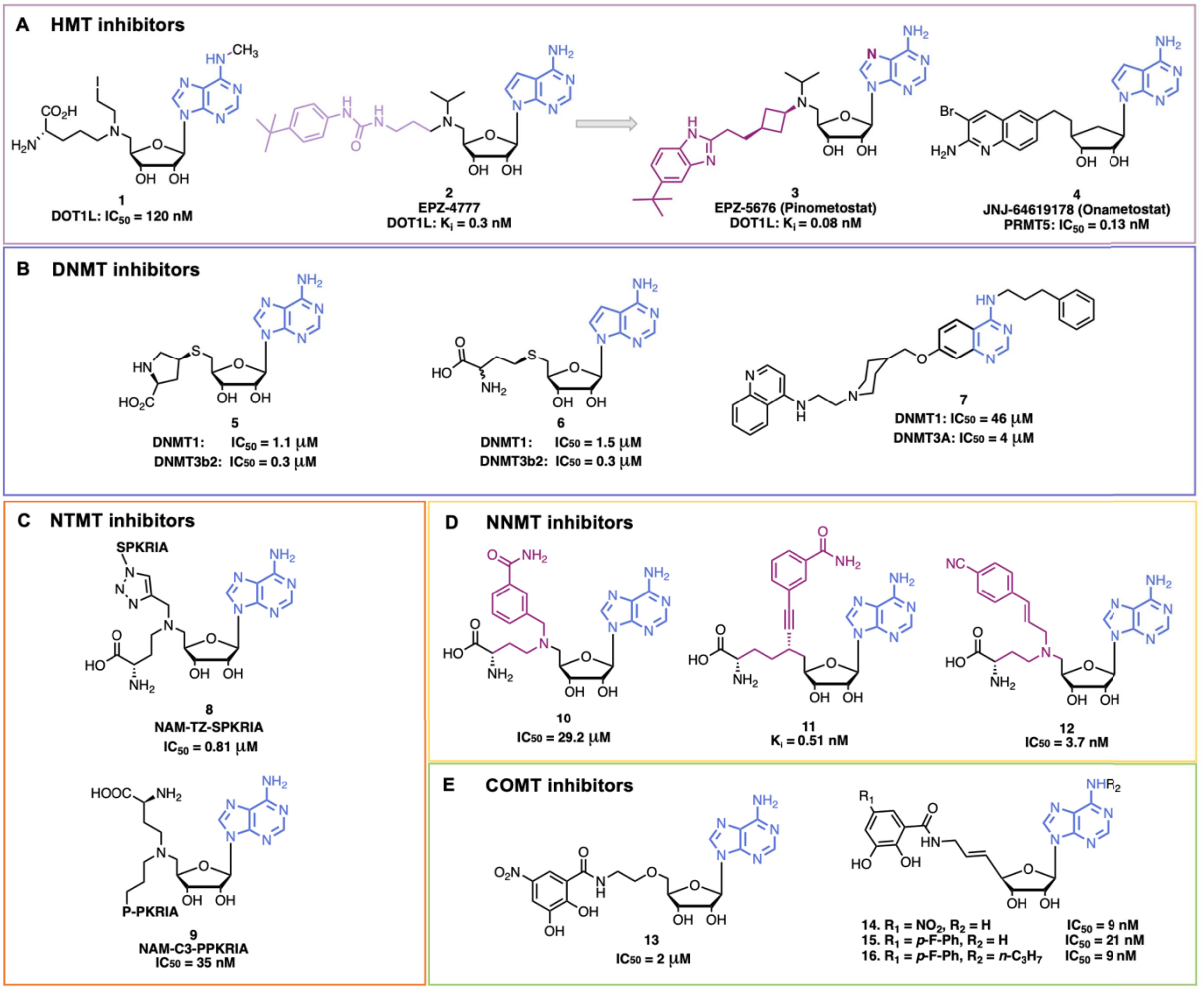

Figure 3. Examples of some SAM/SAH inhibitors. (A) HMT inhibitors; (B) DNMT inhibitors; (C) NTMT inhibitors; (D) NNMT inhibitors; (E) COMT inhibitors.

2.1. *Histone MethylTransferases (HMT) inhibitors*

HMTs are a broad class of enzymes with more than 50 members of KMTs and 9 PRMTs [30]. KMTs catalyze mono- (Kme1), di- (Kme2) or tri- (Kme3) methylation of lysine residues, whereas PRMTs catalyze monomethylation of arginines (Rme1) or dimethylation of arginines (in a symmetrical (Rme2s) or asymmetrical (Rme2a) manner) (Figure 2B). HMTs are involved in various diseases, in particular cancers and infectious diseases, and are thus very interesting therapeutic targets [31–35]. SAM and SAH scaffolds were exploited to develop numerous HMT inhibitors [36]. We chose few examples among the large literature to show the design and application of adenine-based inhibitors (Figure 3).

SAH is an endogenous inhibitor of many MTases and shows, for example, a similar inhibitory potency for PRMT4, G9a and DOT1L ($IC_{50} \approx 1.5$ µM). Hence, co-crystal structures of SAH complexed with different HMTs were exploited to develop HMT inhibitors. DOT1L, the only HMT that catalyzes H3K79 methylation, attracted the interest notably because it is a major target for acute leukemia with Mix Lineage Leukemia (MLL) translocations. Interestingly, DOT1L is a KMT that does not bear the catalytic SET domain but rather shows a similarity in the 3D

structure of the catalytic pocket with the PRMT's one, and exhibits a unique hydrophobic subpocket in the adenosine binding site [37]. Following this rational, Yao et al. designed a potent and selective compound, **1** (Figure 3A), with a methyl substitution on the N6 position of SAH (to protrude interactions in the hydrophobic pocket specific of DOT1L) and the C–S bond of SAH was replaced by a C–N bond (DOT1L, IC_{50} = 120 nM) (Figure 3A) [38]. In 2011, Epizyme Inc. developed a new potent DOT1L inhibitor EPZ-4777, **2**, where the 7-deaza SAM mimics is linked to a bulky 4-*tert*-butylphenyl group to occupy also the substrate pocket (DOT1L, K_i = 0.3 nM ± 0.1) [39,40]. This compound is a SAM competitive inhibitor and the 4-*tert*-butylphenyl group occupies a newly opened hydrophobic subpocket. EPZ-4777 efficiently inhibits the proliferation of MLL-rearranged leukemia cell lines but the poor pharmacokinetic properties of the compound blocked its progress. To improve the pharmacokinetic parameters, a new compound EPZ-5676, **3** (Pinometostat), was developed. In EPZ-5676 the propyl chain of EPZ-4777 is replaced by a *cis*-cyclobutyl ring and the benzimidazole moiety replaces the aryl-substituted urea group. Moreover, the adenosine part of SAM is conserved in EPZ-5676 [41]. The compound is very potent (DOT1L, K_i = 0.08 nM ± 0.03) and is selective towards DOT1L. In addition, EPZ-5676 shows better residence time (>24 h versus 1 h) and entered clinical trials (NCT03701295). Interestingly, since EPZ-4777 weakly inhibits PRMT5 (at 30 μM), it served at starting point for the development of new PRMT5 SAM-competitive inhibitors. After extensive SAR exploration, compound JNJ-64619178, **4** (by Johnson and Johnson), was developed (Figure 3A). It is a bisubstrate inhibitor composed of a 7-deaza SAM mimics and a substituted quinoline moiety, occupying the second substrate binding pocket. JNJ-64619178 is potent (PRMT5, IC_{50} = 0.13 nM) and selective towards PRMT5; it displays favorable pharmacokinetic properties [42] and entered clinical trial notably for the treatment of advanced solid tumors (NCT03573310) [9].

2.2. *DNA MethylTransferases (DNMT) inhibitors*

DNA methylation, mediated by DNMTs, contributes to maintain normal cell function and to embryonic development. DNMT1 catalyzes methylation of newly synthesized DNA strands, while DNMT3A/B are responsible for *de novo* DNA methylation [43]. In humans, DNA methylation mainly takes place on position 5 of cytosine in a CpG dinucleotide context and is generally associated with gene repression when in promoters. Abnormal DNA methylation patterns and alterations in DNMTs activity can induce tumor development and maintenance. DNMTs are thus interesting anticancer targets [27]. Azacitidine (Vidaza™) and Decitabine (Dacogen®), are two DNMT inhibitors approved by the FDA (US Food and Drug Administration) [44,45]. These drugs are cytosine analogues that replace cytosine in DNA, and in RNA for the former. However, they lack selectivity towards CpGs and show poor stability. More recently, a new class of reversible DNMT1-selective inhibitors has been developed by GlaxoSmithKline (GSK), targeting allosteric sites. The compound GSK-3484862 that contains a dicyanopyridine moiety is promising with its low cytotoxicity and great specificity [46,47]. In addition, adenine analogues have been investigated to mimic SAH. MethylGene Inc. performed structural modifications of SAH and showed that substituting the homocystein with a proline mimics confers potent activity (compound **5** in Figure 3B) [48], while the 7-deaza SAH, **6**, showed similar activity as SAH [49]. Finally, DNMT bisubstrate inhibitors with a quinazoline moiety as adenine mimic were developed by our laboratory and others [50–53]. Compound **7** inhibited DNMT3A and DNMT1 at 4 μM and 46 μM respectively (Figure 3B) [54].

2.3. *N-Terminal MethylTransferase (NTMT) inhibitors*

Protein N-Terminal MethylTransferase 1 (NTMT1) methylates the N-terminal amine of proteins and recognizes the canonical motif X-P-K (with X = A, P or S) [55]. Dysregulation of NTMT1 is associated with several cancers and aging processes [56]. NTMT inhibitors have been developed notably to study the biological functions of Nα methylation. A first NMT1 bisubstrate inhibitor NAM-TZ-SPKRIA, **8**, has been developed by Zhang et al. (Figure 3C) [57]. It is composed of 5′-N SAM analogue coupled to an hexapeptide (SPKRIA) via a triazole linker. The compound is very potent (IC_{50} = 0.81 ± 0.13 μM) and shows a 60-fold selectivity over other representative

MTases. Later, Chen et al., developed a new series of NTMT1 bisubstrate inhibitors [58]. With a new synthetic route, they replaced the first serine residue of the SPKRIA peptide by a proline residue giving the NAM-C3-PPKRIA, **9** (Figure 3C), exhibiting an improved potency (IC_{50} = 35 ± 2 nM) and more than 100-fold selectivity over NTMT1 against a panel of MTases. However, the compound showed a poor cell permeability preventing cell-based studies. Nonetheless, this work enabled to obtain the first co-crystal structure of inhibitors with NTMT1 that would help for the development of novel NTMT1 inhibitors.

2.4. *Nicotinamide N-MethylTransferase (NNMT) inhibitors*

NNMT catalyzes methylation of nicotinamide using the SAM cofactor (Figure 2E). NNMT has a major role in cell detoxification and metabolism. Indeed, NNMT can recognize a broad range of substrates (pyridines, quinolines, diverse heterocyclic metabolites) and catalyzes their methylation, which is followed by their excretion [59]. Nicotinamide is also the precursor of NAD^+. Moreover, NNMT balances SAM/SAH ratio that impacts indirectly gene expression [60]. Indeed, it has been reported that NNMT is also involved in the development and progression of cancers, neurodegenerative diseases, diabetes and obesity [61–63]. To better understand the role of NNMT in these diseases, several NNMT inhibitors have been developed, as potent bisubstrate compounds composed of SAM and nicotinamide mimics covalently bound through a linker. In 2017, Van Haren et al. developed the first bisubstrate compound **10** targeting NNMT (IC_{50} = 29.2 ± 4.0 μM) [64], followed by other derivatives [65,66]. In particular, Policarpo et al. synthesized a new potent bisubstrate compound **11** with an increased potency in the namomolar range (K_i = 0.51 ± 0.08 nM) [67]. They figured out that an alkyne linker between the NAM-like and SAM-like fragments was optimal to mimic the transition state geometry. Recently, Gao et al. developed a novel potent bisubstrate compound **12** (IC_{50} = 3.7 ± 0.2 nM) with a *para*-cyano substituted styrene scaffold in the nicotinamide mimic that replaces the common benzamide moiety [68]. However, the compound was not potent in cell-based assays probably due to a poor cell permeability. All these findings help the further design and development of new NNMT inhibitors.

2.5. *Catechol O-Methyltransferases (COMT) inhibitors*

COMT catalyzes methylation of catecholamines (e.g. dopamine and epinephrine) but also of Levodopa (L-dopa) producing 3-*O*-Methyldopa (Figure 2D). L-Dopa is the precursor of dopamine and is used to treat the symptoms of Parkinson Disease (PD) [69]. Administrating COMT inhibitors avoids L-dopa deactivation and prolongs the effects of PD treatment [70]. COMT bisubstrate inhibitors were developed. Based on the crystal structure of COMT with Mg^{2+}, SAM and 3,5-dinitrocatechol, the bisubstrate compound **13** was designed [71]. Compound **13** is a competitive inhibitor of SAM and a non-competitive inhibitor of catechol. The potency was increased by rigidifying the linker with a double bond giving compound **14** (IC_{50} = 9 nM) [72]. To avoid hepatotoxicity, the nitro group was replaced by fluoro-substituted phenyl moiety giving the potent compound **15** (IC_{50} = 21 nM) [73]. Substitution of the OH at position 3 of ribose gave compound **16** (IC_{50} = 9 nM) [74].

3. Adenine scaffold in kinase inhibitors

Protein kinases catalyze the transfer of a γ-phosphate group from ATP to a substrate as for example tyrosine, serine or threonine residues of proteins (Figure 4A). Approximately 538 kinases have been identified in the human genome so far [75]. Kinases play major roles in numerous cellular processes such as cell proliferation, transcription, apoptosis and cell survival. However, they are also involved in the development and progression of numerous diseases, especially cancers but also inflammatory, neurological and cardiovascular diseases [1]. Kinases are thus validated drug targets. Over 70 kinase inhibitors targeting more than 20 different protein kinases have been approved with most of them used for cancer treatment [76]. Kinase inhibitors can be classified according to their binding mode: *Type I inhibitors* are ATP-competitive inhibitors and bind to the active conformation of kinases, *Type II inhibitors* bind to the inactive conformation of kinases, *Type III inhibitors* bind to an allosteric pocket adjacent to

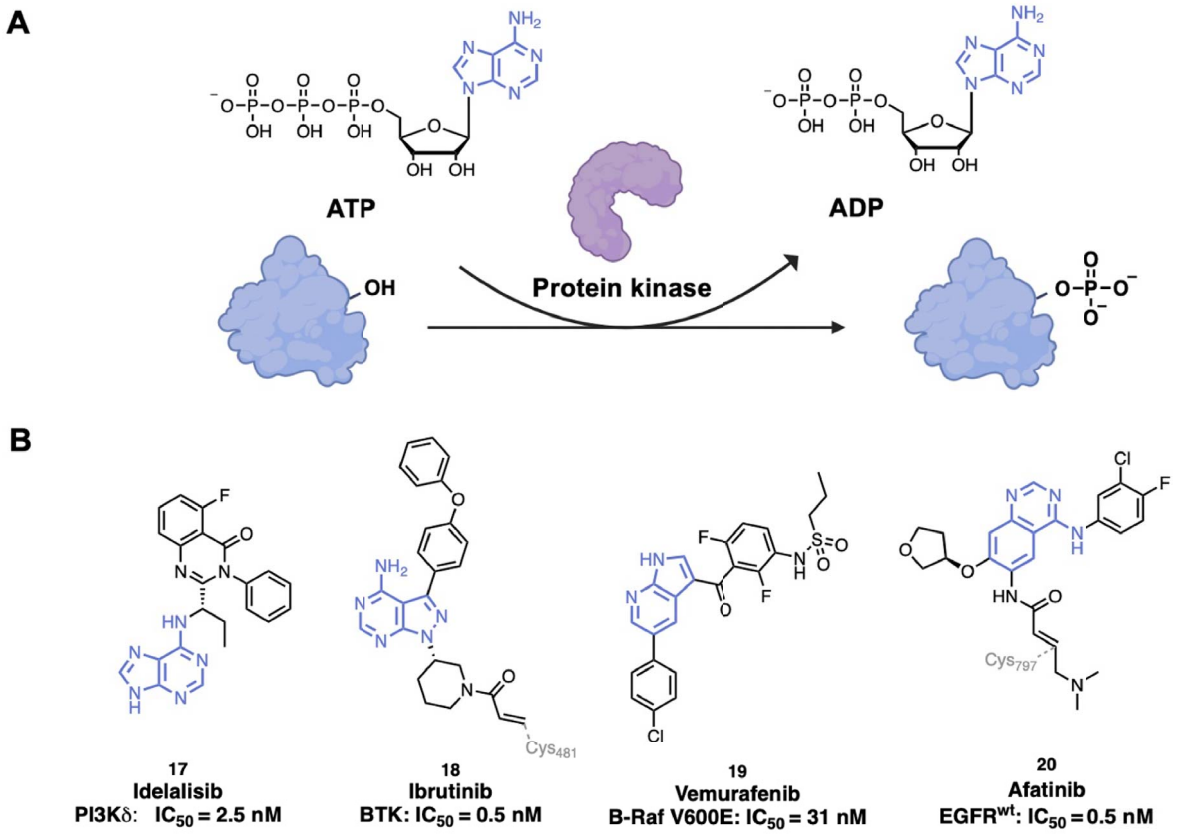

Figure 4. (A) Protein phosphorylation-catalyzed reaction by protein kinases; (B) examples of kinase inhibitors with an adenine analogue scaffold. (Biorender.com was used to prepare part of the figure.)

the ATP-binding pocket and *Type IV inhibitors* bind to an allosteric pocket distant to the ATP-binding pocket [77].

Most of the kinase inhibitors bind to the ATP-binding site. ATP mimics bind making hydrogen bonds to the kinase hinge backbone similarly to the ATP adenine ring [77]. Different chemical scaffolds of adenine analogues are used (Figure 4B). Some of them present the *purine scaffold* that occupies the adenine pocket such as Idelalisib, **17**, (Zydelig®, by Gilead Sciences), a PhosphoInositide 3-Kinase δ (PI3Kδ) inhibitor approved to treat relapsed Chronic Lymphocytic Leukemia (CLL) [78]. Idelalisib establishes a type II binding [79]. The 5-fluoroquinazolinone part binds to an induced hydrophobic specificity pocket and the purine moiety occupies the adenine pocket by forming a key hydrogen bond between the N6 position of the adenine ring and Val828 [80,81]. The *pyrazolo aminopyrimidine scaffold* is also used as adenine mimic in inhibitors such as in Ibrutinib, **18**, (Imbruvica®, by Pharmacyclics Inc.), a Non-Receptor protein Tyrosine Kinase (NRTK) targeting Burton's Tyrosine Kinase (BTK) that was approved to treat mantle cell lymphoma and CLL [82]. Crystallography studies showed that Ibrutinib is an irreversible BTK inhibitor, which covalently binds through Michael addition with Cys481 of BTK [83]. However, some insights on the mechanism of action remain to be understand, as more recently, the determination of the structure of Ibrutinib with SRC (a non-receptor protein tyrosine kinase, PDB ID: 6L8L) showed that Ibrutinib binds *via* a non-covalent manner to the protein [84]. *Pyrrolo pyridine scaffolds* are also used, as in Vemurafenib, **19**, (Zelboraf®, licensed to Roche), an inhibitor of the serine/threonine B-Raf enzyme (member of the Raf kinase family) approved for late-stage melanoma [85]. The structure of Vemurafenib

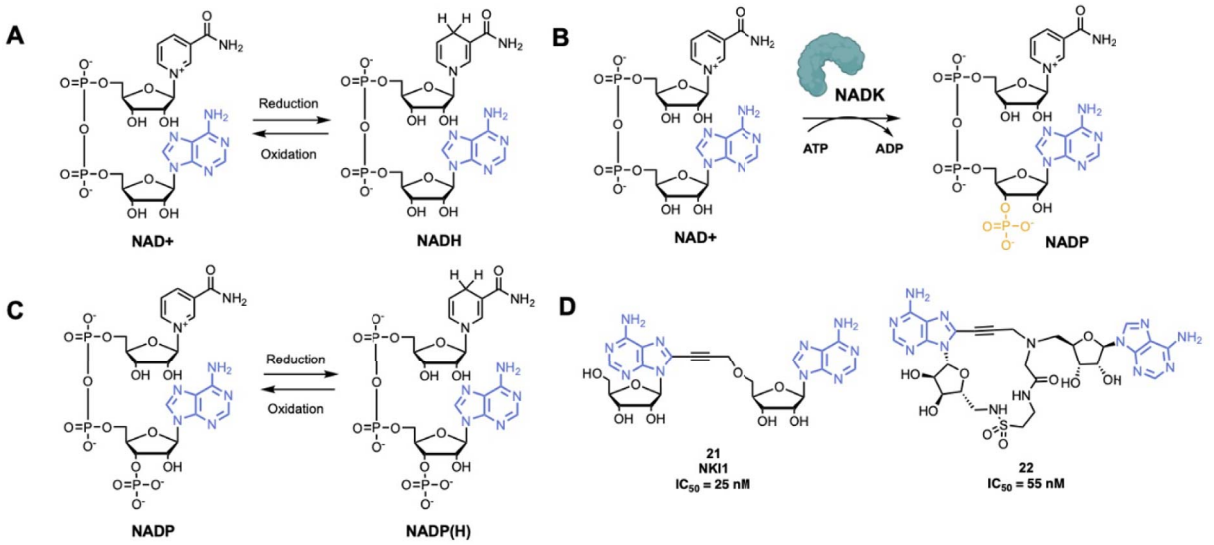

Figure 5. (A) Reduction–oxidation reaction of NAD^+/NADH; (B) NAD^+ phosphorylation-catalyzed reaction by NADK; (C) reduction–oxidation reaction of NADP/NADP(H); (D) examples of NADK inhibitors. (Biorender.com was used to prepare part of the figure.)

complexed with V600E B-Raf, determined by X-ray crystallography (PDB ID: 3OG7), showed a type I inhibition mechanism. The pyrrolo pyridine core of Vemurafenib mimics the adenine core of ATP by forming hydrogen bonds with hinge residue Cys532 and Gln530. Moreover, the sulfonamide moiety interacts through hydrogen bonds to the DFG residues and the 4-chlorophenyl moiety is exposed to the solvent [86]. Since resistance has appeared with mutations in the protein, new inhibitors have been designed (Belvarafenib by Hanmi Pharmaceutical/Genetech and Lifirafenib by Novartis for example) [87]. Kinase inhibitors with a fused six-membered ring system such as a *quinazoline*, *quinoline* or *isoquinoline* moiety are the most used ATP mimics (18 FDA approved inhibitors) [77]. For instance, Afatinib, **20**, (Gilotrif®, by Boehringer Ingelheim), composed of a quinazoline moiety, is an irreversible inhibitor of Human epidermal growth factor receptor 2 (Her2) and Epidermal Growth Factor Receptor (EGFR) kinase. It was the first irreversible kinase inhibitor clinically approved for treatment of Non-Small Cell Lung Carcinoma (NSCLC) [88]. A type I binding mode was shown with co-crystal structures of EGFR-Afatinib (PDB ID: 4G5J) and mutant T790M EGFR-Afatinib (PDB ID: 4G5P). The quinazoline core binds with a conserved hydrogen bond to the hinge residue Met793 [89].

It is worth mentioning that kinase inhibitors are also used to treat non-oncologic diseases such as inflammatory diseases, autoimmune diseases, cardiovascular diseases, diabetes and some neurodegenerative disorders [90]. Noteworthy, some promising kinase inhibitors with as adenine scaffold are currently in preclinical trials for Amyotrophic Lateral Sclerosis (ALS) [91].

4. Nicotinamide Adenine Dinucleotide (NAD) analogues to target Nicotinamide Adenine Dinucleotide Kinases (NADK)

Nicotinamide adenine dinucleotide is an essential cofactor in energy metabolism. NAD is a dinucleotide containing an adenine and nicotinamide linked together through a ribose-phosphodiester backbone (Figure 5A). NAD can be in two forms: in an oxidized form (NAD^+) or in a reduced form (NADH). NADK catalyze the phosphorylation of NAD on the 3′-OH of the adenosine to NADP, which is further reduced to NADP(H) (Figure 5B–C) [92,93]. NADK is the unique enzyme producing NADP *de novo* and is essential to control the balance of NADH and NADP(H) in various metabolic pathways. NADK has crucial roles in

pathogenic bacteria such as *Mycobacterium tuberculosis*, *Staphylococcus aureus*, *Bacillus subtilis* and *Listeria monocytogenes* [12,94–98]. Thus, NADK is a very promising therapeutic target for the development of novel antibiotics [99,100].

A series of adenosine derivatives targeting recombinant *L. monocytogenes* and *S. aureus* NADKs has been recently developed by the group of Pochet [12,101–103]. This work led to the synthesis of the first NADK inhibitor NKI1, **21** (Figure 5D), showing activity in mice infected with *S. aureus* [12]. NKI1 is a dinucleoside of adenosine coupled through a propargyl linker. This linker confers a restricted conformation that is essential for the binding to the NAD-binding site of bacterial NADK. It was suggested that even more constrained compounds would have better affinity and specificity for NADKs [104,105]. Thus, macrocycle compounds were investigated. The potent compound **22** was developed and the macrocyclization was performed by intramolecular amide bond (Figure 5D). Compound **22** is active at 55 nM on recombinant NADK from *L. monocytogenes* (*Lm*NADK1) and represents the best NADK-binder described to date [106].

5. Adenosine analogues as adenosine receptor agonists

Adenosine is a major cell regulator that is involved in numerous physiological processes such as the nervous system, vascular function, immune system, and platelet aggregation. More precisely, adenosine interacts with four G Protein-Coupled Receptors (GPCR) Adenosine Receptors (ARs): A1, A2A, A2B and A3 (Figure 6A) [107,108]. ARs exhibit seven-passed transmembrane α-helix structures, the amino terminus being extracellular and the carboxyl terminus intracellular. Receptors A1 and A3 activate G_i proteins that inhibit the activity of the Adenylyl Cyclase (AC) and consequently reduce the intracellular level of cAMP. On the contrary, receptors A2A and A2B are coupled to G_s proteins that activate AC and induce an increase in the cAMP level. ARs are distributed throughout the body, for example receptors A1 are distributed in the brain, the spinal cord, heart muscles, kidney. Receptors A2A are mainly found in the immune system and the stratum, while receptors A2B are at high concentration in the respiratory pathway. Receptors A3 are located into hippocampus, thalamus, astrocytes, epithelial cells, inflammatory cells etc... [109].

By their role, ARs are involved in various pathological functions in several human diseases as for example in central nervous system disorders, cardiovascular diseases, asthma, and cancer. ARs are thus interesting therapeutic targets and several drugs including agonists, antagonists and allosteric enhancers have been developed and approved. The drugs targeting adenosine signaling pathways are described in a recent review by Kutryb-Zając et al. [14]. A major strategy for the design of agonists of ARs consists in modifying the *N*-6 position of adenine and the 5′-position of ribose.

5.1. *Specific A2A receptor agonist*

Regadenoson, **23** (Lexiscan®), is the only A2A receptor agonist that has been approved by the FDA (Figure 6B). Regadenoson is a pyrazole derivative of adenosine that induces coronaries dilatation by binding to A2A receptors of the coronary arteries [110,111]. Regadenoson is more than 100 times more potent than adenosine as an agonist of A2A receptor. It is used as a stress agent in conjunction with Myocardial Potential Imaging (MPI) for diagnosis of Coronary Artery Disease (CAD). Regarding its therapeutic use, Regadenoson is currently in phase I/II study for the treatment of COVID-19. Indeed, by inhibiting hyperinflammation, Regadenoson could reduce COVID-19 induced lung injury and ameliorate recovery of patients [112].

5.2. *Specific A3 receptor agonists*

The A3 receptor is a promising therapeutic target because it is highly expressed in the skin of psoriasis patients, in inflamed tissues of arthritic patients and in several solid tumor cells (breast, pancreatic, melanoma...) [113–115]. Importantly, A3 agonists inhibit cytokine production and downregulate the NF-κB pathway in cancer and inflamed tissues. Piclidenoson, **24** (Figure 6B), is an adenosine A3 agonist showing anti-inflammatory effects in arthritis and inflammatory bowel disease [116,117]. A phase II study showed that the drug was safe and well-tolerated for patients with rheumatoid arthritis [118]. Piclidenoson was tested in phase III to treat patients with moderate to severe plaque psoriasis (NCT03168256) [119].

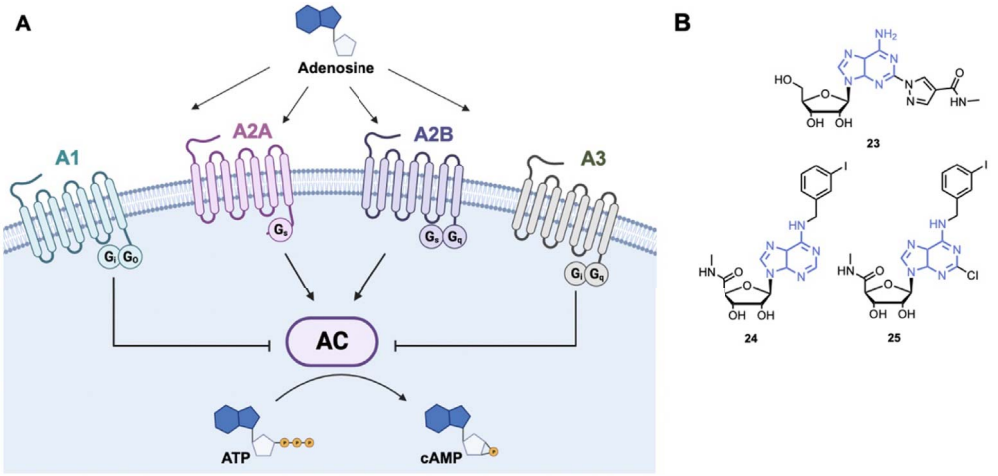

Figure 6. (A) Schematic representation of adenosine signaling; (B) examples of adenosine receptor agonists. AC: Adenylyl Cyclase. (Biorender.com was used to prepare panel A.)

The A3 receptor is also overexpressed in HepatoCellular Carcinoma (HCC) tissues and it has been shown that the A3 agonist Namodenoson, **25** (Figure 6B), inhibits tumor cell growth *in vitro* and *in vivo* [120,121]. Namodenoson is currently in phase III to treat advanced HCC (NCT05201404) [119].

Targeting adenosine receptors has shown promising results, however due to the complexity of the AR signaling and the wide distribution in the body of ARs, only a small amount of adenosinergic drugs have been approved. Development of new drugs is currently explored.

6. cyclic Adenosine MonoPhosphate (cAMP) analogues as Exchange Proteins Activated by cAMP (EPAC) agonist modulators

cAMP is a versatile chemical second messenger that mediates extracellular signals to intracellular responses in most types of cells. Many biological processes are regulated by cAMP such as cell activation, proliferation, migration or apoptosis regulation [122]. The cAMP response is first initiated by primary signaling molecules (hormones, neurotransmitters or prostaglandins) that activate mainly G-Protein-Coupled Receptors (GPCR), which in turn activate adenylyl cyclases (Figure 7A). ACs catalyze ATP cyclization to produce cAMP [123]. There are several intracellular receptors for cAMP, as the Protein Kinase A (PKA) family, EPACs and CNG channels [124–126]. Deregulations in local cAMP signaling has been correlated to various pathophysiological disorders such as cancer, diabetes, cardiac dysfunction and immunological diseases [127–129].

EPACs activate Ras-like small GTPases (Rap1 and Rap2) that are involved in cell-cell adhesion [122,125, 130]. EPAC1 and EPAC2 have been identified as potent targets for several human diseases, as in cancer and cardiovascular diseases, thus small molecules modulating EPAC have been developed. EPAC modulators can be classified into cAMP analogues and non-cyclic nucleotide molecules (for a specific review see Wang et al.) [13]. Here we focused on the cAMP analogues (Figure 7B). cAMP analogues display EPAC agonist activity. Bos et al. first showed that 2′-OH modification increases selectivity EPAC/PKA selectivity. For example, substitution of the 2′-OH by a methoxy group led to compound **26** with about 10- to 60-fold selectivity EPAC/PKA [131]. Then, bulky substitution on adenine at the C8-position gave EPAC agonist **27** with an half-maximal EPAC1 activation at 2.2 μM and about 100-fold EPAC/PKA selectivity [132]. However, compound **27** showed poor membrane penetrating capability. Then, a prodrug, compound **28** (Figure 7B) was developed with esterification of the 4-phosphate group. Compound **28** was over 100-fold more potent than compound **27** and did not affect EPAC/PKA selectivity but acted also as a PhosphoDiEsterases (PDE) inhibitor [133].

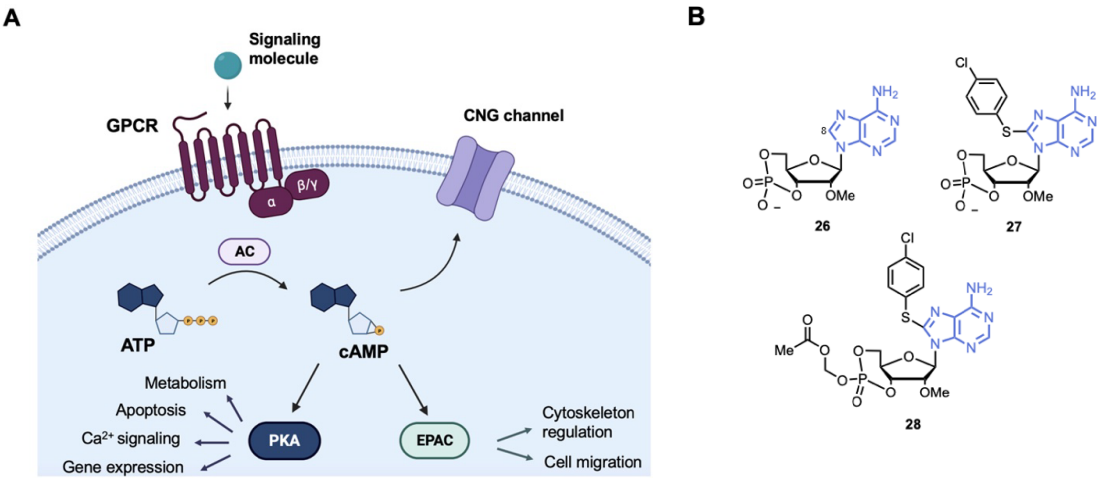

Figure 7. (A) Schematic representation of the intracellular cAMP signaling cascade; (B) examples of cAMP analogues used to target EPACs (Exchange Proteins Activated by cAMP). AC = Adenylyl Cyclase; CNG = Cyclic Nucleotide Gated; PKA = Protein Kinase A. (Biorender.com was used to prepare panel A.)

7. Adenosine analogues as antiviral and anticancer agents

Nucleoside analogues are widely used for antiviral and anticancer therapy by targeting DNA or RNA replication of the virus or the rapidly replicating cancer cells. Nucleoside analogues are mainly "*chain terminators*" and belong to the inhibitors described as anti-metabolites (Figure 8A). After penetration in the cell, the nucleoside analogues are tri-phosphorylated by viral or human cells. The triphosphorylated compounds are then recognized by polymerases and incorporated into the growing DNA/RNA chain. During DNA/RNA chain elongation, the $(n+1)$ nucleoside triphosphate is attached to the 3′-OH of the n terminal nucleotide of the growing chain. The 3′-OH group is thus essential for chain elongation and "*obligate chain terminators*" nucleoside analogues lack the 3′-OH group so that their incorporation consequently results in chain termination [134]. Either the 3′-OH group is substituted with a non-reactive group (–H, –Cl, –F, –Br and $–N_3$ for example) or the deoxyribose is replaced by arabinose derivatives. In general, only few modifications are performed on the nucleobase in order to facilitate the incorporation of the nucleoside analogues as its natural counterpart [135]. Several adenosine analogues are used as "*chain terminators*" for the treatment of cancer or viral infection.

7.1. *Antiviral agents*

One example of chain terminator antiviral agent is Adefovir dipivoxil, **29** (Hepsera®), that was approved by the FDA in 2002 for the treatment of Hepatis B Virus (HBV) (Figure 8B) [136]. It is a ester prodrug of a viral replication terminator Adefovir that blocks the HBV reverse transcriptase and is the prototype of acyclic adenosine phosphonate analogues. The phosphonate bond (–PC–) mimics the 5′-monophosphate of natural nucleotides and enables Adefovir to be phosphorylated by kinases to phosphono-diphosphate form. Adefovir diphosphate competes with the natural substrate dATP and its incorporation results in blockage of the viral polymerase causing chain termination. The phosphonate bond is more stable than the phosphate bond and cannot be cleaved by phosphodiesterases [137]. Based on this efficient strategy, several similar acyclic nucleoside phosphonate compounds have been optimized. In parallel, some nucleoside analogues display a "*delayed chain termination*" mechanism [138]. These compounds exhibit a locked sugar conformation, and after their incorporation in the growing chain, two or three other nucleotides can be further incorporated. Then, due to steric hindrance and displacement of the growing chain in the catalytic site, strand elongation is impeded [134]. This mechanism was developed to avoid exonucleolytic re-

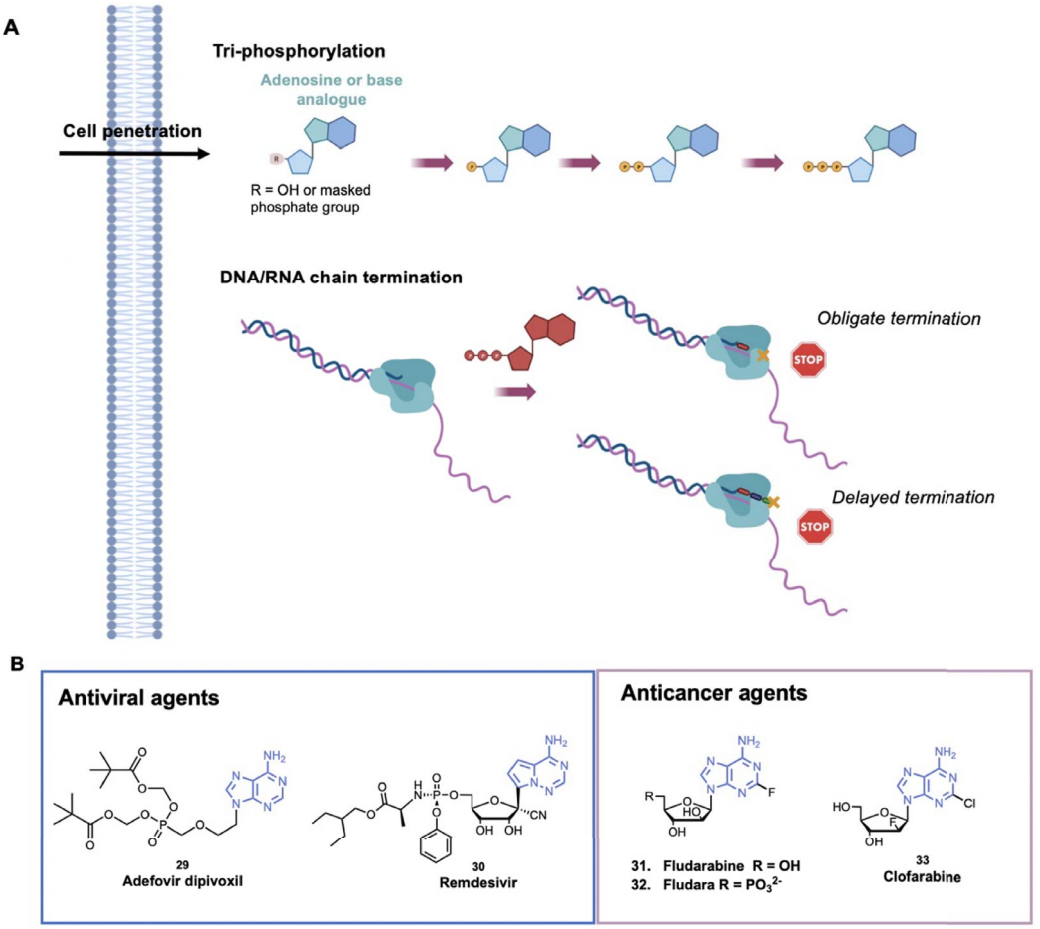

Figure 8. (A) Schematic representation of the main mechanisms of nucleoside analogues to inhibit DNA/RNA synthesis; (B) examples of adenosine analogues as antiviral and anticancer agents. (Biorender.com was used to prepare panel A).

moval of nucleoside analogues. For example, Remdesivir, **30** (Veklury®), is a delayed chain terminator that has been recently approved by the FDA for the treatment of COVID-19 [139,140]. More precisely, Remdesivir is a prodrug of adenosine, the 1′-cyano group avoids the translocation of coronavirus polymerases. According to molecular modeling data, repulsion between the cyano group and S861 in the protein pocket would inhibit the polymerase translocation to position $(n+4)$ [141].

7.2. *Anticancer agents*

Fludarabine, **31** (F-ara-A), was approved by the FDA for the treatment of B-cell chronic lymphotic leukemia (Figure 8B). After cell penetration in its nucleoside form, Fludarabine is triphosphorylated (forming F-ara-ATP) and competes with the natural substrate. Incorporation of F-ara-ATP into DNA by DNA polymerase triggers chain termination [142]. Then, to improve solubility, the 5′-monophosphate derivative, **32** (Fludara®), was designed. Fludara® is then converted into fludarabine by phosphatase (Figure 8B). Clofarabine, **33** (Clolar™, Genzyme), a next-generation deoxyadenosine analogue, was approved by the FDA in 2004 to treat relapsed or refractory Acute Lymphoblastic Leukemia (ALL) (Figure 8B). Clofarabine showed an improved stability in the acidic gastric environment and in plasma, notably thanks to the fluorine group at the 2′-position that

increases its stability at acidic pH. After its triphosphorylation by kinases, Clofarabine competes with the natural dATP for binding to DNA polymerase $-\alpha$ and $-\varepsilon$. At high ratios of Clofarabine/dATP, Clofarabine is inserted into internal and terminal sites of DNA and inhibits DNA elongation [143]. The anticancer activity of Clofarabine is also due to the inhibition of ribonucleotide reductase and induction of apoptosis [144]. These compounds belong to the antimetabolites that are used in the treatment of cancer based on the higher proliferation of the cancer cells, however they target all proliferating cells showing the well-known side effects (e.g. hair loss).

8. Conclusion and perspectives

This review highlights the role of the adenine in the biology of cells and shows through examples the design of adenine-based drugs and their use to treat human diseases, such as cancer, neurological or infectious diseases. The adenine scaffold is involved in many essential biological processes and participate to a broad range of mechanisms, as energy source, cofactor, ... As these mechanisms are aberrant in diseases, they constitute potential targets for treatment and thus the adenosine scaffold is a chemical starting point for the design of drugs in medicinal chemistry. Many chemical modifications have been carried out on the heterocycle moiety and on the side chain giving extensive chemical libraries of adenine derivatives with comprehensive SAR studies. Moreover, it enabled to develop and investigate novel methods in purine synthesis [145–147].

Importantly, membrane permeability and bioavailability remain an issue and many efforts are carried out to improve the pharmacological properties and extend the adenine analogues repertoire and explore adenine prodrugs. For example, adenosine fleximers, in which the purine base is split into two heterocycles connected by a bond allowing rotation, have been developed (Figure 9A) [148]. Thanks to their flexible structure, these derivatives have shown advantages compared to the corresponding purine-base nucleosides, as they can exert new interactions with the protein partner that are not possible with the corresponding nucleoside or their extended structure can give access to new space in the protein pocket [149]. Indeed, the replacement of a guanine by fleximer in Acyclovir greatly improved its biological activity and the ability of the fleximer analogue to adopt the *syn* conformation was able to inhibit efficiently a SAH hydrolase [150]. These compounds have many promising applications in particular for their antiviral activity but also as molecular probes and antitumor agents [150].

Another emerging and promising topic consists of the development of new modified cyclic dinucleotides targeting STimulator of INterferon Genes protein (STING). STING recognizes 2′3′ cyclic GMP-AMP (cGAMP), which is produced by the cyclic GMP-AMP synthase (cGAS) after recognition of cytosolic endogenous or exogenous DNA (Figure 9B) [151]. The STING activation induces a signaling cascade and transcription of antiviral and proinflammatory genes [152]. Several cyclic dinucleotides with adenosine derivatives are developed to activate STING (Figure 9C), by mimicking cGAMP [153]. Such compounds should be further explored and could be used to improve vaccination, control autoimmune disease or treat cancer.

It is worth mentioning that the quinazoline core is also a common mimic of adenine and used more broadly in the design of drugs as we can see in many kinase and DNA methyltransferase inhibitors for example.

Finally, the adenine scaffold is also used to develop fluorescent probes. To confer and modulate fluorescence properties, modifications are mainly carried out on the C8-position of adenine (and few examples with modifications on C2-position) (Figure 9D). By mimicking the natural non-fluorescent adenine, these compounds have many biological applications such as probing the structure of nucleic acids and their interactions with biological molecules [154–156]. Finally, purine chemical libraries are extended with the guanine scaffold that is also used in many biological applications including anticancer and antiviral therapy [5,157].

The interest in the design of analogues of cofactors (SAM, NAD, ...) is increasing for both anticancer, antiviral and antibiotics applications. Interesting, the advances in the technologies to detect RNA modifications (epitranscriptomics) pointed out their role in diseases, increasing the research on the design of analogues to target SAM-based enzymes, ribozymes, deoxyribozymes [158–162].

To conclude, adenine plays a major role in various biological processes but is also involved in processes

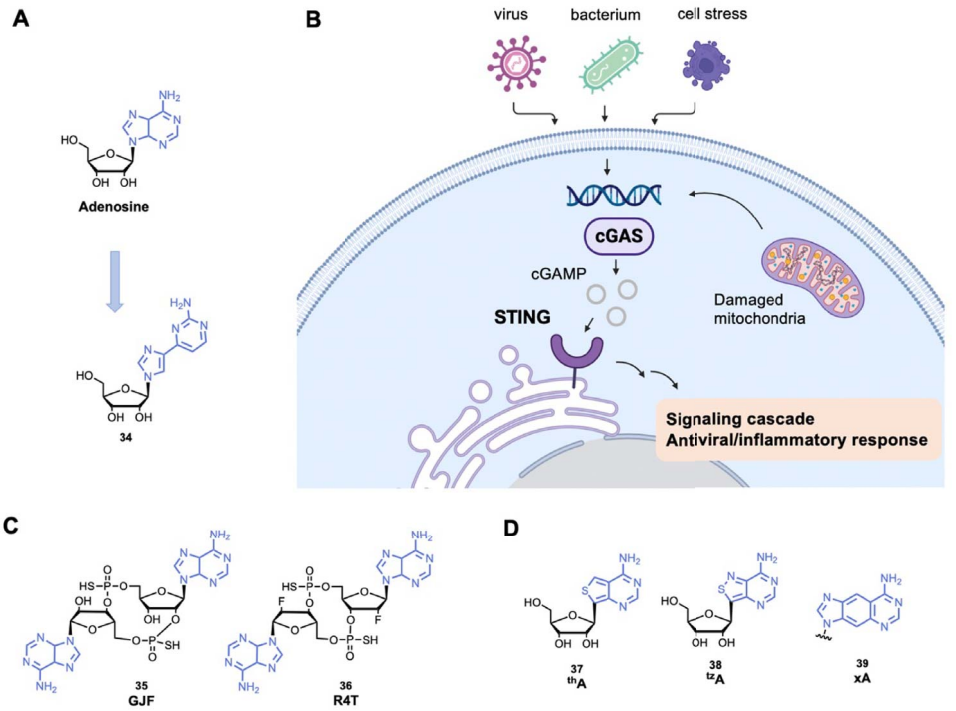

Figure 9. (A) Example of fleximer of adenosine; (B) schematic representation of the STING pathway; (C) examples of cGAMP analogues and (D) examples of adenosine derivatives used as fluorescent probes. (Biorender.com was used to prepare panel B.)

that are aberrant in diseases. Therefore, it is worth continuing to develop new inhibitors based on this scaffold.

Abbreviations

AC	Adenylyl Cyclase
Acetyl-CoA	Acetyl-CoenzymeA
ALS	Amyotrophic Lateral Sclerosis
AR	Adenosine Receptors
ATP	Adenosine TriPhosphate
cAMP	cyclic Adenosine MonoPhosphate
BTK	Burton's Tyrosine Kinase
5mC	5-methylCytosine
CAD	Coronary Artery Disease
CLL	Chronic Lymphocytic Leukemia
CNG	Cyclic Nucleotide-Gated channels
COMT	Catechol *O*-MethylTransferases
DNMT	C5 DNA MethylTransferases
EPAC	Exchange Protein Activated by cAMP
EGFR	Epidermal Growth Factor Receptor
FAD	Flavin Adenine Dinucleotide
FDA	U.S Food and Drug Administration
cGAS	cyclic GMP-AMP Synthase
cGMP	2′3′ cyclic GMP-AMP
GPCR	G-Protein-Coupled Receptors
HBV	Hepatis B Virus
HCC	HepatoCellular Carcinoma
Her2	Human epidermal growth factor receptor 2
HMT	Histone MethylTransferase
KMT	Lysine MethylTransferase
MLL	Mix Lineage Leukemia
MPI	Myocardial Potential Imaging
MTase	MethylTransferase
NAD	Nicotinamide Adenine Dinucleotide
NADK	Nicotinamide Adenine Dinucleotide Kinase
NNMT	Nicotinamide *N*-MethylTransferase
NRTK	Non-Receptor protein Tyrosine Kinase
NSCLC	Non-Small Cell Lung Carcinoma
NTMT	*N*-Terminal MethylTransferases
PDE	PhosphoDiEsterases

PI3Kδ	PhosphoInositide 3-Kinase δ
PKA	Protein Kinase A
PRMT	Protein arginine MethylTransferase
SAH	*S*-Adenosyl-*L*-Homocystein
SAM	*S*-Adenosyl-*L*-Methionine (or AdoMet)
sSAR	Structure-Activity Relationships
STING	STimulator of INterferon Genes protein.

Declaration of interests

The authors do not work for, advise, own shares in, or receive funds from any organization that could benefit from this article, and have declared no affiliations other than their research organizations.

Fundings and acknoweldgements

Authors acknowledge the French National Research Priority Plan PPR Antibioresistance for grant AMI-AMR-2020_ANR-20-PAMR-0011 TheraEPI (to PBA) and The French Minister of Higher Education, Research and Innovation for the ENS Paris Ulm CDSN PhD fellowship to AF.

Biorender.com was used to make parts of Figures graphical abstract, 2, 4, 5, 6, 7, 8 and 9.

References

[1] D. Fabbro, S. W. Cowan-Jacob, H. Moebitz, *Br. J. Pharmacol.*, 2015, **172**, 2675-2700.

[2] Q. Sun, M. Huang, Y. Wei, *Acta Pharm. Sin. B*, 2021, **11**, 632-650.

[3] A. J. Covarrubias, R. Perrone, A. Grozio, E. Verdin, *Nat. Rev. Mol. Cell Biol.*, 2021, **22**, 119-141.

[4] C. Patra, K. Foster, J. E. Corley, M. Dimri, M. F. Brady, *StatPearls*, StatPearls Publishing, Treasure Island (FL), 2023.

[5] X. Lin, C. Liang, L. Zou, Y. Yin, J. Wang, D. Chen, W. Lan, *Eur. J. Med. Chem.*, 2021, **214**, article no. 113233.

[6] S. Man, Y. Lu, L. Yin, X. Cheng, L. Ma, *Drug Discov. Today*, 2021, **26**, 1490-1500.

[7] C. Wang, Z. Song, H. Yu, K. Liu, X. Ma, *Acta Pharm. Sin. B*, 2015, **5**, 431-441.

[8] P. Wu, T. E. Nielsen, M. H. Clausen, *Trends Pharmacol. Sci.*, 2015, **36**, 422-439.

[9] M. Vieito, V. Moreno, A. Spreafico, I. Brana, J. S. Wang, M. Preis, T. Hernández, S. Genta, A. R. Hansen, B. Doger *et al.*, *Clin. Cancer Res.*, 2023, **29**, 3592-3602.

[10] A. A. Zenchenko, M. S. Drenichev, I. A. Il'icheva, S. N. Mikhailov, *Mol. Biol.*, 2021, **55**, 786-812.

[11] J. Shelton, X. Lu, J. A. Hollenbaugh, J. H. Cho, F. Amblard, R. F. Schinazi, *Chem. Rev.*, 2016, **116**, 14379-14455.

[12] M. Gelin, J. Paoletti, M.-A. Nahori, V. Huteau, C. Leseigneur, G. Jouvion, L. Dugué, D. Clément, J.-L. Pons, L. Assairi *et al.*, *ACS Infect. Dis.*, 2020, **6**, 422-435.

[13] P. Wang, Z. Liu, H. Chen, N. Ye, X. Cheng, J. Zhou, *Bioorg. Med. Chem. Lett.*, 2017, **27**, 1633-1639.

[14] B. Kutryb-Zając, A. Kawecka, K. Nasadiuk, A. Braczko, K. Stawarska, E. Caiazzo, P. Koszałka, C. Cicala, *Biomed. Pharmacother.*, 2023, **165**, article no. 115184.

[15] J. Martin, *Curr. Opin. Struct. Biol.*, 2002, **12**, 783-793.

[16] Y. Dor, H. Cedar, *Lancet*, 2018, **392**, 777-786.

[17] Y. Zhou, Y. Kong, W. Fan, T. Tao, Q. Xiao, N. Li, X. Zhu, *Biomed. Pharmacother.*, 2020, **131**, article no. 110731.

[18] X. Zhang, H. Wen, X. Shi, *Acta Biochim. Biophys. Sin.*, 2012, **44**, 14-27.

[19] A. Roberti, A. F. Fernández, M. F. Fraga, *Mol. Metab.*, 2021, **45**, article no. 101165.

[20] E. Abdelraheem, B. Thair, R. F. Varela, E. Jockmann, D. Popadić, H. C. Hailes, J. M. Ward, A. M. Iribarren, E. S. Lewkowicz, J. N. Andexer *et al.*, *ChemBioChem*, 2022, **23**, article no. e202200212.

[21] A. Struck, M. L. Thompson, L. S. Wong, J. Micklefield, *ChemBioChem*, 2012, **13**, 2642-2655.

[22] S. Jahan, J. R. Davie, *Adv. Biol. Regul.*, 2015, **57**, 173-184.

[23] K. Hyun, J. Jeon, K. Park, J. Kim, *Exp. Mol. Med.*, 2017, **49**, article no. e324.

[24] R. Di Blasi, O. Blyuss, J. F. Timms, D. Conole, F. Ceroni, H. J. Whitwell, *ACS Chem. Biol.*, 2021, **16**, 238-250.

[25] R. Huang, *ChemBioChem*, 2019, **20**, 976-984.

[26] K. Diaz, Y. Meng, R. Huang, *Curr. Opin. Chem. Biol.*, 2021, **63**, 115-122.

[27] M. Lopez, J. Gilbert, J. Contreras, L. Halby, P. B. Arimondo, in *DNA Methyltransferases - Role and Function* (A. Jeltsch, R. Z. Jurkowska, eds.), vol. 1389, Springer International Publishing, Cham, 2022.

[28] P. Bastos, T. Gomes, L. Ribeiro, in *Reviews of Physiology, Biochemistry and Pharmacology* (B. Nilius, P. De Tombe, T. Gudermann, R. Jahn, R. Lill, O. H. Petersen, eds.), vol. 173, Springer International Publishing, Cham, 2017.

[29] J. Zhang, Y. G. Zheng, *ACS Chem. Biol.*, 2016, **11**, 583-597.

[30] S. K. Tewary, Y. G. Zheng, M.-C. Ho, *Cell. Mol. Life Sci.*, 2019, **76**, 2917-2932.

[31] M. E. Neganova, S. G. Klochkov, Y. R. Aleksandrova, G. Aliev, *Semin. Cancer Biol.*, 2022, **83**, 452-471.

[32] M. Barbachowska, P. B. Arimondo, *Epigenetics*, 2023, **18**, article no. 2242689.

[33] M. Y. Wang, P. Liow, M. I. T. Guzman, J. Qi, *ACS Chem. Biol.*, 2022, **17**, 744-755.

[34] M. J. G. Eldridge, M. A. Hamon, *PLOS Pathog.*, 2021, **17**, article no. e1010173.

[35] D. Schator, S. Mondino, J. Berthelet, C. Di Silvestre, M. Ben Assaya, C. Rusniok, F. Rodrigues-Lima, A. Wehenkel, C. Buchrieser, M. Rolando, *Nat. Commun.*, 2023, **14**, article no. 2154.

[36] A. Talukdar, A. Mukherjee, D. Bhattacharya, *J. Med. Chem.*, 2022, **65**, 1662-1684.

[37] C. Bon, Y. Si, P. B. Arimondo, in *Histone Modifications in Therapy* (P. Castel-Branco, C. Jeronimo, eds.), vol. 19, Academic Press, 1st ed., 2020, Section II–9, ISBN: 9780128164228.

[38] Y. Yao, P. Chen, J. Diao, G. Cheng, L. Deng, J. L. Anglin, B. V. V. Prasad, Y. Song, *J. Am. Chem. Soc.*, 2011, **133**, 16746-16749.

[39] S. R. Daigle, E. J. Olhava, C. A. Therkelsen, C. R. Majer, C. J.

Sneeringer, J. Song, L. D. Johnston, M. P. Scott, J. J. Smith, Y. Xiao *et al.*, *Cancer Cell*, 2011, **20**, 53-65.
[40] A. Basavapathruni, L. Jin, S. R. Daigle, C. R. A. Majer, C. A. Therkelsen, T. J. Wigle, K. W. Kuntz, R. Chesworth, R. M. Pollock, M. P. Scott *et al.*, *Chem. Biol. Drug Des.*, 2012, **80**, 971-980.
[41] S. R. Daigle, E. J. Olhava, C. A. Therkelsen, A. Basavapathruni, L. Jin, P. A. Boriack-Sjodin, C. J. Allain, C. R. Klaus, A. Raimondi, M. P. Scott *et al.*, *Blood*, 2013, **122**, 1017-1025.
[42] H. Lin, M. Wang, Y. W. Zhang, S. Tong, R. A. Leal, R. Shetty, K. Vaddi, J. I. Luengo, *ACS Med. Chem. Lett.*, 2019, **10**, 1033-1038.
[43] W. Ren, L. Gao, J. Song, *Genes*, 2018, **9**, article no. 620.
[44] E. Kaminskas, A. T. Farrell, Y.-C. Wang, R. Sridhara, R. Pazdur, *Oncologist*, 2005, **10**, 176-182.
[45] S. D. Gore, C. Jones, P. Kirkpatrick, *Nat. Rev. Drug Discov.*, 2006, **5**, 891-892.
[46] M. B. Pappalardi, K. Keenan, M. Cockerill, W. A. Kellner, A. Stowell, C. Sherk, K. Wong, S. Pathuri, J. Briand, M. Steidel *et al.*, *Nat. Cancer*, 2021, **2**, 1002-1017.
[47] Q. Chen, B. Liu, Y. Zeng, J. W. Hwang, N. Dai, I. R. Corrêa, M. R. Estecio, X. Zhang, M. A. Santos, T. Chen *et al.*, *NAR Cancer*, 2023, **5**, article no. zcad022.
[48] L. Isakovic, O. M. Saavedra, D. B. Llewellyn, S. Claridge, L. Zhan, N. Bernstein, A. Vaisburg, N. Elowe, A. J. Petschner, J. Rahil *et al.*, *Bioorg. Med. Chem. Lett.*, 2009, **19**, 2742-2746.
[49] O. M. Saavedra, L. Isakovic, D. B. Llewellyn, L. Zhan, N. Bernstein, S. Claridge, F. Raeppel, A. Vaisburg, N. Elowe, A. J. Petschner *et al.*, *Bioorg. Med. Chem. Lett.*, 2009, **19**, 2747-2751.
[50] C. Bon, L. Halby, P. B. Arimondo, *Epigenomics*, 2020, **12**, 1479-1482.
[51] A. Bouchut, D. Rotili, C. Pierrot, S. Valente, S. Lafitte, J. Schultz, U. Hoglund, R. Mazzone, A. Lucidi, G. Fabrizi *et al.*, *Eur. J. Med. Chem.*, 2019, **161**, 277-291.
[52] D. Rotili, D. Tarantino, B. Marrocco, C. Gros, V. Masson, V. Poughon, F. Ausseil, Y. Chang, D. Labella, S. Cosconati *et al.*, *PLoS One*, 2014, **9**, article no. e96941.
[53] F. Nardella, L. Halby, E. Hammam, D. Erdmann, V. Cadet-Daniel, R. Peronet, D. Ménard, B. Witkowski, S. Mecheri, A. Scherf *et al.*, *ACS Cent. Sci.*, 2020, **6**, 16-21.
[54] L. Halby, Y. Menon, E. Rilova, D. Pechalrieu, V. Masson, C. Faux, M. A. Bouhlel, M.-H. David-Cordonnier, N. Novosad, Y. Aussagues *et al.*, *J. Med. Chem.*, 2017, **60**, 4665-4679.
[55] C. E. Schaner Tooley, J. J. Petkowski, T. L. Muratore-Schroeder, J. L. Balsbaugh, J. Shabanowitz, M. Sabat, W. Minor, D. F. Hunt, I. G. Macara, *Nature*, 2010, **466**, 1125-1128.
[56] R. Huang, *ChemBioChem*, 2019, **20**, 976-984.
[57] G. Zhang, S. L. Richardson, Y. Mao, R. Huang, *Org. Biomol. Chem.*, 2015, **13**, 4149-4154.
[58] D. Chen, G. Dong, N. Noinaj, R. Huang, *J. Med. Chem.*, 2019, **62**, 3773-3779.
[59] M. J. Van Haren, J. Sastre Toraño, D. Sartini, M. Emanuelli, R. B. Parsons, N. I. Martin, *Biochemistry*, 2016, **55**, 5307-5315.
[60] H. Sperber, J. Mathieu, Y. Wang, A. Ferreccio, J. Hesson, Z. Xu, K. A. Fischer, A. Devi, D. Detraux, H. Gu *et al.*, *Nat. Cell Biol.*, 2015, **17**, 1523-1535.
[61] D. Sartini, S. Morganti, E. Guidi, C. Rubini, A. Zizzi, R. Giuliante, V. Pozzi, M. Emanuelli, *Cell Biochem. Biophys.*, 2013, **67**, 865-873.
[62] R. B. Parsons, M.-L. Smith, A. C. Williams, R. H. Waring, D. B. Ramsden, *J. Neuropathol. Exp. Neurol.*, 2002, **61**, 111-124.
[63] D. Kraus, Q. Yang, D. Kong, A. S. Banks, L. Zhang, J. T. Rodgers, E. Pirinen, T. C. Pulinilkunnil, F. Gong, Y. Wang *et al.*, *Nature*, 2014, **508**, 258-262.
[64] M. J. Van Haren, R. Taig, J. Kuppens, J. Sastre Toraño, E. E. Moret, R. B. Parsons, D. Sartini, M. Emanuelli, N. I. Martin, *Org. Biomol. Chem.*, 2017, **15**, 6656-6667.
[65] Y. Gao, M. J. Van Haren, E. E. Moret, J. J. M. Rood, D. Sartini, A. Salvucci, M. Emanuelli, P. Craveur, N. Babault, J. Jin *et al.*, *J. Med. Chem.*, 2019, **62**, 6597-6614.
[66] N. Babault, A. Allali-Hassani, F. Li, J. Fan, A. Yue, K. Ju, F. Liu, M. Vedadi, J. Liu, J. Jin, *J. Med. Chem.*, 2018, **61**, 1541-1551.
[67] R. L. Policarpo, L. Decultot, E. May, P. Kuzmič, S. Carlson, D. Huang, V. Chu, B. A. Wright, S. Dhakshinamoorthy, A. Kannt *et al.*, *J. Med. Chem.*, 2019, **62**, 9837-9873.
[68] Y. Gao, M. J. Van Haren, N. Buijs, P. Innocenti, Y. Zhang, D. Sartini, R. Campagna, M. Emanuelli, R. B. Parsons, W. Jespers *et al.*, *J. Med. Chem.*, 2021, **64**, 12938-12963.
[69] J. P. M. Finberg, *J. Neural Transm.*, 2019, **126**, 433-448.
[70] C. Waters, *J. Am. Geriatr. Soc.*, 2000, **48**, 692-698.
[71] B. Masjost, P. Ballmer, E. Borroni, G. Zürcher, F. K. Winkler, R. Jakob-Roetne, F. Diederich, *Chem. Eur. J.*, 2000, **6**, 971-982.
[72] C. Lerner, B. Masjost, A. Ruf, V. Gramlich, R. Jakob-Roetne, G. Zürcher, E. Borroni, F. Diederich, *Org. Biomol. Chem.*, 2003, **1**, 42-49.
[73] R. Paulini, C. Lerner, R. Jakob-Roetne, G. Zürcher, E. Borroni, F. Diederich, *ChemBioChem*, 2004, **5**, 1270-1274.
[74] M. Ellermann, R. Jakob-Roetne, C. Lerner, E. Borroni, D. Schlatter, D. Roth, A. Ehler, M. G. Rudolph, F. Diederich, *Angew. Chem. Int. Ed.*, 2009, **48**, 9092-9096.
[75] R. R. Naik, A. K. Shakya, *Front. Pharmacol.*, 2023, **13**, article no. 1064472.
[76] R. Roskoski, *Pharmacol. Res.*, 2023, **187**, article no. 106552.
[77] M. M. Attwood, D. Fabbro, A. V. Sokolov, S. Knapp, H. B. Schiöth, *Nat. Rev. Drug Discov.*, 2021, **20**, 839-861.
[78] A. Markham, *Drugs*, 2014, **74**, 1701-1707.
[79] A. Berndt, S. Miller, O. Williams, D. D. Le, B. T. Houseman, J. I. Pacold, F. Gorrec, W.-C. Hon, P. Ren, Y. Liu *et al.*, *Nat. Chem. Biol.*, 2010, **6**, 117-124.
[80] J. R. Somoza, D. Koditek, A. G. Villaseñor, N. Novikov, M. H. Wong, A. Liclican, W. Xing, L. Lagpacan, R. Wang, B. E. Schultz *et al.*, *J. Biol. Chem.*, 2015, **290**, 8439-8446.
[81] P. Wu, Y. Hu, *MedChemComm*, 2012, **3**, 1337-1355.
[82] S. A. Rushworth, D. J. MacEwan, K. M. Bowles, *N. Engl. J. Med.*, 2013, **369**, 1277-1279.
[83] A. T. Bender, A. Gardberg, A. Pereira, T. Johnson, Y. Wu, R. Grenningloh, J. Head, F. Morandi, P. Haselmayer, L. Liu-Bujalski, *Mol. Pharmacol.*, 2017, **91**, 208-219.
[84] M. Guo, S. Dai, D. Wu, Y. Duan, J. Li, L. Qu, L. Jiang, Z. Chen, X. Chen, Y. Chen, *Bioorg. Med. Chem. Lett.*, 2021, **34**, article no. 127757.
[85] G. Kim, A. E. McKee, Y.-M. Ning, M. Hazarika, M. Theoret, J. R. Johnson, Q. C. Xu, S. Tang, R. Sridhara, X. Jiang *et al.*, *Clin. Cancer Res.*, 2014, **20**, 4994-5000.
[86] G. Bollag, P. Hirth, J. Tsai, J. Zhang, P. N. Ibrahim, H. Cho,

W. Spevak, C. Zhang, Y. Zhang, G. Habets *et al.*, *Nature*, 2010, **467**, 596-599.
[87] B. Agianian, E. Gavathiotis, *J. Med. Chem.*, 2018, **61**, 5775-5793.
[88] R. T. Dungo, G. M. Keating, *Drugs*, 2013, **73**, 1503-1515.
[89] F. Solca, G. Dahl, A. Zoephel, G. Bader, M. Sanderson, C. Klein, O. Kraemer, F. Himmelsbach, E. Haaksma, G. R. Adolf, *J. Pharmacol. Exp. Ther.*, 2012, **343**, 342-350.
[90] Z. Xie, X. Yang, Y. Duan, J. Han, C. Liao, *J. Med. Chem.*, 2021, **64**, 1283-1345.
[91] V. Palomo, V. Nozal, E. Rojas-Prats, C. Gil, A. Martinez, *Br. J. Pharmacol.*, 2021, **178**, 1316-1335.
[92] E. T. McGuinness, J. R. Butler, *Int. J. Biochem.*, 1985, **17**, 1-11.
[93] G. Magni, G. Orsomando, N. Raffaelli, *Mini-Rev. Med. Chem.*, 2006, **6**, 739-746.
[94] K. Kobayashi, S. D. Ehrlich, A. Albertini, G. Amati, K. K. Andersen, M. Arnaud, K. Asai, S. Ashikaga, S. Aymerich, P. Bessieres *et al.*, *Proc. Natl. Acad. Sci. USA*, 2003, **100**, 4678-4683.
[95] C. M. Sassetti, D. H. Boyd, E. J. Rubin, *Mol. Microbiol.*, 2003, **48**, 77-84.
[96] R. R. Chaudhuri, A. G. Allen, P. J. Owen, G. Shalom, K. Stone, M. Harrison, T. A. Burgis, M. Lockyer, J. Garcia-Lara, S. J. Foster *et al.*, *BMC Genom.*, 2009, **10**, article no. 291.
[97] C. Mary, M. H. Soflaee, R. Kesavan, M. Gelin, H. Brown, G. Zacharias, T. P. Mathews, A. Lemoff, C. Lionne, G. Labesse *et al.*, *Mol. Cell*, 2022, **82**, 3299-3311, e8.
[98] J. Paoletti, L. Assairi, M. Gelin, V. Huteau, M.-A. Nahori, O. Dussurget, G. Labesse, S. Pochet, *Eur. J. Med. Chem.*, 2016, **124**, 1041-1056.
[99] G. Magni, M. Di Stefano, G. Orsomando, N. Raffaelli, S. Ruggieri, *Curr. Med. Chem.*, 2009, **16**, 1372-1390.
[100] A. Depaix, J. Kowalska, *Molecules*, 2019, **24**, article no. 4187.
[101] G. Poncet-Montange, L. Assairi, S. Arold, S. Pochet, G. Labesse, *J. Biol. Chem.*, 2007, **282**, 33925-33934.
[102] M. Gelin, G. Poncet-Montange, L. Assairi, L. Morellato, V. Huteau, L. Dugué, O. Dussurget, S. Pochet, G. Labesse, *Structure*, 2012, **20**, 1107-1117.
[103] J. Paoletti, L. Assairi, M. Gelin, V. Huteau, M.-A. Nahori, O. Dussurget, G. Labesse, S. Pochet, *Eur. J. Med. Chem.*, 2016, **124**, 1041-1056.
[104] R. Kho, B. L. Baker, J. V. Newman, R. M. Jack, D. S. Sem, H. O. Villar, M. R. Hansen, *Proteins Struct. Funct. Bioinforma.*, 2003, **50**, 589-599.
[105] M. Fujii, Y. Kitagawa, S. Iida, K. Kato, M. Ono, *Bioorg. Med. Chem. Lett.*, 2015, **25**, 5133-5136.
[106] D. A. Clément, M. Gelin, C. Leseigneur, V. Huteau, L. Mondange, J.-L. Pons, O. Dussurget, C. Lionne, G. Labesse, S. Pochet, *Eur. J. Med. Chem.*, 2023, **246**, article no. 114941.
[107] S. Sheth, R. Brito, D. Mukherjea, L. Rybak, V. Ramkumar, *Int. J. Mol. Sci.*, 2014, **15**, 2024-2052.
[108] F. Vincenzi, S. Pasquini, C. Contri, M. Cappello, M. Nigro, A. Travagli, S. Merighi, S. Gessi, P. A. Borea, K. Varani, *Biomolecules*, 2023, **13**, article no. 1387.
[109] A. Saini, R. Patel, S. Gaba, G. Singh, G. D. Gupta, V. Monga, *Eur. J. Med. Chem.*, 2022, **227**, article no. 113907.
[110] K. O. Elkholy, O. Hegazy, A. Okunade, S. Aktas, T. Ajibawo, *Cureus*, 2021, **13**, article no. c12940.
[111] H. Eggebrecht, *Vasc. Health Risk Manag.*, 2008, **4**, 337-340.
[112] J. Rabin, Y. Zhao, E. Mostafa, M. Al-Suqi, E. Fleischmann, M. R. Conaway, B. J. Mann, P. Chhabra, K. L. Brayman, A. Krupnick *et al.*, *PLOS One*, 2023, **18**, article no. e0288920.
[113] P. Fishman, S. Cohen, *Clin. Rheumatol.*, 2016, **35**, 2359-2362.
[114] K. A. Jacobson, S. Merighi, K. Varani, P. A. Borea, S. Baraldi, M. Aghazadeh Tabrizi, R. Romagnoli, P. G. Baraldi, A. Ciancetta, D. K. Tosh *et al.*, *Med. Res. Rev.*, 2018, **38**, 1031-1072.
[115] P. Fishman, S. M. Stemmer, A. Bareket-Samish, M. H. Silverman, W. D. Kerns, *Purinergic Signal.*, 2023, **19**, 513-522.
[116] C. Gallo-Rodriguez, X. Ji, N. Melman, B. D. Siegman, L. H. Sanders, J. Orlina, B. Fischer, Q. Pu, M. E. Olah, *J. Med. Chem.*, 1994, **37**, 636-646.
[117] S. Bar-Yehuda, L. Rath-Wolfson, L. Del Valle, A. Ochaion, S. Cohen, R. Patoka, G. Zozulya, F. Barer, E. Atar, S. Piña-Oviedo *et al.*, *Arthritis Rheumatol.*, 2009, **60**, 3061-3071.
[118] M. David, L. Akerman, M. Ziv, M. Kadurina, D. Gospodinov, F. Pavlotsky, R. Yankova, V. Kouzeva, M. Ramon, M. H. Silverman *et al.*, *J. Eur. Acad. Dermatol. Venereol.*, 2012, **26**, 361-367.
[119] P. Fishman, *Molecules*, 2022, **27**, article no. 3680.
[120] S. Bar-Yehuda, S. M. Stemmer, L. Madi, D. Castel, A. Ochaion, S. Cohen, F. Barer, A. Zabutti, G. Perez-Liz, L. Del Valle, P. Fishman, *Int. J. Oncol.*, 2008, **33**, 287-295.
[121] S. Cohen, S. M. Stemmer, G. Zozulya, A. Ochaion, R. Patoka, F. Barer, S. Bar-Yehuda, L. Rath-Wolfson, K. A. Jacobson, P. Fishman, *J. Cell. Physiol.*, 2011, **226**, 2438-2447.
[122] A. Bhadra, J. L. Hewes, A. Scruggs, C. Zhou, J. Y. Lee, N. Bauer, *Adv. Biol.*, 2021, **5**, article no. 2101064.
[123] M. Kamenetsky, S. Middelhaufe, E. M. Bank, L. R. Levin, J. Buck, C. Steegborn, *J. Mol. Biol.*, 2006, **362**, 623-639.
[124] D. A. Walsh, J. P. Perkins, E. G. Krebs, *J. Biol. Chem.*, 1968, **243**, 3763-3765.
[125] J. De Rooij, F. J. T. Zwartkruis, M. H. G. Verheijen, R. H. Cool, S. M. B. Nijman, A. Wittinghofer, J. L. Bos, *Nature*, 1998, **396**, 474-477.
[126] K. W. Yau, *Proc. Natl. Acad. Sci. USA*, 1994, **91**, 3481-3483.
[127] M. G. Gold, T. Gonen, J. D. Scott, *J. Cell Sci.*, 2013, **126**, 4537-4543.
[128] F. Lezoualc'h, L. Fazal, M. Laudette, C. Conte, *Circ. Res.*, 2016, **118**, 881-897.
[129] A. R. Moore, D. A. Willoughby, *Clin. Exp. Immunol.*, 2008, **101**, 387-389.
[130] H. Rehmann, J. de Rooij, J. L. Bos, in *Handbook of Cell Signaling* (R. A. Bradshaw, E. A. Dennis, eds.), Academic Press, 2nd ed., 2010, Chapter 186, 1525-1529.
[131] A. E. Christensen, F. Selheim, J. De Rooij, S. Dremier, F. Schwede, K. K. Dao, A. Martinez, C. Maenhaut, J. L. Bos, H.-G. Genieser *et al.*, *J. Biol. Chem.*, 2003, **278**, 35394-35402.
[132] J. M. Enserink, A. E. Christensen, J. De Rooij, M. Van Triest, F. Schwede, H. G. Genieser, S. O. Døskeland, J. L. Blank, J. L. Bos, *Nat. Cell Biol.*, 2002, **4**, 901-906.
[133] M. J. Vliem, B. Ponsioen, F. Schwede, W. Pannekoek, J. Riedl, M. R. H. Kooistra, K. Jalink, H. Genieser, J. L. Bos, H. Rehmann, *ChemBioChem*, 2008, **9**, 2052-2054.
[134] P. N. Kamzeeva, A. V. Aralov, V. A. Alferova, V. A. Korshun, *Curr. Issues Mol. Biol.*, 2023, **45**, 6851-6879.
[135] A. J. Berdis, *Front. Mol. Biosci.*, 2017, **4**, article no. 78.
[136] T. M. Dando, G. L. Plosker, *Drugs*, 2003, **63**, 2215-2234.

[137] E. D. Clercq, A. Holý, *Nat. Rev. Drug Discov.*, 2005, **4**, 928-940.
[138] E. P. Tchesnokov, A. Obikhod, R. F. Schinazi, M. Götte, *J. Biol. Chem.*, 2008, **283**, 34218-34228.
[139] C. J. Gordon, E. P. Tchesnokov, E. Woolner, J. K. Perry, J. Y. Feng, D. P. Porter, M. Götte, *J. Biol. Chem.*, 2020, **295**, 6785-6797.
[140] G. Kokic, H. S. Hillen, D. Tegunov, C. Dienemann, F. Seitz, J. Schmitzova, L. Farnung, A. Siewert, C. Höbartner, P. Cramer, *Nat. Commun.*, 2021, **12**, article no. 279.
[141] L. Zhang, D. Zhang, X. Wang, C. Yuan, Y. Li, X. Jia, X. Gao, H.-L. Yen, P. P.-H. Cheung, X. Huang, *Phys. Chem. Chem. Phys.*, 2021, **23**, 5852-5863.
[142] P. Huang, A. Sandoval, E. Van Den Neste, M. Keating, W. Plunkett, *Leukemia*, 2000, **14**, 1405-1413.
[143] A. Zhenchuk, K. Lotfi, G. Juliusson, F. Albertioni, *Biochem. Pharmacol.*, 2009, **78**, 1351-1359.
[144] P. L. Bonate, L. Arthaud, W. R. Cantrell, K. Stephenson, J. A. Secrist, S. Weitman, *Nat. Rev. Drug Discov.*, 2006, **5**, 855-863.
[145] M. Legraverend, *Tetrahedron*, 2008, **64**, 8585-8603.
[146] M. Guinan, C. Benckendorff, M. Smith, G. J. Miller, *Molecules*, 2020, **25**, article no. 2050.
[147] Y. Yoshida, M. Honma, Y. Kimura, H. Abe, *ChemMedChem*, 2021, **16**, 743-766.
[148] K. L. Seley, L. Zhang, A. Hagos, *Org. Lett.*, 2001, **3**, 3209-3210.
[149] K. Seley-Radtke, *Antivir. Chem. Chemother.*, 2018, **26**, article no. 204020661875678.
[150] K. L. Seley-Radtke, C. H. M. Kutz, J. E. Thames, in *Handbook of Chemical Biology Nucleic Acids* (N. Sugimoto, ed.), Springer Nature Singapore, Singapore, 2023.
[151] X. Kong, H. Zuo, H.-D. Huang, Q. Zhang, J. Chen, C. He, Y. Hu, *J. Adv. Res.*, 2023, **44**, 119-133.
[152] A. Decout, J. D. Katz, S. Venkatraman, A. Ablasser, *Nat. Rev. Immunol.*, 2021, **21**, 548-569.
[153] C. Coderch, J. Arranz-Herrero, E. Nistal-Villan, B. De Pascual-Teresa, S. Rius-Rocabert, *Int. J. Mol. Sci.*, 2023, **24**, article no. 9032.
[154] W. Xu, K. M. Chan, E. T. Kool, *Nat. Chem.*, 2017, **9**, 1043-1055.
[155] Y. Saito, R. H. E. Hudson, *J. Photochem. Photobiol. C Photochem. Rev.*, 2018, **36**, 48-73.
[156] D. Dziuba, P. Didier, S. Ciaco, A. Barth, C. A. M. Seidel, Y. Mély, *Chem. Soc. Rev.*, 2021, **50**, 7062-7107.
[157] E. De Clercq, G. Li, *Clin. Microbiol. Rev.*, 2016, **29**, 695-747.
[158] D. Coelho, L. Le Corre, K. Bartosik, L. Iannazzo, E. Braud, M. Ethève-Quelquejeu, *Chem. Eur. J.*, 2023, **29**, article no. e202301134.
[159] V. Meynier, L. Iannazzo, M. Catala, S. Oerum, E. Braud, C. Atdjian, P. Barraud, M. Fonvielle, C. Tisné, M. Ethève-Quelquejeu, *Nucleic Acids Res.*, 2022, **50**, 5793-5806.
[160] T. Okuda, A.-K. Lenz, F. Seitz, J. Vogel, C. Höbartner, *Nat. Chem.*, 2023, **15**, 1523-1531.
[161] A. Bollu, A. Peters, A. Rentmeister, *Acc. Chem. Res.*, 2022, **55**, 1249-1261.
[162] R. Micura, C. Höbartner, *Chem. Soc. Rev.*, 2020, **49**, 7331-7353.

ACADÉMIE DES SCIENCES
INSTITUT DE FRANCE

Comptes Rendus. Chimie
2024, Vol. 27, Special issue S2, p. 161-177
https://doi.org/10.5802/crchim.284

Research article

Women Chemists in France in 2024

Stable and inert manganese complexes for magnetic resonance imaging

Daouda Ndiaye [a] and Éva Tóth [a,*]

[a] Centre de Biophysique Moléculaire, CNRS UPR4301, Université d'Orléans, Rue Charles Sadron, 45071 Orléans, France

Current address: Laboratoire Chimie et Biologie des Métaux, CEA-Grenoble, France (D. Ndiaye)

E-mail: eva.jakabtoth@cnrs-orleans.fr (É. Tóth)

Abstract. Paramagnetic Mn^{2+} complexes are intensively investigated as alternatives to replace the currently used, Gd-based clinical contrast agents in Magnetic Resonance Imaging (MRI). Manganese is an essential metal which alleviates its potential toxicity and the environmental concerns related to the use of Gd^{3+}. Thanks to its five unpaired electrons and slow electron spin relaxation, Mn^{2+} is a very efficient relaxation agent. Given the high doses required for *in vivo* MRI, Mn^{2+} needs to be chelated in thermodynamically stable and kinetically inert complexes, despite its natural presence in the body. We survey here the latest developments in the chemistry and the preliminary *in vivo* MRI evaluation of Mn^{2+} complexes. We specifically focus on the molecular ligand design, including linear, macrocyclic and bicyclic (bispidine) chelators that allowed for substantially enhanced kinetic inertness of the complexes, as well as for ligand selectivity for Mn^{2+} versus the main biological competitor Zn^{2+}. In addition to the +2 form of manganese, Mn^{3+} is also paramagnetic in the high-spin state, with promising relaxation properties among porphyrin complexes. Finally, examples will be presented to demonstrate the first steps towards the development of redox sensors based on the Mn^{2+}/Mn^{3+} switch, detectable in ^{1}H or in ^{19}F MRI.

Keywords. Manganese, MRI contrast agent, Relaxation agent, Bispidine.

Manuscript received 28 November 2023, revised and accepted 15 January 2024.

1. Introduction

Starting with the discovery of X-ray at the end of the 19th century and its immediate application to visualize the inside of the body [1], imaging technologies have revolutionized the way medical doctors work. The imaging field witnessed a spectacular progress from the 1970s, with the introduction of computerized image construction procedures as well as novel technologies based on various physical phenomena, including ultrasound, magnetic resonance or radioactive emission. Imaging has also become a major investigation tool in biological research to understand function and distribution of biomolecules *in vivo* or *in cellulo*. Finally, the pharmaceutical industry is also increasingly integrating imaging into the drug development process, to follow drug biodistribution, metabolic fate or therapeutic effect.

Introduced in the early 1980s, Magnetic Resonance Imaging (MRI) has become a widespread and powerful tool for establishing clinical diagnosis and monitoring therapy. The use of paramagnetic metal complexes as contrast-enhancing agents has greatly contributed to this success [2]. MRI is based on

* Corresponding author

the nuclear relaxation properties of mostly water protons. Paramagnetic (or superparamagnetic) materials can substantially reduce the relaxation rates of surrounding nuclei, thereby improving image contrast between different tissues [3].

Today, clinically approved MRI contrast agents are complexes of the rare earth metal ion gadolinium (Gd^{3+}). With its seven unpaired electrons ($S = 7/2$) and exceptionally slow electron spin relaxation due to a symmetric electron configuration, Gd^{3+} is the most paramagnetic metal ion in the periodic table and a very efficient relaxation agent. Gd^{3+} complexes were considered for a long time as safe drugs which are fully eliminated from the body shortly after their injection. However, since 2006, several Gd^{3+}-related toxicity cases were reported, mostly in kidney-impaired patients presenting slow renal excretion [4]. In this novel, occasionally fatal disease called nephrogenic systemic fibrosis, Gd deposition was detected in the body, originating from the dissociation of the injected agent releasing free, non-complexed Gd^{3+}. This could be directly related to the low kinetic inertness, thus low resistance of the chelates to dissociation. The drug safety agencies in the USA and Europe rapidly responded by the withdrawal of several, less inert chelates and by restricting the use of any Gd^{3+}-based agent in kidney-impaired patients. Long-term accumulation of very small, but detectable amounts of Gd^{3+} has been also observed in various organs of patients, without toxic effects [5]. Lately, the presence of Gd in river and coastal waters due to contrast agent applications is arising as an important environmental pollution issue [6,7]. Altogether, these problems have promoted intensive research in the community of coordination chemists to identify safer alternatives to Gd^{3+} complexes.

Among potential metal ions, Mn^{2+} is the most obvious candidate to replace Gd^{3+} in MRI contrast agent applications [8,9]. In its high-spin state, Mn^{2+} has five unpaired electrons ($S = 5/2$) and slow electron spin relaxation, which are the most critical requirements for a significant relaxation effect. The first relaxation agent used in MRI by Lauterbur was $MnCl_2$ [10], and Mn^{2+} continues to be applied in specific animal experiments to track excitable cells like neurons and cardiac cells where it enters as a Ca^{2+} surrogate (Manganese-Enhanced MRI = MEMRI) [11].

Manganese is an essential metal, having multiple biological roles. Despite the natural presence of manganese in the body, injecting free Mn^{2+} at the typically high MRI contrast agent doses (0.05–0.30 mmol per kg body weight) could be problematic, potentially causing neurotoxicity and Parkinson-like symptoms [12]. Therefore, Mn^{2+} needs to be chelated in stable and inert complexes for *in vivo* applications.

In this context, a great number of novel ligands have been proposed for Mn^{2+} chelation during the last decade [8,13]. Stable and inert complexation of Mn^{2+} is, however, a coordination chemistry challenge. Indeed, in the high spin d^5 electron configuration, Mn^{2+} has no ligand-field stabilization energy, thus its complexes are less stable than those formed with other divalent transition metal analogues, including the most relevant biological competitor Zn^{2+}. The thermodynamic stability of the metal chelates is expressed by the stability constant, $\log K_{ML}$ ($K_{ML} = [ML]/[M][L]$, where the values in brackets correspond to equilibrium concentrations of the complex ML, the metal M and the fully deprotonated ligand L, respectively). Conditional stabilities are often compared for different complexes in order to get rid of the difference in ligand protonation constants. For potential Mn^{2+}-based contrast agents, conditional stability is most commonly expressed with the $pMn = -\log[Mn]$ value, where [Mn] is the equilibrium concentration of free Mn^{2+}, calculated for 10^{-5} M total concentrations of the metal and the ligand each, at pH 7.4 [14]. In addition to the thermodynamic stability, the kinetic inertness, i.e. resistance of the chelate to dissociation, which would lead to the release of free metal ion in biological media, is another important requirement for *in vivo* use. Dissociation of metal complexes typically occurs by acid- and metal-mediated processes. Concerning the metal-catalysis, endogenous metal ions, such as Cu^{2+} or Zn^{2+} are the most important to promote transmetallation, thus Mn^{2+} release [15]. Kinetic inertness is often regarded as even more relevant than high thermodynamic stability, because once the complex is injected into the body, it is not in thermodynamic equilibrium; yet it should stay intact all along its way through the body until full excretion. Mn^{2+} complexes are typically labile, and until very recently, it seemed extremely challenging to attain substantial increase in their kinetic inertness.

For good MRI efficiency, Mn^{2+} complexes need to contain at least one water molecule in their inner coordination sphere which makes high thermodynamic stability and kinetic inertness even more difficult to achieve. The MRI efficiency of a contrast agent is given by its relaxivity (r_1), which is defined as the paramagnetic enhancement of the longitudinal water proton relaxation rate induced by a unity (millimolar) concentration of the probe (the metal ion) [3]. The relaxation effect of the paramagnetic metal complex on the surrounding water protons is governed by two major contributions, called outer and inner sphere relaxivity, both linearly dependent on $S(S+1)$. This implies that relaxivities will be lower for Mn^{2+} ($S = 5/2$) than for Gd^{3+} ($S = 7/2$) complexes provided the other determining parameters are similar [16], thus higher doses might be required for Mn^{2+}-based MRI agents to achieve a similar contrast enhancement effect.

Outer sphere relaxivity arises from dipole–dipole interactions between the electron spin of the metal and the nuclear spin of the water protons diffusing around the complex. The inner-sphere term, which is more interesting since it can be optimized by rational molecular design, is related to water (or proton) exchange between the inner sphere of the metal ion and bulk water. As dipolar interactions are strongly dependent on the distance between the electron and nuclear spins, inner sphere protons experience a much stronger paramagnetic relaxation effect, and this is then transferred to the surrounding water by chemical exchange of the inner sphere water. Inner sphere relaxivity is thus dependent on different structural and dynamic parameters of the complex, such as the number of water molecules directly coordinated to the metal ion (hydration number, q), the rate of exchange of these water molecules with bulk water (k_{ex}), the rotational motion of the complex characterized by the rotational correlation time (τ_R), and the relaxation times of the electron spin of the metal (T_{1e} and T_{2e}). Inner sphere relaxivity is linearly proportional to the hydration number, however, given the relatively low stability of Mn^{2+} complexes, it seems difficult to increase relaxivity by designing bishydrated chelates.

One Mn^{2+} complex was previously approved for clinical contrast agent use (Teslascan®), but later withdrawn. This non-hydrated MnDPDP chelate (DPDP = N,N′-dipyridoxylethylenediamine-N,N′-diacetate-5,5′-bis(phosphate); Scheme 1) is not stable *in vivo*, but releases free Mn^{2+} which is mostly responsible for its relaxation effect. Although no toxicity problems were associated to the use of MnDPDP, it is obvious that today no Mn^{2+} complex with such limited stability could be accepted for human applications.

Beside the 2+ oxidation state, manganese can also exist as a Mn^{3+} cation in aqueous solution, including under biological conditions. High spin Mn^{3+} is also paramagnetic. Although Mn^{3+} has lower electron spin ($S = 4/2$) and typically faster electron spin relaxation than Mn^{2+}, several examples, in particular in the family of Mn^{3+} porphyrin complexes, evidence that this higher oxidation state can also have interesting relaxation properties with potential applications in MRI [17].

In addition, the transformation between the Mn^{3+} and Mn^{2+} forms mediated by biological redox active species can be exploited for the design of redox responsive MRI probes. As the Mn^{3+} and Mn^{2+} states are characterized by different relaxation properties, a redox change will be detectable on the Magnetic Resonance images, and this can report on the redox state of the biological environment [18].

We should also mention that Mn has a positron-emitting radionuclide, ^{52}Mn, with interesting decay features for application in Positron Emission Tomography (PET) ($t_{1/2}$ = 5.6 d, β^+-decay intensity: 29.6%, max. β^+-energy: 575 keV). The relatively long half-life makes ^{52}Mn suitable for the imaging of the slow biodistribution of macromolecules (such as monoclonal antibodies), over periods of days. For PET applications, highly stable and inert Mn chelation is very important to prevent off-target signals originating from released free ^{52}Mn.

The increasing interest in ^{52}Mn is also related to the important advances in bimodal PET/MRI. Mn^{2+} is the only example where a *unique* metal ion offers detection capability in both MRI and PET, which obviously alleviates the chemical design of bimodal PET/MRI agents [19]. Instead of conjugating individual PET and MRI probes, an appropriate isotopic $^{52/nat}Mn$ mixture provides the bimodal PET/MR tracer with ease, ensures that PET and MR reporter complexes are present in a concentration adapted for each imaging modality (PET is $>10^6$ times more sensitive than MRI) and have strictly identical *in vivo* biodistribution.

In overall, for any bioimaging application, Mn^{2+} needs to be chelated in complexes of high thermodynamic stability and kinetic inertness. When MRI applications are concerned, such high stability and inertness of the complex need to be maintained while preserving one inner sphere water molecule to ensure relaxation efficiency. Another feature to consider is the rich redox chemistry of Mn, which implies that the ligand should stabilize the required redox state under biological conditions. To meet all these requirements together, novel ligands have to be designed.

Here, we give an overview of the recent advances in the development of Mn-based potential MR imaging agents. In parallel to the on-going progress in the chemistry of imaging agents, the first steps have also been made towards clinical translation, as two small molecular weight Mn^{2+} chelates passed to Phase 1 human trials as potential extracellular, "general-purpose" MRI probes to replace the current Gd^{3+}-based agents [20,21]. Our objective is not to be exhaustive in this review. We will mainly focus on the chemical design of the ligand in order to tackle the most challenging questions: how to improve the kinetic inertness for the Mn^{2+} complexes and how to achieve selectivity for Mn^{2+} over the main biological competitor Zn^{2+}. While we will select examples from different ligand families including also the design of smart imaging agents, derived from the best chelators, we will survey more closely the latest results obtained with bispidine-type complexes, which brought spectacular progress in these respects. Finally, concerning Mn^{3+} chelates, there is much less data available in the literature, but some recent examples indicate that novel opportunities might be opened in this field.

2. Linear chelators for Mn^{2+} complexation

Mn^{2+} complexes of ethylenediamine-tetraacetate (EDTA) and its derivatives have been known for more than 50 years. These chelates are typically seven-coordinated with one inner sphere water molecule, which made them also interesting early on for paramagnetic relaxation studies [22]. In the context of MRI contrast agent development, derivatization of MnEDTA with hydrophobic moieties such as an ethoxybenzyl (EOB), a benzothiazole-aniline (BTA) or a benzyloxymethyl (BOM) has been more recently reported to target the liver (Mn(EOB-EDTA), Mn(BTA-EDTA)) [23,24] or to induce non-covalent binding to human serum albumin (Mn(EDTA-BOM)) [25] for angiographic imaging (Scheme 1). These modifications influence the biological fate of the complexes, but have limited impact on their thermodynamic stability or kinetic inertness, and in particular, this latter remains relatively low. The relaxivity is slightly increased for Mn(EDTA-BOM) or Mn(EDTA-BOM_2) complexes (3.60 and 4.30 $mM^{-1}\cdot s^{-1}$, 20 MHz, 25 °C) [25] versus MnEDTA (3.00 $mM^{-1}\cdot s^{-1}$) [25], in accordance with the increased molecular size.

The most important developments in this family concern the rigidification of the ligand skeleton in the objective of improving kinetic inertness. Several design elements have been tested in this direction. First of all, the ethylene backbone was replaced with considerably less flexible moieties such as a cyclohexane, a benzene or a pyridine ring, and this led to improved resistance to complex dissociation. The effect of rigidity was first demonstrated by comparing the kinetic inertness of MnEDTA and Mn(*t*-CDTA) (*t*-CDTA = *trans*-1,2-diaminocyclohexane-N,N,N′,N′-tetraacetate; Scheme 1) in Cu^{2+} exchange reactions [26]. These evidenced a two orders of magnitude slower proton-assisted dissociation for Mn(*t*-CDTA), resulting in a dissociation half-life of $t_{1/2}$ = 12 h estimated for physiological conditions, versus 0.076 h for MnEDTA (pH 7.4 and 10^{-5} M Cu^{2+} concentration). The two stereoisomer forms of the cyclohexane-based CDTA ligand, the *trans t*-CDTA and the *cis c*-CDTA provide a different coordination cage for metal complexation; it is considerably larger for *t*-CDTA with a maximum distance of 4 Å between the two nitrogen atoms, as compared to 3.1 Å for *c*-CDTA [27]. Yet, DFT calculations indicate only minor differences in the metal coordination environments in the solution structures, with bond distances differing in less than 0.035 Å. The DFT results suggest remarkably higher stability for the *trans* than for the *cis* analogue, with an energy difference of 35.4 $kJ\cdot mol^{-1}$. This was linked to the more strained geometry of the ligand in the *cis*- than in the *trans*-stereoisomer in accommodating the relatively large Mn^{2+} ion [28]. Experimental data confirm these findings. Although the thermodynamic stability constants for Mn(*c*-CDTA) and Mn(*t*-CDTA) are similar ($\log K_{MnL}$ values are 14.19 and 14.32, respectively), the

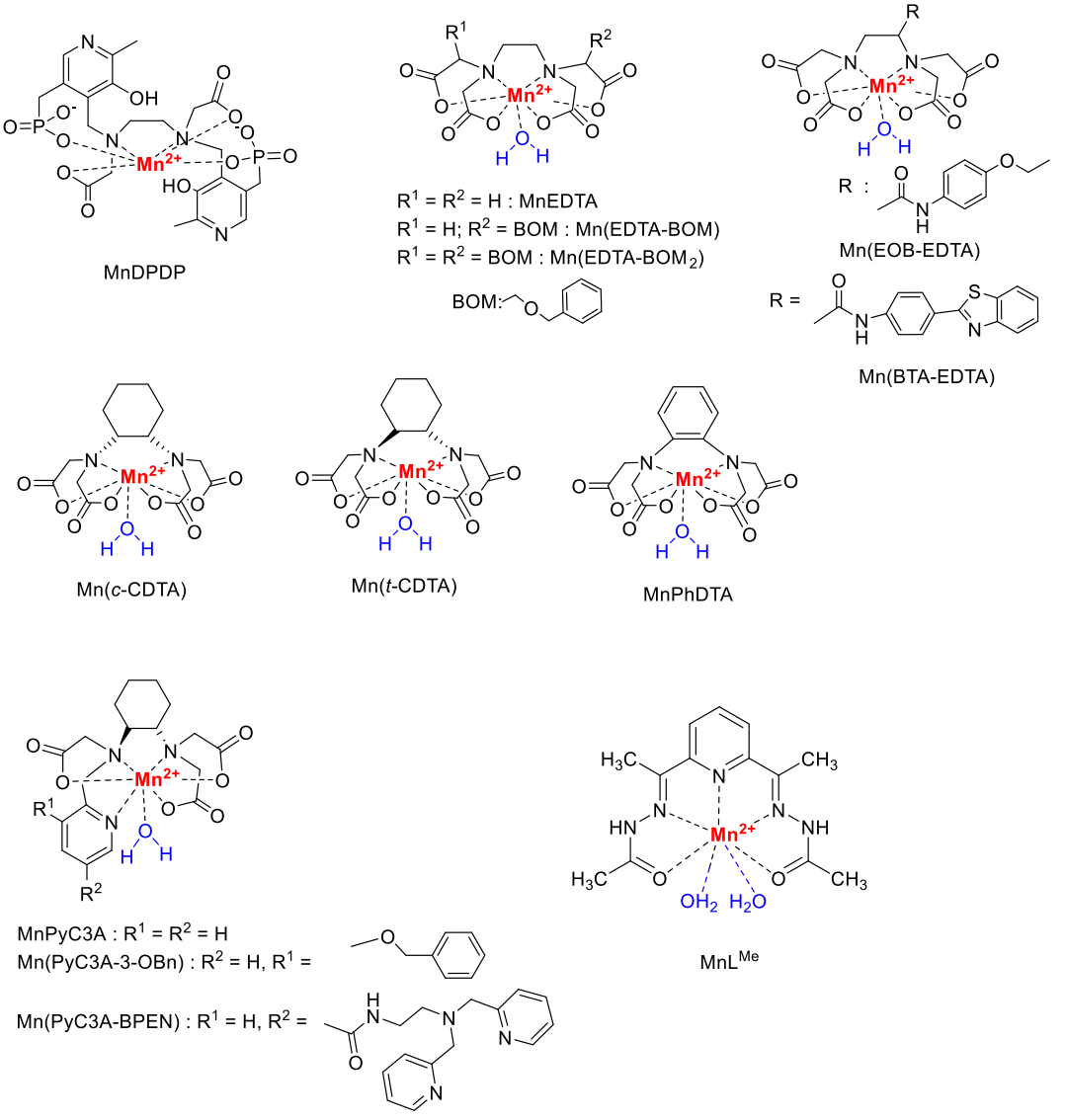

Scheme 1. Mn^{2+} complexes formed with linear ligands.

conditional stability as expressed by the pMn value is higher for Mn(*t*-CDTA) (8.68 versus 7.82; $c_L = c_{Mn} = 10^{-5}$ M, pH 7.4). The most striking difference is in the kinetic inertness of the complexes, the *trans*-isomer being 250 times more inert than the *cis*-analogue, as it was assessed in Cu^{2+} transmetalation reactions [28]. The *t*-CDTA was then used for the development of a bifunctional chelator, and the Mn^{2+} complex was evaluated with respect to its MRI properties [29].

The kinetic inertness is further improved with the PhDTA ligand, where an aromatic benzene ring rigidifies the molecular skeleton (PhDTA = *o*-phenylenediamine-N,N,N′,N′-tetraacetate; Scheme 1). The dissociation half-life of MnPhDTA is estimated to be $t_{1/2}$ = 19 h at pH 7.4 [30]. On the other hand, the conditional stability constant (pMn = 8.16) and the relaxivity (3.72 $mM^{-1}{\cdot}s^{-1}$; 20 MHz, 25 °C) remain similar to those of Mn(*t*-CDTA). Other ligands containing a pyridine in their backbone were

also investigated, however, these ligands did not lead to improved inertness of the Mn^{2+} complexes [31].

Amphiphilic anionic *t*-CDTA derivatives have been recently reported for specific uptake by hepatocytes through one or two bi-directional transmembrane Organic Anion Transporting Polypeptide (OATP) transporters. The complexes have been characterized through relaxivity measurements, *in vivo* liver imaging in mice, and quantitation of *in vitro* cell uptake through ectopically expressed human OATP1 transporters [32].

The group of Caravan developed the N-picolyl-N,N′,N′-trans-1,2-cyclohexylenediaminetriacetate (PyC3A; Scheme 1) ligand by further rigidifying *t*-CDTA by the substitution of one carboxylate with a pyridine. MnPyC3A was proposed in 2015 as an extracellular contrast agent alternative to Gd^{3+}-based contrast agents [33], and it reached Phase 1 human studies in 2022 [20]. MnPyC3A is endowed with good thermodynamic and conditional stability ($\log K_{MnL}$ = 14.14 and pMn = 8.17), and its kinetic inertness exceeds that of the clinical contrast agent GdDTPA; in the presence of 25-fold excess of Zn^{2+}, pH 6, 37 °C, the dissociation is 20-times faster for GdDTPA than for MnPyC3A. The relaxivity of MnPyC3A is 3.3 $mM^{-1}\cdot s^{-1}$ (20 MHz, 25 °C), in coherence with its molecular size and monohydrated nature, and it is slightly increased in serum due to moderate interaction with serum proteins.

Thanks to its slightly lipophilic structure, MnPyC3A undergoes combined hepatobiliary and renal excretion, and no *in vivo* degradation was detected for the complex. MR Imaging evaluation of this potential contrast agent has been realized in various animal models with side-by-side comparison to clinical agents. In a nonhuman primate model, MnPyC3A provided signal enhancement in arteries versus muscle which was comparable to GdDTPA in a standard dynamic MR angiography protocol [34]. Pharmacokinetics was also found comparable to that of clinically used extracellular Gd-based agents [34]. In rat models of breast cancer and metastatic liver disease, it was found to be equally efficient to delineate tumors as the clinical Gd^{3+} probes [35]. MnPyC3A was recently tested in pigs for tissue characterization of acute myocardial infarction, and it appeared to be equally effective as gadolinium-based agents for the assessment of myocardial infarction location and size [36].

Several liver-specific probes have been also derived from MnPyC3A. In a family of nine complexes, a lead compound substituted with a benzyloxy-moiety on the pyridine was retained based on its high relaxivity, rapid blood clearance and avid hepatocellular uptake, the two latter properties directly correlated with the log*P* values [37]. Injection of this lead Mn(PyC3A-3-OBn) complex (Scheme 1) into a mouse model with colorectal liver metastasis resulted in excellent tumor visualization as hypointense spots.

MnPyC3A was conjugated to bis-pyridyl-ethylamine (BPEN), the well-known Zn^{2+}-binding moiety, to derive a responsive agent for the *in vivo* detection of Zn^{2+}released in different mouse tissues, in particular to image β-cell function in the pancreas and glucose-stimulated zinc secretion in the prostate [38]. Mn(PyC3A-BPEN) (Scheme 1), like previously reported Gd-based zinc-responsive agents based on BPEN, shows only a modest r_1 increase in the presence of Zn^{2+} alone, but when Human Serum Albumin (HSA) is also present, a ternary Mn(PyC3A-BPEN)-Zn-HSA complex forms with significantly enhanced relaxivity, allowing for Zn^{2+} detection. Interestingly, the presence of the BPEN unit was found to improve the kinetic inertness of the complex toward transmetalation by Zn^{2+} and transchelation by HSA. Biodistribution and excretory characterization studies indicated that Mn(PyC3A-BPEN) is eliminated from mice without dissociation, by combined renal and hepatobiliary pathways.

Stasiuk and collaborators reported a pentadentate Schiff-base type Mn^{2+} complex, MnL^{Me} which was obtained in a single-pot template reaction [39] (Scheme 1). In solution, this chelate has two inner sphere water molecules, and correspondingly elevated proton relaxivity which further increases in the presence of serum albumin (r_1 = 5.7 $mM^{-1}\cdot s^{-1}$ and 21.1 $mM^{-1}\cdot s^{-1}$, respectively, 298 K, 20 MHz). The inertness of this complex might be insufficient for further development. In the presence of 25-fold excess of Zn^{2+} at pH 6.4, MnL^{Me} was found to fully dissociate in ~10 min. After injection of MnL^{Me} in a clinical dose (0.1 $mmol\cdot kg^{-1}$) in a healthy mouse, urine samples were collected and analyzed by LC-MS, showing that at 40 min post injection, 24% of the applied MnL^{Me} was excreted into the bladder in an intact form.

3. Macrocyclic chelators for Mn^{2+} complexation

A great number of macrocycles of different sizes and bearing various coordinating functions have been investigated for Mn^{2+} complexation in the last two decades. The most important studies involve 9-, 12- and 15-membered azamacrocycles and aza- or aza-oxa crown ethers, many of these have been recently reviewed [13]. We will only focus on 12-membered rings, based either on the cyclen or on the pyridine-containing pyclen macrocycle.

MnDOTA (DOTA = 1,4,7,10-tetraazacyclododecane-1,4,7,10-tetraacetate) is known for a long time to be very stable and highly inert [15,40], however, with eight coordinating functions from the ligand, there is no space for inner sphere water in this complex, which limits its relaxation efficacy to an outer sphere effect. One has to remove at least two carboxylates from DOTA to allow for inner sphere water coordination in the Mn^{2+} complexes. Interestingly, for MnDO2A chelates, the hydration state depends on the position of the two carboxylate functions. A combined ^{17}O NMR, NMRD (Nuclear Magnetic Relaxation Dispersion) and DFT study indicated a hydration equilibrium between nonhydrated ($q = 0$) and monohydrated ($q = 1$) species in solution, with clear prevalence of the monohydrated form for Mn(1,4-DO2A) (average q is 0.9), while Mn(1,7-DO2A) was essentially non-hydrated (1,4-DO2A = 1,4,7,10-tetraazacyclododecane-1,4-diacetate; 1,7-DO2A = 1,4,7,10-tetraazacyclododecane-1,7-diacetate; Scheme 2) [41]. In accordance with this, proton relaxivities amount to 2.1 $mM^{-1}{\cdot}s^{-1}$ for Mn(1,4-DO2A) and to 1.5 $mM^{-1}{\cdot}s^{-1}$ for Mn(1,7-DO2A) (25 °C, 30 MHz). It is surprising that despite this difference in the coordination mode, the thermodynamic stabilities and the kinetic inertness of the two isomers are comparable [42]. A detailed transmetalation study of the complexes with Zn^{2+} or Cu^{2+} ions revealed that the dissociation proceeds primarily by acid catalysis, and metal-assisted pathways are negligible. The complexes are about 20 times more labile than MnDOTA, with dissociation half-lives of 48.3 h (Mn(1,4-DO2A)) and 56.8 h (Mn(1,7-DO2A)) estimated for pH 7.4, to be compared to 1061 h for MnDOTA. 1,4-DO2A was further functionalized with long aliphatic C12 and C16 chains on the secondary amines to promote micellization in solution [43]. For the corresponding Mn^{2+} chelates, this leads to important decrease in the rotational motion, with a concomitant enhancement of the proton relaxivity, up to seven-fold at 30 MHz, where rotation is an important factor for relaxivity [(r_1 = 15.3 $mM^{-1}{\cdot}s^{-1}$ for the Mn(1,4-DO2A)-$(C16)_2$ derivative with two C16 chains, 298 K (Scheme 2)].

The incorporation of a pyridine into the 12-membered cyclen macrocycle also rigidifies the molecules, as in the case the linear chelators. Monofunctionalization of this pyclen cycle with one acetate (PC1A = 6-carboxymethyl-3,6,9,15-tetraazabicyclo[9.3.1] pentadeca-1(15),11,13-triene) or one methylenephosphonate group (PC1P = 6-dihydroxyphosphorylmethyl-3,6,9,15-tetraazabicyclo[9.3.1] pentadeca-1(15),11,13-triene) results in Mn^{2+} complexes which are six-coordinate with one inner sphere water (Scheme 2), but they do not have sufficient thermodynamic and redox stability, nor kinetic inertness [44]. Two acetate functions were introduced on the pyclen either at the 3,6 or at the 3,9 positions (3,6-PC2A and 3,9-PC2A, respectively, Scheme 2), and the corresponding Mn^{2+}complexes were compared in a detailed physical-chemical study [45]. In contrast to the DO2A analogues, there is no difference in the hydration state of the Mn(3,6-PC2A) and Mn(3,9-PC2A) chelates, which are both monohydrated, as evidenced by ^{17}O chemical shifts and relaxation rates. The relaxivities are also similar, and typical of small monohydrated chelates (2.72 and 2.91 $mM^{-1}{\cdot}s^{-1}$, for Mn(3,6-PC2A) and Mn(3,9-PC2A), respectively, 298 K, 0.49 T). The regioisomer Mn(3,9-PC2A) with the two acetate groups in *trans* position is endowed with a slightly higher thermodynamic stability constant than Mn(3,6-PC2A) ($\log K_{MnL}$ = 17.09 versus 15.53, respectively) and conditional stability (pM = 8.64 versus 8.03; $c_L = c_{Mn} = 10^{-5}$ M, pH 7.4), while kinetic inertness is better for Mn(3,6-PC2A), as shown by the longer dissociation half-life calculated ($t_{1/2}$ = 63.2 h versus 21.0 h for Mn(3,6-PC2A) and Mn(3,9-PC2A), respectively; pH 7.4). Interestingly, DFT calculations showed important differences in some nitrogen-Mn distances between the two isomers, indicating more steric strain for Mn(3,6-PC2A), which might be the reason for its lower stability. In overall, both chelates satisfy the requirements of good stability and inertness.

The symmetrical 3,9-PC2A has been chosen for the design of various molecular imaging

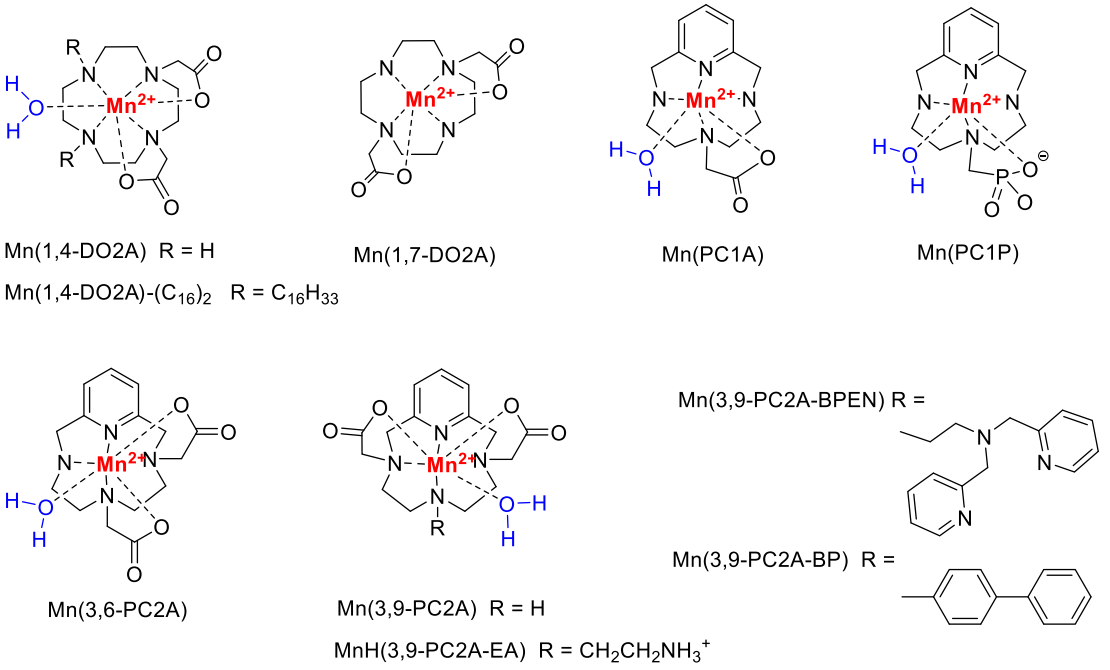

Scheme 2. Mn^{2+} complexes formed with macrocyclic ligands.

agents. The pH-responsive probe Mn(3,9-PC2A-EA) (Scheme 2) [46] undergoes protonation on the ethyleneamine side-chain with logK_a of 6.88 which can thus coordinate/decoordinate to/from the metal ion as a function of its protonation state. As a consequence, the hydration number, thus the relaxivity of Mn(3,9-PC2A-EA) increases from $q = 0$ and $r_1 = 2.04$ $mM^{-1}{\cdot}s^{-1}$, respectively, at pH 8.4 to $q = 1$ and $r_1 = 3.54$ $mM^{-1}{\cdot}s^{-1}$ at pH 6.0 (0.49 T, 25 °C). By attaching the BPEN Zn^{2+} sensitive unit to 3,9-PC2A, the Zn^{2+}-responsive probe Mn(PC2A-BPEN) was prepared (Scheme 2) [47]. This probe functions according to a similar mechanism described above for Mn(PyC3A-BPEN) by forming a ternary complex with Zn^{2+} and HSA, accompanied by a relaxivity increase. Mn(PC2A-BPEN) could be used to visualize glucose-stimulated Zn^{2+} secretion in the prostate of a healthy mouse.

The same 3,9-PC2A unit was also derivatized with a biphenyl moiety which induces HSA-binding (Scheme 2) [48]. This leads to a prolonged residential time of Mn(3,9-PC2A)-BP in the blood which makes it interesting for angiographic imaging. Indeed, it could be used to highlight microvasculature of the mouse brain.

4. Bispidine chelators

All data on linear or macrocyclic Mn^{2+} chelates indicate that rigidity and preorganization of the ligand are key design elements to promote kinetic inertness. This made us explore bispidine (3,7-diazabicyclo[3.3.1]nonane) derivatives for Mn^{2+} complexation. Bispidine-type chelators constitute a versatile family in coordination chemistry with a highly preorganized and rigid structure [49,50]. The bicyclic amine core can be appended with various coordinating functions and in different positions in order to match the coordination requirements of a large variety of metal ions of various sizes, coordination numbers or coordination geometries. As a function of the size and/or the position of the substituents, the bicyclic skeleton can adopt different conformations and configurations, among which the chair–chair conformer, with a "bicyclic coordination cage" is the best suited for metal complexation (Scheme 3a). Bispidines were extensively studied for the complexation of various transition metal and lanthanide ions, and many recent reports were dedicated to the development of bispidine complexes as nuclear imaging agents [51]. Interestingly, Mn^{2+} was

rarely in the scope of such studies, and all previous Mn^{2+}-related data were restricted to the solid state or to non-aqueous solvents.

We have first investigated the 2,4-pyridyl-disubstituted bispidol derivative H_4Bisp1 bearing one carboxylate (from a lysine) for Mn^{2+} complexation [52]. This ligand can coordinate the metal in a five-dentate manner, involving the nitrogens from the two pyridines, the heterobicycle (N3 and N7) as well as the methylene carboxylate (Scheme 3), leaving one coordination site for a water molecule in the coordination sphere of the metal ion, important for good relaxivity in MRI application. The thermodynamic stability of MnBisp1, determined by pH-potentiometry, is relatively modest ($\log K_{MnL}$ = 12.21, pMn = 6.65). However, once the complex is formed, it is extremely resistant to dissociation. In a standard transmetalation test carried out in the presence of 10 or 50 equiv. of Zn^{2+} at pH 6 and 37 °C, no dissociation at all was observed for 140 days, while the most inert non-bispidine chelate, Mn(3,9-PC2A-BPEN) has a dissociation half-life of 64.5 h under similar conditions (37 °C, pH 6.0, 25 Zn^{2+} equivalents) [47]. Such high kinetic inertness is unprecedented for a Mn^{2+} chelate. MnHBisp1 (protonated on the lysine amine) has also excellent relaxation properties, comparable to those of Gd^{3+}-based agents, despite the difference in the electron spin of the metals. The two non-coordinating carboxylate groups create an additional second sphere contribution to relaxivity which, together with the slightly higher molecular weight with respect to typical small molecular weight contrast agents, is responsible for the unusually high relaxivity (r_1 = 4.28 $mM^{-1}\cdot s^{-1}$ and 3.37 $mM^{-1}\cdot s^{-1}$ at 25 °C and 37 °C, respectively, 20 MHz, pH 7 in water). The *in vivo* imaging potential of MnHBisp1 was evaluated in a preliminary MRI experiment in healthy mice at 7 T. Following intravenous injection of MnHBisp1 at 0.06 mmol/kg dose, the signal intensity was monitored over time in various organs, which showed renal clearance and practically no liver uptake (Figure 1). This was further confirmed by *ex vivo* ICP-OES biodistribution measurements of Mn in various tissues. Moreover, Bisp1 was successfully labeled with $^{52}Mn^{2+}$, and the radiocomplex proved to be stable in biological media. In addition to the MRI potential of MnHBisp1, this opens interesting perspectives also for immunoPET applications, after further conjugation of the bifunctional ligand Bisp1 to biomolecules, such as antibodies.

Analogous bispidine ligands bearing methylenephosphonate (Bisp2) and methylenecarboxylate (Bisp3) substituents instead of the lysine have been also synthesized, and their Mn^{2+} complexes have shown similarly remarkable inertness and good proton relaxivities [53]. $^{52}Mn^{2+}$ radiolabeling of the phosphonate derivative was realized with excellent yields and the radiocomplex showed high stability.

In a recent comprehensive study combining structural NMR, potentiometric, relaxometric and kinetic experiments with DFT calculations, we have addressed how the substituents on the two nitrogens of the heterobicycle (N3 and N7) affect the conformation of the Mn^{2+} complexes [54]. In these studies, we have included a series of ligands Bisp3, Bisp4 and Bisp5 that possess methylenecarboxylate substituents at the N7 or N3 positions or both, respectively (Scheme 3b). We could conclude that in this family the conformation of the bispidine is determined by the nature of the N3 substituent (methyl or methylenecarboxylate), with very important consequences on the thermodynamic stability, kinetic inertness, hydration state and relaxation properties of the complexes. Only ligands without N3-appended methylenecarboxylate adopt the chair–chair conformation. Dissociation (as well as complex formation) is several orders of magnitude slower for the Mn^{2+} chelates in chair–chair conformation. The hydration number and the relaxation properties are also dependent on the ligand conformation: Mn^{2+} chelates in boat-chair conformation have less than one inner sphere water molecule, as shown by ^{17}O NMR data, which is unfavorable as it results in lower relaxivities. In overall, we could evidence that chair–chair conformation is required for the favorable properties of Mn^{2+} bispidines. Another ligand, Bisp6 (Scheme 3b) was also investigated to address how steric crowding introduced on the α carbon of the N7 methylenecarboxylate substituent affects the kinetic inertness of the Mn^{2+} complex. As it was previously found in the family Ln^{3+}-tetraazamacrocycles [55], this modification on the methylenecarboxylate arm further increases the resistance of the Mn^{2+} chelate to dissociation, leading to a dissociation half-life which is roughly doubled for MnBisp6 with respect to the MnBisp3 analogue.

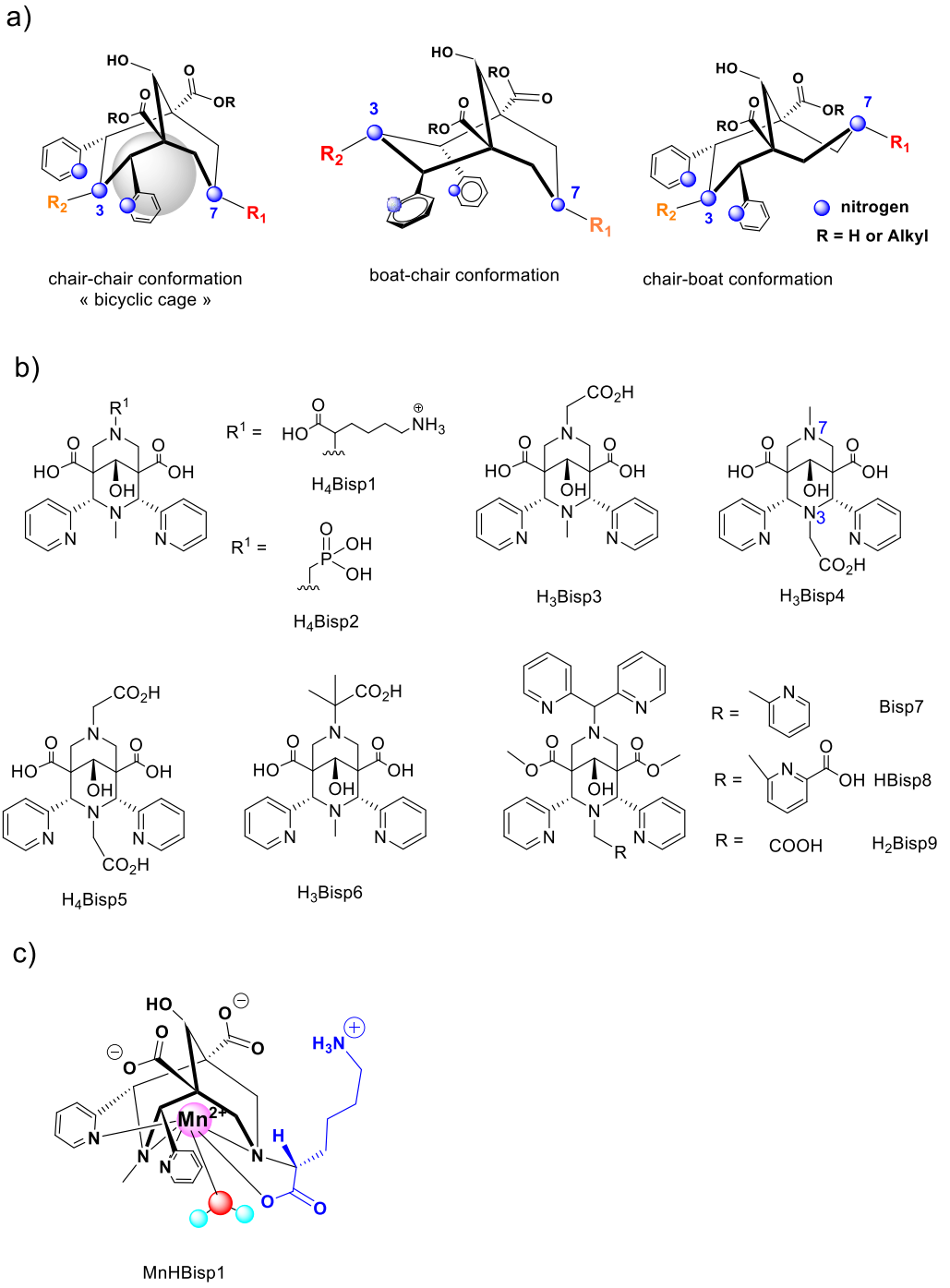

Scheme 3. (a) Bispidine conformations, (b) bispidine ligands for Mn^{2+} complexation and (c) the putative structure of MnHBisp1.

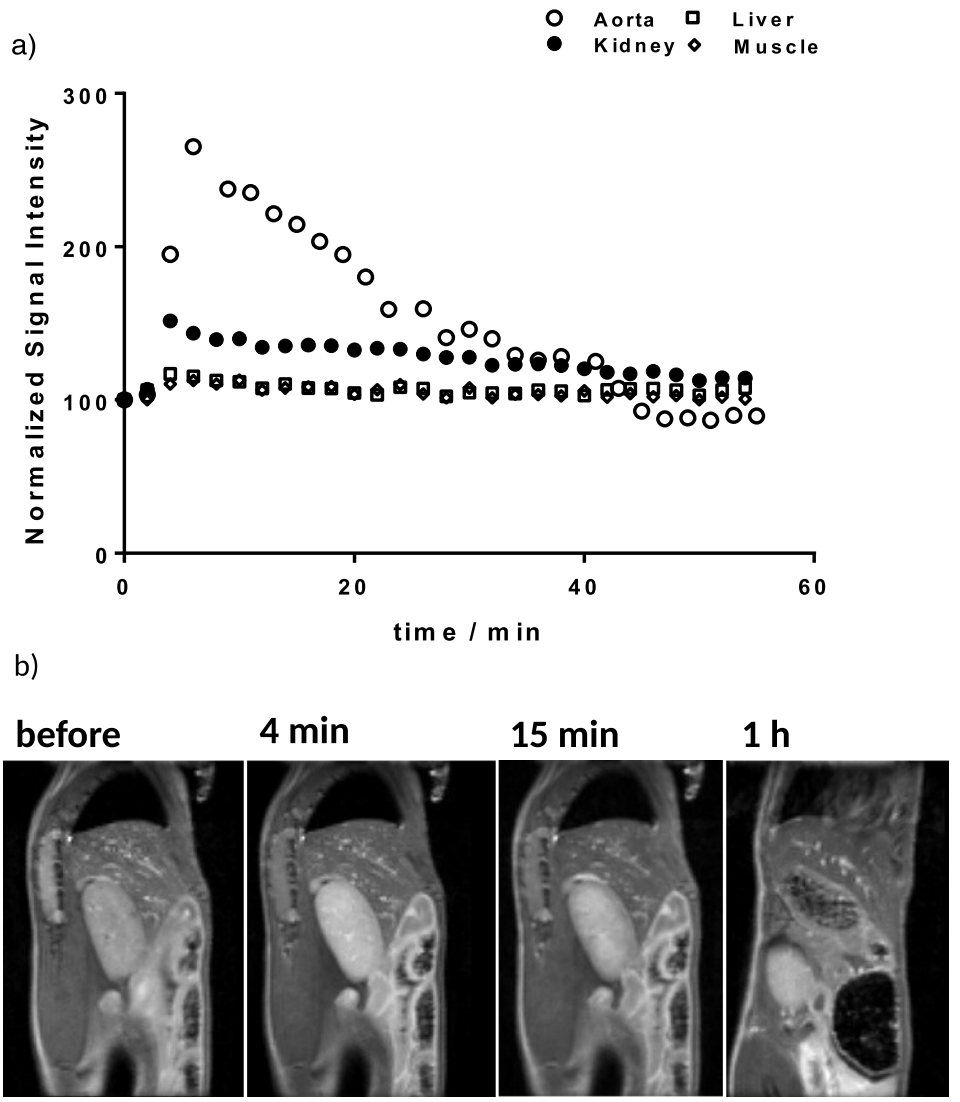

Figure 1. MRI of healthy mice at 7 T following intravenous injection of MnBisp1 at 0.06 mmol/kg dose. (a) Normalized signal intensity in the kidney, muscle, liver and aorta plotted as a function of time. Measurements were performed every 2 min for 4 mice. (b) Sagittal T1-weighted MR images prior to injection and at 4, 15 min and 1 h post intravenous injection of the complex. Reproduced with permission from reference [52].

Bispidine ligands of higher denticity have been also investigated for Mn^{2+} complexation and found to exhibit other extraordinary coordination chemistry features. While high kinetic inertness, as well as relatively high thermodynamic stability could be now achieved for Mn^{2+} chelates, none of them so far provided selectivity for Mn^{2+} over other transition metal ions, in particular Zn^{2+}, its major biological competitor. This directly derives from the large ionic radius of Mn^{2+} and the spherical distribution of its *d* electrons. The Irving–Williams series describes the order of complex stabilities with a particular ligand in the first row of divalent transition metal cations, and Mn^{2+} complexes are usually the least stable: $Mn^{2+} < Fe^{2+} < Co^{2+} < Ni^{2+} < Cu^{2+} > Zn^{2+}$. We hypothesized that the rigid and preorganized nature of

bispidines make them appropriate to design ligands with high denticity and a perfectly adapted coordination cavity for the ~10% larger size of Mn^{2+} versus Zn^{2+}. This cavity would be too large for Zn^{2+}, which could not accommodate all of the donor groups in its coordination sphere. The higher number of coordinating functions would then lead to a higher stability for Mn^{2+} as compared to Zn^{2+}. Some previous observations were already in support of preferential coordination of larger metal ions by the rigid bispidine cavity, resulting in divergence from the Irving–Williams series [56,57].

Hepta- and octadentate bispidine ligands Bisp7, Bisp8 and Bisp9 have been thus synthesized (Scheme 3) [58,59]. The Mn^{2+} and Zn^{2+} complexes have been subject of solid-state X-ray and computational studies to address their structure, and pH-potentiometric, relaxometric and kinetic investigations have been conducted to characterize their stability and inertness in aqueous solution. The solid-state structures show octadentate coordination for the Mn^{2+}, and hexadentate coordination for the Zn^{2+} complexes, evidencing that the coordination cavity provided by these ligands is well-suited for Mn^{2+} but too large for Zn^{2+}. The good match for Mn^{2+} and the misfit for Zn^{2+} was further demonstrated by empirical force field calculations which indicated that Mn^{2+} has an optimum size, while Zn^{2+} coordination induces a ligand-based strain of ~50 kJ/mol. Thermodynamic stability constants determined by pH-potentiometric (Zn^{2+}) or relaxometric (Mn^{2+}) titrations, further corroborated with ^{1}H NMR and UV–Vis data, confirmed the expectations from the structural and computational studies. There is a spectacular, 5–10 orders of magnitude difference in stability in favor of the Mn^{2+} complexes over the Zn^{2+} analogues ($\log K_{MnL}$ = 24.2, 24.7 and 19.47 for MnBisp7, MnBisp8 and MnBisp9, versus $\log K_{ZnL}$ = 14.30, 14.70 and 15.04 for ZnBisp7, ZnBisp8 and ZnBisp9, respectively). These complexes represent the first examples of real Mn^{2+} selectivity in aqueous solution. The kinetic inertness of these chelates also remains excellent, though slightly lower than that of MnHBisp1.

MnBisp9 has been fully characterized for its relaxation properties [59]. Its relaxivity (4.44 $mM^{-1}{\cdot}s^{-1}$ at 20 MHz, 25 °C) is slightly superior to that of MnBisp1 which can be accounted for the 17% higher molecular weight, thus slower rotation. This overbalances the lack of second-sphere contribution to relaxivity which operates for MnBisp1 thanks to the non-coordinating carboxylate groups, but which is not present for MnBisp9 where the carboxylates are replaced by esters. A preliminary *in vivo* MRI study has been carried out with MnBisp9 in mice at 7 T. Even at an unusually low injected dose (0.02 mmol/kg, 80% below typical doses), good contrast is observed in the kidneys. The signal variation over time indicates rapid renal clearance and no significant liver uptake. *Ex vivo* ICP-MS data point to full elimination of the complex from the mice after 24 h.

5. Mn^{3+} complexes and redox-responsive MRI agents based on the Mn^{2+}/Mn^{3+} switch

The stabilization of the Mn^{3+} state in aqueous solution and physiological pH is by far not obvious, due to the strong tendency of this cation to hydrolysis as well as to dismutation yielding Mn^{2+} and Mn^{4+}. The need for an inner sphere water in MRI applications makes stabilization even more difficult, and indeed, only few types of Mn^{3+} complexes are known with coordinated water molecule at pH 7. Among these, Mn^{3+} porphyrins represent a specific class endowed with high stability, and they were indeed considered in MRI and studied for their relaxation properties a long time ago. Mn^{3+} porphyrins have two water molecules coordinated to the metal ion, above and below the porphyrin plane. The relaxivities measured for some water soluble Mn^{3+} porphyrins such as the (5,10,15,20-tetrakis-(*p*-sulfonatophenyl) porphinate) derivative Mn(tpps) (Scheme 4) were considered as anomalously high for the given molecular size and electron spin, and this was tentatively explained by the anisotropy of the electron density at the metal center resulting in a closer approach of the Mn^{3+} spin density to the coordinated water protons [60,61]. More recently, there has been a renewed interest in Mn^{3+} porphyrins. Zhang and collaborators added carboxylates on the porphyrin periphery to increase hydrophilicity and facilitate *in vivo* clearance of the Mntcp complex (Scheme 4) [17,62]. The relaxivity, as well as the biodistribution have been modulated by further structural modifications of this carboxylated derivative, dimers endowed with HSA-binding capability have been developed for blood pool imaging [63], and specific liver targeting was generated by introducing a 4-ethoxyphenyl

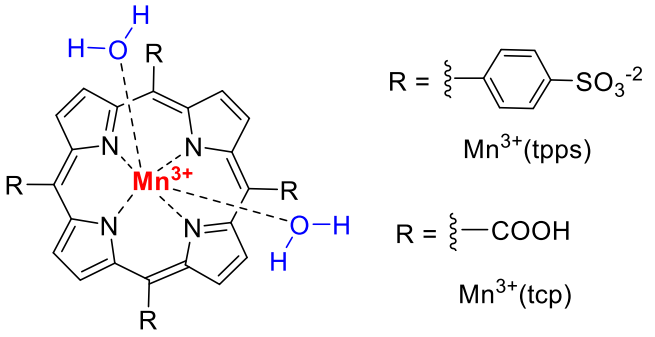

Scheme 4. Porphyrin Mn^{3+} complexes.

substituent on the porphyrin [64]. Cell-penetrating Mn^{3+} porphyrin derivatives containing a Zn^{2+}-binding unit have been also developed and successfully used for Zn^{2+} detection [65,66]. Phtalocyanine complexes of Mn^{3+} have been also investigated [67], but like for porphyrins, water solubility remains often limited.

Mn porphyrins have been further explored in the objective of developing redox sensitive agents. The redox state is an important characteristic of tissues, and redox imbalance is associated to many pathologies which can induce oxidative stress, generate reactive oxygen species, etc. The redox homeostasis in cells and tissues is governed by different biological molecules, such as cysteine, glutathione, hydrogen peroxide, nicotinamide adenine dinucleotide (NADH), etc., and their imaging detection has great interest. Given the different relaxation properties of Mn^{2+} and Mn^{3+}, this redox pair is very promising for the design of redox sensitive MRI probes (Figure 2) [18]. For this, the system needs to satisfy several requirements, including (a) stable and inert complexation of both redox forms of the metal to prevent free metal release, (b) a redox switch of the probe which is rapid and occurs at a biologically relevant potential, and (c) a significant relaxivity change between the two redox states allowing for MRI monitoring.

Following the pioneering work by Aime and collaborators on Mn^{2+}/Mn^{3+}(tpps) [68], as well as other examples of redox responsive Mn-probes based on linear chelators such as the Janus ligand JED (Scheme 5) [69–72], we have been recently exploring a PEGylated Mn-porphyrin derivative, Mn(pfpp$(PEG)_4$) (Scheme 5) [73]. The PEG chains have been introduced on the molecule to increase water solubility, and additionally, fluorine atoms have been added to modulate the redox potential. Both Mn^{2+} and Mn^{3+} forms are stably complexed in aqueous solution, with a reversible switch between them. In the presence of ascorbic acid or β-mercaptoethanol, the Mn^{3+} form undergoes reduction, which is slowly but fully reversed in the presence of air oxygen. This is accompanied by a ~150% relaxivity increase from the oxidized to the reduced form at 20 MHz. No reduction was observed with glutathione or cysteine, which can be explained by the coordination of the glutathione carboxylate to the metal ion by replacing one coordinated water molecule as evidenced by NMR data. Also, Mn(pfpp$(PEG)_4$) had no detectable *in vitro* cytotoxicity in the typical MRI concentration range.

With such fluorinated Mn-porphyrins, the redox detection can be extended to ^{19}F MRI in addition to ^{1}H MRI, as we demonstrated with another derivative, Mn(TPP-*p*-CF_3) (Scheme 5) [74]. The two Mn redox states induce very different ^{1}H and ^{19}F relaxometric properties which allow for differential redox MRI detection. The ^{19}F relaxation rates in these paramagnetic systems are strongly dependent on the Mn^{3+}–F distance. In Mn^{3+}(TPP-*p*-CF_3), it is 9.7–10 Å, as determined from DFT calculations. This distance seems well tailored to allow for adequate paramagnetic effect of Mn^{3+} on ^{19}F relaxation without excessive line-broadening, which would be detrimental for ^{19}F MRI detection. Reduction of Mn^{3+}(TPP-*p*-CF_3) with ascorbic acid and its re-oxidation with air oxygen can be monitored by UV–Vis spectrometry, ^{19}F NMR and ^{1}H relaxivity measurements. Upon reduction, the ^{1}H and ^{19}F NMR

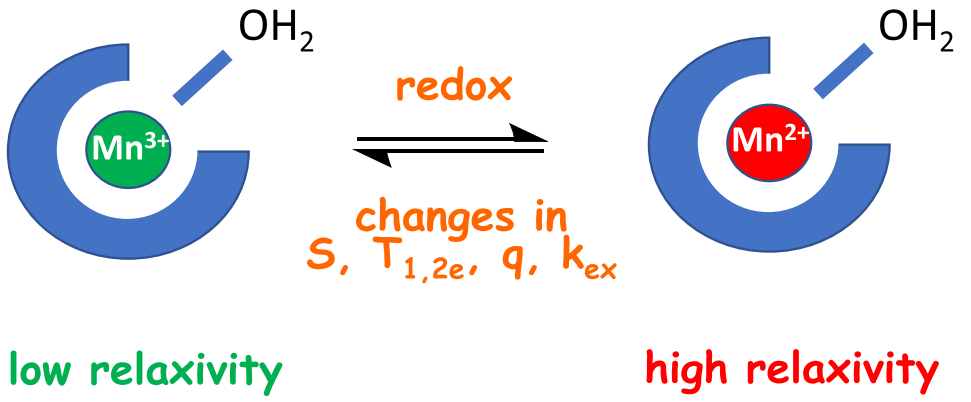

Figure 2. The redox switch between Mn^{3+} and Mn^{2+} states is accompanied by a change in the relaxivity of the complexes, as a consequence of variation in the electron spin (S), electron spin relaxation times ($T_{1,2e}$), hydration number (q), or water exchange rate (k_{ex}).

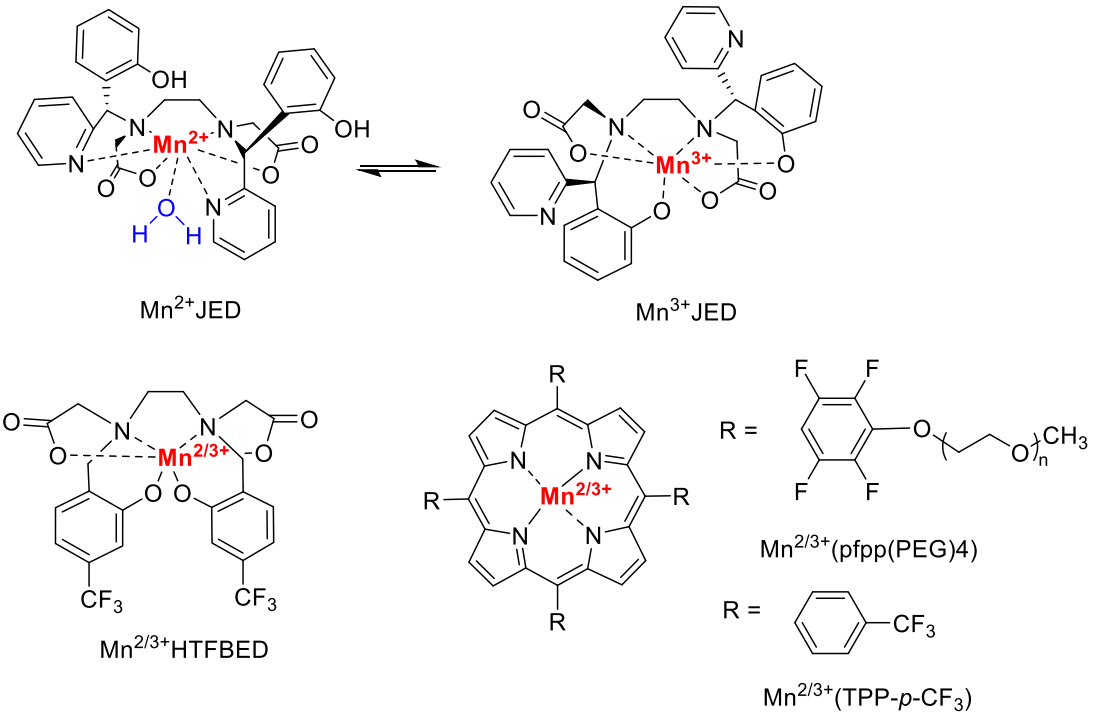

Scheme 5. Mn^{2+}/Mn^{3+} complexes investigated as redox responsive probes.

signals of Mn^{3+}(TPP-*p*-CF_3) largely broaden and disappear. The reduction/oxidation process can be readily visualized on phantom ^{19}F images acquired in DMSO/water mixture (Figure 3).

^{19}F MRI detection of Mn^{2+}/Mn^{3+} redox changes was also realized using the HTFBED ligand (Scheme 5) [72]. The complexes respond to different redox active species of the biological environment including ROS, ascorbic acid or glutathione with concomitant changes in the ^{19}F as well as in the ^{1}H MRI signal intensity. In particular, an eight-fold increase of the ^{19}F signal was detected upon

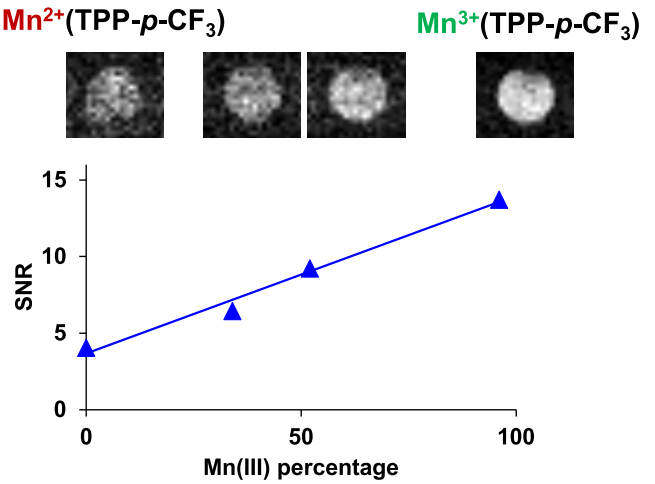

Figure 3. Monitoring oxidation of Mn^{2+}(TPP-*p*-CF_3) (c_{MnL} = 1.6 mM in DMSO) by air oxygen. Variation of the Signal to Noise Ratio (SNR) in MRI phantoms as a function of the oxidized Mn^{3+}(TPP-*p*-CF_3) content (%). The ^{19}F MRI phantom images for each point are represented above. B = 7 T; TR: 60 ms; TE: 1.3 ms; FA: 90°; NA: 256; acquisition time 8 min 11 s. The signal of the Mn^{2+} complex was saturated with a selective pulse. Adapted with permission from ref. [74].

oxidation from Mn^{2+} to Mn^{3+} form, and the responsive properties of these probes could be also validated at the cellular level in HepG2 cells.

6. Conclusion

Mn^{2+} complexes represent the most viable alternatives to replace Gd^{3+}-based MRI contrast agents in the clinical practice. In this context, many chelators, including open-chain, macrocyclic and bicyclic structures, have been explored in the last years for Mn^{2+} complexation, and recently there has been important progress in substantially improving the thermodynamic stability, the selectivity and the kinetic inertness of Mn^{2+} chelates. Endowed with a highly preorganized and rigid skeleton, bispidine ligands proved to provide unprecedented properties in Mn^{2+} coordination chemistry, such as extreme kinetic inertness, complex stability and Mn^{2+} selectivity, which can be further combined with excellent relaxation properties. An increasing number of Mn^{2+} complexes are successfully characterized in *in vivo* preclinical imaging, and some of them have reached human clinical trials as potential MRI agents. The Mn^{3+} state is also increasingly explored, mainly in porphyrin complexes. Finally, efforts are still being made in order to develop Mn-based redox responsive agents.

Declaration of interests

The authors do not work for, advise, own shares in, or receive funds from any organization that could benefit from this article, and have declared no affiliations other than their research organizations.

References

[1] A. Feldman, *RadioGraphics*, 1989, **9**, 1113-1128.
[2] J. Wahsner, E. M. Gale, A. Rodríguez-Rodríguez, P. Caravan, *Chem. Rev.*, 2019, **119**, 957-1057.
[3] E. Toth, L. Helm, A. Merbach, in *The Chemistry of Contrast Agents in Medical Magnetic resonance Imaging* (A. Merbach, L. Helm, E. Toth, eds.), John Wiley & Sons, Chichester, 2nd ed., 2013, 25-81.
[4] T. Grobner, *Nephrol. Dial. Transplant.*, 2006, **21**, 1104-1108.
[5] E. Di Gregorio, G. Ferrauto, C. Furlan, S. Lanzardo, R. Nuzzi, E. Gianolio, S. Aime, *Invest. Radiol.*, 2018, **53**, 167-172.
[6] K. Inoue, M. Fukushi, A. Furukawa, S. K. Sahoo, N. Veerasamy, K. Ichimura, S. Kasahara, M. Ichihara, M. Tsukada, M. Torii, M. Mizoguchi, Y. Taguchi, S. Nakazawa, *Marine Pollut. Bull.*, 2020, **154**, article no. 111148.
[7] S. Le Goff, J. A. Barrat, L. Chauvaud, Y. M. Paulet, B. Gueguen, D. Ben Salem, *Sci. Rep.*, 2019, **9**, article no. 8015.
[8] A. Gupta, P. Caravan, W. S. Price, C. Platas-Iglesias, E. M. Gale, *Inorg. Chem.*, 2020, **59**, 6648-6678.
[9] B. Drahos, I. Lukes, E. Toth, *Eur. J. Inorg. Chem.*, 2012, 1975-1986.
[10] P. G. Lauterbur, *Nature*, 1973, **242**, 190-191.
[11] A. P. Korestky, A. C. Silva, *NMR Biomed.*, 2004, **17**, 527-531.

[12] M. G. Cersosimo, W. C. Koller, *Neurotoxicology*, 2006, **27**, 340-346.
[13] S. Lacerda, D. Ndiaye, É. Tóth, in *Advances in Inorganic Chemistry, Recent Highlights I* (C. D. Hubbard, R. Van Eldik, eds.), vol. 78, Elsevier, 2021, 109-142.
[14] B. Drahos, J. Kotek, P. Hermann, I. Lukes, E. Toth, *Inorg. Chem.*, 2010, **49**, 3224-3238.
[15] B. Drahos, V. Kubicek, C. S. Bonnet, P. Hermann, I. Lukes, E. Toth, *Dalton Trans.*, 2011, **40**, 1945-1951.
[16] M. Botta, F. Carniato, D. Esteban-Gomez, C. Platas-Iglesias, L. Tei, *Future Med. Chem.*, 2019, **11**, 1461-1483.
[17] W. Cheng, I. E. Haedicke, J. Nofiele, F. Martinez, K. Beera, T. J. Scholl, H.-L. M. Cheng, X.-a. Zhang, *J. Med. Chem.*, 2014, **57**, 516-520.
[18] S. M. Pinto, V. Tomé, M. J. F. Calvete, M. M. C. A. Castro, É. Tóth, C. F. G. C. Geraldes, *Coord. Chem. Rev.*, 2019, **390**, 1-31.
[19] C. M. Lewis, S. A. Graves, R. Hernandez, H. F. Valdovinos, T. E. Barnhart, W. Cai, M. E. Meyerand, R. J. Nickles, M. Suzuki, *Theranostics*, 2015, **5**, 227-239.
[20] https://clinicaltrials.gov/ct2/show/NCT05413668.
[21] https://www.gehealthcare.com/about/newsroom/press-releases/ge-healthcare-announces-completion-of-phase-i-subject-recruitment-in-early-clinical-development-program-for-a-first-of-its-kind-macrocyclic-manganese-based-mri-contrast-agent.
[22] M. S. Zetter, E. J. Wood, J. P. Hunt, H. W. Dodgen, M. W. Grant, *Inorg. Chem.*, 1972, **11**, 2701-2706.
[23] M. K. Islam, S. Kim, H. K. Kim, Y. H. Kim, Y. M. Lee, G. Choi, A. R. Baek, B. K. Sung, M. Kim, A. E. Cho, H. Kang, G. H. Lee, S. H. Choi, T. Lee, J. A. Park, Y. Chang, *Bioconj. Chem.*, 2018, **29**, 3614-3625.
[24] M. K. Islam, S. Kim, H.-K. Kim, S. Park, G.-H. Lee, H. J. Kang, J.-C. Jung, J.-S. Park, T.-J. Kim, Y. Chan, *J. Med. Chem.*, 2017, **60**, 2993-3001.
[25] S. Aime, P. L. Anelli, M. Botta, M. Brocchetta, S. Canton, F. Fedeli, E. Gianolio, E. Terreno, *J. Biol. Inorg. Chem.*, 2002, **7**, 58-67.
[26] F. K. Kalman, G. Tircso, *Inorg. Chem.*, 2012, **51**, 10065-10067.
[27] J. Charlier, E. Merciny, J. Fuger, *Anal. Chim. Acta*, 1985, **178**, 299-306.
[28] E. Molnar, B. Varadi, Z. Garda, R. Botar, F. K. Kalman, E. Toth, C. Platas-Iglesias, I. Toth, E. Brucher, G. Tircso, *Inorg. Chim. Acta*, 2018, **472**, 254-263.
[29] C. Vanasschen, E. Molnar, G. Tircso, F. K. Kalman, E. Toth, M. Brandt, H. H. Coenen, B. Neumaier, *Inorg. Chem.*, 2017, **56**, 7746-7760.
[30] K. Pota, Z. Garda, F. K. Kalman, J. L. Barriada, D. Esteban-Gomez, C. Platas-Iglesias, I. Toth, E. Brucher, G. Tircso, *New J. Chem.*, 2018, **42**, 8001-8011.
[31] S. Laine, C. S. Bonnet, F. K. Kalman, Z. Garda, A. Pallier, F. Caille, F. Suzenet, G. Tircso, E. Toth, *New J. Chem.*, 2018, **42**, 8012-8020.
[32] S. W. McRae, M. Cleary, D. DeRoche, F. M. Martinez, Y. Xia, P. Caravan, E. M. Gale, J. A. Ronald, T. J. Scholl, *J. Med. Chem.*, 2023, **66**, 6567-6576.
[33] E. M. Gale, I. P. Atanasova, F. Blasi, I. Ay, P. Caravan, *J. Am. Chem. Soc.*, 2015, **137**, 15548-15557.
[34] E. M. Gale, H.-Y. Wey, I. Ramsay, Y.-F. Yen, D. E. Sosnovik, P. Caravan, *Radiology*, 2018, **286**, 877-884.
[35] D. J. Erstad, I. A. Ramsay, V. C. Jordan, M. Sojoodi, B. C. Fuchs, K. K. Tanabe, P. Caravan, E. M. Gale, *Invest. Radiol.*, 2019, **54**, 697-703.
[36] B. P. Bonner, S. R. Yurista, J. Coll-Font, S. Chen, R. A. Eder, A. N. Foster, K. D. Nguyen, P. Caravan, E. M. Gale, C. Nguyen, *J. Am. Heart Assoc.*, 2023, **12**, article no. e026923.
[37] J. Wang, H. Wang, I. A. Ramsay, D. J. Erstad, B. C. Fuchs, K. K. Tanabe, P. Caravan, E. M. Gale, *J. Med. Chem.*, 2018, **61**, 8811-8824.
[38] S. Chirayil, V. C. Jordan, A. F. Martins, N. Paranawithana, S. J. Ratnakar, A. D. Sherry, *Inorg. Chem.*, 2021, **60**, 2168-2177.
[39] S. Anbu, S. H. L. Hoffmann, F. Carniato, L. Kenning, T. W. Price, T. J. Prior, M. Botta, A. F. Martins, G. J. Stasiuk, *Angew. Chem. Int. Ed.*, 2021, **60**, 10736-10744.
[40] A. Bianchi, L. Calabi, C. Giorgi, P. Losi, P. Mariani, D. Palano, P. Paoli, P. Rossi, B. Valtancoli, *J. Chem. Soc. Dalton Trans.*, 2001, 917-922.
[41] G. A. Rolla, C. Platas-Iglesias, M. Botta, L. Tei, L. Helm, *Inorg. Chem.*, 2013, **52**, 3268-3279.
[42] Z. Garda, A. Forgacs, Q. N. Do, F. K. Kalman, S. Timari, Z. Baranyai, L. Tei, I. Toth, Z. Kovacs, G. Tircso, *J. Inorg. Biochem.*, 2016, **163**, 206-213.
[43] G. Rolla, V. De Biasio, G. B. Giovenzana, M. Botta, L. Tei, *Dalton Trans.*, 2018, **47**, 10660-10670.
[44] B. Drahos, J. Kotek, I. Cisarova, P. Hermann, L. Helm, I. Lukes, E. Toth, *Inorg. Chem.*, 2011, **50**, 12785-12801.
[45] Z. Garda, E. Molnár, N. Hamon, J. L. Barriada, D. Esteban-Gómez, B. Váradi, V. Nagy, K. Pota, F. K. Kálmán, I. Tóth, N. Lihi, C. Platas-Iglesias, É. Tóth, R. Tripier, G. Tircsó, *Inorg. Chem.*, 2021, **60**, 1133-1148.
[46] R. Botár, E. Molnár, G. Trencsényi, J. Kiss, F. K. Kálmán, G. Tircsó, *J. Am. Chem. Soc.*, 2020, **142**, 1662-1666.
[47] R. Botár, E. Molnár, Z. Garda, E. Madarasi, G. Trencsényi, J. Kiss, F. K. Kálmán, G. Tircsó, *Inorg. Chem. Front.*, 2022, **9**, 577-583.
[48] F. K. Kálmán, V. Nagy, B. Váradi, Z. Garda, E. Molnár, G. Trencsényi, J. Kiss, S. Même, W. Même, É. Tóth, G. Tircsó, *J. Med. Chem.*, 2020, **63**, 6057-6065.
[49] P. Comba, M. Kerscher, W. Schiek, in *Progress in Inorganic Chemistry* (K. D. Karlin, ed.), vol. 55, John Wiley & Sons, 2007, 613-704.
[50] A. M. Nonat, A. Roux, M. Sy, L. J. Charbonniere, *Dalton Trans.*, 2019, **48**, 16476-16492.
[51] P. Comba, M. Kerscher, K. Rueck, M. Starke, *Dalton Trans.*, 2018, **47**, 9202-9220.
[52] D. Ndiaye, M. Sy, A. Pallier, S. Meme, I. de Silva, S. Lacerda, A. M. Nonat, L. J. Charbonniere, E. Toth, *Angew. Chem. Int. Ed.*, 2020, **59**, 11958-11963.
[53] M. Sy, D. Ndiaye, I. da Silva, S. Lacerda, L. J. Charbonnière, É. Tóth, A. M. Nonat, *Inorg. Chem.*, 2022, **61**, 13421-13432.
[54] D. Ndiaye, M. Sy, W. Thor, L. J. Charbonniere, A. M. Nonat, E. Toth, *Chem. Eur. J.*, 2023, **29**, article no. e202301880.
[55] S. Aime, M. Botta, Z. Garda, B. E. Kucera, G. Tircso, V. G. Young, M. Woods, *Inorg. Chem.*, 2011, **50**, 7955-7965.
[56] P. Comba, H. Rudolf, H. Wadepohl, *Dalton Trans.*, 2015, **44**, 2724-2736.

[57] P. Comba, M. Kerscher, K. Rück, M. Starke, *Dalton Trans.*, 2018, **47**, 9202-9220.
[58] P. Cieslik, P. Comba, B. Dittmar, D. Ndiaye, É. Tóth, G. Velmurugan, H. Wadepohl, *Angew. Chem. Int. Ed.*, 2022, **61**, article no. e202115580.
[59] D. Ndiaye, P. Cieslik, H. Wadepohl, A. Pallier, S. Même, P. Comba, É. Tóth, *J. Am. Chem. Soc.*, 2022, **144**, 22212-22220.
[60] S. H. Koenig, C. Baglin, R. D. Brown, *Magn. Reson. Med.*, 1984, **1**, 496-501.
[61] S. H. Koenig, R. D. Brown Iii, M. Spiller, *Magn. Reson. Med.*, 1987, **4**, 252-260.
[62] W. Cheng, T. Ganesh, F. Martinez-Santiesteban, J. Lam, H. Yoon, R. Macgregor, T. Scholl, H.-L. Cheng, X.-A. Zhang, *J. Biol. Inorg. Chem.*, 2014, **19**, 229-235.
[63] H. L. Liu, W. R. Cheng, S. L. Dong, D. F. Xu, K. Tang, X. A. Zhang, *Pharmaceuticals*, 2020, **13**, 282-293.
[64] N. N. Nystrom, H. L. Liu, F. M. Martinez, X. A. Zhang, T. J. Scholl, J. A. Ronald, *J. Med. Chem.*, 2022, **65**, 9846-9857.
[65] T. Lee, X.-a. Zhang, S. Dhar, H. Faas, S. J. Lippard, A. Jasanoff, *Chem. Biol.*, 2010, **17**, 665-673.
[66] X.-a. Zhang, K. S. Lovejoy, A. Jasanoff, S. J. Lippard, *Proc. Natl. Acad. Sci. USA*, 2007, **104**, 10780-10785.
[67] S. M. A. Pinto, V. A. Tomé, M. J. F. Calvete, M. M. Pereira, H. D. Burrows, A. M. S. Cardoso, A. Pallier, M. M. C. A. Castro, É. Tóth, C. F. G. C. Geraldes, *J. Inorg. Biochem.*, 2016, **154**, 50-59.
[68] S. Aime, M. Botta, E. Gianolio, E. Terreno, *Angew. Chem. Int. Ed.*, 2000, **39**, 747-750.
[69] E. M. Gale, C. M. Jones, I. Ramsay, C. T. Farrar, P. Caravan, *J. Am. Chem. Soc.*, 2016, **138**, 15861-15864.
[70] E. M. Gale, S. Mukherjee, C. Liu, G. S. Loving, P. Caravan, *Inorg. Chem.*, 2014, **53**, 10748-10761.
[71] G. S. Loving, S. Mukherjee, P. Caravan, *J. Am. Chem. Soc.*, 2013, **135**, 4620-4623.
[72] H. Chen, X. Tang, X. Gong, D. Chen, A. Li, C. Sun, H. Lin, J. Gao, *Chem. Commun.*, 2020, **56**, 4106-4109.
[73] S. M. A. Pinto, M. J. F. Calvete, M. E. Ghica, S. Soler, I. Gallardo, A. Pallier, M. B. Laranjo, A. M. S. Cardoso, M. M. C. A. Castro, C. M. A. Brett, M. M. Pereira, É. Tóth, C. F. G. C. Geraldes, *Dalton Trans.*, 2019, **48**, 3249-3262.
[74] S. M. A. Pinto, A. R. R. Ferreira, D. S. S. Teixeira, S. C. C. Nunes, A. de Carvalho, J. M. S. Almeida, Z. Garda, A. Pallier, A. Pais, C. M. A. Brett, E. Tóth, M. P. M. Marques, M. M. Pereira, C. Geraldes, *Chem. Eur. J.*, 2023, **29**, article no. e202301442.

ACADÉMIE DES SCIENCES
INSTITUT DE FRANCE

Comptes Rendus. Chimie
2024, Vol. 27, Special issue S2, p. 179-195
https://doi.org/10.5802/crchim.294

Research article

Women Chemists in France in 2024

Dye-based fluorescent organic nanoparticles made from polar and polarizable chromophores for bioimaging purposes: a bottom-up approach

Jonathan Daniel[a], **Ophélie Dal Pra**[a], **Eleonore Kurek**[a], **Chloé Grazon**[a] and **Mireille Blanchard-Desce**[*,a]

[a] Univ. Bordeaux, CNRS, Bordeaux INP, ISM, UMR 5255, F-33400 Talence, France
E-mail: mireille.blanchard-desce@u-bordeaux.fr (M. Blanchard-Desce)

Dedicated to the memory of Michel Vaultier

Abstract. In the last decades, inorganic nanoparticles have attracted growing attention in the field of nanophotonics, especially for bioimaging purposes. Among them luminescent metal-, semiconductor- or oxide-based "hard" nanoparticles have been the most widely used. Yet, they raise concern with respect to toxicity and degradability issues. In that context, we have developed innovative bottom-up approaches towards ultrabright dye-based fluorescent organic nanoparticles (dFONs). Our strategy is based on the design and synthesis of custom-designed (multi)polar and polarizable dyes (PPDs) as building blocks of dFONs. These nanoparticles are readily prepared using expeditious and green protocols involving nanoprecipitation of the hydrophobic dyes in water. Their luminescence can be tuned in the whole visible region down to the Near Infra-Red I (NIR-I) region while their nonlinear optical responses can be enhanced thanks to cooperative effects. Intriguingly, the implemented strategy also enables modulating and improving the dFONs colloidal and structural stability as well as their photostability. As a result, dFONs made from PPDs that combine unprecedented brightness (up to $10^8\,M^{-1}\cdot cm^{-1}$ and 10^6 GM), remarkable colloidal stability and absence of toxicity, have been elaborated, providing superior substitutes to Quantum Dots. Such dFONs can be used as ultrasensitive contrast agents for in vivo two-photon angiography in small animals, while hyper-bright NIR-emitting FONs, that show remarkable photostability and excellent biocompatibility, can be successfully imaged and tracked at the single particle level in water. Furthermore, ultrabright dFONs of different colors that internalize into cells can be tracked within living cells allowing real-time multicolor single particles tracking. In contrast, stealth emitters are required for tracking cell-surface receptors or exploring the extracellular space. In this direction, spontaneously stealth, size-tunable, ultrabright and red to NIR emitting dFONs were developed. Thanks to these unique properties, these dFONs could be imaged and tracked up to 150 μm deep in brain tissue.

Keywords. Organic dyes, Luminescent nanoparticles, Two-photon absorption, Confinement effects, In vivo imaging, Stealthiness, Single particle tracking.

Funding. Conseil general d'Aquitaine, University of Bordeaux, CNRS, Bordeaux-INP, ERC COMET (101077364).

Manuscript received 4 January 2024, revised 14 January 2024, accepted 30 January 2024.

[*] Corresponding author

1. Introduction

Fluorescence imaging has become a groundbreaking tool to study and image biological environments and processes, in domains ranging from medical applications to fundamental research in biology. In that context, a wide variety of fluorescent dyes and probes have been developed as tools for high contrast microscopy and cell imaging [1]. Ideal fluorescent probes should be bright, photostable and non-toxic. Additional key parameters are their absorption range and emission color. In terms of brightness, fluorescent organic dyes may be surpassed by luminescent nanoparticles [2,3]. Indeed, in the last decades, inorganic nanoparticles have attracted growing attention in the field of biophotonics, in relation with various applications including new imaging modalities. Among them luminescent metal-, semiconductor- or oxide-based nanoparticles have been by far the most widely studied [4]. Luminescent metallic and semiconducting nanoparticles have been heralded as major nanomaterials due to their unique electronic and optical properties, giving rise to the blooming field of plasmonics in the case of metallic nanoparticles. In parallel, semiconductor quantum dots (QDs) have motivated many studies and have become extremely popular for bioimaging uses. Their luminescence properties can be tuned in the visible to the near-infrared (NIR) region by adjusting their size in relation with quantum confinement and they may show giant brightness [4] (both one-photon brightness [3]: up to 10^6 $M^{-1}{\cdot}cm^{-1}$, and two-photon brightness [5–8]: up to 10^4 GM). Yet, such luminescent inorganic nanoparticles suffer from several drawbacks: their inorganic core is inherently water-insoluble, requiring them to be coated by solubilizing agents (polymeric coating, surfactants, etc.) for use in bioimaging. In addition, several luminescent inorganic nanoparticles raise questions with respect to environmental issues (ecotoxicity, biodegradability) due to their content or composition (heavy metal or toxic components). In that perspective, fully organic nano-objects may offer interesting alternatives. The most widely used typically are polymeric such as dendrimers [9–12], lipid-based [13] or "frozen" micelles systems where fluorescent probes are either encapsulated in [14,15] or covalently linked [16] to the nanoparticle. In contrast, self-stabilized organic nanoparticles generated from the nano-aggregation of dedicated hydrophobic dyes in water represent a much less traveled route. Actually, this type of fully organic luminescent nanoparticles is often overlooked in the literature and some prominent reviews do not even mention them [3,17]. Yet they offer promise for a wide range of applications, including biological applications [18,19]. We propose to name these organic nanoparticles dFONs (for *dye-based fluorescent organic nanoparticles*) to distinguish them from the multitude of fluorescent organic nanoparticles, which otherwise create a somewhat fuzzy domain and some misunderstandings or confusion. We stress that we use the name dFONs to describe *organic nanoparticles made only of pure dyes*, requiring *no stabilizers or additives, nor coatings* to be made dispersible and stable in water or aqueous environments.

The ultimate molecular confinement of pure dyes may look like a counterintuitive approach as most of the time this generates aggregation-caused quenching of fluorescence (ACQ) due to symmetry reasons (in the case of π-stacking notably) or to competitive deactivation processes (such as photoinduced electron transfer (PET) favored by the close proximity of dyes within dFONs) that inhibit fluorescence. Yet by adjusting the electronic structure of the dye (to prevent PET) while adding suitable bulky substituents that hinder π-stacking, such effects can be circumvented. A supposedly similar strategy has been used extensively in the so-called "aggregation-induced emission" (AIE) [20] or aggregation-induced emission enhancement (AIEE) domain. In compounds designed for AIE, appending moieties preventing π-stacking and allowing for efficient non-radiative rotational deactivation processes in non-viscous environments are added to dyes, thus generating loss of fluorescence in solutions. When such dyes are placed in viscous solvents or in the solid state where rotations are restricted, their fluorescence is restored.

2. dFONs design: polar and polarizable dyes (PPDs) as dFONs building blocks

Key criteria for luminescent nanoparticles to be of interest for bioimaging purposes typically are large brightness for enhanced sensitivity (with the ultimate goal of detecting single emitters), photostability, colloidal stability as well as biocompatibility.

In addition, for in vivo bioimaging in tissues or small animals, they should preferably absorb and emit light above 650 nm—i.e., within the biological transparency window(s) (650–950 nm and 1000–1200 nm) [21]. In that perspective, two-photon excitation has attracted much interest giving rise to two-photon laser scanning microscopy (TPLSM) [22], which has nowadays become a popular fluorescence bioimaging technique. Two-photon absorption (2PA) is a nonlinear optical phenomenon defined by the simultaneous absorption of two low-energy photons [23] by an excitable compound (Scheme 1). The wavelength used for two-photon excitation is thus favorably redshifted as compared to that used for one-photon excitation and allows for instance the replacement of excitation in the near UV–blue visible region by excitation in the deep red–NIR-I region. Dyes which have much higher two-photon absorption cross-sections (σ_2) than endogenous chromophores (typically orders of magnitude larger, i.e., over 10^3 GM) are thus required not only to allow deeper imaging in biological tissues thanks to reduced scattering, but also to significantly reduce background fluorescence and provide more selective excitation compared to standard one-photon excitation [24]. In that perspective, we were interested in the design of biocompatible dFONs combining tunable emission, giant brightness (both for standard excitation, i.e., confocal fluorescence microscopy, and TPLSM), excellent colloidal and photostability in bioenvironments, aiming at various imaging modalities (including single particle tracking and two-photon imaging).

Two main strategies are used to prepare dFONs directly as a colloidal suspension in water (or aqueous media): (i) laser-assisted photofragmentation of a suspension of micro-crystals in water [25] or (ii) nanoprecipitation [26,27] (Scheme 2). In the latter, a minute amount of a stock solution of the dye dissolved in a water-miscible organic solvent (typically THF, ethanol, acetone, DMSO ...)—which acts as the good solvent for the hydrophobic dye—is added in a large volume of pure water (or buffer etc.) under either magnetic stirring or sonication. For bioimaging applications, no more than 1% (v/v) of organic solvent should be used and the residual amount can be eliminated by evaporation under vacuum or dialysis. As the good (organic) solvent for the hydrophobic dyes is dispersed in the bad solvent (water), dyes aggregate to form clusters then nanoparticles [26]. If nanoparticles are indeed formed, a colored (thanks to the dispersion of hydrophobic dyes in water) and non-turbid (thanks to the nanometric size of organic aggregates) aqueous suspension is obtained. We stress that this process is a kinetically controlled step contrary to crystallization and that hydrophobic interactions play a definite role as water is used to conduct nanoprecipitation. Hence, the organization of dyes within dFONs might be different from that in the crystal obtained by a thermodynamically controlled slow process. dFONs prepared by nanoprecipitation usually have a spherical shape. We emphasize that the colloidal stability of such dFONs suspensions is a major issue in view of their usefulness: their natural fate is to agglomerate, then deposit upon evolution towards the low-energy thermodynamic state. The nature of the dyes as well as their self-organization are extremely important in that respect as the kinetics of these processes may be rendered extremely slow depending on the type of dye and surface properties of dFONs.

To achieve dFONs that meet the requirements mentioned above for bioimaging, we developed a successful bottom-up strategy based on the molecular engineering of specific chromophores, *namely Polar and Polarizable Dyes (PPDs)* as dFONs building blocks. Such dyes bear electron-releasing (D) and electron-withdrawing (A) moieties or substituents that interact via π-conjugated linkers, giving rise to intramolecular charge transfer(s) (ICT), i.e., electronic redistribution from the D to the A moieties upon excitation. The ICT phenomenon is responsible for the strong absorption of PPDs as well as for their unique nonlinear optical properties, especially two-photon absorption [28–31]. PPDs may have different symmetry including dipolar, quadrupolar, or octupolar dyes (Figures 1–2) [32–42].

The presence of dipolar subunits in those dyes has strong implications that explain the specificity and peculiarities of dFONs made from PPDs:

(i) The dipolar interactions between dyes are strong and longer-ranged ($\propto 1/r^3$) than Keesom interactions ($\propto 1/r^6$) due to the dyes' immobilization and ultimate confinement within dFONs. These electrostatic interactions play a crucial role in the structural cohesion of dFONs and explain their *structural stability though there is no covalent bonding*

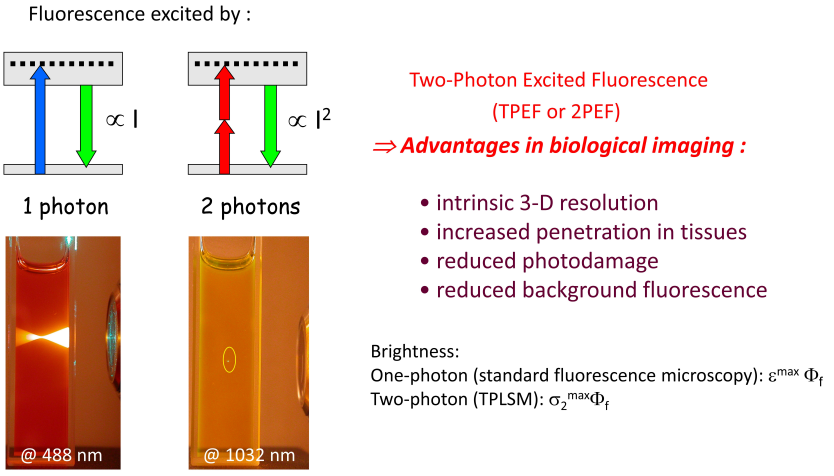

Scheme 1. Two-photon excited fluorescence: principles and advantages in bioimaging.

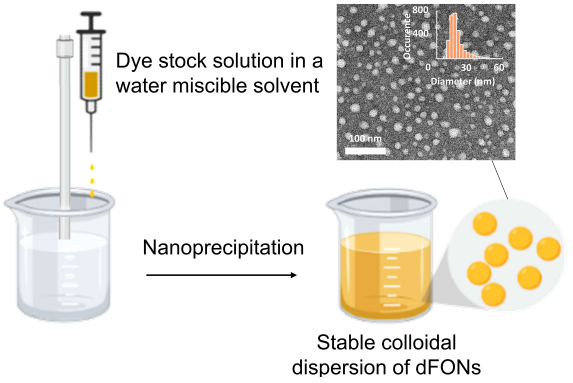

Scheme 2. Typical nanoprecipitation protocol for the preparation of dFONs.

between dyes, contrary to polymeric organic particles.

(ii) The dipolar interactions also play a major role in the self-organization of PPD dyes within dFONs during the nano-aggregation process [43,44]. In that respect, molecular engineering of PPDs is crucial to prevent antiparallel stacking of dipolar dyes or π-staking of quadrupolar dyes [45] that are deleterious to fluorescence. To prevent such processes, we have used dedicated appending moieties such as diphenylamino end-groups (which have a non-planar propeller shape and are also electron-releasing moieties), as in dipolar and quadrupolar dyes shown in Figures 1 and 2. Alternatively, conjugated linkers (or cores) including fluorenyl moieties bearing alkyl substituents that extend above and below the plane of the π-conjugated system have been used. These substituents act as bulky spacers of tunable size, as in bis-dipolar and quadrupolar dyes shown in Figures 1 and 2. The geometry of the dyes, as well as the position and size of the bulky appending moieties, are very important in tuning their self-organization upon aggregation and offer a powerful handle for bottom-up engineering of the dFONs' fluorescence properties (Figure 3).

(iii) The dipolar subunits create strong local electric fields in their close vicinity. As a result, due to the intrinsic high polarizability of PPDs, these local electric fields may change the polarization of the proximal dyes resulting in a modification of their electronic distribution (and polarization) and subsequently of their optical properties (i.e., modification of the electronic gap [46–51]) and even more markedly nonlinear optical properties [30,52,53]. Hence, depending on the self-orientation of the dipolar subunits within dFONs and on the distance between PPDs dyes (which can be tuned by adjusting the geometry of the dyes as well as

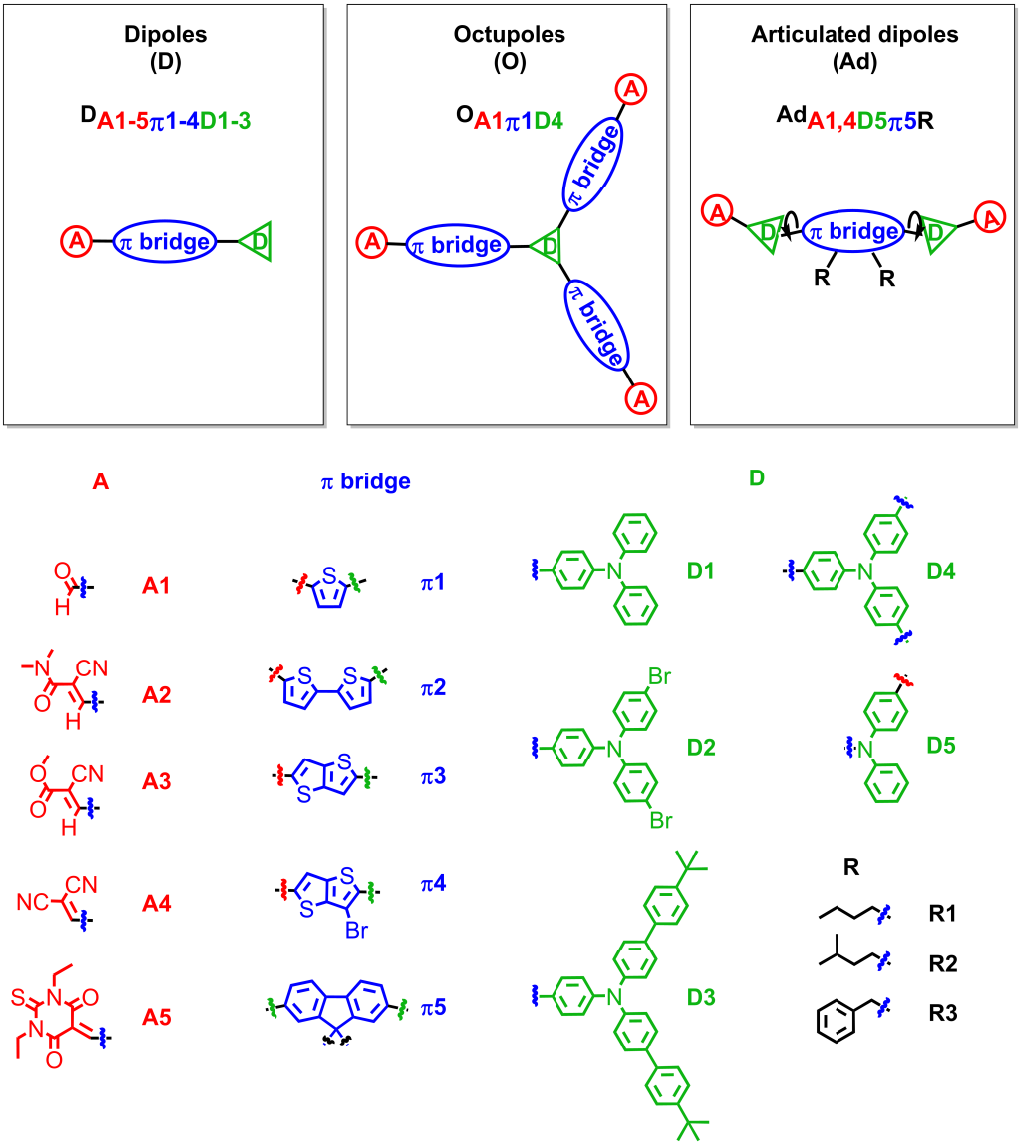

Figure 1. Examples of dipolar, octupolar and bis-dipolar dyes developed in the team for the bottom-up molecular engineering of bright dFONs for bioimaging. Adapted from Refs. [32–35,38,40,42].

the bulkiness and position of substituents—Figure 3), sizeable variations in the optical properties can be expected for dyes with similar optical (and NLO) properties in solution as a result of confinement effects.

(iv) Finally, the nature of the PPDs may significantly influence their orientation at the surface of dFONs resulting in short-range order [54]. We stress that almost all push–pull dyes that we investigated bear electron-withdrawing end-groups that are susceptible to favor electrostatic interaction or H-bonds with water molecules surrounding the surface of the dFONs. Such orientations may result in large surface potentials (as in lipid membranes), emphasizing the specificity of dFONs made from PPDs in terms of the nature and properties of their surface.

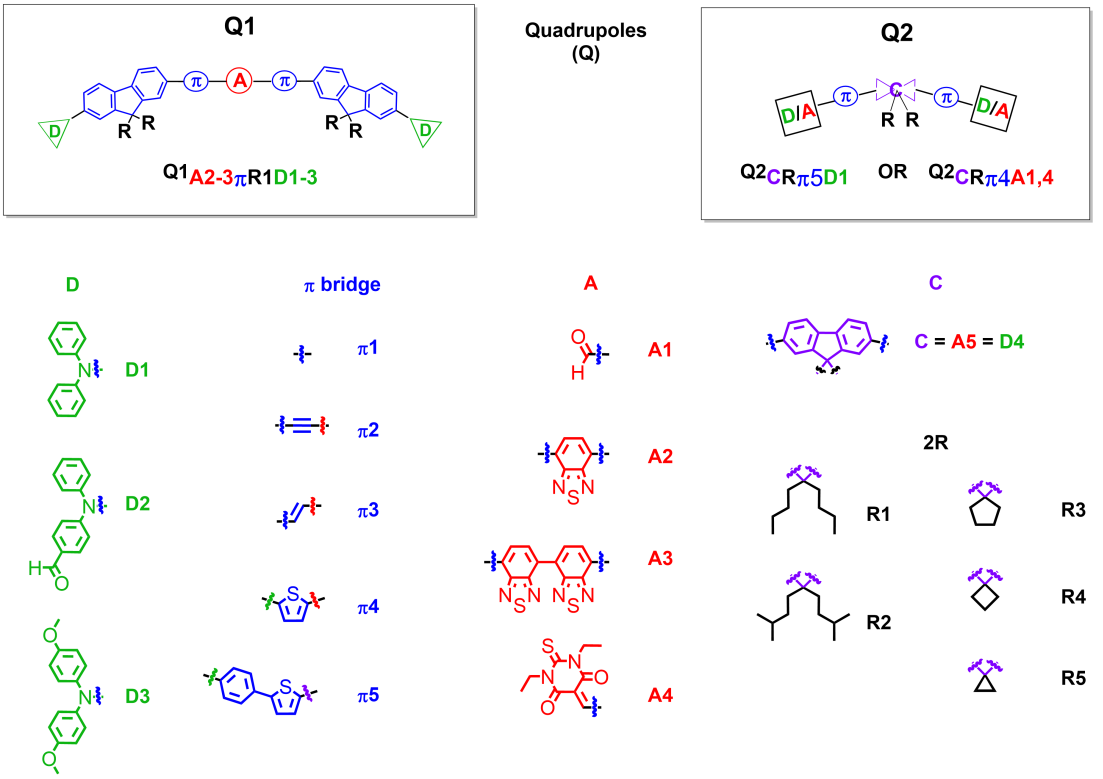

Figure 2. Examples of quadrupolar dyes developed in the team for the bottom-up molecular engineering of bright dFONs for bioimaging. Adapted from Refs. [36,37,39–41].

3. Bottom-up engineering of optical properties

In view of optical bioimaging, "redder is better" due to improved penetration depth and easier detection. In that perspective, we have been keen on red-shifting the absorption and emission of dFONs (bathochromic shift) and increasing their one- and two-photon response (hyperchromic effect) as well as their one- and two-photon brightnesses.

3.1. *Adjusting the strength of D and A moieties*

A classical strategy involves the increase in the D/A strength or the extension of the π-linker. Such a strategy is illustrated in Figure 4A for dipolar dyes. We note that a bathochromic shift is observed both in solution and in dFONs when increasing the strength of the donor or acceptor. A hyperchromic shift is also observed, such that for dFONs of similar size (i.e., same amount of dye subunits), the ones with a stronger donor or acceptor have a larger absorptivity. A bathochromic shift of the emission is also observed such that *dFONs made from dipolar dyes* $\mathbf{D_{D3\pi2A1}}$ *and* $\mathbf{D_{D3\pi2A5}}$ *are respectively red–orange and NIR-I emitters that show huge brightnesses in water, larger than those of* QDs *without the need for surfactants or coating.* We also note the effect of the size of substituents on fluorescence intensity: dFONs made from $\mathbf{D_{D3\pi2A1}}$ have an almost twice larger quantum yield than dFONs made from $\mathbf{D_{D1\pi2A1}}$, emphasizing the role of substituent size on the organization of PPDs within dFONs (Figure 4A).

Subtle tuning can be achieved by tweaking the donor strength or the acceptor strength both for dipolar [33,40] and quadrupolar dyes [41] (Figure 4B).

3.2. *Adjusting the π-linker's nature and length*

Similarly, a hyperchromic and bathochromic shift can be achieved by adjusting the length and nature

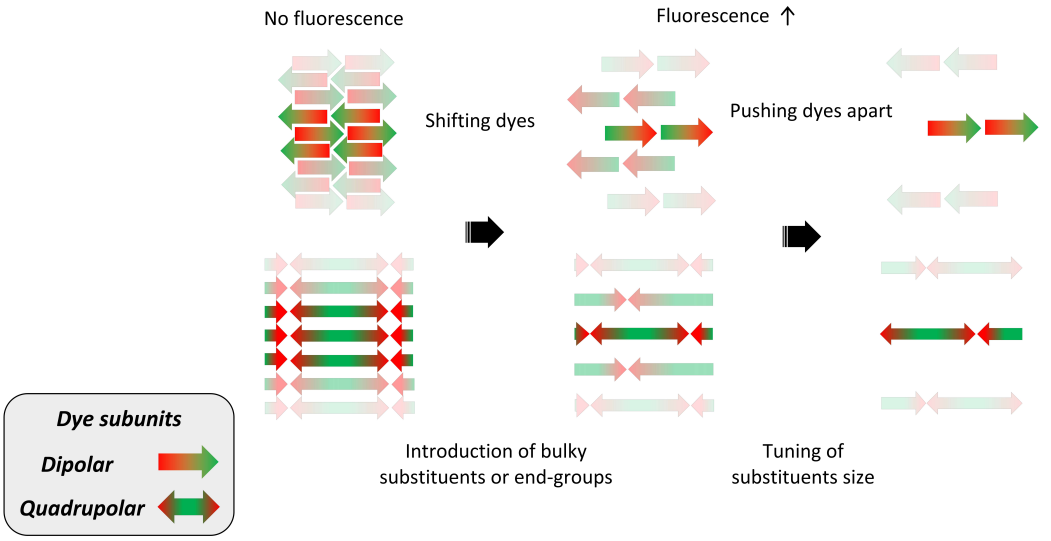

Figure 3. Tuning the organization of dipolar (arrow) and quadrupolar (double arrow) dye subunits in dFONs and its impact on fluorescence intensity.

of the π-linkers as illustrated in Figure 4A for dipolar dyes and in Figure 5 for quadrupolar dyes [37,40].

We note that similar trends are observed for dyes in solution and dFONs. On the other hand, the observed changes in fluorescence quantum yield emphasize the impact of dye size and geometry on dye packing within dFONs in the case of quadrupolar dyes. Indeed dFONs made from $\mathbf{Q1_{A2\pi3R1D1}}$ show a much lower fluorescence quantum yield than dFONs made from $\mathbf{Q1_{A2\pi1R1D1}}$ and $\mathbf{Q1_{A2\pi2R1D1}}$ and even than dFONs made from $\mathbf{Q1_{A2\pi4R1D1}}$ although the latter are significantly redshifted (Figure 5). As a result, *dFONs made from quadrupolar dyes* $\mathbf{Q1_{A2\pi1R1D1}}$ *and* $\mathbf{Q1_{A2\pi4R1D1}}$ *are respectively orange–red and deep red emitters that exhibit a very large brightness.*

3.3. *Adjusting the geometry of the PPDs and the size of substituents to tune packing and fluorescence properties*

Not only may the geometry of the PPDs significantly influence the fluorescence quantum yield (and thus affect the brightness) of dFONs, but it can also be used to change the emission color by controlling and exploiting the local environment created by local dipoles within dFONs. Indeed, whereas dipolar $\mathbf{D_{A1\pi1D1}}$ and related octupolar $\mathbf{O_{A1\pi1D4}}$ PPDs have identical fluorescence properties in solution (fluorescence quantum yields and lifetimes) and show the same emission solvatochromism (blue emission in toluene, green emission in chloroform and orange emission in DMSO), dFONs made from $\mathbf{D_{A1\pi1D1}}$ are green emitters whereas dFONs made from $\mathbf{O_{A1\pi1D4}}$ are orange emitters: the three-branched geometry of $\mathbf{O_{A1\pi1D4}}$ imposes a different packing from the rod-like $\mathbf{D_{A1\pi1D1}}$, generating a stronger local electric field such that $\mathbf{O_{A1\pi1D4}}$ dyes experience a larger polarity within dFONs (similar to DMSO) and its emission is redshifted [32].

Another way to influence the packing of PPDs and tune their luminescence properties is to adjust the size of the bulky substituents. A striking example is given in Figure 6 for a series of quadrupolar dyes built from a fluorenyl core. All dyes bear the same electron-withdrawing end-groups and π-linker, the only difference being the nature of the substituents; cyclopentyl, cyclobutyl and cyclopropyl for dyes with a spirofluorene core or two *iso*pentyl chains for dyes with a bis-alkyl fluorene core. Whereas all quadrupolar dyes show identical optical properties in solution, dFONs fluorescence is strongly affected [55]. Decreasing the size of the cycle in spirofluorenyl derivatives generates a redshift of the dFONs fluorescence, allowing one to tune the dFONs fluorescence from blue (cyclopentyl), to cyan (cyclobutyl)

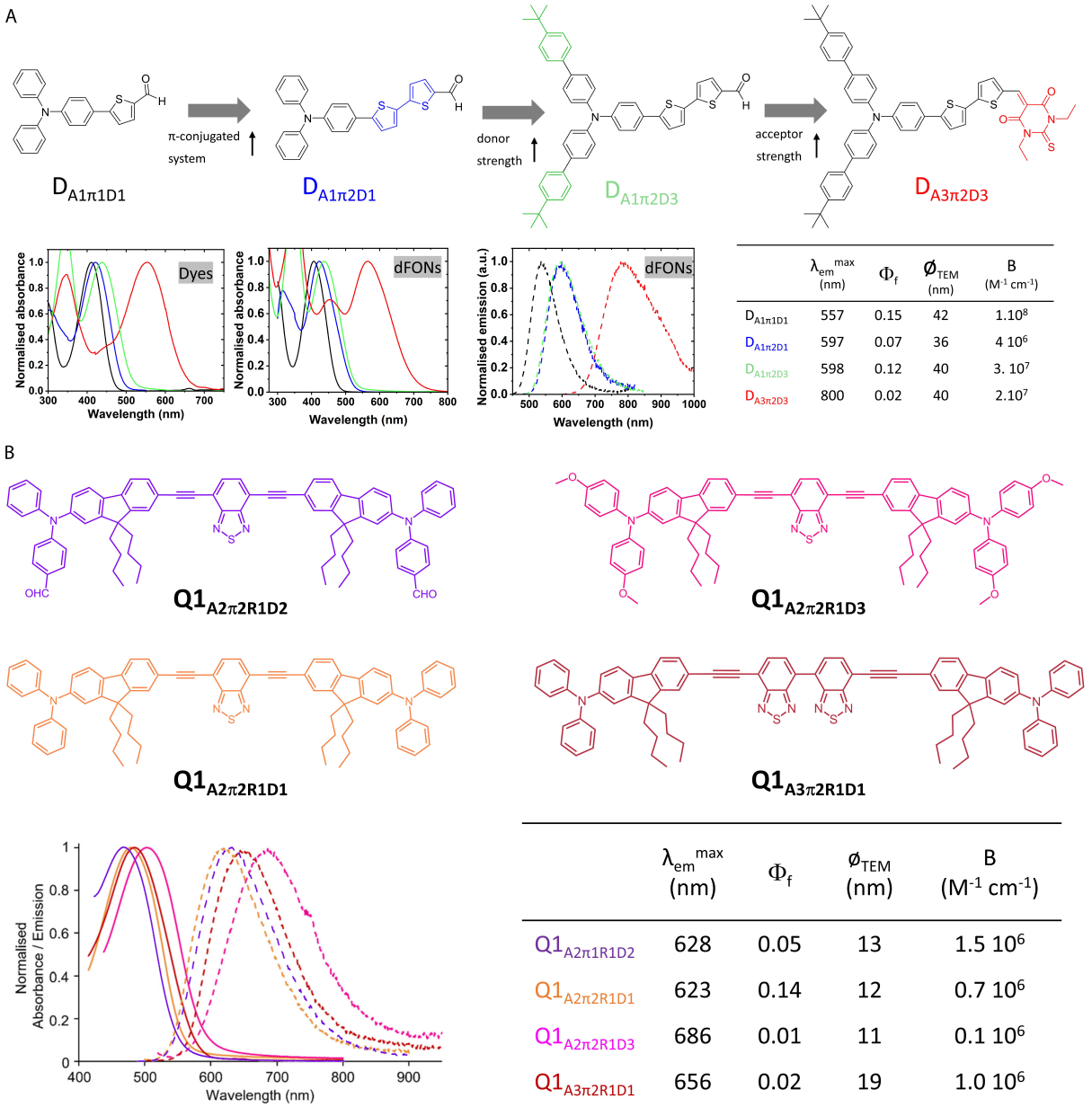

	λ_{em}^{max} (nm)	Φ_f	$\varnothing_{TEM}$ (nm)	B (M^{-1} cm^{-1})
$D_{A1\pi1D1}$	557	0.15	42	1.10^8
$D_{A1\pi2D1}$	597	0.07	36	$4\ 10^6$
$D_{A1\pi2D3}$	598	0.12	40	$3.\ 10^7$
$D_{A3\pi2D3}$	800	0.02	40	2.10^7

	λ_{em}^{max} (nm)	Φ_f	$\varnothing_{TEM}$ (nm)	B (M^{-1} cm^{-1})
$Q1_{A2\pi1R1D2}$	628	0.05	13	$1.5\ 10^6$
$Q1_{A2\pi2R1D1}$	623	0.14	12	$0.7\ 10^6$
$Q1_{A2\pi2R1D3}$	686	0.01	11	$0.1\ 10^6$
$Q1_{A3\pi2R1D1}$	656	0.02	19	$1.0\ 10^6$

Figure 4. Effect of donor and acceptor end-group strength and π-linker length on the optical properties of dFONs made from dipolar ("push–pull") dye (A: top) and quadrupolar dyes (B: bottom). Adapted from Refs. [32,34,35] and [40,41].

and to red–orange (cyclopropyl). This illustrates the effect of subtle tuning of the side-chain size on the packing of the dyes and thus on fluorescence. We note that the quadrupole with two *iso*pentyl chains leads to dFONs whose fluorescence is both red-shifted (green emission) compared to its spiro (cyclopentyl) analog and enhanced by a factor of 2, demonstrating the effect of substituent size and bulkiness on dye packing and its consequences on optical properties.

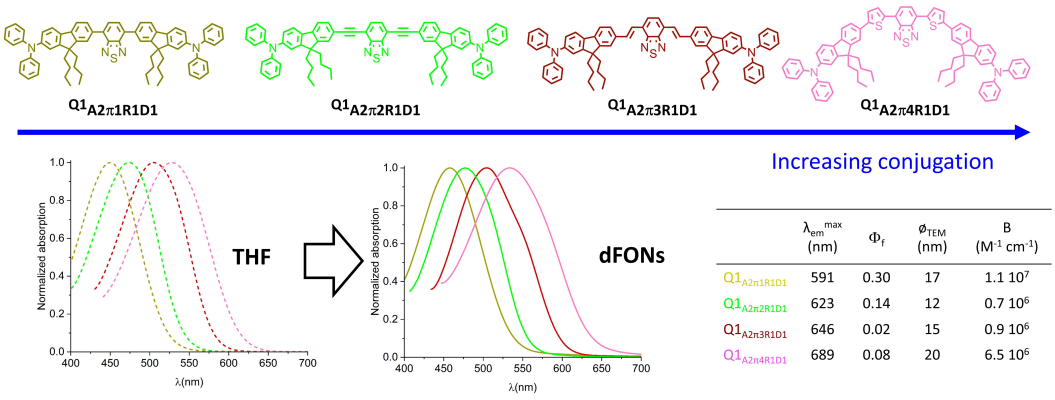

	λ_{em}^{max} (nm)	Φ_f	ϕ_{TEM} (nm)	B (M^{-1} cm^{-1})
$Q1_{A2\pi1R1D1}$	591	0.30	17	1.1 10^7
$Q1_{A2\pi2R1D1}$	623	0.14	12	0.7 10^6
$Q1_{A2\pi3R1D1}$	646	0.02	15	0.9 10^6
$Q1_{A2\pi4R1D1}$	689	0.08	20	6.5 10^6

Figure 5. Effect of π-linker length and structure on the optical properties of dFONs made from quadrupolar dyes. Adapted from Ref. [37].

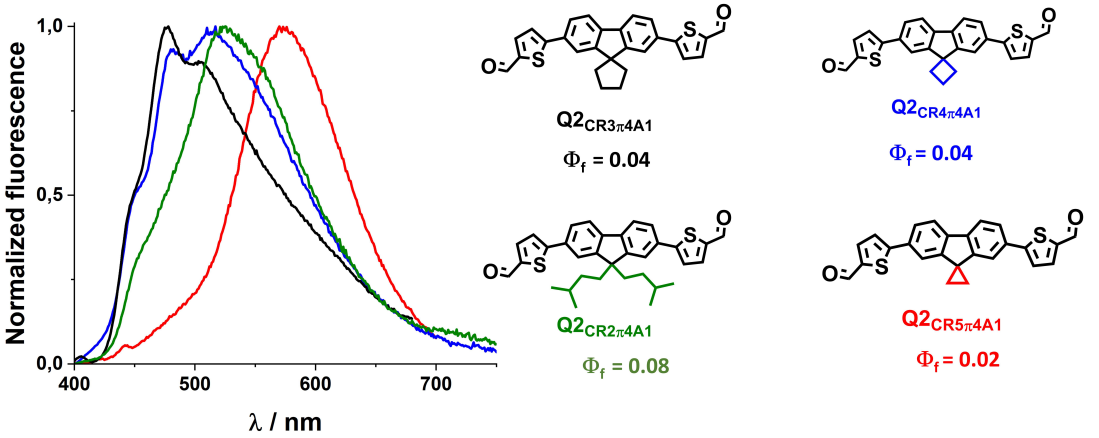

Figure 6. Influence of the substituents on the fluorenyl core of quadrupolar dyes on the fluorescence emission of corresponding dFONs in water.

3.4. *Enhancing two-photon absorption. Effects of confinement*

The two-photon absorption of dipolar and quadrupolar dyes can be modulated by molecular engineering, adjusting the donor and acceptor groups as well as the length and nature of the π-conjugated linker [28,29,31,52]. Increasing the strength of the donor or acceptor groups in dipolar thienothiophene [33] or bisthienyl [40] dyes allows one to significantly increase their response in solution as illustrated in Figure 7A. Yet, the molecular confinement of dipolar dyes within dFONs has a major effect on their 2PA response; either a major decrease (by a factor of 3 or 2 for $\mathbf{D_{A4\pi3D1}}$ and $\mathbf{D_{A4\pi3D3}}$) or an increase ($\mathbf{D_{A1\pi3D1}}$ and $\mathbf{D_{A4\pi3D2}}$) of the 2PA cross-section of the dipolar dyes is observed upon confinement within dFONs (Figure 7A). This phenomenon can be ascribed to electrostatic interactions between dipolar and polarizable dyes depending on their relative orientation and proximity [11,30]. The striking difference between the 2PA response of dyes $\mathbf{D_{A4\pi3D1}}$ and $\mathbf{D_{A4\pi3D2}}$ into dFONs illustrates the positive role of the Br substituent in tuning the packing and allowing a cooperative enhancement of the 2PA [11], as is also the case for $\mathbf{D_{A1\pi3D1}}$ (Figure 7A). Although the fluorescence quantum yields of NIR-I-emitting dFONs made from dipolar dyes $\mathbf{D_{A4\pi3D2}}$ and $\mathbf{D_{A4\pi3D3}}$ remain low in water, their large 2PA response and number of dye subunits in dFONs lead to a very large two-photon brightness at 1070 nm (Figure 7A). As such, they

provide interesting nanoprobes for NIR-II to NIR-I bioimaging in living tissues.

The increase in length leads to a redshift of the 2PA as was the case for the 1PA, but it also induces a major increase in the two-photon absorption response of the quadrupolar dyes, both in solution and as dFONs building blocks. (Figure 7B). The nature of the elongating moieties (ethynyl, vinyl or thienyl) influences not only the fluorescence quantum yield and the emission color (see Section 3.2) but also the 2PA response: an enhancement is observed upon increased conjugation [37]. Interestingly, in all cases, confinement does not reduce the 2PA response of the dyes but rather leads to broadening of the 2PA spectrum [37]. Thanks to the combined variation of the 2PA responses and of the fluorescence quantum yields values, the orange–red and deep red emitting dFONs made from $\mathbf{Q1_{A2\pi1R1D1}}$ and $\mathbf{Q1_{A2\pi4R1D1}}$ also show the largest 2P brightness. As such, they represent bright nanoprobes for NIR-I to red bioimaging [37].

3.5. *Enhancing brightness by increasing size*

The brightness of dFONs made from PPDs can be enhanced simply by increasing the size of the dFONs, as is the case for QDs. This can be achieved by adjusting the nanoprecipitation conditions, notably the dye concentration of the stock solution in the organic solvent [27]. Contrarily to QDs, this does not lead to a change of the luminescence properties (emission spectrum, fluorescence quantum yield) as shown in the case of dFONs made from dipolar dye $\mathbf{D_{A1\pi2D1}}$ [35] and quadrupolar dye $\mathbf{Q1_{A2\pi1D1}}$ [36]. Hence, dFONs with a similar emission color but different sizes (and thus brightnesses) can be obtained from PPDs, as can dFONs with a similar size but different emission colors [32,35,37].

4. Bottom-up engineering of surface properties

4.1. *Molecular engineering of dFONs stability*

Strikingly, molecular engineering of the PPDs also allows tuning of the surface properties of dFONs. dFONs made from PPDs show good colloidal stability in relation with large surface potentials. This kinetic stability can be further enhanced by adjusting the structure of the PPDs. As illustrated in Figure 8, increasing the size of the π-conjugated linker [35] or adding bulky substituents on the donor end-group [33] or the nature of the acceptor end-group [34] of dipolar dyes allow increasing the colloidal and structural stability of dFONs. The evolution of the fluorescence quantum yield values over time is of major importance for the usability of dFONs for bioimaging but also the signature of the structural stability of dFONs made from dipolar dyes: the decrease in fluorescence over time is related to the exchange of dyes from the surface to the bulk water back to the surface, leading to surface defects that are responsible for fluorescence quenching. Hence, the larger the interaction energy of the dyes with the surface (i.e., the energy required to extract a surface dye from the surface to the bulk), the slower the process [54]. Therefore stronger electrostatic interchromophoric interactions within dFONs and addition of hydrophobic substituents allow improving their colloidal and structural stability. As a result, dFONs made from $\mathbf{D_{A5\pi2D3}}$ show very high colloidal and structural stability [34].

4.2. *Molecular engineering of dFONs cell internalization and stealthiness*

Strikingly, the interaction of dFONs with cell membranes can also be "bottom-up-engineered" by adjusting the structure of the PPDs. dFONs made from the dipolar dyes $\mathbf{D_{A5\pi2D3}}$ were found to be non-toxic and to internalize within cells while retaining their structural integrity [34]. In contrast, articulated dipoles ($\mathbf{Ad_{A1D5\pi5R}}$, Figure 1) bearing two long hydrophobic chains were found to show no non-specific interactions with cell membranes, exhibiting an intrinsically stealth behavior [42]. Hence, such *dFONs made only of pure PPDs* do not require specific coatings (PEG or zwitterionic) to be made stealth. As such, thanks to their high brightness and intrinsic stealth character, they hold promise for imaging of specific receptors in cells once surface-functionalized with specific targeting moieties.

Similarly, dFONs made from quadrupolar dyes built from a spiroflurenyl core ($\mathbf{Q_{2CR3\pi5D1}}$ and $\mathbf{Q_{2CR3\pi4A4}}$) were found to internalize within cells [39] while retaining their structural integrity. In contrast, quadrupoles $\mathbf{Q1_{A2\pi1R1D1}}$ [36], $\mathbf{Q1_{A2\pi2R1D1}}$ [37], $\mathbf{Q1_{A2\pi2R1D2}}$ [41], $\mathbf{Q1_{A2\pi21RD3}}$ [41] and $\mathbf{Q1_{A2\pi4R1D1}}$ [37], with a rigid elongated

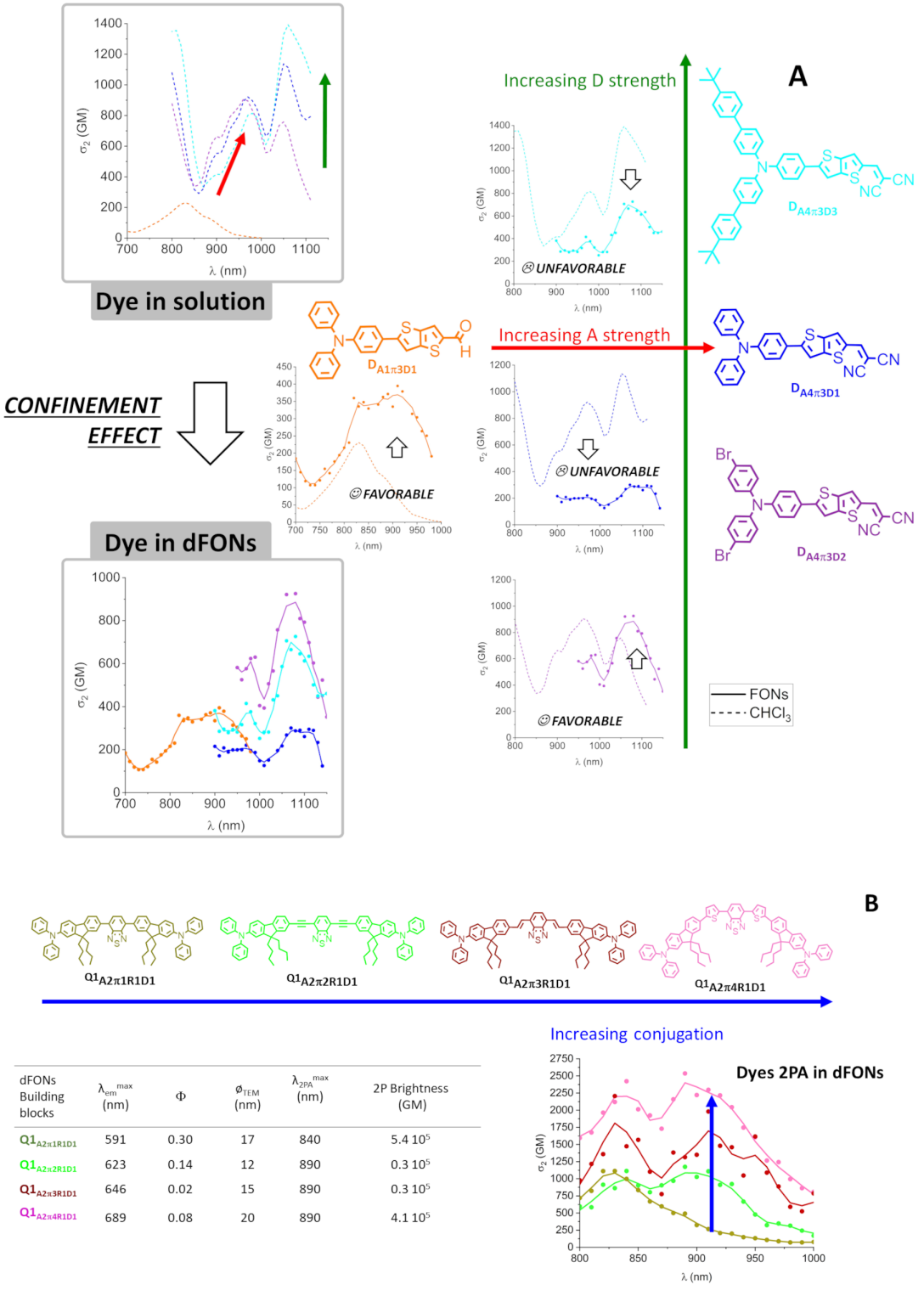

dFONs Building blocks	λ_{em}^{max} (nm)	Φ	ϕ_{TEM} (nm)	λ_{2PA}^{max} (nm)	2P Brightness (GM)
$Q1_{A2\pi1R1D1}$	591	0.30	17	840	$5.4\ 10^5$
$Q1_{A2\pi2R1D1}$	623	0.14	12	890	$0.3\ 10^5$
$Q1_{A2\pi3R1D1}$	646	0.02	15	890	$0.3\ 10^5$
$Q1_{A2\pi4R1D1}$	689	0.08	20	890	$4.1\ 10^5$

Figure 7. Molecular engineering of the two-photon absorption of dFONs made from dipolar [33] (A: top) or quadrupolar [37] (B: bottom) dyes.

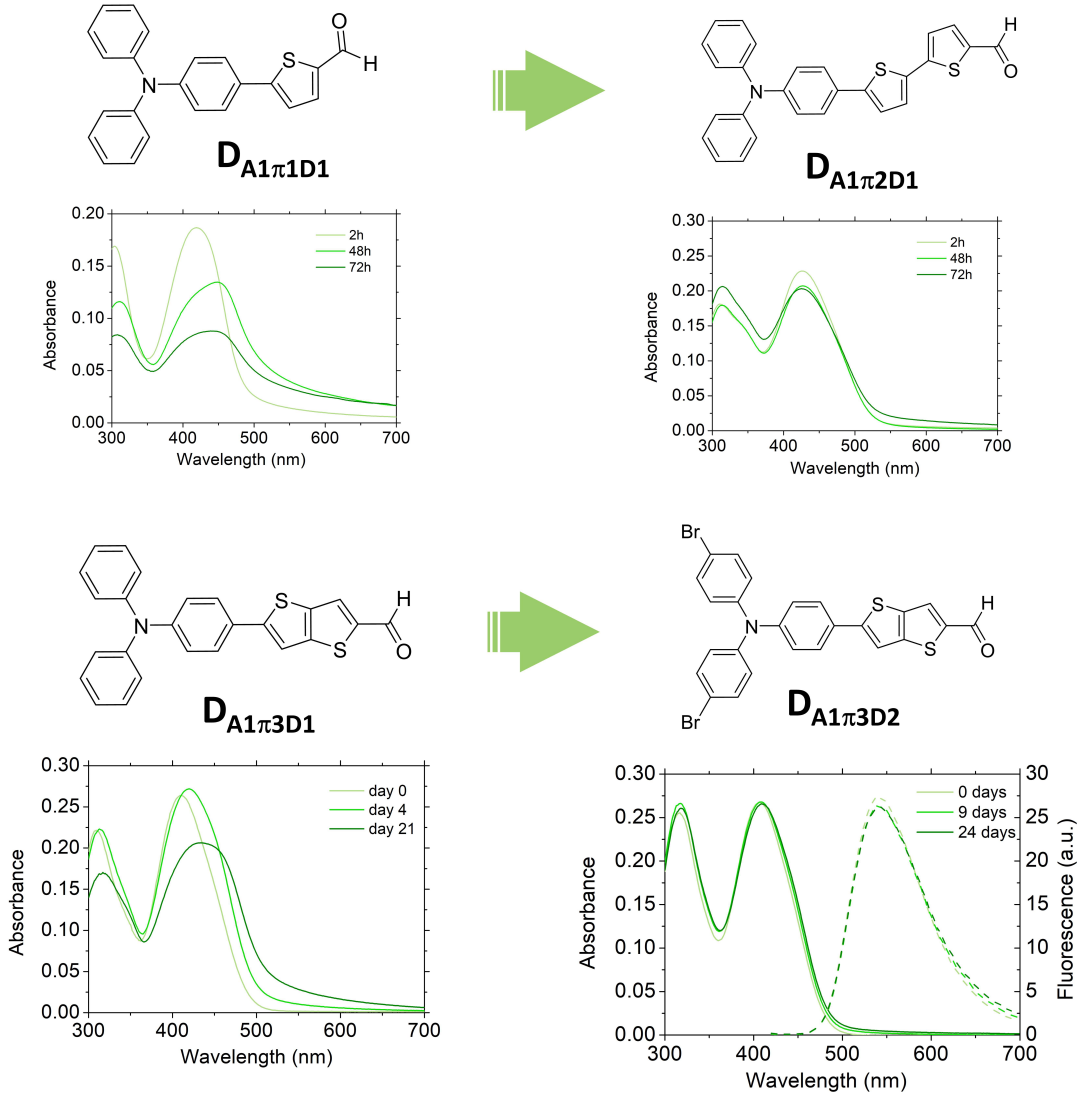

Figure 8. Molecular engineering of the colloidal and structural stability of dFONs made from dipolar dyes. Adapted from Refs. [33] and [35].

conjugated system bearing four hydrophobic alkyl chains were found to be non-toxic and to exhibit a stealth behavior. Interestingly **Q1$_{A2\pi3R1D1}$** does not show a stealth behavior indicating that both the presence of several lipophilic chains and the nature of the π-conjugated system are decisive in controlling the nano-bio interface [37,41].

Furthermore, thanks to their highly negative surface potential, these dFONs can be surface-coated by a polycationic polymer, resulting in a reversal of the surface potential. This change in surface potential triggers the internalization of the dFONs within cells, opening a promising route towards innovative drug delivery protocols [37].

5. Bioimaging applications (in vitro and in vivo)

The unique combination of high colloidal stability, small size, giant brightness and tunability of dFONs made from PPDs makes them ideal candidates for bioimaging in dilute conditions (i.e., nM range).

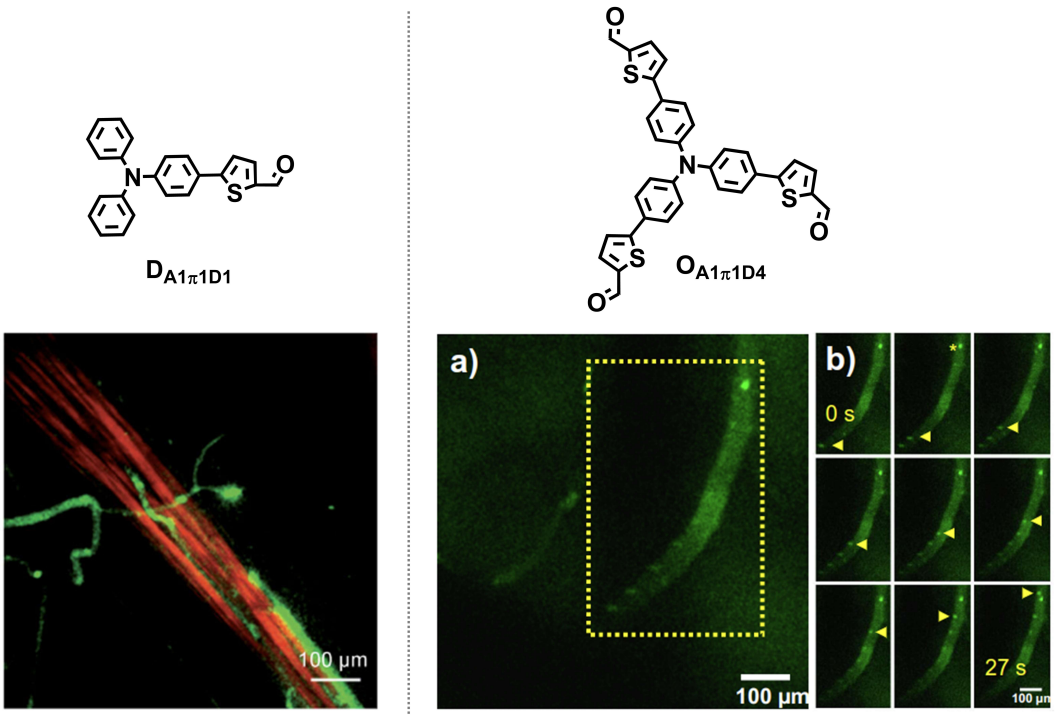

Figure 9. Two-photon angiography in small animals. Left, 3D projection Two-Photon Excitation Fluorescence (TPEF) and SHG (λ^{2P} @820 nm) image 90 min after injection of dFONs made from $\mathbf{D_{A1\pi1D1}}$. Right, 3D projection TPEF (λ^{2P} @820 nm) image 90 min after injection of dFONs made from $\mathbf{O_{A1\pi1D4}}$. For all images, the red color corresponds to the endogenous SHG signal (second harmonic generation at 410 nm) that arises from muscle tissue, while the green corresponds to the TPEF signal generated in vivo by the dye (460–590 nm). Scale bar: 100 µm. Adapted from Ref. [32].

5.1. *Two-photon angiography in small living animals [32]*

As discussed earlier, the molecular design of PPDs is crucial for dFONs properties with consequences on bioimaging applications. A typical case is the difference between dFONs made from dipolar dye $\mathbf{D_{A1\pi1D1}}$ and from its three-branched (octupolar) version $\mathbf{O_{A1\pi1D4}}$ when used as a contrast agent for angiography [32]. Both dFONs show a very large two-photon brightness (10^6 and 2×10^5 GM respectively for dFONs of about 35 nm in diameter) [32], one being a green emitter and the other an orange emitter. These dFONs were injected in the blood circulation of living *Xenopus laevis* tadpoles. The tail of the tadpole was then imaged by two-photon-excited fluorescence (TPEF) 20 min and 90 min after injection. Both dFONs allow the high contrast and high resolution visualization of blood vessels in the tiny animal (Figure 9) by two-photon excitation in the NIR region (820 nm) and detection of the green or red–orange fluorescence emitted by dFONs made from $\mathbf{D_{A1\pi1D1}}$ or $\mathbf{O_{A1\pi1D4}}$ dyes. Thanks to their nanoscale, the dFONs do not permeate through the walls of the blood vessels, thus allowing their imaging with high resolution. Furthermore, no toxicity is observed for the dFONs made from $\mathbf{D_{A1\pi1D1}}$. Yet, this is no longer true for the dFONs made from $\mathbf{O_{A1\pi1D4}}$, which quickly agglomerate into large micro-agglomerates resulting in a deadly clogging of the blood vessels. Hence, not only does the geometry of the dye influence the optical properties of dFONs (see Section 3.3), but it also dramatically impacts the nature of their nano–bio interface and consequently their usability as a contrast agent for angiography by TPEF.

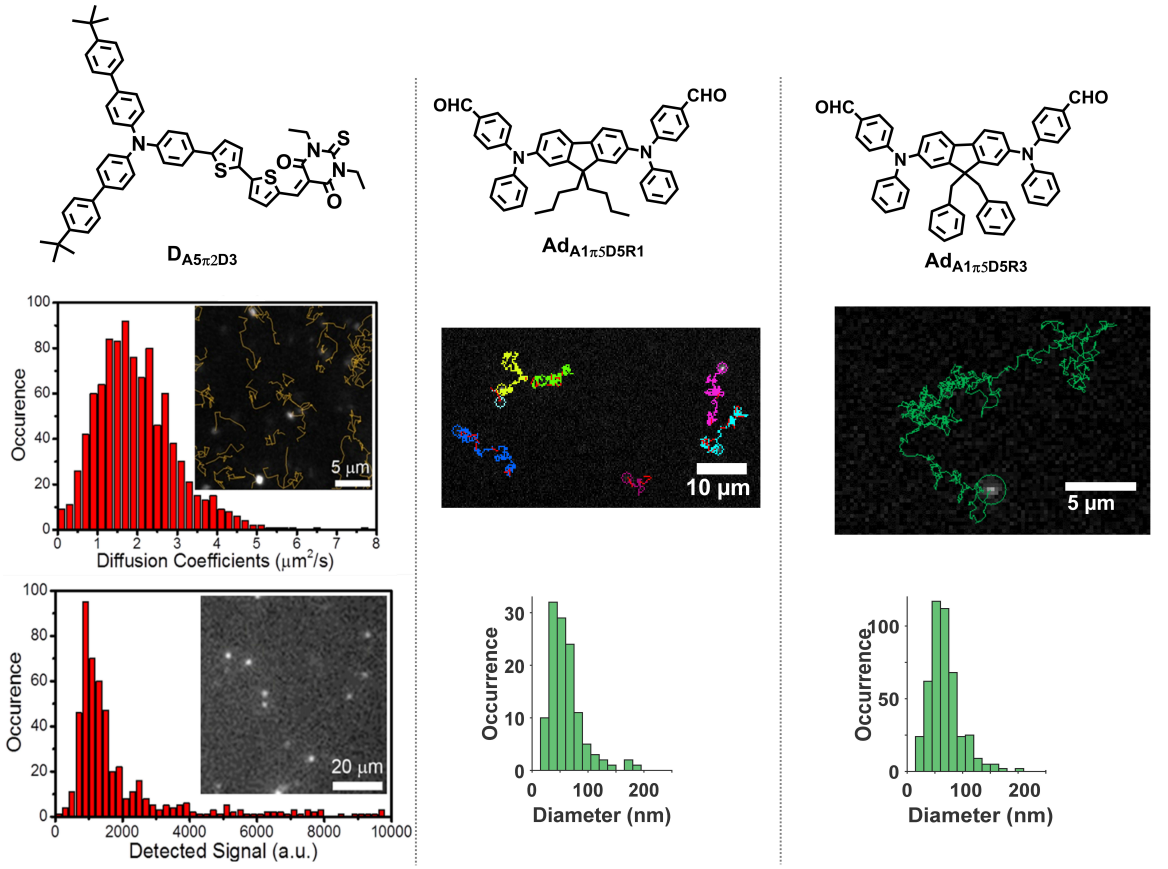

Figure 10. Single-particle tracking of dFONs made from $\mathbf{D_{A5\pi2D3}}$, $\mathbf{Ad_{A1D5\pi5R1}}$ and $\mathbf{Ad_{A1D5\pi5R3}}$ in water. Single-particle tracking of dFONs made from $\mathbf{D_{A5\pi2D3}}$ (left), $\mathbf{Ad_{A1\pi5D5R1}}$ (middle) in water and $\mathbf{Ad_{A1\pi5D5R3}}$ (right) in phosphate buffer saline (with 10% of fetal bovine serum). Examples of traces of single particles with corresponding histograms of hydrodynamic diameter are given. Adapted from Refs. [34] and [42].

5.2. *Single-particle tracking in solutions, cells and in the brain*

Single-particle tracking (SPT) is a class of techniques that allow one to dynamically follow the fate of single molecules in living tissues. In this respect, QDs are the most widely used nanoparticles thanks to their unprecedented brightness and photostability. Due to the giant brightness of dFONs made from PPDs (similar or higher than those of QDs), they represent promising candidates for SPT and their usability for SPT in aqueous solutions was investigated. A critical parameter in that respect is their photostability. Organics are recognized to be much less photostable than inorganics. Yet depending on the structure of the PPDs, we found that the brightness of dFONs made from dipolar ($\mathbf{D_{A5\pi2D3}}$) or quadrupolar ($\mathbf{Q_{2CR3\pi5D1}}$ and $\mathbf{Q_{2CR3\pi4A4}}$) dyes allows performing single particle tracking with adequate [34], good [39] to excellent photostability (up to 3 min) [39]. The reconstruction of the trajectories of single particles gives access to the hydrodynamic diameter of the nanoparticles. The hydrodynamic size of dFONs made from articulated dipole-based ($\mathbf{Ad_{A1D5\pi5R1}}$, $\mathbf{Ad_{A1D5\pi5R2}}$ and $\mathbf{Ad_{A1D5\pi5R3}}$) was found to be similar to the dry diameter measured by transmission electronic microscopy [42]. Interestingly, SPT experiments conducted in saline aqueous buffer containing proteins (i.e., PBS with fetal bovine serum) reveal that the hydrodynamic size of articulated dipole-based ($\mathbf{Ad_{A1D5\pi5R1}}$, $\mathbf{Ad_{A1D5\pi5R2}}$ and $\mathbf{Ad_{A1D5\pi5R3}}$) dFONs increases by ~30–40% (Figure 10) as compared to that determined in pure water [42]. Such an increase reveals the formation of

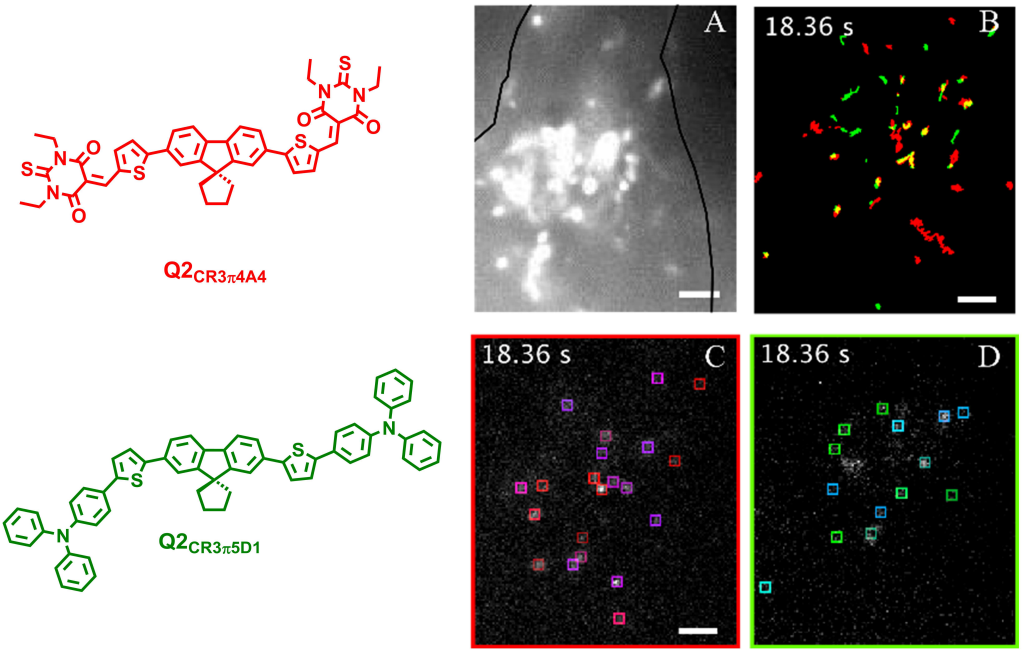

Figure 11. Simultaneous bicolor single-particle tracking within COS cells. Simultaneous bicolor single-particle tracking of dFONs made from $\mathbf{Q2_{CR3\pi4A4}}$ and $\mathbf{Q2_{CR3\pi5D1}}$ in live COS7 cells; A. wide field, COS7 cell contour is drawn in black; B. Merged single particle tracks on green and red channels; C. Live tracking of $\mathbf{Q2_{CR3\pi4A4}}$ dFONs (boxes) in COS7 cells on red channel; D. Live tracking of $\mathbf{Q2_{CR3\pi5D1}}$ dFONs (boxes) in COS7 cells on green channel; Scale bar = 5 μm, excitation at 488 nm (P = 306 W·cm^{-2}). Adapted from Ref. [39].

a protein corona at the surface of the nanoparticles, thus preventing aggregation of dFONs despite the ionic strength of the solution. The presence of such a corona is definitely an advantage for bioimaging in live cells when dFONs are used as tracers.

SPT experiments can also be performed with quadrupolar dye-based ($\mathbf{Q_{2CR3\pi5D1}}$ and $\mathbf{Q_{2CR3\pi4A4}}$) dFONs *within cells*. Interestingly, due to their different sizes (43 nm and 14 nm for $\mathbf{Q_{2CR3\pi5D1}}$ and $\mathbf{Q_{2CR3\pi4A4}}$, respectively) and different absorption spectra (λ_{abs}^{max} = 400 nm and 503 nm for $\mathbf{Q_{2CR3\pi5D1}}$ and $\mathbf{Q_{2CR3\pi4A4}}$, respectively), the two dFONs show similar and large brightnesses at 488 nm (wavelength of the blue laser). Yet their emission can be discriminated easily as dFONs made from $\mathbf{Q_{2CR3\pi5D1}}$ are green emitters while dFONs made from $\mathbf{Q_{2CR3\pi4A4}}$ are NIR-I emitters. Thanks to these unique properties, these dFONs that internalize into cells (see Section 4.2) can be tracked at the single-particle level and used together for *simultaneous bicolor SPT within cells* (Figure 11) [39].

To date, the wealth of information provided by SPT was mostly obtained in simplified systems such as cell monolayers. However, the microenvironment of a cell highly regulates its behavior and its molecular dynamics. There is therefore a need to perform SPT deep in intact tissues. Using small (10 nm in diameter), bright red-emitting and stealth dFONs made from quadrupolar dyes $\mathbf{Q1_{A2\pi1R1D1}}$, it was possible to explore the extracellular brain space deeper into tissues than with the equivalent QDs (i.e., QD655). The small dFONs diffuse deep into organotypic brain slices and can be tracked down to 150 μm depth while QD655 are no longer detected [36] (Figure 12).

6. Conclusion and perspectives

The molecular engineering of dedicated polar ("push–pull") and polarizable dyes as dFONs building blocks has proven to be a successful approach to achieve ultrabright small luminescent organic nanoparticles that compete with QDs for bioimaging

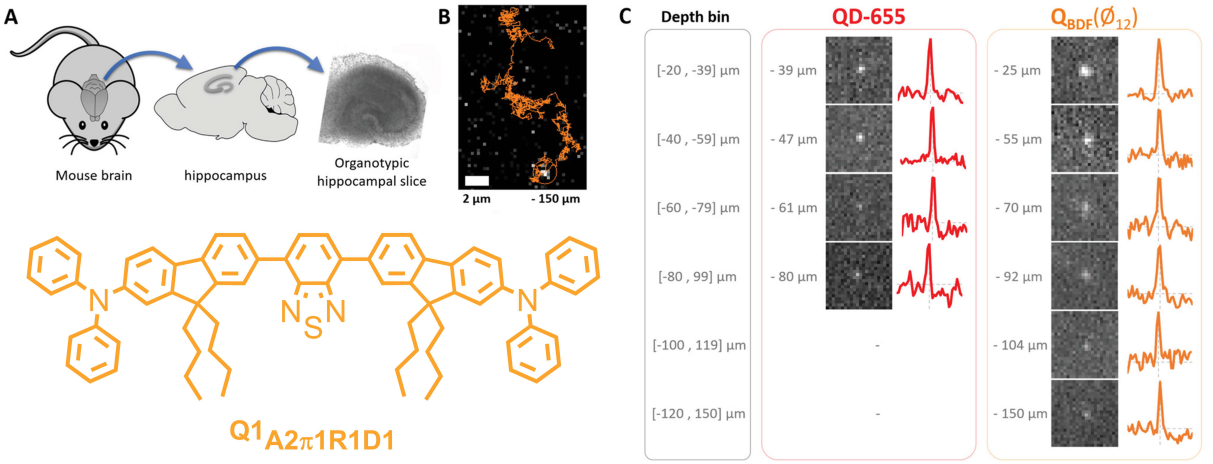

Figure 12. Single-particle tracking deep into brain tissues. Single-particle tracking of small (10 nm) dFONs made from $\mathbf{Q1_{A2\pi1D1}}$ in organotypic brain slices. (A) Organotypic brain slices preparation after extraction of the mouse brain and dissection of the hippocampus. (B) Trace of single-particle tracking for 11 s, 150 µm below the surface of an organotypic brain slice. (C) Fluorescence images of single QDs-655 and $\mathbf{Q1_{A2\pi1D1}}$ dFONs recorded at the indicated depths (an intensity profile of single particle is provided on the right). Fields of view are 6.5 µm wide. Adapted from Ref. [36].

purposes. Not only can their optical properties be modulated, but their (photo)stability and surface properties can be tuned by adjusting the structure of the PPDs. This demonstrates that organics can also play an important role in the field of Nanobiotechnologies, opening new routes for nanotools for drug delivery or super-resolution imaging. dFONs made from PPDs is a highly versatile approach benefiting from the wide wealth of organic dyes. Compared to inorganics, such dFONs may provide a safer and more sustainable alternative: their toxicity can be tuned by adjusting the structure of the dyes, while their synthesis can benefit from green protocols.

An important aspect is their surface functionalization for applications such as early diagnostic, ultrasensitive sensing and super-resolution imaging. In that respect, two main approaches are developed: non-covalent (electrostatic-based) functionalization [37] and covalent functionalization [56]. We are currently investigating these routes.

Declaration of interests

The authors do not work for, advise, own shares in, or receive funds from any organization that could benefit from this article, and have declared no affiliations other than their research organizations.

Funding

The Conseil general d'Aquitaine is acknowledged for financial support (Chaire d'Excellence Grant to MBD). Financial supports for ODP and EK is provided through the MESRI via the University of Bordeaux. Continuous support from Univ. Bordeaux, CNRS and Bordeaux-INP is acknowledged. This work was also supported by the ERC COMET (101077364).

References

[1] L. D. Lavis, R. T. Raines, *ACS Chem. Biol.*, 2008, **3**, 142-155.
[2] A. H. Ashoka, I. O. Aparin, A. Reisch, A. S. Klymchenko, *Chem. Soc. Rev.*, 2023, **52**, 4525-4548.
[3] W. R. Algar, M. Massey, K. Rees, R. Higgins, K. D. Krause, G. H. Darwish, W. J. Peveler, Z. Xiao, H.-Y. Tsai, R. Gupta, K. Lix, M. V. Tran, H. Kim, *Chem. Rev.*, 2021, **121**, 9243-9358.
[4] K. D. Wegner, N. Hildebrandt, *Chem. Soc. Rev.*, 2015, **44**, 4792-4834.
[5] R. Gui, H. Jin, Z. Wang, L. Tan, *Coord. Chem. Rev.*, 2017, **338**, 141-185.
[6] D. R. Larson, W. R. Zipfel, R. M. Williams, S. W. Clark, M. P. Bruchez, F. W. Wise, W. W. Webb, *Science*, 2003, **300**, 1434-1436.

[7] S.-C. Pu, M.-J. Yang, C.-C. Hsu, C.-W. Lai, C.-C. Hsieh, S. H. Lin, Y.-M. Cheng, P.-T. Chou, *Small*, 2006, **2**, 1308-1313.

[8] J. Dimitrijevic, L. Krapf, C. Wolter, C. Schmidtke, J.-P. Merkl, T. Jochum, A. Kornowski, A. Schüth, A. Gebert, G. Hüttmann, T. Vossmeyer, H. Weller, *Nanoscale*, 2014, **6**, 10413-10422.

[9] O. Mongin, T. R. Krishna, M. H. V. Werts, A.-M. Caminade, J.-P. Majoral, M. Blanchard-Desce, *Chem. Commun.*, 2006, **8**, 915-917.

[10] A. Sourdon, M. Gary-Bobo, M. Maynadier, M. Garcia, J.-P. Majoral, A.-M. Caminade, O. Mongin, M. Blanchard-Desce, *Chem. Eur. J.*, 2019, **25**, 3637-3649.

[11] F. Terenziani, V. Parthasarathy, A. Pla-Quintana, T. Maishal, A.-M. Caminade, J.-P. Majoral, M. Blanchard-Desce, *Angew. Chem. Int. Ed.*, 2009, **48**, 8691-8694.

[12] T. R. Krishna, M. Parent, M. H. V. Werts, L. Moreaux, S. Gmouh, S. Charpak, A.-M. Caminade, J.-P. Majoral, M. Blanchard-Desce, *Angew. Chem. Int. Ed.*, 2006, **45**, 4645-4648.

[13] J. J. Gravier, F. P. N. Y. Garcia, T. Delmas, F. Mittler, A.-C. Couffin, F. Vinet, I. Texier-Nogues, *JBO*, 2011, **16**, article no. 096013.

[14] R. Méallet-Renault, A. Hérault, J.-J. Vachon, R. B. Pansu, S. Amigoni-Gerbier, C. Larpent, *Photochem. Photobiol. Sci.*, 2006, **5**, 300-310.

[15] A. Reisch, P. Didier, L. Richert, S. Oncul, Y. Arntz, Y. Mély, A. S. Klymchenko, *Nat. Commun.*, 2014, **5**, article no. 4089.

[16] C. Grazon, J. Rieger, R. Méallet-Renault, G. Clavier, B. Charleux, *Macromol. Rapid Commun.*, 2011, **32**, 699-705.

[17] O. S. Wolfbeis, *Chem. Soc. Rev.*, 2015, **44**, 4743-4768.

[18] A. Patra, Ch. G. Chandaluri, T. P. Radhakrishnan, *Nanoscale*, 2012, **4**, 343-359.

[19] S. Fery-Forgues, *Nanoscale*, 2013, **5**, 8428-8442.

[20] F. Würthner, *Angew. Chem. Int. Ed.*, 2020, **59**, 14192-14196.

[21] A. M. Smith, M. C. Mancini, S. Nie, *Nat. Nanotech.*, 2009, **4**, 710-711.

[22] W. Denk, J. H. Strickler, W. W. Webb, *Science*, 1990, **248**, 73-76.

[23] M. Göppert-Mayer, *Ann. Phys.*, 1931, **401**, 273-294.

[24] A.-C. Robin, S. Gmouh, O. Mongin, V. Jouikov, M. H. V. Werts, C. Gautier, A. Slama-Schwok, M. Blanchard-Desce, *Chem. Commun.*, 2007, 1334-1336.

[25] T. Asahi, T. Sugiyama, H. Masuhara, *Acc. Chem. Res.*, 2008, **41**, 1790-1798.

[26] D. Horn, J. Rieger, *Angew. Chem. Int. Ed.*, 2001, **40**, 4330-4361.

[27] H. Nakanishi, H. Oikawa, in *Single Organic Nanoparticles* (H. Masuhara, H. Nakanishi, K. Sasaki, eds.), NanoScience and Technology, Springer, Berlin, Heidelberg, 2003, 17-31.

[28] F. Terenziani, C. Katan, E. Badaeva, S. Tretiak, M. Blanchard-Desce, *Adv. Mater.*, 2008, **20**, 4641-4678.

[29] M. Pawlicki, H. A. Collins, R. G. Denning, H. L. Anderson, *Angew. Chem. Int. Ed.*, 2009, **48**, 3244-3266.

[30] F. Terenziani, M. Morone, S. Gmouh, M. Blanchard-Desce, *ChemPhysChem*, 2006, **7**, 685-696.

[31] M. Albota, D. Beljonne, J.-L. Brédas, J. E. Ehrlich, J.-Y. Fu, A. A. Heikal, S. E. Hess, T. Kogej, M. D. Levin, S. R. Marder, D. McCord-Maughon, J. W. Perry, H. Röckel, M. Rumi, G. Subramaniam, W. W. Webb, X.-L. Wu, C. Xu, *Science*, 1998, **281**, 1653-1656.

[32] V. Parthasarathy, S. Fery-Forgues, E. Campioli, G. Recher, F. Terenziani, M. Blanchard-Desce, *Small*, 2011, **7**, 3219-3229.

[33] C. Mastrodonato, P. Pagano, J. Daniel, M. Vaultier, M. Blanchard-Desce, *Molecules*, 2016, **21**, article no. 1227.

[34] E. Genin, Z. Gao, J. A. Varela, J. Daniel, T. Bsaibess, I. Gosse, L. Groc, L. Cognet, M. Blanchard-Desce, *Adv. Mater.*, 2014, **26**, 2258-2261.

[35] K. Amro, J. Daniel, G. Clermont, T. Bsaibess, M. Pucheault, E. Genin, M. Vaultier, M. Blanchard-Desce, *Tetrahedron*, 2014, **70**, 1903-1909.

[36] M. Rosendale, J. Flores, C. Paviolo, P. Pagano, J. Daniel, J. Ferreira, J.-B. Verlhac, L. Groc, L. Cognet, M. Blanchard-Desce, *Adv. Mater.*, 2021, **33**, article no. 2006644.

[37] P. Pagano, M. Rosendale, J. Daniel, J.-B. Verlhac, M. Blanchard-Desce, *J. Phys. Chem. C*, 2021, **125**, 25695-25705.

[38] J.-B. Verlhac, J. Daniel, P. Pagano, G. Clermont, M. Blanchard-Desce, *C. R. Chim.*, 2016, **19**, 28-38.

[39] J. Daniel, A. G. Godin, M. Palayret, B. Lounis, L. Cognet, M. Blanchard-Desce, *J. Phys. D: Appl. Phys.*, 2016, **49**, article no. 084002.

[40] P. Pagano, "Design and Synthesis of Ultra-Bright Organic Nanoparticles (ONPs) for Bioimaging", These de doctorat, Université de Bordeaux, Bordeaux, 2017.

[41] M. Rosendale, J. Daniel, F. Castet, P. Pagano, J.-B. Verlhac, M. Blanchard-Desce, *Molecules*, 2022, **27**, article no. 2230.

[42] M. Rosendale, G. Clermont, J. Daniel, C. Paviolo, L. Cognet, J.-B. Verlhac, M. Blanchard-Desce, *Proc. SPIE*, 2020, **11360**, article no. 1136005.

[43] F. Würthner, *Acc. Chem. Res.*, 2016, **49**, 868-876.

[44] L. Lescos, P. Beaujean, C. Tonnelé, P. Aurel, M. Blanchard-Desce, V. Rodriguez, M. de. Wergifosse, B. Champagne, L. Muccioli, F. Castet, *Phys. Chem. Chem. Phys.*, 2021, **23**, 23643-23654.

[45] J. Gierschner, S. Y. Park, *J. Mater. Chem. C*, 2013, **1**, 5818-5832.

[46] E. E. Jelley, *Nature*, 1936, **138**, 1009-1010.

[47] G. Scheibe, *Angew. Chem.*, 1937, **50**, 212-219.

[48] J. Gierschner, J. Shi, B. Milián-Medina, D. Roca-Sanjuán, S. Varghese, S. Park, *Adv. Opt. Mater.*, 2021, **9**, article no. 2002251.

[49] M. Kasha, H. R. Rawls, M. Ashraf El-Bayoumi, *Pure Appl. Chem.*, 1965, **11**, 371-392.

[50] D. Bialas, C. Zhong, F. Würthner, F. C. Spano, *J. Phys. Chem. C*, 2019, **123**, 18654-18664.

[51] H. Zhang, Z. Zhao, A. T. Turley, L. Wang, P. R. McGonigal, Y. Tu, Y. Li, Z. Wang, R. T. K. Kwok, J. W. Y. Lam, B. Z. Tang, *Adv. Mater.*, 2020, **32**, article no. 2001457.

[52] M. Barzoukas, M. Blanchard-Desce, *J. Chem. Phys.*, 2000, **113**, 3951-3959.

[53] M. Barzoukas, C. Runser, A. Fort, M. Blanchard-Desce, *Chem. Phys. Lett.*, 1996, **257**, 531-537.

[54] J. Daniel, F. Bondu, F. Adamietz, M. Blanchard-Desce, V. Rodriguez, *ACS Photon.*, 2015, **2**, 1209-1216.

[55] J. Daniel, "Nano Outils Moléculaires Biphotoniques Pour Le Vivant", These de doctorat, Université de Bordeaux, Bordeaux, 2015.

[56] O. Dal Pra, J. Daniel, M. Blanchard-Desce, C. Grazon, "Surface functionalisation of dye-based fluorogenic organic nanoparticles: towards hyperbright biomarkers" (submitted).

ACADÉMIE DES SCIENCES
INSTITUT DE FRANCE

Comptes Rendus. Chimie
2024, Vol. 27, Special issue S2, p. 197-212
https://doi.org/10.5802/crchim.286

Research article

Women Chemists in France in 2024

Development of an analytical method for the simultaneous determination of 22 Polycyclic Aromatic Hydrocarbons (PAHs) in maternal and umbilical cord blood

Stéphanie Swiha [a, b], Valérie Pichon [*, a, c], Thierry Fournier [b, d, e], Sophie Gil [b, d, e] and Nathalie Delaunay [a]

[a] Laboratory of Analytical and Bioanalytical Sciences and Miniaturization, UMR CBI 8231 CNRS – ESPCI Paris, PSL University, Paris, France

[b] INSERM U1139, Faculté de Pharmacie, Paris, France

[c] Sorbonne Université, Paris, France

[d] Université Paris Descartes, UMR-S 1139, Sorbonne Paris Cité, Paris, France

[e] Fondation PremUP, Paris, France

Current address: LSABM, UMR CBI 8231 CNRS – ESPCI Paris, PSL University, 10 rue Vauquelin, 75231 Paris cedex 05, France (V. Pichon)

E-mail: valerie.pichon@espci.fr (V. Pichon)

Abstract. Pregnant women and their fetuses, a very fragile population, are exposed to polycyclic aromatic hydrocarbons (PAHs) and subject to potentially serious health risks. Consequently, the determination of PAHs in maternal serum and umbilical cord blood is necessary but challenging, due to their highly varied physico-chemical properties and trace presence. The aim of this project was to develop a method enabling, for the first time, the simultaneous determination of 22 listed PAHs from small volumes (100 µL) of maternal serum and umbilical cord blood, including a sample pre-treatment reducing as far as possible the quantity of solvents used. A solid-phase extraction step on C18-grafted silica was optimized by studying the effect of different parameters (nature and proportion of organic solvent added to the sample, washing and elution conditions) on extraction yields. The evaporation step was carefully controlled to limit the loss of the most volatile PAHs. Then, to break any interactions between PAHs and serum proteins, a precipitation step prior to solid-phase extraction was optimized using a design of experiments. The final sample processing procedure led to extraction yields of between 27 and 57% and between 34 and 69% for 22 PAHs in serum and umbilical cord blood, respectively, with standard deviation values of less than 11%. Limits of quantification between 0.2 and 3.1 µg/L were achieved for PAHs fluorescing in spiked real samples, close to the concentrations expected in biological samples.

[*] Corresponding author

Keywords. Polycyclic aromatic hydrocarbons, Maternal serum, Umbilical cord blood, Solid phase extraction, Liquid chromatography.

Funding. The authors gratefully acknowledge the Région Ile-de-France and the DIM Analytics for their financial support.

Manuscript received 29 November 2023, revised 5 December 2023 and 8 December 2023, accepted 19 January 2024.

1. Introduction

Polycyclic Aromatic Hydrocarbons (PAHs) are pollutants that are emitted naturally or produced by human activities, due to incomplete combustion or pyrolysis of organic materials (industries, road traffic, heating…) [1]. They are present in environment, but also in food, leading to a constant exposure of humans [2–4]. They are carcinogens and genotoxic substances. After entering the human body, due to their hydrophobic properties, PAHs are transported to all lipid-rich tissues. This is why a long-term exposure may lead to their accumulation in adipose tissue, liver, and kidney [4,5]. They can also undergo different metabolic transformations resulting to the formation of reactive electrophilic intermediates able to bind cellular macromolecules such as proteins and nucleic acids. It is now well established that these pollutants are chemical hazard to human health. Long-term exposure increases the risk of a series of cancers. Moreover, an exposure during pregnancy can lead to fetal malformations, prematurity and even disorders in children and adults [6–8]. This may come from a contamination of the placenta, which ensures multiple functions directly involved in the initiation and outcome of gestation, fetal growth and possibly the initiation of parturition, and/or of the fetal tissues through a transfer of PAHs via the placenta. This is why it is highly interesting to determine PAHs in both maternal and umbilical cord bloods and also in placenta.

Today, 24 different PAHs are listed as priority pollutants: 16 by the United State Environmental Protection Agency (US-EPA) and 16 by the European Food Safety Authority (EFSA), eight of them belonging to both lists. The 24 listed PAHs belong to a wide range of Log P values reported in Figure S1 (see Supplementary Information) [9–12], thus rendering their determination in biological samples particularly difficult but necessary as human contamination has multiple sources and because the EFSA PAHs are quite different from the US-EPA PAHs (higher number of aromatic cycles). Focusing on the determination of PAHs in blood, in most of the cases, only the US-EPA PAHs were targeted [13] except Pleil and coworkers who quantitated also 6 EFSA PAHs [14]. Typical blood, plasma, and serum used volumes range from 1 to 12 mL, which are quite large values, limiting the access to epidemiological cohort samples, with one exception of a study using pipette-tip solid-phase extraction (SPE) and only 200 µL of blood to determine the 16 US-EPA HAPs [15]. The most used technique for sample pretreatment consists in extracting the PAHs by liquid–liquid extraction (LLE) [6,14,16–26], but with some drawbacks such as the large volumes of used solvent and being time consuming as it involves several successive LLE steps, often three, to improve the extraction yields. Most of the time, the LLE steps were followed by SPE using C18-bonded silica, silica or silica/alumina packed in cartridge [17–19,21,24–26] to improve the clean-up of the sample extract by removing matrix interferents that could disturb the PAH quantitation.

SPE can also be used alone as an alternative approach to LLE to extract the PAHs from blood, plasma or serum prior to their chromatographic analysis [27–31]. It requires a lower volume of solvent than LLE and simple less-time consuming manipulations. Indeed, 1 mL [30] or 2 mL [28,29,31] of blood, plasma or serum were percolated on an apolar sorbent, C18-bonded silica when this information is given [27–29]. The SPE step was followed by an analysis with either gas chromatography coupled to mass spectrometry [27–29,31] or liquid chromatography (LC) coupled to a fluorescence detection (FD) [30]. Unfortunately, in some of these papers, several analytical data are missing, such as the nature of the SPE sorbent [30,31], the enrichment factors [28,31], the extraction yields in real samples [31], and the limits of quantitation (LOQs) in the biological matrices [28,31], whereas these data are necessary to be sure that the presented results are consistent. Moreover, only between seven and 16 PAHs were targeted and they only belong to the US-EPA list [27–31], even for the last study dealing with miniaturized pipette-tip SPE format involving 200 µL of sample [15].

Concerning the detected concentrations of PAHs in blood, plasma or serum, they were most often normalized with lipid content and reported in ng/g lipid. A study demonstrated that the mean lipid content in 283 maternal sera was 7.33 ± 1.86 g/L [32]. Using this value for the lipid content, it is therefore possible to convert the data reported in each study in the same unit and then to compare these estimated values, with the hypothesis that all the reported values are consistent. The highest mean values were observed by Song et al. with up to 37 μg/L of benzo[a]anthracene (BaA) in the blood of heavy-taste food consumers and a minimum mean value of 0.3 μg/L of pyrene (PYR) in the blood of Chinese non-smokers [27]. Similar values, between 0.05 and 2.7 μg/L, were determined for each of 13 US-EPA PAHs in blood plasma collected from Hong Kong residents [29]. These values are in accordance with the ones determined in sera of autopsied people in Tennessee, where the sum of the concentrations of 13 US-EPA PAHs varied between 0.1 and 12 μg/L [31]. Focusing on both maternal and cord sera, there are two Chinese studies reported values between 0.1 and 2.5 μg/L for 11 of the 16 US-EPA PAHs (the five other US-EPA PAH concentrations were below the LOQs) [28] and between 0.1 and 9.5 μg/L for the 9 targeted US-EPA PAHs [30]. This gives an idea of the PAH concentrations that one can expect in these kind of samples.

Due to the lack of consistent data of contamination level in literature, especially for the PAHs listed for food, there is still a great societal need to determine PAH concentrations in biological tissues or fluids to increase knowledge of their health effects, especially on at-risk populations such as pregnant women and their fetus. Therefore, the objective of this study is to develop a simple and low solvent consuming sample preparation step able to extract simultaneously the maximum of the 24 listed PAHs from maternal and umbilical cord sera. One of the challenges of this work is to obtain the best possible sensitivity from low volumes of sera in order to access to precious samples from epidemiological cohorts. For this, a protocol involving protein precipitation, SPE, and evaporation-redissolution before PAH analysis was developed. The key parameters of each sample pretreatment step were optimized. At last, to highlight the potential of the developed method, the extraction yields and LOQs were determined in both real spiked maternal and umbilical cord sera.

2. Materials and methods

2.1. *Chemicals*

HPLC grade methanol, acetonitrile (CH_3CN), propan-2-ol, and tetrahydrofuran (THF) were supplied by Carlo Erba (Val de Reuil, France). High purity water was dispensed by a milli-Q purification system (Millipore, Saint Quentin en Yvelines, France). The PAH standards were supplied by Cluzeau Info Labo (Sainte-Foy-La-Grande, France): acenaphthylene (ACY) 99%, cyclopenta[cd]pyrene (CPcdP) 99%, benzo[c]fluorene (BcF) 97%, benzo[j]fluorene (BjF) 99.7%, dibenzo[a,l]pyrene (DalP) 99.8%, dibenzo[a,e]pyrene (DaeP) 99.8%, dibenzo[a,h] pyrene (DahP) 99%, dibenzo[a,i]pyrene (DaiP) 99% at 10 mg/L in CH_3CN and a standard mixture of the 16 US-EPA PAHs at 100 mg/L in CH_3CN.

A stock solution mixture containing 100 μg/L of each PAH was prepared in CH_3CN and stored at 4 °C until further use. An aqueous solution containing 10% (w/v) sodium dodecyl sulfate (SDS) was purchased from Thermofisher Scientific (Villebon-Courtaboeuf, France). A synthetic serum was prepared from Earle's balanced salt solution containing albumin at 25 g/L and spiked with a mixture of 16 representative PAHs at 4 μg/L for each PAH in CH_3CN.

2.2. *Apparatus and analytical conditions*

The LC-diode array detector (DAD)/FD analyses were performed using an Agilent 1200 series system (Agilent Technologies, Massy, France) that was controlled by the Chemstation software. The separation was performed on a Pursuit PAH column (100 × 2.1 mm, 3 μm, Agilent Technologies) maintained at 35 °C with a column oven (Croco-cil, Interchim, Montluçon, France). Samples were analyzed using a linear gradient elution with water (A) and a mixture of CH_3OH:CH_3CN (6:4, v/v) (B). The gradient started at 50% of B and increased to 90% of B in 27 min, held for 13 min, and increased to 100% of B in 1 min, held for 10 min, and finally returned to initial composition within 1 min and let 10 min to equilibrate the system. The flow-rate was set at 0.2 mL/min

Table 1. LOQs (S/N = 10) in μg/L obtained with fluorescence and UV detections and estimated by injecting 10 μL of a solution of PAHs at 1, 5, and 20 μg/L in CH_3CN:water (1:1, v/v)

Compounds	λ_{UV} (nm)	λ_{ex}, λ_{em} (nm)	LOQ_{FD} (μg/L)	LOQ_{UV} (μg/L)
NAPH	220	269, 327	1.2	2.2
ACY	230	-	-	2.1
ACE	230	227, 315	0.5	2.3
FLO	260	227, 315	1.1	13.2
PHE	250	250, 364	0.4	1.5
ANT	250	250, 364	0.9	0.7
FLT	230	234, 454	0.9	4.8
PYR	240	237, 388	0.2	0.9
BcF	230	237, 388	0.3	8.0
CPcdP	230	-	-	6.8
BaA	275	265, 376	1.5	8.7
CHR	270	265, 376	0.1	6.3
5MCHR	270	265, 376	0.2	5.5
BjF	240	-	-	4.9
BbF	260	290, 440	0.3	4.6
BkF	240	290, 440	0.1	5.7
BaP	260	290, 440	0.2	4.5
DahA	295	292, 428	0.3	3.6
DalP	315	292, 428	0.4	6.7
BghiP	285	292, 428	0.3	15.9
IcdP	300	-	-	9.3
DaeP	310	280, 404	0.8	5.7
DaiP	240	390, 439	0.4	6.2
DahP	310	260, 456	0.4	2.0

and the injection volume was 5 or 10 μL. ACY, CPcdP, BjF, and indeno[1,2,3-cd]pyrene (IcdP) were quantified by UV, at 230 nm for both ACY and CPcdP, 240 nm for BjF, and 300 nm for IcdP. For the other PAHs, a time program of the excitation and emission wavelengths was performed and they were quantified with FD. The wavelengths are reported in Table 1.

2.3. *SPE procedure*

The SPE cartridges were Hypersep (25 mg of trifunctional octadecyl non-end-capped silica, 40–63 μm, 60 Å, 520 m^2/g, 21–23% carbon, ThermoFisher Scientific), Versaplate (25 mg of trifunctional octadecyl end-capped silica, 40 μm, 60 Å, 500 m^2/g, 17.4% carbon, Agilent Technologies) and BondElut SPEC (30 mg of trifunctional octadecyl non-end-capped silica, 70 Å, 220 m^2/g, 7% carbon, Agilent Technologies). The first SPE developments were carried out by percolating ultra-pure water spiked at 5 μg/L with PAHs on the Hypersep cartridges. Except when it is mentioned, the protocol was as follows: the cartridge was conditioned with 300 μL each of THF, CH_3OH, and H_2O:CH_3CN (1:1, v/v). After percolating 100 or 200 μL of a H_2O:CH_3CN (1:1, v/v) mixture spiked with PAHs, a washing step with 100 μL of H_2O:CH_3CN (1:1, v/v) was carried out and the cartridge was next dried. Finally, the PAHs were eluted with 300 μL of THF. The elution fraction was diluted with water to obtain a THF:H_2O mixture (1:1, v/v) before injection in LC-DAD/FD system or subjected to evaporation.

2.4. *Optimization of the evaporation step*

To enrich the SPE elution fraction, the optimization of an evaporation step was carried out by evaporating 200 µL of THF spiked with 5 µg/L of 20 PAHs to dryness or partially when 10 or 40 µL of an aromatic solvent (xylene, trimethylbenzene, or toluene) were added to THF. For both approaches, after the evaporation step, the extract was recovered in CH_3CN before its injection in LC-DAD/FD (5 µL).

2.5. *Optimization of the protein precipitation procedure with a design of experiment*

The optimization of the protein precipitation parameters was performed with a design of experiment (DOE). The DOE was constructed with two levels for the percentage of CH_3CN and heating and three levels for the percentage of SDS. The DOE was realized with an Earle's balanced salt solution containing albumin at 25 g/L (synthetic serum) and spiked at 4 µg/L with 16 PAHs (acenaphthene (ACE), fluorene (FLO), phenanthrene (PHE), anthracene (ANT), fluoranthene (FLT), PYR, BcF, chrysene (CHR), 5-methylchrysene (5MCHR), benzo[b]fluoranthene (BbF), benzo[k]fluoranthene (BkF), benzo[a]pyrene (BaP), dibenzo[a,h]anthracene (DahA), DalP, DaeP, and DahP) to prevent from wasting precious sera samples. For these experiments, only 16 PAHs among the 24 were selected in order to cover the whole range of hydrophobicity, except the less hydrophobic compounds, naphthalene (NAPH) and acenaphthylene (ACY) because of their higher LOQs. All samples were introduced in 2 mL Protein Lobind tubes (Eppendorf, Montesson, France). The denaturation and the precipitation of the albumin were carried out by adding an aqueous solution containing 10% of SDS (w/v) to achieve a final concentration of 0.1 or 0.2%. Some samples were next heated at 60 °C during 25 min. Then, different volumes of CH_3CN were added to obtain a final content of 50 or 70% (v/v) and samples were vortexed. Finally, a centrifugation at 4500 rpm at 4 °C during 30 min was carried out and the supernatants were collected. Before SPE, as the samples already contained 700 µL of CH_3CN, a dilution with water to achieve a final content of 50% of CH_3CN in the sample was implemented. After conditioning the SPE cartridge, 400 µL of the diluted supernatant were percolated. A washing step with 100 µL of H_2O:CH_3CN (1:1, v/v) was done and the cartridge was dried. Finally, the PAHs were eluted with 300 µL of THF and a partial evaporation with the addition of 40 µL of toluene and a recovered volume of 35 µL of CH_3CN was performed before injection in LC-DAD/FD system (5 µL). The measured responses were the PAH extraction recoveries. The data treatment was performed using JMP 10.0 (S.A.S Institute Inc, Cary, NC, USA) software.

2.6. *Extraction of PAHs from maternal and umbilical cord sera*

2.6.1. *Sample collection and storage*

Biological samples were obtained following informed written patient consent and approval from our local ethics committee (CPP 2015-Mai-13909). Umbilical cord and maternal blood were collected with harmonized procedures from patients delivered in Obstetric Units of Paris' Hospitals. Sera were obtained after blood centrifugation at 3000 rpm during 15 min and stored at −20 °C in Protein Lobind tubes.

2.6.2. *Sera pretreatment procedure*

100 µL of maternal or umbilical cord serum were spiked at 10 µg/L with each PAH except at 20 $\mu g \cdot L^{-1}$ for CPcdP and IcdP. A solution containing 10% of SDS was next added to achieve a final concentration of 0.2% (w/v). Sample was vortexed and 225 µL of CH_3CN were added. A centrifugation at 4500 rpm during 30 min at 4 °C was carried out. 300 µL of supernatant were then collected and 120 µL of water were added to obtain a final content of 50% of CH_3CN (v/v). 400 µL of this sample were percolated on SPE cartridge. A washing step with 100 µL of CH_3CN:H_2O (1:1, v/v), a drying and an elution with 300 µL of THF were implemented. 40 µL of toluene were added to the elution fraction that was next vortexed and evaporated. The final extract was suspended in 100 µL of CH_3CN:H_2O (1:1, v/v) before injection in LC-DAD/FD system (10 µL).

3. Results and discussions

3.1. *Limits of quantitation of the LC-DAD/FD analysis*

The analysis of the 24 PAHs by LC-DAD/FD was carried out with an Agilent Pursuit PAH (100 × 2.1 mm,

3 μm) column containing a polymeric C18-bonded silica stationary phase, chosen for its shape selectivity towards PAHs [33]. Considering the wide polarity range of the 24 targeted PAHs with log P values from 3.3 up to 7.7 (see Figure S1) [9–12], different temperatures (30 and 35 °C), mobile phases (CH_3CN and water, CH_3OH and water, CH_3OH plus CH_3CN and water), and gradients were tested to find optimal conditions implementing a ternary gradient with water, CH_3CN, and CH_3OH (see Figure S2).

The FD detection schedule was optimized by studying the excitation and emission fluorescence spectra of each PAH. Nevertheless, some compromises were necessary as it is only possible to change the wavelengths when the time gap between two peaks is sufficient. Table 1 presents the LOQ values (defined as the concentration level that gives a signal to noise ratio of 10) determined with the optimized fluorescence schedule. They ranged from 0.1 to 1.5 μg/L for an injection volume of 10 μL. It is worthwhile to notice that no values are given for four PAHs (ACY, CPcdP, BjF, and IcdP) in FD. Indeed, ACY and CPcdP do not fluoresce while BjF have a poor fluorescence. Concerning IcdP, its quantification in UV was preferred because the resolution was insufficient to change the excitation and emission wavelengths in order to better detect it in FD. The LOQs were also determined in UV, at the maximal absorption wavelength of each PAH (see Table 1), and are comprised between 0.7 and 15.9 μg/L. As expected, except for ACY, CPcdP, BjF, IcdP and ANT, these LOQ values are significantly better in FD than in UV, by factors of 1.8 to 63. This is why FD was used for quantitation of all these PAHs. For ANT, LOQs in LC-UV and -FD are very close and FD was chosen in order to exploit its specificity for the analysis of real samples. It can also be noticed that the obtained LOQs for these standard solutions are close to the expected concentrations in sera already determined in literature thus indicating that the sample pretreatment method does not necessitate to provide a high enrichment factor. This should favor the possibility of using reduced sample volumes, which is often required by cohort leader.

3.2. *Development of the SPE procedure*

In order to determine PAHs at trace level in sera that are complex biological samples, a purification and extraction by SPE on C18-bonded silica-based sorbent was optimized in order to remove as much as possible matrix components.

3.2.1. *Choice of the percolation solvent*

The solubility of some PAHs is very low in aqueous solutions, particularly for the high molecular weight PAHs. This can induce their adsorption on the vial or cartridge walls and consequently their loss and then the underestimation of their concentration in samples. The strategy to avoid their adsorption consists in adding some organic solvent in the sample. Moreover, the treatment of serum samples as envisaged in this study, generally required a first precipitation step usually carried out in organic solvent that will also prevent the risk of loss of PAHs by adsorption to proteins. Therefore, the critical parameters are the solvent nature and its proportion to add in the sample without reducing too much the breakthrough volume of the lowest molecular weight PAHs. Preliminary experiments were performed by percolating water containing 30% of CH_3OH, CH_3CN or isopropanol and spiked with CHR, BaP, and DaiP, i.e. three PAHs selected to be representative of some of the most hydrophobic targeted ones. For the washing step, an CH_3CN:H_2O (1:1, v/v) mixture was chosen to remove some potential interferents that could be present latter in real samples since it has a slightly higher eluent strength than the percolation media. A volume of 100 μL of this solution was introduced to limit the risk of reaching the breakthrough volume of the most polar PAHs. For the elution step, one has to select a solvent able to disrupt the interactions between the analytes and the sorbent with a volume as low as possible to either lead to some enrichment or to limit the time of the potential subsequent evaporation step. In literature, THF [34] or mixtures of hexane:CH_2Cl_2 (1/1) [28,29] and CH_3CN:butyl chloride (55/45) [31] or ethyl acetate [30] were used. THF was selected, with an elution volume of 300 μL. Figure 1 shows the resulting average extraction recoveries obtained with this SPE protocol, percolating 100 μL of hydro-organic mixtures (7:3, v/v) spiked at 5 μg/L with the three PAHs on 25 mg of a C18-bonded silica (Hypersep). It appears that the DaiP concentration in the elution fraction was below the LOQ whereas it was not the case with CH_3CN and isopropanol. CH_3OH appears as too polar to ensure the solubilization of this highly hydrophobic

PAH (log P(DaiP) = 7.3), leading to its adsorption on the vial or cartridge walls. Therefore, CH_3OH was removed for the end of the study.

An ANOVA test (α = 5%) demonstrated that the recoveries of the three PAHs obtained after percolating them in 30% of CH_3CN or isopropanol were not significantly different. Nevertheless, CH_3CN led to lower standard deviation (SD) values than isopropanol and was thus preferred. Its proportion in the sample was next increased up to 50% to favor the PAH solubility, especially for the most hydrophobic ones. It appears in Figure 1 that the obtained extraction recoveries did not significantly change for CHR and BaP (ANOVA test, α = 5%), but was increased for DaiP. Therefore, for the rest of the development of the SPE step, a content of 50% of CH_3CN was added in the percolation media.

3.2.2. *Choice of the eluting solvent*

Another solvent with a higher elution strength (ε_0), CH_3CN, was evaluated for the desorption of the retained PAHs on the cartridge. The experiments were performed with a spiked CH_3CN:H_2O (1:1, v/v) mixture solution and the same washing conditions described in Section 3.2.1 (n = 3). It was observed that CH_3CN did not allow the elution of DaiP, and led to not significantly different extraction recoveries for CHR, and lower ones (47%) for BaP (ANOVA test, α = 5%) compared to THF (68%). Therefore, THF was the best choice as eluting solvent and the results were in good agreements with the ε_0 values of CH_3CN (ε_0 = 3.1) and THF (ε_0 = 3.7), which give a measure of their elution strength on a C18-based sorbent [35].

3.2.3. *Comparison of three different SPE sorbents*

In order to select a C18-based sorbent favoring the PAH extraction and leading to the best recoveries, three SPE cartridges containing 25 or 30 mg of C18-bonded silica from different suppliers that mainly differ by their carbon content were evaluated (see Section 2.3) by applying the optimized conditions. For these experiments, nine PAHs among the 24 were selected in order to cover the whole range of hydrophobicity, except the less hydrophobic compounds, NAPH and ACY, because of their higher LOQ (see Table 1). After conditioning the SPE sorbents, 200 µL of H_2O:CH_3CN (1:1, v/v) spiked with the nine PAHs were percolated. After washing and drying, PAHs were eluted with 300 µL of THF. Results are reported in Figure 2. High extraction recoveries between 65% and 98% were obtained. An ANOVA test (α = 5%) demonstrated that the recoveries obtained on the three sorbents for each PAH were not significantly different. The single exception was for 5MCHR, which has a significantly higher extraction recovery with the Hypersep cartridge. Therefore, the Hypersep cartridge was preferred for the end of the study.

3.2.4. *Study of the evaporation step*

At this stage of the study, the SPE elution fraction had never been evaporated before its LC analysis. The introduction of an evaporation step was next evaluated to improve the enrichment factor and the method sensitivity, but this step can also induce some loss of the most volatile PAHs. To evaluate this risk, 200 µL of THF was spiked with 20 PAHs and was evaporated to dryness and further reconstituted in 50 µL of CH_3CN before analysis. Results are reported in Figure 3. This evaporation step led to the partial loss of the five most volatile PAHs (NAPH, ACE, FLO, PHE, and ANT). Their recoveries ranged from 15% (NAPH) to 54% (ANT) with SD values up to 20%. For the other PAHs, the losses were lower and the recoveries were higher than 70%. To improve the recoveries of the most volatile PAHs, a small volume of an aromatic solvent having a low volatility and able to develop π–π interactions with PAHs was added in the extract before starting the evaporation and the evaporation was stopped before a complete dryness in order to trap all PAHs in this small residual volume of the aromatic solvent, this volume being controlled thanks to the shape of the used vials. For these experiments, three aromatic solvents were selected: toluene (boiling point (BP): 110.6 °C, vapor pressure (VP): 0.29 kPa), xylene (BP: 144.4 °C, VP: 0.8 kPa), and trimethylbenzene (BP: 175 °C, VP: 0.18 kPa). First, 10 µL of each aromatic solvent was added in 200 µL of THF spiked at 5 µg/L with each PAH. The evaporation was stopped before dryness (last drop) and the extract was diluted with 50 µL of CH_3CN before analysis. Figure 3 presents the obtained results.

With xylene, the quantitation of NAPH, BcF, and BaA was not possible because of the presence of co-eluting peaks in the chromatogram due to xylene and its impurities. There was a similar problem with trimethylbenzene, which prevents from the quantitation of ACE and FLO. Therefore, toluene was selected.

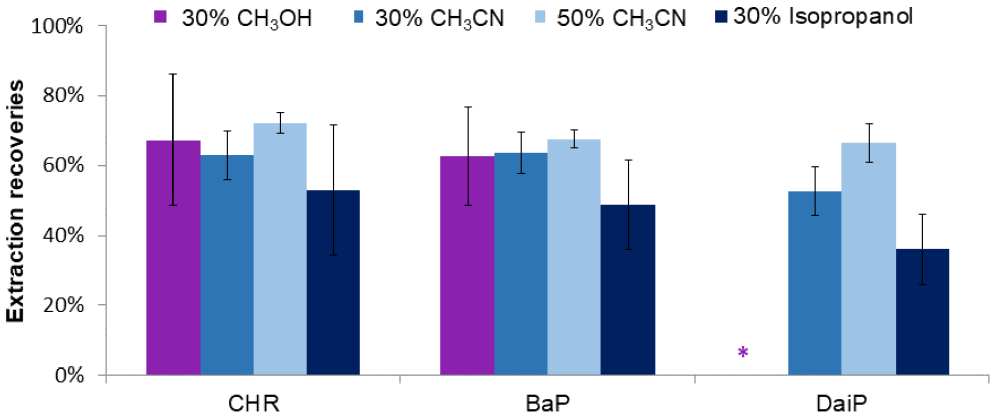

Figure 1. Effect of the nature and the volume of organic solvent (30% or 50%) introduced in spiked water on the extraction recoveries. SPE procedure (Hypersep cartridge): percolation of 100 µL of water containing 30 or 50% of the organic studied solvent and spiked with 5 µg/L of each PAH, washing with 100 µL of CH_3CN:H_2O (1:1, v/v), and elution with 300 µL of THF, dilution of the THF extract with water (THF:H_2O, v:v, 1/1) ($n = 3$). * not quantifiable PAH.

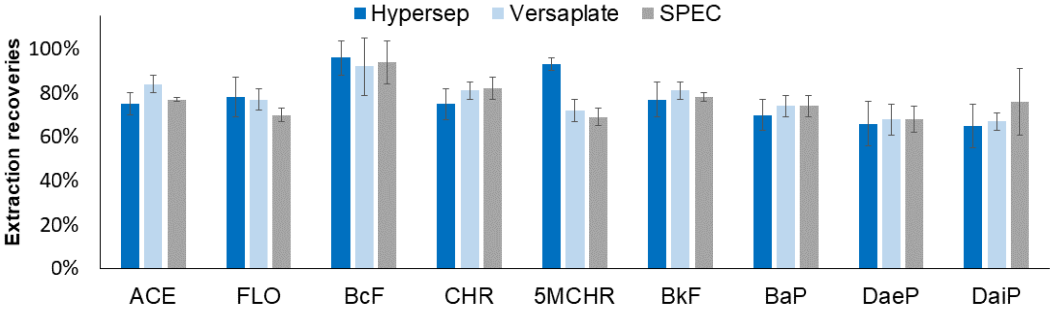

Figure 2. Comparison of the extraction recoveries obtained using three different SPE sorbents. SPE procedure: percolation of 100 µL of CH_3CN:H_2O sample (1:1, v/v) spiked with 5 µg/L of each PAH, washing with 100 µL of CH_3CN:H_2O (1:1, v/v) and elution with 300 µL of THF ($n = 3$).

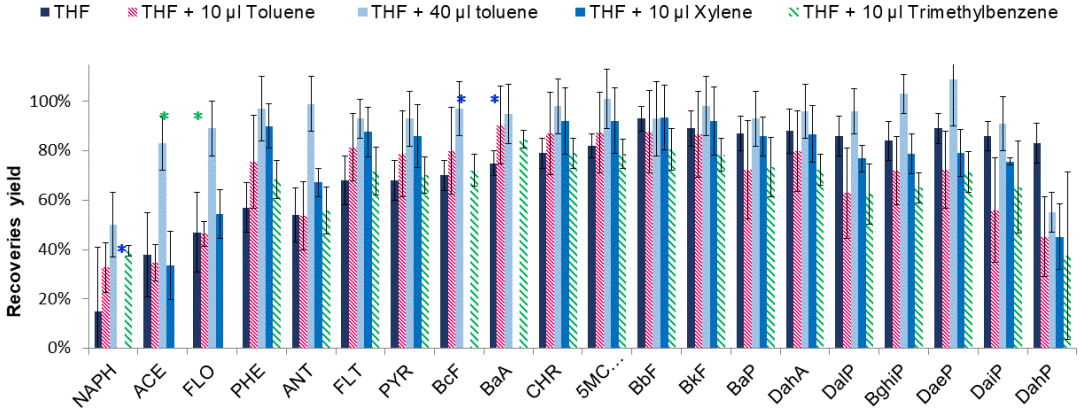

Figure 3. Effect of the nature and the volume of the aromatic solvent added in 200 µl of THF and spiked with 5 µg/L of each PAH on extraction recoveries. The extract was recovered in 50 µL of CH_3CN before analysis ($n = 3$). * not quantifiable PAHs.

Nevertheless, 10 μL of toluene were not sufficient to ensure high recoveries for NAPH, ACE, FLO, and ANT. Then, the effect of the addition of 40 μL of toluene was evaluated. In that case, the recoveries for the five most volatile PAHs were improved: about 50% for NAPH, 60% for DahP, and above 80% for all the other PAHs. Only DahP has a lower recovery than without the addition of an aromatic solvent. The addition of 40 μL of toluene in the SPE extract before its evaporation was then selected to limit the loss of most of the PAHs.

Then, different volumes of CH_3CN (50, 100, and 150 μL) were tested for the dilution of the extracts after evaporation and before injection in LC. According to the ANOVA test ($\alpha = 5\%$), the extraction yields were similar for all the tested volumes except for DahP (data not shown) for which a volume of 150 μL of CH_3CN gave higher extraction recoveries (87%). Therefore, 150 μL of CH_3CN was selected for the optimization of the next step.

3.2.5. *Optimization of the elution volume*

As described previously, two elution solvents were tested, CH_3CN and THF, and THF was preferred. At this stage, 300 μL of THF were used for the elution but it is important to ensure that this volume is sufficient to elute the most hydrophobic PAHs from the SPE cartridge. This is why an increase in the elution volume was studied. Three volumes of THF were tested: 300, 400 and 500 μL and Figure 4 presents the obtained recoveries. An ANOVA test ($\alpha = 5\%$) demonstrated that they are not significantly different except for NAPH and IcdP. NAPH is the most polar and the most volatile PAH and its recovery decreases when the elution volume increases. This cannot be due to a problem of desorption from the SPE cartridge but rather to the subsequent evaporation step that takes a longer time, leading to an increasing lost of this volatile compound. For IcdP, there is a decrease in the recovery with the increase in the elution volume. This unexpected result for this highly hydrophobic compound may be also due to the evaporation step. Indeed, with a higher elution volume to evaporate, the compound may adsorb on the entire walls of the vials and may become more difficult to recover within a resuspension volume of 150 μL of CH_3CN even after vortexing. This is why a volume of 300 μL of THF was finally selected.

3.2.6. *Improvement of the enrichment factor*

At this stage of the study, almost all the parameters of the pretreatment steps were optimized except the sample volume and the final volume of solvent to recover compounds after the evaporation just before analysis. Both are key parameters for the recoveries and enrichment factors of the SPE procedure, that have to be as high as possible to detect the PAHs present at trace levels in real samples. The loading volume was first increased from 200 to 400 μL. The obtained extraction recoveries are presented in Figure 5. For the first four less hydrophobic PAHs, a dramatic decrease was observed. Indeed, a loading volume of 400 μL followed by a washing volume of 100 μL may exceed their breakthrough volumes. For the other PAHs, the obtained extraction recoveries were quite similar and SD values were between 2 and 17% for both conditions. As the aim of this study was to quantify the 24 listed PAHs at trace levels, a compromise had to be made and a loading volume of 400 μL was chosen to favor the enrichment factor.

The volume needed for recovering all the PAHs after the evaporation and before analysis was finally studied. For this, three volumes of CH_3CN were tested: 35, 100, and 150 μl. According to the results presented in Figure 6 and the ANOVA test ($\alpha = 5\%$), the extraction recoveries were not significantly different. To improve LOQs, the injection volume of 5 μL used for all the injection achieved for the development of the SPE procedure was increased to 10 μL, which prevents from the use of 35 μL as volume use to dilute the final extract after the evaporation step. Therefore, a volume of 100 μL was selected. However, an injection volume of 10 μL of PAHs in CH_3CN induced a peak deformation for the first eluted PAHs. Therefore, the 100 μL of CH_3CN was replaced by the addition of 50 μL of CH_3CN for resuspension followed by 50 μL of H_2O. Finally, the optimized SPE protocol with spiked pure media, at this stage, was: percolation of 400 μL of H_2O:CH_3CN (1:1, v/v), washing with 100 μL of H_2O:CH_3CN (1:1, v/v), drying, elution with 300 μL of THF, addition of 40 μL of toluene in the elution fraction, partial evaporation (last drop), and dilution of the extract with 100 μL of H_2O:CH_3CN (1:1, v/v) before analysis.

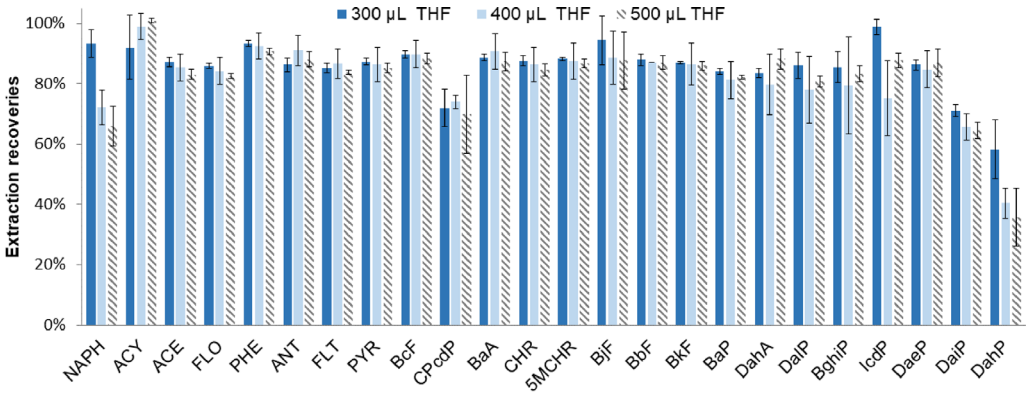

Figure 4. Optimization of the SPE elution volume. SPE procedure (Hypersep cartridge): percolation of 200 µL of CH_3CN:H_2O (1:1, v/v) spiked with 5 µg/L of each PAH except ACY, CPcdP, BjF, and IcdP at 50 µg/L, washing with 100 µL of CH_3CN:H_2O (1:1, v/v), elution with THF, and partial evaporation (addition of 40 µL of toluene in the elution fraction). The extract was recovered with 150 µL of CH_3CN before analysis ($n = 3$).

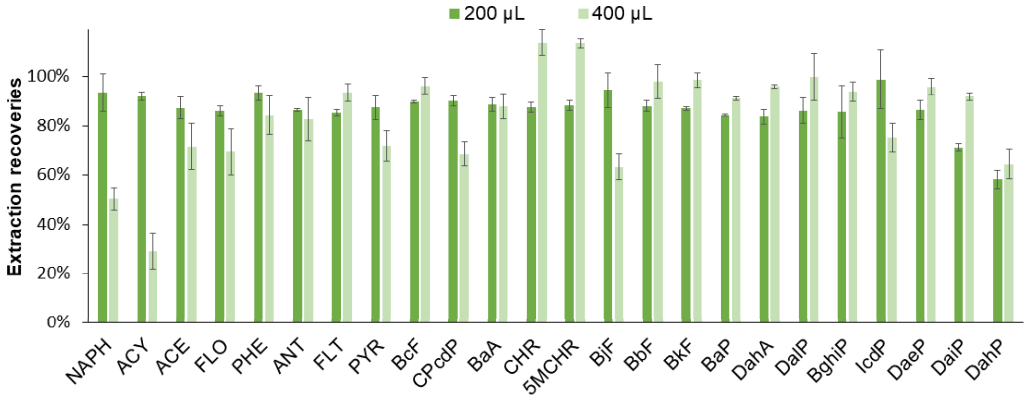

Figure 5. Optimization of the SPE percolation volume. SPE procedure (Hypersep cartridge): percolation of 200 µL or 400 µL of CH_3CN:H_2O sample (1:1, v/v) spiked with 5 µg/L of each PAH except for ACY, CPcdP, BjF, and IcdP at 50 µg/L, washing with 100 µL of CH_3CN:H_2O (1:1, v/v), elution with 300 µL of THF and partial evaporation (addition of 40 µL of toluene in the elution fraction). The extract was recovered with 150 µL of CH_3CN before analysis ($n = 3$).

3.3. *Optimization of the protein precipitation procedure by a DOE*

Previous results were obtained for spiked pure media. Nevertheless, the analysis of real sera is targeted. Therefore, it is necessary to proceed first to the precipitation of the proteins contained in the sera minimizing PAHs losses that may occur due to their potential interactions with the serum proteins. The traditional approach involves the addition of an organic solvent, but also of a surfactant, such as SDS [36–39]. The CH_3CN percentage, SDS concentration, and temperature may affect these interactions. A DOE-based approach was selected to study the potential effects and interactions of these three factors and determine the optimum precipitation conditions.

According to literature and the conventional protocols used for protein precipitation, the low and high levels for the CH_3CN content was fixed at 50

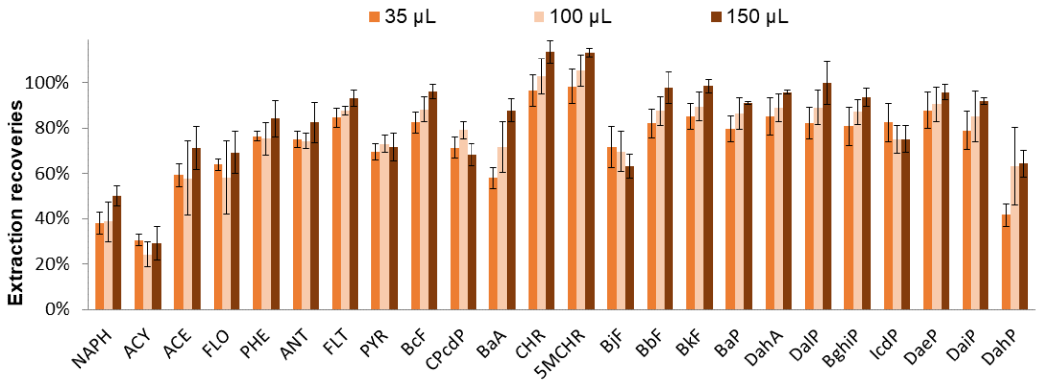

Figure 6. Optimization of the resuspension volume after evaporation before LC analysis. SPE procedure (Hypersep cartridge): percolation of 400 µL of CH_3CN:H_2O sample (1:1, v/v) spiked with 5 µg/L of each PAH except for ACY, CPcdP, BjF, and IcdP at 50 µg/L, washing with 100 µL of CH_3CN:H_2O (1:1, v/v), elution with 300 µL of THF, and partial evaporation (addition of 40 µL of toluene in the elution fraction). The extract was recovered with 35, 100 or 150 µL of CH_3CN ($n = 3$).

and 70% (v/v), respectively [36,37], the three levels of SDS were fixed at 0, 0.1, and 0.2% (v/w) [38], and the precipitation was carried out at 25 °C (rt) for 2 min or at 60 °C during 25 min [39]. Table 2 presents the coded and non-coded values for each factor. The experiments were next carried out with 16 PAHs representative of the log P range of the 24 targeted ones (except for NAPH and ACY, the less hydrophobic compounds because of their higher LOQs) and, it is worthwhile to notice it, with a synthetic serum (Earle's balanced salt solution containing albumin at 25 g/L). Indeed, to carry out this DOE with sera, 4.5 mL (300 µL × 15 experiments) would have been necessary whereas sera are highly precious samples.

The considered responses were the recoveries of the 16 PAHs and these data are reported in Table S1. A polynomial model was used to identify the factors impacting the PAH recoveries during the protein precipitation step. Using a classical least-squares multiple linear regression, the model coefficients were estimated to evaluate factor effects. Coefficient significance was evaluated using a t-test comparing the coefficient estimate to its standard-deviation obtained from the repeated experiments and the results are presented Figure S3. A factor or an interaction was considered as significant with a 5% risk of the first kind if the value of $P > t$ was lower than 0.05. First, the change from 50 to 70% of CH_3CN had no significant effect for all the studied PAHs except for FLO. It seems then that 50% of CH_3CN are sufficient to disrupt the PAH–protein interactions. Similarly, the SDS content had no significant effect on the PAH recoveries. Considering temperature, a negative effect on PAH recoveries was observed for all the PAHs except DahP. Moreover, the interaction between SDS content and temperature had also a significant negative effect for 11 of the 16 studied PAHs. Finally, the interaction between the SDS content and CH_3CN percentage had a negative significant effect for seven PAHs.

The Derringer's desirability function was next used to determine the precipitation conditions giving rise to the highest PAH recoveries. Each response was transformed on a scale between 0 (corresponding to the most undesirable value) and 1 (representing the value that most fulfilled the requirements). The value of each transformed response was called "desirability value". The global desirability was calculated by multiplying all the individual desirability values. Finally, this global desirability was maximized to determine the predicted optimum (see Figure S4): the coded values of the predicted optimum were (1, −1, 3), which correspond to 70% of CH_3CN (v/v), 0.2% of SDS (w/v), and precipitation done at rt for 2 min.

This optimum corresponded to one of the experimental points tested during the DOE, for which it appeared that the obtained PAH recoveries are very close to the ones obtained with another experimen-

Table 2. 2 × 2 × 3 factorial design with the different factors studied for their potential impact on the PAH recoveries during the protein precipitation (test with a synthetic serum: Earle's balanced salt solution containing albumin at 25 g/L spiked with 16 PAHs at 4 μg/L each)

Order	Coded values			Experimental values		
	[CH_3CN]	Precipitation conditions	[SDS]	[CH_3CN] (%, v/v)	Precipitation conditions	[SDS] (%, w/v)
1	+1	+1	3	70	25 min at 60 °C	0.2
2	+1	+1	1	70	25 min at 60 °C	0
3	+1	+1	1	70	25 min at 60 °C	0
4	−1	−1	2	50	2 min at 25 °C	0.1
5	+1	−1	2	70	2 min at 25 °C	0.1
6	+1	−1	3	70	2 min at 25 °C	0.2
7	+1	−1	3	70	2 min at 25 °C	0.2
8	−1	−1	3	50	2 min at 25 °C	0.2
9	−1	+1	1	50	25 min at 60 °C	0
10	−1	+1	1	50	25 min at 60 °C	0
11	+1	−1	1	70	2 min at 25 °C	0
12	+1	+1	2	70	25 min at 60 °C	0.1
13	−1	+1	2	50	25 min at 60 °C	0.1
14	−1	+1	3	50	25 min at 60 °C	0.2
15	−1	−1	1	50	2 min at 25 °C	0

tal condition using the same content of CH_3CN (70%) and no heating, but with only 0.1% of SDS. Therefore, both experimental conditions were tested again, but with the 24 PAHs at a spiking level of 10 μg/L. For the predicted optimum, extraction recoveries were between 28 and 82% with SD values lower than 16%, in agreement with the predicted recoveries, whereas for the other experimental condition, they were between 33% and 81% with SD values lower than 14%. An ANOVA test (α = 5%) demonstrated that the extraction recoveries were not significantly different for both conditions (data not shown). Therefore, the predicted optimum by the DOE was preferred.

3.4. *Extraction of the PAHs from maternal and umbilical cord sera*

After the optimization of the different steps of the sample handling with spiked pure media and a synthetic serum, the extraction efficiency of this procedure was evaluated in real biological fluids for the 24 PAHs by spiking pooled maternal and umbilical cord sera at 10 μg/L for each PAH except for CPcdP and IcdP at 20 μg/L. 100 μL of pooled maternal and umbilical cord sera were used for each experiment carried out in triplicate. The protein precipitation was made by adding 233 μL of CH_3CN plus 0.2% SDS. 300 μL of the supernatant were taken and water was added to decrease the CH_3CN proportion from 70 to 50%. 400 μL of this mixture were percolated through the SPE cartridge and were recovered after elution and evaporation in 100 μL of H_2O:CH_3CN (1:1, v/v) before analysis. Figure 7 shows the resulting chromatograms and Table 3 the calculated extraction recoveries. It is worthwhile to notice that the pooled sera were also analyzed without spiking to evaluate the potential presence of endogenous PAHs and correct the resulting extraction recoveries, but no PAHs were detected in this pooled sample.

Extraction recoveries were between 27 and 57% for maternal sera and between 34 and 69% for umbilical cord sera, with SD values lower than 11% thus highlighting the reliability of the developed method applied to complex samples. These recoveries are quite inferior to the ones obtained with spiked pure media (between 24 and 82%) (Table 3), but for which

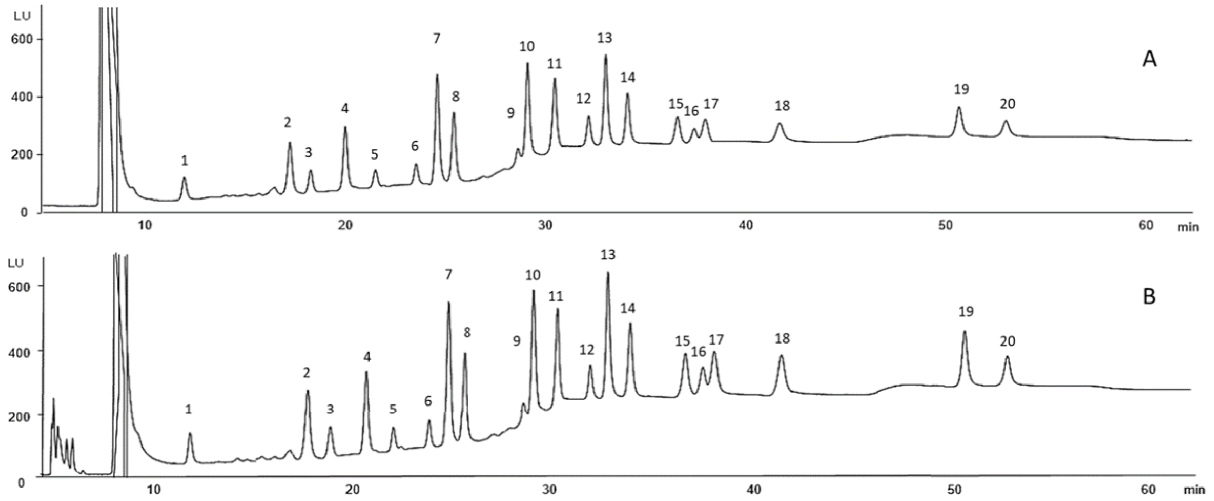

Figure 7. LC/UV/FD chromatograms of the extracted pooled maternal (A) and umbilical cord (B) sera spiked with 24 PAHs at 10 μg/L except CPcdP and IcdP at 20 μg/L. Other conditions: see Section 2.2. 1, NAPH; 2, ACE; 3, FLO; 4, PHE; 5, ANT; 6, FLT; 7, PYR; 8, BcF; 9, BaA; 10, CHR; 11, 5MCHR; 12, BbF; 13, BkF; 14, BaP; 15, DahA; 16, DalP; 17, BghiP; 18, DaeP; 19, DaiP; 20, DahP.

no precipitation was involved. This may also result from a matrix effect. Moreover, the extraction recoveries for maternal sera are lower than those obtained with umbilical cord sera, especially for BaA to DahP. Therefore, the matrix effect seems to be different for both kinds of sera. Unfortunately, it was not possible to quantitate CPcdP and IcdP, because some impurities co-eluted with them. This is why it is possible to conclude that the developed whole sample pretreatment led to good extraction recoveries for 22 of the 24 listed PAHs. These extraction recoveries are inferior to the values given in literature [6,19,20,24], ranging from 77 to 122%, but it is worthwhile to notice that here 22 compounds with a wide range of log P were targeted against only between five and 16 US-EPA PAHs in literature.

The whole sample pretreatment led to ratio between the sample volume and the final extract volume of 0.95. Considering the extraction recoveries, enrichment factors ranged from 0.3 to 0.5 and from 0.3 to 0.7 for maternal and umbilical cord sera, respectively. This led to LOQs in sera between 0.2 and 3.1 μg/L for the 20 fluorescent PAHs and between 7.0 and 14.5 μg/L for the two others PAHs (calculation for a signal to noise ratio equal to 10), which are close to the expected concentrations in real samples [6,14,21,27–31]. In literature, LOQ values between 0.01 and 2.5 μg/L were reached, but requiring a serum volume at least 10 times larger, i.e. 1 or 2 mL of serum [6,20,21,24].

The optimized sample handling, separation, and detection steps require a total analysis time of 1 h 40 and the SPE and analytical steps can be automated. This constitutes also a significant improvement over the literature where serum sample handling always required at least three LLE steps followed most often by an additional SPE step [6,19–21,24,25]. After validation, it should allow the analysis of a large number of real samples.

4. Conclusions

The analysis of the 24 listed PAHs by LC-DAD/FD was developed. Then, different parameters governing the SPE procedure were studied to optimize the extraction recoveries on C18 silica of the 24 PAHs belonging to a large range polarity (lop P values between 3.3 and 7.7). The use of an aromatic solvent was proposed to minimize the loss of the most volatile PAHs during the evaporation step. A DOE was used to optimize the protein precipitation conditions. The performances of the whole sample pretreatment were determined for 22 PAHs and for

Table 3. Extraction recoveries (*R*%) and SD (n = 3) of 24 PAHs in spiked CH_3CN:H_2O mixture, pooled maternal and umbilical cord sera

PAHs	Spiked CH_3CN:H_2O (1:1, v/v)		Spiked maternal serum		Spiked umbilical cord serum	
	R (%)	SD (%)	*R* (%)	SD (%)	*R* (%)	SD (%)
NAPH	27	13	46	11	47	11
ACY	24	5	31	2	34	2
ACE	35	10	40	7	48	4
FLO	38	7	40	5	48	4
PHE	47	5	45	10	51	2
ANT	51	4	39	5	53	2
FLT	64	5	52	8	62	5
PYR	66	9	57	6	68	9
BcF	62	7	53	5	64	4
CPcdP	64	6	NQ	-	NQ	-
BaA	55	5	51	4	68	2
CHR	67	7	55	3	69	3
5MCHR	71	8	51	6	64	4
BjF	71	2	41	6	60	2
BbF	68	7	51	3	69	5
BkF	69	8	51	4	67	4
BaP	68	8	48	3	65	4
DahA	74	9	46	2	68	7
DalP	70	6	33	1	66	10
BghiP	82	8	40	1	59	3
IcdP	75	6	NQ	-	NQ	-
DaeP	77	9	37	2	61	4
DaiP	72	8	28	1	54	5
DahP	67	8	27	2	47	3

Precipitation step: 0.2% of SDS and 70% of CH_3CN. SPE *(Hypersep cartridge)*: percolation of 400 μL of spiked sample with 10 μg/L of each PAH except for CPcdP, BjF and IcdP at 20 μg/L, washing with 100 μL of CH_3CN:H_2O (1:1, v/v), elution with 300 μL of THF and partial evaporation (addition of 40 μL of toluene in the elution fraction). The extract was further recovered with 100 μL of CH_3CN:H_2O (1:1, v/v). NQ: Non-quantifiable.

a reduced volume of 100 μL of maternal and umbilical cord sera. The LOQs obtained for both matrices were between 0.2 and 3.1 μg/L for the fluorescent PAHs and between 7.0 and 14.5 μg/L for ACY and BjF (UV detection). The optimized sample handling, separation, and detection steps require a total analysis time of only 1 h 40 and the SPE and analytical steps can be automated. The next step will consist in validating this method, which will allow its use for the analysis of numerous real samples. The consistency of the resulting data will enable to carry out epidemiologic studies.

Abbreviations

ACE, acenaphthene; ACY, acenaphthylene; ANT, anthracene; BaA, benzo[a]anthracene; BaP, benzo[a]pyrene; BbF, benzo[b]fluoranthene; BcF, benzo[c]fluorene; BghiP, benzo[g,h,i]pyrene; BjF, benzo[j]fluorene; BkF, benzo[k]fluoranthene; CHR,

chrysene; CPcdP, cyclopenta[cd]pyrene; DaeP, dibenzo[a,e]pyrene; DahA, dibenzo[a,h]anthracene; DahP, dibenzo[a,h]pyrene; DaiP, dibenzo[a,i]pyrene; DalP, dibenzo[a,l]pyrene; FLO, fluorene; FLT, fluoranthene; IcdP, indeno[1,2,3-cd]pyrene; 5MCHR, 5-methylchrysene; NAPH, naphthalene; PHE, phenanthrene; PYR, pyrene; SDS, sodium dodecyl sulfate.

Declaration of interests

The authors do not work for advise, own shares in, or receive funds from any organization that could benefit from this article, and have declared no affiliations other than their research organizations.

Ethical approval

All procedures performed in studies involving human participants were in accordance with the ethical standards of the institutional and/or national research committee and with the 1964 Helsinki declaration and its later amendments or comparable ethical standards. This article does not contain any studies with animals performed by any of the authors.

Informed consent

Informed consent was obtained from all individual participants included in the study.

Supplementary data

Supporting information for this article is available on the journal's website under https://doi.org/10.5802/crchim.286 or from the author.

References

[1] N.-D. Dat, M. B. Chang, *Sci. Total Environ.*, 2017, **609**, 682-693.

[2] P. Zhang, Y. Chen, *Sci. Total Environ.*, 2017, **605-606**, 1011-1020.

[3] M. A. Mallah, L. Changxing, M. A. Mallah, S. Noreen, Y. Liu, M. Saeed, H. Xi, B. Ahmed, F. Feng, A. A. Mirjat, W. Wang, A. Jabar, M. Naveed, J.-H. Li, Q. Zhang, *Chemosphere*, 2022, **296**, article no. 133948.

[4] L. Wright, L. Zhang, I. Cheng, J. Aherne, G. R. Wentworth, *Aerosol Air Qual. Res.*, 2018, **18**, 1953-1992.

[5] E. Błaszczyk, D. Mielżyńska-Švach, *J. Appl. Genet.*, 2017, **58**, 321-330.

[6] Y. Guo, X. Huo, K. Wu, J. Liu, Y. Zhang, X. Xu, *Sci. Total Environ.*, 2012, **427**, 35-40.

[7] J. Wu, H. Hou, B. Ritz, Y. Chen, *Sci. Total Environ.*, 2010, **408**, 2312-2318.

[8] D. Yi, Y. Yuan, L. Jin, G. Zhou, H. Zhu, R. H. Finnell, A. Ren, *NeuroToxicology*, 2015, **46**, 73-78.

[9] Y. Wang, X. Wang, F. Lee, *Se Pu*, 1999, **17**, 424-426, http://europepmc.org/abstract/MED/12552873.

[10] F. Alves de Lima Ribeiro, M. M. C. Ferreira, *J. Mol. Struct. THEOCHEM*, 2003, **663**, 109-126.

[11] S. K. Sahu, G. G. Pandit, *J. Liq. Chromatogr. Relat. Technol.*, 2003, **26**, 135-146.

[12] M. T. O. Jonker, *Environ. Toxicol. Chem.*, 2016, **35**, 1371-1377.

[13] P. M. Santos, M. del Nogal Sánchez, J. L. P. Pavón, B. M. Cordero, *TrAC Trends Anal. Chem.*, 2019, **113**, 194-209.

[14] J. D. Pleil, M. A. Stiegel, J. R. Sobus, S. Tabucchi, A. J. Ghio, M. C. Madden, *J. Chromatogr. B*, 2010, **878**, 1753-1760.

[15] Y. Zhang, Y.-G. Zhao, W.-S. Chen, H.-L. Cheng, X.-Q. Zeng, Y. Zhu, *J. Chromatogr. A*, 2018, **1552**, 1-9.

[16] X. Xu, J. Liu, C. Huang, F. Lu, Y. M. Chiung, X. Huo, *Chemosphere*, 2015, **139**, 295-302.

[17] V. K. Singh, D. K. Patel, Jyoti, S. Ram, N. Mathur, M. K. J. Siddiqui, *Clin. Biochem.*, 2008, **41**, 152-161.

[18] N. Madhavan, K. Naidu, *Hum. Exp. Toxicol.*, 1995, **14**, 503-506.

[19] X. Zhang, X. Li, Y. Jing, X. Fang, X. Zhang, B. Lei, Y. Yu, *Environ. Pollut.*, 2017, **222**, 267-275.

[20] I. Al-Saleh, A. Alsabbahen, N. Shinwari, G. Billedo, A. Mashhour, Y. Al-Sarraj, G. E. D. Mohamed, A. Rabbah, *Sci. Total Environ.*, 2013, **444**, 565-578.

[21] K. Sexton, J. J. Salinas, T. J. McDonald, R. M. Z. Gowen, R. P. Miller, J. B. McCormick, S. P. Fisher-Hoch, *Int. J. Environ. Res. Public Health*, 2011, **8**, 3365-3379.

[22] N. M. Al-Daghri, *Int. J. Occup. Med. Environ. Health*, 2008, **21**, 211-217, https://api.semanticscholar.org/CorpusID:4539191.

[23] A. Kamal, M. Qayyum, I. U. Cheema, A. Rashid, *BMC Public Health*, 2011, **11**, article no. 467.

[24] S. Yin, M. Tang, F. Chen, T. Li, W. Liu, *Environ. Pollut.*, 2017, **220**, 1429-1437.

[25] Y. Yu, X. Wang, B. Wang, S. Tao, W. Liu, X. Wang, J. Cao, B. Li, X. Lu, M. H. Wong, *Environ. Sci. Technol.*, 2011, **45**, 10235-10242.

[26] V. K. Singh, D. K. Patel, S. Ram, N. Mathur, M. K. J. Siddiqui, J. R. Behari, *Arch. Environ. Contam. Toxicol.*, 2008, **54**, 348-354.

[27] X. F. Song, Z. Y. Chen, Z. J. Zang, Y. N. Zhang, F. Zeng, Y. P. Peng, C. Yang, *Environ. Int.*, 2013, **60**, 97-105.

[28] H. L. Tsang, S. Wu, C. K. M. Leung, S. Tao, M. H. Wong, *Environ. Int.*, 2011, **37**, 142-151.

[29] Y. Y. Qin, C. K. M. Leung, C. K. Lin, A. O. W. Leung, H. S. Wang, J. P. Giesy, M. H. Wong, *Environ. Sci. Technol.*, 2011, **45**, 1630-1637.

[30] Q. Chen, T. Zheng, B. A. Bassig, Y. Cheng, B. P. Leaderer, S. Lin, T. R. Holford, J. Qiu, Y. Zhang, K. Shi, Y. Zhu, J. Niu, Y. Li, H. Guo, X. Hu, Y. Jin, *Open J. Air Pollut.*, 2014, **3**, 100-110.

[31] A. Ramesh, A. Kumar, M. P. Aramandla, A. M. Nyanda, *Int. J. Environ. Res. Public Health*, 2015, **12**, 322-334.

[32] B. Wang, L. Jin, A. Ren, Y. Yuan, J. Liu, Z. Li, L. Zhang, D. Yi, L. Wang, Y. Zhang, X. Wang, S. Tao, R. H. Finnell, *Environ. Sci. Technol.*, 2015, **49**, 588-596.

[33] S. A. Wise, L. C. Sander, M. M. Schantz, *Polycycl. Aromat. Compd.*, 2015, **35**, 187-247.

[34] G. Kiss, Z. Varga-Puchony, J. Hlavay, *J. Chromatogr. A*, 1996, **725**, 261-272.
[35] V. J. Barwick, *TrAC Trends Anal. Chem.*, 1997, **16**, 293-309.
[36] S. Souverain, S. Rudaz, J.-L. Veuthey, *J. Pharm. Biomed. Anal.*, 2004, **35**, 913-920.
[37] C. Polson, P. Sarkar, B. Incledon, V. Raguvaran, R. Grant, *J. Chromatogr. B*, 2003, **785**, 263-275.
[38] K. L. Gudiksen, I. Gitlin, G. M. Whitesides, *Proc. Natl. Acad. Sci. USA*, 2006, **103**, 7968-7972.
[39] H. Y. Hernández-Unzón, M. L. Ortega-Delgado, *Plant Foods Hum. Nutr.*, 1988, **38**, 211-223.

Comptes Rendus

Chimie

Objet de la revue

Les *Comptes Rendus Chimie* sont une revue électronique évaluée par les pairs de niveau international, qui couvre l'ensemble des domaines de la discipline. Ils publient principalement des numéros spéciaux, mais également des articles originaux de recherche, des annonces préliminaires, des articles de revue, des mises en perspective historiques, des textes à visée pédagogique ou encore des actes de colloque, sans limite de longueur, en anglais ou en français. Les *Comptes Rendus Chimie* sont diffusés selon une politique vertueuse de libre accès diamant, gratuit pour les auteurs (pas de frais de publications) comme pour les lecteurs (libre accès immédiat et pérenne).

À propos de la revue

Toutes les informations concernant la revue, y compris le texte des articles publiés qui est en accès libre intégral, figurent sur le site https://comptes-rendus.academie-sciences.fr/chimie/.

Informations à l'attention des auteurs

Pour toute question relative à la soumission des articles, les auteurs peuvent consulter le site https://comptes-rendus.academie-sciences.fr/chimie/.

Contact

Académie des sciences
23, quai de Conti, 75006 Paris, France
CR-Chimie@academie-sciences.fr

Comptes Rendus
de l'Académie des sciences

Chimie

Volume 27, nº S2, 2024

Special issue / *Numéro spécial*
Women Chemists in France in 2024 / *Femmes chimistes en France en 2024*

Guest editor / *Rédactrice en chef invitée*
Janine Cossy (ESPCI Paris – PSL, CNRS, 75005 Paris, France)

Cover illustration / *Illustration de couverture*
Photo: Julien Desmarets.

Contents / *Sommaire*

Guest Editor 1-1

Janine Cossy
A Collection of Articles Highlighting Women Chemists in France in 2024 3-3

Odile Eisenstein
Nucleophilic addition to carbonyl groups from qualitative to quantitative computational studies. A historical perspective 5-19

Sabine Choppin, Joanna Wencel-Delord, Françoise Colobert
Control of atropoisomerism: an access to valuable compounds 21-32

Lucas Bacheley, Gérard Guillamot, Phannarath Phansavath, Virginie Ratovelomanana-Vidal
Direct ring fluorination of 3-substituted 5-(1,3-dioxane) acetal isoxazoles: application to the formal synthesis of a bioactive fluorinated isoxazole 33-38

Anne-Marie Caminade, Valérie Maraval
Selected properties of phosphorus dendrimers: green approaches to catalysis 39-55

Léa Ibos, Emmanuelle Schulz
Non-covalent interactions in supported asymmetric catalysis: a brief account 57-83

Arthur Lasbleiz, Franck Pelissier, Jean-Hugues Renault, Claire M. Grison, Yves-Marie Legrand, Claude Grison
A new generation of ecocatalysts®—from Invasive Alien Species to sustainable and biosourced glyceryl fatty esters 85-97

Juliette Martin
The need for Open Labs for fostering interdisciplinarities in Modern Chemistry. Biocatalysis: a necessary tool for synthetic chemists 99-115

Clotilde Policar, Nicolas Delsuc, Hélène Charlotte Bertrand
Metal complexes in cells: from design of catalytic antioxidants to imaging metal ions and designing metal-based probes in X-ray fluorescence and IR-imaging, a multidisciplinary collaborative journey in bioinorganic chemistry and inorganic chemical biology 117-141

Alexandra Fillion, Sophie Vichier-Guerre, Paola Barbara Arimondo
Adenine, a key player in biology and medicinal chemistry 143-160

Daouda Ndiaye, Éva Tóth
Stable and inert manganese complexes for magnetic resonance imaging 161-177

Jonathan Daniel, Ophélie Dal Pra, Eleonore Kurek, Chloé Grazon, Mireille Blanchard-Desce
Dye-based fluorescent organic nanoparticles made from polar and polarizable chromophores for bioimaging purposes: a bottom-up approach 179-195

Stéphanie Swiha, Valérie Pichon, Thierry Fournier, Sophie Gil, Nathalie Delaunay
Development of an analytical method for the simultaneous determination of 22 Polycyclic Aromatic Hydrocarbons (PAHs) in maternal and umbilical cord blood 197-212

1878-1543 (electronic)

Académie des sciences — Paris

COMPTES RENDUS
DE L'ACADÉMIE DES SCIENCES

Chimie

Volume 27, nº S2, 2024